ANL-NSE-1

Safety Analysis and Technical Basis for Establishing an Interim Bunup Limit for Mark-V and Mark-VA Fueled Subassemblies in EBR-II

Nuclear Science and Engineering Division

About Argonne National Laboratory
Argonne is a U.S. Department of Energy laboratory managed by UChicago Argonne, LLC under contract DE-AC02-06CH11357. The Laboratory's main facility is outside Chicago, at 9700 South Cass Avenue, Argonne, Illinois 60439. For information about Argonne and its pioneering science and technology programs, see www.anl.gov.

DOCUMENT AVAILABILITY

Online Access: U.S. Department of Energy (DOE) reports produced after 1991 and a growing number of pre-1991 documents are available free via DOE's SciTech Connect (http://www.osti.gov/scitech/)

Reports not in digital format may be purchased by the public from the National Technical Information Service (NTIS):
U.S. Department of Commerce
National Technical Information Service
5301 Shawnee Rd
Alexandria, VA 22312
www.ntis.gov
Phone: (800) 553-NTIS (6847) or (703) 605-6000
Fax: (703) 605-6900
Email: **orders@ntis.gov**

Reports not in digital format are available to DOE and DOE contractors from the Office of Scientific and Technical Information (OSTI):
U.S. Department of Energy
Office of Scientific and Technical Information
P.O. Box 62
Oak Ridge, TN 37831-0062
www.osti.gov
Phone: (865) 576-8401
Fax: (865) 576-5728
Email: **reports@osti.gov**

Disclaimer
This report was prepared as an account of work sponsored by CRADA No. 1201201. Neither the United States Government nor any agency thereof, nor UChicago Argonne, LLC, nor any of their employees or officers, makes any warranty, express or implied, or assumes any legal liability or responsibility for the accuracy, completeness, or usefulness of any information, apparatus, product, or process disclosed, or represents that its use would not infringe privately owned rights. Reference herein to any specific commercial product, process, or service by trade name, trademark, manufacturer, or otherwise, does not necessarily constitute or imply its endorsement, recommendation, or favoring by the United States Government or any agency thereof. The views and opinions of document authors expressed herein do not necessarily state or reflect those of the United States Government or any agency thereof, Argonne National Laboratory, or UChicago Argonne, LLC.

ANL-NSE-1

Safety Analysis and Technical Basis for Establishing an Interim Bunup Limit for Mark-V and Mark VA Fueled Subassemblies in EBR-II

Compiled by
L.L. Briggs, L. K. Chang, and D. J. Hill
Reactor Analysis Division, Argonne National Laboratory

Contributors:
J. Ahrens[1], M. Billone[3], D. C. Crawford[4] E. Filewicz[2] P. J. Finck[1] E. K. Fujita[1], K. Grimm[1], K. C. Gross[1], S. Kamal[2], J. Kramer[2], J. Ku[1], C. Lahm[4], M. Lee[4] Y. Liu[3], D. Meneghetti[1], R. Pahl[4], W. A. Ragland[1] R. W. Schaefer[5], D. L. Porter[4], H. C. Tsai[3], A. M. Yacout[1]
[1]Reactor Analysis Division, Argonne National Laboratory
[2]Reactor Engineering Division, Argonne National Laboratory
[3]Energy Technology Division, Argonne National Laboratory
[4]Fuesl and Engineering Division, Argonne National Laboratory
[5]IFR Operations Division, Argonne National Laboratory

March 9, 1995 (Compilation of Version 1.2)
May 23, 2018 (Publication)

Table of Contents

1 INTRODUCTION 1-1
1.1 Background 1-4
1.2 Safety Analysis 1-5
1.2.1 Strategy 1-6
2 DESIGN BASES 2-1
2.1 Fuel Design Bases 2-1
2.1.1 Functional Requirements 2-1
2.1.2 Operational Requirements 2-2
2.1.3 Key Physical Phenomena 2-3
2.1.4 Design Criteria 2-11
2.2 Structure Evaluation Criteria for the Fuel Subassembly 2-27
2.2.1 Allowable Stresses and Strains 2-28
2.2.2 Creep-Fatigue Damage 2-30
2.2.3 Deformation Limits for Functional Adequacy 2-30
2.2.4 Non-Ductile Failure Protection 2-31
2.2.5 Special Requirements for Weldments 2-32
2.3 Summary 2-33
3 DESIGN DESCRIPTION OF EBR-II DRIVER SUBASSEMBLIES WITH MARK-V AND MARK-VA FUEL PINS 3-1
3.1 Fuel Pins 3-1
3.2 316SS Driver Subassembly 3-2
3.2.1 Basic Design Features 3-2
3.2.2 Subassembly Hardware Description 3-4
3.2.2.1 Lower Preassembly 3-4
3.2.2.2 Upper Preassembly 3-5
3.2.2.3 Final Assembly 3-5
3.3 HT9 Driver Subassembly 3-6
3.3.1 Basic Design Features 3-6
3.3.2 Subassembly Hardware Description 3-6
3.3.2.1 Lower Preassembly 3-6
3.3.2.2 Upper Preassembly 3-10
3.3.2.3 Final Assembly 3-11
4 METHODS FOR DESIGN EVALUATION OF MARK-V AND MARK-VA FUEL SUBASSEMBLIES 4-1

4.1 Mark-V and Mark-VA Fuel Qualification 4-1
4.1.1 Irradiation Plan 4-2
4.1.2 Examination and Evaluation 4-3
4.1.3 Evaluation of Results 4-3
4.2 Fuel Pin Steady-State Performance 4-4
4.2.1 LIFE-METAL Code 4-4
4.2.2 LIFE-METAL Validation 4-5
4.3 Fuel Pin Transient Performance 4-8
4.3.1 FPIN2 Code 4-8
4.3.2 FPIN2 Validation 4-12
4.3.3 DEFORM-5 Validation 4-13
4.4 Thermal-Hydraulic Performance 4-14
4.4.1 SASSYS/EBR Model 4-14
4.4.2 PPS and Code Validation 4-15
4.5 Uncertainty Factors 4-17
4.5.1 Direct Factors 4-22
4.5.1.1 Power Level Measurement 4-22
4.5.1.2 Transient Overload 4-23
4.5.2 Statistical Factors 4-24
4.5.2.1 Flow Rate Through Subassembly 4-24
4.5.2.2 Flow Profile Within Subassembly 4-26
4.5.2.3 Cladding Thickness 4-27
4.5.2.4 Fissile Fuel Content 4-28
4.5.2.5 Clad Thermal Conductivity 4-28
4.5.2.6 Fuel Thermal Conductivity 4-29
4.5.2.7 Film Heat Transfer Coefficient 4-30
4.5.2.8 Neutron and Gamma Flux Distribution 4-30
4.5.3 Additional Uncertainties 4-31
4.5.3.1 Interchannel Coolant Mixing 4-31
4.5.3.2 Wire Wrap Orientation 4-31
4.5.3.3 Coolant Properties 4-31
4.5.3.4 Loop Temperature Imbalance 4-31
4.5.4 Hot Channel Factors Analyses 4-32
4.5.4.1 Selection of A Method for Analysis 4-32
4.5.4.2 Hot Channel Factors for Steady State Analysis 4-32

4.5.4.2.1 Fuel Hot Channel Factors 4-32
4.5.4.2.2 Cladding Hot Channel Factors 4-35
4.5.5 Uncertainty Factors for Transient Analysis 4-38
4.5.6 Summary 4-42
4.6 Duct Performance 4-43
4.6.1 Duct Description 4-43
4.6.2 Code and Model Description 4-44
4.6.3 Model Validation 4-47
4.6.4 Application of the Model for Duct Analysis 4-49
5 TESTING EXPERIENCE AND PLANS 5-1
5.1 Purpose 5-1
5.2 Irradiation Data Base 5-1
5.2.1 Steady State Experiments in EBR-II 5-2
5.2.1.1 Fuel Swelling 5-2
5.2.1.2 Fuel Constituent Redistribution 5-3
5.2.1.3 Fission Gas Behavior 5-6
5.2.1.4 Cladding Mechanical Performance 5-14
5.2.1.4.1 HT9 Cladding Diametral Strain 5-14
5.2.1.4.2 316SS Cladding Diametral Strain 5-18
5.2.1.5 Cladding Wastage by Fuel/Cladding Chemical Interaction (FCCI) 5-18
5.2.1.5.1 HT9 Wastage Data 5-20
5.2.1.5.2 316SS/D9 Wastage Data 5-20
5.2.1.6 Cladding Failure 5-21
5.2.2 Cladding Breach Experience in EBR-II 5-22
5.2.3 High Temperature Furnace Tests 5-26
5.2.4 Transient Tests in TREAT 5-33
6 NUCLEAR DESIGN 6-1
6.1 Background and Nuclear Design Methods 6-1
6.1.1 Measurements in Support of EBR-II Neutronics and Gamma Analysis 6-1
6.1.2 Neutron and Gamma Analysis Methodology 6-4
6.1.3 Measurements in Support of EBR-II Reactivity Feedback Analysis 6-7
6.1.4 Reactivity Feedback Analysis Methodology 6-8
6.1.5 Measurements in Support of EBR-II Depletion Analysis 6-11
6.1.6 Depletion Analysis Methodology 6-12

6.2 Mark-V Core Design 6-13
6.2.1 Design Description 6-14
6.2.1.1 Six-Row Core Model 6-14
6.2.1.2 Six-Plus-Row Core Model 6-15
6.2.1.3 Mark-V U-20Pu-10Zr HT9 Clad Subassembly Model 6-17
6.2.1.4 Mark-V U-20Pu-10Zr 316SS Clad Subassembly Model 6-18
6.2.1.5 Control/Safety U10Zr 316SS Clad Subassembly Model 6-18
6.2.2 Analysis 6-18
6.2.2.1 Six-Row Core Analysis 6-18
6.2.2.2 Six-Plus-Row Core Analysis 6-25
6.3 Reactivity Feedbacks 6-26
6.4 Depletion Characteristics 6-31
6.5 Surveillance of Core Neutronics Properties 6-37
6.5.1 Background 6-37
6.5.2 Measurements 6-39
6.5.3 Analysis 6-41
6.6 Summary 6-42
7 DUTY CYCLE AND CATEGORIZATION OF EVENTS 7-1
7.1 Operation History and Equipment Failure Mechanism 7-1
7.2 Equipment Failure Probability 7-3
7.3 Off-normal Events and Categorization 7-4
7.4 Selection of "Umbrella" Transients 7-9
7.4.1 Normal Operation 7-9
7.4.2 Anticipated Events 7-11
7.4.3 Unlikely Events 7-13
7.4.4 Extremely Unlikely Events 7-14
7.4.5 Beyond Design Basis Events 7-14
7.5 Summary of Transients for Thermal-Hydraulic Analysis 7-15
7.6 Input Descriptions for Off-Normal Event Analysis 7-16
8 STRUCTURAL ANALYSIS OF SUBASSEMBLY DUCTS 8-1
8.1 Introduction 8-1
8.2 Loading on the Duct 8-2
8.3 Structural Analysis 8-3
8.4 Structural Evaluation 8-13
8.5 Conclusions 8-20

9 THERMAL-HYDRAULIC SAFETY ANALYSIS 9-1
9.1 Introduction 9-1
9.2 Operational Limits 9-4
9.3 Steady-State Thermal Analysis 9-6
9.3.1 Thermal Analysis of Reference Mark-V Fueled Subassemblies 9-6
9.3.2 Thermal Analysis of Reference Mark-VA Core Fueled Subassemblies 9-8
9.4 Thermal and Mechanical Steady-State Fuel Performance Analysis Using LIFE-METAL 9-10
9.4.1 Thermal Analysis 9-10
9.4.2 Wastage 9-16
9.4.3 Stress 9-18
9.4.4 Cladding Damage 9-21
9.4.5 Summary of Expected Behavior of Mark-V and Mark-VA Fuel in the Reference Cores 9-22
9.5 Fuel Performance Sensitivity Analysis 9-22
9.6 Determination of Limiting Initial Conditions for Transient Analysis 9-27
9.7 Safety Analysis 9-35
9.7.1 Normal Events 9-38
9.7.2 Anticipated Events 9-38
9.7.2.1 Protected Loss of a Single Pump, AN-1 9-39
9.7.2.2 Protected Loss of Flow Due to Loss of Normal Power, AN-2 9-42
9.7.2.3 Protected TOP Due to a Single Control Rod Runout, AN-3 9-45
9.7.2.4 Protected TOP During Reactor Startup, AN-4 9-48
9.7.2.5 Limited Operation up to Power/Flow Ratio of 1.15, AN-5 9-48
9.7.3 Unlikely Events 9-49
9.7.3.1 Protected LOF Due to Double Clutch Breaker Trip, UN-1 9-49
9.7.3.2 Protected LOF Due to Seizure of One Pump and Clutch Breaker Trip of One Pump, UN-2 9-51
9.7.3.3 Protected TOP Due to a Single Control Rod Runout with Delayed Reactor Scram, UN-3 9-51
9.7.3.4 Protected TOP Due to Double Control Rod Runout, UN-4 9-53
9.7.3.5 Protected TOP During Reactor Startup with Delayed Reactor Scram, UN-5 9-54
9.7.4 Extremely Unlikely Events 9-55
9.8 Safety Evaluation 9-64
9.8.1 Normal Operation 9-64

9.8.1.1 Mark-V Fuel Pin 9-65
9.8.1.2 Mark-VA Fuel Pin 9-66
9.8.2 Off-Normal Events 9-66
9.8.2.1 Mark-V Fuel Pin 9-68
9.8.2.2 Mark-VA Fuel Pin 9-68
9.9 Discussion and Conclusions 9-68
10 ANCILLARY ISSUES 10-1
10.1 Containment Design Basis 10-1
10.2 Local Faults 10-4
10.3 Mark-III and Mark-IIIA Fueled Subassemblies 10-4
10.4 Safety Considerations for Blanket Fuel 10-6
10.5 The Effect of β_{eff} on the Safety Case 10-10
10.6 The Effect of Reactor Inlet Temperature on the Safety Case 10-13
10.7 Startup TOP Events 10-17
10.8 Duct Dilations of Control, Safety and Blanket Subassemblies 10-18
10.9 Bowing of Safety and Control Subassemblies 10-25
10.10 Adequacy of the Cover Gas Cleanup System (CGCS) for the Mark-V Fuel 10-26
10.11 Safety Consideration of Major Components 10-27
10.12 Adequacy of Argon Cooling System Fuel Transfer Criteria for Mark-V and Mark-VA Fuels 10-28
10.13 Mark-IIC and Mark-IICS Fueled Subassemblies 10-29
11 SUMMARY 11-1
12 QUALITY ASSURANCE 12-1
A APPENDIX: ENVIRONMENTAL AND MATERIAL CONSIDERATIONS A-1
A.1. Irradiation-Induced Swelling; Creep Deformation A-1
A.1.1 HT9 Swelling A-2
A.1.2 HT9 Creep A-2
A.1.3 Creep and Swelling of 20% and 12% Cold-Worked 316 SS A-4
A.2. Stress Rupture Properties A-6
A.2.1 20% Cold-worked 316SS A-7
A.2.2 Normalized and Tempered HT9 ..... A-9
A.3. Tensile Properties A-10
A.3.1 Generalized Plastic Flow Behavior of 316SS A-11
A.3.2 Generalized Plastic Flow Behavior of HT9 ..... A-13
A.3.3 Yield and Ultimate Tensile Strength A-15

A.3.4 Ductility A-16
A.3.5 Fracture Toughness A-17
A.4. Cladding Wastage A-22
A.4.1 Cladding/Coolant Interaction A-22
A.4.2 Wastage A-24
A.4.3 Eutectic Liquefaction Threshold A-30
A.4.4 Eutectic Penetration Rate A-30
A.5. Effect of Fuel and Cladding Swelling A-34
A.6. Effect of Fuel Constituent Redistribution A-35
A.7. Thermal Properties of Fuel and Cladding A-37
A.7.1 Properties of U-20 wt % Pu-10 wt % Zr A-37
A.7.2 Properties of HT9 Cladding A-40
A.7.3 Properties of 316 Stainless Steel A-42
B APPENDIX: REFERENCE CORE LOADINGS AND STEADY-STATE ANALYSIS.. B-1
B.1. Thermal Analysis of Reference Mark-V Fueled Subassemblies B-1
B.2. Thermal Analysis of Reference Mark-VA Core Fueled Subassemblies B-29
C APPENDIX: POWER AND FLOW DATA FROM THE OFF-NORMAL TRANSIENT ANALYSES C-1

Table of Figures

Figure 2-1 Cladding Wastage Mechanisms 2-7

Figure 2-2 Summary of HT9 Pressurized Tube Failure Strain Data (Data from Refs. 2.6 and 2.7) 2-16

Figure 3-1 Mark-III Subassembly Design (for Mark-V Fuel Pins 3-3

Figure 3-2 Mark-V Fueled Subassembly Design..... 3-7

Figure 3-3 Mark-IV Fueled Subassembly Design - Basis for Mark-V Design 3-8

Figure 3-4 Mark-V Subassembly Mechanical Attachment 3-9

Figure 4-1 LIFE-METAL vs. Data for U-19Pu-10Zr/HT9 Peak Cladding Strains..... 4-7

Figure 4-2 Reactivity Insertion Corresponding to Single Rod Insertion (from Ref. 4.29)..... 4-17

Figure 4-3 Power History of a Transient Overpower Event (Reactor Scrammed by SOT Trip Function) 4-18

Figure 4-4 History of a Loss-of-Flow Event Due to Clutch Breaker Trips of Both Pumps (Reactor Scrammed by Flow Trip Function) 4-19

Figure 4-5 Three-Dimensional Finite-Element Model of the Duct 4-45

Figure 4-6 Two-Dimensional Finite-Element Model of One-Sixth of a Duct..... 4-46

Figure 4-7 Diametrical Dilation of 316SS Ducts Considering Interaction Between Adjacent Subassemblies 4-48

Figure 5-1 Liquidus/Solidus Temperatures of U-20 wt.% Pu-yZr vs. Zr Content 5-4

Figure 5-2 Radial Constituent Profile for U-19Pu-10Zr Fuel from the X420 Test after ~5.5 at.% Burnup at $x/\ell_0 = 0.12$..... 5-7

Figure 5-3 Radial Constituent Profile for U-19Pu-10Zr Fuel from the X420 Test after ~5.5 at.% Burnup at $x/\ell_0 = 0.60$..... 5-8

Figure 5-4 Radial Constituent Profile for U-19Pu-10Zr Fuel from the X420 Test after ~5.5 at.% Burnup at $x/\ell_0 = 0.88$..... 5-9

Figure 5-5 Radial Constituent Profile for U-19Pu-10Zr Fuel from the X421 Test after ~10 at.% Burnup at $x/\ell_0 = 0.10$..... 5-10

Figure 5-6 Radial Constituent Profile for U-19Pu-10Zr Fuel from the X421 Test after ~10 at.% Burnup at $x/\ell_0 = 0.60$..... 5-11

Figure 5-7 Radial Constituent Profile for U-19Pu-10Zr Fuel from the X421 Test after ~10 at.% Burnup at $x/\ell_0 = 0.86$..... 5-12

Figure 5-8 Predicted Fission Gas Release in U-20Pu-10Zr Fuel..... 5-13

Figure 5-9 Maximum Observed Diametral Strain in the X425, X429, X441, and X447 Pins Clad in HT9 5-17

Figure 5-10 Lower Bound on the Fuel (19-26% Pu)/Cladding Liquefaction Temperature 5-30

Figure 5-11 Bounding Results for HT9 Wastage After > 10 at.% Bu U-19Pu-10Zr FBTA Tests... 5-30

Figure 5-12 Bounding Results for 316SS/D9 Wastage After > 10 at.% Bu U-19Pu-10Zr FBTA Tests 5-31
Figure 5-13 Predictions vs. HT9 FBTA Fuel (> 10 at.% Bu U-19Pu-10Zr) Liquefaction Data 5-31
Figure 5-14 Predictions vs. 316SS/D9 FBTA Fuel (> 10 at.% Bu U-19Pu-10Zr) Liquefaction Data 5-32
Figure 6-1 Six-Row-Core Loading Configuration 6-16
Figure 6-2 Six-Plus-Row-Core Loading Configuration 6-17
Figure 6-3 EBR-II Generic Mark-V Design, U-20Pu-10Zr, HT9, 62.5 MWt 6-33
Figure 7-1 Schematic Representation of EBR-II Primary Pumps 7-2
Figure 7-2 Pump Coastdown in EBR-II 7-3
Figure 8-1 Gap Variation of Mark-V/316SS Duct Subassembly in Row 2 8-6
Figure 8-2 Gap Variation of Mark-V/316SS Duct Subassembly in Row 6 8-7
Figure 8-3 Gap Variation of Mark-VA/316SS Duct Subassembly in Row 2 8-7
Figure 8-4 Gap Variation of Mark-VA/316SS Duct Subassembly in Row 6 8-8
Figure 8-5 Temperature Difference Across Duct Walls of Adjacent Subassemblies During an Unlikely Transient Overpower Event (UN-3) 8-11
Figure 8-6 Temperature Difference Across Duct Walls of Adjacent Subassemblies During an Unlikely Transient Overpower Event (UN-4) 8-12
Figure 8-7 Temperature Difference Across Duct Walls of Adjacent Subassemblies During an Unlikely Loss-of-Flow Event (UN-1) 8-12
Figure 8-8 Ultimate Strength of HT9 (from Ref. 8.5) 8-15
Figure 8-9 Ultimate Strength of Irradiated 20% CW 316SS (from Ref. 8.5) 8-16
Figure 9-1 Mark-V and Mark-VA Cladding Midwall EOL Hoop Stress for 5% Overpower ... 9-21
Figure 9-2 Mark-V and Mark-VA Cladding EOL Diametral Strain for 5% Overpower 9-22
Figure 9-3 LIFE-METAL Predictions of Mark-V and Mark-VA Design Lifetimes vs. PICT .. 9-26
Figure 9-4 Fuel Temperature Radial Configuration Across the Hottest Pin of the T. S. Limiting Mark-V Fueled Subassembly in Row 1 at 105% Power in a Six-Row Core 9-36
Figure 9-5 Fuel Temperature Radial Configuration Across the Hottest Pin of the T. S. Limiting Mark-VA Fueled Subassembly in Row 1 at 105% Power in a Six-Row Core 9-37
Figure 9-6 Thermal Response of the T. S. Limiting Pin in Row 6L for Mark-V Fuel During a Loss of a Single Pump Event (AN-1), with Uncertainties 9-42
Figure 9-7 Thermal Response of the T. S. Limiting Pin in Row 6L for Mark-VA Fuel During a Loss of a Single Pump Event (AN-1), with Uncertainties 9-43
Figure 9-8 Thermal Response of the T. S. Limiting Pin in Row 6L for Mark-V Fuel During a Loss of Flow Due to Loss of Normal Power (AN-2), with Uncertainties 9-43
Figure 9-9 Thermal Response of the T. S. Limiting Pin in Row 6L for Mark-VA Fuel During a Loss of Flow Due to Loss of Normal Power (AN-2), with Uncertainties 9-44
Figure 9-10 Thermal Response of the T. S. Limiting Pin in Row 1 for Mark-V Fuel During a

Control Rod Runout Event (AN-3), with Uncertainties 9-46

Figure 9-11 Thermal Response of the T. S. Limiting Pin in Row 6L for Mark-V Fuel During a Control Rod Runout Event (AN-3), with Uncertainties 9-46

Figure 9-12 Thermal Response of the T. S. Limiting Pin in Row 1 for Mark-VA Fuel During a Control Rod Runout Event (AN-3), with Uncertainties 9-47

Figure 9-13 Thermal Response of the T. S. Limiting Pin in Row 6L for Mark-VA Fuel During a Control Rod Runout Event (AN-3), with Uncertainties 9-47

Figure 9-14 Lower Bound on Time to Reach 5%-Clad/10%-Fuel Liquefaction for Mark-V Fuel.. 9-50

Figure 9-15 Thermal Response of the T. S. Limiting Pin in Row 6L for Mark-V Fuel During a Loss of Flow Due to a Double Clutch Breaker Trip Event (UN-1), with Uncertainties 9-54

Figure 9-16 Thermal Response of the T. S. Limiting Pin in Row 6L for Mark-VA Fuel During a Loss of Flow Due to a Double Clutch Breaker Trip Event (UN-1), with Uncertainties 9-55

Figure 9-17 Thermal Response of the T. S. Limiting Pin in Row 6L for Mark-V Fuel During a Loss of Flow Due to Seizure of One Pump and Clutch Breaker Trip of One Pump (UN-2), with Uncertainties 9-56

Figure 9-18 Thermal Response of the T. S. Limiting Pin in Row 6L for Mark-VA Fuel During a Loss of Flow Due to Seizure of One Pump and Clutch Breaker Trip of One Pump (UN-2), with Uncertainties 9-57

Figure 9-19 Thermal Response of the T. S. Limiting Pin in Row 1 for Mark-V Fuel During a Control Rod Runout with Delayed Scram (UN-3), with Uncertainties 9-57

Figure 9-20 Thermal Response of the T. S. Limiting Pin in Row 6L for Mark-V Fuel During a Control Rod Runout with Delayed Scram (UN-3), with Uncertainties 9-58

Figure 9-21 Thermal Response of the T. S. Limiting Pin in Row 1 for Mark-VA Fuel During a Control Rod Runout with Delayed Scram (UN-3), with Uncertainties 9-58

Figure 9-22 Thermal Response of the T. S. Limiting Pin in Row 6L for Mark-VA Fuel During a Control Rod Runout with Delayed Scram (UN-3), with Uncertainties 9-59

Figure 9-23 Thermal Response of the T. S. Limiting Pin in Row 1 for Mark-V Fuel During a Double Rod Runout Event (UN-4), with Uncertainties 9-59

Figure 9-24 Thermal Response of the T. S. Limiting Pin in Row 6L for Mark-V Fuel During a Double Rod Runout Event (UN-4), with Uncertainties 9-60

Figure 9-25 Thermal Response of the T. S. Limiting Pin in Row 1 for Mark-VA Fuel During a Double Rod Runout Event (UN-4), with Uncertainties 9-60

Figure 9-26 Thermal Response of the T. S. Limiting Pin in Row 6L for Mark-VA Fuel During a Double Rod Runout Event (UN-4), with Uncertainties 9-61

Figure 9-27 Thermal Response of the T. S. Limiting Pin in Row 1 for Mark-V Fuel During a Protected TOP During Reactor Startup with Delayed Reactor Scram (UN-5), with Uncertainties 9-61

Figure 9-28 Thermal Response of the T. S. Limiting Pin in Row 6L for Mark-V Fuel During a

Protected TOP During Reactor Startup with Delayed Reactor Scram (UN-5), with Uncertainties 9-62

Figure 9-29 Thermal Response of the T. S. Limiting Pin in Row 1 for Mark-VA Fuel During a Protected TOP During Reactor Startup with Delayed Reactor Scram (UN-5), with Uncertainties 9-62

Figure 9-30 Thermal Response of the T. S. Limiting Pin in Row 6L for Mark-VA Fuel During a Protected TOP During Reactor Startup with Delayed Reactor Scram (UN-5), with Uncertainties 9-63

Figure 9-31 Thermal Response of the T. S. Limiting Pin in Row 6L for Mark-V Fuel During a Loss of Flow Due to a Double Clutch Breaker Trip Event with One Stuck Rod (EU-1), with Uncertainties 9-63

Figure 9-32 Thermal Response of the T. S. Limiting Pin in Row 6L for Mark-VA Fuel During a Loss of Flow Due to a Double Clutch Breaker Trip Event with One Stuck Rod (EU-1), with Uncertainties 9-64

Figure 10-1 Peak Temperature Reached in Cladding of Hottest Mark-V Driver Fuel Pin for Power-Level Trip, SOT Trip, and Period Trip as a Function of Initial Power 10-19

Figure 10-2 CDF of Worst Cladding Damage of Mark-V Driver Fuel Pin for Power-Level Trip, SOT Trip, and Period Trip as a Function of Initial Power 10-20

Figure 10-3 Peak Fuel Temperature Reached in Low-Zr Zone of Hottest Mark-V Driver Fuel Pin for Power-Level Trip, SOT Trip, and Period Trip as a Function of Initial Power 10-21

Figure 10-4 Peak Temperature Reached in Cladding of Hottest Mark-VA Driver Fuel Pin for Power-Level Trip, SOT Trip, and Period Trip as a Function of Initial Power 10-22

Figure 10-5 CDF of Worst Cladding Damage of Mark-VA Driver Fuel Pin for Power-Level Trip, SOT Trip, and Period Trip as a Function of Initial Power 10-23

Figure 10-6 Peak Fuel Temperature Reached in Low-Zr Zone of Hottest Mark-VA Driver Fuel Pin for Power-Level Trip, SOT Trip, and Period Trip as a Function of Initial Power 10-24

Figure 10-7 Total Xenon Inventory for Mark-III (U-10Zr) and Mark-V (U-20Pu-10Zr) Fuel as a Function of Irradiation Time 10-27

Figure 10-8 Total Krypton Inventory for Mark-III (U-10Zr) and Mark-V (U-20Pu-10Zr) Fuel as a Function of Irradiation Time ..... 10-27Figure A-1 Yield Strength of HT9 (from Ref. A.15) A-16

Figure A-2 Ultimate Strength of HT9 (from Ref. A.15) A-17

Figure A-3 Yield Strength of 20% CW 316SS (from Ref. A.14) A-18

Figure A-4 Ultimate Strength of 20% CW 316SS (from Ref. A.14) A-18

Figure A-5 Ductility of HT9 (from Ref. A.15) A-19

Figure A-6 Ductility of 20% CW 316SS (from Ref. A.14) A-19

Figure A-7 Fracture Toughness Behavior of Irradiated HT9 (from Ref. A.15) A-20

Figure A-8 Temperature Dependence of KIC for the ACO-1 Duct Sample (from Ref. A.17) A-20

Figure A-9 Effect of Temperature on the K_c of Irradiated 20 CW 316SS(from Ref. A.18) .. A-21

Figure A-10 Effect of Temperature on Fracture Toughness of Irradiated 20 CW 316SS (from Ref. A.18) A-22
Figure A-11 LIFE-METAL Predictions for HT9/U-19Pu-10Zr and HT9/U-10Zr ID Wastage A-28
Figure A-12 Predictions vs. Data for 316SS and D9 Local Wastage A-29
Figure A-13 LIFE-METAL Predictions (with Mark-V Correlation) vs. Data for Peak Wastage in HT9 ..... A-29
Figure A-14 316SS/D9 Wastage (fission product attack) Data and Correlations A-31
Figure A-15 LIFE-METAL Predictions vs. Data and Local Fission Product Depth in HT9 Cladding A-32
Figure A-16 LIFE-METAL Predictions vs. Data for Peak Wastage in 316SS/D9 ..... A-32
Figure A-17 Comparison of D9 and 316SS ID Fission Product Attack Correlations to T581 316SS/U-19Pu-10Zr Data A-33
Figure A-18 Swelling Data of U-19Pu-10Zr Fuel A-36
Figure A-19 Solidus/Liquidus Temperatures for Mark-V Fuel (U-20Pu-10Zr) vs. Zr Content A-37
Figure A-20 The Effect of Fuel Burnup on the Thermal Conductivity of the Mark-V Fuel A-42
Figure A-21 Thermal Expansion of HT9 (from Ref. A.25) A-43
Figure B-1 EBR-II and SUPERENERGY-2 Pin Numbering System of the Mark-V Fuel Pins B-4
Figure C-1 Power Histories for Anticipated LOF Events in the 6-Row Core C-3
Figure C-2 Flow Histories for Anticipated LOF Events in the 6-Row Core C-3
Figure C-3 Power/Flow Ratio Histories for Anticipated LOF Events in the 6-Row Core C-6
Figure C-4 Power History for Anticipated TOP Event AN-3 in the 6-Row Core C-8
Figure C-5 Power History for Anticipated TOP Event AN-4 in the 6-Row Core C-8
Figure C-6 Power Histories for Unlikely LOF Events in the 6-Row Core C-10
Figure C-7 Flow Histories for Unlikely LOF Events in the 6-Row Core C-10
Figure C-8 Power/Flow Ratio Histories for Unlikely LOF Events in the 6-Row Core C-15
Figure C-9 Power Histories for Unlikely TOP Events UN-3 and UN-4 in the 6-Row Core (T_{inlet} = 690°F for UN-3) C-15
Figure C-10 Power History for Unlikely TOP Event UN-5 in the 6-Row Core C-19

Table of Tables

Table 1-1 Nominal Design Parameters for EBR-II Driver Fuel 1-2
Table 2-1 Design Criteria for Mark-V Fuel 2-14
Table 2-2 Design Criteria for Mark-VA Fuel (316SS Cladding) 2-15
Table 4-1 Plant Protection System Trip Functions 4-15
Table 4-2 Hot Channel Factors Used in Ref. 4.34 for Thermal Analysis of Fuel Pins 4-21
Table 4-3 Uncertainty and Hot Channel Factors for Thermal Analysis of Mark-V Fuel 4-22
Table 4-4 Hot Channel Factors Analysis for Mark-V Fuel Pin in Row 2 4-34
Table 4-5 Extended Hot Channel Factors Analysis for Mark-V Fuel Pin in Row 2 4-36
Table 4-6 Hot Channel Factors Analysis for Mark-V Fuel Pin in Row 6 4-37
Table 4-7 Extended Hot Channel Factors Analysis for Mark-V Fuel Pin in Row 6 4-38
Table 5-1 Radial Composition Profiles of U-19Pu-10Zr Fuel Observed Near Core Midplane at ~2 at.% Burnup 5-5
Table 5-2 Detailed Radial Composition Profile Used as the Base Case for Mark-V/VA Thermal Analysis 5-6
Table 5-3 Design Data for X425, X429, X441, X447 HT9 Pins 5-15
Table 5-4 Summary of Fuel/Cladding Chemical Interaction Wastage Data 5-19
Table 5-5 Summary of Peak Wastage Depth Data for HT9-Clad Pins Irradiated Under Normal Operating Conditions 5-20
Table 5-6 Summary of Peak Wastage Depth Data for 316SS- and D9-Clad Pins Irradiated Under Normal Operating Conditions 5-21
Table 5-7 FBTA Database for Cladding ID Wastage and Fuel Liquefaction for 10-14 at.% Burnup HT9/U-19Pu-10Zr at T ≤ 800ºC 5-28
Table 5-8 FBTA Database for Cladding ID Wastage and Fuel Liquefaction for 10-14 at.% Burnup D9/ and 316SS/U-19Pu-10Zr at T ≤ 800ºC 5-29
Table 5-9 IFR Tests on Metallic Fuel Pins 5-34
Table 6-1 Eigenvalues and Core-Masses for a Fresh Mark-II U-5Fs-Fueled Loading, a Fresh Mark-III U-10Zr-Fueled Loading, and Two Fresh Mark-V U-20Pu-10Zr-Fueled Loadings in EBR-II 6-21
Table 6-2 Fast Flux (> 0.111 MeV) Increases for Fresh Mark-V U-20Pu-10Zr Fuel (Relative to Fresh Mark-III U-10Zr Fuel) in Axial Regions of a Six-Row Core Loading Configuration 6-22
Table 6-3 Thermal-Hydraulic Quantities for a Fresh Mark-II U-5Fs-Fueled Loading, a Fresh Mark-III U-10Zr-Fueled Loading, and Two Fresh Mark-V U-20Pu-10Zr-Fueled Loadings in EBR-II 6-24

Table 6-4 Driver, Safety Rod, and Control Rod Row-wise Average Power and Average Flow Rate (plus related ratio quantities) for a Mark-V U-20Pu-10Zr-Fueled Six-Row Core Loading with HT9 Cladding and a Six-Plus-Row Core Loading with 316SS Cladding (Safety and Control Rods are U-10Zr-Fueled with 316SS Cladding) 6-26

Table 6-5 Reactivity Feedback Components of Fresh U-20Pu-10Zr-, of Fresh U-10Zr- and of Fresh U-5Fs-Fueled EBR-II* 6-28

Table 6-6 Power, Power-to-Flow, and Inlet-Temperature Integral Coefficients and Pertinent LOFWS and LOHSWS Quantities 6-30

Table 6-7 REBUS-3 Depletion Calculations for Generic EBR-II Models 6-32

Table 6-8 Effect of Cadmium Addition to U-20Pu-10Zr Mark-V Fuel 6-35

Table 6-9 Transmutation of Fuel in Equilibrium Cycle With and Without Recycle 6-36

Table 7-1 Probabilities of Equipment Failures 7-5

Table 7-2 Categorization of Events Based on Frequency of Occurrence 7-7

Table 7-3 Event Categorization and Duty Cycles Through Life of the Fuel 7-10

Table 7-4 Comparison of Hydraulic Characteristics of Various EBR-II Cores 7-17

Table 8-1 Summary of Duct Structural Evaluation 8-14

Table 9-1 Design and Safety Calculational Sequence 9-2

Table 9-2 Mark-V or Mark-VA Fuel Pins, U-20Pu-10Zr Fuel – HT9 Clad, Hottest Subassembly Power and Flow Rate 9-7

Table 9-3 Maximum Conditions in Mark-V Subassemblies and Mark-II Control and Safety Rods, Beginning-of-Life Conditions, 6-Row Core 9-8

Table 9-4 Maximum Conditions in Mark-VA Subassemblies, Beginning-of-Life Conditions, 6-Plus-Row Core 9-9

Table 9-5 Mark-V and Mark-VA Cases for LIFE-METAL Analysis 9-11

Table 9-6 LIFE-METAL Results for the Mark-V and Mark-VA Calculations 9-14

Table 9-7 Radial distributions for Zr weight fraction W_z and solidus (T_s) and liquidus (T_l) temperatures 9-15

Table 9-8 End-of-Life Wastage Values for LIFE-METAL Cases 9-19

Table 9-9 Maximum Gas Pressure (P_p), Interface Pressures (P_{fc}) and Mid-wall Cladding Hoop Stresses σH for the LIFE-METAL Cases in Table 9-5 9-20

Table 9-10 Summary of End-of-Life Strains and Cumulative Damage Fractions for Mark-V and Mark-VA Cases 9-23

Table 9-11 Summary of Sensitivity Study for Lifetime vs. Peak Inner Cladding Temperature (PICT) for Mark-V and Mark-VA Cases 9-25

Table 9-12 Limiting Conditions and Associated Physical Quantities for Mark-V and Mark-VA Fuel Based Upon Steady State Sensitivity Analysis to 10 at. % Burnup 9-28

Table 9-13 Limiting Conditions for Mark-V Fueled Subassemblies in the 6-Row Core 9-30

Table 9-14 Limiting Conditions for Mark-V Fueled Subassemblies in the 6-Plus-Row Core.. 9-31

Table 9-15 Limiting Conditions for Mark-VA Fueled Subassemblies in the 6-Row Core 9-32
Table 9-16 Limiting Conditions for Mark-VA Fueled Subassemblies in the 6-Plus-Row Core 9-33
Table 9-17 Mark-V Fuel Safety Parameters for Anticipated Events 9-40
Table 9-18 Mark-VA Fuel Safety Parameters for Anticipated Events 9-41
Table 9-19 Mark-V Fuel Safety Parameters for Unlikely Events 9-52
Table 9-20 Mark-VA Fuel Safety Parameters for Unlikely Events 9-53
Table 9-21 LCOs for Mark-V and Mark-VA Fuels 9-69
Table 10-1 Mark-III Fuel Safety Parameters for LOF Events 10-6
Table 10-2 Mark-IIIA Fuel Safety Parameters for LOF Events 10-7
Table 10-3 Mark-V Fuel Safety Parameters as a Function of Reactor Inlet Temperature 10-16
Table 10-4 Mark-VA Fuel Safety Parameters as a Function of Reactor Inlet Temperature ... 10-17
Table 10-5 Mark-IIC Fuel Safety Parameters for LOF Events (Row 3) 10-31
Table 10-6 Mark-IICS Fuel Safety Parameters for LOF Events (Row 5) 10-32
Table 11-1 LCOs for Mark-IIC, Mark-IICS, Mark-III, Mark-IIIA, Mark-V and Mark-VA Fuels in EBR-II 11-3
Table 12-1 Summary of Mark-V/VA Safety Analysis Information 12-2
Table A-1 Enthalpy and Heat Capacity of Unirradiated U-15Pu-10Zr A-39
Table A-2 Thermal Conductivity of Unirradiated U-20Pu-10Zr A-41
Table A-3 Heat Capacity and Thermal Conductivity of HT9 ..... A-44
Table A-4 Heat Capacity and Thermal Conductivity of 316 Stainless Steel A-45
Table B-1 Mark-V or Mark-VA Fuel Pins, 6-Row Core, U-20Pu-10Zr Fuel – HT9 Clad, Hottest Subassembly Power and Flow Rate B-2
Table B-2 BOL Peak Powers and Temperatures of Mark-V and Mark-IIC Fueled Subassemblies B-3
Table B-3 Maximum Heat Rating and Temperatures, Mark-V Fuel Pins, Position 1A1, Beginning-of-Life Conditions B-5
Table B-4 Maximum Heat Rating and Temperatures, Mark-V Fuel Pins, Position 2F1, Beginning-of-Life Conditions B-7
Table B-5 Maximum Heat Rating and Temperatures, Mark-V Fuel Pins, Position 3E2, Beginning-of-Life Conditions B-10
Table B-6 Maximum Heat Rating and Temperatures, Mark-V Fuel Pins, Position 4E2, Beginning-of-Life Conditions B-13
Table B-7 Maximum Heat Rating and Temperatures, Mark-V Fuel Pins, Position 5E2, Beginning-of-Life Conditions B-16
Table B-8 Maximum Heat Rating and Temperatures, Mark-V Fuel Pins, Position 6E3, Beginning-of-Life Conditions B-18

Table B-9 Maximum Heat Rating and Temperatures, Mark-V Fuel Pins, Position 6F1, Beginning-of-Life Conditions B-21

Table B-10 Maximum Heat Rating and Temperatures, Safety Rod Mark-IIC Fuel Pins, Position 3A1, Beginning-of-Life-Conditions B-24

Table B-11 Maximum Heat Rating and Temperatures, Control Rod Mark-IICS Fuel Pins, Position 5B3, Beginning-of-Life-Conditions B-27

Table B-12 BOL Peak Powers and Temperatures of, Mark-VA Fueled Subassemblies, U-20Pu-10Zr Unswollen Fuel B-30

Table B-13 Maximum Heat Rating and Temperatures, Mark-VA Fuel Pins, Position 1A1, Beginning-of-Life-Conditions B-31

Table B-14 Maximum Heat Rating and Temperatures, Mark-VA Fuel Pins, Position 2F1, Beginning-of-Life-Conditions B-33

Table B-15 Maximum Heat Rating and Temperatures, Mark-VA Fuel Pins, Position 3E2, Beginning-of-Life-Conditions B-36

Table B-16 Maximum Heat Rating and Temperatures, Mark-VA Fuel Pins, Position 4E2, Beginning-of-Life-Conditions B-39

Table B-17 Maximum Heat Rating and Temperatures, Mark-VA Fuel Pins, Position 5E2, Beginning-of-Life-Conditions B-42

Table B-18 Maximum Heat Rating and Temperatures, Mark-VA Fuel Pins, Position 6E3, Beginning-of-Life-Conditions B-44

Table B-19 Maximum Heat Rating and Temperatures, Mark-VA Fuel Pins, Position 6F1, Beginning-of-Life-Conditions B-47

Table C-1 Power, Flow, and Power/Flow Ratio Histories for the AN-1 Transient C-4

Table C-2 Power, Flow, and Power/Flow Ratio Histories for the AN-2 Transient C-5

Table C-3 Power History for the AN-3 Transient C-7

Table C-4 Power History for the AN-4 Transient C-9

Table C-5 Power, Flow, and Power/Flow Ratio Histories for the UN 1 Transient C-11

Table C-6 Power, Flow, and Power/Flow Ratio Histories for the UN 2 Transient C-13

Table C-7 Power History for the UN-3 Transient (T_{inlet} = 690°F) C-16

Table C-8 Power History for the UN-4 Transient C-17

Table C-9 Power History for the UN-5 Transient C-18

LIST OF ACRONYMS

AGHCF	Alpha-Gamma Hot Cell Facility
ANL	Argonne National Laboratory
ANL-W	Argonne National Laboratory-West
ASLRB	Atomic Safety and Licensing Review Board
ASME	American Society of Mechanical Engineers
ASTM	American Society for Testing and Materials
BDBE	Beyond Design Basis Event
BDI	Bundle-Duct Interaction
BOC	Beginning of Core
BOL	Beginning of Life
BU(u)	Burnup
CD	Carbon Depletion
CDF	Cumulative Damage Function
CEDE	Committed Effective Dose Equivalent
CGCS	Cover Gas Cleanup System
CPU	Central Processing Unit
CRBR(P)	Clinch River Breeder Reactor (Plant)
CW	Cold Work
DBT(T)	Ductile-Brittle Transition (Temperature)
DN	Delayed Neutron
DOE	Department of Energy
EBR-II	Experimental Breeder Reactor-II
EFL	Experimental Fuels Laboratory
EFPD	Effective Full Power Days
EOC	End of Core
EOL	End of Life
EPDF	Effective Pressure Drop Fraction
ESRG	Experiment Safety Review Group (ANL)
ET	Energy Technology Division (ANL)
FBTA	Fuel Behavior Test Apparatus
FCCI	Fuel-Cladding Chemical Interaction
FCF	Fuel Cycle Facility (later Fuel Conditioning Facility)
FCMI	Fuel-Cladding Mechanical Interaction
FCTT	Fuel Cladding Transient Tester
FAD	Fuels and Engineering Division (ANL)
FERD	Fuel Element Rupture Detector
FFTF	Fast Flux Test Facility
FG	Fission Gas
FMF	Fuel Manufacturing Facility
FP	Fission Product
FSAR	Final Safety Analysis Report
FUM	Fuel Unloading Machine
HEDL	Hanford Engineering Development Laboratory
HWCR	High Worth Control Rod

IBC	Inter-Building Cask (Coffin)
ICS	Irradiation Creep Strain
ID	Inside Diameter
IDMS	Isotope Dilution Mass Spectroscopic
IFR	Integral Fast Reactor
IFRO	Integral Fast Reactor Operation Division (ANL)
IHX	Intermediate Heat Exchanger
IPR	Initial Pressure Regulator
ITC	Isothermal Temperature Coefficient
JCL	Job Control Language
LCC	Liquid Cadmium Cathode
LCO	Limiting Condition for Operation
LMR	Liquid Metal Reactor
LOCP	Loss of Constant Power
LOF(WS)	Loss of Flow (Without Scram)
LOHS(WS)	Loss of Heat Sink (Without Scram)
LSSS (or LS^3)	Limiting Safety System Setting
M-G	Motor-Generator
NE	Nuclear Energy
NSMH	Nuclear Systems Materials Handbook
NRC	Nuclear Regulatory Commission
OD	Outside Diameter
ORNL	Oak Ridge National Laboratory
PC	Power Coefficient
PICT	Peak Inner Cladding Temperature
PIE	Post-Irradiation Examination
PPS	Plant Protection System
PRA	Probabilistic Risk Assessment
PRD	Power Reactivity Decrement
PRISM	Power Reactor Innovative Small Module
PSAR	Preliminary Safety Analysis Report
PSRG	Plant Safety Review Group (ANL)
QA	Quality Assurance
RA	Reactor Analysis Division (ANL)
RA	Reduction in Area
RBCB	Run-Beyond-Cladding Breach
RE	Reactor Engineering Division (ANL)
RHTH	Reactor Hydraulic Test Facility
RSRC	Reactor Safety Review Committee (ANL)
S/A	Subassembly
SAP	Subassembly Profilometry
SAR	Safety Analysis Report
SHRT	Shutdown Heat Removal Test
SOT	Subassembly Outlet Temperature
SR	Safety Rod
SPM	Special Material
SST	Stainless Steel

TAV	Turbine Admission Valve
TC	Temperature Coefficient
TCS	Thermal Creep Strain
TF	Triaxility Factor
TLD	Thermoluminescent Detector
TOP(WS)	Transient Overpower (Without Scram)
TREAT	Transient REActor Test Facility
T.S.	Technical Specifications
WPF	Whole-Pin Furnace
ZPR	Zero Power Reactor

1 INTRODUCTION

This document describes the technical basis and safety analysis for introduction of the Mark-V and Mark-VA fuel subassemblies into the core of EBR-II. An interim burnup limit of 10 at. % is specified for the Mark-V and Mark-VA fuel pins in driver subassemblies. As more information on fuel pin lifetime and hexcan behavior is gathered a final burnup limit will be sought.

1-1 describes the key features of the Mark-V and Mark-VA fuels and compares them with earlier fuel types such as Mark-II, Mark-III, Mark-IIIA and Mark-IV. The main difference is the presence of plutonium (20% by weight) in the fuel slug, and it is this feature, together with remote manufacturing and accumulated fission products left after recycling, which identifies this fuel as the prototype IFR fuel. Initially subassemblies may be constructed in the Fuel Manufacturing Facility (FMF) but once the Fuel Cycle Facility (FCF) becomes operational manufacture of the Mark-V fuel will take place in that facility. The combination of a Liquid Metal Reactor fueled by recycled fuel produced by an integral facility is the embodiment of the IFR concept.

The technical basis described herein utilizes the information available at the end of 1993, prior to the completion of the FCF refurbishment project. As a result of this timing, fuel behavioral modelling has to be based upon data from fuels fabricated in other facilities which do not use reprocessed fuel. Therefore, a number of conservatisms have been included in the fuel design criteria and analysis. As experience is acquired with the manufacture and performance of Mark-V and Mark-VA fuel these criteria may be altered to allow more operational flexibility as long as the basic overriding requirement for safe operation is not compromised.

Ideally, conservatism would always be incorporated into the design criteria and safety analysis by using 3σ parameters. This has been done wherever phenomena are well-understood and adequate data are available to allow evaluation of true statistical uncertainty. However, understanding of some phenomena (e.g., lanthanide penetration) is incomplete and an adequate database is not available to provide true statistical uncertainty evaluation. In these cases, conservatism is achieved by using limiting values which bound all known results.

Table 1-1 Nominal Design Parameters for EBR-II Driver Fuel

Designation: Mark-	**II**	**III**	**III A**	**IV***	**V**	**VA**	**Units**
Fuel	U-5FS	U-10Zr	U-10Zr	U-10Zr	U-20Pu-10Zr	U-20Pu-10Zr	
Clad	SA316SS	20% CWD-9	CW316SS	HT9	HT9	CW316SS	CW=20% Cold Work SA=Solution Annealed
Bond	Na	Na	Na	Na	Na	Na	
Wire Wrap	SA316SS	SAD-9	CW316SS	HT9	HT9	CW316SS	CW=10% Cold Work SA=Solution Annealed
Clad O.D.	0.174 (0.442)	0.230 (0.584)	0.230 (0.584)	0.230 (0.584)	0.230 (0.584)	0.230 (0.584)	inch (cm)
Clad Thickness	.012 (0.03)	0.15 (0.038)	.015 (0.038)	.018 (0.046)	.018 (0.046)	.015 (0.038)	inch (cm)
1-2 Element Length	25.0 (63.5)	29.5 (74.9)	29.5 (74.9)	29.5 (74.9)	29.5 (74.9)	29.5 (74.9)	inch (cm)
Fuel/Clad Diametral Gap	.02 (0.051)	.027 (0.069)	.027 (0.069)	.026 (0.066)	.026 (0.066)	.027 (0.069)	inch (cm)
Fuel Slug O.D.	.130 (.33)	.173 (.439)	.173 (.439)	.168 (.427)	.168 (.427)	.173 (.439)	inch (cm)
Fuel Slug l	13.5 (34.3)	13.5 (34.3)	13.5 (34.3)	13.5 (34.3)	13.5 (34.3)	13.5 (34.3)	inch (cm)
Smear Density	75%	75%	75%	75%	75%	75%	-
W/W diam.	.049 (.124)	.042 (.107)	.042 (.107)	.042 (.107)	.042 (.107)	.042 (.107)	inch (cm)
W/W pitch	6.0 (15.24)	6.0 (15.24)	6.0 (15.24)	6.0 (15.24)	6.0 (15.24)	6.0 (15.24)	inch (cm)
Vol. Plenum	2.41	7.55	7.55	7.1	7.1	7.55	cc @ 25°C
Na. Vol.	0.434	2.0	2.0	1.88	1.88	2.0	"

Designation: Mark-	**II**	**III**	**III A**	**IV***	**V**	**VA**	**Units**
Na Level	0.65 (1.65)	0.5 (1.27)	0.5 (1.27)	0.5 (1.27)	0.5 (1.27)	0.5 (1.27)	inch (cm) above fuel
Plenum Gas	Ar/He	Ar/He	Ar/He	Ar/He	Ar	Ar	
Number of pins per subassembly	91	61	61	61	61	61	
Duct	SA304SS CW316SS	CW316SS	CW316SS	HT9	HT9 or CW316SS	CW316SS	CW=12% Cold Work SA=Solution Annealed
Duct Fixtures, etc.	304SS	304SS	304SS	304SS	304SS	304SS	
S/A pitch	2.32 (5.89)	2.32 (5.89)	2.32 (5.89)	2.32 (5.89)	2.32 (5.89)	2.32 (5.89)	inch (cm)
Flat to Flat I.D.	2.21 (5.61)	2.21 (5.61)	2.21 (5.61)	2.21 (5.61)	2.21 (5.61)	2.21 (5.61)	inch (cm)
Duct Wall Thickness	.04 (.1)	.04 (.1)	.04 (.1)	.04 (.1)	.04 (.1)	.04 (.1)	inch (cm)
Button Thickness	.014 (.036)	.014 (.036)	.014 .036	.014 (.036)	.014 (.036)	.014 (.036)	inch (cm)

* Never adopted as an approved driver fuel

Note: Fuel is named after the fuel pin design

1.1 Background

In 1986 the EBR-II core was converted to Mark-III and Mark-IIIA fuel, the Mark-IV fuel form was planned as the next step in this process but material availability (HT9) obstructed this process and the Mark-III and Mark-IIIA fuels have been utilized to fuel EBR-II to the present day [1.1] [1.2]. The experience with these fuels is that very high burnups are attainable, up to 20 at. %, with no new life limiting phenomena having been identified although swelling of the cladding would prevent use of full bundles to these burnups. The ducts used with the Mark-IIIA design are 12% cold-worked Type 316 Stainless Steel which approaches the point at which swelling in the steel reaches the limits imposed at an equivalent fuel burnup of 10 at. %. For the central section of the subassembly duct the fast fluence per at. % in a completely Mark-V fueled core is predicted to be about 5% higher than that for a Mark-III fueled core. The same burnup limit of 10 at. % is imposed on Mark-V and Mark-VA subassembly ducts based on analysis presented in this document, although the limit will be expressed in terms of the fluence rather than equivalent burnup.

Progression to the Mark-V fuel is required to make use of fuel produced in the Fuel Cycle Facility and demonstrate closure of the fuel cycle. Mark-V and Mark-VA, as defined in 1-1, are two variants that are retained in order to preserve the option to continue to use 316SS as a clad material as well as the advanced ferritic alloy HT9. In addition, the Mark-V fueled subassemblies can be used, up to the interim burnup limit of 10 at. %, with either HT9 or 316SS ducts. The swelling of 316SS ducts precludes their use past 10 at. % burnup. The differential expansion between an HT9-clad fuel bundle and a 316SS duct does lead to some increase in bypass flow around the bundle and therefore flow diversion from the pins; however the effect is small and is easily bounded by the conservatisms built into the fuel safety analysis. This issue is discussed further at the end of Sec. 9.9 and is examined in detail in Ref. 9.12

Retaining the option of 316SS for both cladding and ducts is necessary for two reasons. First, supplies of HT9 may at times be difficult to procure. Second, 316SS is considerably less expensive than HT9. The desire to close the fuel cycle could well lead to designating some Mark-V subassemblies to be removed from the reactor and reprocessed in the Fuel Cycle Facility at a burnup well below the requested limit. Subassemblies which are slotted for early removal

will therefore probably use 316SS ducts as a means of cutting costs and reserving limited supplies of HT9. Thus, 316SS may well dominate the early processing. Argonne National Laboratory has ample supplies of 316SS duct and cladding to support such a campaign should it be deemed desirable.

It should be noted that the Mark-V fuel pin has HT9 cladding which is .018 inch (.046 cm) thick while the Mark-VA has 316SS cladding of .015 inch (.038 cm) thickness, but the outside cladding diameters of both fuel forms are identical, see 1-1. This difference leads to a design choice which must be made; either to use the same fuel slug outer diameter which leads to a different smear density or to preserve the smear density and require Fuel Cycle Facility to manufacture two types of fuel slug. The latter option was adopted, primarily because the overwhelming majority of the fuel database is at the 75% smear density chosen. The additional requirements on Fuel Cycle Facility Equipment are not onerous.

1.2 Safety Analysis

The structure of the analysis presented here is patterned after the Standard Review Plan [1.3] and the CRBR PSAR [1.4] in format and content. This structure has been adopted to allow the safety case for a future IFR prototype easier to make and defend and to facilitate the reformatting of the EBR-II Safety Analysis Report. The logic adopted by these formats and followed here is to specify fuel design requirements and to define design criteria appropriate to meet these goals, Section 2.0. The fuel subassembly design is specified in Section 3.0 and Section 4.0 describes the methods used to assess the performance of the fuel against these requirements. The methods are both analytic, therefore requiring validation, and experimental through a surveillance plan. The knowledge base for the fuel design is described in Section 5.0, as are the planned experiments designed to further broaden the data base. Section 6.0 describes the expected neutronic behavior of complete cores of Mark-V fuel and the impact upon design of the fuel pins, i.e. ^{235}U enrichment, the effect upon existing components such as control rods and blankets and the limitations that these effects impose.

The safety analysis is covered in the next sections. Section 7.0 describes the duty cycle chosen for the Mark-V fuel subassembly and gives the basis for the selection. Sections 8.0 and

9.0 describe the results of structural and thermal hydraulic safety analyses in both steady-state and transient conditions. Section 10.0 addresses various ancillary issues associated with introduction of Pu-bearing fuel, especially whether the containment design basis is not exceeded. Section 11.0 summarizes the conclusions and Section 12.0 provides the quality assurance for the calculations performed in support of the Mark-V safety case.

In fact, for EBR-II the approval is not sought for this document in itself but for Technical Specification changes associated with the transition. This document is the supporting material to justify the proposed changes.

1.2.1 Strategy

Apart from the fuel behavioral issues discussed in detail herein there are a number of important neutronic changes which will arise as plutonium is added to the core. Most particularly, all the Technical Specification limits are expressed in dollar units for uranium, β _ .007, and the full Mark-V core will have β _ .0053 thus changing the "value" of the dollar. This has important implications for how the transition to a Mark-V core is carried out.

Since the conversion to a full IFR (Mark-V) core will have to proceed slowly, (constrained by the rate at which subassemblies are manufactured and the desire to extract maximum life from existing fuel), the safety case and Technical Specification changes required to effect a full core change will be staged. The first set of changes addresses fuel behavior issues and seeks to demonstrate that the fuel will behave as intended. The transition to a fully Mark-V core will be constrained by existing Technical Specifications, and the core surveillance plan will ensure that the physical effects of the transition are monitored and well understood. With this information in hand the case will be made to make the Technical Specification changes appropriate to a full core of Mark-V fuel. Finally, at some later date, a third and final change will be sought to increase the burnup to the final desired level.

The gradual change of core environment will mean that for several years the EBR-II core will be a mixture of Mark-IIIA and Mark-V subassemblies. The first Mark-V subassemblies will be part of the qualification plan described in the attachment and as such will be designated as experiments, Xnnn, and have their own safety documentation. However, that safety

documentation will rely on arguments presented herein.

To address the fuel behavioral issues associated with the introduction of Mark-V and Mark-VA a full thermal hydraulic analysis of all the relevant accidents in the duty cycle is required, and this is shown to be essentially independent of β_{eff} and therefore the precise core loading. Where the change in β_{eff} will potentially have the most impact is in the reactivity limits for fuel handling. In this case it is conservative to continue to use the existing limits in dollar units because as β_{eff} decreases this implies an increasing constraint of the absolute reactivity. A full discussion of the reactivity limits and how they are affected by the change in β_{eff} is given in Section 10.

Section 1 References

1.1 J. F. Koenig, "Safety Analysis and Performance History as a Basis for Establishing an Interim Burnup Limit for Mark-III, Mark-IIC and Mark-IICS Fuel Elements," February 1988.

1.2 J. F. Koenig, et. al., "Safety Analysis and Performance History as a Basis for Establishing an Interim Burnup Limit for Mark-IIIA Fuel Elements," ANL Internal Document, March 1989.

1.3 U.S.N.R.C., "Standard Review Plan," NUREG-0800, July 1981.

1.4 "Clinch River Breeder Reactor Project Preliminary Safety Analysis Report," Project Management Corporation, April 1978.

2 DESIGN BASES

2.1 Fuel Design Bases

The fuel subassemblies used in EBR-II have been designed to satisfy the general performance requirement during reactor operation by performing their functions in a safe and reliable manner over their design lives. The functional requirements, operational requirements and design criteria to achieve this objective are delineated in the following subsections.

2.1.1 Functional Requirements

The primary functions of the fuel subassemblies in EBR-II are to provide, protect and position the nuclear fuel in order to produce heat for the reactor heat transport system; and to provide neutrons for experimental and blanket subassemblies. Specific design features in the fuel subassemblies also serve important safety functions. The fuel pin cladding acts as the primary fission product barrier and the duct helps to protect the reactivity control system and the primary cooling system, both during normal operation and during off-normal events. The design requirements for the fuel assure that these functions will be fulfilled in accordance with the General Design Criteria for Nuclear Power Plants given in Appendix A of 10 CFR Part 50 [2.1]. The two principal requirements that have been established to meet the safety and reliability functions for the Mark-V and Mark-VA fuel subassemblies are:

1. Ensure that sufficient fuel pin reliability is maintained so as to statistically prevent a "significant" number of fuel pin breaches during normal and off-normal reactor operation (up to and including unlikely events). A "significant" number of breaches may be defined as that which challenges the safe operation or performance goals of the EBR-II reactor. This has previously been defined as ensuring that no more than one fuel pin breach is expected per core loading. In other words, a 95% confidence that no more than one in 3000 pins will breach.

The fuel reliability requirement is demonstrated through an analytical performance assessment (see Section 9.0) and a follow-on fuel qualification program (see attachment). The calculable

performance guidelines, as shown subsequently in Table 2-1 and Table 2-2, have been formulated to ensure this reliability requirement. Factors involved in the assessment and guarantee of reliability are 1) prevention of stress-rupture of the cladding, which involves fuel pin materials choices that ensure the peak cladding temperature is below the minimum fuel/cladding eutectic temperature for steady-state operation and a burnup limit at which point creep damage caused by fuel and fission-product induced stress does not compromise cladding integrity, and 2) a fuel design and fabrication specification which will statistically eliminate manufacturing defects sufficient to cause reduced reliability. The latter, while drafted on best engineering judgement, is demonstrated by the qualification program.

2. Maintain a coolable geometry of both the fuel pin and the fuel pin bundle for the useful lifetime of the subassembly, including normal operation and all off-normal events.

The coolability requirement is demonstrated by analytical performance assessment (See Section 9.0) and by in-reactor experimental data (See Section 4.0). During normal operation, anticipated events and unlikely events, the low probability of fuel pin failure assures that the fuel pins will remain intact and, therefore, that the coolable pin bundle geometry will be maintained. In addition, the limits that have been established (see Section 2.1.4) on fuel melting, fuel/cladding eutectic formation, maximum cladding stress and maximum cladding strain assure no "significant" number of pin failures for these events. For very low probability extremely unlikely events, multiple fuel pin failures are allowed. However, the governing criteria of no sodium boiling and cumulative eutectic penetration of less than 5% of the wall thickness assure that significant disruption of the fuel geometry cannot occur.

2.1.2 Operational Requirements

The operational requirements for the Mark-V and Mark-VA subassemblies describe the nature of the reactor operation that the subassemblies must endure. This is expressed as a limiting steady state power, duty cycle and the use of uncertainty factors and other worst-case conditions to evaluate the fuel performance.

The duty cycle through the life of the fuel is defined in Section 7.0, and includes normal, anticipated (upset), unlikely (emergency) and extremely unlikely (faulted) events; these duty

cycles have been used in the safety assessment of the Mark-V fuel subassembly. The number of duty cycles in this report is defined in a conservative manner and is based on operation experience, engineering judgement and probabilistic risk analysis (PRA) of EBR-II, [2.2]. Off-normal transients considered include loss of primary and secondary flows, loss of balance of plant, and reactivity insertion due to control-rod, primary-flow and secondary-flow runouts. At nominal flow, the Mark-V subassemblies are able to operate at 105% of 62.5 MWt steady-state power condition below the threshold for eutectic formation and without fuel-cladding failure. This corresponds to the normal power envelope in EBR-II.

In the thermal-hydraulic safety assessment of the fuel performance, the analysis has been performed based on worst-case scenarios. Uncertainty factors of 3σ level are applied to the nominal calculations for normal and off-normal analyses. At this 3σ uncertainty level, the probability of the actual temperature exceeding the calculated temperature is about 0.1%. In the previous Shutdown Heat Removal Testing (SHRT) program [2.3], the results indicate that the measured temperatures agree very well with the nominal predictions. When uncertainties are considered, the code calculations consistently give over-predictions when compared with observations. The use of 3σ level uncertainty factors in the present thermal-hydraulics calculations is therefore conservative.

The following loading conditions of fuel pin and hexcan have been considered:

1. Applied load required during fuel handling.
2. Hydraulic pressure on the hexcan.
3. Interaction forces between fuel pin and the hexcan due to differential thermal expansion and swelling.
4. Thermal loadings during steady-state and transient conditions.
5. Pressure loading in the fuel pin due to fission gas release.
6. Fuel cladding mechanical interaction (FCMI) due to differential fuel and cladding expansion.

2.1.3 Key Physical Phenomena

Design criteria have been established to assure that the Mark-V and Mark-VA fuel will perform

in EBR-II in a safe and reliable manner. The fuel damage mechanisms that govern this performance depend on a few key physical phenomena. These phenomena are 1) mechanical deformation of the cladding, 2) cladding wastage and 3) fuel melting. A brief description of the key phenomena and their relationship to the fuel design bases are given here in order to provide the rationale for the selection of the fuel design criteria that are given in the next section. Detailed discussion of the phenomena, references, and the role of the key phenomena in the safety analyses are contained in subsequent sections of this report.

The fuel pin cladding provides the primary barrier to the release of radioactive materials. Because of this, the cladding strength must be sufficient to assure that the probability of cladding failure is acceptably low during normal reactor operation and during off-normal reactor transient events that may occur over the life of the fuel (See Section 7.3 for the event categorizations). Very low probability extremely unlikely events have also been included in the design basis, even though none of these events is expected during the fuel lifetime. For these events fuel failures may occur, although the pin geometry must remain intact so that the core remains coolable.

In addition to providing a barrier to the release of radioactive materials, the fuel system must also provide a stable geometry. As mentioned above, this geometry has to be such that the sodium coolant flow can always provide a path for heat removal. Furthermore, the fuel itself (i.e., the U-Pu-Zr alloy slug) must maintain its geometry to the extent that fuel motion does not lead to unacceptable changes in reactivity or to regions of high smear density.

The reliability of the cladding as a barrier to the release of radioactive materials depends on the inherent strength of the cladding materials in response to the applied loadings. The two cladding materials that have been selected for the Mark-V and Mark-VA fuel pins are ferritic-martensitic alloy HT9 and austenitic alloy Type 316 stainless steel, respectively. The mechanical behavior of both of these alloys is relatively well understood and both are routinely used in the FFTF reactor as fuel pin and duct materials. Details of the fuel, cladding and duct materials properties used in the present safety evaluations are given in Appendix A of this report. The two properties that are used directly in the design criteria to assess cladding failure are the cladding plastic strain correlations and the stress rupture correlations. To some extent the design criteria based on these phenomena are redundant since most of the mechanisms that lead to cladding

rupture are related to plastic straining. In the case of the stress-rupture correlations, the Cumulative Damage Function (CDF) method is used to apply the stress-rupture correlations to variable load and temperature conditions.

Another important factor determining cladding strength is cladding wastage. Cladding wastage is defined here as that part of the original cladding wall that is assumed to no longer contribute to carrying the applied loading. Mechanisms that have been identified as contributing to cladding wastage in the Mark-V/VA fuel and cladding systems are 1) scratches on the cladding surfaces, 2) solid-state diffusion of fuel constituents and fission products (especially lanthanides) into the cladding, 3) eutectic liquefaction at the fuel-cladding interface, and 4) sodium/cladding interaction causing corrosion and carbon/nickel depletion at the cladding outer diameter. A graphical representation of the various zones that may form in the cladding is shown in Figure 2-1.

The standard ASTM specifications (A 771-83) for fast reactor cladding call for external and internal surfaces to be free of scratches, dents, scuff marks or pitting that exceeds 1.0 mils (25 microns) in depth. The cladding materials for the Mark-V/VA fuel pins have sufficient ductility at operating temperatures [2.29, 2.30] so that flaws of this type will not lead to brittle fracture of the cladding. However, some general reduction in strength might be expected because of the local reduction in load-bearing area. The computer codes that have been used to assess the performance of Mark-V and Mark-VA fuels assume an axisymmetric geometry and, therefore, cannot model the three-dimensional nature of these imperfections. An assumption of a uniform wastage of 1.0 mil (25.4 microns) would be conservative but would be much too severe for modeling the effect of small flaws of random length and random orientation. Instead, as noted in Section 9.4.2, an effective scratch depth of 0.5 mils (12.7 microns) is used.

Solid-state diffusion of fuel constituents and/or fission products into the cladding form an FCCI (Fuel Cladding Chemical Interaction) band on the inside of the cladding. This band forms during steady-state irradiation and can grow larger during transients, as shown in Figure 2-1. The FCCI zone is indicated by optical microscopy as a band that has a microstructure that is distinctly different from the cladding. Although the composition of the zone is complex, it is usually rich in lanthanides. Because the mechanical properties of the FCCI band are not known, and because

it often contains cracks, it is assumed here to be strengthless and part of the wastage.

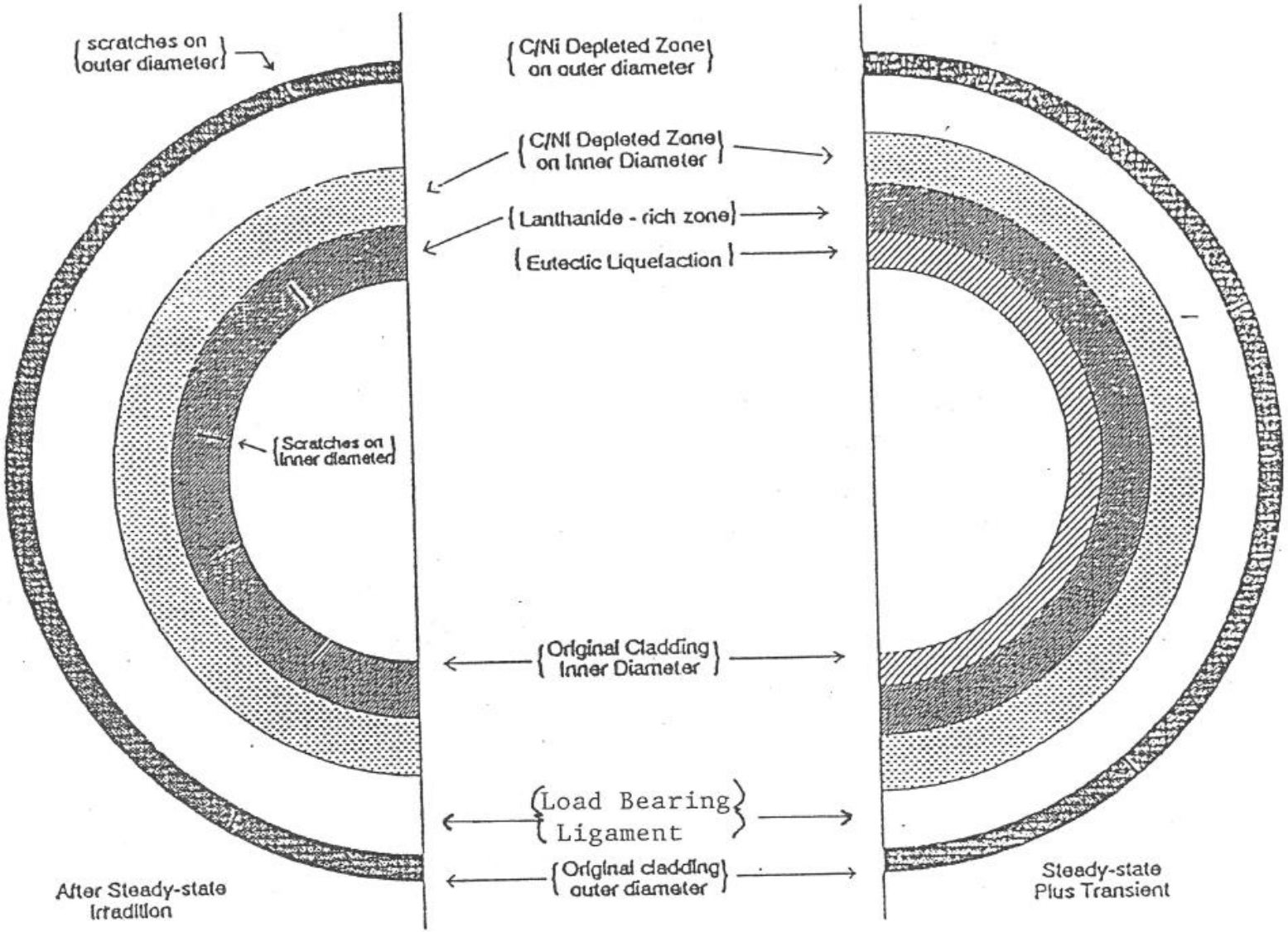

Figure 2 1 Cladding Wastage Mechanisms

Eutectic liquefaction is the term given to the formation of low melting point phases at the fuel-cladding interface. These phases are formed primarily by interpenetration of iron and nickel from the clad and uranium and fission products from the fuel. Plutonium does not participate significantly in these phases, as discussed in more detail in Sec. 5.0. There is a threshold temperature below which there is no liquid formation at the fuel-cladding interface; above this temperature the liquefaction of the cladding proceeds at a certain rate, which is temperature dependent. For high burnup U-20Pu-10Zr fuel with HT9 cladding the threshold temperature (T_e) has been determined to be $650 < T_e \leq 660°C$. For Mark-VA fuel (316SS/U-20Pu-10Zr), the threshold temperature is higher ($660 < T_e \leq 700°C$). These results are based on a series of out-of-pile experiments described fully in Section 5.0. Evidence exists which shows that, at lower burnups, the threshold temperature is much higher. In this safety evaluation the limit temperatures of 650°C for Mark-V and 660°C for Mark-VA are applied <u>irrespective</u> of burnup or exact quantity of plutonium or other actinides in the fuel. This is a very conservative position; a less extreme position may be adopted in the future once the performance characteristics of this fuel are fully developed. One reason for adopting this position is to bound the effects of lanthanide fission products and actinide carryover in the recycled fuel. The lanthanides appear to play a major role in clad wastage, and therefore this assumption is adopted to ensure that the process is treated conservatively.

During off-normal transients, eutectic liquefaction at the fuel-cladding interface may consume part of the original solid-state interdiffusion zone in the cladding or may propagate into cladding that had not previously been wasted. In addition, for high burnup fuels the solid-state FCCI band may advance in front of the liquid zone. Regardless of how the wastage progresses, the important quantity is the remaining tendon of unaffected cladding that is available to carry the loading. In this regard it should be noted that the determinations of cladding wastage and eutectic penetration rates discussed in Section 5.0 necessarily rely on measuring inward from the cladding outer surface and subtracting the thickness of the unaffected tendon from the original cladding thickness. Thus, the cladding wastage and penetration rate correlations yield the correct thickness of the load-bearing portion of the cladding, which is the quantity of greatest interest. It should also be noted that the transient penetration rate correlation for the Mark-V and Mark-VA fuels includes both the liquid penetration and the advance of the FCCI band in front of it. The total wastage for transient analyses of fuel pin behavior can therefore be determined by adding the

steady-state wastage to the calculated incremental amount of penetration during the transient. In developing the transient wastage rate correlation, the steady-state wastage prior to Fuel Behavior Test Apparatus (FBTA) and Whole-Pin Furnace (WPF) overheating events is subtracted from the total wastage measured after the overheating event. This incremental wastage is divided by the test time to determine a transient wastage rate. In performing these analyses, the total wastage from multiple transients is assumed to be cumulative.

Nickel depletion and carbon depletion at both the inner and outer cladding surface can also degrade the strength of the cladding materials. Nickel depletion is primarily of concern for the Type 316 stainless steel austenitic alloy, whereas carbon depletion is primarily of concern for the HT9 ferritic-martensitic alloy. Such depletion does not necessarily constitute wastage because the cladding materials retain a significant fraction of their strength, especially when the depletion is not sufficient to cause recrystallization and grain growth. The depleted zones on the inner and outer cladding diameter are also illustrated in Figure 2-1.

Nickel and carbon depletion at the cladding outer surface are caused by interaction with the sodium coolant. In addition to matrix depletion there is also a certain amount of erosion of the surface and intergranular penetration. Correlations for cladding/coolant interaction are given in Appendix A. The penetration depths on the outer surface are minor. Their treatment here as having zero strength is conservative, but it has little impact on the design results. The incremental increases in this type of wastage during the short times of off-normal transients are negligible.

Nickel and carbon depletion at the cladding inner surface is caused by the presence of metallic fuel and fission products. The depth of the nickel depletion band in Type 316 stainless steel can generally be associated with the depth of the FCCI diffusion band. Since this band is considered to be part of the wastage, the effect of nickel depletion on the mechanical properties of Type 316 stainless steel does not need to be addressed separately. Depletion of the minor amounts (0.3 to 0.8 wt.%) of nickel in HT9 cladding also occurs in the FCCI zone, which is again included as part of the wastage.

In HT9 cladding a separate carbon depleted band is often identified at high temperature (>630°C) in advance of the FCCI zone, as illustrated in Figure 2-1. This band forms during normal operation and grows in width during high temperature transients. The carbon depleted

band is distinguished by its difference in microstructure from normal HT9 cladding and from the FCCI zone, by a general absence of fuel and/or fission product constituents in the band and by a modest decrease in cladding hardness. It is inferred from these observations that carbon has been lost from this band to the fuel or to the FCCI zone. In spite of the fact that the hardness numbers would indicate only a modest decrease in strength, this band is considered as part of the wastage for the present safety case. This is a very conservative assumption which may be relaxed in subsequent safety analyses.

The absence of fuel melting has traditionally served as one of the design criteria for nuclear reactor fuels. In the case of metallic fuels, it is important to distinguish between bulk melting of the fuel itself and limited eutectic liquefaction at the fuel-cladding interface. Bulk fuel melting is often referred to as fuel centerline melting, or simply fuel melting. This occurs when the fuel temperature exceeds the local fuel solidus temperature. It should be noted that for metallic fuels the first bulk melting may not begin exactly at the fuel centerline because of fuel constituent redistribution. The primary reason that fuel melting has traditionally been used as a design criterion is that, at least for the case of oxide fuels, centerline melting can lead to contact of molten fuel with the cladding and rapid cladding failure. Metallic fuels have much lower melting temperatures than oxide fuels (1100°C compared to 2700°C) and are therefore much less prone to cladding failure caused by this mechanism. Nevertheless, as a conservatism, fuel melting will not be allowed for the Mark-V/VA fuels during normal operation or during anticipated or unlikely off-normal events.

The effect of eutectic liquefaction at the fuel-cladding interface on cladding wastage and cladding failure was discussed above. The liquid that is formed contains both cladding constituents and fuel constituents and therefore the interaction zone spreads both into the cladding and into the fuel. As is the case for bulk fuel melting, limits have been placed on the amount of eutectic melting in order to preclude fuel motion. The penetration rate correlations provided in Appendix A give the liquid penetration rate into the cladding. A simple estimate for the liquid penetration rate into the fuel can be derived by assuming that the atom ratio of fuel to cladding constituents in the liquid always has the same ratio as the eutectic in the uranium-iron binary system (0.65/0.35). The limit of 5% of the cladding wall thickness that has been established as a design criterion for transient eutectic penetration corresponds to 10% liquefaction of the fuel cross

section. The methodology of treating incremental transient wastage as liquid penetration and assuming a 2:1 ratio of percent fuel liquefaction to percent cladding liquefaction has been validated to FBTA data (which are discussed in Sec. 5.2.3). This limited amount of local fuel liquefaction is only allowed over the short times of off-normal transients where capillary forces and viscous forces are sufficient to prevent fuel motion; eutectic liquefaction is not allowed during normal operation.

2.1.4 Design Criteria

The EBR-II Mark-V fuel subassembly functional and operational requirements have been identified in subsections 2.1.1 and 2.1.2. The criteria presented herein establish the detailed criteria that the fuel pin design must satisfy in order to meet the general requirements and establish the methodology that should be utilized. These criteria were selected so that the fuel pins will satisfy their functional requirements and performance objectives in a safe and reliable manner based on current technology.

The design criteria and analysis methods that are presented in this section address the geometry, temperature regimes and loading mechanisms that are expected to influence fuel performance both during normal and off-normal operation. Certain loading conditions are not reflected by the criteria because they have been eliminated by proper design of the fuel system. Most notable here is Bundle-Duct-Interaction (BDI) which could impose a limit on the total cladding strain. The primary concern is that differential expansion between the fuel bundle and the duct may induce local bending stresses in the cladding that may affect the cladding CDF predictions. The amount of bundle deformation required to load the duct is design and materials dependent, as the duct also expands during start-up and operation. It would be difficult to provide a reasonable value on the total cladding strain to serve as a design criterion because the BDI is a function of material, fluence, burnup and pressure loading conditions of both cladding and duct. Although no rigid limit is imposed on the diametral expansion of each pin, analyses are to be performed to insure that fuel pin dilation leading to BDI does not occur within the goal burnup (see Section 8.5).

Evaluations of steady-state operation are made using current, state-of-the-art metallic fuel behavior models as incorporated in the LIFE-METAL computer code described in subsection 4.2. Evaluations of the transient behavior of Mark-V fuel are performed as an integral part of the whole-

core analyses of the response of EBR-II to reactor accident conditions. The SASSYS code with the DEFORM-5 fuel pin model is used for these evaluations. The material properties of Mark-V and Mark-VA fuel and cladding are obtained from the Metallic Fuels Handbook [2.4], with the exception of those additions and/or corrections noted in Appendix A. Justification for the simple pressurized tube model of metallic fuel pin behavior used in DEFORM-5 is supported by more-detailed FPIN2 transient fuel pin behavior code calculations and by experimental results, as discussed in subsection 4.3.

The design criteria given below are separated into those that are applicable to normal operation of the fuel and those that are applicable to off-normal operation (see Section 7.3 for the categorization of off-normal events). Although it may be desirable to have a single set of criteria for all conditions, it is recognized that, because of the widely different time scales that are involved, separate criteria are necessary. This is particularly true for HT9 cladding where extrapolations of short-term mechanical behavior to long times, and extrapolations of long-term mechanical behavior to short times, are not possible because of changes in the microstructure of the alloy that occur during its service. In order to account for the accumulation of fuel pin damage during normal operation and during off-normal transients, it is assumed that damage (e.g. life fractions, cladding plastic strain, fuel-cladding metallurgical interaction) is additive. This procedure is conservative in the sense that the data on which the transient design criteria are based were obtained from tests on irradiated fuel pins, or sections from irradiated fuel pins. Prior damage due to steady-state irradiation is, therefore, already incorporated into the transient fuel pin failure correlations.

The reference cladding for Mark-V fuel is ferritic/martensitic alloy HT9. An alternative cladding for which this safety case is also being made is austenitic 20% cold worked Type 316 Stainless Steel, the Mark-VA cladding. This latter cladding alloy is the same alloy that was used in the Clinch River Breeder Reactor (CRBR) design. Although CRBR was never built, a PSAR [2.5] was written and the Atomic Safety and Licensing Review Board (ASLRB) of the USNRC issued a Memorandum of Findings which would have resulted in the granting of a construction permit. Because of the precedent set by the CRBR PSAR, the design criteria given in the following paragraphs for Mark-V fuel follow the format in Chapter 4 of the CRBR PSAR [2.5, Section 4.2.1.1.2.2]. For the 316SS option, the criteria given for EBR-II Mark-VA fuel pins are

essentially the same as the CRBR criteria, with the exception of those differences that are due to differences in the fuel type (metal alloy vs. mixed oxide). The justifications for the 316SS criteria are given in the CRBR PSAR (again with the exception of those that apply specifically to the fuel type) and are not repeated here. For the reference HT9 cladding both the new criteria and their justification are presented, again using the CRBR format. The design criteria for both cladding types are summarized in Table 2-1 and Table 2-2.

The design criteria are as follows:

1.0 During steady state (normal) operation, the thermal component of the plastic diametral strain for HT9 cladding shall be less than 1%. The comparable limit for 20% Cold Worked Type 316 Stainless Steel is 0.2%.

The total in-reactor, permanent strain consists of a volumetric swelling strain and an in-reactor creep strain. Based on a very extensive data base for Type 316 Stainless Steel [2.6, Section 5, Appendix A], large swelling strains can be tolerated without imposing a failure ductility limit on the material. Also, at low temperature and stress, where thermal creep is negligible, the material can deform without any observable limit due to irradiation enhanced creep. Thus, the in-reactor ductility of a pressurized tube is often associated with the thermal creep strain component.

For HT9 cladding, there is a smaller data base for failure strain. Figure 2-2 summarizes that data for out-of-reactor [2.6, Section 10] and in-reactor [2.7] pressurized tube tests. The lowest observed failure strain is 2.1%. Thus, the 1% limit is conservative. Also, based on the temperature to cause failure, whether the test was performed in-reactor or out-of-reactor. This observation supports the concept that it is the thermal creep component that is damaging for HT9 cladding, as is the case for 316SS.

Very few HT9 breaches have occurred in irradiated metallic fuel pins. Two breaches, out of fifteen, occurred in HT9/U-10Zr pins from EBR-II Subassembly X447A at 10 at. % burnup. These fifteen pins were operated at a peak nominal beginning-of-life cladding temperature of 644±12°C. The maximum diametral strain for unfailed sibling pins reached 2%, which is above the prescribed design limit for Mark-V fuel.

Table 2-1 Design Criteria for Mark-V Fuel

DESIGN CRITERIA	DESIGN BASIS EVENTS			
	Normal Operation	**Anticipated Events**	**Unlikely Events**	**Extremely Unlikely Events**
1.0	$\epsilon_{THN} < 1\%$			
2.0	$CDF_N < 0.05$			
3.0	No fuel melting			
4.0	No eutectic liquefaction at the fuel-cladding interface			
5.0	$\overline{\sigma}_H < 150$ MPa			
6.0		$\sum_{i=1}^{M}\sum_{j=1}^{N_i}(\Delta r_A)_{ij} + \Delta r_U + \Delta r_{EU} < 5\%$ wall thickness		
7.0		$\sum_{i=1}^{M}\sum_{j=1}^{N_i}(CDF_A)_j\, CDF_U \leq 0.1$		
8.0		$\sum_{i=1}^{M}\sum_{j=1}^{N_i}(\epsilon_{HA})_j + \epsilon_{HU} \leq 1\%$		
9.0	Core remains coolable			

KEY TO TABLE 2.1

ε_{THN}	=	Thermal component of plastic hoop strain during normal operation
CDF_N	=	Cumulative damage function during normal operation
$\overline{\sigma}_H$	=	Radially averaged primary hoop stress
$\sum_{i=1}^{M}\sum_{j=1}^{N_i}(\Delta r_A)_{ij}$	=	Total cladding eutectic penetration for all M anticipated events and all N_i occurrences
Δr_U	=	Cladding eutectic penetration for single most damaging unlikely event
Δr_{EU}	=	Cladding eutectic penetration for the extremely unlikely event
$\sum_{i=1}^{M}\sum_{j=1}^{N_i}(CDF_A)_j$	=	Cumulative damage function during all M anticipated events and all N_i occurrences
CDF_U	=	Cumulative damage function during single most damaging unlikely event
$\sum_{i=1}^{M}\sum_{j=1}^{N_i}(\epsilon_{HA})_j$	=	Total plastic hoop strain for all M anticipated events and all N_i occurrences
ϵ_{HU}	=	Plastic hoop strain for single most damaging unlikely event

Table 2-2 Design Criteria for Mark-VA Fuel (316SS Cladding)

DESIGN CRITERIA	DESIGN BASIS EVENTS			
	Normal Operation	**Anticipated Events**	**Unlikely Events**	**Extremely Unlikely Events**
1.0	$\epsilon_{THN} < 0.2\%$			
2.0	$CDF_N < 0.05$			
3.0	No fuel melting			
4.0	No eutectic liquefaction at the fuel-cladding interface			
5.0	$\overline{\sigma}_H < 150$ MPa			
6.0		$\sum_{i=1}^{M}\sum_{j=1}^{N_i}(\Delta r_A)_{ij} + \Delta r_U + \Delta r_{EU} < 5\%$ wall thickness		
7.0		$\sum_{i=1}^{M}\sum_{j=1}^{N_i}(CDF_A)_j\, CDF_U \leq 0.1$		
8.0		$\sum_{i=1}^{M}\sum_{j=1}^{N_i}(\epsilon_{HA})_j + \epsilon_{HU} \leq 0.1\%$		
9.0	Core remains coolable			

KEY TO TABLE 2.2

ε_{THN}	=	Thermal component of plastic hoop strain during normal operation
CDF_N	=	Cumulative damage function during normal operation
$\overline{\sigma}_H$	=	Radially averaged primary hoop stress
$\sum_{i=1}^{M}\sum_{j=1}^{N_i}(\Delta r_A)_{ij}$	=	Total cladding eutectic penetration for all M anticipated events and all N_i occurrences
Δr_U	=	Cladding eutectic penetration for single most damaging unlikely event
Δr_{EU}	=	Cladding eutectic penetration for the extremely unlikely event
$\sum_{i=1}^{M}\sum_{j=1}^{N_i}(CDF_A)_j$	=	Cumulative damage function during all M anticipated events and all N_i occurrences
CDF_U	=	Cumulative damage function during single most damaging unlikely event
$\sum_{i=1}^{M}\sum_{j=1}^{N_i}(\epsilon_{HA})_j$	=	Total plastic hoop strain for all M anticipated events and all N_i occurrences
ϵ_{HU}	=	Plastic hoop strain for single most damaging unlikely event

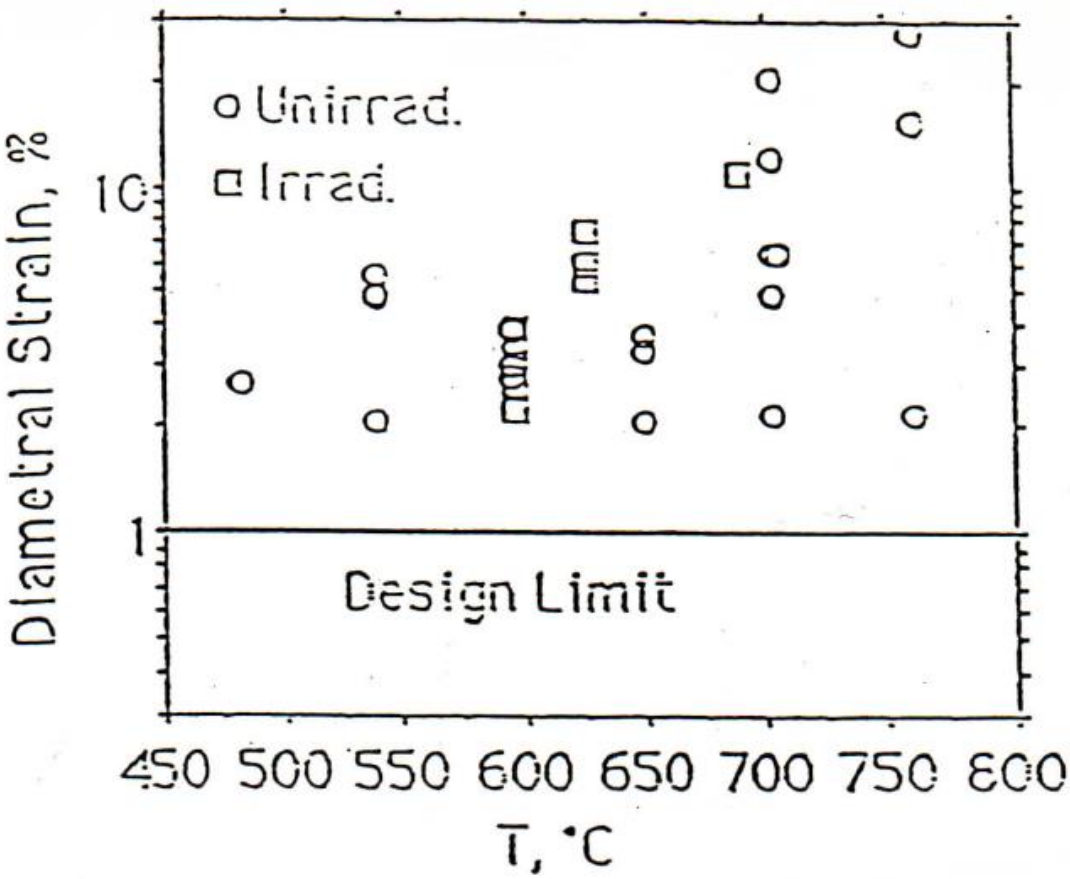

Figure 2-2 Summary of HT9 Pressurized Tube Failure Strain Data
(Dadta from Refs. 2.6 and 2.7)

2.0 During steady state operation, the cumulative damage function (CDF) for HT9 cladding shall be limited to 0.05. The same damage fraction shall apply to Type 316SS.

The separation of the allowable CDF into a steady-state component and a transient component departs somewhat from the format used in the CRBR PSAR. For CRBR, the equivalent requirement was that the sum of the steady-state CDF plus the accumulated CDF for all transients should be less than 1.0 - ε, where ε designated an unspecified total uncertainty in the CDF. Here a CDF of 0.05 for steady-state operation and an accumulated CDF of 0.1 (see criterion 7.0 below) for all transients have been allowed. The sum of these two is obviously less than 1.0, even if all of the transients were to occur at the end of life of the fuel.

The CDF for 316SS and HT9 cladding are to be calculated using the long term stress-rupture correlations given in Section A.2 of this document. The hoop stress used in this

correlation is to be calculated from the plenum gas pressure and/or the fuel-cladding interface pressure using the same formula as was used to correlate the data.

The CDF, or life fraction, is a widely used method for predicting failure of components that are subjected to creep damage at elevated temperatures and has been accepted as a means for predicting fuel pin failure in LMR systems [2.8]. The CDF method allows rupture time data from creep tests at constant stress and temperature to be used to predict failure under similar loading conditions, but with time-varying stress and temperature. The basic assumption is that creep damage is linearly additive so that the damage over a given time interval dt is proportional to the ratio of the time interval to the time t_r that would cause failure at the instantaneous stress and temperature levels. The CDF is then defined as the sum of these fractions, or

$$\mathrm{CDF} = \int_0^t \frac{dt}{t_r}$$

The expected value of the CDF at failure should equal 1.0 in order to be consistent with the data base for t_r. However, in practice the allowable CDF is usually chosen to be smaller than 1.0 to account for differences in loading conditions from those assumed, uncertainties in the applied temperature and stress histories and scatter in creep-rupture data base.

The CRBR PSAR [2.5] utilized the CDF as a design criterion to assure that fast reactor cladding satisfies its functional requirements during the fuel lifetime. The CDF method is also specified in Case N-47-22 of the ASME Boiler and Pressure Vessel Code [2.9] for the analysis of components in elevated temperature service (alloy HT9 and irradiation effects are not treated in this code case).

The CDF methodology has been validated by comparing the results of variable-load and -temperature tests with predictions based on results of constant-load and -temperature tests along with the CDF law. Validation of the law for austenitic stainless steels has been provided by extensive work at ORNL [2.10] where it was found that a damage summation of 0.65, as opposed to 1.0, was adequate to assure, at a 95% confidence level, that the observed life in variable-load and -temperature tests would be equal to or greater than the predicted life. Less direct evidence of the validity of the CDF method for predicting HT9 cladding lifetime is its successful use in the analyses of the TREAT tests and the Whole Pin Furnace tests (See Section 5) on HT9 clad metallic fuel pins. It should also be noted that the CDF failure criterion and the strain-to-failure criterion

given above are not totally independent so that satisfying both of the design requirements adds a degree of conservatism through redundancy. The relationship between the two criteria comes from the definition of the CDF along with the Monkman-Grant relationship [2.11] which empirically relates the secondary creep strain rate $\dot{\epsilon}$ to the rupture time t_r by

$$\dot{\epsilon} t_r = \text{constant.}$$

The allowable CDF of 0.05 during steady state operation of Mark-V fuel pins with HT9 cladding is based on the HT9 out-of-reactor stress-rupture data and LIFE-METAL code calculations for fuel pins with HT9 cladding that have been irradiated in EBR-II. With regard to the time-to-rupture correlation used in the CDF formulation, it is fit to the unirradiated stress-rupture data for pressurized HT9 tubes. A statistical analysis [2.12] of these data shows the logarithm (base 10) of the CDF at failure is distributed normally. With 95% confidence, the mean and standard deviation of the probability distribution are -0.0354 and 0.1885, respectively. Thus, the failure probability will be less than 1 in 3000 if the logarithm of the CDF is less than -0.6771, or the CDF is less than 0.21. The allowable value of the steady-state CDF of 0.05 that is used in the current safety case is considerably smaller than this value. The additional conservatism is based on the precedent set by CRBR and PRISM reactor analyses, engineering judgement and the desire to select a suitably low value of the steady-state CDF so that it can be argued that the transient performance of the cladding in not significantly degraded by the steady-state operation. It is expected that this limit can be relaxed when additional fuel pin failure data become available from the Mark-V/VA qualification program.

It is worthwhile to also consider the data base for irradiated HT9/U-Pu-Zr fuel pins. In terms of the calculated (using the LIFE-METAL Code) CDF values for HT9/U-19Pu-10Zr fuel pins which <u>did</u> <u>not</u> fail, most of the calculated values are in the range of 10^{-6} to 10^{-8} for peak burnups of 10-12 at. %. However, four fuel pin from subassembly X441 which had high smear densities (85%) reached 10 at. % burnup without failure. The calculated CDF was 0.2 for these pins which experienced substantial fuel-cladding mechanical interaction.

The LIFE-METAL approach for calculating cladding wastage, cladding ID pressures, cladding stresses and strains, and failure probability based on CDF and thermal creep strain (TCS) limits was validated to the data from experimental subassembly X447. Of the 15 hot (PICT =

644±12°C) HT9/U-10Zr pins which were irradiated to 10 at. % burnup, two pins failed. An ID wastage rate correlation which was the best fit to the FCCI layer (fission-product attack) data from all HT9 pins examined, resulted in very good agreement with the measured peak cladding strains for these pins and gave a failure probability of 2/15 based on the 2% failure strain limit. However, the CDF predictions were lower than those required to give 2/15 failure probability. Recall that for Mark-V, the design limit is set based on either CDF or TCS exceeding limiting values. However, to be conservative, a second set of calculations was performed by raising the wastage rate (by 67%) to achieve the implied 2/15 failure statistics based on CDF. However, this case resulted in much higher-than-observed peak strains and peak wastage layers. An intermediate case was recommended for Mark-V design analysis with a wastage rate that is 41% higher than the best fit correlation. This case gave a more reasonable bound to the failure statistics (5/15 based on 2% TCS limit), to the observed peak cladding strains, and the observed FCCI layers. The resulting wastage prediction for the 15 pins was 6.43± 0.66 mils (0.016±0.0017 cm), as opposed to a 4.7±1.5 mil (0.012±0.0038 cm) FCCI layer measured and a 6.9±0.5 mil (0.018±0.0013 cm) FCCI + carbon-depleted layer measured. Thus, the predicted wastage is within the boundaries of the two zones.

The same basic approach is used for predicting Mark-VA cladding performance, although the 316SS/D9 data base for U-Pu-Zr is too limited to allow direct validation. D9/U-19Pu-10Zr pins have been irradiated to 20 at. % burnup with only one failure occurring in the fuel-column cladding. The peak CDF value (using nominal operating conditions) calculated by LIFE-METAl is 0.069 and the peak TCS is 0.091% for this relatively low temperature pin (T084 from subassembly X420B) at about 17 at. % burnup. While the implied failure probability is low based on these CDF and TCS values, it should be realized that a very large number of pins operating under similar conditions have survived this burnup. Thus, the validation of the design-analysis methodology for Mark-VA is based indirectly on the success of the methodology in predicting HT9 performance and more directly on predicting peak cladding strains and peak FCCI zones for U-Pu-Zr fuel clad in 316 SS and D9 – both austenitic materials with very similar compositions.

In the previous discussion, the calculated nominal temperatures and operating conditions were used to validate the LIFE-METAL CDF and TCS methodologies for predicting fuel pin failure probability. It is worth mentioning that if three-sigma uncertainties were used in the

predictions of cladding temperatures, the calculated CDF and TCS values would have exceeded failure limits for all failed pins and many unfailed pins. Thus, while some conservatism has been used in the fuel performance modeling and the design criteria, the real confidence that Mark-V and Mark-VA will reach their goal of < 1/3000 failures if the design criteria are satisfied comes from the conservatism and pessimism used in calculating the three-sigma uncertainty temperatures.

3.0 During steady-state operation, all Anticipated Events, and all Unlikely Events, the power in the hottest fuel pins, regardless of cladding type, shall be less than the minimum values for incipient bulk fuel melting. The redistribution of fuel alloying elements shall be considered in satisfying this criterion.

The purpose of the above requirement is to provide sufficient margin up to the over-power reactor trip points so that incipient fuel melting is precluded. This is not meant to imply that incipient fuel melting under these conditions is, in itself, detrimental. Rather, by providing such a margin, the task of demonstrating that reactor accident transients can be terminated with limited fuel damage becomes easier.

It has been traditional practice in license applications to the Nuclear Regulatory Commission to assume that failure of nuclear reactor fuel pins will occur if bulk (centerline) fuel melting takes place [2.13]. The origin of this assumption comes from light water reactor practice for uranium oxide fuels where the criterion was established to assure that molten fuel could not come into contact with the cladding. Because the melting point of uranium dioxide (2700°C) is much greater than the melting point of the cladding (~1400°C for iron-based materials), contact of the cladding by molten oxide fuel can lead to melt-through or significant weakening of the cladding. The damage caused to the cladding depends on the mass of the molten fuel that finds its way to the cladding through cracks in the fuel pellets. This is obviously difficult to predict with any degree of certainty. Consequently, it is easier for light water reactor fuel safety analyses to simply exclude fuel melting.

Bulk fuel melting is less likely to cause cladding damage in metallic fuel pins because the melting temperature of the fuel (~1100°C) is less than the melting temperature of the cladding. The relatively benign effect of bulk melting in metallic fuels is illustrated by the results from

experimental irradiations of EBR-II Mark-IA fuel fabricated with bond sodium only in the lower half of the pins [2.14,2.15]. Even though the absence of the bond caused extensive fuel melting, the molten fuel simply relocated to close the fuel-cladding gap and froze in place without failing the cladding. Only a small area of eutectic interaction with the cladding was noted with a maximum wall penetration of 10% of the thickness.

In spite of the conservatism, the criterion of not allowing bulk fuel melting during normal operation and all off-normal events is retained here. This has been accomplished by limiting the maximum pin power so that fuel melting will not occur for powers up to the scram setting of 15% overpower. A similar approach was taken in the CRBR PSAR [2.5]. Elimination of bulk fuel melting eliminates the need to consider the effect of molten fuel in the cladding failure analyses. It also eliminates the need to consider the consequences of molten fuel relocation on reactivity and the possibility of molten fuel relocation leading to axial locations in the fuel with high smear density which could cause excessive fuel-cladding mechanical interaction. In addition, the criterion eliminates the need to consider the effects of molten fuel relocation into the coolant channels on core coolability.

It should be noted here that the bulk fuel melting criterion is being applied to the fuel alloy itself (U-Pu-Zr) and not to the low melting point fission products or to alloys that these fission products may form with the fuel constituents. Just as it is impossible to preclude local melting in the vicinity of fission tracks, it is impossible to preclude small amounts of liquid formation caused by the fission products. This microscopic melting is not damaging to the fuel or to the cladding.

4.0 Within the bounds of normal operation and reactor maneuvering, the power-to-flow ratio and power in the hottest fuel pins, regardless of cladding type, shall be less than the minimum values for macroscopic eutectic liquefaction at the fuel-cladding interface.

Exceeding the eutectic liquefaction temperature while within the bounds of normal operation is not acceptable in order to meet functional requirement (1), Section 2.1.1. However, as will be discussed below in criterion 6.0, the temperature threshold can be exceeded for short times during off-normal reactor operation, outside the bounds of normal operation, without excessively damaging the fuel pins.

The source of the eutectic liquefaction at the interface is the metallurgical interaction of metallic U-Pu-Zr fuel and fission products with the iron-based cladding to form a low melting point phase. Just as it is impossible to preclude microscopic melting within the bulk of the fuel, it is equally impossible to preclude microscopic fuel melting at the interfaces between certain phases that may form at the fuel-cladding interface. However, the safety and reliability concerns involve assuring that the cladding remains intact and that fuel motion cannot lead to increases in reactivity or regions of high smear density. The above limits are designed to satisfy these concerns. For U-20Pu-10Zr fuel the maximum interface temperature for which macroscopic liquefaction does not occur is taken to be 650°C (1202°F) for Mark-V (HT9) and 660°C (1220°F) for Mark-VA (316SS). The FBTA results discussed in Section 5.0 of this report provide the bases for these values.

5.0 During normal operation the plenum pressure shall be less than that which would cause a peak, radially-averaged hoop stress in the cladding of 150 MPa in the hottest pin.

The purpose of this limit is to preclude unstable plastic deformation. The parallel criterion in the CRBR PSAR [2.5] was that the primary equivalent stress remains below 90% of the yield strength. However, the yield strength of cladding materials at high temperatures depends on the strain rate at which the defining tensile tests are performed. Thus, using the yield strength as a limit does not uniquely define the criterion unless the strain rate is specified. On the other hand, the flow stress for both HT9 and 316SS cladding materials does become nearly strain-rate independent above a certain stress, which depends on the temperature. If the cladding is subjected to stresses near this level, the strain rates increase very rapidly. The primary loading due to internal gas pressure is most damaging in this regime because it can lead to plastic instability. Stresses caused by secondary loads, such as thermal stresses, do not lead to plastic instability since the plastic deformation acts to relieve the stresses. Since internal gas pressure is the only loading which leads to plastic instability, a limit on gas pressure, or, rather, on the radially-averaged hoop stress caused by gas pressure, is the appropriate criterion for precluding plastic instability. Criterion 5.0 therefore includes only the hoop stress produced by gas pressure, not stress from fuel-cladding mechanical interaction (FCMI), since stress from FCMI does not lead to plastic instability.

The value of 150 MPa for the hoop stress limit was set by limiting the gas pressure, or hoop

stress, to levels below which burst failures do not occur in pressurized cladding tubes. This was the approach that was taken in developing the safety package [2.16] for the continued irradiation of subassemblies X425B and X429B in EBR-II. In that safety package it was argued that plastic instability would not occur if the cladding hoop stress remained below the high stress branch of the biaxial stress rupture curves. The locus of points that define the intersection of the high stress and low stress branches of these curves is a weak function of temperature for both 316SS and HT9 cladding materials (see Figure 1, Property Code 2202, Section 5; and Figure 1, Property Code 2202, Section 10 of Ref. 2.17). The high stress branches always begin at hoop stresses greater than 150 MPa for temperatures less than 650°C.

The 150 MPa limit can be compared with the 90% yield strength criterion by comparing the equivalent stress with the cladding yield strengths. For this purpose a peak cladding temperature of 650°C will be assumed and the increase in yield strength that radiation hardening causes will be neglected. Assuming 2:1 biaxial gas pressure loading, the equivalent stress in the cladding equals 130 MPa if the hoop stress is 150 MPa. On the other hand, 90% of the yield strength of 316SS at 650°C is 305 MPa, and 90% of the yield strength of HT9 at 650°C is 170 MPa, both measured at a strain rate of 10^{-4} s^{-1}. Thus, the 150 MPa limit is somewhat more conservative than the CRBR limit.

EBR-II has an additional limit upon predicted gas pressure in fuel pins of 1800 psi imposed in order to ensure that there will be no damage to hex ducts caused by pressure loading after fuel pin failure. Imposition of the design criteria that the plenum pressure should lead to a peak, radially-averaged hoop stress in the cladding of less than 150 MPa in the hottest pin ensures that this limit will be met.

6.0 During all Anticipated Events, the single most-damaging Unlikely Event, and the Extremely Unlikely Event, the cumulative eutectic penetration of both HT9 and 316SS cladding shall be less than 5% of the wall thickness.

At temperatures above the eutectic liquefaction threshold (see Criterion 4.0) the time scales for eutectic penetration into the cladding and liquefaction of the fuel are comparable to the time scales of accident transients [2.18]. The damage done to the cladding at these temperatures is implicitly accounted for in the transient CDF and strain limits (Criterion 7.0 and 8.0 below) since

the analyses of cladding mechanical behavior include eutectic penetration as one of the forms of cladding wastage (see Section 2.1.3). The purpose of the additional restriction on the total amount of cladding attack to 5% of the wall thickness is to limit quantity of liquid formation to 10%.

The value of 5% was chosen to be consistent with the current EBR-II Mark-II fuel limit on eutectic attack during accident transients. Although this limit is stated in terms of a temperature-time limit of 1500°F (816°C) for 60 s, its origin is based on a maximum of 5% reduction in cladding wall thickness [2.19]. The corresponding quantity of liquid formation can be estimated by assuming that the atom ratio of the fuel to cladding constituents in the liquid has the same ratio as the eutectic in the uranium-iron binary system (0.65/0.35). It should be noted that, because of the Arrhenius temperature dependency of the eutectic penetration rate, only limited amounts of fuel at the hottest axial elevations of the hottest pins in the core liquify during transients where the eutectic threshold is exceeded. Capillary and viscous forces are capable of preventing the relocation of such small amounts of fuel over the time scale of accident transients [2.20]. This is consistent with the results of the FBTA tests discussed in Section 5.2.3 where the liquid eutectic formed at the fuel-cladding interface remained in place in spite of the fact that the small segments of test fuel were open at both ends.

7.0 During all Anticipated Events and the single most-damaging Unlikely Event, the cumulative transient CDF for both 316SS and HT9 cladding shall be less than 0.1. The effect of steady-state and transient wastage due to metallurgical interaction between the fuel and the cladding shall be accounted for by assuming that any interaction zones are strengthless.

The basis for the CDF approach and its relationship to the CRBR design requirements were given in Criterion 2.0 above. The transient CDF correlations, (see Sections A.2.1.2 and A.2.2.2) for both cladding types are based on the results of the HEDL (Westinghouse Hanford Company) Fuel Cladding Transient Tester (FCTT) tests [2.21]. In these tests, cladding tubes cut from irradiated fuel pins are pressurized and subjected to transient heating at various temperature ramp rates. The measured failure temperatures are used to determine time-to-rupture correlations as a function of stress and temperature. The transient failure strains are also measured.

The complete data base for 20% Cold-Worked Type 316 Stainless Steel cladding is given in Ref. 2.22. Based on these data, the Transient Pin/Cladding Failure Criteria Task Force [2.23]

recommended that the TDC-2 correlation [2.24] be adopted as the principal cladding failure correlation for 316SS. An evaluation of this criterion for application to transient cladding failure analysis in oxide-fueled fast reactors is given in Ref. 2.25.

The TDC-2 correlation is also being used for the analysis of the transient behavior of metal-fueled fast reactors with austenitic stainless steel cladding (316SS and D9). However, for metallic fuels there is no evidence of the "Fuel Adjacency Effect" [2.26] so that the term FAE in the TDC-2 correlation is set equal to zero. The validation of the TDC-2 model for application to metallic fuels is based on calculations of the failure of D9-clad fuel pins in the TREAT M Series tests, as discussed in Sections 4.3 and 5.0.

The data and transient time-to-rupture correlation for HT9 cladding are reported in Ref. 2.27. This correlation has been incorporated into FPIN2, LIFE-METAL and DEFORM-5 (see Sections 4.2 and 4.3) and has been extensively validated for analyzing metallic fuel failure using the results from the TREAT tests and the WPF tests (see Section 5.0). The basis for the allowable transient CDF value of 0.1 is a statistical analysis of the FCTT data where it was shown that a transient CDF less than 0.103 is sufficient to assure, with 95% confidence, that the failure probability will be less than 1/3000 [2.28].

8.0 During all Anticipated Events and the single most-damaging Unlikely Event, the cumulative thermal component of the plastic diametral strain for HT9 cladding shall be less than 1%. The comparable limit for 20% Cold Worked Type 316 Stainless Steel Cladding is 0.1%. The effect of steady-state and transient wastage due to metallurgical interaction between the fuel and the cladding shall be accounted for by assuming that any interaction zones are strengthless.

In the CRBR PSAR [2.5] the total allowable permanent strain in 316SS cladding was 0.3% for normal operation plus all transients. Requirements 1.0 and 8.0 for Mark-V fuel with 316SS cladding are equivalent to the CRBR design requirement. In addition, the requirement of 0.1% transient plastic strain is consistent with the results of the FCTT tests [2.21] on 316SS cladding samples cut from regions of oxide fuel pins that were not adjacent to the fuel column. The diametral strain in regions near the failure site ranged from 0.2 to 2%, with the exception of one test at a pressure (14,300 psi, or 98.6 MPa) much greater than that of interest here.

The ductility of irradiated HT9 cladding is considerably greater than that of irradiated

austenitic cladding materials. This can be seen by comparing the measured strains from the FCTT tests on HT9 cladding [2.27] with those for 316SS cladding [2.21]. In the HT9 FCTT tests the peak plastic strain measured by the extensometer ranged from 2% to 18%, except for a single measurement at 1.0%. In addition, the uniform strains measured by averaging the diameter changes along the samples after the tests were greater than 3% for pressures less than 5000 psi (34 MPa). The tests at higher pressures, which are not relevant here, tended to cause very localized failures because of plastic instability.

It should also be noted that the HT9 transient cladding deformation model (see Section A.3.2) that is being used to analyze the response of Mark-V fuel pins to accident events has been validated using the results of the FCTT tests. A plastic strain-to-failure of 6% was found to predict the failure temperature measured in the tests. This observation, in addition to the measured plastic strains, suggests that the design requirement of 1% is sufficiently conservative to preclude cladding failure during accident transients.

9.0 For all Design Basis Events, including Extremely Unlikely Events, the core shall remain coolable.

The only functional requirement for Extremely Unlikely Events is that the core remain coolable. Fuel pin failures may occur and the core may be damaged to the extent that it has to be replaced.

Core coolability is guaranteed if two conditions are met:

1. The cladding does not melt.
2. Cladding failures do not lead to significant blockages.

Condition 1 is met if no coolant boiling occurs, since it is impossible for the cladding to melt if the sodium remains below the boiling point. Condition 2 is met if insufficient molten material is available to form blockages or if the cladding failures are of the pinhole type.

In the case of metallic fuels, assurance of no sodium boiling precludes cladding melting, since it is impossible to reach the bulk melting temperature of the cladding (about 1400°C) unless coolant boiling occurs. Also, criterion 3.0 assures that there will be no bulk fuel melting during

anticipated or unlikely events. A certain amount of fuel-cladding interfacial melting may occur during off-normal events. However, both in-pile and out-of-pile metallic fuel cladding breach experiments consistently indicate that these breaches are of the pinhole type and are therefore benign with respect to blockage formation (see Secs. 5.2.2, 5.2.3, and 5.2.4 for discussion of cladding breach experiment results). In the specific case of Mark-V/VA fuels, the results of the thermal-hydraulic analyses presented in Sec. 9.7 indicate that no fuel melting occurs even during the extremely unlikely event and that only very small amounts of eutectic form during the low flow transients within the design basis. Therefore, neither significant flow blockages nor pin-to-pin failure propagation are indicated for Mark-V/VA fuels. Consequently, core coolability during design basis off-normal events is assured if the bulk sodium temperature remains below the boiling point.

2.2 Structure Evaluation Criteria for the Fuel Subassembly

Structural evaluation criteria are an important part of demonstrating that a design can safely and reliably perform its function during its service life. These evaluation criteria specify limits on stresses, strains, deformations, and other parameters that the design can tolerate under the maximum postulated loadings. The evaluation criteria of the Mark-V fuel subassembly are based on the NE Standards F9-7, -8, and -9 [2.31 - 2.33] which specifically address core components in fast breeder reactors. Section III of the ASME Code (Subsection NB and Code Case N-47 [2.34] serves as a conservative guide to what a complete set of criteria should cover. The criteria are consistent with experience with similar subassemblies that have been irradiated in EBR-II and other reactors.

An important element to satisfy the NE-Standard criteria is the service classification of the structural components for various plant events and transients. This classification reflects the effect of the component response on the overall plant response. Basically, component classification determines the service limits (limits on stresses and other parameters) that can be tolerated by the component for a given event. A component could have one of four levels of service limits (Levels A, B, C, or D), with Level A service being the most stringent and Level D service the least stringent. The Mark-V fuel subassembly is conservatively considered as a component that must withstand loadings with a high degree of confidence and thus will be assigned the Level A service limits for normal operation and anticipated faults. The subassembly will be

assigned Level B service limits for unlikely faults and either Level C limits or Level D limits for extremely unlikely faults.

The present structural evaluation criteria cover all parts of the fuel subassembly excluding the fuel bundle, which is considered only in terms of its interaction with the hexagonal ducts. The evaluation criteria will concentrate on the ducts, since they are an integral part of the reactor core and as a result are subjected to large neutron fluences that depend heavily on the core composition and fuel burnup. Two alternative duct materials are used in Mark-V fueled subassemblies: HT-9 alloy steel and CW Type 316 stainless steel. Physical properties for both materials are taken from Ref. 2.6.

2.2.1 Allowable Stresses and Strains

Reference 2.31 is intended to provide protection against ductile rupture from short- term loadings and gross distortion from incremental collapse and ratcheting by setting upper limits on either the stresses or inelastic strains. Stresses are to be determined by elastic analyses in which mechanical loadings, thermal loadings, and interaction between subassembly and neighboring components are modeled. The stress limits that need to be satisfied can be summarized as follows:

(1) Primary Membrane Stress Intensity Limit:

$$P_m < \alpha * S_F,$$

where

S_F = Minimum $\{1.66\ S_y\ ,\ S_u\}$

S_y = Yield stress

S_u = Ultimate stress

α = 0.55, 0.66, and 0.75 for Service Levels A, B, and C, respectively.

(2) Primary Membrane Plus Bending Stress Intensity Limit:

$$P_L + P_b < \alpha * K_t * S_F,$$

where

P_L = Local primary membrane stress

P_b = Bending stress

K_t = Bending shape factor [2.32].

(3) Primary Plus Secondary Stress Intensity Limit:

(i) For axisymmetric structures subjected to axisymmetric loadings and for material exhibiting a minimum uniform elongation of 1% at the time under consideration, the sum

$$(P_L + (P_b/K_t))_{max}/S_y + (Q)_{max}/S_y$$

as a function of axial location is restricted to be within a modified shakedown boundary, defined in Figure 5 in Ref. 2.31, for all normal operation and anticipated faults. The S_y in this expression is the average yield stress at the maximum and minimum section temperatures during the period of time under consideration and $(Q)_{max}$ is the maximum range of secondary stress intensity. The structure is considered unstable beyond the shakedown boundary.

(ii) For material with a minimum uniform elongation less than 1%,

$$(P_L + P_b + Q)_{max} < \chi * S_u,$$

where χ = 0.60, 0.75, 0.90 for Service Levels A, B, and C, respectively.

(4) Maximum Primary Principal Stress Limit:

$$S_{max} < S_u$$

for RA/TF < 10%, where RA is the reduction in area and TF is the stress triaxiality factor [2.31]. The S_{max} is the largest principal stress, including the effect of stress concentration.

Reference 2.31 permits stresses higher than the above limits on condition that the design meet requirements on inelastic strains that are limited by material ductility. In this case, a complete inelastic analysis must be performed which covers elastic, thermal, plastic, thermal-creep, irradiation-creep, and irradiation swelling strains. Limits are then imposed on the two types of strains: (i) membrane plastic plus thermal creep strains at locations away from local structural

discontinuities and (ii) peak plastic strain at any structural point. The allowable strain limits have to be determined from material test data as functions of temperature and neutron fluence.

It is important to point out that Ref. 2.31 does not impose limits on the amounts of irradiation creep and swelling strains, as these types of strains are not considered to be ductility limited. However, the effects of both irradiation creep and swelling on stress and strain calculations must be included in a complete inelastic analysis. In addition, the effects of these irradiation-induced strains must be taken into account to satisfy the deformation limits for functional adequacy described in Section 2.2.3.

2.2.2 Creep-Fatigue Damage

The total cumulative damage (D) is the sum of the creep damage (D_c) and the fatigue damage (D_f). This total damage is to be maintained below a specified limit (β) which depends on the service limit classification of the component. The β value is to be maintained below 0.1 for Level A service limits, 0.5 for Level B service limits, and 0.9 for level C service limits. This means that D (based on the fuel subassembly classification provided earlier) due to normal plus anticipated faulted events should be below 0.1, while D due to these events plus the unlikely faulted events should be below 0.5. More details about the procedures for calculating D_c and D_f are given in Section 7 of Ref. 2.32.

2.2.3 Deformation Limits for Functional Adequacy

For core subassemblies, functional requirements are particularly important since they usually are the limiting design criteria. The essential functional requirements of the fuel subassembly are: (i) provide support and protection for the fuel pin-bundle and other components of the subassembly; (ii) provide a controlled path for the primary coolant; (iii) provide a compact structural unit that can be easily moved in and out of the reactor core by the refueling machine; and (iv) interact with adjacent subassemblies, retaining ring, and core support plates in a manner that assures safe and predictable reactor geometry.

With regard to duct dilation, the maximum dilation of any subassembly is limited to 1.016 mm (40 mils) by the size of the hole in the storage basket. This limit is considered to be an operational limit since it has no impact on reactor safety. Duct dilation is to be determined as accurately as possible by an inelastic analysis that takes into account thermal creep, irradiation-

induced creep, irradiation-induced swelling, and plasticity.

Limits on subasembly bowing will be imposed indirectly in terms of the effect of subassembly bowing on the interassembly forces during reactor operation and refueling. During refueling, large interassembly forces could impede the removal or insertion of the subassemblies. The present settings of the EBR-II fuel handling system are as follows: gripper pull and push forces at 2224N (500 lb_f) each, and hold-down push force (holding the six neighboring subassemblies) at 1779N (400 lb_f). The gripper forces can be increased up to 2891N (650 lb_f) by a special procedure. In order for the subassembly handling operation to be classified as normal, the largest force required (determined analytically) to remove a fuel subassembly must not exceed two-thirds the value of the normal settings, i.e. 1481N (333 lb_f). Testing indicated that the subassembly could withstand a pull force of 8896N (2000 lb_f). The 2891N (650 lb_f) load is considered to be the limit in fuel handling in the structural evaluation.

2.2.4 Non-Ductile Failure Protection

The non-ductile failure of the subassemblies is addressed since alloy HT-9 is a ferritic stainless steel which exhibits a marked drop in ductility at low temperatures or high fluence. Non-ductile fracture could lead to subassembly failure at stresses well below those corresponding to ductile failure [2.35]. Generally, there are two important parameters to consider in the the non-ductile failure of ferritic materials: (i) the operating temperature relative to the material Ductile-Brittle Transition Temperature (DBTT) and (ii) the amount of material embrittlement induced by fast flux irradiation. The material embrittlement is manifested in the form of an increase in the DBTT and also in a lower upper-shelf of fracture toughness at temperatures above the DBTT. References 2.36 and 2.29 investigated the issue of HT9 ductility and provided an assessment for the effect of irradiation at various temperatures. The largest increase in the DBTT reported in Ref. 2.29 occurs when the material is irradiated at 360°C with the DBTT increasing from 0°C (for the unirradiated condition) to 180°C.

The evaluation of non-ductile failure protection in the case of fuel subassembly ducts made of HT-9 alloy steel will be as follows:

(1) The DBTT of HT-9 is 180°C. For temperatures that are at least 33°C above the DBTT, HT-9 steel, whether unirradiated or irradiated, is considered to be sufficiently

ductile that no non-ductile evaluation is required. At EBR-II reactor operation conditions, the subassembly temperature is always higher than 213°C, and so no analysis is required.

(2) During fuel handling in the inter-building coffin and the fuel unloading machine, the duct temperature is below 213°C. For temperatures below 213°C, detailed fracture mechanics calculations as outlined in Ref. 2.32 are used to demonstrate that the duct material can withstand the applied loads. According to Ref. 2.32, it is required to demonstrate that the largest stress intensity factor is less than one-half the fracture toughness of the material. A duct fracture analysis under these conditions is discussed in Sec. 8.4., item (5).

Pressure vessels made of austenitic stainless steels normally do not require consideration of non-ductile failure [2.34]. However, when irradiated to high neutron fluences, these steels show a sharp drop in ductility exhibited in the form of smaller elongation and lower fracture toughness. Pronounced drop of fracture toughness has been demonstrated in Ref. 2.30 for a number of annealed austenitic steels. Type 316 base metal and Type 308 weld were among the austenitic steels tested. Fracture toughness of 20% CW Type 316SS was also measured at various temperatures before and after irradiation and reported in Ref 2.37. Unlike the case of ferritic steels, the drop in the fracture toughness of these austenitic steels is attributed not to higher DBTT but to lower upper-shelf energy levels.

Fracture mechanics procedures are used to demonstrate that the 316SS duct will withstand the applied mechanical and thermal loads. The stress intensity factor for the largest postulated cracks permitted by the pre-service inspection is shown to be less than one-half the fracture toughness at the worst combination of temperature and fluence.

2.2.5 Special Requirements for Weldments

The special requirements for weldments provided in Article T-1710 of Ref. 2.34 are taken into account in the evaluation of the Mark-V subassembly design. These requirements guard against the potential for limited ductility of weldments at elevated temperatures and the potential for high strain concentrations, particularly in the heat-affected zone of weldments. The special requirements in Ref. 2.34 affect the inelastic strain limits and creep fatigue damage evaluation.

The inelastic strains (only those strains that are limited by material ductility) in the weld region are limited to one-half the strain values permitted for the parent material. The creep fatigue damage evaluation utilizes reduced values for the allowable number of design cycles N_d and the allowable time duration T_d.

The N_d value for weldments are one-half the value permitted by the parent material. The T_d is determined by multiplying the parent material strength values by weld strength (stress rupture) reduction factors. These weld strength reduction factors depend on the parent material and weld material as well. They are provided in Ref. 2.34 for those materials permitted for pressure vessels in elevated temperature service only. The stress rupture factors of the annealed Type 316SS (provided in Ref. 2.34) are used with the CW form of the same steel.

Weldments are not a concern for the HT-9 ferritic steel duct, since the duct is connected to the upper and lower preassemblies mechanically, rather than by weldments.

2.3 Summary

This section has presented the design and operational requirements imposed upon the Mark-V and Mark-VA fuels, the specific design criteria that they must meet in order to satisfy the requirements and the key physical phenomena of the fuel and cladding that determine the evaluation of the fuel types against the specific design criteria. Structural evaluation criteria for the Mark-V fuel subassembly design have also been discussed.

Section 2 References

2.1 *Code of Federal Regulations*, Title 10, Part 50 (January 1, 1991).

2.2 D. J. Hill, W. A. Ragland and J. Roglans-Ribas, "EBR-II Level 1 Probabilistic Risk Assessment," Revision 2 June 30, 1991, Argonne National Laboratory.

2.3 H. P. Planchon et al., "The Experimental Breeder Reactor II Inherent Shutdown and Heat Removal Test - Results and Analysis," *Nucl. Eng. Des.*, 91, 1986.

2.4 G. L. Hofman, et al., "Metallic Fuels Handbook," Argonne National Laboratory, ANL-IFR-29 (November 1985).

2.5 Clinch River Breeder Reactor Project Preliminary Safety Analysis Report, Project Management Corporation (April, 1978).

2.6 *Nuclear Systems Materials Handbook*, Vol. 1: Design Data, Oak Ridge National Laboratory Report TID 26666. (Note: Correlations and data used represent the most recent contributions as of October 1991)

2.7 C. Martinez and R. J. Puigh, "Interim Report on Pressurized Tube Data from MOTA-1E (Cycle 9)," Westinghouse Hanford Company Report WHC-SP-0227 (January, 1988).

2.8 D. C. Jacobs, "The Development and Application of a Cumulative Mechanical Damage Function for Fuel-Pin Failure Analysis in LMFBR Systems," Clinch River Breeder Reactor Plant Report CRBR-ARD-0115 (August, 1976).

2.9 ASME Boiler and Pressure Vessel Code, 1983 Code Cases, Nuclear Components, The American Society of Mechanical Engineers, New York (1983).

2.10 R. L. Huddleston, "An Assessment of the Linear Time-Fraction Damage Theory Utilized for Design of Liquid-Metal Reactor Structural Components," Oak Ridge National Laboratory Report ORNL-6109 (January, 1985).

2.11 F. C. Monkman and N. J. Grant, "An Empirical Relation Between Rupture Life and Minimum Creep Rate in Creep Rupture Tests," *Proc. American Soc. for Testing Materials*, 56, 593 (1956).

2.12 J. M. Kramer, Argonne National Laboratory, unpublished information, (1992).

2.13 U.S.N.R.C., "Standard Review Plan," NUREG-0800, July 1981.

2.14 J. F. Koenig et al., "Irradiation of Mark IA Fuel Element with Bond Sodium Defects," Argonne National Laboratory Progress Report, ANL-RDP-30, 1.10, (July, 1974).

2.15 J. F. Koenig et al., "Irradiation of Mark IA Fuel Element with Bond Sodium Defects," Argonne National Laboratory Progress Report, ANL-RDP-45, 1.14, (November, 1975).

2.16 Argonne National Laboratory, unpublished information (1989).

2.17 Nuclear Systems Materials Handbook, Vol. 2: Supporting Documentation for Design Data, Oak Ridge National Laboratory Report TID 26666. (Note: Correlations and data used represent the most recent contributions as of October 1991)

2.18 T. H. Bauer, G. R. Fenske and J. M. Kramer, "Cladding Failure Margins for Metallic Fuel in the Integral Fast Reactor," *Transactions of the 9th International Conference on Structural Mechanics in Reactor Technology*, Lausanne, (August 17-19, 1987).

2.19 E. M. Dean and J. I. Sackett, "Response of EBR-II to Off-Normal Primary Coolant Flow," Argonne National Laboratory Report ANL-75-40 (August, 1976).

2.20 J. M. Kramer, Argonne National Laboratory, unpublished information (1991).

2.21 G. D. Johnson and C. W. Hunter, "Mechanical Behavior of Fast Reactor Fuel Pin Cladding Subjected to Simulated Overpower Transients," Hanford Engineering Development Laboratory Report HEDL-TME 78-13 (June, 1978).

2.22 C. W. Hunter, "Transmittal of FCTT Data Base for Cladding Failure Criteria," letter to A. Biancheria, D. B. Atcheson and G. D. Johnson (March 9, 1982).

2.23 "Final Report of the Transient Pin/Cladding Failure Criteria Task Force," C. W. Hunter, Chairman, Draft Report (January, 1983).

2.24 W. F. Brizes and M. L. Hamilton, "Development of a New Transient Damage Correlation for CW 316 Fuel Pin Cladding," in Hanford Engineering Development Laboratory Report HEDL TC-160-35, 201 (1982).

2.25 J. M. Kramer and R. J. DiMelfi, "An Evaluation of Transient Fuel Pin Cladding Failure Criteria for Application to Inherently Safe LMFBR Designs," Argonne National Laboratory Report ANL/RAS 84-6 (March, 1984).

2.26 C. W. Hunter and G. D. Johnson, "Fuel Adjacency Effects on Fast Reactor Cladding Mechanical Properties," Proceedings of the International Conference on Fast Breeder Reactor Fuel Performance, Monterey, California, 478, ISBN 0-89488-105-3, (March 5-8, 1979).

2.27 M. L. Hamilton and N. S. Cannon, "HT9 Transient Data Base and Failure Correlation," Hanford Engineering Development Laboratory Report HEDL-TC-2681 (March 1985).

2.28 O. Derollepot, Argonne National Laboratory, unpublished information (1991).

2.29 F. H. Huang, "Effect of Irradiation on the Fracture Behavior and Tensile Properties of an HT9 Duct," Westinghouse Hanford Company Report WHC-SP-0454 (May 1989).

2.30 W. J. Mills, "Fracture Toughness of Irradiated Stainless Steel Alloys," *Nuclear Technology*, 82, 290 (1988).

2.31 "Structural Design Guideline for FBR Core Components - Structural Design Criteria," RDT F9-7, Draft, August 1978.

2.32 "Structural Design Guidelines for FBR Core Components - Guidelines for Analysis," RDT F9-8, Draft, August 1978.

2.33 "Structural Design Guideline for FBR Core Components - Rational," RDT F9-9, Draft, August 1978.

2.34 *ASME Boiler and Pressure Vessel Code*, Section III, Class 1 Components in Elevated Temperature Service, Case N-47-28, July 27, 1988.

2.35 E. A. Little, "Fracture Mechanics Evaluations of Neutron Irradiated Type 312 Austenitic Steel," *Journal of Nuclear Materials*, Vol. 139, pp. 261-279, 1986.

2.36 G. D. Johnson, "The Mechanical Properties of Alloy HT9," Westinghouse Hanford Company, Westinghouse Hanford Company Report WHC-SP-0230, February 1989.

2.37 M. L. Hamilton et al., "Mechanical Properties of Irradiated FFTF First Core Stainless Steel," Hanford Engineering Development Laboratory, HEDL-TC-2223, pp. 28-31, September 1982.

3 DESIGN DESCRIPTION OF EBR-II DRIVER SUBASSEMBLIES WITH MARK-V AND MARK-VA FUEL PINS

3.1 Fuel Pins

The EBR-II Driver Subassembly is designed to utilize 61 fuel pins with external dimensions of 0.230 inch (5.84 mm) diameter cladding, 0.042 inch (1.07 mm) diameter spacer wire and overall length of 29.500 inches (0.75 m) [3.1]. The fuel pins are attached to a grid which maintains the bottom of the fuel slug at the bottom of the core, an elevation of 24.562 inches (0.624 m) above the top of the reactor grid. The Mark-V fuel pins are planned to be fabricated of both HT9 and 316SS stainless steel clad materials (designated Mark-V and Mark-VA respectively). Both Mark-V and Mark-VA fuel pins will be used in the subassembly design that has a 316SS duct. The cladding thickness and fuel slug diameter for the Mark-VA fuel pins are 0.015 and 0.173 inches (0.38 and 4.4 mm) respectively, the cladding thickness and fuel slug diameter of the Mark-V fuel pins are 0.018 and 0.168 inches (0.46 and 4.27 mm), respectively, while the fuel pins have the same outside diameters. A subassembly with an HT9 duct is also included, however this will be used only for the HT9 fuel pins.

A fuel specification has been developed for the Mark-V and Mark-VA fuel which combines the intent of dimensional and chemical requirements that have traditionally been utilized in the Mark-III, Mark-II and Mark-IIIA fuel fabrication process with those additional requirements necessary to be addressed for reprocessed U-Pu-Zr fuel fabricated remotely in the FCF hot cells. In addition, the quality assurance requirements necessary to assure that the fuel pins are leak tight and that the fuel is properly bonded to the cladding for thermal transfer, as adapted to the FCF manufacturing process, are included. The chemical requirements further ensure that the fuel will perform in a predictable manner with respect to swelling, fuel/cladding compatibility, etc. This will ensure that conservative assumptions made in this document with respect to "eutectic" temperature, fuel solidus temperature, etc. remain conservative.

The fuel specification is intended to assure that a fuel pin is produced that performs in a consistently reliable manner, and that has a consistent fissile content to allow accurate prediction

of individual pin, subassembly, and core performance. The requirements that have traditionally been utilized for EBR-II driver fuel have been shown to produce fuel with these characteristics. Fuel slug size, weight, and chemical specifications are combined in the manufacturing process to ensure production of fuel which meets these requirements. The fuel reliability has also been shown to be statistically consistent. This latter characteristic is further proven for each new fuel type, built to the specification, with a full in-reactor qualification program.

As the remote reprocessing and fabrication are first accomplished, the product will be extremely well characterized in regards to the factors specific to this new fabrication process. These may include fission-product carryover, and the remote blending of feedstock from various sources available in the process scheme. The fuel specification will therefore be a "living" document at first which is designed to match characteristics of the new fabrication processes with performance as predicted in this document, and as demonstrated by the qualification program.

The uncertainties in the fuel specification have been allowed for in the analyses presented in this document by,

(1) Uncertainty analyses for fissile mass, see Section 4.5,
(2) Use of conservative material properties to bound behavior of thermal conductivity etc.,
(3) Use of a threshold temperature of 655 ± 5°C, irrespective of burnup, to bound the effect of lanthanide carryover or cladding wastage, and
(4) Inclusion of 0.7 wt.% Americium in the dose calculations of Section 10.1 (a maximum of 0.5 wt.% is allowed by the fuel specification).

3.2 316SS Driver Subassembly

3.2.1 Basic Design Features

The subassembly design with 316SS duct is identical to the Mark-III design as shown in Figure 3-1. The basic design features are:

1. The subassembly is designed to position the fuel slug of the pins at the same elevation in the reactor as those in all other driver subassemblies and to conform to other dimensional requirements as specified on EBR-II drawing EB-1-25961-E.

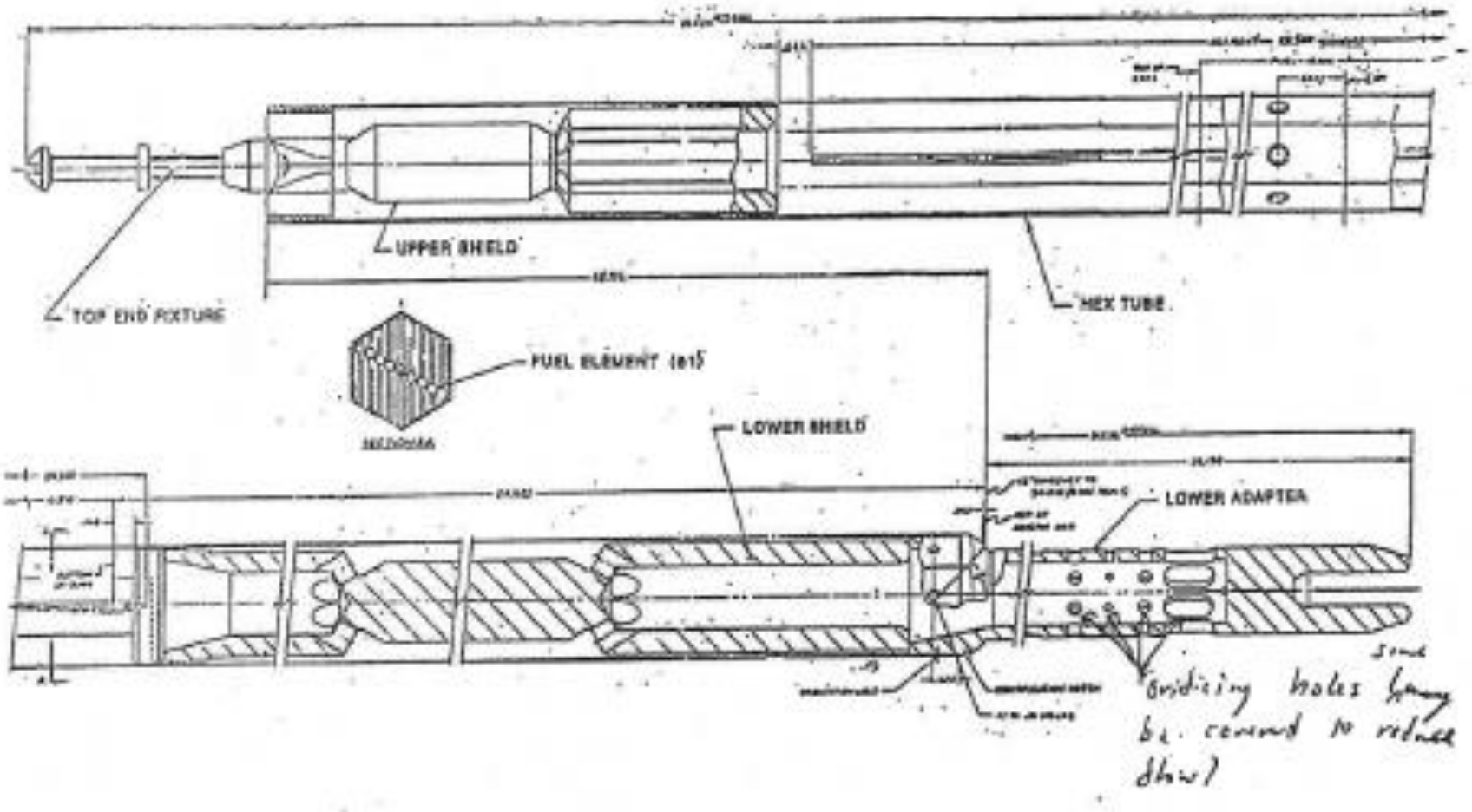

Figure 3-1 Mark-III Subassembly Design (for Mark-V Fuel Pins)

2. The subassembly is designed to be compatible with existing reactor handling equipment and procedures.
3. Radiation shielding is provided in the subassembly to protect reactor structures.
4. Sodium drainage is provided for all internal spaces.
5. The subassembly is designed to withstand a 2000 lb. (8900M) axial pull test at room temperature without permanent deformation.

3.2.2 Subassembly Hardware Description

Other than the fuel pins, the subassembly is made up of two major components, the upper and lower preassemblies, which are described below.

3.2.2.1 Lower Preassembly

The lower preassembly consists of the lower adapter, lower shield, and element grid; all three forming a welded assembly. The lower adapter is 304 stainless steel and is designed to insert and seat on the reactor grid at the specific core or blanket region position for which it is designated. It is oriented in the grid by means of a key slot at its lower end. The pole piece portion and the key slot are sized to prevent inadvertent insertion of the subassembly in other than its designated position. A spherical shoulder is provided to seat on the 45° chamfered hole of the reactor grid. The upper portion is a hexagonal form sized to accept the outer hexagonal tube and lower shield for weld attachment. Flow holes are provided in the pole piece to direct a predetermined amount of coolant through the subassembly.

The lower shield is 304 stainless steel and is provided to protect the reactor grid from neutron radiation. It is designed as two hex forms separated by a center pole with flow holes directed from the center of each hex form to the outside of the center pole. The lower shield is butt welded to the lower adapter.

The element grid is 304 stainless steel containing 9 round type grid bars brazed to a hexagonal thin walled form. The fuel pin tips are slotted with a round hole to fit the grid bars. The grid bars are spaced to accept the aforementioned 61 fuel pins. The hexagonal form of the grid is plug/fillet welded to the top end of the lower shield.

3.2.2.2 Upper Preassembly

The upper preassembly consists of the hexagonal duct, upper shield, and top end fixture, all three forming a welded assembly.

The hexagonal duct is of 316-12% cold worked stainless steel to provide improved radiation swelling characteristics to the subassembly. It has an external dimension of 2.290 inches (58 mm) nominal across flats and a wall thickness of 0.040 inches (1.02 mm). Six (6) buttons about 0.375 inches (9.5 mm) in diameter are press-formed externally to a dimension across flat of 2.319 inches (58.9 mm) maximum and are located about 1.547 inches (39 mm) above centerline of the reactor core. The buttons are provided to maintain an approximately 0.030 inches (0.8 mm) clearance between hex duct faces when contacting like buttons on adjacent subassemblies in the core.

The top end fixture is the standard handling adapter for subassemblies to be transported by the reactor's fuel handling system, which includes the core gripper, fuel unloading machine gripper and transfer arm. The top end fixture is of 304 stainless steel and includes a hexagonal base for attachment to the hexagonal duct and a pole piece for gripper handling. The pole piece has a conical nose piece for gripper entry and pickup, and is slotted for gripper sense orientation. A collar is located at the pole's mid-length for resting in the transfer arm pickup fitting and includes a rectangular section to maintain radial orientation during transfer. The top end fixture is either plug/fillet or fusion spot welded to the hexagonal tube.

3.2.2.3 Final Assembly

Final assembling of the subassembly requires installing the 61 fuel pins on the element grid of the lower preassembly, lowering the hexagonal duct over the fuel pins until seated on a shoulder of the lower adapter. The hexagonal duct is welded to the lower adapter by either plug/fillet or fusion spot welds. The completed subassembly is load tested at a 2000 lb. (8900 N) pull force. Final assembly can be performed remotely in a hot cell.

The subassembly overall length is 91.656 inches.

3.3 HT9 Driver Subassembly

When compared to the 316SS Driver Subassembly, the proposed HT9 design allows for a longer in-reactor lifetime, up to ≥ 18 at. %, should it be desired. However, the attachment of the hexagonal duct to the lower preassembly must be accomplished remotely in the Fuel Cycle Facility Hot Cell. The chosen method of attachment is by mechanical means, in lieu of making HT9 to HT9 welds which was judged unacceptable for remote fabrication.

3.3.1 Basic Design Features

The HT9 (Mark-V) subassembly design shown in Figure 3-2 and described in Ref. 3.2 is similar to the HT9 (Mark-IV) design shown in Figure 3-3 and described in Ref. 3.3. The difference between the two is that the Mark-V hex duct is attached to the HT9 hex collar of both the top end fixture and lower preassembly by a mechanical screw connection (as shown in Figure 3-4) instead of being welded.

The basic design features listed in Section 3.2.1 for the 316SS Driver Subassembly also apply to the HT9 Driver Subassembly.

3.3.2 Subassembly Hardware Description

Other than the fuel pins the Subassembly is made up of two major components, the upper and lower preassemblies which are described below.

3.3.2.1 Lower Preassembly

The lower preassembly consists of the lower adaptor, lower shield assembly (shield, hex collar, and collar retainer) and element grid; all forming a welded assembly. Six connection screws are included prior to attaching the hex duct at final assembly.

The lower adaptor is 304 stainless steel and except for the size of the upper hex portion is identical to that described for the Mark-III (316SS) Subassembly. The upper hex portion is sized at least .009 inches (0.23 mm) smaller than the HT9 hex duct to accommodate the differential thermal expansion and swelling.

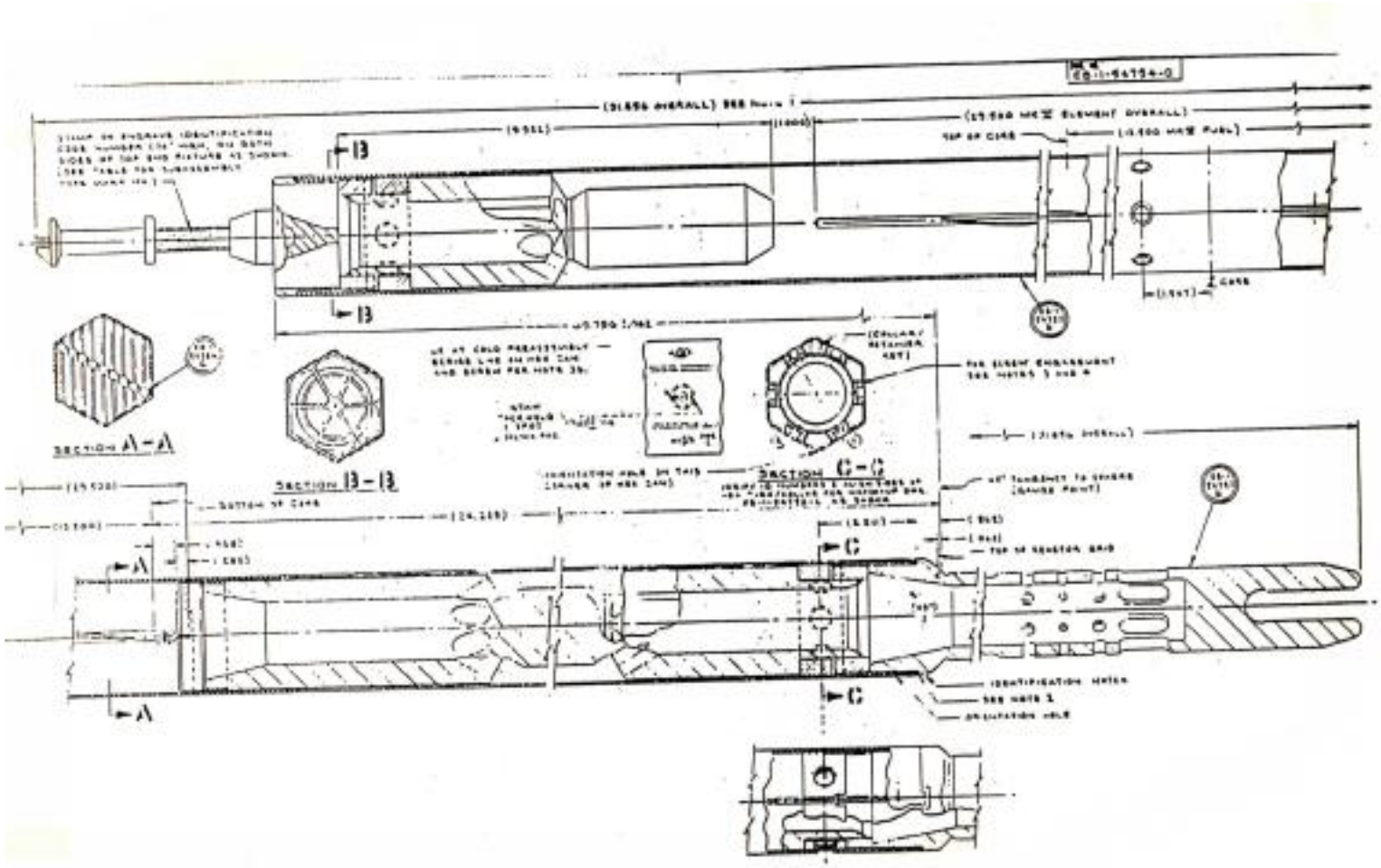

Figure 3-2 Mark-V Fueled Subassembly Design

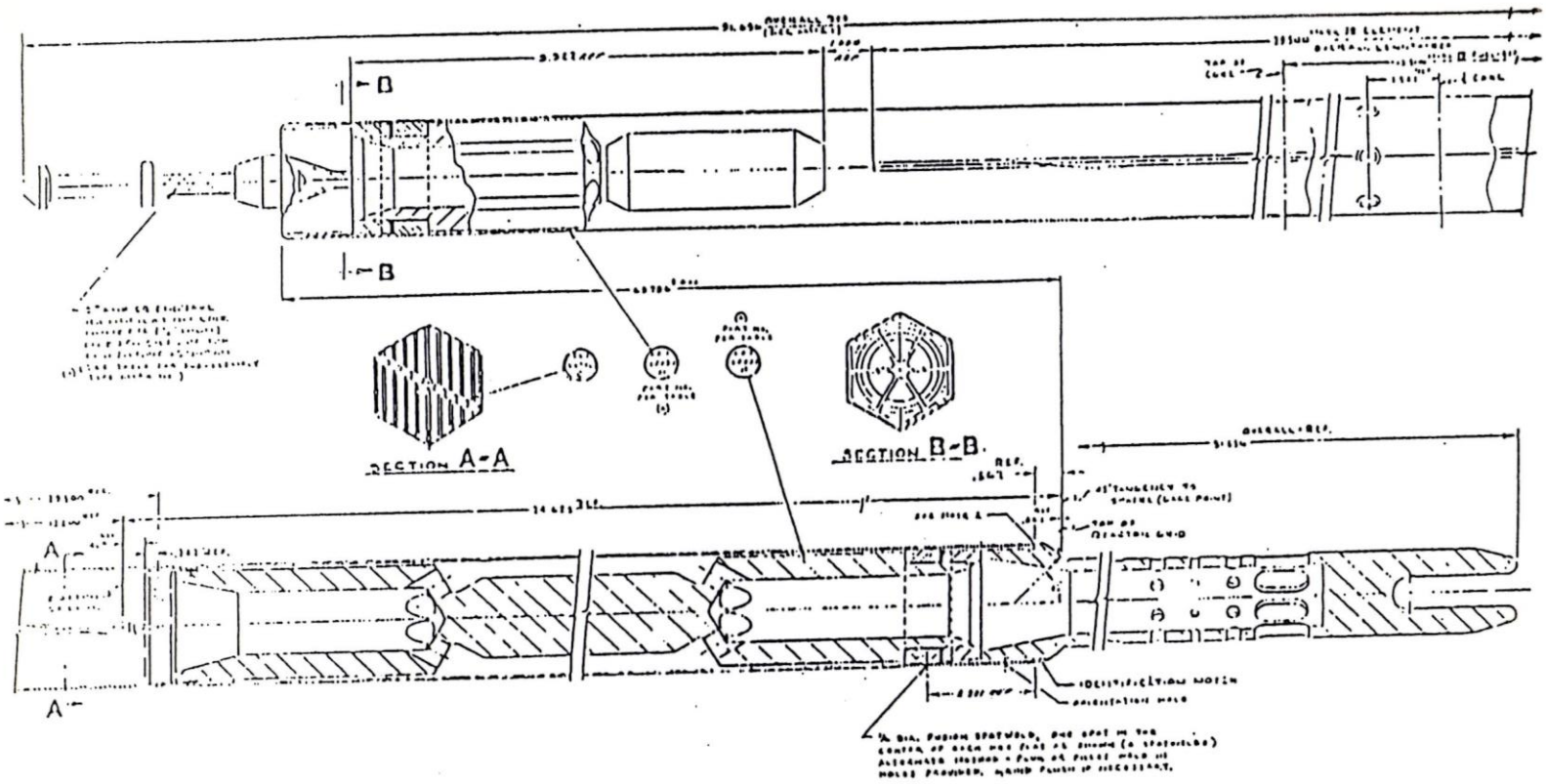

Figure 3-3 Mark-IV Fueled Subassembly Design - Basis for Mark-V Design

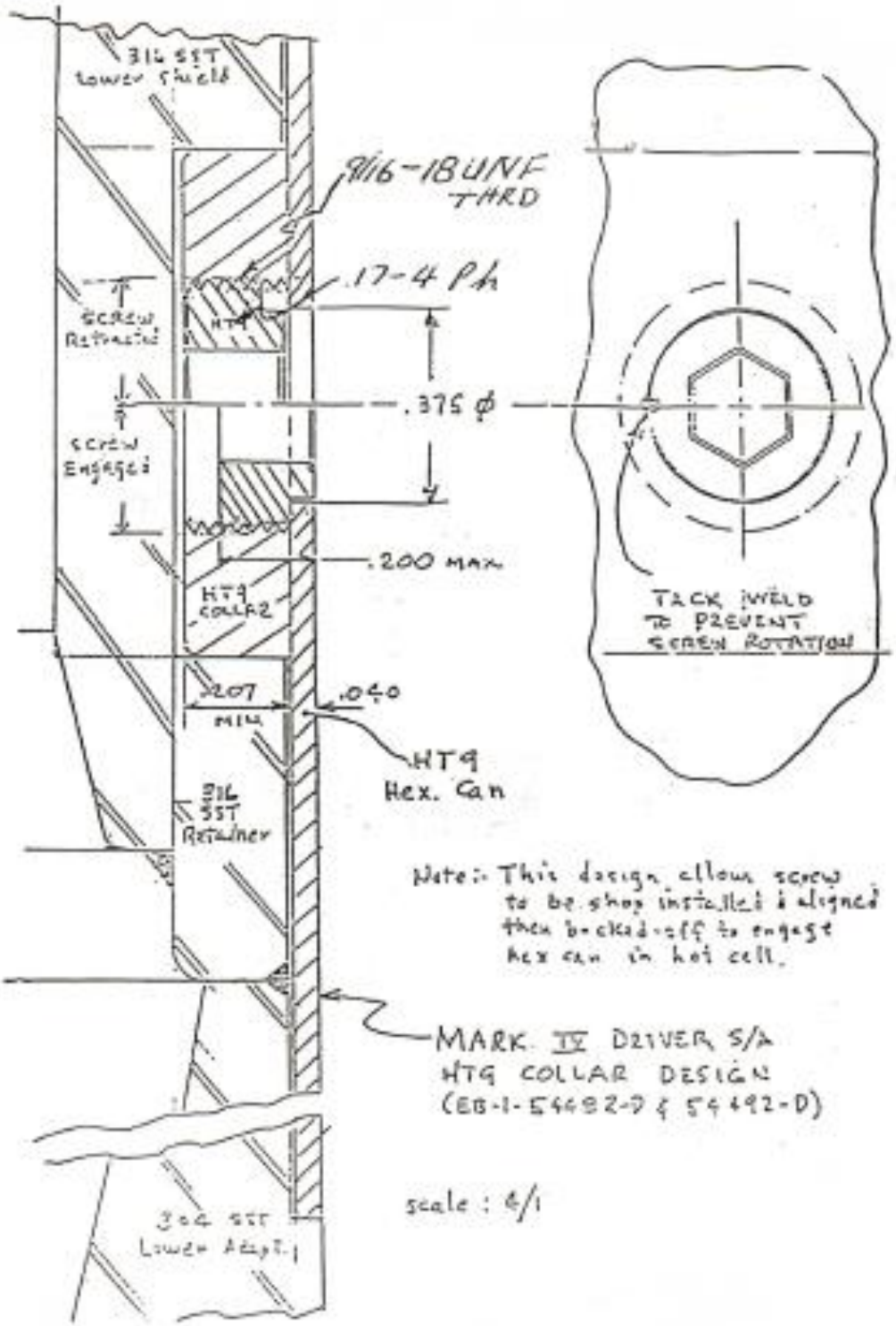

Figure 3-4 Mark-V Subassembly Mechanical Attachment

The lower shield assembly consists of a 316SS shield, HT9 hex collar, 17-4 Ph SS screws and a 316SS collar retainer. The lower shield is designed as two hex forms separated by a smaller center pole with flow holes directed from the center of each hex form to the outside of the center pole. The hex collar is captured by the collar retainer welded at the bottom of the shield. The HT9 hex collar fits with a 0.001 inch (0.0254 cm) minimum clearance to the HT9 hex duct. Each flat of the hex collar incorporates a threaded hole to accept (6) pre-installed screws (Figure 3-4) made of 17-4 Ph stainless steel hardened to Rockwell C44. The collar retainer has a face key on one end that fits into the hex collar's groove to maintain hexagonal alignment with minimum rotational clearance. The collar retainer is welded to the lower adapter for attaching the lower shield assembly.

The element grid is 316 stainless steel containing 9 round type grid bars brazed to a hexagonal thin-walled shell sized with .017 inches (0.43 mm) minimum clearance to the HT9 hex duct. The fuel pin tips are slotted with a round hole to fit the grid bars. The grid bars are spaced to accept the aforementioned 61 fuel pins. The hexagonal form of the grid is plug/fillet welded to the top end of the lower shield.

3.3.2.2 Upper Preassembly

The upper preassembly consists of the hexagonal duct, upper shield assembly (shield, hex collar and collar retainer), top end fixture, and six connection screws. The upper shield assembly and the end fixture are a welded unit to which the hex duct is mechanically attached.

The hex duct is of HT9 ferritic steel. Except for holes to attach the hex duct at the lower adaptor and top end fixture, the hex duct is identical to that described for the Mark III, Section 3.2.2.2.

The upper shield assembly consists of a 316SS shield, HT9 SS hex collar and 316 SS collar retainer. The upper shield is designed as an integral hex form stepped down to a center pole configuration with flow holes directed from the outside of the center pole to the center of the hex form. The hex collar is captured by the collar retainer welded at the top of the upper shield. The HT9 hex collar fits with a .001 inch (0.0254) minimum clearance to the HT9 hex duct.

The collar retainer has a face key on one end that fits into the hex collar's groove to maintain

hexagonal alignment with minimum rotational clearance. The collar retainer is welded to the top end fixture for attaching the upper shield assembly.

The connection of the hex duct to the hex collar is the screwed connection mentioned for the lower shield (Section 3.3.2.1).

The top end fixture is 304 stainless and is identical to that described for the Mark III Subassembly (Section 3.2.2.2) except for sizing the hex form with adequate clearance with the HT9 hex duct.

3.3.2.3 Final Assembly

Final assembly is done remotely in a hot cell and requires installing the 61 fuel pins on the element grid of the lower preassembly, lowering the hex duct of the upper preassembly over the fuel pins until seated on a shoulder of the lower adapter, manipulating the hex duct to align its screw holes with the pre-installed screws in the hex collar of the lower shield, and backing-out the screws until fully engaged in the hex duct. The screws will then be lightly tack-welded to prevent loosening.

The completed subassembly is load tested at 2000 lb (8900 N) pull force.

The subassembly overall length is 91.656 inches (2.328 m.).

Section 3 References

3.1 EBR-II Technical Memorandum No. 167, "Design and Pressure Drop Characteristics of EBR-II Mark-III Core and Blanket Region Core Subassemblies," Dated January 29, 1987.

3.2 EBR-II Technical Memorandum No. 184, "Design Characteristics of the EBR-II Mark-V Driver Subassembly, Core and Blanket Region Core," Dated June 23, 1992, (Draft).

3.3 EBR-II Technical Memorandum No. 172, "Design Characteristics of the EBR-II Core and Blanket Region Core Subassemblies Mark-IV," Dated September 12, 1988.

4 METHODS FOR DESIGN EVALUATION OF MARK-V AND MARK-VA FUEL SUBASSEMBLIES

The design evaluation of the fuel subassemblies will be carried out by a combination of proof by analysis and by a program of qualification subassemblies which will lead the introduction of the Mark-V fuel into the core. This section describes the qualification, surveillance and post-irradiation examination plans for the Mark-V and Mark-VA fuels and describes the nature and validation of the fuel behavior codes to be used in the proof-by-analysis sections later in this evaluation. The EBR-II thermal-hydraulic model validation is then discussed, and the uncertainty factors which are applied in the safety analysis are derived. Finally, the duct structural analysis models used for duct dilation prediction are described.

4.1 Mark-V and Mark-VA Fuel Qualification

Mark-V/VA fuel will be qualified for driver fuel operation under both transient and steady state conditions. Steady-state performance will be demonstrated using qualification subassemblies as described later in this section. Transient performance will be demonstrated for normal events using qualification subassemblies. Fuel performance during off-normal events has been demonstrated through testing of irradiated pins in ex-reactor simulated heating tests, which are discussed in Sec. 5.0. Qualification of Mark-V and Mark-VA fuel will be accomplished with an irradiation and testing program having the following objectives:

1) demonstrate that irradiation of Mark-V/VA fuel to the interim burnup limit is adequately enveloped by the safety case presented in this document, and that fuel behavior meets performance and safety criteria;
2) establish a margin-to-failure for Mark-V/VA fuel pins irradiated to the interim burnup limit;
3) obtain performance data that will provide a basis for extending the burnup limit beyond the interim value.

The qualification program (discussed in greater detail in the attachment [Mark-V/VA Fuel Qualification, Experiment, and Surveillance Plan, D.C. Crawford, 1992.]) will encompass

irradiation of the HT9 subassembly design to high exposure (fluences near 2 x 10^{23} n/cm^2) as well as all forms of fuel produced in the Fuel Cycle Facility (FCF) as process equipment and capability is incrementally put into operation. The first driver fuel pins expected from the FCF will likely be produced from "cold" (i.e. unreprocessed) feedstock materials. Therefore, this fuel product will be qualified as the initial Mark-V/VA driver fuel. Subsequent operation of different parts of the FCF process is expected to produce fuel product with more impurities than the initial "cold" product. Because of this, a new set of qualification subassemblies will be irradiated to qualify any fuel product that contains more impurities than the tolerances given in the fuel specification.deviations in fuel composition or fuel pin design which fall within the tolerances of the fuel specification but which, though they will not affect the burnup limit, are judged to merit further attention will be assessed through surveillance programs that can be used to address specific changes to the design.

4.1.1 Irradiation Plan

A set of qualification subassemblies consists of four subassemblies, each operating at a controlled set of irradiation conditions. These conditions include peak pin power levels and peak inside cladding temperature. Pin power level determines fuel temperature and the temperature gradient across the radius of the fuel slug. These parameters can influence phenomena such as migration of lanthanide elements to the cladding, fuel constituent migration, and fuel cracking. Similarly, peak inside cladding temperature can influence the solid state interaction between fuel and cladding as well as the ability of the cladding to withstand internal gas pressure. The four qualification subassemblies in each set will encompass the following irradiation conditions:

1) Near the maximum expected linear power rating (~18 kW/ft (59 kW/m) with uncertainty; see Section 9.4.1) for a six-row core and the associated peak inside cladding temperature;
2) Near the maximum expected peak inside cladding temperature (~615°C with uncertainty; see Section 9.4.1) for a six-row core;
3) Nominal conditions for row 4 and row 6 subassemblies in a six-row core.

To ensure that the qualification subassemblies will lead all subsequent driver subassemblies in burnup, the qualification subassemblies will be the first four subassemblies of any distinguishable fuel type produced by the FCF. In addition, these subassemblies will be treated as experimental subassemblies and xenon-tagged, aiding in identifying breach.

Therefore, any unforeseen limitations to fuel lifetime that result in premature breach will be discovered with tagged qualification subassemblies before any untagged driver subassemblies can attain similar burnup.

4.1.2 Examination and Evaluation

Performance assessment of Mark-V/VA qualification and experimental subassemblies will include both destructive and non-destructive examinations. Pins that will be returned to the reactor for further irradiation will be evaluated through several types of non-destructive examinations. Neutron radiography can be used to assess dimensional changes, axial elongation in particular, in the fuel slugs within the pins. Cladding profilometry, and possibly bow and length measurements, can be used to determine dimensional changes of the fuel pin and dilation of the cladding. Axial-dependent gamma spectroscopy (gamma scan) can be used to assess migration of fission products along the length of the fuel column.

Pins that do not require further irradiation can be examined destructively. Such examinations may include laser puncturing of pins for measurements of plenum volumes and fission gas release.

Sectioning of fuel pins can allow analyses of fuel burnup and composition. In addition, metallographic sections can be examined to assess fuel-clad chemical interaction, fuel restructuring, and fuel constituent redistribution.

The data obtained from examinations of qualification or experimental fuel pins will be assessed to ensure that the observed behavior is enveloped by the safety case presented in this document. Such data and subsequent analyses will demonstrate that fuel behavior meets the performance criteria discussed in Section 2.1.4. In addition, fuel performance data will provide guidance for further irradiation for subsequent qualification irradiations and for extending the fuel burnup limit beyond the interim limits set herein.

4.1.3 Evaluation of Results

The data obtained from examinations of surveillance or qualification fuel pins will be used to provide guidance for further irradiation of sibling subassemblies and to provide burnup limits for use by EBR-II. The performance criteria of Section 2.1.4 will be used to determine

acceptance of the fuel burnup limits. Several fuel pins in the qualification program will be irradiated until breach to provide data for evaluating margin to clad failure.

4.2 Fuel Pin Steady-State Performance

As part of the design evaluation, fuel performance codes are used to predict the performance of the Mark-V and Mark-VA fuel pins. This section describes the LIFE-METAL code [4.1] used to assess fuel pin steady-state performance.

4.2.1 LIFE-METAL Code

The LIFE-METAL fuel performance code has been developed to predict the behavior of metallic fuel rods [4.1]. The code has evolved from the LIFE series of codes which perform steady-state and design-basis-transient analyses for the thermal, mechanical, and radiation behavior of nuclear fuel rods. The LIFE-4CN code, which forms the basis for LIFE-METAL, includes two fuel options [(U, Pu)C and (U, Pu)N], two fuel/cladding thermal-bond options (He and Na), numerous cladding options (e.g., solution-annealed and 20% cold-work Type-316 stainless steels, etc.), and one coolant option (Na). A detailed thermomechanical analysis is performed in the radial direction with provisions to specify up to 20 radial rings for the fuel/cladding system. Axial variations in operating conditions are accounted for by inputting powers and fast fluxes for up to nine fuel axial nodes and one plenum node. Thermally, the axial nodes are coupled through the calculated coolant temperatures. However, axial heat conduction is ignored (a good approximation), and there are no provisions for mechanical coupling between axial nodes.

A detailed mechanical analysis is performed for both fuel and cladding utilizing the generalized-plane-strain assumption for each axial segment and incorporating a large strain capability. The solution procedure involves iteration on local total strain within each time step, and the solution procedure is explicit in time.

In converting LIFE-4CN to LIFE-METAL, a number of fuel properties and models were changed and/or added. Fuel properties correlations for U-5Fs and U-xPu-yZr were first developed as continuous functions of temperature, porosity, alloy composition, stress, fission rate, burnup, etc. These are documented in the IFR Metallic Fuels Handbook [4.2]. The physical

and thermal properties include density, phase-change temperatures, specific heat, thermal expansion, thermal conductivity, and alloy and fission product distributions. The mechanical properties include elastic moduli, fracture strength, and thermal and fission enhanced creep.

Physical, thermal, mechanical, and irradiation properties correlations for the test and design cladding materials (e.g., austenitic 316, austenitic D9, and ferritic HT9) are taken directly from the Nuclear Systems Materials Handbook (NSMH) [4.3], which includes both the correlations and the properties data base. Some work has been done during LIFE-METAL development in improving the correlations (e.g., D9 creep and swelling) to get a better fit to the data base within the operating range of interest for metallic fuels. The wastage correlation for sodium/cladding interaction and time and strain-failure correlations are also taken from NSMH. Models were developed for Ni depletion from D9 and carbon depletion from HT9 due to the fuel/sodium/cladding chemical interaction (FCCI). Empirical eutectic penetration correlations, based upon FBTA and IFR whole-pin-furnace test data are also incorporated into LIFE-METAL.

The focus of LIFE-METAL development has been on verifying the algorithms and validating the models for predicting fuel-pin behavior important in design analysis under normal operating conditions. Predictions of interest in the nuclear design are fuel length changes and changes in fissile content due to burnup and breeding. Thermal predictions of interest are fuel temperature, design margins to fuel melting, and design margins to low-melting-temperature alloy (e.g., U-Fe) formation. Mechanical predictions of interest to designers are cladding damage and design margin to cladding failure due to fission gas pressure loading, fuel-cladding mechanical interaction (FCMI) and FCCI, and cladding deformation and design margin to significant coolant flow area reduction.

4.2.2 LIFE-METAL Validation

The validation effort has been extensive. Post-irradiation data are available from a large number of fuel-pin irradiations for "global" integrated parameters such as fission gas release, fuel volumetric change, and fuel length change. Axial profiles are available for fuel radial growth at low burnup (prior to and including initial fuel-cladding contact) and for cladding radial growth for a wide range of burnups and fast fluences. Other data available on a more limited basis are radial and axial variations in U, Pu, Zr, and fission gas porosity, axial variations in fraction of porosity filled (logged) with Na, and depth of C-depleted and Ni-depleted zones in HT9 and D9,

respectively. Fairly complete sets of data are currently available for 80 fuel-pin irradiations. Limited data (e.g., fuel length change, cladding diameter change) are available for hundreds of irradiated fuel pins.

While more validation has been done for D9 than HT9-clad pins, a particularly relevant HT9 data set from EBR-II subassembly X441 has been used. This data set is of interest to the Mark-V safety case as the peak cladding temperature (600°C) and the peak linear heat rating (16 kW/ft (52.5 kW/m)) are close to the upper limits for the Mark-V pins. The reference X441 pins are identical to the Mark-V design except that the cladding thickness was 15 mils (0.038 cm) for X441 as opposed to 18 mils (0.046 cm) for Mark-V. The design variables included in X441 are Zr content (6-14 wt. %), plenum-to-fuel volume ratio (1.0-2.1), and fuel smear density (70-85%). Code predictions were compared to experimental data for cladding strain, fuel length change, and fission gas release. Figure 4-1 shows the good agreement between the LIFE-METAL predictions and the data for the peak HT9 cladding strains (circles) for 75% smear density U-19Pu-10Zr pins. The cases with the reference plenum and fuel composition are indicated by the dark circles. The difference between LIFE predictions and data is generally within the uncertainty and pin-to-pin scatter (±0.087%). Also included in Figure 4-1 are some data from subassembly X425 at lower power, cladding temperature and plenum-to-fuel volume ratio. Each point in the figure represents about 4 pins. Less effort has been expended on validating LIFE-METAL to data for the 316SS/U-19Pu-10Zr combination. However, because of the similar mechanical behavior and in-reactor behavior (up to the goal burnup of 10 at. %) of 316SS and D9, the D9 effort can be used to validate the code for the Mark-VA case, as well. The peak linear heat ratings for the X441 test are high relative to the ones calculated for Mark-VA. The data from other experimental subassemblies (e.g., X419, X420, X421, etc.) at lower operating power (11-14 kW/ft (36-46 kW/m)) are more appropriate for Mark-VA validation. The difference between calculated and measured values are given in Figure 4-1, which shows that the agreement between LIFE-METAL-predicted peak cladding strain and data is quite good for the D9 cases. In addition, the predicted strain profiles for the D9 cases shown in Figure 4-1 agree quite well with the data. These cases all had a plenum-to-fuel volume ratio of about 1.

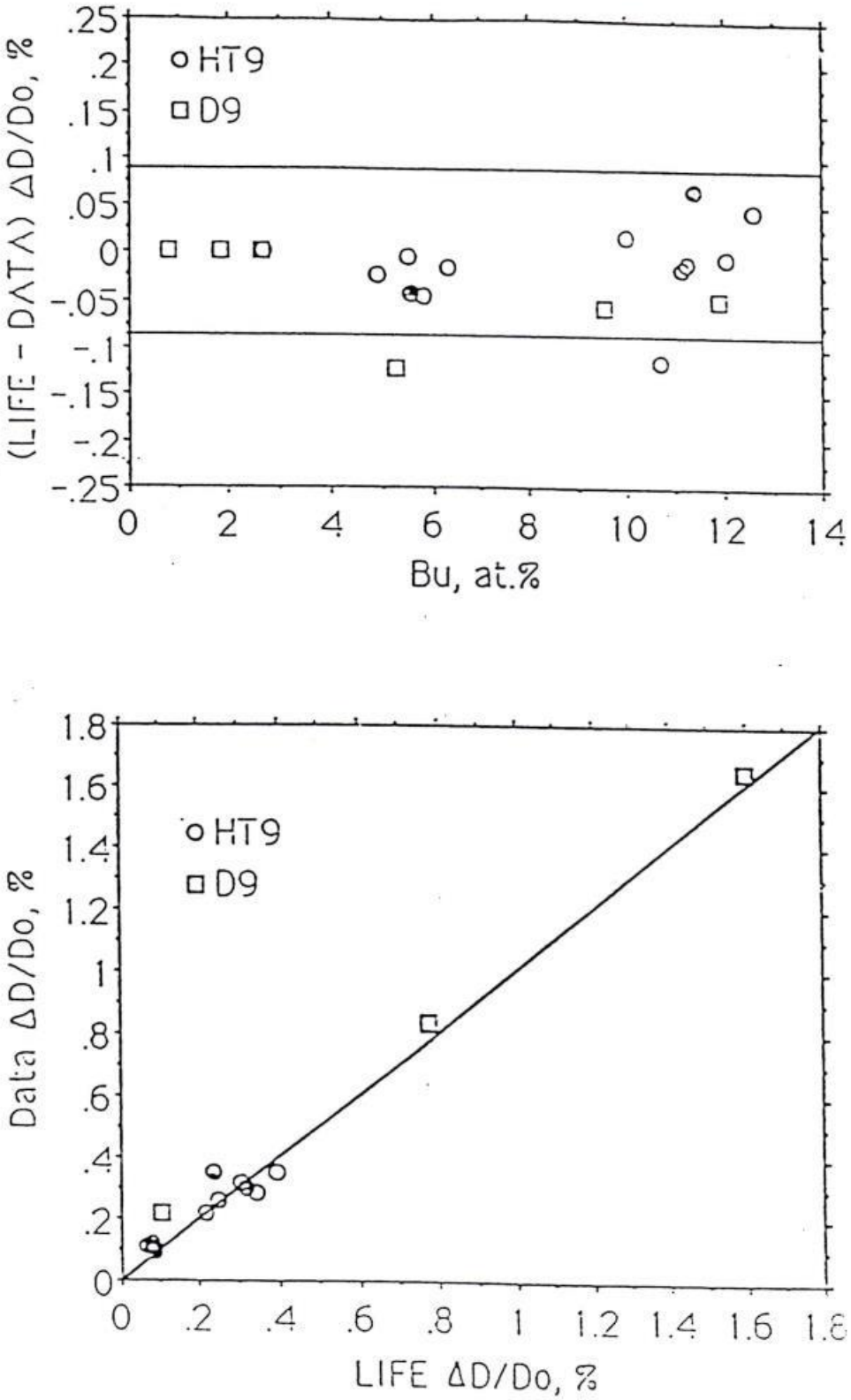

Figure 4-1 LIFE-METAL vs. Data for U-19Pu-10Zr/HT9 Peak Cladding Strains

4.3 Fuel Pin Transient Performance

Transient fuel performance during reactor accidents depends strongly on the reactor power, coolant flow and overall plant response to the accident initiator. It is advantageous, therefore, to perform the thermal and mechanical analyses of transient fuel pin behavior using the same computer code that is being used to perform the whole-plant analyses. The fuel pin behavior calculations in large, multi-channel whole-plant analyses must necessarily be simple if they are to be practical because of limitations in computer running time. Certain characteristics of metallic fuels allow such simplified analyses of the transient behavior of metal-fueled pins [4.4]. This is particularly true for the calculation of fuel pin damage, which is of primary concern for the Mark-V safety case. The reason for this is that the high conductivity of metallic fuels leads to cladding temperatures and cladding damage that peak near the top of the fuel column. If the fuel-cladding gap is open at the top of the fuel at high burnup, as predicted by the LIFE-METAL calculations given in Section 9.4, the only loading on the high temperature section of the cladding is the plenum pressure. Furthermore, during undercooling accidents the gaps tend to open even more because the cladding expands more than the fuel. Even during transient overpower events, where the gaps close, Fuel-Cladding Mechanical Interaction (FCMI) does not damage the cladding significantly [4.4] because of similarities in the fuel and cladding expansion and because the fuel near the top of the pin is hottest and therefore most compliant. Because of these characteristics it is often adequate to model transient cladding damage in metallic fuel pins by considering the deformation and failure of a cladding tube pressurized only by the plenum gases. This is essentially the fuel pin mechanical behavior model that is contained in the DEFORM-5 module of the SASSYS code, as described later. In order to justify this model for the Mark-V analyses, supporting calculations have been performed using the detailed, state-of-the-art transient fuel pin behavior code FPIN2. The supporting calculations included analyses of the response of the hottest end-of-life Mark-V pins to the most severe transient overpower and loss of cooling accidents. FPIN2 analyses have also been performed in order to relate the results from the TREAT tests M2-M7 to the transient fuel pin failure margins for Mark-V fuel, as described in Section 5.0 of this report. The following paragraphs describe the models contained in FPIN2 and their validation.

4.3.1 FPIN2 Code

The FPIN2 code is a detailed, state-of-the-art computer code that has been developed to

analyze the complex thermal-mechanical phenomena that govern fast reactor fuel pin behavior during accident transients. The analysis determines the fuel and cladding temperatures, stresses and displacements during overpower and undercooling events. The basic program includes a group of subroutines to calculate the temperature of the fuel, cladding, coolant and associated structure; and a separate group of subroutines to calculate the mechanical behavior of the fuel and cladding. Relevant pretransient fuel characterization parameters are input into FPIN2 based on sibling pin information or on LIFE-METAL code calculations. The heat transfer section in FPIN2 uses an implicit finite difference algorithm, while the mechanical analysis uses a non-linear finite element procedure. A major reason for choosing the finite element method is that it allows a convenient modular coding structure for the fuel pin mechanics so that different models for material behavior can be easily implemented into the code and the importance of phenomena assessed.

A detailed description of the FPIN2 code and the models used in the code to analyze the behavior of metallic fast reactor fuel pins is given in Reference 4.5. The FPIN2 code simulates the behavior of a single fuel pin along with its associated coolant and structure. Axial symmetry of temperatures and external loads is assumed. At the beginning of the transient, the fuel pin is assumed to be in mechanical equilibrium with the plenum pressure and in thermal equilibrium with steady-state power and flow conditions. For the Mark V calculations, other parameters that characterize the pretransient fuel condition were obtained directly from output from the LIFE-METAL fuel performance code. In order to facilitate this process, a small computer routine was written that reads the LIFE-METAL data from a special output file and transforms it into the FPIN2 input format. The routine performs all of the calculations that convert between the units used in LIFE and the units used in FPIN2, and interpolates between the LIFE fuel mesh (equal volume rings) and the FPIN2 mesh (equal thickness rings). The input from LIFE-METAL includes 1) the burnup, power profile and cladding fluence, 2) steady-state fuel and cladding dimensions, 3) plenum volume, pressure and temperature, 4) porosity, zirconium and plutonium distributions, and 5) the quantity of fission gas retained within the fuel. Consistency checks are available in the FPIN2 output at the beginning of the transient to assure that the input fuel characterization matches the LIFE-METAL results.

Although the primary emphasis in the FPIN2 code is on the mechanical analysis of the fuel

and cladding, a complete heat transfer analysis is also included. The basic assumption is that heat is conducted only radially in the fuel and cladding and is convected axially by the sodium coolant. The one-dimensional heat transfer equations for the fuel, bond sodium, cladding, coolant and structure are solved using the Crank-Nicholson implicit finite difference method. Since the thermal conductivity and heat capacity are temperature dependent, the finite difference equations are nonlinear. These equations are solved by simple iteration in which the material properties are evaluated using the most recently calculated temperatures. Although minor solid-state phase changes are modeled using an "effective heat capacity", the large enthalpies of fusion associated with melting are modeled explicitly giving an accurate accounting of the solid and liquid fractions during the thermal arrest.

The mechanical analysis in the FPIN2 code uses the finite element method based on a force-displacement formulation. Both large strain and small strain options are available by setting a single input parameter. Axial symmetry and generalized plane strain are assumed so that the analysis is essentially one-dimensional. The finite elements are defined by first dividing the fuel pin into a number of axial segments (as many as 20) and then further dividing each axial segment radially into a number of equal thickness rings (as many as 20 in the fuel and up to 10 in the cladding). The elements are assumed to interact only at the radial boundaries, or nodes, and the displacements at the nodes are the basic unknowns in the analysis. The displacements within the elements are approximated by simple linear functions of the nodal displacements. The finite element equilibrium equations are derived using the principle of virtual work. For each axial segment, the equations for both the fuel and the cladding elements are assembled into a single matrix equation for the unknown radial and axial displacements. In this way, Fuel-Cladding Mechanical Interaction (FCMI) forces come out of the analysis without a separate iteration. Simple modifications during the matrix assembly are used to account for cases where the fuel and cladding are not in contact and when they are free to slip in the axial direction. When fuel melts, the number of radial elements included in the mechanical analysis decreases. In FPIN2 the number of equilibrium equations is kept fixed and the extraneous equilibrium equations describing molten fuel are replaced by simple identities. Eutectic penetration of the cladding is handled somewhat differently by reducing the contributions of the hoop stress and the axial stress to the equilibrium equations for a given element by the fraction of the element that has liquified.

The finite element solution procedure used in the FPIN2 mechanical analysis is general enough to allow for a wide range of material behavior. Superposition of strains is assumed to hold so that the total strain can be written as the sum of the elastic strain, thermal strain, non-elastic (plastic, creep, etc) strain and swelling strain. The form of the constitutive equations for these strains can be quite general. With the exception of the fuel swelling strain, discussed in the following paragraph, the strain components for Mark-V fuel and cladding were determined from properties given in Appendix A of this document.

Several of the models in FPIN2 that contribute significantly to the calculations for Mark-V fuel warrant further elaboration. The first is the fuel swelling model. A study [4.6] of gas-bubble growth mechanisms in metallic fuels suggests that the transient swelling of metallic fuels is dominated by the diffusive growth of grain boundary bubbles. This is the only mechanism that can explain the rapid swelling of irradiated fuel samples that were tested in a hot cell at various temperatures and pressures. A grain boundary bubble swelling model based on this work was implemented into FPIN2 and has been used in all of the code validation studies. Because the model predicts that metallic fuels can swell significantly during transient heating, it also predicts that the fuel can be easily compressed. This fact, along with the similarity in the transient thermal expansion of metallic fuels and their cladding, gives rise to much lower FCMI loads than for oxide fuels.

The second model is the plenum model. In FPIN2 it is assumed that the space above the fuel column is occupied by bond sodium and by fission gases. The bond sodium height is input based on sibling pin information or, for the Mark-V safety case, from LIFE-METAL results. Similarly, the quantity of gas in the plenum is determined from the input plenum pressure at a specified temperature. During the transient calculation the plenum pressure is determined implicitly by using a simple volume accounting procedure and assuming that the plenum temperature is always at the sodium outlet temperature. Changes in the gas volume can occur because of axial fuel expansion, extrusion of molten fuel into the plenum, transfer of bond sodium between the plenum and the fuel-cladding gap, thermal expansion of the sodium in the plenum and radial and axial expansion of the cladding in the plenum region. In this latter contribution the only mechanical strains that are presently included are the elastic strains; non-elastic deformation in the plenum is not modeled.

4.3.2 FPIN2 Validation

Over the past decade the FPIN2 code has undergone extensive verification and validation. The verification is based on the comparison of code calculations with the analytical solutions for simple test problems. The references for these verification comparisons along with the references for all of the earlier oxide fuel validation studies are given in an Argonne IFR report [4.7]. This report also describes the preliminary metallic fuel validation studies using results from the TREAT tests M2, M3 and M4 on EBR-II Mark-II uranium-fissium fuel. In this report FPIN2 calculations are compared with experimental measurements of flowtube temperatures, melt fractions, cladding failure time and location, cladding plastic strain, eutectic penetration, fuel axial expansion and liquid fuel extrusion into the plenum. The sensitivities of some of the calculated results to uncertainties in the prior irradiation history of the test pins and to the experiment conditions is also discussed. Extension of the FPIN2 validation to ternary U-Pu-Zr and binary U-Zr fuels is reported in Reference 4.8. A summary of the TREAT tests that have been run thus far and the plans for future TREAT tests are discussed in Section 5 of the present document.

More recently, the FPIN2 validation studies have concentrated on the results from the Whole Pin Furnace (WPF) tests on irradiated IFR fuel pins. These tests are also described in Section 5. In the Whole Pin Furnace tests intact irradiated EBR-II fuel pins are heated externally inside a hot cell using a radiant furnace. The furnace is computer controlled and the fuel pin is contained in a capsule which is cooled by flowing helium. This system is able to achieve a reasonable simulation of the temperatures that an actual fuel pin would experience during a reactor accident. This is because the radial temperature gradients in metallic fuel pins are not large, even prior to scram. Following scram, the temperature gradients rapidly collapse and there is very little difference between the in-reactor temperatures and those that can be achieved by external heating. The advantage of the WPF tests over the TREAT tests is that the WPF tests can be run for longer times, which simulate both the initial phase of the accident and the period following scram where the fuel cools to temperatures below normal operating temperatures.

Both FPIN2 and LIFE-METAL have been used to make pre-test and post-test predictions for the initial WPF tests FM-1, FM-2, FM-3, FM-4 and FM-5. As discussed in Section 5, tests FM-4 and FM-5 were conducted specifically to support the Mark-V safety case. The FPIN2 calculations [4.9,4.10,4.11, 4.12] used the LIFE-METAL steady-state output to characterize the

pre-test condition of the irradiated test pins. Comparisons of calculated results with the test results include the time of pin failure, the location of pin failure, the cladding diametral strain profile and the extent of cladding eutectic attack. In general the agreement between the calculations and measurements is within the expected scatter, with the FPIN2 results tending to be conservative in the sense that they predict more cladding strain and earlier pin failure than was measured.

4.3.3 DEFORM-5 Validation

The DEFORM-5 code [4.13] incorporates a simpler fuel behavior treatment than the FPIN2 code, neglecting the effect of FCMI. This treatment has been validated by comparison with FPIN2 and experiment. As described above metal fuel is easily compressed and therefore FCMI loads are small. This code is part of the SASSYS code, which predicts transient thermal response of the fuel pin, and this information is used by DEFORM-5 to predict the thermal-mechanical behavior of fuel pin including cladding failure mechanism. The failure of the cladding is primarily caused by stress/strain of the cladding due to fission gas pressure, and cladding thinning due to eutectic penetration and large strain increase. Both phenomena were modeled in DEFORM-5, using the plastic flow equation in Ref. 4.14 for strain predictions and the eutectic penetration correlation of Ref. 4.15 for clad thinning. The results were then incorporated in the cladding margin to breach predictions.

The DEFORM-5 solution method involves first determining the eutectic penetration thinning of the cladding. The new cladding thickness is then studied to determine if breach has occurred over the time interval. If breach has not occurred, a damage fraction is calculated, and this is accumulated with any previous damage.

One of the other areas of modelling involves the axial relocation of molten fuel within the intact cladding. If the cladding remains intact, it is possible for the top fuel sections to melt and release the molten fuel upward. The code can determine the amount of molten fuel relocation.

The DEFORM-5 code has been validated with the TREAT experiments M2, M3, and M4 [4.16] and there is good agreement between DEFORM-5 predictions and the experimental data [4.13].

4.4 Thermal-Hydraulic Performance

4.4.1 SASSYS/EBR Model

The EBR-II models were developed and were incorporated into the general thermal-hydraulic-neutronic system analysis computer code, SASSYS [4.17], to predict steady-state and transient thermal responses of the EBR-II plant. SASSYS provides a detailed thermal-hydraulic and neutron kinetics treatment of the reactor core, coupled with a general thermal-hydraulic treatment of the primary and intermediate heat transport systems. The code is especially suited for predicting the transient response of the reactor plant. The code has been used heavily in support of the Integral Fast Reactor concept [4.18] and of innovative LMR designs, such as PRISM [4.19] and many others. Application of SASSYS modeling to EBR-II has been developed [4.20], and was employed in the present safety analysis. This model is referred to as SASSYS/EBR in the present report. Included in the SASSYS depiction of EBR-II are models of all the main heat transfer components in the primary and secondary systems. Validation of the SASSYS/EBR model was aided by analysis of early Shutdown Heat Removal Testing (SHRT) data [4.21], among which the measurements from a protected loss-of-flow (LOF) transient initiated from full power and flow conditions provided validation of primary and secondary heat transport models [4.20, 4.22]. Analysis of the mild reactor flow and inlet temperature perturbation tests in the SHRT program provide validation of the EBR-II reactivity feedback model in SASSYS [4.22]. The combined effects of the thermal-hydraulic and reactivity models were investigated by applying the SASSYS/EBR model to the analysis of loss-of-flow without scram (LOFWS) and loss-of-heat-sink without scram (LOHSWS) tests of the SHRT program [4.20]. Results indicated that analytical predictions and measurement are generally in good agreement.

The steam system model has not been included in the current SASSYS/EBR model, instead the sodium temperature drops across the superheaters and the evaporators are specified as a function of time to establish the ultimate heat transfer boundary condition. Since the off-normal transients considered in the safety analysis are rapid thermal transients, the heat transfer boundary conditions of the superheaters and the evaporators have insignificant effect on the temperatures of the transients considered.

In the SASSYS/EBR model, the subassemblies connected to the high pressure plenum are

modeled as 11 core channels. The subassemblies are grouped into channels based on similarity in composition, flow rate, and operating power. The thermal response of an average subassembly or a hot pin in a subassembly is represented by a single pin in a single channel. However, intersubassembly heat transfer is not considered in the modeling. When the hottest pin is considered in the safety evaluation, the effects of flux tilt and edge flow can be compensated by applying a "peaking factor" to the hot pin considered. In the safety analysis, the safety issues are addressed to the hottest pin, and the analysis is considered to be conservative when intersubassembly heat transfer is neglected.

4.4.2 PPS and Code Validation

In the safety analysis of the protected off-normal duty cycle events, the plant protection system (PPS) plays an important role in the thermal responses of the reactor plant as well as the subassembly. Thus, it is essential to have a PPS model available in order to assess the overpower and loss-of-flow transients. The EBR-II PPS is simulated by utilizing the SASSYS generalized control system module [4.23]. Four types of trip functions are considered which are caused by monitoring of various system quantities and are triggered due to their respective safety system settings. These trips include power-level trip, flow trip, subassembly-outlet-temperature (SOT) trip, and period trip. Two sets of input decks were generated to include the EBR-II T.S. and the best-estimate values of the on-site components for trip settings. Table 4-1 shows the PPS trips included in the simulation [4.24].

Table 4-1 Plant Protection System Trip Functions

Function	Safety Settings (Tech. Spec.)	Safety Settings (Best Estimate)
Power-level trip	115%	110%
Reactor-outlet low-flow (total flow) trip	88%	94%
No. 2 high-pressure-plenum low-flow trip	88%	94%
Low-pressure-plenum low-flow trip	85%	87%
Upper-plenum low-flow trip	88%	94%
Selected subassembly-outlet-temperature trip, ΔT	115%	110%
Period trip (power below 25MWt)	17 sec	25 sec

Power, flow, SOT, and period trip functions of the SASSYS/EBR PPS model have been validated, as described in Ref. 4.24. The voltage step-function (the basic control action) has been employed to verify that the EBR-II T.S. requirements for response time of each PPS channel are met. The calculated result from the power step-function shows good agreement with the analytical solution. Results from the step-functions for reactor flow and SOT trips are in good agreement with the results from DSNP [4.25] and NATDEMO [4.26] reported, respectively, in Refs. 4.27 and 4.24. Step-function results for the period trip agree well with results from the EROS code [4.28]. The study shows that the analytical solution is approached when time-step-size is small.

Four of the fault cases associated with either transient overpower (TOP) or loss-of-flow (LOF) were simulated. Two of the cases simulated are the TOP events (e.g., due to uncontrolled insertion of a control rod) which can be terminated by trip functions activated due to a signal either from the neutron flux (fission power) sensors or the SOT detectors, if the power trip function fails. Two LOF events were simulated in the validation; they are the LOF due to clutch breaker trips of both pumps and the LOF due to one pump seizure and the clutch breaker trip of the other pump, and in both events the reactor is scrammed by the flow trip function.

In the simulation, the reactor is considered to be at full power (62.5 MW) before transient initiation, and the SASSYS core loading is based on Run 148B, which consists mainly of Mark-II, Mark-III, and Mark-IV fuel subassemblies. Under conditions of normal operation, the primary loop flow is 0.57 m^3/s (9000) gpm with core inlet temperature of 644 K (700°F), and the secondary loop flow is 0.35 m^3/s (5600 gpm) with the IHX secondary inlet temperature of 582 K (588°F). In the TOP events, the power increase is initiated by reactivity insertion as shown in Figure 4-2, which is the same as that used in Ref. 4.29. In SASSYS calculation, the steady state decay heat, φ, is a normalized value based on the steady state total power, which is also used as a reference value for normalization of fission power and decay heat during the transient. Thus the fission power setpoint is $(1-\varphi)$ times 1.15. In the LOF events, pump speed versus time tables of both primary pumps, as used in Ref. 4.29, were used for the simulation of the pump coastdown due to clutch breaker trips. In the case of one pump seizure, the pump is assumed to stop in 0.2 sec. The auxiliary pump provides 3.3% flow throughout the transient. The protective action of the PPS in the simulation is the insertion of shutdown reactivity of $3.7 linearly in 0.45 s, as used in

Ref. 4.29.

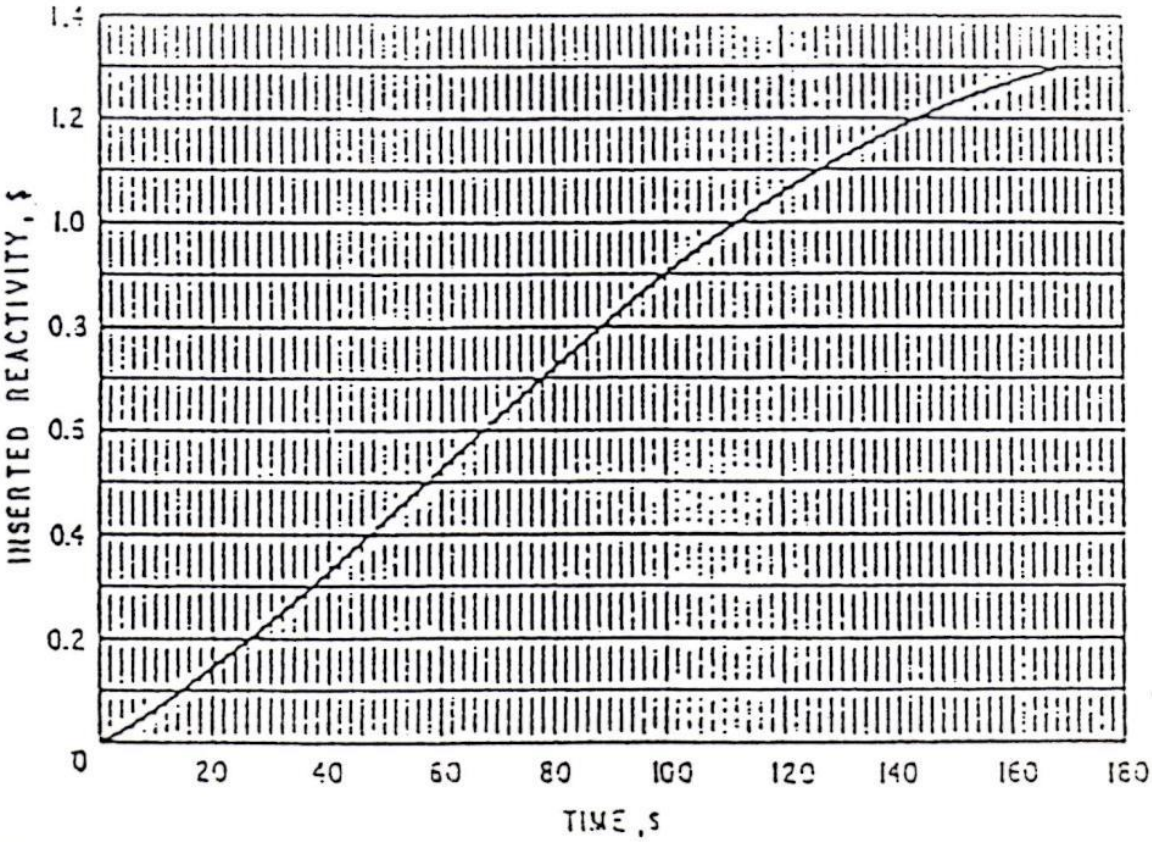

Figure 4-2 Reactivity Insertion Corresponding to Single Rod Insertion (from Ref. 4.29)

Results of the SASSYS/EBR PPS models were verified against results from the EROS and DSNP codes, and sample results are given in Figure 4-3 and Figure 4-4, respectively, for the TOP event with reactor scram by the SOT trip function and the LOF event due to clutch breaker trips of both pumps with reactor scram by the flow trip function. The results of all the TOP and LOF cases simulated are, respectively, in good agreement with the EROS and DSNP code results reported in Ref. 4.30. The present work shows that the SASSYS/EBR PPS model adequately simulates the EBR-II PPS as described in Refs. 4.29 and 4.31.

4.5 Uncertainty Factors

The uncertainty factor analysis presented herein has been based upon requirements for Mark-III, Mark-IIIA and Mark-IV fuel types, together with engineering judgment. The uncertainty factor analysis has been reviewed for compatibility with the fuel specification [4.32]

for Mark-V and Mark-VA fuel pins. The details of this review are documented in Ref. 4.33. The only factor affected by the fuel specification is the uncertainty in fissile fuel content, which falls under the category of manufacturing deviations, as discussed below. The fuel specification allows a 5% uncertainty in fissile fuel content. As a conservatism, the present analysis assumes a 6% uncertainty in fissile fuel content, thereby bounding the fuel specification.

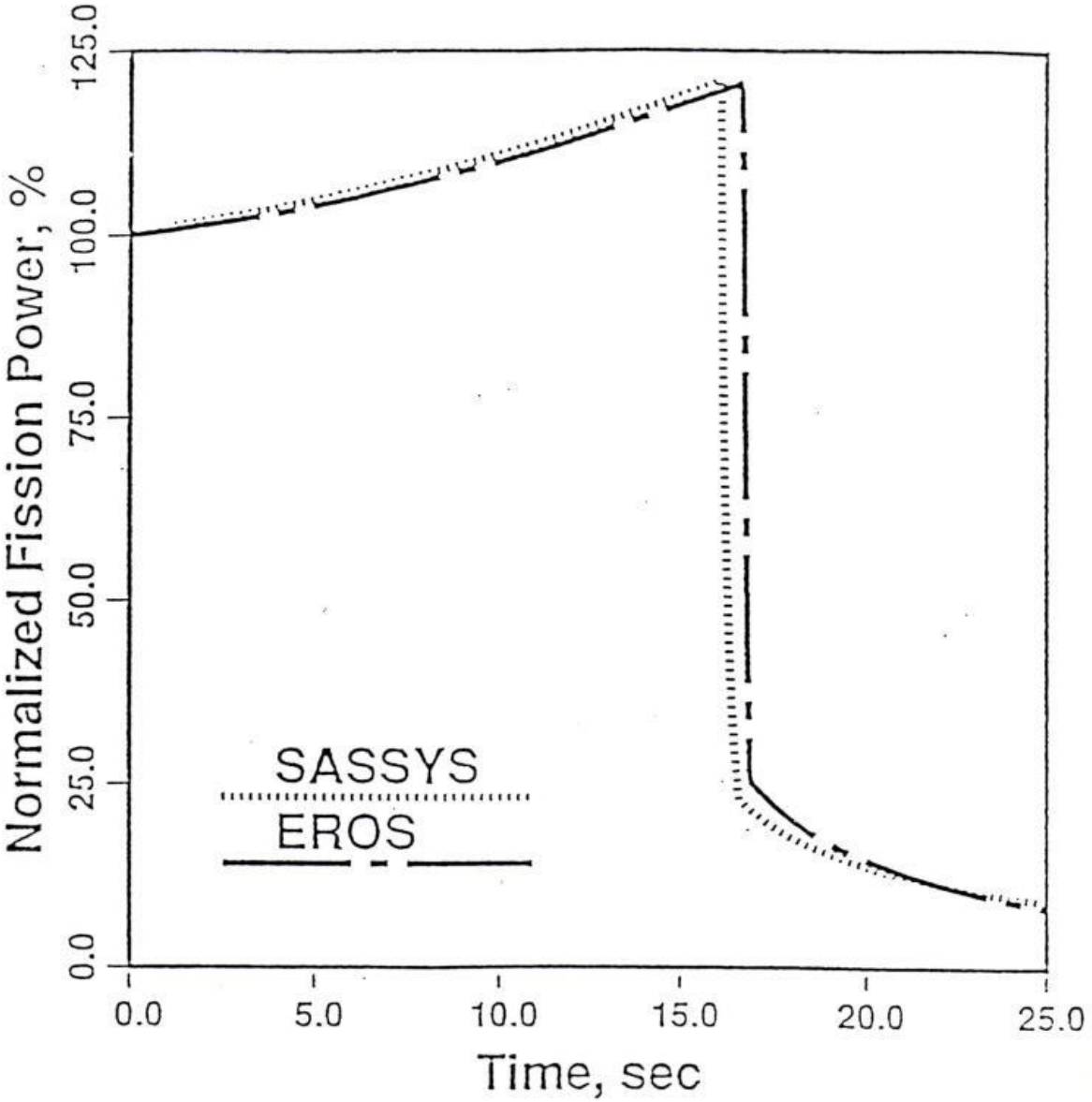

Figure 4-3 Power History of a Transient Overpower Event
(Reactor Scrammed by SOT Trip Function)

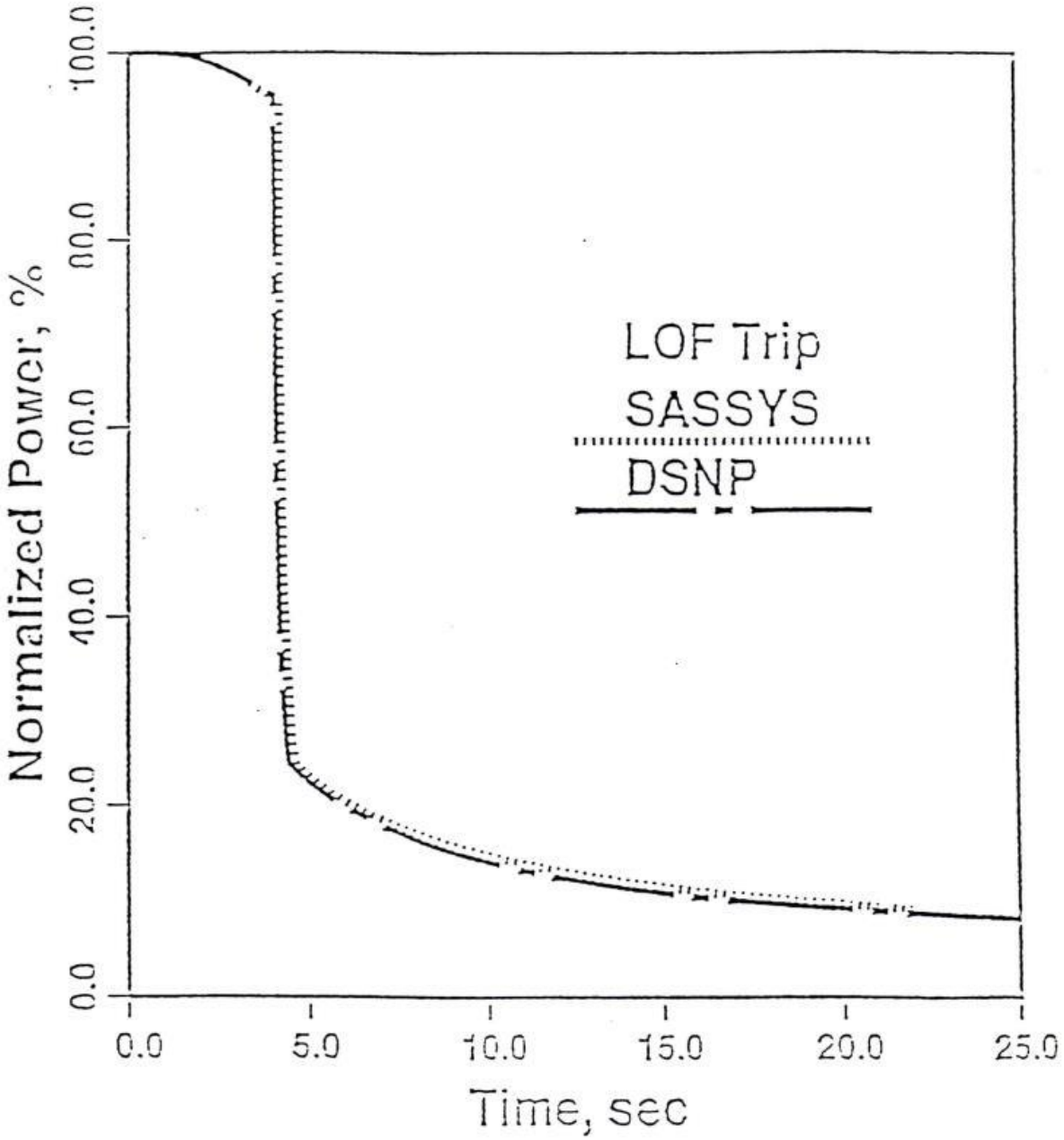

Figure 4-4 History of a Loss-of-Flow Event Due to Clutch Breaker Trips of Both Pumps (Reactor Scrammed by Flow Trip Function)

An uncertainty factor is a factor representing a design parameter associated with an uncertainty and is applied to hot channel factors analyses. According to the origin of the uncertainty in individual parameters, uncertainty factors are separated into two principal categories; they are direct uncertainty factors due to biases and statistical uncertainty factors due to random uncertainties.

The heat transport path from fuel to coolant is divided into five consecutive regions, i.e., fuel, fuel-cladding gap, cladding, film, and coolant, and a hot channel factor is assigned to each of the five regions as a result of the application of the uncertainty factor. Table 4-2 shows the uncertainty factors in Ref. 4.34 used for previous thermal analyses of fuel pins. The original factors listed separately for clad-bond and bond-uranium interfaces, and sodium bond, in Ref. 4.34 are combined to a single uncertainty factor for the fuel-cladding gap in Table 4-2. This combination proves to be consistent with many researchers [4.35-4.43].

In a review of the hot channel factors analyses in the literature, it was found that the two terms, "uncertainty factor" and "hot channel factor," were used interchangeably to some extent in many references [4,34, 4.37-4.40, 4.42, 4.44]. The "hot channel factor" defined in this report is the factor applied to the nominal temperature calculation in the channel to include input uncertainties such as power, flow, thermal conductivity, etc.

The uncertainty factors, along with the hot channel factors, for thermal analyses of Mark-V fuel pins [4.45] are presented in Table 4-3. Results from fuel thermal conductivity experiments [4.46] indicate that the highest fuel temperature occurs when the metal fuel reaches about 2 at. % burnup due to the low thermal conductivity of the fuel. When Mark-V fuel is irradiated Zr redistributes and forms three zones based upon Zr atom fraction. The fuel solidus temperature in the intermediate zone of fuel is the lowest due to the low zirconium fraction. The factors listed in Table 4-3 for thermal analyses of Mark-V fuel are obtained for the low conductivity condition. The major differences between Table 4-2 and Table 4-3 are the uncertainties in fuel thermal conductivity and in flow rate through a subassembly. The reasons for the differences will be discussed later.

Uncertainties of parameters can be categorized as of either statistical or non-statistical origin. This was done by judging the argument and rationale given in the hot channel factors analyses in the literature. Then, a hot channel factors analysis method, which allows treatment of uncertainty factors of different origins, was chosen to demonstrate the procedures for obtaining overall hot channel factors for peak fuel and cladding temperatures for steady state analysis. Finally, separate composite uncertainty factors, each composed of uncertainties attributable to parameters that directly affect reactor power, flow rate, or heat transport, were derived for transient analysis.

Table 4-2 Hot Channel Factors Used in Ref. 4.34 for Thermal Analysis of Fuel Pins

Thermo-Physical Quantity	Coolant	Film	Cladding	Gap	Fuel
Precision of Power Level Measurement	1.02	1.02	1.02	1.02	1.02
Precision in Neutron and Gamma Flux Distribution	1.07	1.10	1.10	1.10	1.10
Precision in Total Coolant Flow Rate Through a Subassembly	1.05	-	-	-	-
Precision in Coolant Flow Profile Within a Subassembly	1.05	-	-	-	-
Manufacturing Deviations from Nominal:					
Clad Dimensions	-	-	1.05	-	-
Bond Dimension	-	-	-	1.04	-
Uranium Dimensions	-	1.02	1.02	1.02	1.02
Fissionable Material Concentration	1.01	1.01	1.01	1.01	1.01
Thermal Conductivity Values:					
Clad	-	-	1.10	-	-
Bond	-	-	-	1.10	-
Uranium	-	-	-	-	1.15
Heat Transfer Coefficient	-	1.20	-	-	-
Possible Transient Overload	1.05	1.05	1.05	1.05	1.05

Sections 4.5.1 and 4.5.2 will discuss the uncertainty factors included in Ref. 4.34, which form the historical background of application of uncertainties to EBR-II safety analyses.

Sections 4.5.1 and 4.5.2 will discuss the uncertainty factors included in Ref. 4.34, which form the historical background of application of uncertainties to EBR-II safety analyses. In addition, Section 4.5.3 will discuss some parameter uncertainties that were not included in Ref. 4.34 but were considered in the CRBRP analysis [4.37]. The hot channel factors analyses will

be presented in Sec. 4.5.4, which will also address the effect of the additional uncertainties on the overall steady-state hot channel factors. Sec. 4.5.5 will discuss generation of uncertainty factors for transient analysis.

Table 4-3 Uncertainty and Hot Channel Factors for Thermal Analysis of Mark-V Fuel

Thermo-Physical Quantity	**Uncertainty Factors**	**Hot Channel Factors**				
		Coolant	**Film**	**Cladding**	**Gap**	**Fuel**
Precision of Power Level Measurement	1.02	1.02	1.02	1.02	1.02	1.013
Precision in Neutron and Gamma Flux Distribution	1.07*	1.07	1.10	1.10	1.10	1.10
Precision in Total Coolant Flow Rate Through a Subassembly	1.07	1.079	1.025	-	-	-
Precision in Coolant Flow Profile Within a Subassembly	1.05	1.056	1.018	-	-	-
Manufacturing Deviations from Nominal:						
Clad Dimensions (Thickness)	1.03	-	-	1.03	-	-
Fissile Content	1.06	1.06	1.06	1.06	1.06	1.04
Thermal Conductivity Values:						
Clad	1.07	-	-	1.08	-	-
Fuel	1.25	-	-	-	-	1.25
Heat Transfer Coef. (Film)	1.16	-	1.20	-	-	-
Transient Overload	1.05#	1.05	1.05	1.05	1.05	1.043

*No measured data available at this time; this value indicates an uncertainty for a combination of fuel Mark I, IA, and II.

Traditionally required in the EBR-II safety analysis; only considered in transient analysis.

4.5.1 Direct Factors

4.5.1.1 Power Level Measurement

The uncertainty in the power level measurement represents the calibration error in power

measurement instrumentation based mainly on water flow rate and feedwater temperature measurement uncertainties in the steam cycle. The essence of this factor is how well the instrumentation is calibrated in measured temperature rise and flow rate within the operation range. This uncertainty could be considered to be statistical, as was done for FFTF. In LWR licensing, however, it is treated as a bias. In CRBRP, this uncertainty was also considered as a direct one and has a value of 2%; this is an example where LWR precedent dictates LMR methodology. EBR-II operating experience has indicated a 2% uncertainty in power level measurements, as shown in the top line of Table 4-2. Since the new fuel will not affect the calibration error in power measurement instrumentation, the uncertainty remains at 2%.

This uncertainty affects all channel temperature rises (or differentials) in a global manner. Results from steady-state SASSYS/EBR-II calculations [4.20, 4.47] show that a 2% calibration error in power measurement instrumentation from the rated value causes approximately a 2% increase in the coolant temperature change axially and in the temperature difference radially across the film, the cladding, and the gap but only about a 1.3% increase in the temperature difference between the fuel surface and the fuel centerline. The increase across the fuel is less than the power increase due to nonlinear fuel thermal conductivity dependence on temperature. Therefore, a hot channel factor of 1.013 for fuel temperature rise is used in the current analysis, instead of the value of 1.02 reported in Ref. 4.34.

The above demonstrates the difference between hot channel and uncertainty factors. That is, an uncertainty factor of 1.02 in power causes a hot channel factor of 1.013 for the fuel temperature rise. This implies that the difference in (nominal) temperature between the fuel centerline and the fuel outer surface will increase by 1.3% if the power level is 2% higher. The 1.3% increase in temperature difference between the fuel centerline and fuel surface temperatures corresponds to a 1.5% increase in the temperature difference between the fuel centerline and the coolant inlet, as is also shown by the SASSYS/EBR-II results.

4.5.1.2 Transient Overload

This uncertainty is considered as a power control deadband allowance and is taken into account only in transient analysis. The effect is conservatively treated as a direct, rather than a statistical factor, even though the reactor power will be at the maximum end of the power control deadband for only a small fraction of time during each operation. In CRBRP, a bounding factor

of 1.03 was used for the combined power level measurement and control system deadband factor, in which 1.01 is due to control deadband. The 1.05 transient overload uncertainty factor is considered conservative for the current analysis. Further discussion is included later in the description of the uncertainty factors used for transient analysis.

4.5.2 Statistical Factors

4.5.2.1 Flow Rate Through Subassembly

This factor accounts for uncertainties in the calculated subassembly flow due to (a) flow maldistribution in the inlet plenum caused by internals structure arrangements and manufacturing tolerances, (b) orificing uncertainties, and (c) primary loop flow imbalances.

The initial modeling and hydraulic testing of the EBR-II primary flow system design was performed on a 0.6 scale water test model by the Franklin Institute in Philadelphia [4.48]. Subsequently, this test model was modified and became known as the Reactor Hydraulic Test Facility (RHTF), [4.49, 4.50] to reassess the reactor subassembly flow distribution after EBR-II was converted to an irradiation test facility, with the reactor loading changed substantially and frequently. In the original hydraulic design of the reactor, as tested by the Franklin Institute and verified by RHTF Phase I [4.50], there was essentially homogeneous core loading yielding virtually a row-wise symmetry in subassembly flow distribution. As a result of this symmetry, the so called row-wise effective pressure drop fraction (EPDF) concept, originally developed by the Franklin Institute, was also used in the RHTF Phase I study. The analytical methodology for using the values determined by row-wise EPDF is performed by the EBRFLOW computer code [4.51] to calculate subassembly flow rates.

By the time reactor Run 56 was made, the core loading had evolved into a heterogeneous mixture of driver and both fueled and nonfueled experimental subassemblies. Therefore, the subsequent RHTF Experimental Phases III and IV [4.52] were performed to provide an assessment of the EPDFs for each of the subassemblies of the high pressure plenum in a core loading hydraulically similar to Run 56. In the data analysis of the RHTF Phases III and IV simulation [4.53], it is found that the row-wise EPDF concept is a viable one for a core loaded with a heterogeneous mixture of driver and experimental subassemblies of widely differing hydraulic characteristics. The EBRFLOW computer code was again used as the primary tool for predicting

subassembly coolant flows on the basis of the EPDF algorithm. However, the analysis indicates that the row-wise EPDFs have in some instances changed substantially from those determined from the Franklin Institute and RHTF Phase I study results. Since the Phase III simulation better represents core loadings of the current type than does the Franklin Institute simulation, the newly obtained Phase III EPDFs were used for EBRFLOW analysis. It was judged based on the Phase III data analysis that a 5% uncertainty in subassembly flow rates would result in assessing a Run 56 type core loading. In addition, the analysis [4.53] recommended a 7% uncertainty in subassembly flow rates when the Phase III distribution is used to assess future loadings. This was obtained by adding arithmetically an additional 2% to the 5% uncertainty in flow to account for the large deviation between the EBRFLOW subassembly flow distributions.

The level of confidence associated with this uncertainty reported in Ref. 4.53, however, is not described. Nevertheless, from the data and the descriptions of the analysis presented therein, the uncertainty is judged by the current study to be of 3σ level of confidence, mainly because the 5% and 2% uncertainties represent the maximum deviations in the calculated results of the accompanying analyses. This 1.07 uncertainty factor is slightly larger when compared to the uncertainty factor of 1.059 recommended for CRBRP with 3σ level of confidence.

Flow reduction affects the coolant enthalpy rise directly and hence the coolant temperature rise. A parametric study using the SASSYS/EBR-II model shows that a 7% reduction in reactor coolant flow will lead to about 7.9% increase in the temperature rise in coolant and nearly 2.5% increase in film, in the hottest channel. Note that there is no increase in the temperature rise in cladding, gap, and fuel although the absolute temperatures in these regions will rise as a result of the coolant and film temperature increases. The temperature rises in cladding, gap, and fuel remain the same since the same amount of heat generated in the fuel is to be removed. The effect of the flow reduction on the film temperature is relatively smaller than on the coolant temperature. This is because the film heat transfer coefficient is tied to the Nusselt number that is equal to a constant coefficient plus a term accounting for the flow-dependent Peclet number. In the flow rate range of interest the constant term is slightly more dominant, so the film temperature change is less sensitive to flow variations than the coolant temperature change. The additional hot channel factor for film, which is omitted from the Addendum, is included for the current analysis even though the effect on the maximum fuel temperature is expected to be insignificant. In FFTF

and CRBRP, a hot channel factor for film was also included. The 1.07 uncertainty factor in subassembly flow rates alone will cause about a 1% increase in the maximum fuel temperature.

4.5.2.2 Flow Profile Within Subassembly

The coolant flow profile within a subassembly is not uniform due to the different flow areas in the interior, edge, and corner subchannels of the subassembly. Together with the effect of power skew in the subassembly, this nonuniform flow profile leads to different coolant temperatures in various subchannels. Subchannel analysis codes such as COTEC [4.54], COBRA [4.55], and THI-3D [4.56] are available for calculations of coolant flow and temperature distributions within various subchannels of a fuel subassembly.

Empirical factors modeling various effects such as turbulent mixing (fraction of axial mass velocity continuously transferred to the adjacent subchannel), cross flow (fraction of the wire wrap transverse flow transferred to the adjacent subchannel), pumping (displacement of coolant by wire wrap), sweeping (forced flow following the wire wrap) in the interior subchannels and swirl in the edge subchannels are selected by calibration of subchannel analysis codes against available experimental data. The lack of complete correspondence between code predictions after calibration and experimental data as well as discrepancies between various sets of data cause an uncertainty that is applied to the nominal temperature distribution predicted by the analysis code. The value of this uncertainty should decrease as more experimental data and analyses become available.

Additionally, the flow areas in individual types of subchannels may also change due to fuel pin bowing and manufacturing tolerances, etc. Flow area variations affect the flow velocity distribution in a subassembly and thus cause changes in flow rates in different subchannels. Analyses had been done in CRBRP to investigate the effects of manufacturing deviations and fuel pin bowing on the subchannel flow areas. As is presented in Section 4.6.3.4, however, the effects on the flow areas, and thus on the hot channel coolant temperature, were found to be insignificant.

Extensive efforts had been made in CRBRP to calibrate the various empirical factors used in the COTEC code against experimental data from several different experiments. Because of the inability of the COTEC model to completely represent the axial and transverse flows and flow split in a wire wrapped bundle, the analysis regarding the statistical calibration uncertainty indicated a

value of 0.058 with 3σ level of confidence. This uncertainty was considered conservative.

There are currently no experimental data for Mark-V subassembly temperature distributions available for subchannel analysis code calibration. In a prior analysis for Mark-III subassembly temperature distributions [4.57], the subchannel friction factors in COBRA were adjusted to give the edge-interior channel flow split based on the flow measurements on subassemblies by Cheng and Todreas [4.58]. One important conclusion of the analysis is that the Cheng-Todreas correlations for predicting subchannel flow distribution result in good correlation between measured and calculated temperatures. The Cheng-Todreas correlations were reported to yield, in their applicable ranges, all flow split data within 5% calibration uncertainty against the available data base. The correlation can be used in the hydrodynamic model of Mark-V fuel subassemblies.

Uncertainty in subassembly flow distribution causes uncertainty in the film temperature rise, as does the inlet flow maldistribution discussed in the above section. It is assumed that the effect of flow changes on the temperature in each region is the same no matter what the flow variation is due to the uncertainty in intrasubassembly or intersubassembly flow distribution. Thus, by proportionality the hot channel factors of 1.056 and 1.018 are assigned for the coolant and film, respectively, due to the 1.05 uncertainty factor compared to the 1.07 uncertainty factor used in Section 4.5.2.1. The hot channel factor for film was also not included previously, as shown in Table 4-2.

4.5.2.3 Cladding Thickness

Two types of cladding materials are under consideration: HT9 and 316SS. For Mark-V fuel, the HT9 cladding OD is required by the manufacturing specifications to be 0.2300±0.0005 in. (0.5842±0.0013 cm) and the cladding ID to be 0.1940±0.0005 in. (0.4928±0.0013 cm). The nominal cladding thickness is thus 0.018 in. (0.046 cm). This leads to a 3σ uncertainty of 3% (actually 2.8%) in the HT9 cladding thickness due to manufacturing deviations as delineated by the tolerances in both OD and ID. For Mark-VA fuel, the 316SS cladding has the same specifications as the cladding of Mark-IIIA fuel; the cladding OD and ID are 0.2300±0.0005 in. (0.05842±0.0013 cm) and 0.2000±0.0005 in. (0.05080±0.0013 cm), respectively. With a nominal thickness of 0.015 in. (0.038 cm), this results in an uncertainty of 3% (really 3.3%) in the cladding thickness for Mark-VA; the 7% uncertainty used in Ref. 4.40 is too conservative.

Cladding thickness affects cladding conductance, and a 3% increase in the cladding thickness will result in a 3% increase in the temperature differential across the cladding, based upon considering the simple heat conduction equation.

4.5.2.4 Fissile Fuel Content

The Mark-V fuel specification [4.32, 4.59] allows a 5% 3σ uncertainty in fissile fuel content, with 4% accounting for chemistry variation (deviations in nuclide masses) and an additional 1% accounting for spatial variations in nuclide specific powers. To allow some room for future refinement in the fissile fuel content uncertainty, the current analysis assumes a 6% uncertainty in this parameter.

Note that earlier EBR-II analyses have used a slightly different approach, in that uncertainties in fuel geometry and fissionable material concentration were considered separately (see Table 2-1), rather than combining these into uncertainty on fissile fuel content. Since the real concern is the effect of the fissionable material uncertainties on power, it is preferable to work with uncertainty in fissile fuel content, which takes into account uncertainty in nuclide specific powers, as well as uncertainties in pin geometry and fissionable material concentration.

4.5.2.5 Clad Thermal Conductivity

Uncertainty in the thermal conductivity of cladding (and fuel as well) exists due to: 1) experimental errors in measurement of this property; and 2) irradiation effects. The thermal conductivity of HT9 as a function of temperature used in the SASSYS/EBR-II code is taken from IFR Metallic Fuels Handbook [4.2]. The actual variation in thermal conductivity is fairly small over the temperature range of interest. The uncertainty is estimated to be about 7%. However, the irradiation effects are not sufficiently well known to establish this uncertainty as of 3σ level of confidence.

The thermal conductivity of unirradiated 316SS cladding has been measured with a high degree of accuracy and the estimated uncertainty is 5% [4.60, 4.61]. However, irradiation effects impose some uncertainty; these include 1.5% due to volumetric swelling [4.62] and 1% due to interstitial lattice defect [4.63]. The overall uncertainty in the thermal conductivity of irradiated 316SS is thus obtained by combining these uncertainties cumulatively to be 7.6%. This is judged to be a 3σ uncertainty.

Calculations from SASSYS/EBR-II code indicate that a 7% decrease in clad thermal conductivity will have about 8% increase in the temperature rise across the cladding region, in the hottest pin in row 2. This yields a hot channel factor of 1.08 for the cladding temperature rise due to the uncertainty in cladding thermal conductivity.

4.5.2.6 Fuel Thermal Conductivity

The subject of uncertainties in the thermal conductivity of U-Pu-Zr fuel is a difficult one because of the limited data base. Furthermore, no data are available for the thermal conductivity of irradiated U-Pu-Zr fuel. The data for the thermal conductivity of U-Pu-Zr fuel are presented in [4.2] along with a recommended correlation. Further discussions can be found in [4.64]. Among the data are those for U-19Pu-10Zr, which is close, in composition, to Mark V fuel, U-20Pu-10Zr. Because of the limited number of compositions tested and the lack of confidence in the data base, an uncertainty of 32% in predicted thermal conductivity of irradiated fuels after porosity interlinkage is conservatively recommended in [4.2]. Later, a new correlation was proposed [4.65] with a recommended uncertainty of 25% at about 2 at. % burnup where the thermal conductivity is a minimum. This correlation is currently used for SASSYS/EBR-II safety calculations for Mark-V fuel and a 25% uncertainty factor is used for the hot channel factors analysis.

The ternary fuel composition does not remain uniform with irradiation; the fuel tends to redistribute zirconium and form three zones. The intermediate zone has a low zirconium fraction and therefore a solidus temperature which is considerably lower than that of the other two zones. However, analysis of melt profiles observed in TREAT tests described in Ref. 4.66 indicates that thermal conductivity varies inversely with zirconium content (i.e., thermal conductivity increases as zirconium content decreases) and that burnup dependence of thermal conductivity is independent of zirconium content. The observed melt profiles were matched using nominal solidus temperatures. Therefore, the uncertainty in fuel melting point, and in zirconium content, is accounted for already by the uncertainty in the fuel thermal conductivity.

The hot channel factor for the fuel temperature rise as a result of the uncertainty in fuel thermal conductivity is found from running the SASSYS/EBR-II model to be 1.25.

4.5.2.7 Film Heat Transfer Coefficient

Uncertainty in the film heat transfer coefficient is determined by the experimental data of the correlation currently used in the SASSYS/EBR-II calculation,

$$Nu = 5.0 + 0.025 \times Pe^{0.8}, \text{ [4.67]}.$$

The use of this equation for Prandtl number of less than 0.1 provides a Nusselt number with an accuracy of 6% from the experimental data. However, the equation was originally meant to be used for internal flow in ducts with uniform duct surface temperature. The application of this correlation to external flow through a fuel bundle introduces an additional uncertainty in the heat transfer coefficient. Thus, an additional arbitrary 10% uncertainty is added arithmetically to the 6% for the current analysis.

The hot channel factor for the film temperature rise due to the uncertainty (16%) in film heat transfer coefficient is found to be 1.20 from the SASSYS/EBR-II calculation.

4.5.2.8 Neutron and Gamma Flux Distribution

Burnup measurements of driver fuel pins from EBR-II compared with calculated burnup values were first reported in [4.68]. The comparisons were limited to driver fuel subassemblies containing only Mark-I and Mark-IA fuel pins. In [4.69], a more elaborate calculational procedure considering also the effects of differing locations and orientations during irradiation of the pins was used, and Mark-II driver pins were included in this analysis. The ratios of calculated-to-measured burnup values range from 0.951 to 1.057. The average value is 0.993, with an estimated standard deviation of 0.024. This standard deviation yields a 3σ uncertainty of 0.072 which is essentially the same value as the one given in [4.34].

The uncertainty obtained from the earlier analysis, 0.07, is employed in the present analysis, so that the hot channel factor of 1.07 as listed in [4.34] for coolant and the hot spot factor of 1.10 for each of the other four regions are adopted for the analysis. There are two possible reasons for the different factors as a result of the uncertainty in neutron and gamma flux distributions: (1) the 1.07 factor for coolant indicates an integrated effect over the entire flow channel whereas the 1.10 factor includes conservatism for a local spot at a particular elevation, (2) the uncertainty factor actually consists of radial and axial subfactors; for the coolant, only the radial

subfactor applies, which is a constant over the entire channel whereas for the rest of the regions, a statistical combination of the radial and axial effects is accounted for.

4.5.3 Additional Uncertainties

Several uncertainties which were not considered in Ref. 4.34 but which were part of the CRBRP uncertainties analysis [4.37] have been examined relative to the Mark-V fuel evaluation. These include uncertainties due to the following effects: interchannel coolant mixing, wire wrap orientation, coolant properties, and loop temperature imbalance. The effect of these uncertainties on the hot channel factors for fuel and cladding is discussed at the end of Secs. 4.5.4.2.1 and 4.5.4.2.2.

4.5.3.1 Interchannel Coolant Mixing

In subassemblies with radial power gradients across the fuel bundle, coolant mixing occurs to reduce the peak subchannel enthalpy rise. Since this phenomenon can only lower pin temperatures, it is conservative for safety analysis to simply neglect it.

4.5.3.2 Wire Wrap Orientation

Due to the swirl flow induced by the wire wrap in subchannels near the subassembly ducts, the flow and temperature distributions in the subassembly depend mildly on the relative orientation of the wire wrap and the power skew. An investigation [4.37] on the power skew range in CRBRP fuel subassemblies and the associated orientations of the wire wrap shows a maximum bounding deviation in the hot channel temperature rise of the order of 1%.

4.5.3.3 Coolant Properties

The polynomial expression used in SASSYS for sodium density fits two empirical equations recommended in [4.70] to within 0.5%. The equation used for sodium specific heat fits the data generated in [4.71] using a thermodynamic relation from [4.72] to within 1.5%. A statistical combination of these two uncertainties yields an uncertainty of 1.6%.

4.5.3.4 Loop Temperature Imbalance

Loop imbalance mixing tests were performed for CRBRP in the Inlet Plenum Feature Model at HEDL [4.73], which was then followed by a Monte Carlo type of analysis. The results

indicate an overall 3σ bounding uncertainty of 4.1°C (including the experimental error) on reactor inlet temperature due to loop temperature imbalance. For EBR-II, the uncertainty is smaller. Under normal operating conditions, the inlet temperature fluctuations (as recorded and retrieved from the Data Acquisition System) in the low-pressure plenum and high-pressure plenum have, in general, a standard deviation of less than 0.27°C (0.5°F) so 0.8°C is adequate as a 3σ bounding uncertainty.

4.5.4 Hot Channel Factors Analyses

Effects of the various uncertainties are accounted for in the hot channel factors analysis, where factors are considered relating the nominal value to one corresponding to the most unfavorable conditions possible. This analysis is necessary to assure safe operation of the reactor.

4.5.4.1 Selection of A Method for Analysis

The semistatistical horizontal method is chosen for the current hot channel factors analyses. This method is selected for the following considerations: a) it allows treatment of uncertainty factors of both direct and statistical types, b) the method has a rigorous analytic basis, c) it yields an estimated overall hot channel factor neither too conservative nor too optimistic and retains the flexibility of specifying an uncertainty type, d) the method was used in the later stage of CRBRP analysis, and e) this method has also been recommended for use in hot spot analyses for reactor analysis [4.43].

4.5.4.2 Hot Channel Factors for Steady State Analysis

During steady-state operation the design criteria require that the peak fuel and cladding temperatures should be below fuel solidus and fuel-cladding eutectic temperatures, respectively. In the present analysis, the hot channel factors were developed for peak temperatures in the fuel low-Zr zone and at the cladding inner surface.

4.5.4.2.1 Fuel Hot Channel Factors

The hot channel factors analysis for the maximum fuel temperature is illustrated in Table 4-4 using the semistatistical horizontal method. The fuel pin under consideration is located in row 2 position which has a coolant channel overall temperature rise of 142°C (255°F). The axial

position of the fuel hot spot is 0.194 m, about 60% of the fuel slug length. Since the redistributed fuel in the low zirconium zone, having a low solidus temperature of 1314 K, is the main constraint, the fule temperature in this analysis is focused on the inner-most location of the intermediate low-Zr zone (about 0.062 cm from fuel centerline).

The values in the parentheses in Table 4-4 are the nominal temperature rises in each of the five regions. The algorithm of the semistatistical horizontal method is explained as follows. First of all, the hot channel factors following the uncertainty factor in each row in Table 4-4 are obtained as discussed in Sections 4.6.1 and 4.6.2. Each nominal temperature rise is multiplied by the hot channel factor(s) resulting from the direct uncertainty factor(s) to obtain an increased temperature rise which is used to account for the statistical uncertainties. For instance, the nominal coolant temperature rise, 82.7°C, is multiplied first by the hot channel factor, 1.02, due to the direct uncertainty in power level measurement to become 84.4°C. To account for the statistical uncertainty in neutron and gamma flux, this new temperature rise is multiplied by 0.07 (the mantissa of the hot channel factor 1.07) to yield 5.9°C as an additional rise in coolant temperature. To account for the uncertainty in fissile fuel concentration, the new temperature rise, 84.4°C, is again multiplied by the mantissa of the corresponding hot channel factor, 1.01. Similar calculations proceed until all the applicable statistical uncertainties for the coolant are considered. The same procedure is performed for each of the remaining four regions (film, cladding, gap, and fuel). The temperature rise in each region due to the same statistical uncertainty is added horizontally to obtain the subtotal temperature rise as a result of the effect of the particular uncertainty. The integrated effect of all the statistical uncertainties is then quantified by taking the square root of the sum of squares of each subtotal uncertainty. That is, the subtotal uncertainty of 46.4 due to neutron and gamma flux is a sum of the five individual temperature rises in the same row (5.9, 1.6, 5.5, 1.5, and 32.0). The value 96.0 is the square root of

$$(46.4^2 + 7.1^2 + 5.0^2 + 1.6^2 + 23.6^2 + 4.4^2 + 80.0^2 + 3.1^2).$$

Table 4-4 Hot Channel Factors Analysis for Mark-V Fuel Pin in Row 2

Row 2 Position (Nominal Peak Coolant Temp. Rise at Subassembly Outlet: 255°F or 142°C)							
Thermo-Physical Quantity (Nom. Temp. Rise at Max. Fuel Temp. Axial Location, °C)	Uncertainty Factor	Coolant (82.7)	Film (15.4)	Cladding (53.5)	Gap (14.6)	Fuel (315.7)	Total Uncertainty
DIRECT:	1.020	1.020	1.020	1.020	1.020	1.013	
Power Level Measurement (Temp. Rise)		84.4	15.7	54.6	14.9	319.8	
STATISTICAL:	1.070	1.070	1.100	1.100	1.100	1.100	
Neutron & Gamma Flux (Temp. Rise)		5.9	1.6	5.5	1.5	32.0	46.4
Flow Rate Thru Subassem.	1.070	1.079	1.025				
(Temp. Rise)		6.7	0.4				7.1
Flow Profile in Subassem.	1.050	1.056	1.018				
(Temp. Rise)		4.7	0.3				5.0
Clad Thickness	1.030			1.030			
(Temp. Rise)				1.6			1.6
Fissile Fuel Content	1.060	1.060	1.060	1.060	1.060	1.042	
(Temp. Rise)		5.1	0.9	3.3	0.9	13.4	23.6
Clad Thermal Conductivity	1.070			1.080			
(Temp. Rise)				4.4			4.4
Fuel Thermal Conductivity	1.250					1.250	
(Temp. Rise)						80.0	80.0
Film Heat Transfer Coef.	1.160		1.200				
(Temp. Rise)			3.1				3.1

						SQRT (SUM (X*X)) =	96.0

T(fuel) = 644.3 + 84.4 + 15.7 + 54.6 + 14.9 + 319.8 + 96.0 = 1229.6 (K)

Overall Hot Channel Factor = (1229.6 - 644.3) / (1126.2 - 644.3) = 1.215

The estimated fuel temperature is obtained by adding the increased temperature rise in each region due to the direct uncertainty and the temperature uncertainty due to all statistical uncertainties to the coolant inlet temperature, as shown near the bottom of Table 4-4. The overall hot channel factor, 1.25, is calculated as presented in the last line of the table, where 1126.2 K is the nominal fuel temperature at the hot spot.

Since the uncertainty in fuel thermal conductivity has increased substantially because of the inclusion of Pu in Mark-V fuel, the thermal conductivity uncertainty factor becomes the dominant term in the temperature calculation. The overall hot channel factor (1.215) for Mark-V is much higher than the factor (1.16) derived for Mark-III fuel.

Another calculation, as shown in Table 4-5, was made to study the effect of the additional uncertainty factors not considered in Ref. 4.34 on the overall hot channel factor. Of the four additional factors, only uncertainties in wire wrap orientation, coolant properties, and loop temperature imbalance are included in the calculation (as noted in Sec. 4.5.3.1, the conservative posture is to take no credit for the effect of interchannel coolant mixing). Note that the temperature uncertainty of 0.8°C due to loop temperature imbalance represents a shift upward in all temperatures and so is added directly to the coolant inlet temperature (644.3 K) in calculating the maximum fuel temperature, as shown near the bottom of the table. The revised calculation indicates that there is only an insignificant increase in the overall hot channel factor (1.216 vs. 1.215). The factor can be decreased slightly by accounting for the interchannel coolant mix which leads to more uniform coolant temperature distribution but was conservatively neglected in the analysis. Conservatism is also provided, as mentioned before, by assuming a normal distribution for the variation in cladding thickness, which would be more appropriately described by a rectangular probability distribution.

4.5.4.2.2 Cladding Hot Channel Factors

The hot channel factors analysis for the maximum cladding temperature is illustrated in Table 4-6 also using the semistatistical horizontal method. The cladding hot spot under consideration is located in the fuel pin in row 6 which has a coolant channel overall temperature rise of 169°C (305°F). The axial position of the cladding hot spot is 0.343 m, at the top of the fuel slug. The constraint for the cladding is the fuel-cladding eutectic temperature, so the cladding temperature in the analysis is focused on the cladding inner surface temperature.

The results indicate that the overall hot channel factor for cladding, 1.15, is slightly smaller when compared to the factor, 1.16, used in Ref. 4.57 for Mark-III fuel cladding. Note that in Ref. 4.57, the same factor, 1.16, derived for predicting maximum fuel temperature was also used for estimating maximum cladding temperature. The overall hot channel factor for cladding temperature in the Mark-III case would have been lower than 1.15 if a separate calculation for the cladding, like the one shown in Table 4-6, had been performed.

Table 4-5 Extended Hot Channel Factors Analysis for Mark-V Fuel Pin in Row 2

Row 2 Position (Nominal Peak Coolant Temp. Rise at Subassembly Outlet: 255°F or 142°)							
Thermo-Physical Quantity (Nom. Temp. Rise at Max. Fuel Temp. Axial Location,°C)	Uncertainty Factor	Coolant (82.7)	Film (15.4)	Cladding (53.5)	Gap (14.6)	Fuel (315.7)	Total Uncertainty
DIRECT:	1.020	1.020	1.020	1.020	1.020	1.013	
Power Level Measurement (Temp. Rise)		84.4	15.7	54.6	14.9	319.8	
STATISTICAL:	1.070	1.070	1.100	1.100	1.100	1.100	
Neutron & Gamma Flux (Temp. Rise)		5.9	1.6	5.5	1.5	32.0	46.4
Flow Rate Thru Subassem.	1.070	1.079	1.025				
(Temp. Rise)		6.7	0.4				7.1
Flow Profile in Subassem.	1.050	1.056	1.018				
(Temp. Rise)		4.7	0.3				5.0
Clad Thickness	1.030			1.030			
(Temp. Rise)				1.6			1.6
Fissile Fuel Content	1.060	1.060	1.060	1.0610	1.060	1.042	
(Temp. Rise)		5.1	0.9	3.3	0.9	13.4	23.6
Clad Thermal Conductivity	1.070			1.080			
(Temp. Rise)				4.4			4.4
Fuel Thermal Conductivity	1.250					1.250	
(Temp. Rise)						80.0	80.0
Film Heat Transfer Coef.	1.160		1.200				
(Temp. Rise)			3.1				3.1
Wire Wrap Orientation	1.010	1.010					
(Temp. Rise)		0.8					0.8
Coolant Properties	1.016	1.016					
(Temp. Rise)		1.3					1.3

						SQRT (SUM (X*X)) =	96.0

T(fuel) = 644.3 + 0.8 + 84.4 + 15.7 + 54.6 + 14.9 + 319.8 + 96.0 = 1230.5 (K)

Overall Hot Channel Factor = (1230.5 - 644.3) / (1126.2 - 644.3) = 1.216

Table 4-6 Hot Channel Factors Analysis for Mark-V Fuel Pin in Row 6

Row 6 Position (Nominal Coolant Temp. Rise, 305°F or 169°C)					
Thermo-Physical Quantity (Nom. Temp. Rise, °C)	Uncertainty Factor	Coolant (169.4)	Film (9.8)	Cladding (27.6)	Total Uncertainty
DIRECT:					
Power Level Measurement	1.020	1.020	1.020	1.020	
(Temp. Rise)		172.8	10.0	28.2	
STATISTICAL:					
Neutron & Gamma Flux	1.070	1.070	1.100	1.100	
(Temp. Rise)		12.1	1.0	2.8	15.9
Flow Rate Thru S-Assem.	1.070	1.079	1.025		
(Temp. Rise)		13.7	0.2		13.9
Flow Profile in S-Assem.	1.050	1.056	1.018		
(Temp. Rise)		9.7	0.2		9.9
Clad Thickness	1.030			1.030	
(Temp. Rise)				0.8	0.8
Fissile Fuel Content	1.060	1.060	1.060	1.060	
(Temp. Rise)		10.4	0.6	1.7	12.7
Clad Thermal Conductivity	1.070			1.080	
(Temp. Rise)				2.3	2.3
Film Heat Transfer Coef.	1.160		1.200		
(Temp. Rise)			2.0		2.0

				SQRT(SUM(X*X)) =	26.7
T(clad) = 644.3 + 172.8 + 10.0 +28.2 + 26.7 = 881.9 (K)					
Overall Hot Channel Factor = (881.9 - 644.3) / (851.1 - 644.3) = 1.149					

Table 4-7 illustrates the effect of the additional uncertainties on the overall hot channel factor for cladding. The factor is increased slightly to 1.154 mainly due to the 0.8°C of loop temperature imbalance.

Table 4-7 Extended Hot Channel Factors Analysis for Mark-V Fuel Pin in Row 6

Row 6 Position (Nominal Coolant Temp. Rise, 305°F or 169°C)					
Thermo-Physical Quantity (Nom. Temp. Rise, °C)	Uncertainty Factor	Coolant (169.4)	Film (9.8)	Cladding (27.6)	Total Uncertainty
DIRECT:					
Power Level Measurement	1.020	1.020	1.020	1.020	
(Temp. Rise)		172.8	10.0	28.2	
STATISTICAL:					
Neutron & Gamma Flux	1.070	1.070	1.100	1.100	
(Temp. Rise)		12.1	1.0	2.8	15.9
Flow Rate Thru S-Assem.	1.070	1.079	1.025		
(Temp. Rise)		13.7	0.2		13.9
Flow Profile in S-Assem.	1.050	1.056	1.018		
(Temp. Rise)		9.7	0.2		9.9
Clad Thickness	1.030			1.030	
(Temp. Rise)				0.8	0.8
Fissile Fuel Content	1.060	1.060	1.060	1.060	
(Temp. Rise)		10.4	0.6	1.7	12.7
Clad Thermal Conductivity	1.070			1.080	
(Temp. Rise)				2.3	2.3
Film Heat Transfer Coef.	1.160		1.200		
(Temp. Rise)			2.0		2.0
Wire Wrap Orientation	1.010	1.010			
(Temp. Rise)		1.7			1.7
Coolant Properties	1.016	1.016			
(Temp. Rise)		2.8			2.8

				SQRT(SUM(X*X)) =	26.9
T(clad) = 644.3 + 0.8 + 172.8 + 10.0 +28.2 + 26.9 = 882.9 (K)					
Overall Hot Channel Factor = (882.9 - 644.3) / (851.1 - 644.3) = 1.154					

4.5.5 Uncertainty Factors for Transient Analysis

A set of transient uncertainty factors were developed to predict the hot channel temperatures of Mark-V fuel pins during transient operation. The uncertainty factors for transient analysis were developed using the methodology of Ref. 4.74. The uncertainties in Table 4-4 were sorted into five groups: one group of uncertainties which directly affect reactor power, another

group which directly affect flow rate, a third group which affect fuel heat transfer, a fourth group which affect cladding heat transfer, and a fifth group which affect film heat transfer. The uncertainties in each group were combined to obtain a preliminary composite uncertainty factor for the physical parameter directly affected by the uncertainties in that group. However, it is not correct to apply the preliminary composite uncertainties directly to the corresponding physical parameters, since this would be treating the composite factors as independent variables, whereas all uncertainties except that in power level measurement are statistical. The integrated effect of the composite factors on calculated temperatures would be the product of each separate effect, which would result in temperatures different from those obtained by applying the steady-state uncertainty factors (which are derived by treating power level measurement directly and all other uncertainties statistically). Therefore, the preliminary composite factors are normalized to produce factors which, when applied directly, predict a steady-state hot channel fuel temperature which is consistent with that calculated by applying the steady-state uncertainty factors to the fuel temperature predicted by a best-estimated steady-state calculation.

Uncertainties in power level measurement, neutron and gamma fluxes, and fissile fuel content in Table 4-4 directly affect power and form one group. Uncertainties in flow rate through a subassembly and flow profile within a subassembly directly affect flow and form a second group. The uncertainty in fuel thermal conductivity affects fuel heat transfer and constitutes a third group. Cladding thermal conductivity and thickness affect cladding heat transfer and make up a fourth group. The uncertainty in the film heat transfer coefficient directly affects film heat transfer and forms a fifth group.

Each of the preliminary composite uncertainty factors is obtained as follows:

1. Power, $P = 1.02 \times (1 + (0.07^2 + 0.06^2)^{0.5})$
   $= 1.114$

where the uncertainty factor, 1.02, of power level measurement is still treated as a direct factor and the remaining three factors are treated statistically;

2. Flow, $F = 1 + (0.07^2 + 0.05^2)^{0.5}$
   $= 1.086$
3. Fuel heat transfer, $H_{fuel} = 1.25$

4. Cladding heat transfer, $H_{clad} = 1 + (0.03^2 + 0.07^2)^{0.5}$

$= 1.076$

5. Film heat transfer, $H_{film} = 1.16$

Application of transient uncertainty factors must produce both fuel and cladding temperatures which conservatively represent the effects of the known parameter uncertainties. Since uncertainty is greater in the fuel temperature than in the cladding temperature, as shown in the hot channel factors analyses of Sec. 4.5.4.2, the transient factors were derived by considering the effect of the uncertainties on the fuel temperature. This approach results in transient factors which bound the steady-state uncertainties in both fuel and cladding temperatures. Since fuel temperature is greatest in the inner rows, the transient factor derivation considered row 1 fuel temperatures.

A parametric study performed for row 1 with the SASSYS/EBR-II code shows that each of the above five composite factors alone will lead to an increase in fuel centerline temperature, relative to coolant inlet temperature, by a factor of 1.102, 1.013, 1.211, 1.007, and 1.005, respectively. If all five composite factors are applied at the same time, the fuel temperature increases by a factor of 1.364 (simple multiplication of the basic numbers yields 1.368; the difference arises from non-constant thermal properties). In doing this, the factors are treated as statistically independent (direct) factors. This is overly conservative, however; it it more accurate, though still conservative, to combine the five factors statistically. This is achieved by adjusting the five preliminary composite factors as described below.

If the increases in fuel temperature due to each of the five composite uncertainty factors are combined statistically the fuel temperature will rise by a factor of

$$1 + (0.102^2 + 0.013^2 + 0.211^2 + 0.007^2 + 0.005^2)^{0.5} = 1.235$$

This statistical factor, 1.235, together with the cumulative factor, 1.364, are used to adjust the five preliminary uncertainty factors so that direct application of the adjusted factors produces the correct fuel temperature, consistent with applying the preliminary factors in a statistical manner. That is, each of the five factors is adjusted by multiplication by the ratio,

$$0.235 / 0.364 = 0.646$$

to yield the refined factors,

$$P = 1 + 0.114 \times 0.646 = 1.074$$

$$F = 1 + 0.086 \times 0.646 = 1.056$$

$$H_{fuel} = 1 + 0.250 \times 0.646 = 1.161$$

$$H_{clad} = 1 + 0.076 \times 0.646 = 1.049$$

$$H_{film} = 1 + 0.160 \times 0.646 = 1.103$$

The highest temperatures arise from a combination of excessive power and reduced flow and heat transfer. The factors F, H_{fuel}, H_{clad}, and H_{film}, minus 1, represent the fraction by which the flow, fuel and cladding thermal conductivities, and film heat transfer coefficient must be reduced to achieve peak temperatures due to uncertainties, whereas the quantity (P - 1) represents the fraction by which the power must be increased. Therefore, power must be increased and flow, thermal conductivity, and film heat transfer coefficient decreased by the following factors (rounded to two decimal places):

$$P = 1.074$$

$$\hat{F} = 1 / (1 - 0.056) = 1.06$$

$$\hat{H}_{fuel} = 1 / (1 - 0.161) = 1.19$$

$$\hat{H}_{clad} = 1 / (1 - 0.049) = 1.05$$

$$\hat{H}_{film} = 1 / (1 - 0.103) = 1.12$$

That is, to obtain the highest temperatures as input for transient calculation, the nominal power should be increased by directly multiplying by the adjusted power uncertainty factor, 1.074, while the nominal flow rate and material heat transfer characteristics should be decreased by being directly divided by the respective uncertainty factors, 1.06, 1.19, 1.05, and 1.12.

To check the validity of this final set of composite uncertainty factors for all rows, null-transient (i.e. transients with no variation of the forcing functions, or quasi-steady-states) calculations were performed with these factors applied directly to the related quantities. In the SASSYS/EBR-II input file, the nominal power was multiplied by 1.074 and the nominal flow rate was divided by 1.06. In addition, the nominal values of fuel thermal conductivity, cladding thermal conductivity, and film heat transfer coefficient were divided, respectively, by 1.19, 1.05, and 1.12 at each time step before being used for relevant computations. The results show that in

row 2, the maximum fuel temperature in the intermediate low Zr zone is 1226.6 K, and in row 6, the maximum cladding temperature is 880.4 K. These temperatures are slightly lower than the temperatures obtained from the hot channel factors analysis for the steady state (shown in Table 4-4 and Table 4-6). So as to keep the temperatures computed from the transient factors conservative with respect to those computed using the steady-state factors, the transient factors were fine-tuned by increasing the adjustment factor from 0.646 to 0.67, which gives

$$P = 1.08$$

$$F = 1.06$$

$$H_{fuel} = 1.2$$

$$H_{clad} = 1.05$$

$$H_{film} = 1.12$$

A null-transient calculation using these factors gives a maximum row 2 fuel temperature in the low-Zr zone of 1232.4 K and a maximum row 6 cladding temperature of 882 K, which are in excellent agreement with the temperatures in Table 4-4 and Table 4-6.

The use of these final transient composite hot channel factors allows direct analysis of transient performance for "hot pins" in each row. This method is more accurate than evaluating the nominal temperature and multiplying by some effective hot channel factor.

4.5.6 Summary

Uncertainty factors for Mark-V fuel have been determined, based primarily on the factors reported in ANL-5719 (Addendum) and in reference to the FFTF and CRBRP works. Most of the factors retain the values given in Ref. 4.34, apart from a few minor changes, except for the large increase in the fuel thermal conductivity uncertainty factor. The large uncertainty in fuel thermal conductivity is due to lack of data; as more conductivity data are acquired for the ternary fuel, this uncertainty will decrease.

Application of uncertainty factors to the hot channel factors analyses is performed to obtain separate overall hot channel factors for fuel and cladding for steady state analysis. The semistatistical horizontal method was used for the analyses. The overall hot channel factor for fuel temperature for Mark-V fuel is larger than that for Mark-III fuel mainly due to the higher

uncertainty in fuel thermal conductivity, whereas the overall hot channel factor for cladding temperature is smaller for Mark-V fuel than for Mark-III fuel. Had a separate hot channel factor been calculated for predicting maximum cladding temperature for Mark-III fuel, the factor would have been smaller than its counterpart for Mark-V fuel.

Additional uncertainty factors (Sec. 4.5.3) that have not been considered in prior EBR-II analyses are also examined. Results of the hot channel factors analyses including additional factors indicate only slight increases in maximum fuel and cladding temperatures due to increase of the overall hot channel factors.

The set of uncertainty factors to be used for transient analysis has also been obtained. The validity of these factors is confirmed by running the null-transient calculations and comparing the results to steady state calculations.

4.6 Duct Performance

Both HT-9 and 316SS have been used as duct materials in earlier fuel designs, see Table 1-1. The performance of the 316SS ducts has been adequate to maintain the fluence equivalent of 10 at.% burnup in a uranium core. While there is less data available concerning HT-9 in EBR-II, HT-9 is a low-swelling alloy intended for high-burnup use that has been used in FFTF and is intended to go to higher fluence levels.

In the EBR-II operation, the duct dilation is limited to 1.016 mm (40 mils) due to the hole size of the storage basket. This duct dilation has no impact on reactor safety, and the dilation calculation is not required in the safety analysis. The basis, therefore, for duct lifetime in EBR-II will be performance-based; nonetheless an analysis model was developed to investigate possible higher fluence limits, HT-9 performance and to identify any 'cliffs', sudden changes in performance, which the Mark-V and Mark-VA subassemblies might be approaching in the modified core environment.

4.6.1 Duct Description

The Mark-V subassembly is shown in Figure 3-1; the top end fixture is made of 304SS, while the duct is made with either HT-9 or 12% CW 316SS. The duct is 1.016 mm. (0.04 in.) thick and has a flat-to-flat inside distance of 56.134 mm. (2.21 in.). The duct is about 1.676 meter

(66 in.) in length and has a button (load pad) about 0.356 mm. (0.014 in.) in depth located at 38.1 mm. (1.5 in.) above the fuel midplane. The gap between subassemblies is about 0.712 mm. (28 mils), and there is practically no gap between buttons of adjacent subassemblies. There are 61 fuel pins arranged in five rows inside the duct, the outside diameter of the fuel-cladding and the wire wraps are 5.842 mm. (0.23 in.) and 1.067 mm. (0.042 in.) respectively.

4.6.2 Code and Model Description

The ANSYS structural analysis code [4.75] was used for the duct analysis. ANSYS is a well-accepted structural analysis code that has been widely used in the static and dynamic analyses of structural components and has been verified by numerous organizations. ANSYS is capable of handling both general linear as well as nonlinear structural problems. The preprocesor and postprocessor are especially powerful in generating and checking inputs and in sorting and processing the results of analysis.

Two finite-element models, one three-dimensional (3-D) and one two-dimensional (2-D), have been developed to assess the performance of the duct during steady-state irradiation. The 3-D model, shown in Figure 4-5, can be applied to part or all of the length of the duct. When the model is applied to a partial length of the duct, plane stress is assumed in the axial direction. The 3-D model is capable of studying the effect of asymmetrical loading on the duct, which is often encountered in the reactor. The numerous elements needed in this 3-D model make it costly to perform creep and swelling calculations, which require many iterations and long CPU time. Consequently, the 2-D model, shown in Figure 4-6, was developed. It focuses on a local area of the duct, and thus fewer elements are needed to perform inelastic analysis. Using the 2-D model results in acceptable CPU time without unacceptable loss of accuracy, since the 3-D model can provide adequate boundary conditions for the 2-D analysis. Thus, use of the 3-D model was limited to defining and validating the boundary conditions specified in the local 2-D model and to examining the global behavior of the duct.

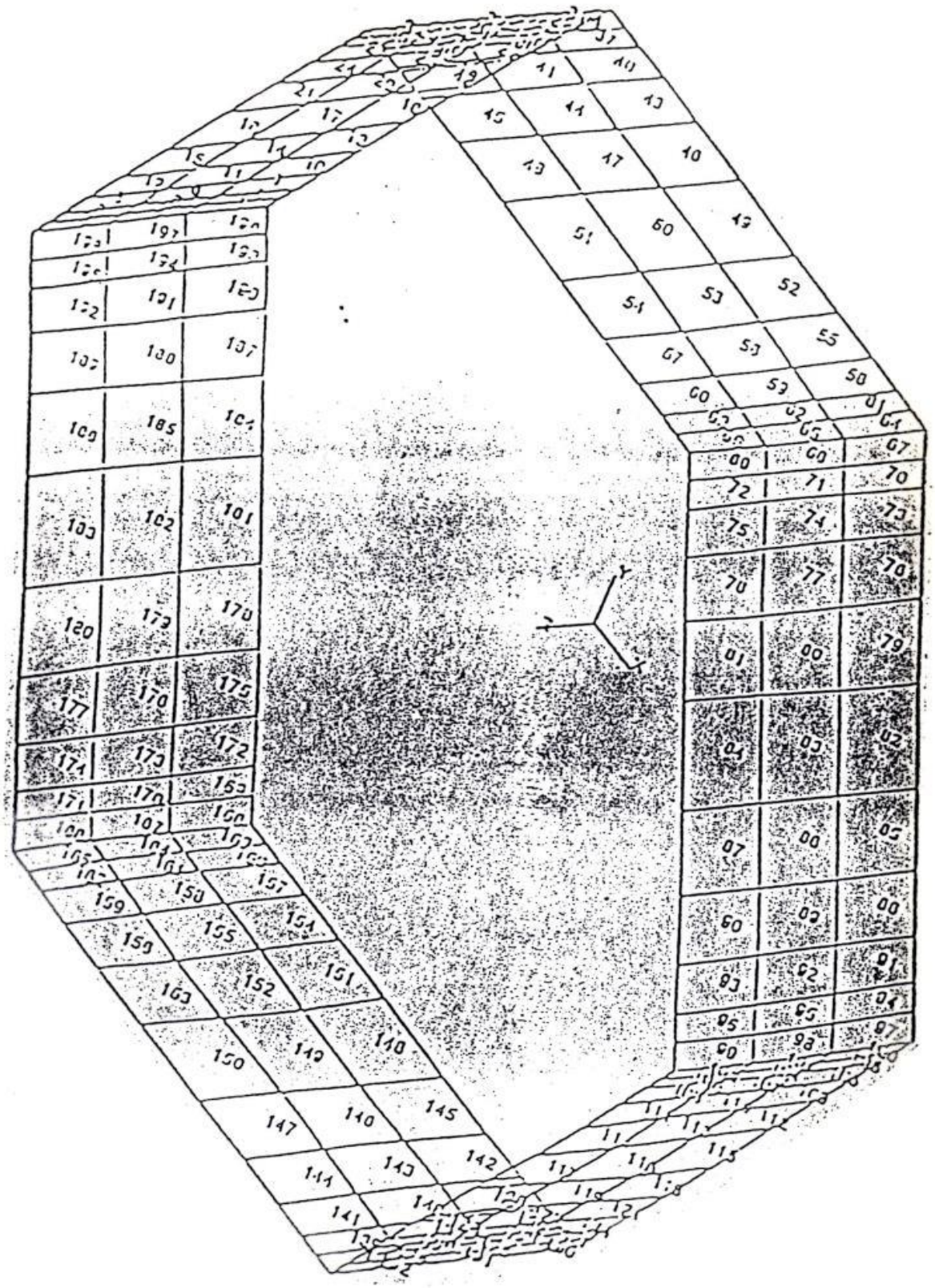

Figure 4-5 Three-Dimensional Finite-Element Model of the Duct

Figure 4-6 shows the model of a one-sixth section of the duct. Gap elements are used to model duct-to-duct interaction behavior. Two-dimensional isoparametric solid elements have been used to describe the cross-thickness details of the flat and corner of the duct. The model calculates the time-dependent inelastic creep and swelling strains over the history of burnup. The duct is assumed to be subjected to symmetrical loading only. For driver subassemblies irradiated in rows 1 through 7 in EBR-II, this assumption is reasonable. The variations of temperature, pressure and fluence across the subassembly are less than 10% of the average values, and the variations are compensated for by conservative assumptions employed in the analysis. The gap elements which simulate the duct-to-duct interaction play an important role in the determination of the duct dilation.

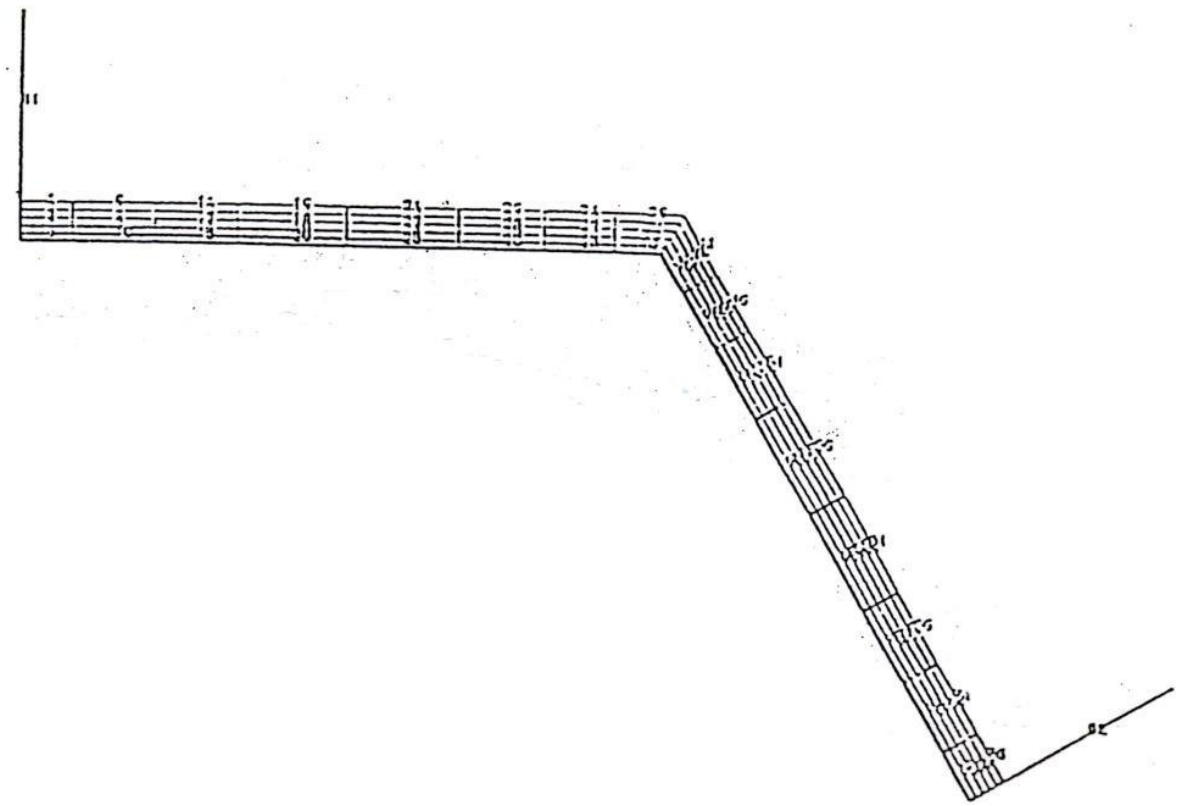

Figure 4-6 Two-Dimensional Finite-Element Model of One-Sixth of a Duct

Since the dilation calculation is highly nonlinear, the time step was kept very small to ensure solution convergence (in the ANSYS calculation the convergence is automatically checked by the code, and a flag is raised when a specified tolerance is exceeded). A burnup of 15 at. % was chosen for the analysis to allow for an increase in the current 10 at. % burnup design limit.

Duct dilation is caused by both creep and swelling, which are a function of pressure and temperature and the irradiation environment. The creep and swelling correlations in Ref. 4.3 were used in the code calculation, and the initial boundary conditions, such as the gap size between subassemblies, were determined based on irradiation histories of a cluster of seven subassemblies. As the fluences increase, the subassembly ducts tend to dilate due to a combination of creep and swelling until the gap between subassemblies is closed. Stress in the duct is then drastically reduced, since the pressure loadings in the ducts cancel each other once duct-to-duct contact is established. Further dilation is caused by swelling only.

4.6.3 Model Validation

Duct models were developed using different numbers and/or types of elements, and the analysis results from these models were compared to ensure that model predictions were consistent and that the model was economically feasible. The calculational results were then compared with a simplified closed-form solution to ensure solution accuracy for the test problem.

In the model validation, the 3-D model was used to study the effect of asymmetric loading and to ensure that adequate boundary conditions are used in the 2-D model analysis. The 2-D finite-element model with gap elements was used for the dilation analysis, in which a unit length and plane strain were assumed in the calculation.

In order to assess the model, the performance of eight 316SS driver subassembly ducts for which there were profilometry measurements was analyzed. The eight subassemblies were categorized into two groups according to fluence and pressure loading during irradiation. The first group included three subassemblies in rows 2 and 3 which had fluences between 8.4 and 10.0 x 10^{22} n/cm^2, with surrounding subassemblies having the same fluence level. In the code calculation, the radial gap of the duct was set to be 0.356 mm (14 mils), and contact was initiated when radial dilation reached about 0.305 mm (12 mils) as shown in Figure 4-7. The second group included five subassemblies located in rows 6 and 7 which had fluences between 6.5 and 8.0 x 10^{22} n/cm^2, with the surrounding subassemblies having a higher fluence level. A portion of the gap was occupied by the surrounding subassemblies, so the gap was, therefore, smaller than the original value. In the calculation, the initial gap was assumed to be 0.254 mm (10 mils), and duct-to-duct contact occurred when the duct radial dilation reached about 0.203 mm (8 mils). (In the analysis presented in Section 8, it was assumed that the initial gap between subassemblies was

the nominal unirradiated gap of 0.711 mm (28 mils)). Determination of the initial gap is necessary for accurate duct dilation prediction. An upper bound for duct dilation can be obtained when the gap size is set to a large value.

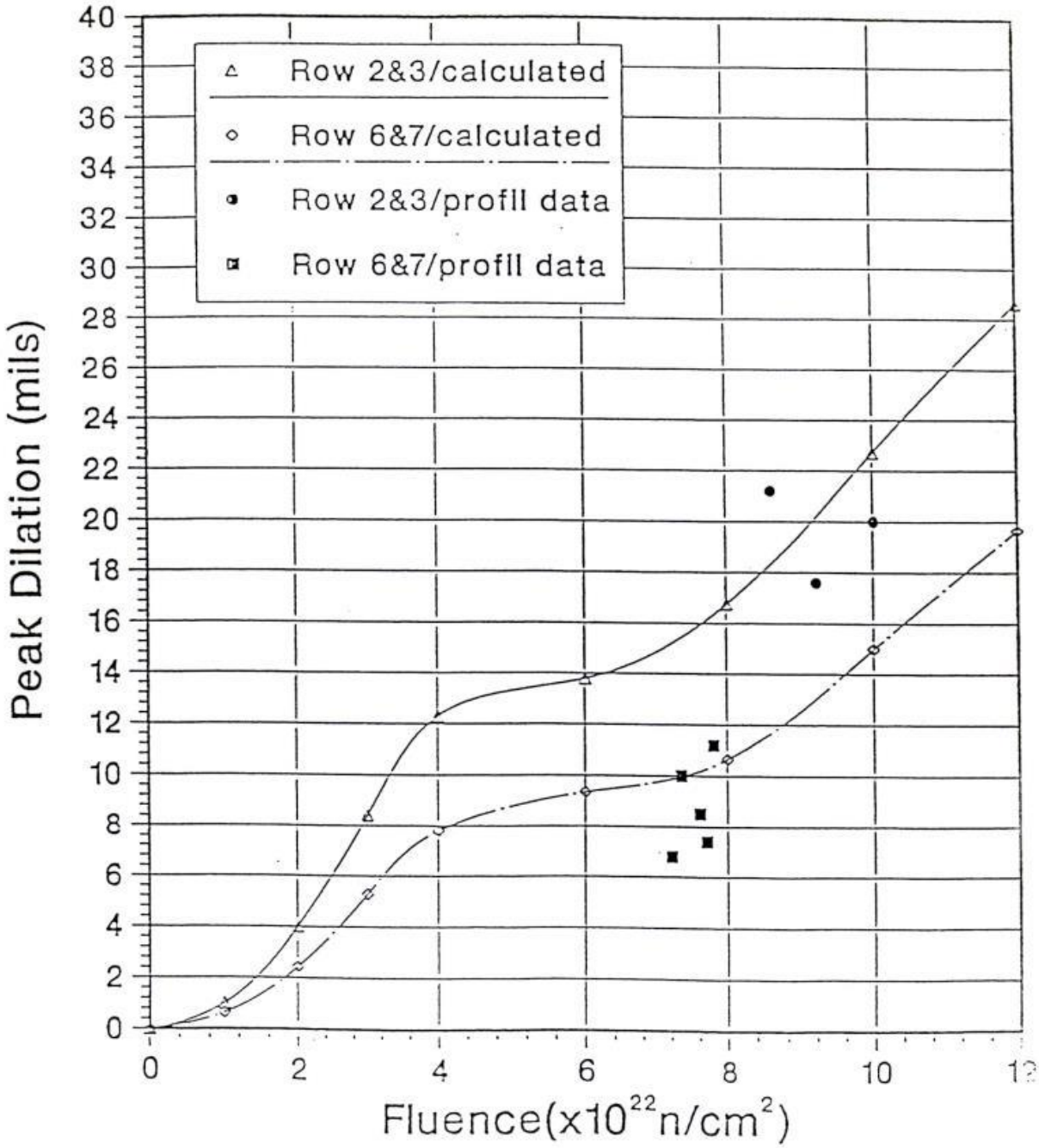

Figure 4-7 Diametrical Dilation of 316SS Ducts Considering Interaction between Adjacent Subassemblies

The calculations confirm that in the early stage of irradiation when gaps exist between subassemblies, the dilation is induced by creep, which is a function of pressure. Since the pressure is higher in the inner-row subassemblies, the duct dilation rate is higher in rows 2 and 3 than in rows 6 and 7. Eventually duct-to-duct interaction is initiated, as shown in Figure 4-7, and the rate of dilation is slowed.

4.6.4 Application of the Model for Duct Analysis

The duct dilation model offers a good representation of the dilation behavior of the SS316 ducts in the EBR-II core. This is evidenced in the good agreement of the predictions with a number of profilometry measurements shown in Figure 4-7. This model will therefore be used to identify any potential problems with SS316 and HT-9 subassemblies at higher fluences and in the modified core environment and to support the performance-based evaluation of SS316 and HT-9 duct in EBR-II.

Section 4 References

4.1 M. C. Billone, Y. Y. Liu, E. E. Gruber, T. H. Hughes, and J. M. Kramer, "Status of Fuel Element Modeling Codes for Metallic Fuels", Proc. ANS International Conference on Reliable Fuels for Liquid Metal Reactors, September 7-11, 1986, p. 5-77.

4.2 G. L. Hofman, et al., "Metallic Fuels Handbook," Argonne National Laboratory, ANL-IFR-29 (November 1985).

4.3 Nuclear Systems Materials Handbook, Vol. 1: Design Data, Oak Ridge National Laboratory, TID 26666.

4.4 J. M. Kramer and T. H. Bauer, "Fuel Damage during Off-normal Transients in Metal-Fueled Fast Reactors," Proc. International Fast Reactor Safety Meeting, Snowbird, Utah, August 12-16, 1990.

4.5 T. H. Hughes and J. M. Kramer, "The FPIN2 Code - An Application of the Finite Element Method to the Analysis of the Transient Response of Oxide and Metal Fuel Elements," Conference on the Science and Technology of Fast Reactor Safety, Guernsey (May 12-16, 1986).

4.6 E. E. Gruber and J. M. Kramer, "Gas-Bubble Growth Mechanisms in the Analysis of Metal Fuel Swelling," Argonne National Laboratory, ANL-IFR-27 (October 1985).

4.7 J. M. Kramer, T. H. Hughes and E. E. Gruber, "Validation of Models for the Analysis of the Transient Behavior of Metallic Fast Reactor Fuel," Argonne National Laboratory, ANL-IFR-66 (April 1987).

4.8 J. M. Kramer, T. H. Hughes and E. E. Gruber, "Validation of Models of the Analysis of the Transient Behavior of Metallic Fast Reactor Fuel," Trans. of the 10th International Conference on Structural Mechanics in Reactor Technology, Vol. C, 65, Anaheim, California (August 1989).

4.9 M. C. Billone and J. M. Kramer, Argonne National Laboratory, unpublished information (1990).

4.10 J. M. Kramer, Argonne National Laboratory, unpublished information (1990).

4.11 J. M. Kramer and T. H. Hughes, Argonne National Laboratory, unpublished information (1990).

4.12 J. M. Kramer, Y. Y. Liu, M. C. Billone and H. C. Tsai, "Modeling the Behavior of Metallic Fast Reactor Fuels During Extended Transients," Journal of Nuclear Materials, Vol. 204, pp. 203-211 (1993).

4.13 K. L. Miles, "Metal Fuel Safety Performance," Proceedings, International Topical Meeting on Safety of Next Generation Reactor, Seattle, Washington, May 1-5, 1988.

4.14 J. M. Kramer and R. J. DiMelfi, "Modeling Deformation and Failure of Fast Reactor Cladding During Simulated Accident Transients," Nucl. Eng. and Design, 63 1981.

4.15 T. H. Bauer, C. R. Fenske, and J. M. Kramer, "Cladding Failure Margins for Metallic Fuel in the Integral Fast Reactor," 9th International Congress on Structural Mechanics in Reactor Technology, Laosanne, Switzerland

4.16 A. E. Wright et al., "Recent Metal Fuel Safety Experiments in TREAT," Science and Technology of Fast Reactor Safety, Guernsey, Channel Islands, U. K., 1986.

4.17 J. E. Cahalan and T. Y. C. Wei, "Modeling Developments for the SAS4A and SASSYS Computer Codes," Proceedings of the 1990 International Fast Reactor Safety Meeting (Snowbird, Utah, August 12-16, 1990), American Nuclear Society, II:123 (1990).

4.18 C. E. Till and Y. I. Chang, "The Integral Fast Reactor Concept," Proceedings of the American Power Conference, Chicago, Illinois, 1986.

4.19 E. L. Gluekler, et. al., "Safety Characteristics of a Small Modular Reactor," Proceedings of the International Topical Meeting on Fast Reactor Safety, Knoxville, Tennessee, 1985.

4.20 J. P. Herzog, "SASSYS Validation with the EBR-II Shutdown Heat Removal Tests," Fifth Proceedings of Nuclear Thermal Hydraulics, 1989 ANS Winter Meeting, pp. 416-423.

4.21 H. P. Planchon, et. al., "The Experimental Breeder Reactor II Inherent Shutdown and Heat Removal Tests-Results and Analysis," Nuclear Engineering and Design, 1986, Vol. 91.

4.22 D. J. Hill, "SASSYS Validation Studies," Proceeding of the International Topical Meeting on Safety of Next Generation Power Reactors, Seattle Washington, 1988.

4.23 R. B. Vilim, T. Y. C. Wei, and F. E. Dunn, "Generalized Control System Modeling for Liquid Metal Reactors," Nuc. Sci. Eng., Vol. 99, pp. 183-196, 1988.

4.24 J. Y. Ku and T. C. Hung, "SASSYS EBR-II Plant Protection System Model and Model Validation," Argonne National Laboratory, ANL-FRA-172, October 1992.

4.25 D. Saphier, "The Simulation Language of DSNP: Dynamic Simulator for Nuclear Power-plants (User Manual)," ANL-CT-77-20, March 11, 1990.

4.26 D. Mohr and E. Feldman, A Dynamic Simulation of the EBR-II Plant with the NATDEMO code, Decay Heat Removal and Natural Circulation in Fast Breeder Reactors, eds. A. Agrawal and J. Guppy (Hemisphere Publishing Co., Washington, 1981) pp. 207-224.

4.27 J. M. Keeton, W. K.. Lehto, R. J. Forrester, and J. I. Sackett, "Final Safety Analysis Addendum to Hazards Summary Report, Experimental Breeder Reactor II (EBR-II): EBR-II Operation in the Limited Transient Mode," ANL-84-70, March 1985.

4.28 J. J. Kaganove, E. M. Dean, and A. V. Campise, "EBR-II Reactor Operation Simulator: Vol. I, A Description of EROS," ANL-7981, August 1974.

4.29 R. N. Curran, E. M. Dean, J. F. Boland, and J. I. Sackett, "Design-Basis Document for Trips Related to Reactivity Change in the EBR-II PPS (in the Operate Mode)," ANL-76-32, December 1980.

4.30 Argonne National Laboratory, unpublished information (1990).

4.31 J. M. Keeton, "Final Safety Analysis Addenda to Hazards Summary Report, Experimental Breeder Reactor II (EBR-II): Upgrading of Plant Protection System, Vol. III," ANL-83-92, January 1984.

4.32 D. L. Porter, et al., "EBR-II Mark-V and -VA Fuel Pins ands Elements Specification," ANL-IFR-246, Section II.B, December 1994.

4.33 L. K. Chang, Argonne National Laboratory, unpublished information (1993).

4.34 L. J. Koch, W. B. Loewenstein, and H. O. Monson, Argonne National Laboratory, unpublished information (1962).

4.35 G. J. Calamai, R. D. Coffield, L. J. Ossens, J. L. Kerian, J. V. Miller, E. H. Novenstern, G. H. Ursin, and P. J. Wood, Steady State Thermal and Hydraulic Characteristics of the FFTF Fuel Assemblies, ARD-FRT-1582, Westinghouse Electric Corp., June 1974.

4.36 J. Muraoka, R. E. Peterson, R. G. Brown, W. D, Yule, D. S. Dutt and J. E. Hanson, Assessment of FFTF Hot Channel Factors, HEDL-TI-75226, Hanford Engineering Development Laboratory, November 1976.

4.37 A. J. Friedland, "CRBRP Core Assemblies Hot Channel Factors Preliminary Analysis," CRBRP-ARD-0050, Westinghouse Electric Corp., February 1980.

4.38 M. D. Carelli and A. J. Friedland, "Hot Channel Factors for Rod Temperature Calculations in LMFBR Assemblies," Nucl. Eng. and Des., 62 (1980) 155-180.

4.39 L. K. Chang and E. E. Feldman, Argonne National Laboratory, unpublished information

(1982).

4.40 J. F. Koenig, Argonne National Laboratory, unpublished information (1988).

4.41 A. E. Waltar and A. B. Reynolds, “Fast Breeder Reactors”, Pergamon Press, New York, 1981.

4.42 Y. S. Tang, R. D. Coffield and R. A. Markley, Thermal Analysis of Liquid Metal Fast Breeder Reactors, ANS, pp. 82-109, 1978.

4.43 R. B. Vilim, "Reactor Hot Spot Analysis," Argonne National Laboratory, FRA-TM-152, ANL, August 1985.

4.44 J. L. Gillette, G. H. Golden, and B. R. Sehgal, "Neutronic and Thermal-Hydraulic Analyses of Mixed Cores for EBR-II," ANL-7778, July 1971.

4.45 H. P. Planchon, D. L. Porter, and W. H. Perry, Argonne National Laboratory, unpublished information (1990).

4.46 P. R. Betten, "In-core Measurements of U-5 wt.% Fissium Alloy Thermal Conductivity," Trans. Am. Nuc. Vol. 50, pp. 239-240 (1985).

4.47 L. L. Briggs, Argonne National Laboratory, unpublished information (1991).

4.48 D. T. Rymsa and G. P. Wachtell, “Flow Model Study of the EBR-II,” The Franklin Institute Philadelphia, Pennsylvania (Final Report, F-A2201), July 15, 1958 to December 2, 1960.

4.49 J. D. Cerchione, F. D. McGinnis, P. M. Long, R. E. Rice, and A. Gopalakrishnan, “Final System Description of the EBR-II Reactor Hydraulic Test Facility (RHTF),” ANL/EBR-6, October 1972.

4.50 W. B. Loewenstein, Argonne National Laboratory, unpublished information (1972).

4.51 A. Gopalakrishnan and J. L. Gillette, "EBRFLOW - A Computer Program for Prediction the Coolant Flow Distribution in the Experimental Breeder Reactor II," Nuclear Technology, Vol. 17, pp. 205-216, 1973.

4.52 J. V. Tokar and E. E. Feldman, Argonne National Laboratory, unpublished information (1976).

4.53 R. G. Staker, Argonne National Laboratory, unpublished information (1976).

4.54 E. H. Novendstern, "Mixing Model for Wire Wrap Fuel Assemblies," Trans. Am. Nucl. Soc., Vol. 15, p. 866, 1972.

4.55 E. P. Coomes, et al., Users' Manual, COBRA-WC: A Version of COBRA for Single-Phase and Multiassembly Thermal-Hydraulic Transient Analysis, PNL-4303, May 1982.

4.56 W. T. Sha and R. C. Schmitt, Argonne National Laboratory, unpublished information (1974).

4.57 J. F. Koenig, Argonne National Laboratory, unpublished information (1991).

4.58 S. K. Cheng and N. E. Todreas, "Hydrodynamics Models and Correlations for Bare and Wire Wrapped Hexagonal Rod Bundles - Bundle Friction Factors, Subchannel Friction Factors, and Mixing Parameters," Nuclear Engineering and Design (1986) 227-251.

4.59 Integral Fast Reactor Program Annual Progress Report, Section II.B, ANL-IFR-246 (1994).

4.60 Nuclear Systems Materials Handbook, Vol. 1 - Design Data, Part I - Structural Materials; Group I - High Alloy Steel: Section 4 - 316SS Annealed.

4.61 Nuclear Systems Materials Handbook, Vol. 2 - Supporting Documentation, Part I - Structural Materials; Group I - High Alloy Steel; Section 4 - 316SS Annealed.

4.62 M. Jakob, "Heat Transfer," Vol. 1, p. 85, John Wiley and Sons, New York, 1949.

4.63 C. A. Bruch and W. E. McHugh, "Radiation Damage Studies of Seven Non-Fissionable Metals," Preprint 37, Session 26, presented at the Nuclear Engineering and Science Conference, March 17-21, 1958, Chicago, Illinois.

4.64 M. C. Billone, Argonne National Laboratory, unpublished information (1990).

4.65 M. C. Billone, Argonne National Laboratory, unpublished information (1991).

4.66 T. H. Bauer and J. W. Holland, "In-Pile Measurement of the Thermal Conductivity of Irradiated Metallic Fuel," ANL-IFR-218, November 1993.

4.67 R. A. Seban and T. T. Shimazaki, "Heat Transfer to a Fluid Flowing Turbulently in a Smooth Pipe with Walls at Constant Temperature," Trans. ASME, Vol. 73, pp. 803-809, 1951.

4.68 D. Meneghetti, E. R. Ebersole, and P. Walker, "Analysis of Burnups in EBR-II Driver-Fuel Elements," Nuclear Technology, Vol. 25, pp. 406-415, February 1975.

4.69 D. A. Kucera, D. Meneghetti and E. R. Ebersole, "Analysis of Burnups in Experimental Fuel Elements Irradiated in EBR-II," Trans. ANS, Vol. 23, pp. 573-574, 1976.

4.70 J. K. Fink and L. Leibowitz, "Thermophysical Properties of Sodium," ANL-CEN-RSD-79-1, May 1979.

4.71 A. Padilla, "High-Temperature Thermodynamic Properties of Sodium," HEDL-TME 77-27, February 1978.

4.72 J. S. Rowlinson, “Liquids and Liquid Mixtures,” 2nd Ed., Plenum Press, New York, 1969.

4.73 P. M. McConnell, F. R. Fisher, and R. G. White, "Inlet Plenum Feature Model Flow Tests of the Clinch River Breeder Reactor: Addendum V Results," HEDL-TME 76-33, March 1976.

4.74 D. Mohr, Argonne National Laboratory, unpublished information (1991).

4.75 "ANSYS Engineering Analysis System", Swanson Analysis Systems, Inc., Revision 4.4, issued May 1, 1989

5 TESTING EXPERIENCE AND PLANS

5.1 Purpose

The purpose of this subsection is to review the irradiation experience to date which is applicable to the Mark-V fuel design and its anticipated performance. Experience relevant to U-20Pu-10Zr fuel clad in HT9 and 316SS will be covered in sufficient detail to show the expected behavior and demonstrate the needed reliability for the core conversion to Mark-V and Mark-VA driver fuel.

5.2 Irradiation Data Base

The irradiation database used for the assessment of Mark-V/VA driver fuel safety and reliability is composed mainly of experimental data for fuel of slightly lower Pu content. For this level of plutonium content, the in-reactor behavior of Mark-V/VA fuel during transients and steady-state is not expected to differ significantly from the U-19Pu-10Zr fuel data which dominates the existing database. The Pu composition for the experimental U-19Pu-10Zr fuel ranged from 18.4 to 19.2 wt. %. Additionally, limited data are available for fuel with 22.2 wt. % Pu. With regard to observable and measurable fuel performance (e.g., fission gas release fraction, fuel swelling, axial length change, etc.,), no sensitivity has been found to the Pu content in the range of 18.4 to 22.2 wt. % Pu.

In organizing the review of the database, an attempt has been made to parallel the key physical phenomena and design criteria specified in Section 2. Fuel phenomena affecting early-in-life (e.g., 0-2 at. % burnup) design considerations are discussed first. These include axial length changes, which influence the core neutronics, and fuel constituent redistribution, which influences the minimum fuel solidus temperature used in the "no-fuel-melting" design constraint (Design Criterion 3.0). Fuel performance with regard to fission gas release and fuel swelling is discussed next. Fission gas release causes plenum pressure loading of the cladding, and fuel swelling influences both the plenum pressure and the local loading of the cladding due to fuel-cladding-mechanical-interaction (FCMI). The gas pressure on the cladding resulting from fission

gas release to the plenum is particularly important in design, as it represents a primary load on the cladding, which could cause plastic instability. Design Criterion 5.0 protects against plastic instability due to gas pressure loading. Both gas pressure and FCMI loading tend to cause monotonic increases in cladding stress, strain, and damage based on both the thermal creep strain (TCS, Design Criteria 1.0 and 8.0) and the cumulative damage function (CDF, Design Criteria 2.0 and 7.0). While only strain is a measurable parameter and no-failure/failure is observable, information in both of these areas may be used to deduce the relative contributions of plenum pressure loading and FCMI. As the loads on the cladding increase with burnup, effective wall-thinning of the cladding due primarily to the embrittling penetration of lanthanides into the cladding and secondarily to carbon and/or nickel depletion from the cladding inner-diameter (ID) and sodium-cladding interactions at the cladding outer diameter (OD) increases with burnup and results in increases in stress, strain, and damage. Because wall thinning has a very strong influence on cladding lifetime Design Criteria 1.0, 2.0, 7.0 and 8.0, the long-time, steady-state data base for this phenomenon is discussed in depth. Finally, enhanced lanthanide penetration of the cladding at the cladding ID due to liquefaction during overheating events and concurrent fuel liquefaction are described. Prohibiting fuel/cladding liquefaction during normal operation is specified in Design Criterion 4.0 and limiting liquefaction during anticipated, unlikely and extremely-unlikely events is explicitly treated in design Criterion 6.0.

5.2.1 Steady State Experiments in EBR-II

In February of 1985, irradiation testing of U-Pu-Zr fuel in support of the Integral Fast Reactor concept began in EBR-II. Based on their promising in-reactor behavior, thousands of experimental and core driver pins have been successfully irradiated to date (1993). The technical basis for a Mark-V core conversion is based largely on the irradiation experience gained since the lead IFR subassemblies were placed in the core. The following compilation of experimental data was obtained from open literature reports, ANL reports, and yet to be published data.

5.2.1.1 Fuel Swelling

Swelling of U-Pu-Zr fuel has been well documented [5.1, 5.2]. All metallic fuel has been observed to swell rapidly in the radial direction so that cladding gap closure is complete over the entire fuel column by 2 at. % burnup independent of the amount of Pu present. The axial growth rate for Pu-bearing fuels is much less, with typical axial strains between 1% and 5% at 2 at. %

burnup. By 10 at. % burnup the expected axial strains will range between 2% and 6%. U-19Pu-10Zr fuel in the D9 and HT9 clad lead subassemblies all showed a strong temperature dependence for axial growth. This behavior is believed to be related to the more rapid alloy redistribution (Section 5.2.1.2) in the hotter inner row fuel (of a given 61 pin bundle). Reference 5.2 showed a two-fold increase in axial strains of X419 fuel for the outer row versus inner row pins (3.7% vs 1.8%). Data from the X441 test at ~6 at. % burnup showed similar effects at a higher linear power rating (15.5 kW/ft (50.91 kW/m) vs 13.5 kw/ft (44.3 kW/m)). Including all plenum to fuel ratios, the 14 inner row U-19Pu-10Zr/HT9 pins averaged only 1.6% strain while the 5 outer row pins averaged 2.8%.

There is a substantial body of data regarding fuel swelling which suggests that the Mark-V/VA fuel will perform as observed in prior inner-row irradiation tests. Swelling data are needed however for Mark-V/VA fuel operating in rows 5, 6, and 7. The expected behavior, based on the lower fuel temperatures, would be that higher axial swelling values would be attained before cladding contact occurred. No performance problems regarding reliability or safety are anticipated, but a surveillance program including PIE (Section 4.1) and regular measurements of reactivity loss rates (Section 6.4) will be implemented to monitor fuel swelling and its effect on core behavior. Some early information will be obtained at ~6 at. % burnup from PIE of X489, an HT9-clad U-19Pu-10Zr fuel test irradiated in row 6.

5.2.1.2 Fuel Constituent Redistribution

While fuel constituent redistribution has a dramatic effect on the <u>local</u> behavior of U-Pu-Zr fuel, and possibly contributes to fuel cracking, the resulting integrated behavior of fission gas release, total fuel swelling and resulting cladding strain profiles seems relatively unaffected by this redistribution. In addition, while the redistribution results in a radial gradient in local thermal conductivity and heat generation rates, LIFE-METAL analyses [5.1] indicate that the calculated fuel temperatures are relatively insensitive to this redistribution. The major design impact of the redistribution, however, is a lowering of the solidus temperature in the resulting low-Zr/high-U zone. Figure 5.1 shows the increase in local solidus (T_s), as well as liquidus (T_1), temperature with Zr content in wt. % for a constant Pu atom fraction. Thus, while U-20Pu-10Zr has a solidus temperature of 1120°C, the solidus temperature of a 2 wt. % Zr zone is reduced to 1040°C. Complete elimination of Zr from a redistributed zone lowers the zone solidus temperature to

1010°C. In the following, some local effects of the redistribution are described, as well as typical radial profiles which have been observed in both high/low power and low/high burnup U-19Pu-10Zr fuels.

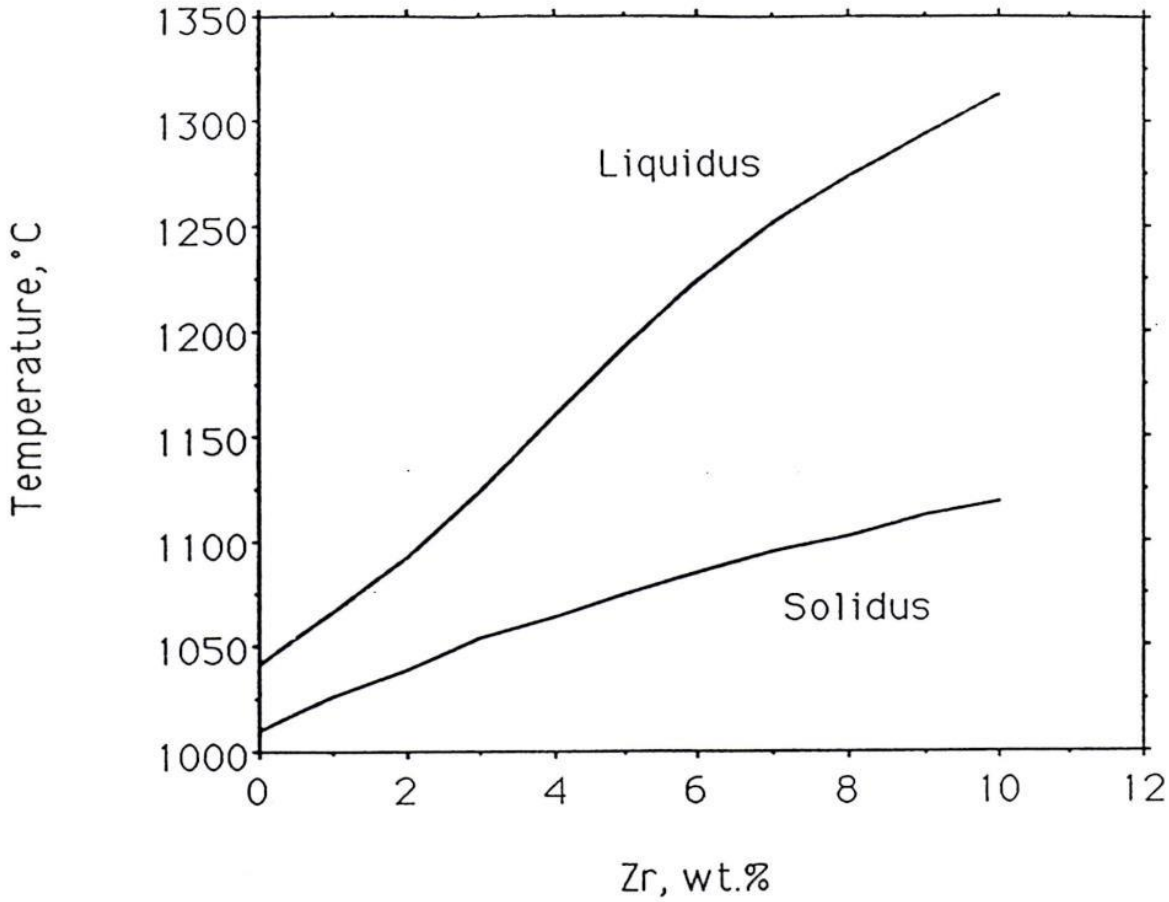

Figure 5-1 Liquidus/Solidus Temperatures of U-20 wt.% Pu-yZr vs. Zr Content

Multiphase boundaries present in U-20Pu-10Zr fuel during operation lead to annular zones which differ in swelling properties and composition. By 2 at. % burnup, an interchange between zirconium and uranium occurs. The plutonium composition profile is essentially uniform when plotted as an atomic fraction rather than a weight fraction. The redistribution produces, in the case of high fuel temperatures, a zirconium-depleted shell, near mid-radius with a zirconium-rich core and outer shell. Current research indicates that the inner-most zone likely begins where there is a single-phase gamma region. This would occur where fuel temperatures reach ~680°C. High temperature fuel therefore can be defined as that where this phase field exists in the inner radius of the fuel. For lower temperature fuel, a zirconium-depleted region at slug center is

encircled by zirconium-rich fuel extending to the slug surface. The microstructural features of the fuel are described in Ref. 5.2. Pie-shaped cracks seen in transverse sections occur due to the swelling rate mismatch, and such features are common at the earliest stages of redistribution. However, they are completely "healed" due to fuel growth by 10 at. % burnup.

Wet chemistry was performed on spark-eroded annular samples from irradiated U-19Pu-10Zr fuel at ~2 at. % burnup [5.3], ~5.5 at. % burnup [5.4] and ~10 at. % burnup [5.5] from the X419, X420 and X421 experiments, respectively. The X419 and X421 tests operated in EBR-II row 3 positions while X420 operated in a row 4 position. These subassemblies should therefore be representative of intermediate row Mark-V drivers, since they operated at power and flow conditions typical of intermediate row drivers.

Table 5-1 and **Error! Reference source not found.** through Figure 5-7 summarize the data from references 5.3, 5.4 and 5.5. (Note that in Reference 5.4 there is a typographical error for the %Pu. This has been corrected for use in Figure 5-2. The sample at x/ℓ_o =.12 for r/r_o = 0.61-0.70 had 18.69 wt % Pu.)

Fuel constituent redistribution in Mark-V/VA fuel is expected to follow the trends of the existing database, which utilized U-19Pu-10Zr at power levels and burnups of interest. Table 5-2 shows the predicted redistribution profile for high-power U-20Pu-10Zr fuel based on a

Table 5-1 Radial Composition Profiles of U-19Pu-10Zr Fuel
Observed Near Core Midplane at ~2 at.% Burnup

		Approximate Composition (at. %)		
Zone	Position (r/r_o)	U	Pu	Zr
Centerline	0 to 0.3	52.3	14.5	33.2
Intermediate	0.4 to 0.6	71.0	16.0	13.0
Outer	0.7 to 0.9	58.5	13.8	27.7

Table 5-2 Detailed Radial Composition Profile Used as the Base Case for Mark-V/VA Thermal Analysis

Ring No.	r/r_o	Zr, wt. %	Pu, wt. %	T_s, °C	T_l, °C
1	0 - 0.289	25	24	1290	1490
2-3	0.289 - 0.500	2	18	1040	1100
4	0.500 - 0.577	4	18	1060	1160
5-10	0.577 - 0.913	11	20	1130	1330
11	0.913 - 0.957	13	21	1150	1360
12	0.957 - 1.000	15	22	1170	1390

scaling of the results for high-power U-19Pu-10Zr fuel at 2 at. % burnup [5.1]. Thermal analysis sensitivity studies were also performed using the distributions in Figure 5-2 through Figure 5-6.

5.2.1.3 Fission Gas Behavior

Gas pressure in the plenum increases with burnup due to the increase in the amount of gas released from the fuel to the plenum and a decrease in plenum volume due to fuel swelling. The decrease in plenum temperature with burnup tends to lessen the rate of increase of gas pressure with burnup. While plenum pressure is relatively easy to bound and to account for in design, it is also very important. Not only does an increase in gas pressure increase cladding CDF and TCS damage, high levels of gas pressure can cause plastic instability leading to cladding failure. From a design viewpoint, plenum pressure can be bounded from above by assuming 100% gas release, no sodium-logging or entry into the fuel pores, and peak beginning-of-life plenum temperatures. In the following, the observed gas release behavior of metallic fuels is discussed.

In the hot cell facilities, a laser is used to puncture the plena of irradiated fuel pins and a calibrated collection system allows for the plenum pressure and volume to be determined at ambient cell temperature. The fractional theoretical release is calculated by taking into account the moles of gas collected along with the heavy metal fuel mass irradiated, the calculated average burnup, the estimated fission yield, and the nominal quantity of He/Ar fill gas present in the as-built plenum.

U-19Pu-10Zr 5.5 at.% Burnup, $L/L_0 = 0.12$

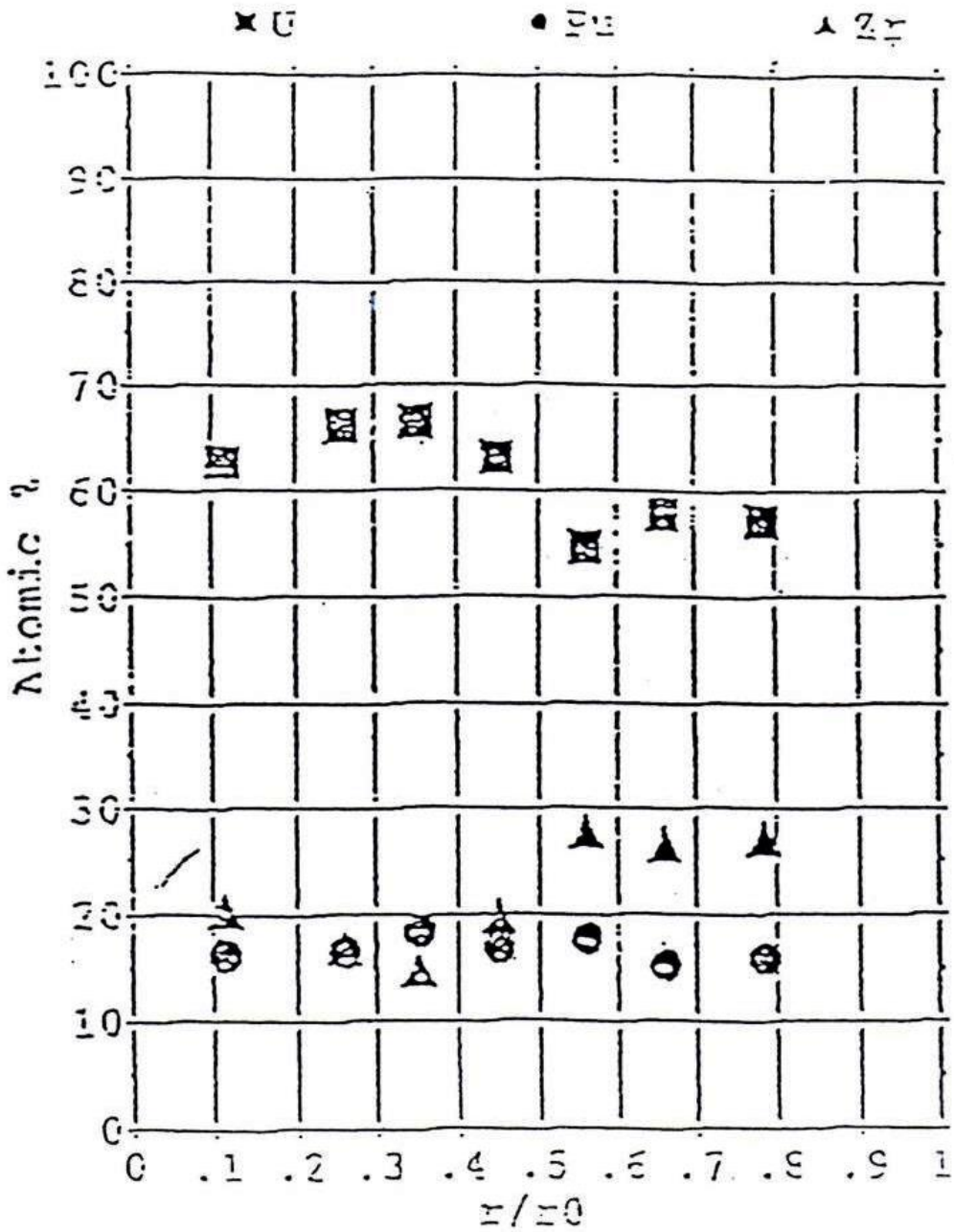

Figure 5-2 Radial Constituent Profile for U-19Pu-10Zr Fuel from the X420 Test after ~5.5 at.% Burnup at $x/l_o = 0.12$

U-19Pu-10Zr 5.5 at.% Burnup, $L/L_0 = 0.60$

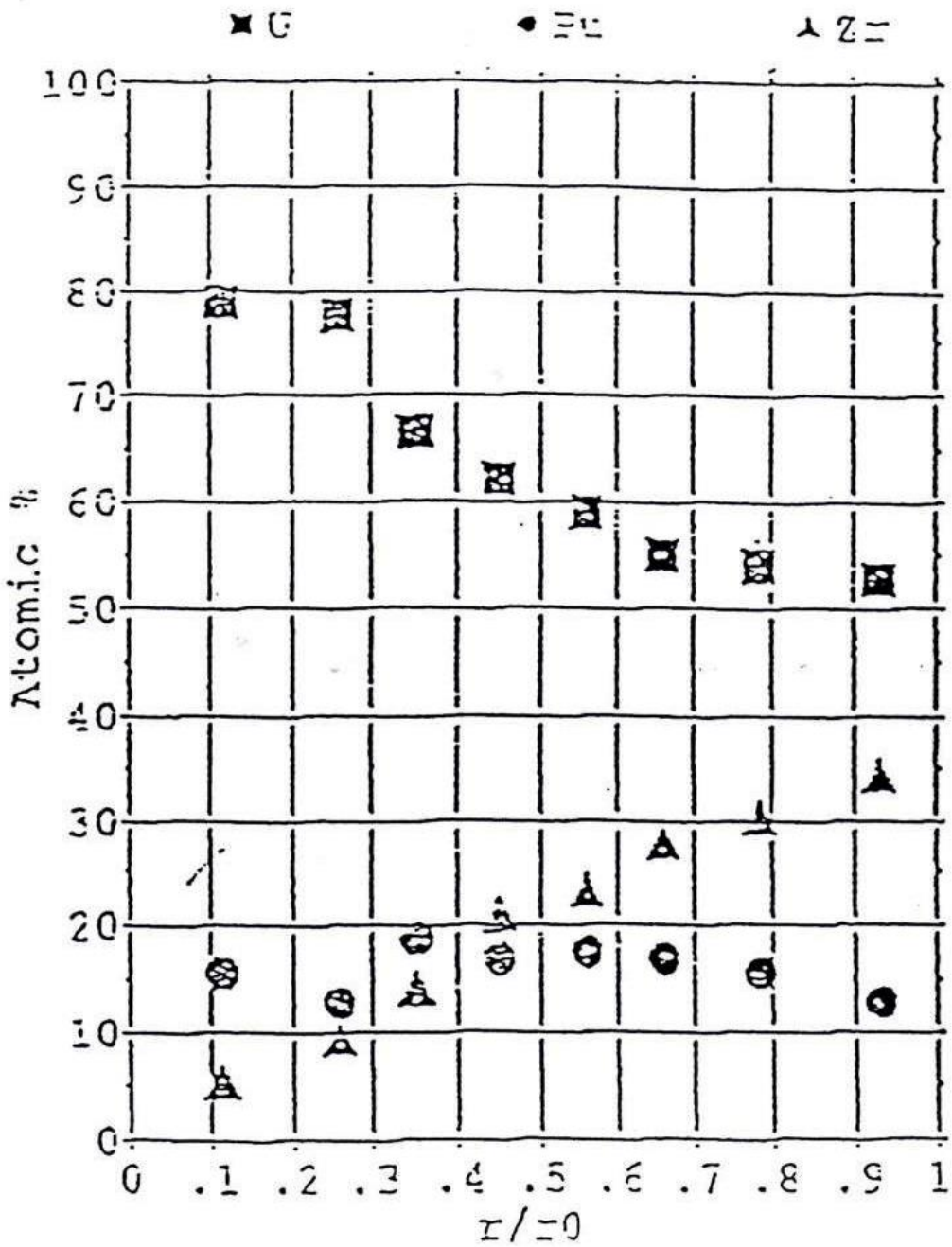

Figure 5-3 Radial Constituent Profile for U-19Pu-10Zr Fuel from the X420 Test after ~5.5 at.% Burnup at $x/l_o = 0.60$

U-19Pu-10Zr 5.5 at.% Burnup, $L/L_0 = 0.88$

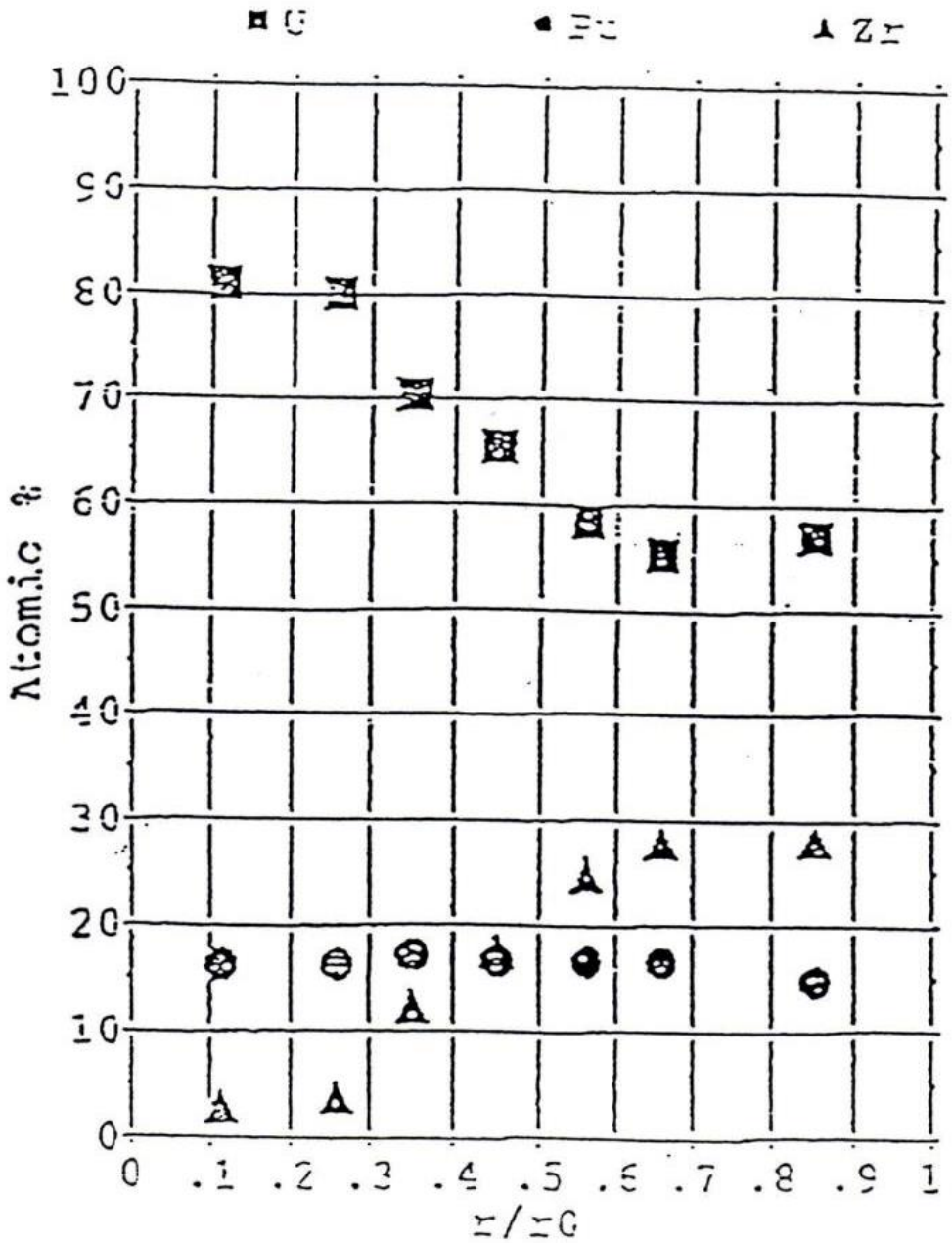

Figure 5-4 Radial Constituent Profile for U-19Pu-10Zr Fuel from the X420 Test after ~5.5 at.% Burnup at $x/\ell_o = 0.88$

U-19Pu-10Zr 10.0 at.% Burnup, $L/L_0 = 0.10$

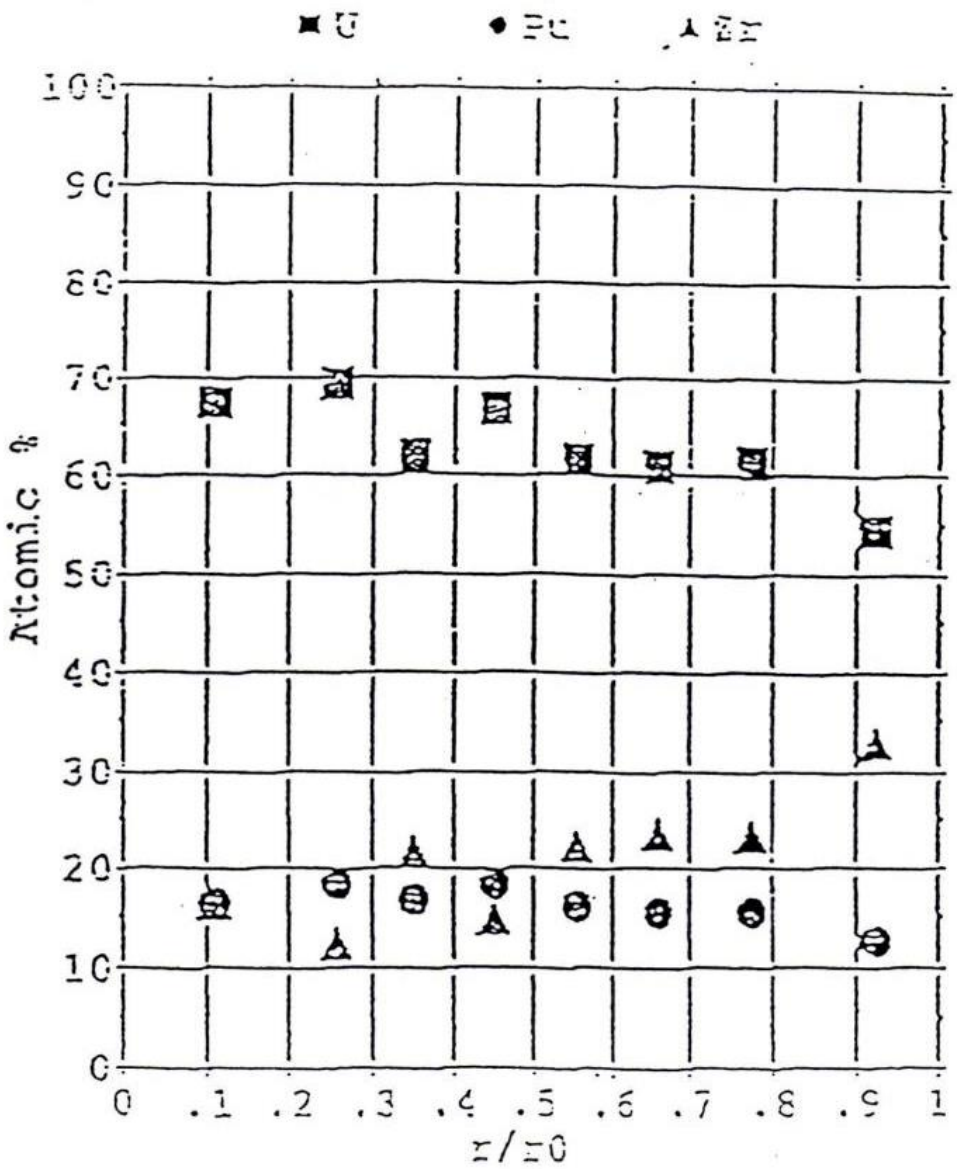

Figure 5-5 Radial Constituent Profile for U-19Pu-10Zr Fuel from the X421 Test after ~10 at.% Burnup at $x/\ell_o = 0.10$

U-19Pu-10Zr 10.0 at.% Burnup, L/L_0 = 0.60

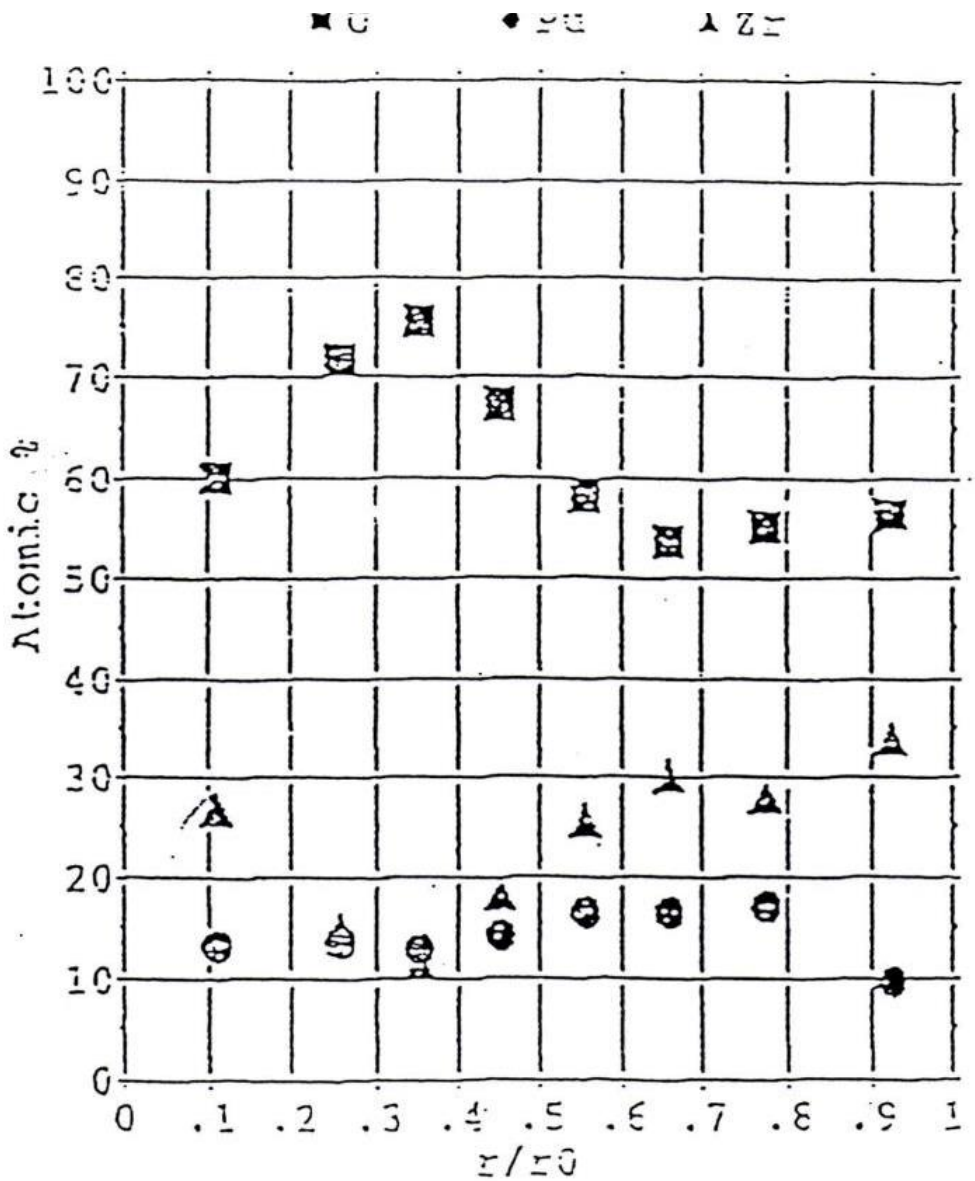

Figure 5-6 Radial Constituent Profile for U-19Pu-10Zr Fuel from the X421 Test after ~10 at.% Burnup at x/ℓ_o= 0.60

U-19Pu-10Zr 10.0 at.% Burnup, $L/L_0 = 0.86$

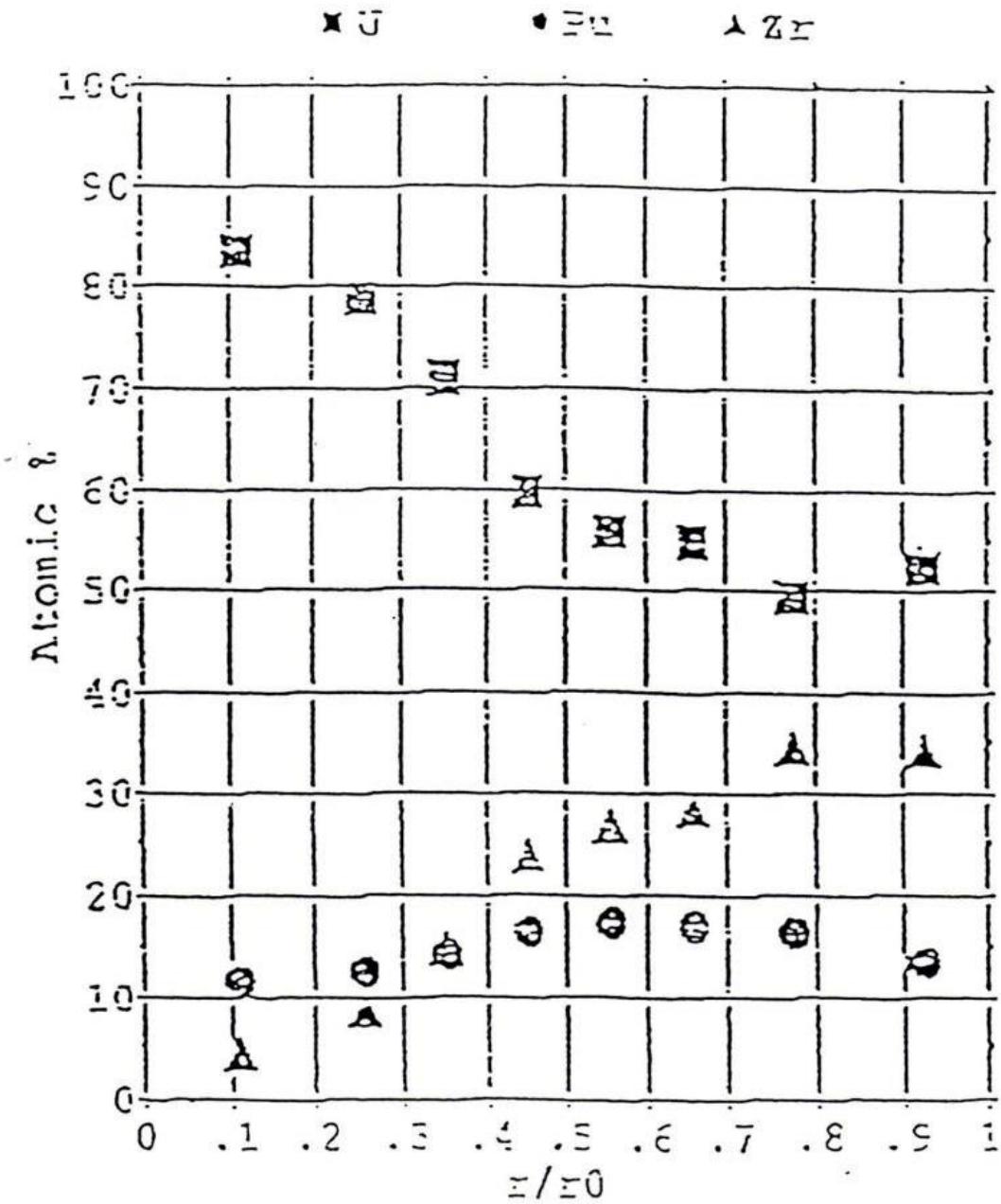

Figure 5-7 Radial Constituent Profile for U-19Pu-10Zr Fuel from the X421 Test after ~10 at.% Burnup at $x/\ell_o = 0.86$

Fission gas behavior in U-Pu-Zr fuel has been well documented [5.6, 5.7]. After an incubation period of ~1 at. % burnup, the molar quantity of gas in the pin plenum increases with burnup in a near linear fashion. Based on the experimental data from Ref. 5.7 a conservative empirical relation between burnup and % gas release for Mark-V/VA fuel would be the following (Figure 5-8):

For burnup < 0.5 at. %, % Release = 0

For 0.5 at. % < burnup < 10 at. %, % Release = 90-(45/at. % Burnup)

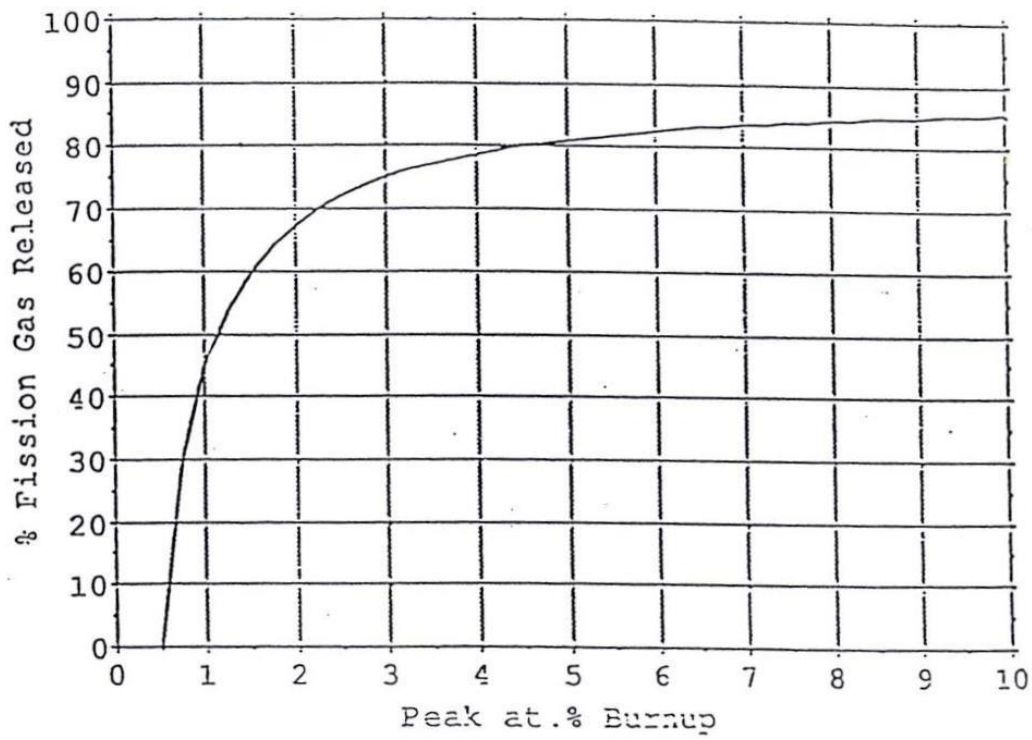

Figure 5-8 Predicted Fission Gas Release in U-20Pu-10Zr Fuel

The data were obtained from the X419, X420, X421, X425 tests described previously. Data from the X441 experiment are consistent with the behavior reported previously. Data from a control test pin from X441 at 5.6 at. % burnup released ~81% of the theoretical generated, while a sibling control pin at 11.4 at. % burnup released ~77% of the theoretical generated gas.

In summary, the fission gas behavior for Mark-V/VA type fuel has been well characterized, and the gas release is expected to be less than ~85% theoretical at any burnup level.

5.2.1.4 Cladding Mechanical Performance

The total cladding diametral strain profile is routinely measured for each irradiated pin. The measured strain is composed of a stress-free swelling strain, an irradiation-induced creep strain and a thermal creep strain. Of these, only the thermal creep strain (TCS) is ductility-limited (see Section 2.1.4). While it is not measured directly, it can be deduced from the data by use of modeling codes (e.g., LIFE-METAL). Also, the end-of-life measured strains represent an integration of the thermal, irradiation and stress histories for the experimental pins. For example, it is possible to determine the relative contributions of gas pressure loading and FCMI by analyzing the cladding diametral strain profiles, as well as plausible stress histories. The thermal and stress histories are significant in that they determine the calculated CDF damage of the cladding.

For most of the experimental test pins, failure was not observed even up to high burnups. In these cases, the calculated CDF and TCS values could not be validated directly. However, failure was observed for several of the test pins. These few failed cases, as well as the numerous unfailed experimental pins, serve as a check of the CDF and TCS failure criteria, as well as the methods for calculating temperature and stress histories which are used as input to the CDF and TCS calculations.

The data base for HT9/U-19Pu-10Zr and 316SS/U-19Pu-10Zr cladding strain is summarized in the following. Because a strong dependence on Pu content has not been observed, the data from lower Pu-bearing fuel are also included to strengthen the data base. Also, because of the similarities in the performance of D9 and 316SS claddings in terms of creep strength, the D9 data base is also summarized. Other than being a lower swelling alloy beyond a certain incubation fluence, some of the D9 behavior is directly applicable to the performance of 316SS. Also, the extensive D9 data base is indirectly relevant because it is used to validate the properties, models, and criteria incorporated into fuel behavior computer codes (e.g., LIFE-METAL).

5.2.1.4.1 HT9 Cladding Diametral Strain

The most pertinent tests performed in EBR-II to date regarding HT9 strain profiles are

experimental subassemblies X425, X429, X447, together with the "control" pins from X441, which are closest to the fuel design chosen for the Mark-V fuel. Each of the subassemblies was irradiated in EBR-II beyond the 10 at. % burnup limit and is either prototypic or "aggressive" regarding pin power, coolant and cladding temperature, cladding stress, etc. Table 5-3 summarizes the range of operating and design conditions for the four experiments and the Mark-V fuel. As explained in Section 9.4, for 10 at. % burnup, the pin behaves as a pressurized tube with fission gas loading dominant over fuel/cladding mechanical interaction. Because plenum pressures for all three alloy types tested are not strongly Pu-dependent, the use of U-10Zr and U-8Pu-10Zr data from the X425, X429 and X447 tests to strengthen the database is justified.

Table 5-3 Design Data for X425, X429, X441, X447 HT9 Pins

Design Parameter	Linear Power, kW/ft Peak Midplane	S/A Outlet Coolant Temp. (~BOL)	Peak Inside Cladding Temp. (~BOL)	Pin Length, in.	Plenum Vol./ Fuel Vol.	Clad. Dia./ Thickness	wt. % Pu, U-Pu-10Zr
X425	12.1	505°C	590°C	25.1	~1.0	15.3	0, 8, 19
X429	13.6	510°C	595°C	24.4	~1.0	15.3	0, 8, 19
X441 (control)	15.5	515°C	600°C	29.5	~1.5	15.3	19
X447	10.0	540°C	660°C	29.5	~1.5	15.3	0
Mark-V	9.0 to 15.6	480°C to 550°C	520°C to 580°C	29.5	~1.5	12.8	20

Contrasting the conditions summarized in Table 5-3 for the Mark-V fuel to the experimental conditions, it is noted that typical X425 and X429 pins would be similar to those of typical row 5 Mark-V driver pins with regard to linear power and coolant temperatures. However, X425 and X429 pins are more aggressive in that their estimated cladding hoop stress is ~80% greater than a Mark-V driver at equivalent burnups, assuming similar gas release fractions. This is due to their smaller plenum to fuel volume ratio (~1.0 vs ~1.5) and thinner cladding wall thickness (0.015" (0.38 mm) vs 0.018" (0.46 mm). In light of these facts, it is very significant that no HT9 clad fuel pins from either X425 or X429 have breached to peak burnups of 19.3 at. % and 13.7 at. %, respectively. There are 43 pins in X425 beyond 13 at. % burnup and 29 beyond 13 at. % burnup in X429.

The X441 and X447 experiments contained a complement of pins that were essentially identical in design to the Mark-V driver fuel pins. The X447 test was intended as a "2 sigma" high temperature test to qualify U-10Zr/HT9 for the FFTF reactor driver fuel pin. As such, it operated at a Beginning-Of-Life (BOL) peak inside cladding temperature of 660°C at 10 kW/ft (33 kW/m) peak linear power, without uncertainties. This power is equivalent to that of a Mark-V drive in a row 6 corner position but with an inside cladding temperature ~100°C above nominal. X447 experienced its first 2 breaches between ~9.5 at .% and ~10 at. % burnup at the top of the fuel region, where the diametral strain is maximum. Note that due to the thinner cladding wall, the X447 pins experienced hoop stresses equivalent to a ~12 at. % burnup Mark-V pin, even neglecting the much higher plenum temperatures in X447. Neglecting the two breached pins, X447 contained a total of 13 pins with burnups exceeding 9.9 at. % burnup [5.8]. The relevance of the two breached pins to the Mark-V safety case is discussed in Sec. 5.2.1.6.

The X441 experiment involved a systematic variation of key design parameters and has been used to validate the LIFE-METAL fuel performance code. The parameters which were varied included zirconium content (U-19Pu-6,10,14Zr), plenum to fuel ratio (1.1, 1.3, 1.5, 2.1), and smear density (70%, 75%, 85%). The "control pins" described in Table 5-3 are essentially identical to Mark-V driver fuel. None of the pins in X441 were breached when the test was terminated at a peak burnup of ~12.7 at. %. A total of 31 HT9 clad ternary fuel pins have achieved peak burnups greater than 9.5 at. % burnup.

Figure 5-9 summarizes the observed peak diametral strains in the 4 tests as measured with post-irradiation spiral contact profilometry. Inspection of the X441 data in Figure 5-9 suggests no more than ~0.4% diametral strain is likely at the Mark-V burnup limit of 10 at. %. This level of strain is indicative of low damage levels in the HT9 material and reduces the likelihood of any significant levels of bundle/duct interaction.

The lead Mark-IV qualification subassembly (X448) was nondestructively examined after reaching ~8.8 at. % peak burnup without breach. Cladding profilometry data from this row two, 61-pin U-10Zr driver fuel subassembly is pertinent to the Mark-V situation since it operated with similar power (15 kW/ft (49 kW/m)) and cladding temperatures (536°C) to inner row Mark-V drivers. The Mark-IV and Mark-V pin designs both employ 0.018" (0.46 mm) thick HT9 cladding, and plenum to fuel volume ratios of ~1.5. A total of seven pins were measured with the helical

contact profilometer. The peak diametral strain ranged from 0.17% to 0.70%, averaging 0.42%.

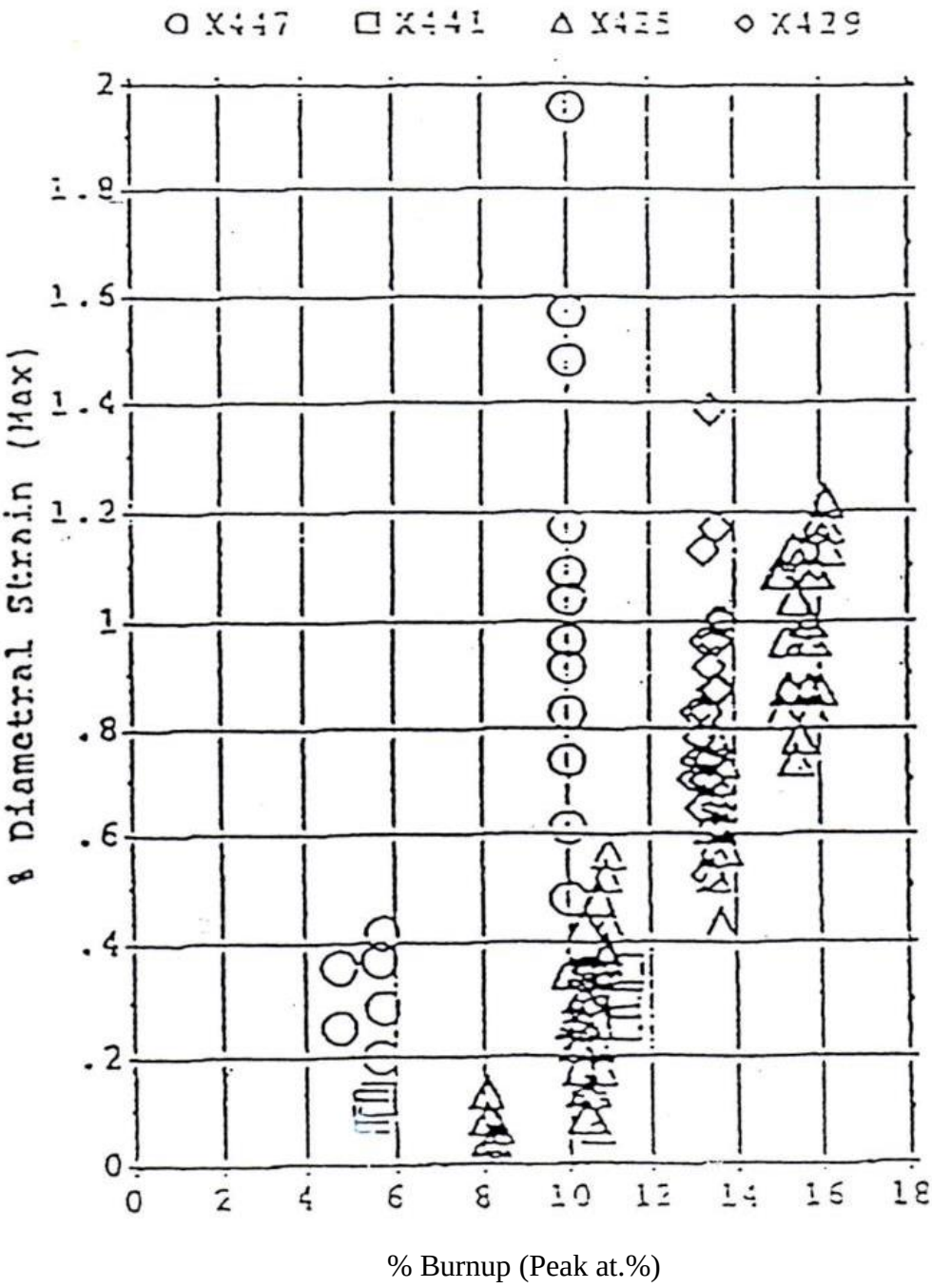

Figure 5-9 Maximum Observed Diametral Strain in the X425, X429, X441, and X447 Pins Clad in HT9

In summary, the applicable database for HT9 cladding diametral strain supports the prediction that low levels of cladding damage (i.e. strain) will occur in Mark-V driver fuel at 10

at. % burnup and that the design criterion of <1% thermal strain will easily be met.

5.2.1.4.2 316SS Cladding Diametral Strain

The lead Mark-IIIA driver qualification subassembly (X483) was nondestructively examined after reaching ~9.5 at. % peak burnup without breach. Analogous to the X448 cladding profilometry data in Section 5.2.1.4.1 above, this row three, 61-pin U-10Zr driver fuel subassembly is pertinent to the Mark-VA situation since it operated with similar power (15 kW/ft (49 kW/m)) and cladding temperatures (552°C) to inner row Mark-VA drivers. The Mark-IIIA and Mark-VA pin designs both employ 0.015" (0.38 mm) thick 20% CW 316SS cladding, and plenum volume to fuel volume ratios of ~1.5. A total of seven pins were measured with the helical contact profilometer. The peak diametral strain ranged from 0.83% to 1.26%, averaging 1.07%. Based on LIFE-METAL calculations, the thermal creep component of these strains is <<0.2%.

Limited data are also available for 316SS/U-19Pu-10Zr fuel from subassembly X429. Peak cladding strains of ~6% were measured at ~14 at. % burnup and a peak inner cladding temperature of 590°C. At least half of this strain is due to swelling. The other half is due to high plenum pressure because of the high burnup and the low plenum-to-fuel volume ratio. While these cases are not directly relevant to Mark-VA design conditions, they were used to validate the LIFE-METAL models and properties for 316SS/U-19Pu-10Zr pins.

In summary, the available data for 316SS cladding strain shows that about 1% peak strain would be expected in Mark-VA driver fuel at 10 at. % burnup, with the thermal creep component calculated to be <<0.2%. No failures of 316SS cladding have been observed under Mark-VA-type design conditions.

5.2.1.5 Cladding Wastage by Fuel/Cladding Chemical Interaction (FCCI)

During irradiation under normal operating conditions, HT9, 316SS, and D9 claddings develop a lanthanide-rich/iron-poor layer at the fuel/cladding interface. This layer is brittle and often observed to be cracked. Thus, this fission-product (FP) penetrated layer cannot be relied on as load-bearing and is considered to be wastage. In addition to the increase in FP concentration and the decrease in Fe concentration, 316SS and D9 austenitic claddings experience a decrease in Ni content in the wasted zone. However, because the nickel-depleted zone does not extend any farther into the cladding than the FP zone, there is no reason to distinguish it for the

purposes of design analysis or modeling. However, in ferritic/martensitic HT9, a carbon-depleted (CD) zone has been observed (at 10 at. % burnup and PICT = 640 - 660°C) to penetrate farther into the cladding than the FP zone. Unlike the FP zone, the CD zone is softer than the base metal and uncracked. Therefore, it represents a region of reduced strength as compared to the base metal.

The database for wastage due to the FP and CD zones was expanded greatly from 1990-1994. Table 5-4 summarizes the cladding/fuel types, the peak inner cladding temperature (PICT), the peak burnup and the number of wastage data points. In general, cladding wastage increases with fuel/cladding interface temperature and burnup. Under comparable conditions the wastage rates for D9 are higher than those for 316SS which, in turn, are higher than those for HT9. Also, U-19Pu-10Zr fuels tend to result in higher cladding wastage rates than U-10Zr fuels.

The cladding wastage data bases are reviewed below. While there is no direct design limit on the solid-state wastage depth into the cladding, the reduction in cladding load-bearing thickness does enter into the CDF and TCS calculations which are limited by Design Criteria 1.0 and 2.0, as well as 7.0 and 8.0.

Table 5-4 Summary of Fuel/Cladding Chemical Interaction Wastage Data

Design	Clad/Fuel	PICT, °C	Peak Bu, at. %	Data Points
Mark-V	HT9/U-20Pu-10Zr	600	18	9
Mark-IV	HT9/U-10Zr	600	13	30
Mark-VA	316SS/U-20Pu-10Zr	590	14	6
Mark-IIIA	316SS/U-10Zr	--	--	0
--	D9/U-20Pu-10Zr	600	17	21
Mark-III	D9/U-10Zr	630	18	14

5.2.1.5.1 HT9 Wastage Data

The 39 HT9 cladding wastage data points in Table 5-4 come from 7 irradiated fuel pins. While all of these 39 points were used for model development and validation, only the peak values for each pin are summarized in Table 5-5. Based on the X441A data for the two pins which are very close in design and operating conditions (DP16 and DP21), it is anticipated that the peak wastage which the hottest (without uncertainties in temperature) Mark-V pin will experience in 10 at. % burnup is about 2 mils (50 microns) or 11% of the initial cladding thickness. For the peak three-sigma temperature uncertainty case (650°C), the wastage could reach as high as 6-8 mils (0.15 - 0.20 mm) at 10 at. % burnup. Section A.4.2 of Appendix A and Section 9.4 contain more in-depth treatments of wastage data, models, model validation, and calculational methodology.

Table 5-5 Summary of Peak Wastage Depth Data for HT9-Clad Pins Irradiated Under Normal Operating Conditions

Subassembly/Pin	Fuel	PICT, °C	Peak Bu, at. %	Peak FP Zone, mils (mm)	Peak (FP & CD) Zone, mils (mm)
X441A/DP16	U-19Pu-10Zr	550	11.5	1.3 (0.033)	1.3 (0.033)
X441A/DP21	U-19Pu-10Zr	569	11.4	2.3 (0.058)	2.3 (0.058)
X425/T459	U-19Pu-10Zr	537	2.8	0.4 (0.01)	0.4 (0.01)
X441A/DP11	U-10Zr	659	10.1	3.0 (0.076)	7.0 (0.18)
X441A/DP04	U-10Zr	653	9.8	3.5 (0.089)	6.0 (0.15)
X441A/DP70	U-10Zr	651	9.8	5.5 (0.14)	7.0 (0.18)
X441A/DP75	U-10Zr	641	9.7	6.7 (0.17)	7.5 (0.19)

5.2.1.5.2 316SS/D9 Wastage Data

The wastage data base for 316SS/U-Pu-Zr pins is very limited. However, there is evidence (see Section A.4.2. of Appendix A) that the 316SS wastage rate is bounded from above by the D9 wastage rate, for which there is an extensive data base.

The 41 D9 and 316 SS data points in Table 5-4 come from 12 irradiated fuel pins. The peak wastage depths from these twelve pins are summarized in Table 5-6. Based on the

316SS/U-19Pu-10/Zr data points, the peak wastage depth for Mark-VA fuel at 10 at. % burnup can be estimated (without three-sigma temperature uncertainties) to be about 2 mils (0.05 mm). However, the three-sigma uncertainty may have to be limited to <650°C in order to prevent excessive cladding wastage for the design case. More details on wastage data, models, model validation and calculational methodology are given in Section A.4.2. of Appendix A and in Section 9.4.

Table 5-6 Summary of Peak Wastage Depth Data for 316SS and D9-Clad Pins Irradiated Under Normal Operating Conditions

Subassembly/Pin	Cladding/Fuel	PICT, °C	Peak Bu, at. %	Peak FP Zone, mils (mm)
X429B/T581	316SS/U-19Pu-10Zr	591	13.5	2.8 (0.07)
X441A/A850	D9/U-19Pu-10Zr	582	11.3	4.1 (0.10)
X420B/T084	D9/U-19Pu-10Zr	566	17.1	6.0 (0.15)
X421A/T106	D9/U-19Pu-10Zr	536	17.4	2.0 (0.05)
X421/T108	D9/U-19Pu-10Zr	536	9.5	1.5 (0.04)
X419B/T112	D9/U-19Pu-10Zr	542	11.9	2.8 (0.07)
X420/T053	D9/U-19Pu-10Zr	566	5.3	2.0 (0.05)
X447A/C709	D9/U-10Zr	629	11.1	6.9 (0.18)
X421/T225	D9/U-10Zr	536	9.7	1.2 (0.03)
X419B/T141	D9/U-10Zr	536	11.8	1.2 (0.03)
X421A/T227	D9/U-10Zr	536	18.0	1.1 (0.028)
X420/T224	D9/U-10Zr	567	5.4	2.8 (0.07)

5.2.1.6 Cladding Failure

The cladding failures most relevant to the Mark-V safety case are the two high-temperature X447A HT9/U-10Zr pins which failed at ~10 at. % burnup. Although the fuel does not contain plutonium, these pins, along with the other 13 hot pins which did not fail, provide validation for the methodology of predicting failure for HT9 based on the cumulative damage function (CDF), the thermal creep strain (TCS) and the hoop stress due to plenum pressure loading. Recall from the design criteria in Section 2.1.4 that limits are placed on CDF, TCS, and the wall-averaged hoop stress to limit the design life such that <1/3000 failures can be assured per core loading. These

criteria are based on values of CDF and TCS which result in failure, along with the statistics associated with these calculated parameters. The 15 hot elements of X447A operated with a calculated peak inner cladding temperature (PICT), not including uncertainties, of 646±8°C, where the ± represents reasonable agreement with the data. It also predicted 2/15 failures based on the 2% TCS criterion. This exercise was also used to determine upper-bound wastage rate parameters for design analysis which result in higher-than-observed failure predictions. Thus, the X447A data set proved to be significant in and of itself, as well as indirectly for validating the methodology adopted for predicting cladding failure based on CDF, TCS, and cladding hoop stress criteria.

5.2.2 Cladding Breach Experience in EBR-II

The characterization and monitoring of metallic fuel breaches is now a significant part of the metallic fuel testing program at EBR-II [5.9]. Irradiation experience with failed metallic fuel now includes natural breaches in the plenum and fuel column regions in lead D9 clad "endurance" tests [5.7] as well as fuel column breaches in intentionally defected fuel pins which have operated for months in the run-beyond-cladding breach (RBCB) mode [5.10]. It has become evident that metallic fuel failures in the EBR-II are benign events. Fission gas release and delayed neutron signals (when present) take a characteristic form. The breaches themselves are nonpropagative, involve insignificant fuel loss and do not disrupt the normal operation of EBR-II. In fact, all of the breach experience to date includes some run-beyond-breach time varying from several days to several months depending on reactor schedule.

Unlike oxide-based liquid metal fast reactor fuel, sodium/fuel reaction products do not form after breach in a metallic fuel pin because the metal fuel is compatible with the sodium coolant. Thus the fuel adjacent to the crack is contained and the cladding itself remains intact. In most cases, the breach site in natural or pre-thinned test pins is a tight pinhole-type crack in the fuel or plenum region oriented parallel to the pin longitudinal axis. Upper closure weld failures are likewise small tight cracks aligned with a notch in the end plug that acted as a stress-riser. During the breach event sodium and fission gas expulsion occurs readily. In the plenum, fission gas is nearly completely vented, with some loss of the sodium bond also possible. No delayed-neutron emitters reach the breach site if it is in the plenum and the fuel structure remains generally unaffected.

The events that follow a fuel column failure are of a somewhat different nature. Monitoring of the fission gas and delayed neutron detectors reveals a steep rise in gas and delayed neutron signals, very nearly coincident in time. Once the sodium bond expulsion ceases, (taking typically 5 to 20 minutes depending on crack size and fuel porosity morphology), delayed neutron signals fall to background level. Fission gas release slows but continues for a few hours until finally only small bubbles of gas are occasionally seen on the fission gas monitor every few days.

In order to identify and monitor metallic fuel breaches in EBR-II, analyses of the fission gas (FG) release-to-birth ratios (R/B) of selected historical breaches have been completed.

Measured fission gas activities are corrected for natural decay and for operation of the cover gas cleanup system. This gives true release rates for individual isotopes. The corresponding birth rates are obtained from knowledge of the failure (from xenon tag), local fission rates, and appropriate fission yields. The slope of a logarithmic plot of the R/B ratio versus isotope half-life can then indicate the dominant mechanism of gas release. The release of stored gas from the plenum of a breached pin will exhibit a slope of -1.0. The slope is -0.5 when release occurs by diffusion out of the fuel structure. When the release mechanism is simple recoil, the slope should be zero; in practice, recoil occurs in conjunction with knockout of gas and this mixed mode of release will exhibit a slope between 0 and -0.4.

The normal fission gas activities in the cover gas due to fissioning of “tramp” uranium in the EBR-II primary circuit give rise to a very distinct R/B signature; with time it appears as a broad band of R/B values scattered between 0 and -0.35. (It should be noted that the R/B value used in this report is the slope of a logarithmic plot of R/B ratio versus isotope half-life.) Although fission gas release from all types of pin failure is clearly detected against such a background, that from an upper closure-weld failure in a sodium-bonded metal pin is the most easily identified. An initial R/B value of -1.0 is followed by a steady decline to zero over 15-25 days; the “tramp” signature then returns. This behavior has been observed a number of times from 1987 to 1990 and identified with specific upper weld failures.

The R/B signature for a fuel column breach is similarly very characteristic. If bond expulsion is rapid enough, I and Br precursors in the sodium give rise to a characteristic DN signal

spike. Subsequently, R/B values rise rapidly to -1.0, indicating release of stored plenum gas through the breach site. Over 3-5 days they decline to values of approximately -0.5, corresponding to diffusional release via the interconnected porosity of the metal fuel. Thereafter, occasional bursts of short and long-lived gas from the fuel interior appear as momentary changes about the -0.5 level.

A sustained delayed neutron signal has been observed only once in a metallic fuel RBCB test [5.9]. In the X429 test the defected 316SS clad U-8Pu-10Zr fuel pin had a 2.0 inch (5.1 cm) long V-groove pre-machined into the cladding (nearly 20% of the wall) in the fuel region prior to irradiation. The defected area split at ~13 at. % burnup under high gas pressure (fuel/cladding mechanical interaction is nearly absent) for almost all its length, giving a rapid release of sodium and delayed neutron precursors, and then stored fission gas. Subsequently, this breach gave not only a steady-state diffusional release of fission gas with a mean release to birth ratio of -0.5 but also a delayed neutron signal of 50-200 cps above background over a 22-day period. This behavior is attributed to the unusual breach geometry which allowed a comparatively large volume of fuel to communicate with the flowing coolant. Such exposure is atypical in normal metal fuel pin failures where pinhole type cracks are usually observed.

Though no significant fuel or solid fission product loss is experienced, both the fuel and the cladding are affected after fuel column breach. The sodium bond (and Cs fission products logged in the interconnected porosity) is vented to some extent, so the effective fuel thermal conductivity decreases. As fuel temperature increases, a sintering of the open porosity occurs at the top of the fuel column which causes the fuel to shrink away from the cladding inner wall. This occurs on a local scale so fuel motion is limited. Also, outward migration of the lanthanide fission products toward the cladding interface accelerates. Because steady-state fuel/cladding chemical interaction normally occurs by interchange of the cladding constituents and the lanthanides, local areas of accelerated attack have been observed in the hotter regions of breached cladding. This interaction has little real significance because the cladding has already been breached and contains little residual fission gas which would lead to additional cladding strain.

There have been a total of only three HT9 breaches in HT9 clad U-Pu-Zr fuel pins to date, despite the high burnup levels attained in the X441 test (12.7 at. %), the X429 test (13.7 at. %) and the X425 test (19.3 at. % burnup). One occurred in a predefected U-19Pu-10Zr fuel pin in the

X482B test (reorificed to operate at ~600°C peak inside cladding temperature) and the other two occurred in the high temperature U-10Zr test X447 (beginning-of-life nominal peak inside cladding temperature of ~660°C). The three breaches proved to be totally benign as expected.

In the X482B test a defect was machined into the clad wall after preirradiation in the X425 test to ~10.5 at. % burnup. The defect was placed near fuel midplane such that only ~1.5 mil (0.04 mm) wall thickness remained, resulting in an unfortunate premature breach in the EBR-II storage basket facility. No subsequent delayed neutron signal was observed during the run beyond breach stage that lasted uneventfully for ~150 EFPD's (~2.5 at. % burnup). Destructive examinations revealed a crack which matched the thinned area in length (~0.44 inches (1.1 cm)) with a maximum opening of ~13 mils (0.3 mm). The fuel adjacent to the breach was intact but did show a tendency to extrude into the crack opening. As described above, post-breach fuel/cladding chemical interaction may be accelerated due to the increased fuel temperature. The depth of interaction ranged between ~2 mils (0.05 mm) and ~3.5 mils (0.09 mm) over the upper ~3/4 inch (19 mm) of fuel column, with no visible interaction at core midplane near the breach.

Two natural breaches occurred in the X447 test at ~9.5 at. % burnup. For the one breach where good signals were recorded, the delayed neutron signal, coincident with the fission gas, rose within minutes to ~135 CPS above background on the open core detector. The signal returned to normal ~15 minutes after the breach.

The HT9 alloy creep strength declines rapidly above ~650°C. Consistent with this characteristic was the breach location at the top of the fuel column in a region of high local thermal strain and wall thinning due to fuel/cladding chemical interaction. Unbreached siblings averaged ~1% diametral strain at this elevation. Destructive examination of one of the two breached pins from the X447 subassembly has been completed. Numerous cracks were found at the hottest position of the cladding, near the top of the core. Considerable necking was found at the major cracks showing good remaining ductility. No burst failures were expected or observed.

In summary, the experimental database for steady-state and breach behavior is sufficient to allow qualification testing of the Mark-V/VA core to proceed. No significant impediments to safe and reliable performance have been discovered within the experimental fuels programs to date.

5.2.3 High Temperature Furnace Tests

The performance of irradiated Mark-V/VA-type fuels under off-normal reactor conditions has been studied in ex-reactor simulated heating tests. These tests were conducted with the Fuel Behavior Test Apparatus (FBTA) [5.11, 5.12] and the Whole-Pin Furnace (WPF) [5.13] system in the Alpha-Gamma Hot Cell Facility [5.14] at ANL-E. In the FBTA, short segments of irradiated fuel pins were subjected to isothermal heating tests in a furnace. After the tests, the specimens were metallographically examined to study the mechanisms and kinetics of interaction between the fuel and cladding. In the WPF tests, intact irradiated fuel pins were heated to elevated temperatures to investigate the combined effect of internal fission-gas pressure loading and interaction-induced cladding thinning on pin cladding integrity. Data from both types of tests are being used to support the development of the fuel-pin behavior codes LIFE-METAL and FPIN2.

In applying the data from the high temperature furnace tests to the design of Mark-V and Mark-VA, there are three areas of interest. The first area is the fuel/cladding liquefaction temperature. Design criterion 4.0 requires that there be no liquefaction during normal operation. This sets an upper limit on the peak inner cladding temperature allowed during normal operation. The second area of interest is the total penetration of lanthanides and molten material into the cladding. The resulting reduced load-bearing thickness of the cladding is reflected in the CDF and TCS calculations in applying Design Criteria 7.0 and 8.0, respectively. As "wasted" cladding is treated as having no load-bearing capability, regardless of whether the wasted zone is solid, liquid or a mixture of the two, it is not significant with respect to CDF and TCS criteria to distinguish liquid from solid in the data base. The third area of interest is directly the fraction of fuel which has been liquefied, and indirectly the corresponding fraction of liquefied cladding. Although Design Criterion 6.0 specified that <5% of the cladding thickness shall be liquefied during the sum of anticipated, unlikely and extremely unlikely events, the intent here is really to limit the fraction of molten fuel at any cross-section to <10%. Based on a simplified analysis of the chemistry of the liquefied zone, there is a two-to-one ratio of U to Fe in the zone based on the formation of U_2Fe and similar U_XM (where M stands for metal) low melting eutectics. Because the chemistry of the HT9/U-20Pu-10Zr+FP system is much more complicated than the simple U-Fe binary system, the 2:1 U:Fe ratio must be viewed as a hypothesis to be validated by comparison to the high temperature data. From this perspective, the fraction of liquefied fuel following a high temperature test is both a measured quantity and a quantity of primary interest in applying

Design Criterion 6.0.

Table 5-7 summarizes the relevant data for total penetration into the cladding and fuel liquefaction fraction following high-temperature FBTA tests for irradiated (>10 at. % burnup) HT9/U-19Pu-10Zr from Refs. 5.15 - 5.17. Similarly, Table 5-8 summarizes the relevant data for irradiated 316SS/U-19Pu-10Zr and D9/U-19Pu-10Zr. The wastage values under the category "SS" refer to estimated values, based on neighboring axial locations and sibling pin results, at the end of normal irradiation. The column marked "Tran" refers to the estimated additional wastage which occurred during FBTA testing. The column marked "Total" refers to the actual measurement taken after FBTA testing. Implicit in the tables are the fuel/cladding liquefaction temperatures. As shown in Table 5-7, in one test no liquefaction was observed after 36 hours at 650°C, while liquefaction was observed after 12 hours at 660°C in another test. As these times exceed the time of any transients considered in the safety case, it is conservative to set 651°C as the liquefaction temperature for Mark-V fuel pins. Additional conservatism is implied by this choice. Figure 5-10 shows that the liquefaction temperature is actually burnup dependent [5.18]. It is greater than 725°C for low-burnup Mark-V-type fuel pins. Thus, added conservatism comes from setting 651°C as the liquefaction temperature for Mark-V for all burnups.

Similarly, the liquefaction temperature for Mark-VA pins is implicit in the results presented in Table 5-8. Because of the scarcity of data on 316SS/U19Pu-10Zr, because of the chemical similarity of 316SS and D9, and because the D9 steady state wastage data bounded from above the 316SS wastage data, the two data sets are combined to strengthen the Mark-VA data set. Here liquefaction was not observed until after 1 hour at 700°C. The 12-hour results of no liquefaction at 660°C are significant because of the duration of the test as compared to Mark-VA transient durations. The no-liquefaction results at 675°C after 1 hour are interesting but not conclusive because of the short duration. Thus, the high burnup liquefaction temperature for Mark-VA pins lies between 660°C and 700°C. Again from the point of design conservatism, 661°C is chosen as the Mark-VA liquefaction temperature for all burnups. Figure 5-10 shows the added conservatism implied in this criterion for the lower burnups.

Table 5-7 FBTA Database for Cladding ID Wastage and Fuel Liquefaction for 10-14 at.% Burnup HT9/U-19Pu-10Zr at T ≤ 800ºC

Test Parameters			Maximum d_i, μm			Fuel Liquefaction, %
X/L	T, °C	t, h	SS	Tran.	Total	
0.88	650	1	29	0	29	0
0.75	650	1	36	10	46	0
0.61	650	12	24	12	36	0
0.59	650	36	20	55	75	0
0.69	660	12	32	78	108	0
0.64	660	12	28	53	81(21%)	12
0.76	675	1	16	0	16	0
0.25	675	1	29	0	29	0
0.72	675	1	35	24	59(15%)	5
0.67	675	12	31	109	140(37%)	31
0.71	700	1	32	21	53	0
0.83	700	1	37	21	58(15%)	9
0.83	700	1	53	23	76(20%)	13
0.73	725	1	32	0	32(8%)	2
0.89	740	1	41	46	87(23%)	18
0.54	740	1	21	37	58(15%)	12
0.85	770	1.0	40	40	80(21%)	66
0.68	800	0.1	39	3	42(11%)	27
0.72	800	0.5	46	33	79(21%)	63
0.52	800	0.5	8	29	37(10%)	58
0.80	800	1	56	44	100(26%)	100
0.73	800	2	48	56	104(27%)	100

Table 5-8 FBTA Database for Cladding ID Wastage and Fuel Liquefaction for 10-14 at.% Burnup D9/ and 316SS/U-19Pu-10Zr at T ≤ 800ºC

Test Parameters			Maximum d_i, μm			Fuel Liquefaction, %
X/L	T, °C	t, h	SS	Tran.	Total	
316SS						
0.91	650	7	65	0	65	0
0.76	675	1	58	10	68	0
0.89	750	2	65	54	119(31%)	19
D9						
0.81	660	12	106	7	113	0
0.76	675	1	88	0	88	0
0.83	700	1	104	3	107(28%)	4
0.71	700	12	108	70	178(47%)	57
0.73	725	1	108	0	108(28%)	7

While the data in Table 5-7 and Table 5-8 are useful as presented, their real value to the Mark-V and Mark-VA safety cases is derived from their use to validate the methodologies used to perform design calculations. As explained in Section 9.4, LIFE-METAL is used to calculate the solid-state wastage during normal operation. The Bauer-Kramer correlation (Section A.4 of Appendix A) is used in SASSYS to calculate additional wastage during a high temperature excursion and the fraction of liquefied fuel and cladding. With regard to the prediction of total penetration following a high-temperature excursion, Figure 5-11 shows that the LIFE-METAL methodology (SSBDF) coupled with the sequential Bauer-Kramer (BK) calculation for transient wastage bounds the FBTA data for irradiated (>10 at. %) HT9/U-19Pu-10Zr with a confidence level of 81%. In the case of Mark-VA-type fuel the same methodology is an upper bound to all of the data (Figure 5-12). The fuel liquefaction predictions vs. data are shown in Figure 5-13 and Figure 5-14. In the case of Mark-V fuel (Figure 5-13), the current practice (SSBDF+BK) results in a 57% confidence level of an upper-bound fuel liquefaction fraction prediction. For the more limited Mark-VA data base, the current methodology results in upper-bound liquefaction predictions to all of the data.

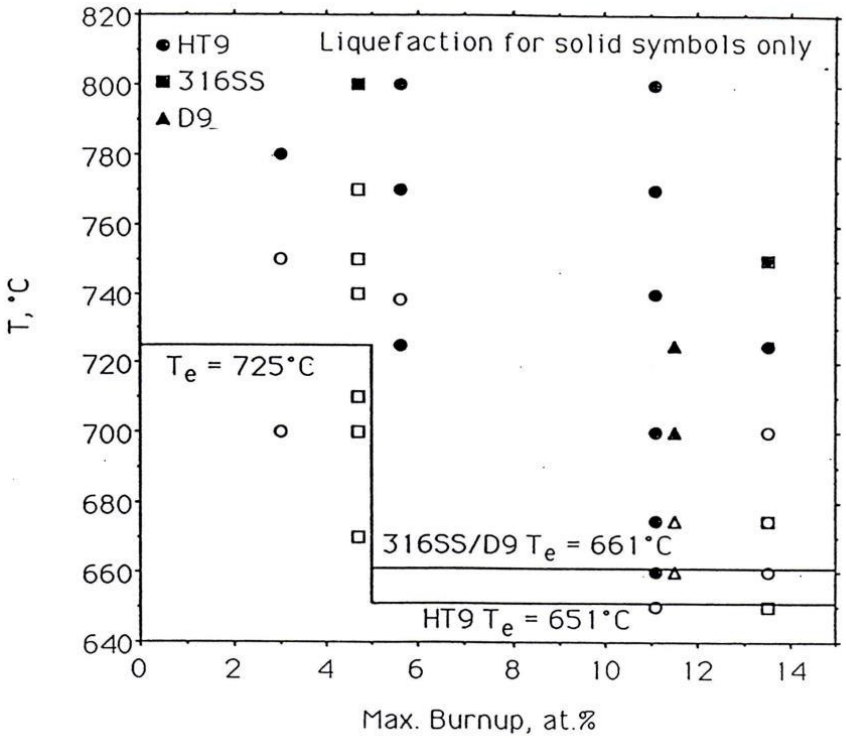

Figure 5-10 Lower Bound on the Fuel (19-26% Pu)/Cladding Liquefaction Temperature

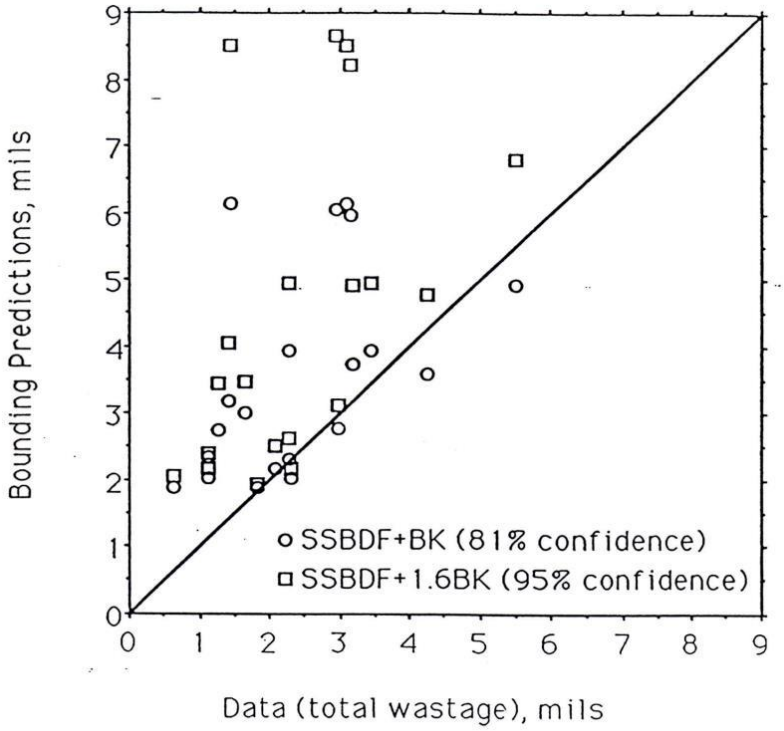

Figure 5-11 Bounding Results for HT9 Wastage After > 10 at.% Bu U-19Pu-10Zr FBTA Tests

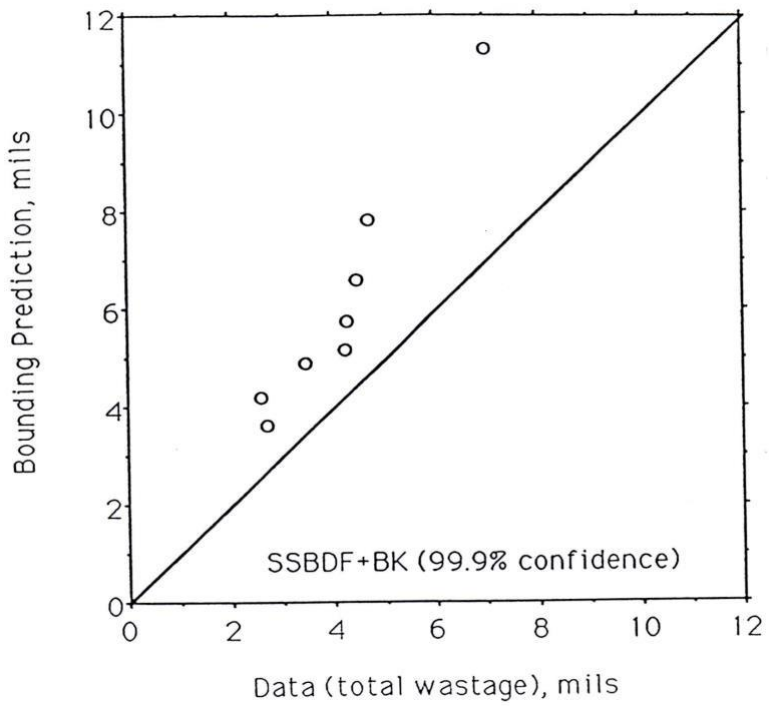

Figure 5-12 Bounding Results for 316SS/D9 Wastage after > 10 at.% Bu U-19Pu-10Zr FBTA Tests

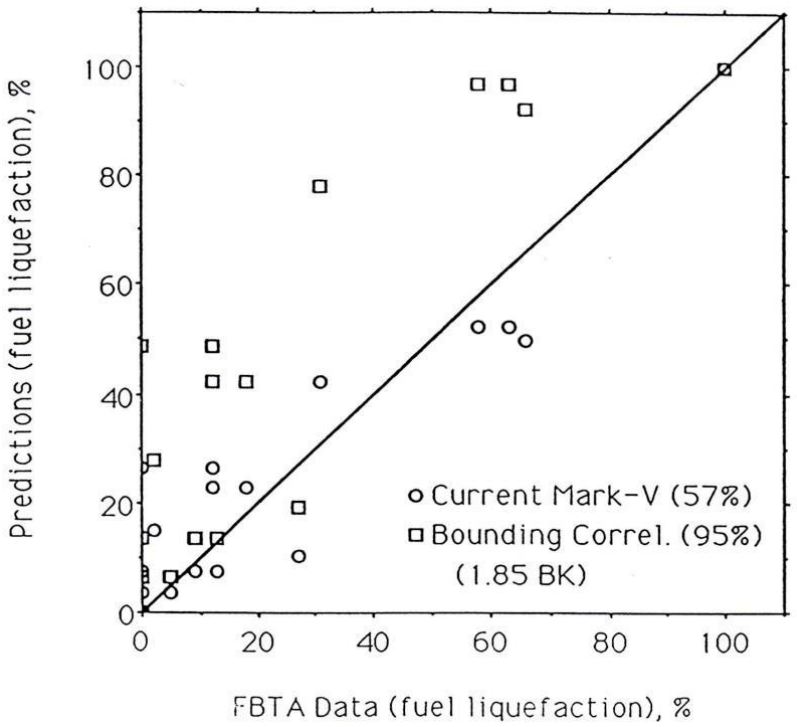

Figure 5-13 Predictions vs. HT9 FBTA Fuel (> 10 at.% Bu U-19Pu-10Zr) Liquefaction Data

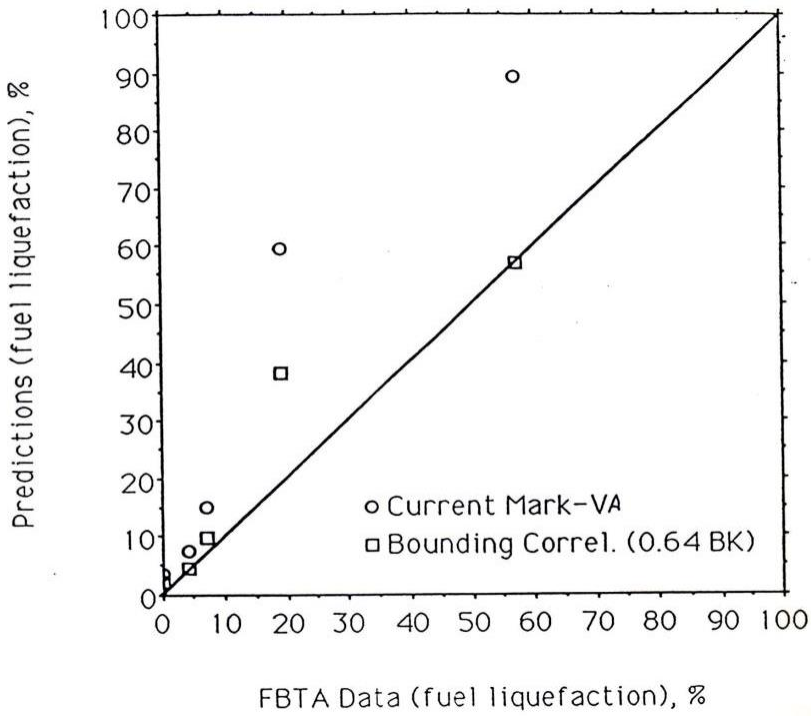

Figure 5-14 Predictions vs. 316SS/D9 FBTA Fuel (> 10 at.% Bu U-19Pu-10Zr) Liquefaction Data

Three integral-pin tests, FM-2, FM-4 and FM-5, have been conducted in the WPF in support of the Mark-V driver development [5.196]. These tests were designed to envelop the umbrella unlikely loss-of-flow (LOF) event, UN-1, during which the calculated peak cladding temperature of the Mark-V driver would reach 750°C for less than 10 seconds (see Figure 9-14).

A low-burnup (3 at. %) pin was used in the FM-2 test, whereas high-burnup (11 at. %) pins were used in both FM-4 and FM-5 tests. The cladding of these pins was thinner than that of the Mark-V driver (15 vs. 18 mils (0.38 vs 0.47 mm)). In addition, the FM-2 pin also had a smaller plenum (1.0 vs. 1.5 P/F). The results from these tests are therefore conservative from the standpoint of Mark-V fuel performance.

The FM-2 and FM-4 tests were conducted as pin-integrity tests at constant temperatures until cladding breach. In the FM-2 test, the pin was held at a peak cladding temperature of 820°C until cladding breach, which occurred at 112 min. into the test. In the FM-4 test, the pin was heated at a peak cladding temperature of 770°C and breach occurred at 68 minutes. Both breaches occurred substantially beyond the UN-1 transient duration of ~2 min. A very significant cladding integrity margin was thus demonstrated in these two tests. The shorter cladding

breaching time in FM-4 at a lower test temperature than FM-2 was due to the higher fission-gas pressure in the high-burnup FM-4 pin. Nondestructive examination of the FM-4 test pin showed a cladding breach in the plenum apparently caused by gas-pressure induced stress rupture. For the breached pin in the FM-2 test, posttest examination showed a cladding breach at the fuel top that was caused by a synergism of cladding thinning (due to fuel/cladding metallurgical interaction) and fission-gas pressure loading. Significant axial fuel expansion (at least 2 in. (5.1 cm)) within the cladding was also noted in the FM-2 test.

The FM-5 test was conducted as a proof test to demonstrate that a high-burnup, Mark-V-type pin can endure a UN-1 LOF event in EBR-II with only minor incremental cladding strain and wastage, and no cladding breach. Results from the test showed that the pin survived the simulated LOF event with no cladding breach. The measured incremental cladding strains were <0.1% in the entire fueled region. Preliminary results from destructive examination of the FM-5 test pin showed no incremental cladding penetration and no fuel liquefaction over the entire region of the fuel [5.19].

5.2.4 Transient Tests in TREAT

In-reactor data on the behavior of metallic fuel pins under transient conditions have been obtained using the TREAT (Transient Reactor Test) facility [5.20, 5,21]. Approximately 175 tests on metallic fuels of earlier designs were performed between 1961 and 1971. More recently, tests on metallic fuels have resumed as part of the Integral Fast Reactor (IFR) Program. It is these latter tests that are most relevant to the Mark-V driver fuel because of similarities in fuel materials, cladding materials, fuel column dimensions, plenum dimensions and burnups.

The seven IFR metallic fuels tests that have been performed thus far are part of the TREAT M series of experiments. After a preliminary test M1 on a small fuel sample in a dry capsule, six tests (M2 through M7) were performed in Mark-III sodium loops. All six investigated the response of the fuel to severe transient overpower (TOP) conditions, in particular the fuel failure mechanisms, prefailure fuel expansion, and early post-failure fuel movement. The parameters in the tests were fuel composition, cladding type, burnup, and fuel conditions at test termination, as indicated in Table 5-9.

Table 5-9 IFR Tests on Metallic Fuel Pins

Test	Fuel Composition	Cladding Composition	Burnup (at. %)	Posttest Condition	Data Report and Analysis
M2	U-5Fs " "	20% C.W. 316 SS " "	0.3 4.4 7.9	intact failed failed	5.17 " "
M3	U-5FS " "	20% C.W. 316 SS " "	0.3 4.4 7.9	intact intact intact	5.17 " "
M4	U-5Fs " "	20% C.W. 316 SS " "	fresh 2.4 4.4	intact failed intact	5.17 " "
M5	U-19Pu-10Zr "	20% C.W. D9 "	0.8 1.9	intact intact	5.18 "
M6	U-19Pu-10Zr "	20% C.W. D9 "	1.9 5.3	intact failed	5.18 "
M7	U-19Pu-10Zr U-10Zr	20% C.W. D9 HT9	9.8 2.9	failed intact	5.18 "

The reference fuel for IFR is a ternary alloy of uranium, plutonium and zirconium. In order for the IFR safety program to progress in parallel with the IFR irradiations program, the first M series experiments on metallic fuel were performed using readily available uranium-fissium EBR-II Mark-II driver fuel. Fissium is a mixture of metals representing an equilibrium composition of solid fission products that would result from using a simple pyrometallurgical fuel cycle. Although some minor differences in the transient behavior of these two fuel types would be expected, models and codes that are applicable to one fuel should be sufficiently general to apply to the other. The last three tests, M5 through M7, used prototypic U-Pu-Zr IFR fuels which are similar to the EBR-II Mark-V driver fuel.

Each fuel pin in test M2-M7 was located in a separate flowtube. The same overpower transient with an 8 s exponential period was used in all of the tests. The data that were obtained from the tests were instrumental in developing models of cladding failure and pre-failure fuel elongation. In the relatively short time frame of the tests, cladding failure was caused by a combination of pin plenum pressure acting hydrostatically through weak partially-molten fuel on cladding that had been thinned by transient-induced formation of a low-melting temperature fuel-cladding eutectic alloy. The relative importance of pressure and cladding thinning was found to

be a strong function of burnup. At low burnups, it was necessary for peak cladding temperatures to reach a value at which the rate of metallurgical attack of the cladding increased sharply by two or three orders of magnitude. For the heating conditions applied in these tests, failure of both U-5Fs and U-19Pu-10Zr fuel in austenitic cladding consistently occurred at conditions corresponding to 4.0 - 4.4 times IFR reference operating power (12 kW/ft (39 kW/m), 150 K coolant temperature rise). The failure threshold for HT9-clad U-10Zr fuel was not reached in these experiments and therefore must exceed 4.8 times nominal conditions. Cladding failure consistently occurred at the very top of the fuel column and was very localized. Nearly all of the molten alloy (roughly half of the fuel) that was present in the pin at the time of failure was expelled through that small breach and was carried upward out of the core region by the flowing sodium. The non-molten alloy at the bottom of the fuel pin remained in place. Although the test geometry did not well represent a pin bundle configuration, the observed propensity of the fuel to monotonically disperse in a manner that would be a strong advantage in mitigating or preventing severe accidents can be considered to be a basic characteristic of the metal fuel.

Pre-failure fuel elongation was found to be sensitive to fuel composition and pre-irradiation power level. In addition, where those parameters led to potentially high elongations, there was strong dependence on burnup. The U-5Fs fuel irradiated at 8 kW/ft (26 kW/m) expanded up to 17% axially at low burnups, but the reference U-Pu-Zr fuel expanded during the tests by only 2-4% and the expansion was nearly independent of burnup.

Of course, the overpower transients imposed by the TREAT tests were much more severe than those that would occur during design basis transient overpower accidents for Mark-V fuel, where the automatic scram system is activated at 1.15 times nominal power. However, the TREAT tests do indicate a wide margin to failure under TOP conditions. The tests also indicate that fuel melting leads to fuel expansion rather than compaction, and that any failures would most likely occur at the top of the fuel column. Consequently, fuel motion reactivity feedback, both pre-failure and post-failure, would be strongly negative.

Comparison of the test matrix in Table 5-9 with the design parameters for the Mark-V fuel shows that none of the test pins was exactly identical to the Mark-V design. However, both 316SS and HT9 cladding were tested, as well as high plutonium fuels at burnups approaching 10 at. %. These tests have formed the basis for the validation of the FPIN2 transient fuel pin

behavior code, as discussed in Section 4.3 of this report. Calculations have been performed in support of the Mark-V safety case using the FPIN2 code to extrapolate the test results to the behavior of Mark-V fuel. The results of these calculations are described in the following paragraph.

Calculations of the thermal and mechanical response of Mark-V fuel to transient overpower events were performed using the detailed FPIN2 transient fuel pin behavior code. A description of the code and its validation are summarized in Section 4.3 of this report. The pretransient characterization (dimensions, fission gas content, porosity, etc.) of the fuel pin were obtained directly from LIFE-METAL code calculations for the hottest end-of-life fuel pin in a typical (Run 141D) core loading in EBR-II. The transient that was analyzed was a single rod insertion at 1 ¢/s. The reactor power and flow were obtained from the SASSYS calculations for the AN-3 event described in Section 9.7.2.3. However, instead of scramming the reactor at 15% overpower, the power was allowed to increase with the pre-scram period (62.5 s) until pin failure was predicted. This is analogous to TREAT tests M2-M7 except, because of TREAT energy limitations, the period in the tests was 8 s. As noted above, the test pin designs were also different from the Mark-V fuel. However, the FPIN2 calculations indicate that these differences are not significant and that the TREAT results are directly applicable to the Mark-V safety case. One of the reasons for this is that the thermal response for an 8 s period and for a 62.5 s period TOP are both essentially quasi-static with the temperatures depending only on the instantaneous power. The second reason is that, in both cases, the failure of the pins is governed primarily by the onset of rapid eutectic penetration which occurs when the cladding interface temperature reaches 1080°C; cladding failure by this mechanism is nearly independent of the heating rate. The FPIN2 calculated overpower for the failure of Mark-V fuel is 4.1 times nominal power, which is similar to that for the TREAT pins that failed in test M2-M7. Failure was also predicted to occur at the very top of the fuel column and pre-failure fuel extrusion was about 2.1%, again consistent with the TREAT results. Thus Mark-V fuel can be expected to have a large margin to failure and any fuel motion would tend to decrease the reactivity.

Section 5 References

5.1 M. C. Billone, Y. Y. Liu, E. E. Gruber, T. H. Hughes and J. M. Kramer, "Status of Fuel Element Modeling Codes for Metallic Fuels", Proc. Intern. Conf. on Reliable Fuels for

Liquid Metal Reactors, p. 5-77, Sept. 7-11, 1986.

5.2 G. L. Hofman, et al.,"Swelling Behavior of U-Pu-Zr Fuel", Metallurgical Transactions A, Vol. 21A, p. 517, March 1990.

5.3 R. G. Pahl, et al.,"Postirradiation Examinations of U-Pu-Zr Fuel Elements from Subassemblies X419 and X419A", ANL-IFR-55, Oct. 1986.

5.4 Argonne National Laboratory, unpublished information (1987).

5.5 Argonne National Laboratory, unpublished information (1987).

5.6 R. G. Pahl, et al., "Experimental Studies of U-Pu-Zr Fast Reactor Fuel Pins in the Experimental Breeder Reactor-II", Metallurgical Transactions A, Vol. 21A, p. 1863, July 1990.

5.7 R. G. Pahl, R. S. Wisner and G. L. Hofman, "Steady-State Irradiation Testing of U-Pu-Zr Fuel to >18% Burnup", Proceedings of the 1990 International Fast Reactor Safety Meeting, American Nuclear Society Topical Meeting, Vol. IV, p. 129, 12-16 August 1990, Snowbird, Utah.

5.8 R. G. Pahl and C. E. Lahm, "The Performance of HT9 Clad Metallic Fuel at High Temperature", ANS Transaction Vol. 66, November 1992.

5.9 R. G. Pahl, et al., "The Characterization and Monitoring of Metallic Fuel Breaches in EBR-II", accepted for the 1991 International Conference on Fast Reactor and its Fuel Cycles, October 29-November 1, 1991, Kyoto, Japan.

5.10 G. L. Batte' and G. L. Hofman, "Run-Beyond-Cladding Breach (RBCB) Test Results for the Integral Fast Reactor (IFR) Metallic Fuels Program", Proceedings of the 1990 International Fast Reactor Safety Meeting, American Nuclear Society Topical Meeting, Vol. IV, p. 207, 12-16 August 1990, Snowbird, Utah.

5.11 H. C. Tsai, "A Versatile Apparatus for Studying the Behavior of Irradiated Fuel," Proc. 37th Conf. on Remote Systems Technology, 1989 Winter Mtg., San Francisco, CA, p. 88, 26-30 Nov. 1989.

5.12 H. C. Tsai, "Fuel/Cladding Compatibility in Irradiated Metallic Fuel Pins at Elevated Temperatures," Proc. 1990 Intl. Fast Reactor Safety Mtg., Snowbird, UT, Vol. II, p. 257, 12-16 Aug. 1990.

5.13 Y. Y. Liu, et al., "Whole-Pin Furnace System: An Experimental Facility for Studying Irradiated Fuel Pin Behavior under Potential Reactor Accident Conditions," ibid., p. 491, Vol. 1.

5.14 L. A. Neimark, et al., "The Alpha-Gamma Hot Cell Facility at Argonne National Laboratory-East," Proc. 27th Conf. on Remote Systems Technology, 1979 Winter Mtg., San Francisco, p. 15, Nov. 11-16, 1979.

5.15 A. B. Cohen, H. Tsai, J. E. Sanecki and L. A. Neimark, "Fuel/Cladding Compatibility in High-Burnup U-19Pu-10Zr/HT9 Clad Fuel at Elevated Temperatures," ANS Transaction Vol. 66, November 1992.

5.16 A. B. Cohen, Argonne National Laboratory, unpublished information (1993).

5.17 H. Tsai, Argonne National Laboratory, unpublished information (1992).

5.18 M. C. Billone, Argonne National Laboratory, unpublished information (1994).

5.19 Y. Y. Liu, H. Tsai, M. C. Billone and J. M. Kramer, "Behavior of EBR-II Mark-V-Type Fuel Elements in Simulated Loss-of-Flow Tests", ANS Transaction Vol. 66, November 1992.

5.20 W. R. Robinson, et al., "IFR Safety Tests M2, M3 and M4 in TREAT: Data and Analysis," Argonne National Laboratory Report, ANL-IFR-18 (June 1985).

5.21 T. H. Bauer et al., "Fast Overpower Tests of Metallic IFR Fuel in TREAT: Data and Analysis from Tests M5, M6 and M7", ANL-IFR-124 (December 1989).

6 NUCLEAR DESIGN

6.1 Background and Nuclear Design Methods

EBR-II was originally designed and operated to provide a small-plant demonstration of a sodium-cooled fast breeder reactor power plant. Following the successful demonstration of the plant, the need for an adequate fast reactor irradiation test and examination facility led to its operation for the testing of fast reactor fuel, structural, and poison materials. In this role, EBR-II has had frequent core loading changes for removal, insertion, and relocation of test-irradiation subassemblies. These core loadings are very heterogeneous and generally have a non-constant core radial periphery. Both for the characterization of the irradiation environments of individual test subassemblies and for the overall specification of the neutronics of the reactor system for operational and reactor modification, extensive reactor physics analyses have been carried out.

The physics analyses of EBR-II loadings, operations, modifications, tests, and of environmental characteristics of each subassembly require extensive usage of current methods of analyses and also development and innovation of techniques. This is due to the heterogeneous complexity of the system, the frequent loading changes, and the user need for detailed environmental characterization. As such, the tests and analyses on EBR-II function also as indicators of the capabilities of the nuclear data and computational methods to accurately predict the nuclear environment of EBR-II. Described below are the experimental programs and analyses performed to support the validation of the EBR-II nuclear computational methodology.

6.1.1 Measurements in Support of EBR-II Neutronics and Gamma Analysis

Studies of measurements in support of EBR-II run-to-run analyses are based upon measured data obtained from zero-power simulations, using the ZPR-3 critical assembly, and from the EBR-II reactor.

The critical assemblies are designated 60, 61, 62, & 63 and were constructed prior to the conversion of the EBR-II to the first nominally four-rowed stainless-steel radially-reflected system, which was for Run 56 in 1972. Assemblies 60, 61, and 62 simulated homogeneous

uranium-fueled cores radially-reflected by depleted-uranium, nickel, or steel respectively [6.1]. Assembly 63 instead consisted of three separate configurations designated A, B, and C of heterogeneous cores radially reflected by steel [6.2].

The neutron data support from the critical assemblies are reaction-rate traverses, dosimetry-foil-packet irradiations, and proton-recoil spectra. The gamma data support are thermoluminescent detector (TLD) traverses including effects of heterogeneities.

Calculated RZ-geometry and measured radial and axial reaction-rate traverses for $^{235}U_f$, $^{238}U_f$, $^{10}B_C$ are compared in Ref. 6.3 for assembly 60, in Ref. 6.4 for assembly 61, and in Refs. 6.5, 6.6, and 6.7 for assembly 62. Comparisons of calculated XY-geometry with measured radial reaction-rate traverses for $^{235}U_f$, $^{238}U_f$, $^{10}B_C$ for the heterogeneous assembly 63 cases are shown in Refs. 6.8, 6.9, and 6.10. Because run-to-run neutronic analysis of EBR-II loadings are carried out in XY-geometry and the loadings are not usually homogeneous, the comparisons for the steel-reflected assembly 63 cases are more applicable. Calculated central fission ratios relative to measured ratios for ^{238}U, ^{234}U, ^{233}U, ^{236}U, ^{239}Pu, ^{240}Pu relative to ^{235}U are shown in Ref. 6.11 for the homogeneous core steel-reflected assembly 62.

Spectrally sensitive neutron-activated foil packets of ^{235}U, ^{238}U, Au, Ni, and Al irradiated at core, interface, and reflector positions in assemblies 60, 61, and 62 were analyzed using XY-geometry discrete-ordinate transport calculations in S_4 approximation, [6.12]. Comparisons with measurements are shown in Table II of Ref. 6.13.

Proton-recoil measurements made at core center, in core near core-reflector interface, and in the reflector of the nickel-reflected and steel-reflected assemblies 61 and 62, respectively, were compared with calculated spectra obtained using 165-energy groups. The comparisons for the nickel-reflected case are shown in Ref. 6.2 and for the more relevant steel-reflected case as Fig. 8 of Ref. 6.14. A spectral comparison at core center using the usual 29-energy structure is shown in Ref. 6.15.

Radial and axial TLD dose mappings were performed in these EBR-II series of ZPR-3 critical assemblies. The measured spatial distributions are compared with RZ-geometry gamma transport calculations, done with 20 energy groups, in Ref. 6.16 for the radial and in Ref. 6.17 for

the axial for assemblies 60, 61, and 62. The calculated results are shown for deposition in iron because the TLDs were enclosed in steel sleeves. In order to determine to what extent two-dimensional, XY-geometry, gamma transport calculations represent the deposition profiles through different subassembly types, TLD's were also exposed through differing subassembly simulated drawers of Assembly 63A. These are shown in Ref. 6.18.

Supporting measurements made in EBR-II include some made before the conversion to the nominally four-row steel-reflector run 56, but subsequently analyzed using post run 56 calculational methods, as well as calculations of post run 56 measurements. Measurements analyzed for these purposes are foil (or wire) dosimetries and burnup measurements.

Analyses of an extensive series of reaction-rate measurements during EBR-II runs 50G and 50H are reported in Ref. 6.19. The run 50G radial and axial ^{235}U and ^{238}U fission measurements were made at low power (≅50kWt) using wires. The run 50H foil measurements were made at full power for a very large number of spectrally-sensitive foils.

Measurements of integral neutron capture-to-fission cross-section ratios and neutron capture rates of samples of ^{233}U, ^{235}U, ^{238}U, ^{239}Pu, ^{240}Pu, and ^{242}Pu at numerous radial and axial positions exposed during the early depleted-uranium-blanketed EBR-II runs 5 through 23 were made. The fission rates were determined by measurement of the fission product ^{137}Cs and the capture rates were determined by mass-spectrometric and alpha-spectrometric analysis. A detailed comparison between measurements and calculations using RZ and XY geometries are reported in Ref. 6.20.

Measured burnup values of about 100 enriched-uranium driver-fuel pins irradiated in EBR-II for various ranges of runs between run 1 and run 55 have been compared with calculated values based on run-to-run subassembly-delineated transport analyses, [6.21]. Experimental-fuel subassemblies often contained pins of non-identical compositions. These subassemblies often occupied differing locations during irradiation, occasionally their orientations were rotated, and a given pin might occupy different locations in differing subassemblies used during its irradiation. A comparison of calculated burnups, taking into considerations these changes, has been made for 28 experimental pins, [6.22]. Calculational comparisons of blanket-pin burnup and plutonium buildup for EBR-II depleted-uranium blanket-pins irradiated near core at fixed and at non-fixed

locations in the EBR-II blanket have also been made, [6.23].

Specific measurements made in EBR-II to support EBR-II analyses were also made subsequent to the conversion to the nominal four-row steel reflector system.

A low-power dosimetry test during run 78C of axial distributions of ^{235}U and ^{238}U fission rates and ^{238}U capture rate at various radial locations in core and in radial steel-reflector subassemblies were made with wires. In addition, midplane reaction rates were measured with dosimeter packets containing an assortment of materials. Calculational analyses of this test are described in Ref. 6.24.

Because of the irradiation-users need for detailed reaction-rates and fluences, dosimetry analyses for core locations have usually been emphasized. Consideration of blanket dosimetry, however, became increasingly important due to increased blanket exposure requiring analyses and dosimetry data to guide the scheduling of blanket subassembly relocations and removals, to support damage and burnup studies, and to obtain a measure of the analyses capability in the blanket regions which are separated from the core by the intervening rows of steel-reflector subassemblies. Comparisons of neutron-rate calculations with absolute dosimetry measurements are reported in Ref. 6.25 for ^{235}U, ^{239}Pu, and ^{238}U fission reactions and for ^{238}U capture reactions.

The comparison between measured and calculated values of these numerous quantities are described and discussed in References 6.1 to 6.25. The agreements between calculated and measured values are generally good, although discrepancies in some details do exist. The overall calculational methodology, however, has been used successfully as the basis for physics guidance for the EBR-II for many years involving numerous loadings and various applications. This gives confidence as to the validity of the integrated methodology for further predictions.

6.1.2 Neutron and Gamma Analysis Methodology

As described in Section 6.1.1, the neutron and gamma environment in EBR-II has been extensively studied from the time of its initial startup to facilitate validation of the EBR-II nuclear computational methodology. Specifically, the experimental program was planned and implemented to establish the accuracy of the computational methods to predict the reaction rates, power profile, and flux levels for each subassembly in the reactor. The discussion below

summarizes the neutron and gamma methodologies used in the analysis of the EBR-II reactor.

An EBR-II modification of the DOT program [6.26] is used to solve the discrete ordinate transport equation in XY geometry for both the neutron and gamma problems. The transport solution represents all driver, reflector, and radial blanket subassemblies as individual regions in the XY geometry midplane description. The model also includes the graphite shielding surrounding the radial blanket and the sodium window through one sector of this graphite shield. Each hexagonal-shaped subassembly is simulated as a rectangle of equal area which employs four mesh points per subassembly. The multigroup analysis uses 30 neutron energy groups in S_4P_0 transport approximation and 20 gamma energy groups in S_4P_3 approximation. In the neutron problem, region dependent axial bucklings [6.27] are used to simulate the axial leakage.

The BURNOUT Code [6.28] tracks the run-to-run heavy metal isotopic changes, relocation, and insertions of driver, experimental, and radial blanket subassemblies. An auxiliary code processes the heavy metal mass data from the BURNOUT code, datafiles which contain the light masses (i.e., Na, Fe, etc.), and other neutronic problem specification parameters to generate the necessary input file for the DOT code system.

The neutron calculations utilize a fixed set of multigroup cross sections derived from the ENDF/B Version-I data. This approach has enabled results from previous work in EBR-II to be factored into the assessment of calculational biases and uncertainties. The neutron cross section library was obtained by processing the ENDF/B-I data through the MC^2 code system [6.29] to generate a 29-group library. This 29-group library was merged with one group thermal cross section data to form a 30-group multigroup library. This set was derived by energy collapse to 30 groups specifically for compositions representing drivers, axial gaps, blankets, axial reflectors, radial reflectors, sodium window, and shield regions.

Similarly, the gamma calculations utilize a fixed set of multigroup cross sections. The gamma-production cross sections are obtained from the POPOP4 code [6.30] which converts spectra of gamma rays from neutron-induced reactions to a required coupled neutron gamma energy-group structure. The gamma yield data used in POPOP4 comes from the POPOP4 library [6.31], which is a compendium of secondary gamma-ray yield and cross-section data for the various neutron-induced reactions. The 20-energy group gamma library was obtained from the

MUG Code [6.32]. The MUG code explicitly accounts for Compton scattering, pair-production, and the photoelectric effect. In addition, the code processes γ-energy absorption cross-sections.

Axial dependence of neutron and gamma energy deposition rates obtained by RZ analysis are employed for axial integration and normalization of power. In particular, the composite of the XY transport solutions and the axial shapes from Run 56''' are used to synthesize 3-D neutron power and gamma power distributions. However, the total integrated gamma energy deposition relative to total fissions as obtained by way of the transport solutions do not necessarily result in the ratio required from fundamental data of reported gamma energy per fission. Thus correction factors derived from an energy balance are applied [6.33]. This is accomplished by requiring the total transport-calculated gamma energy rate deposited in the reactor to be consistent with basic data on the energy released per fission. Based on the total gamma energy resulting from fissions in ^{235}U, ^{238}U, and ^{239}Pu, and the relative fission rates in a EBR-II system, the average-gamma energy has been estimated [6.34] to be 28.3 MeV/fission of a total of about 202.8 MeV/fission. Assuming negligible gamma leakage about 8.75 MWt of gamma heating occurs at 62.5 MWt operating power. The power normalization is carried out using the SUBPOWER Code [6.35].

The results of the power normalization are input to the EBRFLOW code [6.36]. The EBRFLOW program is used in the thermal hydraulic characterization of the changing core loadings in EBR-II and in analyses in support of reactor design changes. This program is based on simple balances of flowrates and pressure drops in the EBR-II system, and on suitable input information from flow-modeling studies and engineering estimates of the leakage flowrates. The program calculates the flowrate, pressure drop, and outlet ΔT for each reactor subassembly, as well as the pressure drops in other parts of the system and the pump discharge pressures.

A post-processor code is utilized to display the results of the neutronic and gamma neutronic analysis for each of the 637 hexagonal lattice positions. The following 2D midplane parameters are displayed: fission and capture rates (per gram of material) for each of the heavy metal isotopes, the ^{10}B capture rate (per gram of material), iron and uranium gamma-energy deposition rates (per gram of material), fast neutron flux ($E \geq 0.111$MeV), and total neutron flux. Subsequent processing of the DOT output files results in the total power, coolant flowrate, and outlet ΔT hexagonal map.

6.1.3 Measurements in Support of EBR-II Reactivity Feedback Analysis

The reactivity feedback characteristics of EBR-II have been studied from the time of its initial startup [6.37]. These feedback characteristics have been re-examined in detail both prior to and during the conduct of the Shutdown Heat Removal Test Program, culminating in the unprotected loss-of-flow and loss-of-heat-sink tests, both conducted successfully from full power on April 3, 1986. The accurate prediction of the results of both tests rested upon, and demonstrated, a thorough understanding of the details of feedback in EBR-II [6.38]. In addition to the SHRT program, other experimental tests and calculational campaigns have been conducted [6.39, 6.40, 6.41, 6.42] to verify and validate the methodology to predict the reactivity feedback characteristics of EBR-II.

Overall feedback reactivity coefficients are generally defined in two ways, according to their application:

1. The isothermal temperature coefficient (ITC) is the change in reactivity that occurs with a 1°F (0.6°C) uniform increase in temperature in a reactor. The ITC of EBR-II is -0.4¢/°F (-0.7¢/°C). The ITC is derived by summing position-dependent components which are average temperature coefficients between the coolant inlet temperature and the applicable positional temperature for full-power (62.5 MWt) and flow conditions.
2. The power coefficient (PC) is the reactivity change in going from zero-power isothermal conditions to a given power divided by that power. The PC of EBR-II corresponding to a power of 62.5 MWt is -0.5¢/MWt.

The major contributor to the strongly negative reactivity feedback in EBR-II is reduction in density of the sodium and structural material in the reactor as the reactor temperature increases; this enhances neutron leakage from the core. Another strong contributor is axial expansion of the metal fuel as its temperature increases; this moves fuel from regions of higher reactivity worth to regions of lower worth, giving a net loss in reactivity. Both of the foregoing effects are very prompt-acting (time constant ≈ 0.3 second) and both are highly reproducible from one core loading to the next. The nuclear Doppler effect in EBR-II is very small (-Tdk/dT = 0.0002, vs. 0.002-0.008 for larger reactors). It must be accounted for in running reactivity-related tests in EBR-II but plays an insignificant role in the safety posture of EBR-II.

The sodium void effect at any point in a reactor is the change in reactivity per unit mass of sodium removed. The effect has three major components:

1. reduction in parasitic capture of neutrons by the sodium that is removed (always positive);
2. spectral hardening due to reduction in sodium moderation (comprised of increased fissions in ^{238}U and increased fissions in ^{235}U and ^{239}Pu relative to parasitic captures; always positive); and
3. increase in neutron leakage (always negative).

The net effect at a given point is the sum of the three components above, and may be positive or negative, depending on whether or not leakage dominates.

In EBR-II, which has a core volume of only about 100 liters and core H/D of about 0.53, leakage dominates everywhere. That is, EBR-II has a negative sodium void effect from the center of the core outwards. The total void worth was determined from criticality measurements made on EBR-II before it was filled with sodium and again after filling [6.43]. The total sodium void effect was determined to be -$6.

6.1.4 Reactivity Feedback Analysis Methodology

For improved understanding of reactivity feedback behavior and because of utilization of the EBR-II for operational-transient studies, a program EBRPOCO [6.44] has been under development to facilitate the calculations and interpretations of the power-reactivity-decrements (PRDs) of EBR-II loadings. The program enables contributions of various components of the PRD to be delineated axially for every subassembly of a loading configuration. Because the loading configurations are heterogeneous and frequently modified, calculations of the sensitivities of various components are of interest for steady-state operations as well as operational-transient studies.

For each core, steel radial-reflector, or depleted-uranium radial-blanket subassembly of an EBR-II loading configuration, the subassembly area-averaged axial distributions of the temperatures of sodium coolant, fuel- and blanket-pin cladding, structural rods and steel reflectors, sodium in gaps, and fuel are calculated. Axial distributions of the components of the PRD for the subassemblies are then obtained for the components resulting from: coolant density (density

reduction of sodium coolant due to temperature), coolant displacement (displacement of sodium coolant by thermal radial expansion of claddings, structural rods, subassembly cans, and lower and upper axial-reflector regions), steel density (density reduction of these steel components due to axial expansion with temperature), bond sodium (resultant of displacement of bond sodium, if present in the open gaps, by differential thermal expansions of fuel and cladding and of density reduction of bond sodium due to temperature), fuel and blanket axial expansions (free axial expansion of fuel if unrestricted by cladding or restricted axial expansion of fuel determined by axial expansion of cladding), Doppler (in fuel and blanket), B_4C-fuel (change in separation of B_4C follower and fuel in the cases of high-worth fueled control rods having B_4C followers), and the rod bank suspension (downward expansion of the control rods because of their being suspended from above). For the rod bank suspension an EBRPOCO program addition, RODCO, calculates the downward expansion of each rod from its banked position. The contributions of the rods to the bank suspension component of the PRD are then obtained by using the measured rod worths together with the measured fractional differential worth curves for the rod types. Furthermore, because EBR-II loadings contain fuels with various burnups, as well as differing fuel types, the type of fuel-cladding interaction assumed for a subassembly is based upon the type of fuel and the estimated average fuel burnup of the subassembly. Thus the fuel subassemblies are assumed to have gaps either: fully open, fully closed with fuel free to move axially, or fully closed with fuel axially restrained by the cladding.

Intra-subassembly information required as direct input for EBRPOCO consists of pin and rod diameter, number of fueled pins, type of fuel, fuel diameter, clad thickness, gap status, number of structural rods which are solid, and number of structural rods designated as non-solid (containing test samples or experiments). The fuel types are designated as metal driver, mixed-oxide, mixed-carbide, and uranium-metal blanket. The gap status is either open or closed. An open gap is specified to contain sodium or helium and if helium-bonded the fraction of xenon tag gas. A closed gap is specified as having fuel expanding axially either freely or as determined by the axial expansion of the cladding. Furthermore, if the fuel is mixed-oxide it must be specified also as being cylindrical or annular.

By the nature of the data it requires, EBRPOCO is inevitably the final step of a computational process involving prior executions of other programs. Three-dimensional

subassembly-wise non-gamma and gamma energy deposition rates are required. These are obtained from XY-geometry neutron and gamma calculations in which every subassembly is represented as a rectangle having four mesh regions. From corresponding azimuthally-homogenized RZ-geometry analyses are obtained non-gamma and gamma axial distributions of the energy deposition rates. These are 30 energy group discrete-ordinate neutronics calculations in S_4P_0 transport approximation and 20 energy group gamma calculations in S_4P_3 approximation using an EBR-II modification of the DOT program. The composite of the results from the two geometries is used to model the required three-dimensional input and to obtain overall power normalization. This synthesis is carried out using an auxiliary EBR-II program.

Required EBRPOCO inputs are also the subassembly-homogenized compositions (used in the XY-geometry calculations) and the axial regional compositions and delineations. The calculated spatial distribution of gamma energy deposition rate per unit mass of steel is also required. The latter input is needed for the EBRPOCO calculation of the gamma energy deposition rates in steel materials of a subassembly, for example, structural rods, hexagonal cans, etc. The sum of these deposition rates is also subtracted from the total gamma energy deposition rate for a given axial interval of a subassembly. The remaining gamma energy deposition rate is then added to the non-gamma deposition rate and the sum attributed to the fuel-containing pins of the subassembly. The program also requires the spatial distributions of isotopic reactivity worths. These are currently obtained from diffusion theory RZ-geometry calculations using the perturbation theory option of the CITATION program [6.45]. Furthermore, for computation of the distributions of the Doppler component a higher temperature neutron cross section set is needed. Subassembly coolant-flow input is obtained from calculations carried out using the EBRFLOW program.

The detailed contributions of both power and power-to-flow feedback components by subassembly types (and fuel gap conditions) and by regions are determined. These linear and Doppler components of the PRDs are calculated using the EBRPOCO program together with the addition to the program RODCO which accounts for the effects of axial positioning of control rods. These enable the PRD to be expressed as the sum of parts from which the PRD for other values of coolant flow may be estimated. The delineations of the components also enhance the understanding of the contributions of the various components and regions in the feedback process

in EBR-II. Separation of the components into power and power-to-flow delineations is made by calculations of the components of the PRD assuming infinite values of thermal conductivity everywhere and comparing with results for finite flow. Subtractions of the infinite-conductivity flow feedback values from the corresponding finite-flow values give the power portions.

The non-linear (primarily subassembly bowing) component can be deduced by differences of these calculated linear components from a measured total PRD value.

6.1.5 Measurements in Support of EBR-II Depletion Analysis

The depletion characteristics of EBR-II have also been studied from the time of its initial startup [6.21, 6.22, 6.23, 6.46, 6.47]. These depletion characteristics have been re-examined in detail [6.48] for the more recent irradiation of binary and ternary Zr-alloy fuel. The EBR-II experimental data available for comparison with calculations include burnup measurements, U and Pu isotopic fraction measurements, and gamma scan data.

The burnup measurements are based on Isotope Dilution Mass Spectroscopic (IDMS) analysis of fission products, such as ^{139}La and ^{148}Nd. Burnup indicators are selected that:

1. are chemically separable from the fuel matrix;
2. have high fission yields;
3. are insensitive to fissioning nuclide and neutron spectrum; and
4. do not migrate in the fuel.

The overall accuracy of the Argonne-West Analytical Laboratory's determination of burnup on irradiated IFR fuel (U-10Zr or U-xPu-10Zr) up to 20 atom percent burnup is estimated to be ± 4%, provided the diffusion of La and Nd is only in the radial (and not axial) direction.

The measurements of U and Pu isotopic fractions are also obtained from mass spectrometer measurements. The achievable accuracy of determining the actinide fractions in irradiated IFR fuel is dependent on:

1. the precision of the mass spectrometer to repetitively perform an isotopic measurement, and

2. the certified uncertainty of the standard reference material used to calibrate the mass spectrometer.

The overall accuracy of performing isotopic measurements on irradiated IFR fuel with the mass spectrometer is estimated to be ~0.2% for ^{235}U, ^{238}U, and ^{239}Pu, and ~1.0% for ^{234}U, ^{236}U, and ^{240}Pu. Radial variation of the U and Pu isotopic fractions has also been measured in IFR fuel [6.49] from radial drillings of irradiated samples.

Many irradiated EBR-II fuel pins, including current IFR binary and ternary Zr alloy fuel pins, have been analyzed with a precision gamma scanner. Energy dependent activity measurements are taken every one or two mils along the entire length of the fuel pins. Although some of the fission products migrate and redistribute within the fuel pin, other fission products, such as ^{95}Nb, appear to remain fixed in the fuel matrix. Therefore, the gamma scan measurement for ^{95}Nb approximates the fission distribution or burnup profile along the fuel pin.

6.1.6 Depletion Analysis Methodology

The current fuel management methodology [6.28] used by EBR-II has focused on uranium-fueled cores. These methods are currently used for core monitoring, SPM accountability, and as input for generation of the EBR-II run reports. Recent modifications in these methods have addressed some of their deficiencies and have extended the depletion chain up to ^{242}Pu. However, the current methodology does not calculate the buildup of higher actinides, in particular, the isotopes of Am and Cm. Although the quantity of these isotopes is small, gradual buildup will occur during the reprocessing of the Mark-V subassemblies.

In anticipation of an integral reprocessing system with recycling uranium or mixed-(U,Pu) fuels for which the concentration of the transuranic isotopes will be important, an extensive core-follow study for EBR-II has been performed using the REBUS-3/RCT methodologies [6.50, 6.51]. The REBUS-3 reactor model of EBR-II is a three-dimensional (hexagonal-Z) full core model which explicitly models each hexagonal subassembly through Row 16. The neutronics solution uses DIF3D nodal diffusion theory [6.52]. The depletion chain used in the REBUS-3 calculations includes U, Np, Am, Pu, and Cm isotopes, as well as explicit treatment of the burnup indicators ^{139}La and ^{148}Nd. The RCT code is used to reconstruct the intra-nodal distributions of

power density, burnup, nuclide densities, group fluxes, and fast and total fluences from the nodal-diffusion/depletion calculations performed in hexagonal-Z geometry using REBUS-3/DIF3D. Several important capabilities have been implemented in RCT to permit its application to a wide range of core designs and fuel management strategies. Specifically, the burnup characteristics can be explicitly calculated for user-defined "special pins" by point depletion using interpolated fluxes at the center of each fuel pin. Rotation of assemblies is allowed (in integer multiples of 60 degrees), and to permit assembly reconstitution, pin-by-pin shuffling is allowed for the special pins.

Details of the EBR-II core-follow study based on the REBUS-3/RCT methodologies are given in Ref. 6.48. In that study, calculated values have been compared with experimental determinations of burnup and U and Pu isotopic weight fractions that have been measured in IFR fueled test subassemblies irradiated in EBR-II. The results of these comparisons are very good.

6.2 Mark-V Core Design

Motivated by the programmatic needs resulting from the Integral Fast Reactor (IFR) fuel cycle demonstration and the new mission of the EBR-II complex as the IFR prototype, the EBR-II reactor will undergo a transition from the binary (uranium and zirconium) fuel form to the ternary (uranium, plutonium and zirconium) fuel form. This core conversion activity requires the core designers to specify the heavy metal enrichment since ^{239}Pu has a higher reactivity worth ($\Delta k/k$) per atom than ^{235}U ((^{239}Pu worth)/(^{235}U worth) ~1.7 for the EBR-II reactor). Therefore, less fissile mass is needed in a uranium/plutonium system to achieve the same eigenvalue as in a corresponding uranium system. Incorporating plutonium in the fuel leads to a higher flux level since, for a given system power and eigenvalue, the ratio of the ^{239}Pu fission cross section to the ^{235}U fission cross section is less than the corresponding worth per atom ratio. In addition, the effective delayed neutron fraction (β) for ^{239}Pu is less than it is for ^{235}U. (Subassembly worths are converted from $\Delta k/k$ units to dollars and cents units by dividing by the system β.) This means the effective delayed neutron fraction in a uranium/plutonium-fueled system will decrease. This will make control-rods, for example, worth more in terms of dollars and cents in a ternary fueled core than in a equivalent binary fueled core. This change is important because all current EBR-II Technical Specifications limits are expressed in dollars and cents.

The current Mark-V subassembly design is based on ternary U-20Pu-10Zr fuel with 18-mil HT9 cladding. The bundle is composed of 61 pins with a clad OD of 0.584 cm (0.230 inches). The fuel smear density is 75% which is prototypic of IFR subassembly designs. An alternative strategy for the core conversion from binary (U-10Zr) fuel to ternary fuel is to use existing supplies of 316SS cladding (0.230-inch (0.584 cm) OD and 15-mil (0.038-cm) thickness) in conjunction with the HT9 option. Since the clad thickness is reduced in the alternative subassembly design, the slug OD would increase in order to retain the 75% smear density. (A smear density of 75% was chosen because almost all the experimental database for Mark-V fuel is based on this smear density.) Another design constraint is to retain the same ^{235}U enrichment for both clad options. The larger fuel slug diameter associated with the 316SS option results in larger excess reactivity for an equivalent loading configuration.

Discussed herein are the scoping calculations used to determine a uranium enrichment, effective delayed neutron fraction, and prompt-neutron lifetime for a six-row EBR-II loading configuration where all the binary-fueled driver, partial-driver and driver-like experimental subassemblies are replaced by equivalent fresh U-20Pu-10Zr-fueled Mark-V subassemblies clad with HT9. Neutronic calculations were also performed for the 316SS option in which the ^{235}U enrichment was the same as with the HT9 option. However, the core layout was modified (six-plus-row core configuration) in an attempt to equalize the BOC excess reactivity between the two design options. In particular, the inner rows contained low worth structural subassemblies to partially compensate for the larger fissile mass (larger slug diameter in the 316SS option) in the core. Also discussed are the effects resulting from the increased flux level and smaller β for the ternary core. In addition, several thermal hydraulic quantities for the two ternary cores considered are compared with each other and with corresponding quantities from both a U-5Fs-fueled configuration and a U-10Zr-fueled configuration.

6.2.1 Design Description

6.2.1.1 Six-Row Core Model

Proposed-run 141D [6.53] was used as the basic loading configuration model for the six-row core. Shown in Figure 6-1 is the row 1-8 loading pattern for that proposed-run. The Mark-V subassembly design is based on U-20Pu-10Zr fuel with 18-mil HT9 cladding (see Section

6.2.1.3). Contained in the 91-subassembly six-row core region of this loading configuration are:

55 drivers (normal-flow and high-flow)
6 experimental drivers (X390, X399, X402, X411, X412, X427)
10 partial (half) drivers
7 high-worth control-rods
1 standard control-rod
1 experimental control-rod
2 safety rods
1 fueled experiment (XY20)
3 structural experiments (X320, XX10, XY16)
5 dummy structural subassemblies (K018).

The experimental drivers were modeled as drivers and the experimental control-rod was modeled as a control-rod. The three structural experiments in rows 1-6 (X320, XX10 and XY16) and the five structural experiments in row 7 (X319, X415, X101, X133 and X416) were left unchanged. Because this six-row loading configuration was based on proposed-run 141D, the radial blanket used in the analysis was assumed to be the radial blanket from proposed-run 141D.

6.2.1.2 Six-Plus-Row Core Model

The six-plus-row core model was used as the loading basis for the 316SS option (see Section 6.2.1.4). In an attempt to balance the excess reactivity at beginning of core conditions (relative to the six-row core model), several structural subassemblies were moved from the outer rows to row 2 and Mark-V drivers loaded into row 7. As is shown in Section 9, the analysis of two different layouts should not pose any safety concerns, since the adjustment of the EBR-II layout to meet the desired performance goals has been done routinely. In addition, the safety case is based on the most conservative results of the two core models.

Shown in Figure 6-2 is the row 1-8 loading pattern for this loading. Contained in the 103-subassembly six-plus-row core region of this loading configuration are:

73 drivers (normal-flow and high-flow)
10 partial drivers

8 high-worth control-rods

1 standard control-rod

2 safety rods

9 dummy structural subassemblies.

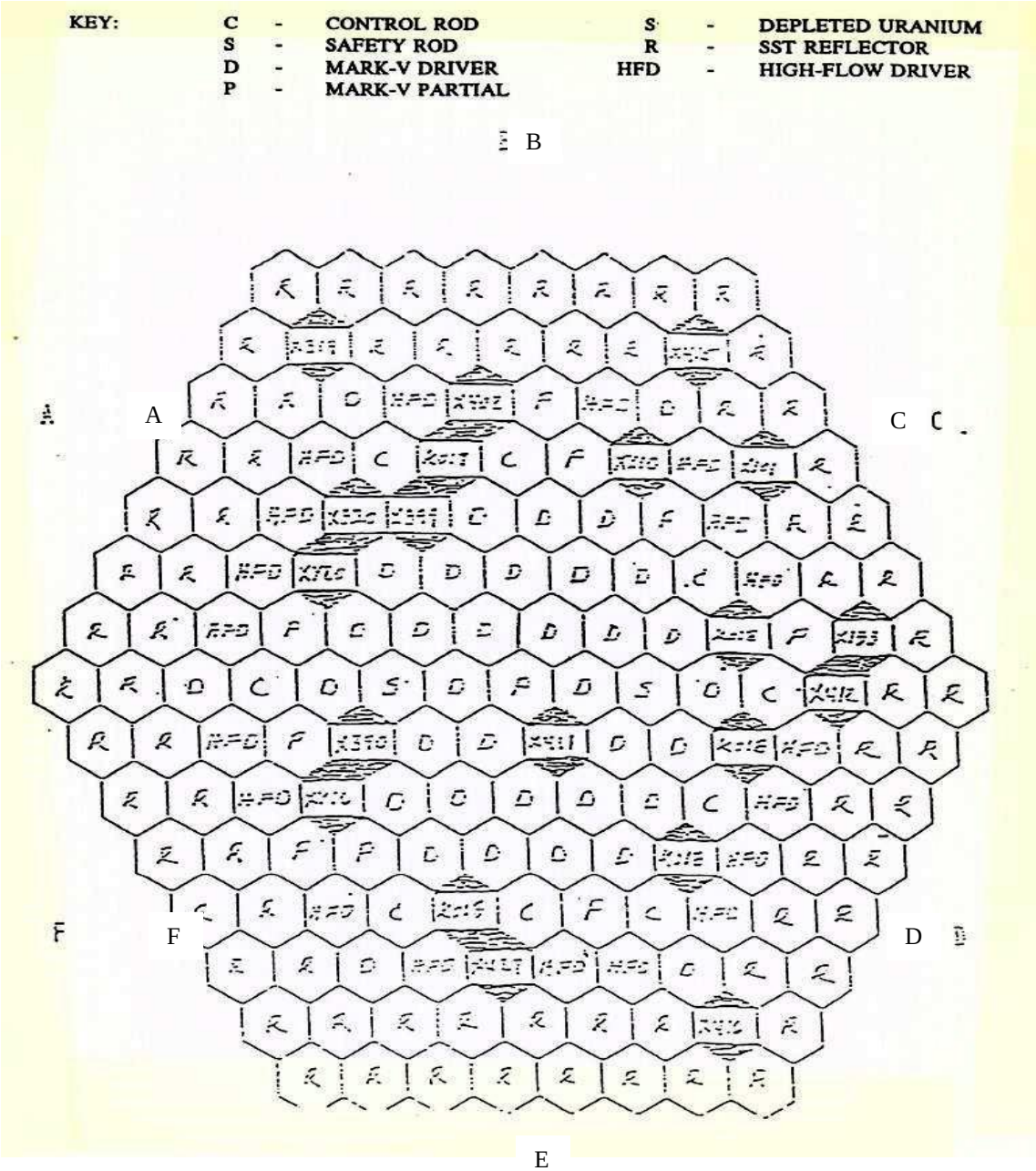

Figure 6-1 Six-Row-Core Loading Configuration

Although this loading configuration was not based on proposed-run 141D, the radial blanket assigned to this loading configuration was taken to be the radial blanket for proposed-run 141D.

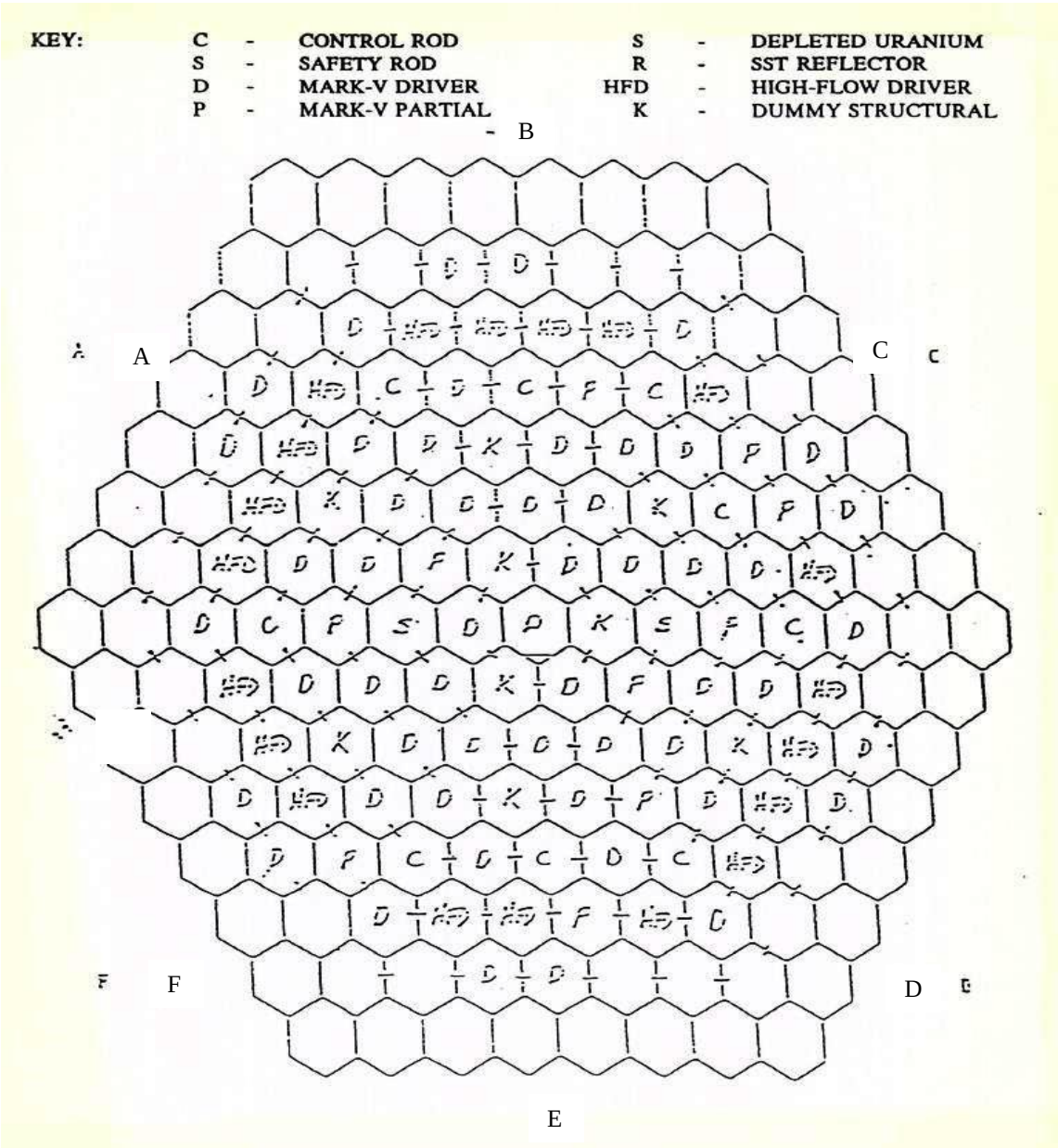

Figure 6-2 Six-Plus-Row-Core Loading Configuration

6.2.1.3 Mark-V U-20Pu-10Zr HT9 Clad Subassembly Model

The dimensions of this fresh Mark-V fuel pin are: clad OD 0.584 cm (0.230 inches), clad

thickness 0.046 cm (0.018 inches) and fuel-slug OD 0.427 cm (0.168 inches) [6.54]. With these dimensions the resultant fuel smear-density is 75%. The U-20Pu-10Zr fuel density was assumed to be 15.8 g/cm^3. The pin cladding, wire-wrap (0.042 inches (0.107 cm) OD) and 40-mil (0.1 cm) hexcan were HT9 (ferritic) steel. The total fuel mass in the 61-pin driver is 4725 g, whereas the total fuel mass in the 31-pin partial is 2444 g. The plutonium was assumed to contain 81% ^{239}Pu, 18% ^{240}Pu and 1% ^{241}Pu [6.55]. For a driver subassembly this translates into 765.5 g ^{239}Pu, 170.1 g ^{240}Pu, and 9.5 g ^{241}Pu whereas a partial driver contains 395.9 g ^{239}Pu, 88.0 g ^{240}Pu, and 4.9 g ^{241}Pu.

6.2.1.4 Mark-V U-20Pu-10Zr 316SS Clad Subassembly Model

The dimensions of this fresh Mark-V fuel pin are: clad OD 0.584 cm (0.230 inches), clad thickness 0.038 cm (0.015 inches) and fuel-slug OD 0.439 cm (0.173 inches). With these dimensions the same fuel smear density (75%) is retained. The U-20Pu-10Zr fuel density was assumed to be 15.8 g/cm^3. The pin cladding, wire-wrap (0.042 inches (0.107 cm) OD) and 40-mil (0.1 cm) hex-can were 316SS (austenitic) steel. The total fuel mass in the 61-element driver is 5018 g whereas the total fuel mass in the 31-pin partial is 2542 g. The plutonium was assumed to contain 81% ^{239}Pu, 18% ^{240}Pu and 1% ^{241}Pu [6.55]. For a driver subassembly this translates into 813.0 g ^{239}Pu, 180.7 g ^{240}Pu, and 10.0 g ^{241}Pu, whereas a partial driver contains 411.7 g ^{239}Pu, 91.5 g ^{240}Pu, and 5.1 g ^{241}Pu.

6.2.1.5 Control/Safety U10Zr 316SS Clad Subassembly Model

The control and safety rods were assumed to be 61-pin fresh U-10Zr fueled rods with an enrichment of 78% and a fuel mass of 2830 g. The control-rod fuel pin dimensions were: clad OD 0.442 cm (0.174 inches), clad thickness 0.030 cm (0.012 inches) and fuel-slug OD 0.330 cm (0.130 inches). The steel in the control and safety rods (clad, wire-wraps and hexcans) was assumed to be 316 stainless steel. These control-rods are the rods currently being used in EBR-II. The safety-rods are located in row 3 and the control-rods are located in row 5.

6.2.2 Analysis

6.2.2.1 Six-Row Core Analysis

The criterion used to determine the enrichment for a six-row core, with HT9 clad U-20Pu-

10Zr fuel, is equality of system eigenvalue with an identical Mark-II U-5Fs-fueled or Mark-III U-10Zr fueled loading configuration. To eliminate burnup related effects on the determination of the enrichment, all calculations are based on fresh fuel in all fueled subassemblies in the six-row core region (except for the experimental subassembly XY-20). All subassemblies outside of row 6 (i.e. structural experiments in row 7, radial steel reflector subassemblies and the radial blanket subassemblies) were not changed.

Neutronic calculations were done for two different uranium enrichments given the six-row core configuration. The final uranium enrichment for the HT9 clad Mark-V fuel was chosen by linear interpolation such that the eigenvalue is equivalent to the Mark-II U-5Fs fueled eigenvalue. (This is the same methodology that was used to determine the enrichment of Mark-III fuel [see Ref. 6.56], thus the comparison results in enrichments which are consistent with the current Mark-III driver loading.) The enrichment estimation was done in both XY-geometry transport theory using S_4 angular quadrature and RZ diffusion theory. (The bucklings used in the XY analyses to model axial leakages were the standard bucklings used in EBR-II run-to-run calculations.) Using the transport theory XY eigenvalues gives a uranium enrichment of 0.449, whereas the diffusion theory RZ eigenvalues give a uranium enrichment of 0.478. Of the two estimated enrichments the 0.478 value is the more credible for two reasons: (1) RZ calculations model axial variations in geometry and isotopic mass better than a constant buckling value and (2) the bucklings that were used for the XY neutronics calculations were determined for an all-uranium system and therefore may not be applicable to a uranium/plutonium system. (More details of this analysis are discussed in Ref. 6.57.)

In the RZ diffusion theory six-row core calculations for the two different enrichment cases, an effective delayed neutron fraction (β) and prompt neutron lifetime (l_p) were calculated. Interpolating these values to an enrichment of 0.478 results in an effective delayed neutron fraction of 0.00526 and a prompt neutron lifetime of 2.6×10^{-7} seconds for the six-row core configuration. The effective delayed fraction for a uranium system (fueled with either Mark-II U-5Fs or Mark-III U-10Zr) is ~0.0070 and the prompt neutron lifetime is 2.6×10^{-7} seconds. Thus for an equal worth in terms of $\Delta k/k$, the U-20Pu-10Zr system worths in terms of dollars will be ~32% (.0070/.0053) larger. Currently the high-worth control-rods in EBR-II are worth 0.7-1.0$. If this 32% factor is applied to these rods they approach the EBR-II Technical Specification control-

rod worth limit ($1.30). In addition, because β will change during the core transition from a uranium-fueled system to a uranium/plutonium-fueled system, the control rod worths (in terms of dollars) may change significantly for a given loading.

In the fresh Mark-V U-20Pu-10Zr fuel there is a small amount of americium [6.54]. In these calculations the americium weight percent was assumed to be 0.0. This implies any americium was, by default, put into the uranium. If the americium weight is between 0 - 2% of the plutonium weight, then the amount of americium in the uranium/americium mixture is between 0.0 - 0.6%. This will have some effect on the calculated uranium enrichment. Using an estimated reactivity worth per atom, relative to ^{235}U, of 1.7 for ^{239}Pu and 0.33 for ^{241}Am, conservation of equivalent ^{235}U atoms with a system containing no americium leads to a uranium enrichment of 0.479 (from 0.478) if 2% of the Pu mass is americium.

^{239}Pu has a higher reactivity worth($\Delta k/k$) per atom than does ^{235}U. Therefore, less fissile mass is needed in a uranium/plutonium system to achieve the same eigenvalue as a corresponding uranium system (see Table 6-1). Since the macroscopic fission cross section (Σ_f) of the Mark-V fuel is lower than the Σ_f of the binary fuel, a higher flux is needed in the U/Pu system for the same power level. Calculations for the six-row core show that the total flux increases ~10-15% in the core regions (~15% at the core center to ~10% in row 6) and ~6-8% in the blanket region (rows 11-16). (The fast flux differences show the same trend but they are somewhat smaller in magnitude.) These higher fluxes mean higher total and fast fluences in some reactor components.

For example, shown in Table 6-2 is the percentage increase in fast flux (fresh Mark-V U-20Pu-10Zr fuel relative to fresh Mark-III U-10Zr fuel) for various non-core axial positions given the six-row core loading configuration. From the table it is seen that the fast flux in non-core regions will increase 8-15% depending on position. Higher fast fluxes (and hence fluences) imply that the onset of swelling, and the effects of swelling on structural components, will appear earlier. In addition, increased flux levels will also increase the ^{60}Co activity in the Stellite liner regions of the reactor cover. (These liners are used to line the control-rod penetrations through the reactor cover.)

The power is higher in the subassemblies that do not contain U-20Pu-10Zr fuel. The flux is increased in the system to maintain system power but the amount of fissile mass in the

control/safety and blanket subassemblies was left unchanged from the uranium (binary fueled) system values. This means higher powers in these regions when compared to what was calculated for the equivalent binary case. Calculations show that the subassembly power increased somewhat in the core center but decreased in the outer rows of the core. This power shift in U-20Pu-10Zr-fueled subassemblies from the outer rows to the inner rows is due to the relative flux peaking in the core inner rows. (Variations in subassembly power will also be seen in experimental subassemblies during and after the core transition to a U/Pu fueled loading.

Table 6-1 Eigenvalues and Core-Masses for a Fresh Mark-II U-5Fs-Fueled Loading, a Fresh Mark-III U-10Zr-Fueled Loading, and Two Fresh Mark-V U-20Pu-10Zr-Fueled Loadings in EBR-II

Identifier	Case	Keff		^{235}U Total Kg in Core	^{239}Pu Total Kg in Core
		XY	RZ		
EBRIFR02 ($\varepsilon = 0.67$)	U-5Fs Mark-II 316SS Clad Six-Row Core	1.087687	1.039893	220.8	0.01
EBRIFR04 ($\varepsilon = 0.67$)	U10Zr Mark-III D9 Clad Six-Row Core	1.099113	1.042854	219.5	0.01
IFRKNG06 ($\varepsilon = 0.48$)	U-20Pu-10Zr Mark-V HT-9 Clad Six-Row Core	1.104583	1.0407276	127.5	50.7
IFRKNG17 ($\varepsilon = 0.48$)	U-20Pu-10Zr Mark-V 316SS Clad Six-Plus-Row Core	1.147681	-	153.5	63.5

Significant power differences are seen in the control and safety rods plus the radial blanket. Calculations show that in the control and safety rods the relative power is larger by ~10% whereas in the blanket subassemblies the power is larger by 5-8%. This implies, given equivalent flow rates, these subassemblies will run hotter. This, coupled with the fact that plutonium will build-up faster, may result in a shorter blanket subassembly lifetime since the radial blanket reaches the EBR-II Technical Specification limit on outlet temperature (1140°F (616°C)) sooner. Higher flux values in the control and safety-rod subassemblies means that they will reach their Tech. Spec.

limits sooner, hence their effective lifetime will decrease.

Table 6-2 Fast Flux (> 0.111 MeV) Increases for Fresh Mark-V U-20Pu-10Zr Fuel (Relative to Fresh Mark-III U-10Zr Fuel) in Axial Regions of a Six-Row Core Loading Configuration

	Fast Flux Increase, %		
Row	Top-End Fixture[(a)]	Spades and Grids	Grid-Plate[(b)]
2	14	10	8
5	13	10	8
7	12	8	8

[(a)] estimated from values at 1.3 cm below the top of the upper reflector region

[(b)] estimated from values at the bottom of the lower reflector region

Technical Specification burnup limits have been established for all standard fuel types. For example, the current Technical Specification burnup limit for Mark-IIIA fuel is 10 atom percent whereas for control rods the burnup limit is 6.4 atom percent for certain types of rods (Mark-IIA, -IIC, and IICS) and 5.5 atom percent for another type of rod (Mark-IIS). Currently there are no fast fluence limits for fueled subassemblies. The Technical Specification burnup limit for U-10Zr fuel has been related to a hex-duct fast fluence limit for creep, swelling, and bowing effects. This relationship will change in a Mark-V core since the fast fluence per atom percent burnup ratio will increase by 5 to 7% for a Mark-V driver in a Mark-V core relative to the corresponding value for a Mark-IIIA driver in a Mark-IIIA core [6.58]. Thus, for the <u>same</u> driver burnup, a Mark-V driver in a Mark-V core will have a larger accumulated fast fluence (larger swelling and bowing) than a corresponding Mark-IIIA driver in a Mark-IIIA core. The same calculations utilized to estimate the fast fluence to burnup ratio for driver fuel were used to estimate the fluence to burnup ratio for identical U10Zr-fueled control rods and blanket subassemblies in each system. The calculations indicate that the fast fluence to burnup ratio for U-10Zr-fueled control rods in a Mark-V system is ~2% less than the fast fluence to burnup ratio for control rods in an identical Mark-IIIA system. For blanket subassemblies the fast fluence to burnup ratio will be ~5% lower in a Mark-V system when compared to an identical Mark-IIIA system. The change in the fast fluence to burnup ratio for the control rod and blanket subassemblies is due to a slight spectral softening when the core is converted from Mark-IIIA to Mark-V fuel. The slight reduction in fast fluence to burnup ratio calculated for control subassemblies should also apply to isolated Mark-IIIA driver subassemblies in a Mark-V dominated core. (The above results were

calculated for Mark-IIIA subassemblies. Similar results are expected for Mark-III subassemblies.)

A summary of significant thermal-hydraulic quantities is given in Table 6-3 for a six-row core. (The number of pins plus the dimensions for the clad OD, wire-wrap OD and hexcan are the same for the Mark-V type driver and partial-driver subassemblies as they are for the corresponding Mark-III U-10Zr-fueled subassemblies. Therefore, the flow coefficients for Mark-V subassemblies were taken to be the same values as those for the equivalent Mark-III subassembly.) From the table it is seen that there is a higher plenum-to-plenum pressure drop (more flow resistance) in both the six-row U-20Pu-10Zr-fueled and six-row U-10Zr-fueled system when compared to the six-row U-5Fs-fueled system. This results in a lower high-pressure-plenum flow rate. In each six-row system, the driver subassembly with the highest peak local coolant temperature is located in row 4. This parameter is monitored because there is a Technical Specification limit on peak coolant outlet temperature in the hottest driver subassembly (for Mark-III drivers the limit is 1040°F (560°C)). The peak outlet coolant temperature in the hottest driver in the six-row U-20Pu-10Zr-fueled loading configuration is between the corresponding temperature in the six-row Mark-II U-5Fs-fueled system and the six-row Mark-III U-10Zr-fueled system. Since these temperatures are within a few degrees, changes in loading pattern may re-arrange this order. What is worth noting however, is that there do not seem to be significant differences in <u>peak</u> local coolant temperature of the <u>hottest</u> driver subassembly among the six-row systems.

The peak coolant temperature in the hottest blanket subassembly in the U-20Pu-10Zr-fueled system will increase because the blanket power increase (5-10%) is more than the blanket flow increase (3-4%). This makes the hottest blanket peak coolant temperature closer to the Technical Specification limit of 1140°F (616°C). (These calculations used the proposed-run 141D blanket. Because of plutonium build-up, the proposed-run 156A blanket peak coolant temperature is 1069°F (576°C.) The control-rods and safety-rods will also run hotter than those for the Mark-III case because of their increased power. As with the subassembly power, temperatures in control-rods, safety-rods, blanket subassemblies, and experimental subassemblies will be a function of core loading during the transition to a U-20Pu-10Zr configuration.

Table 6-3 Thermal-Hydraulic Quantities for a Fresh Mark-II U-5Fs-Fueled Loading, a Fresh Mark-III U-10Zr-Fueled Loading, and Two Fresh Mark-V U-20Pu-10Zr-Fueled Loadings in EBR-II

Item	U-5Fs (ε = 0.67) Mark-II 316SS Clad Six-Row Core	U10Zr (ε=0.67) Mark-III D9 Clad Six-Row Core	U-20-Pu10-Zr (ε = 0.48) Mark-V HT9 Clad Six-Row Core	U-20Pu-10Zr (ε = 0.48) Mark-VA Six-Plus-Row Core
Flow in High Pressure Plenum Subassemblies	7417.2 gpm (0.468 m^3/s	7363.5 gpm (0.465 m^3/s)	7363.6 gpm (0.465 m^3/s)	7420.1 gpm (0.468 m^3/s)
Plenum-to-Plenum Pressure Drop	40.7 psi (0.28MPa)	44.0 psi (0.30 MPa)	44.0 psi (0.30 MPa)	40.5 psi (0.28 MPa)
Peak Coolant Temperature in Hottest Normal-Flow Driver+	997.5°F (4E2)* (536.4°C)	1005.5°F (4E2) (540.8°C)	1001.4°F (4E2) (538.6°C)	1003.4°F (5A4) (539.7°C)
Coolant Flow Rate in Hottest Normal-Flow Driver	94.7 gpm (5.97 x 10^{-3} m^3/s)	93.2 gpm (5.88 x 10^{-3} m^3/s)	93.2 gpm (5.88 x 10^{-3} m^3/s)	75.3 gpm (4.75 x 10^{-3} m^3/s)
Peak Coolant Temperature in the Hottest High-Flow Driver+	1001.6°F (6E3) (538.7°C)	994.9°F (6E3) (534.9°C)	983.1°F (6E3) (528.4°C)	851.7°F (6A4) (455.4°C)
Coolant Flow Rate in Hottest High-Flow Driver	74.3 gpm (4.69 x 10^{-3} m^3/s)	76.0 gpm (4.79 x 10^{-3} m^3/s)	76.0 gpm (4.79 x 10^{-3} m^3/s)	72.8 gpm (4.59 x 10^{-3} m^3/s)
Outlet Temperature in Hottest Safety-rod	867.7°F (3A1) (464.3°C)	856.5°F (3A1) (458.1 °C)	878.0°F (3A1) (470.0°C)	851.7°F (3A1) (455.4°C)
Coolant Flow Rate in Hottest Safety-rod	94.6 gpm (5.97 x 10^{-3} m^3/s)	98.7 gpm (6.23 x 10^{-3} m^3/s)	98.6 gpm (6.22 x 10^{-3} m^3/s)	94.4 gpm (5.96 x 10^{-3} m^3/s)
Outlet Temperature in Hottest Control-rod	919.4°F (5E3) (493.0°C)	903.8°F (5E3) (484.3°C)	931.0°F (5E3) (499.4°C)	906.0°F (5B3) (485.6°C)
Coolant Flow Rate in Hottest Control-rod	61.6 gpm (3.89 x 10^{-3} m^3/s)	64.2 gpm (4.05 x 10^{-3} m^3/s)	64.2 gpm (4.05 x 10^{-3} m^3/s)	61.5 gpm (3.88 x 10^{-3} m^3/s)
Flow in Low Pressure Plenum Subassemblies	1462.8 gpm (0.0923 m^3/s)	1516.5 gpm (0.0957 m^3/s)	1516.4 gpm (0.0957 m^3/s)	1459.9 gpm (0.0921 m^3/s)
Outer Blanket Region Pressure Drop	11.4 psi (0.079 MPa)	12.2 psi (0.084 MPa)	12.2 psi (0.084 MPa)	11.4 psi (0.079 MPa)
Peak Coolant Temperature in Hottest Blanket++	1005.2°F (11F10) (540.7°C)	994.7°F (11F10) (534.8°C)	1016.9°F (11F10) (547.2°C)	1016.5°F (11F10) (546.9°C)
Coolant Flow Rate in Hottest Blanket	3.2 gpm (2.02 x 10^{-4} m^3/s)	3.3 gpm (2.08 x 10^{-4} m^3/s)	3.3 gpm (2.08 x 10^{-4} m^3/s)	3.2 gpm (2.02 x 10^{-4} m^3/s)

*Reactor Position

+Peak Coolant Temperature = 700 + Average Coolant Temperature Increase/0.794°F = 371 + Average Coolant Temperature Increase/0.794 °C

++Peak Coolant Temperature = 700 + Average Coolant Temperature Increase +60 °F = 371 + Average Coolant Temperature Increase + 33.3 °C

6.2.2.2 Six-Plus-Row Core Analysis

Calculations were also done for a loading configuration where the pins in the fueled driver and partial-driver subassemblies were modeled using the 15-mil (0.038 cm) 316SS clad U-20Pu-10Zr fuel mentioned above. This fuel would use the 316SS cladding that is currently available at EBR-II. This loading configuration, shown in Figure 6-2 and described above as the six-plus-row core model, is more representative of current sized EBR-II loadings. Note that there are two low-worth structural subassemblies in row 2. This was done to partially compensate for the added fissile mass in the core. (The control and safety rods were unchanged from both the six-row HT9 and Mark-III loading configuration calculations.) The uranium enrichment, however, was kept at 48%. Eigenvalues, core-masses, and significant thermal quantities are shown, respectively, in Table 6-1 and Table 6-3 for this loading configuration. From the eigenvalues in Table 6-1 it is seen that this fresh-fueled loading configuration will have more excess reactivity than the six-row fresh-fueled configuration. From Table 6-3 it is seen that the hottest driver and hottest high-flow driver peak outlet coolant temperatures, while not occurring at the same subassembly location as in the six-row core configuration, are relatively unchanged from the hottest peak coolant outlet temperatures in the six-row system.

Shown in Table 6-4 are average powers and flows (plus related ratios) for various subassembly types given the ternary-fueled six-row loading configuration and the ternary-fueled six-plus-row loading configuration. The results show that while flow rates are reduced uniformly (4%), powers are reduced more in the inner rows than in the outer rows. (Both power and flow per subassembly are reduced in the six-plus-row loading configuration because there are more driver subassemblies in that configuration and <u>all</u> results, independent of loading, are normalized to a system power of 62.5 MWt and a system flow rate of 9340 gpm (0.59 m^3/s) at the primary pumps.) The average power decreases more than the flow decreases in the inner rows of the six-plus-row loading configuration. Therefore, coolant temperature increments will decrease in the inner rows. However, in the outer rows the coolant temperature increment may increase slightly because the power decrease is less than the flow decrease. When compared with the ternary-fueled six-row core configuration, the power decreases in the two safety-rods by an average of 19% (18% and 20%) and in the nine control-rods by an average of 12% (6-15%). (These values vary, especially in the control-rods, because of the surrounding subassembly compositions). In

addition, the outlet ΔT for the control and safety rods is smaller because the flow reduction (4%) is smaller than any of the power reductions.

Table 6-4 Driver, Safety Rod, and Control Rod Row-wise Average Power and Average Flow Rate (plus related ratio quantities) for a Mark-V U-20Pu-10Zr-Fueled Six-Row Core Loading with HT9 Cladding and a Six-Plus-Row Core Loading with 316SS Cladding (Safety and Control Rods are U-10Zr-Fueled with 316SS Cladding)

	Average Power (KW)		Power Ratio	Average Flow (gpm (10^{-3} m^3/s))		Flow Ratio	ΔT Ratio[a]
Row Item	IFR06[b]	IFR17[c]	IFR17/IFR06	IFR17	IFR17	IFR17/IFR06	IFR17/IFR06
1-Driver	-[d]	796	-	-	132.0 (8.33)	-	-
2-Driver	977	796	0.82	134.9	129.1 (8.14)	0.96	0.85
3-Driver	915	768	0.84	119.3	114.2 (7.20)	0.96	0.88
3-Safety	662	534	0.81	98.6	94.4 (5.96)	0.96	0.84
4-Driver	808	727	0.90	93.3	89.4 (5.64)	0.96	0.94
5-Driver	-	665	-	-	75.4 (4.76)	-	-
5-Control	521	459	0.88	64.2	61.5 (3.88)	0.96	0.92
6-Driver (Standard Flow)	558	553	0.99	67.8	65.0 (4.10)	0.96	1.03
6-Driver (High Flow)	615	600	0.98	76.0	72.8 (4.59)	0.96	1.02
7-Driver	-	538	-	-	65.4 (4.13)	-	-

[a] ΔT (Coolant Temperature Increment) Ratio = Power Ratio (IFR17/IFR06)/Flow Ratio (IFR17/IFR06)
[b] Drivers U-20Pu-10Zr (Enrichment = 48%), 18-mil (0.046 cm) HT9 clad, six-row core loading configuration
[c] Drivers U-20Pu-10Zr (Enrichment = 48%), 15-mil (0.038 cm) 316SS clad, six-plus-row core loading configuration
[d] The six-row loading configuration did not have driver subassemblies in rows 1, 5, and 7

6.3 Reactivity Feedbacks

Calculational comparisons of detailed reactivity feedback components in regions of a U-20Pu-10Zr-fueled (Mark-V) Experimental Breeder Reactor II (EBR-II) with the corresponding components of an analogous U-10Zr-fueled (Mark-III) and an analogous U-5Fs-fueled (Mark-II) EBR-II have been made. In these analyses the descriptions for the reactor are the same except for the fuel types, the fuel-cladding, and a thicker cladding with a concomitant smaller radial dimension for the U-20Pu-10Zr fuel. Rows 1 to 6 of the reactor description constitute the core, rows 7 to 10 the radial steel reflector, and rows 11 to about 16 the radial blanket of essentially depleted uranium. For each of these fuel types three sets of components were calculated. These correspond to: bond-sodium gap fully open; bond-sodium gap fully closed, the fuel not adhering to the clad, and no sodium in the fuel porosity; and bond-sodium gap fully closed, the fuel adhering

to the clad (such that the fuel axial expansion is that of the clad), and about one-third of the fuel porosity contains sodium.

Regional linear (and Doppler) components comprising the power reactivity decrement (PRD) and the corresponding temperature coefficients of reactivity were calculated [6.59, 6.60]. The PRD at a power is the negative of the reactivity that must be added to bring the reactor from zero power hot-critical to that power. The PRD components were also separately delineated into power-to-flow dependent and into solely power dependent parts, [6.61]. These delineations, together with the components of the temperature coefficients of reactivity, are also useful for indicating relative potential inherent safety characteristics, [6.61, 6.62].

The linear and Doppler components of the PRDs were calculated using the EBRPOCO program [6.44] together with an addition (RODCO) to the program which estimates the power-reactivity effects of axial positions of control rods. The corresponding components of the temperature coefficients of reactivity were calculated using the TEMCO addition [6.63] to the EBRPOCO code. These temperature coefficients correspond to average temperature coefficients between the coolant inlet temperature and the applicable positional temperature for the power and coolant flowrate of the reactor. The grid-plate radial-expansion component of the temperature coefficient and some aspects of the net rod-bank suspension component of the temperature coefficient, which are additional components of inlet-temperature coefficients, were calculated separately from the EBRPOCO and TEMCO programs. The former was derived from calculated differences in eigenvalues between a uniformly radially-expanded system and the corresponding reference system. The latter was calculated using the method described in Ref. 6.60 together with RODCO-calculated values of the reactivity change resulting from unit change in the core to rod-bank relative axial displacements at the assumed rod-bank position.

The reactivity feedback components of the PRD, the power-to-flow dependent components, the solely power dependent components, and the components of the temperature coefficients summed over various reactor regions are given in Table 6-5 for core loadings of fresh fuels having the sodium-bond-gaps fully open. The components are: coolant density (density reduction of sodium coolant due to temperature), coolant displacement (displacement of sodium coolant by thermal radial-expansions of cladding, structural rods, subassembly ducts, and lower

and upper axial-reflector regions), steel density (density reductions of these steel components due to axial expansions with temperature), bond sodium (resultant of displacement of bond sodium, by differential thermal expansions of fuel and cladding, and of density reduction of bond sodium due to temperature), fuel and blanket axial expansions, Doppler (in fuel and blanket), B_4C-fuel (change in separation of B_4C follower and fuel in the case of high-worth fueled control rods having B_4C followers), and rod-bank suspension (downward expansion of the control rods, relative to the core, because of overhead suspension). The grid-plate temperature coefficient of reactivity is that resulting from a uniform change in its temperature. It contributes to the overall inlet-temperature coefficient.

Table 6-5 Reactivity Feedback Components of Fresh U-20Pu-10Zr-, of Fresh U-10Zr- and of Fresh U-5Fs-Fueled EBR-II*

Case	Components	Coolant Density	Coolant Displ.	Steel Density	Bond Sodium	Fuel Axial Exp.	Dopp.	B_4C-Fuel	Rod Bank Susp.	Grid Plate	Sum
U-20Pu-10Zr-Fueled (Mark-V) ($\beta_{eff} \cong 0.0053$)	PRD[a]	-92.3	-23.9	-21.2	-15.4	-86.4	-6.9	+ 1.2	-57.3	-	-302.2
	P/Q[b]	-92.3	-17.7	-14.7	- 6.5	-24.5	-3.5	+ 1.2	-56.6	-	-214.5
	P[c]	0.0	- 6.2	- 6.5	- 8.9	-61.9	-3.4	0.0	- 0.7	-	- 87.7
	TC[d]	-0.933	-0.189	-0.200	- 0.079	- 0.251	-0.031	+0.009	- 0.018	-0.964	- 2.65
U-10Zr-Fueled (Mark-III) ($\beta_{eff} \cong 0.0070$)	PRD	-93.3	-30.2	-23.3	-14.5	-59.9	-5.1	+ 1.2	-56.0	-	-281.1
	P/Q	-93.3	-22.6	-16.4	- 6.2	-19.1	-2.9	+ 1.2	-55.3	-	-214.6
	P	0.0	-7.6	- 6.9	- 8.3	-40.8	-2.2	0.0	- 0.7	-	- 66.5
	TC	-0.953	-0.224	-0.211	- 0.073	- 0.189	-0.027	+0.011	- 0.018	-0.887	- 2.58
U-5Fs-Fueled (Mark-II) ($\beta_{eff} \cong 0.0069$)	PRD	-102.0	-27.3	-24.3	-11.3	-56.8	-4.3	+1.2	-53.2	-	-277.9
	P/Q	-102.0	-20.8	-17.5	-5.4	-20.5	-3.0	+1.2	-52.6	-	-220.6
	P	0.0	-6.5	-6.8	-5.9	-36.3	-1.3	0.0	-0.6	-	-57.3
	TC	-1.02	-0.212	-0.215	-0.065	-0.231	-0.027	+0.010	-0.017	-0.885	- 2.66

*62.5 MWt. power, coolant flow rate of 9340 gpm (0.59 m^3/s at the pumps, and fresh fuels
[a] Power reactivity decrement, units of 10^{-5} $\Delta k/k$
[b] Power-to-flow component, units of 10^{-5} $\Delta k/k$
[c] Power component, units of 10^{-5} $\Delta k/k$
[d] Temperature coefficient of reactivity, units of 10^{-5} $\Delta k/k$ per °F. Multiply by 1.8 for units of 10^{-5} $\Delta k/k$ per °C.

The ratios of the sums of the components of the quantities designated by PRD, P/Q, P, and TC for the U-20Pu-10Zr-fueled loading relative to the U-10Zr-fueled loading are about 1.1, 1.0, 1.3, and 1.0, respectively. The larger ratio for the P-quantity is because of the larger fuel-axial-expansion reactivity component. This relatively larger component results primarily from a larger average temperature of the fuel and from a larger average temperature coefficient of expansion of the fuel because of its larger fuel temperature. The larger fuel temperature is due to the smaller thermal conductivity of the U-20Pu-10Zr fuel.

The ratios of the sums of the components of the quantities designated by PRD, P/Q, P, and TC for the U-10Zr-fueled loading relative to the U-5Fs-fueled loading are about 1.0, 1.0, 1.2, and 1.0, respectively. The larger ratio for the P-quantity is because of the larger fuel-axial-expansion reactivity component and because of the larger bond-sodium reactivity component. These relatively larger components result from the larger average temperature of the fuel and the concomitant larger sodium-bond temperature which are caused by the larger diameter Mark-III fuel pins having 61 pins per subassembly (as has also the Mark-V fuel) compared to the smaller diameter Mark-II fuel pins having 91 pins per subassembly.

Divisions of the sums of the components of listed PRD, P/Q, and P values, respectively, by the power of 62.5 MWt give the integral coefficients of power while holding flow and inlet temperature fixed (A+B), of power-to-flow while holding power and inlet temperature fixed (B), and of power while holding power-to-flow and inlet temperature fixed (A). These, together with the sums of the temperature coefficient components (C), are given in Table 6-6. These integral coefficients enable the reactivity change $\Delta\rho$ due to a power increment ΔP, a power-to-flow increment $\Delta(P/Q^*)$, and a change ΔT_i in inlet temperature to be approximated by $\Delta\rho \cong A\Delta P+B\Delta(P/Q^*)+C\Delta T_i$, where Q^* is the fraction of the reference flow. Listed also are corresponding quantities of interest in loss-of-flow-without-scram (LOFWS) and loss-of-heat-sink-without-scram (LOHSWS) situations assuming these loadings. Although such unprotected transients are not within the scope of the required safety evaluations, the differences in response between ternary- and binary-fueled cores are of interest. For LOFWS the quantity A/B is significant because the ratio of the final coolant temperature increment through the system at equilibrium conditions can, for purposes of these intercomparisons, be approximated by: $\Delta T_f/\Delta T_o \cong 1+A/B$, where ΔT_f and ΔT_o are the final and initial coolant temperature increments

across the system. For LOHSWS, the quantity (A+B)/C is significant because the increase in coolant inlet-temperature required so that the negative reactivity will compensate for the otherwise positive reactivity resulting from the return of the PRD due to the power decrease to zero can be approximated by ΔT_i = (A+B) P/C. (Non-inclusion of a subassembly bowing component in B should not significantly affect the LOFWS quantities. Non-inclusion of a subassembly-bowing component in B, however, most likely would cause the listed inlet coolant temperature increases, ΔT_i, to be too large because in EBR-II the bowing component of the PRD is usually positive.) The quantity φ_o (see footnote e. of Table 6-6) is significant because it is an indicator of the relative peak temperature overshoot in LOFWS situations in that if φ_o is smaller, the relative overshoot is larger and vice-versa.

Table 6-6 Power, Power-to-Flow, and Inlet-Temperature Integral Coefficients and Pertinent LOFWS and LOHSWS Quantities

Case	Coefficient Or Quantity	Open-Gap	Closed-Gap Fuel-Free	Closed-Gap Fuel-Restr. Na in 1/3 Pores
U-20Pu-10Zr-Fueled ($\beta_{eff} \cong 0.0053$)	(A+B)[a]	-4.84 (-0.91)	-5.87(-1.11)	-3.80(-0.72)
	B[a]	-3.44(-0.65)	-3.59(-0.68)	-3.38(-0.64)
	A[a]	-1.40(-0.26)	-2.28(-0.43)	-0.42(-0.08)
	C[b]	-2.65(-0.50)	-2.73(-0.52)	-2.55(-0.48)
	$(\Delta T_f/\Delta T_o)$[c]	1.41	1.64	1.12
	ΔT_i[d]	114(63)	134(74)	93(52)
	φ_o[e]	0.45	0.63	0.28
U-10Zr-Fueled ($\beta_{eff} \cong 0.0070$)	(A+B)	-4.50(-0.64)	-4.77(-0.68)	-4.01(-0.57)
	B	-3.44(-0.49)	-3.60(-0.51)	-3.55(-0.51)
	A	-1.06(-0.15)	-1.17(-0.17)	-0.46(-0.06)
	C	-2.58(-0.37)	-2.58(-0.37)	-2.58(-0.37)
	$(\Delta T_f/\Delta T_o)$	1.31	1.33	1.13
	ΔT_i	109(61)	116(64)	97(54)
	φ_o	0.29	0.32	0.23
U-5Fs Fueled ($\beta_{eff} \cong 0.0070$)	(A+B)	-4.45(-0.64)	-4.75(-0.69)	-3.97(-0.58)
	B	-3.53(-0.51)	-3.66(-0.53)	-3.59(-0.52)
	A	-0.92(-0.13)	-1.09(-0.16)	-0.38(-0.06)
	C	-2.66(-0.39)	-2.68(-0.39)	-2.62(-0.38)
	$(\Delta T_f/\Delta T_o)$	1.26	1.30	1.11
	ΔT_i	105(58)	111(62)	95(53)
	φ_o	0.28	0.31	0.22

[a]Units of 10^{-5} $\Delta k/k$ per MWt (Units of cents per MWt)
[b]Units of 10^{-5} $\Delta k/k$ per °F (Units of cents per °F). Multiply by 1.8 for units of 10^{-5} $\Delta k/k$ per °C (units of cents per °C).
[c]$\Delta T_f/\Delta T_o = 1 + (A/B)$.
[d]ΔT_i = (A+B)P/C in °F (in °C), P = 62.5 MWt.
[e] $\varphi_o = (-\lambda\tau/\beta_{eff})[(A+B)^2/B]P$ in \$, $\lambda = 0.08\ s^{-1}$ and $\tau = 7$ s

Thus, for situations having fuels not adhering to clads, the U-20Pu-10Zr case has relatively larger $\Delta T_f/\Delta T_o$ (in LOFWS) and ΔT_i (in LOHSWS) values; but for this case, the relative values of φ_o, indicate less peak temperature overshoot in LOFWS. For situations having fuels adhering to clads, however, the respective values of these quantities are essentially the same for the three fuel types.

6.4 Depletion Characteristics

Depletion calculations for generic EBR-II cores have been performed [6.64] to investigate the differences in the burnup reactivity swing between the Mark-III binary-fueled and Mark-V ternary-fueled cores. Because ^{239}Pu is more reactive than ^{235}U in EBR-II (which is a burner and not a breeder core), the Mark-V fuel will have a larger δk swing due to burnup. This is demonstrated in the depletion results given in Table 6-7, which represent REBUS-3 equilibrium calculations for generic (one-sixth core, hex-Z) models of EBR-II (see Figure 6-3). The generic model has been selected to approximate the configuration of Ref. 6.50, i.e., the core occupies Rows 1-7 (only half of the Row 7 positions contain fuel) and includes 85 driver S/A's, 12 CR's, 12 SST dummy S/A's and 18 (Row 7) SST reflector S/A's. The burn cycle is 100.0 days and the residence time is 4 cycles for the drivers in Rows 1-5 and 6 cycles for the drivers in Rows 6 and 7.

The various cases shown in Table 6-7 are as follows. Case 1 is simply the static eigenvalue calculation (RZ Diffusion Theory) of Ref. 6.50 for the fresh Mark-V (U-20Pu-10Zr) core. The comparison between the binary- and ternary-fueled cores is made in Cases 2 and 3, respectively. Case 2 utilizes binary U-10Zr fuel (Mark-IIIA with 15 mil (0.038 cm) 316SS clad) in all driver positions. Case 3, which is the reference calculation for the other ternary-fueled cases, utilizes ternary U-20Pu-10Zr fuel (Mark-V with 18 mil (0.046 cm) HT9 clad). The uranium enrichment is taken to be the same as Case 1, i.e., ^{235}U/U = 0.478, and the Pu isotopic weight fractions (239/240/241/242) are 0.805/0.175/0.015/0.005. Cases 4 through 8 are each simple variations from the reference Mark-V case. Case 4 is identical (to Case 3) except the ^{235}U enrichment is increased by 1.0 w/o, to study the sensitivity of eigenvalue to U enrichment (for comparison with previous Mark-V study). Case 5 includes "dirty" plutonium, i.e., higher weight fraction of ^{241}Pu, and Cases 6 and 7 add 1.5 w/o ^{241}Am. (In Cases 6 and 7, the Pu fraction in the

fuel is maintained at 20 w/o, with the ^{241}Am replacing uranium in the former and replacing ^{241}Pu in the latter.) Case 8 represents a Mark-VA core, substituting 15 mil (0.038 cm) 316SS clad while maintaining the fuel composition and density.

Table 6-7 REBUS-3 Depletion Calculations for Generic EBR-II Models

Case	**Fuel (Clad)**	**Fresh Core**	**Equilibrium Core**		
U w/o: 234/235/236/238 Pu w/o: 239/240/241/242		**k_{eff} (BOC)**	**k_{eff} (BOC)**	**k_{eff} (EOC)**	**δk (Burnup)**
1. Mark-V U w/o: Pu w/o:	U-20Pu-10Zr (.018HT9) 0.0/47.8/0.0/52.2 81.0/18.0/1.0/0.0	1.0399 (RZ Diffusion Theory)			
2. Mark-IIIA U w/o: Pu w/o:	U-10Zr (.015 SS316) 0.5/66.9/0.5/32.1 none	1.0410	1.0185	1.0052	0.0134
3. Mark-V U w/o: Pu w/o:	U-20Pu-10Zr (.018 HT9) 0.5/47.8/0.5/51.2 80.5/17.5/1.5/0.5	1.0397	1.0107	0.9935	0.0172
4. Mark-V U w/o: Pu w/o:	U-20Pu-10Zr (.018 HT9) 0.5/48.8/0.5/50.2 80.5/17.5/1.5/0.5	1.0452	1.0163	0.9992	0.0171
5. Mark-V U w/o: Pu w/o:	U-20Pu-10Zr (.018 HT9) 0.5/47.8/0.5/51.2 80.0/15.0/4.5/0.5	1.0449	1.0156	0.9983	0.0174
6. Mark-V U w/o: Pu w/o:	U-20Pu-10Zr (.018 HT9) 0.5/47.8/0.5/51.2 (1.5 ^{241}Am) 80.0/15.0/4.5/0.5	1.0444	1.0152	0.9978	0.0173
7. Mark-V U w/o: Pu w/o:	U-20Pu-10Zr (.018 HT9) 0.5/47.8/0.5/51.2 80.0/15.0/3.0/0.5 (1.5 ^{241}Am)	1.0436	1.0145	0.9972	0.0173
8. Mark-"VA" U w/o: Pu w/o:	U-20Pu-10Zr (.015 SST) 0.5/47.8/0.5/51.2 80.5/17.5/1.5/0.5	1.0749	1.0471	1.0306	0.0165

As shown in Table 6-7, the calculated eigenvalues for a fresh core for Cases 1, 2, and 3 are all extremely close (k_{eff} ~ 1.04). Furthermore, the burnup reactivity swing is ~28% greater for the equilibrium Mark-V core (for all cases) relative to the Mark-III core (Case 2). This "additional" reactivity loss, -(0.0172 - 0.0134) δk or -0.38% δk, may be thought of in terms of additional ^{235}U enrichment required to achieve a 100-day burn cycle. The sensitivity of eigenvalue to ^{235}U enrichment (from Case 3 vs. Case 4) is 0.5424% δk /% ^{235}U, which is in good agreement with the value (0.5430) derived in Ref. 6.50. Therefore, the greater burnup reactivity

swing may be converted to an additional ^{235}U enrichment requirement of 0.70 w/o.

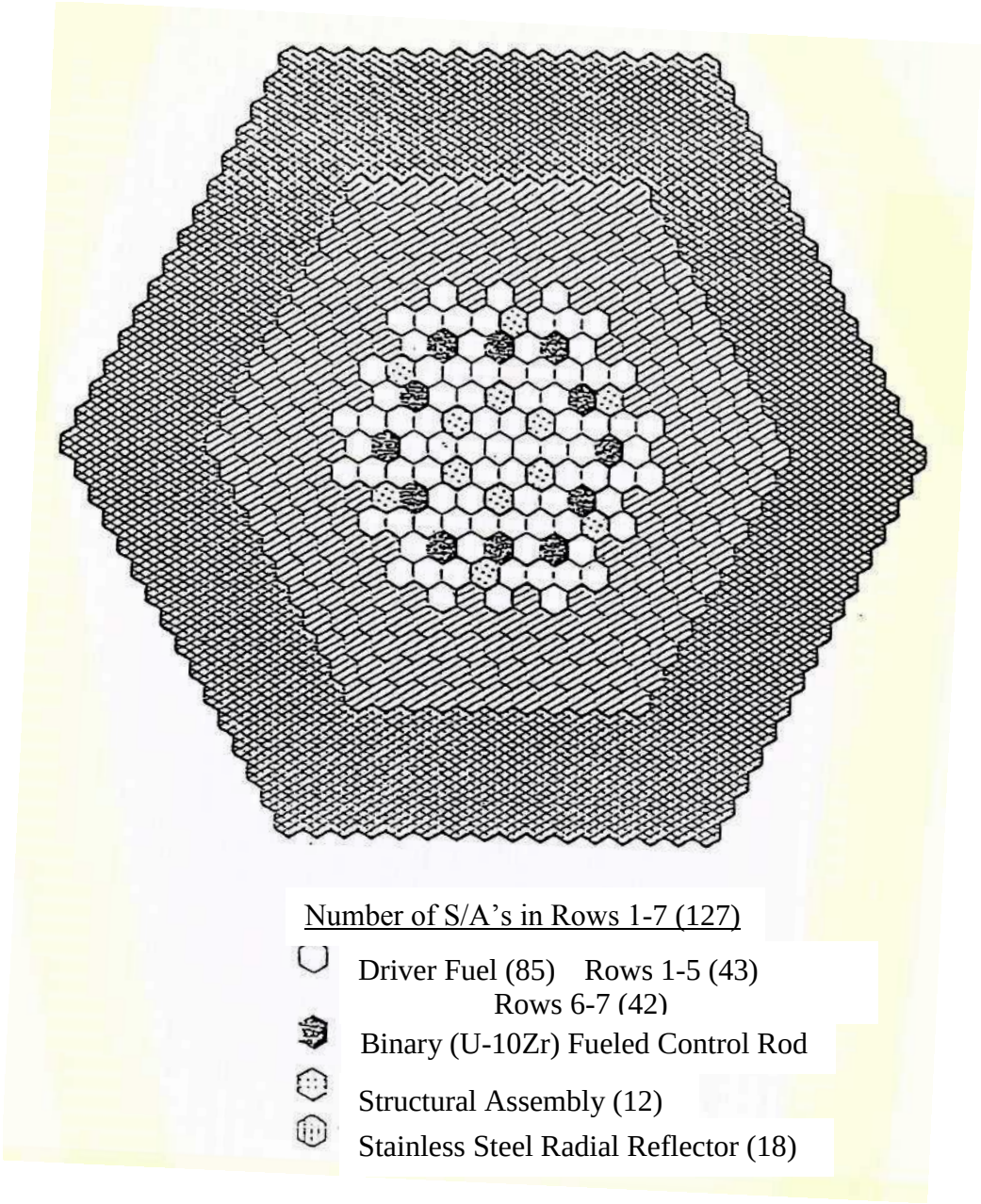

Figure 6-3 EBR-II Generic Mark-V Design, U-20Pu-10Zr, HT9, 62.5 MWt

The results for Case 5 illustrate the greater reactivity worth of ^{241}Pu (relative to ^{239}Pu and ^{240}Pu). The eigenvalues for Case 5 are each ~0.50 % δk higher (than Case 3). Again, this may be viewed as reducing the ^{235}U enrichment requirement by ~0.9 w/o. The reactivity effect of including 1.5 w/o ^{241}Am, replacing either U feedstock or ^{241}Pu (Cases 6 and 7, respectively) are

very small. That is, the eigenvalues are each ~0.5 % δk higher than Case 3 and are, respectively, 0.05 % δk and 0.15 % δk lower than Case 5. It may be noted that Ref. 6.50 projected that the effect of replacing 2% of the uranium with ^{241}Am would require increasing the ^{235}U weight fraction from 0.478 to 0.479. This is analogous to Case 6 in which 1.5 w/o ^{241}Am reduces the eigenvalue by 0.0005, that is, 2 w/o ^{241}Am would require a ^{235}U enrichment of [0.478 + (2.0/1.5)(0.05/0.5424)(0.01)] = 0.4792.

The final case shown in Table 6-7 is for a Mark-VA six-plus-row core. The burnup reactivity swing is very similar to the Mark-V six-row cores; however, the higher fuel volume fraction for the Mark-VA six-plus-row core yields much higher (~3.5 % δk) eigenvalues. Two additional Mark-VA configurations have been analyzed to calculate the "edge" worth of Mark-VA driver subassemblies. In each case, the core contains successively six fewer driver subassemblies (i.e., 1 driver is removed from the one-sixth core model). In the first case, the model shown in Figure 6-1 has the six Row 6 SST dummy subassemblies replaced with Mark-VA drivers and has twelve "corner" Row 7 Mark-VA drivers replaced with SST reflector subassemblies (i.e., only six driver subassemblies remain in Row 7 and they are located at the center of each "flat"). The effect of moving six drivers inward and removing six drivers from the edge was to lower the eigenvalue by ~0.7% δk. In the second case, the six remaining Row 7 Mark-VA driver subassemblies are replaced with SST reflectors and the eigenvalue is reduced an additional 2.1% δk. The eigenvalue for the fresh core is 1.0486, which is comparable to the Mark-V six-row core values.

The results of another series of equilibrium depletion calculations are given in Table 6-8. The cases in Table 6-8 reflect addition of various trace amounts of cadmium to the fuel. (It is postulated that trace amounts of cadmium might remain in the fuel after the electro-refining process.) The reference for these cases is the same reference U-20Pu-10Zr Mark-V model given in Table 6-7 (Case 3). In successive calculations, cadmium was added to the fuel at levels of 50, 100, 500, 1000 and 10000 ppm. The impact on reactivity (or enrichment requirements) is truly negligible for these levels. Note the edit of eigenvalues shown in Table 6-8 must display 6 decimal places in order that the differences for all but the largest cadmium addition (1 w/o) even appear. The small reactivity effect (about -0.0005 δk/100 ppm Cd) is extremely linear over the range of values calculated.

Table 6-8 Effect of Cadmium Addition to U-20Pu-10Zr Mark-V Fuel

Case	ppm Cd	Fresh Core k_{eff} (BOC)	Equilibrium Core		δk (Rel. to 100 ppm Cd)
			k_{eff} (BOC)	k_{eff} (EOC)	
1.	0	1.039726	1.010730	0.993499	----
2.	50	1.039723	1.010727	0.993499	2×10^{-6}
3.	100	1.039721	1.010725	0.993497	4×10^{-6}
4.	500	1.039702	1.010705	0.993475	24×10^{-6}
5.	1000	1.039678	1.010679	0.993448	50×10^{-6}
6.	10000	1.039250	1.010219	0.992962	508×10^{-6}

Finally, one set of depletion calculations has been used to study the "eventual" or long-term buildup/depletion of higher actinides for FCF. This was approximated by running a series of ten equilibrium REBUS-3 calculations, where the initial feed for the first calculation is the standard U-20Pu-10Zr Mark V fuel (E=0.478) with 3 w/o ^{241}Pu and 1.5 w/o ^{241}Am (Case 7 of Table 6-7). The feed to each subsequent equilibrium calculation is the discharged heavy metal (i.e., fission products are removed) from the previous calculation[****]. In principle, the time frame for each of the ten equilibrium calculations corresponds to an EBR-II "lifetime". Therefore, the series of calculations conservatively spans the buildup of isotopes discharged from EBR-II with recycle of the Mark-V ternary fuel. The calculated mass flows are summarized in Table 6-9. A comparison is made of the isotopic masses in the first and last (tenth) equilibrium cycles of the driver heavy metal inventory. Values are given (in grams) for a single (central) S/A at BOC and EOC, and (in kg) for the EOC reactor loading (i.e., isotopic masses of 85 driver subassemblies at various stages of burnup). These values indicate a small buildup of higher actinides and an increase (to ~54%) in the uranium enrichment (required because of the shift in isotopics of the plutonium).

[****]These calculations assumed the next fuel isotopic composition to be that from the previous discharge composition without any makeup material. Without any makeup material, these calculations show the most conservative buildup of higher actinides.

Table 6-9 Transmutation of Fuel in Equilibrium Cycle With and Without Recycle

Isotope	Without Recycle			With Recycle*		
	Fresh S/A, gm	Discharged (1A1) S/A, gm	Equilibrium Reactor Core EOC (85 S/A's), kg	Fresh S/A, gm	Discharged (1A1) S/A, gm	Equilibrium Reactor Core E0C (85 S/A's), kg
U^{234}	16.43	15.19	1.34	15.61	15.00	1.28
U^{235}	1570.46	1339.20	121.73	1722.82	1564.73	133.91
U^{236}	15.70	51.24	3.33	430.90	442.07	37.70
U^{238}	1682.21	1644.00	141.06	1035.94	1021.24	86.91
Np^{237}	--	1.47	6.8-2	53.97	57.82	4.92
Pu^{236}	--	5.4-6	1.6-7	6.3-4	7.6-4	5.8-5
Pu^{238}	--	0.43	2.1-2	17.63	18.51	1.61
Pu^{239}	765.72	660.48	59.94	564.60	514.82	44.19
Pu^{240}	143.58	142.80	12.32	313.79	302.50	25.92
Pu^{241}	28.72	25.15	2.27	38.72	37.05	3.18
Pu^{242}	4.78	5.16	0.43	18.30	18.17	1.55
Am^{241}	14.36	13.78	1.21	25.66	24.74	2.14
Am^{242m}	--	0.20	1.1-2	1.61	1.59	0.14
Am^{243}	--	8.6-2	5.0-3	2.10	2.17	0.19
Cm^{242}	--	0.35	2.1-2	0.65	0.70	5.4-2
Cm^{243}	--	1.8-3	9.4-5	3.0-2	3.0-2	2.6-3
Cm^{244}	--	2.1-3	1.1-4	0.37	0.40	3.5-2
Cm^{245}	--	2.6-5	1.2-6	3.3-2	3.7-2	3.2-3
Cm^{246}	--	9.2-8	4.1-9	1.2-3	1.4-3	1.2-4
BU (MWD/HT)	0.0	7.72+4	--	0.0	7.80+4	--
BU (a/o)	0.0	8.14	--	0.0	8.22	--

* These values represent fresh and discharged isotopic masses for the last of a series of ten equilibrium calculations with feed to each from discharged heavy metal from the preceding equilibrium calculation.

In addition to fuel burnup, another mechanism for core reactivity loss is related to burnup induced fuel axial growth: when the fuel grows axially, fissile material is shifted from higher worth central positions to lower worth axial positions, resulting in a net reactivity loss. Note that radial fuel growth has a negligible reactivity effect. The net loss of reactivity is proportional to the reactivity loss per unit length of fuel growth, and to the actual length of fuel growth. The reactivity loss per unit length of fuel growth can be easily calculated using the standard physics analysis models and tools used for the Mark-V core design. Calculations (for a row 1 subassembly) indicate that the reactivity loss per inch-growth (cents/inch) of a Mark-V subassembly in a Mark-V core will be ~56% larger than the corresponding value for a Mark-IIIA

subassembly in a Mark-IIIA core. Of this increase, ~20% is due to an increase in the reactivity loss rate in terms of δk and ≈30% results from the reduction in beta. The actual change in rod-length will be considerably smaller; the average fuel elongation for U-19Pu-10Zr is ~1/3 the value of U-10Zr fuel [6.65]. Thus it is estimated that, for a given burnup, the axial expansion reactivity loss (cents) for a Mark-V subassembly in a Mark-V core will be ~1/2 of the value of a corresponding Mark-IIIA subassembly in a Mark-IIIA core. This estimate is for a row 1 subassembly; for other rows the effect is expected to be similar. (The above results were calculated for Mark-IIIA subassemblies. Similar results are expected for Mark-III subassemblies.)

6.5 Surveillance of Core Neutronics Properties

6.5.1 Background

The core neutronics properties constitute one of the principal determinants of the safety of the ternary-fuel core. The temperature changes from steady state conditions to transient conditions are determined by metallurgical properties of the fuel and clad, and by thermal, hydraulic and neutronic design parameters. Given a postulated accident initiator, core properties determine the transient temperature and equilibrium temperature behavior.

The neutronic response to accident initiators will change as the core evolves from a binary-fuel to ternary-fuel loading. A core surveillance program has been developed to monitor and evaluate these changes, with the goal of assuring that the changes are known and that safety margins will not be violated.

The predicted neutronics changes were described in Sections 6.2 and 6.3. The fundamental quantities in which changes are important to safety margins are the effective delayed neutron fraction (β_{eff}) and the level and spatial distribution of the neutron flux. Of these quantities, only the flux level corresponding to a given power output can be observed in EBR-II. The inability to observe the others is not a problem because their importance derives from their impact on observable quantities that directly determine the neutronics response. Rod worths and feedback reactivity are the quantities of direct importance.

The increase in control rod worths is the most important change. Rod worths in dollars

are expected to increase about 32% due to the change in β_{eff} and perhaps as much as another 10% due to changes in the neutron flux distribution. This has a beneficial safety impact for accident scenarios where a scram occurs (protected), since there will be a more pronounced negative reactivity from the scram. The impact will be detrimental for unprotected rod run-in accidents, since there will be a larger insertion reactivity. This drawback is relatively unimportant for two reasons: 1) a scram failure is extremely unlikely ($\approx 10^{-6}$), and 2) only the worth increase independent of β_{eff} is relevant (see below).

The safety implications of the expected feedback reactivity changes are not as complex as the tables of data in Section 6.3 might suggest. First, although the breakdown into components in Table 6-5 provides insight into the origin of the changes, it is only the net reactivity that affects accident outcomes. Second, in Table 6-6 it is only the difference between U-20Pu-10Zr and U-10Zr fuels that is of direct interest. The U-5Fs results are just given to illustrate that, when expressed in $\Delta k/k$ units (in which normalization to β_{eff} is not done), many of the feedback coefficient changes expected to occur in going to ternary fuel are comparable to changes already experienced in going from U-5Fs to U-10Zr driver fuel. Third, the three columns of Table 6-6 are associated with fuel burnup states and it is primarily the last column that is of interest; the fuel behavior should change nearly uniformly from the first state (open-gap) to the second during the first 2 at. % burnup, and then the properties in the last column should apply until the fuel reaches the 10 at. % burnup limit. Finally, the effect of the change in β_{eff} depends on the accident behavior being considered; dynamic temperature peaks depend on reactivity in cents (and thus on differences in β_{eff}), while asymptotic temperatures in unprotected transients depend on ratios of reactivity coefficients (which are independent of β_{eff}).

With this perspective, the data in Table 6-6 imply the following behavior. The feedback coefficients in cents increase, generally by 20% to 40%. This tends to improve safety for protected transients because it retards the power rise before the scram takes effect. Peak temperatures in unprotected loss-of-flow and loss-of-normal-power events should also be reduced. Except for the power coefficient contribution from low burnup (<2 at. %) fuel, feedback coefficient ratios governing the asymptotic temperatures in unprotected transients change less than 10% and more often decrease than increase. The effects of the increased power coefficient magnitude and the potentially larger control rod worths on asymptotic temperatures in unprotected accidents could

be slightly adverse; this could be significant for transient overpower but not for loss of heat sink, loss of flow and loss of normal power - asymptotic temperatures for these are very far from safety limits. Overall, then, the feedback changes tend to have a beneficial effect on safety.

The situation for the dominant type of unprotected transient overpower event, rod run-in, is not as unfavorable as it might appear. According to quasi-static analysis, the peak temperature depends on the ratio of insertion reactivity to combinations of feedback coefficients. This means that most of the rod worth increase, the 32% due to the β_{eff} change, is not relevant; peak temperatures increase only to the extent that rod worth changes are greater than feedback coefficient changes.

6.5.2 Measurements

The considerations discussed in Sec. 6.5.1 guided the formulation of a core neutronics surveillance program [6.66]. The goal is to measure those reactor parameters that determine the global power behavior of the reactor in response to changes in reactor forcing functions. There are only three such functions: reactor inlet temperature, primary flowrate and control rod position. The reactor is safe if measurements of the parameters that determine reactor behavior as driven by these forcing functions fall within safe levels. The parameters, described below, will be measured at the start of reactor-power operation after changes in core loading.

On the approach to criticality during startup, the controlling rod actual position will be continually monitored and compared to the estimated critical position. This is a current EBR-II operating instructions requirement.

Once criticality has been achieved, the delayed-neutron parameters will be measured. Both the precursor relative yields (a_i) and the decay constants (λ_i) will be used later for rod worth determination. To measure delayed-neutron parameters, a rod will be dropped at zero power critical. Experiments performed in EBR-II have shown that about 20 cents is sufficient [6.67] and yields a set of values that differ by only a few percent from those calculated from knowledge of the core composition. Prior to the development of this technique, a calculated (a_i-λ_i) set was used in place of a measured set. A measured set reduces the likelihood of error that exists when generating calculated values.

Another benefit of a_i-λ_i measurements is that they will provide an indicator of how delayed neutron properties are changing as ternary fuel is introduced. The relative delayed neutron yield for precursor family i, a_i, is defined as

$$a_i = \beta_{eff}^i/\beta_{eff}, \text{ where } \beta_{eff} = \Sigma\beta_{eff}^i \ .$$

Thus an experimental determination of the a_i values provides information related to β_{eff}. The expected change as binary fuel is replaced with ternary fuel is smaller for the a_i than for β_{eff}, less than 10% compared to 32%.

Once values for the delayed-neutron parameters have been obtained, rod worths will be measured by perturbing rod positions at zero power critical. Inverse kinetics are used to determine the reactivity in cents associated with moving a rod a small amount. The reactor operating instructions already prescribe a procedure for doing this. Measuring rod worth allows monitoring of the change in rod worths as ternary fuel becomes the dominant driver fuel.

At this point, values have been obtained for those parameters that determine the response of the reactor to reactivity insertions when temperature effects are not present. If temperature effects are included, the quasi-static reactor response can be described by introducing the three reactivity feedback parameters, A, B and C given in the quasi-static reactivity balance

$$\rho = A(1 - P) + B(1 - P/W) + C\ \delta T_i,$$

where P is normalized reactor power, W is normalized coolant flow rate, δT_i is reactor inlet temperature change, and A, B, and C are the integral feedback coefficients discussed in Sec. 6.3. These parameter values will be measured by performing inlet temperature and primary flowrate changes and fitting the above equation to the power response of the reactor [6.68]. Except for the hypothesized event of a sudden core shift, producing a step change in reactivity, the quasi-static representation adequately describes reactor behavior during all transient scenarios that can develop, as discussed in [6.68].

The rate of reactivity loss will also be monitored, as currently required by the operating instructions. A deviation of the loss rate from the normal value would indicate anomalous reactivity behavior.

Determination of the prompt power coefficient of reactivity is required by the Technical Specifications if the average power coefficient is less than 85% of the previously measured value or if the average power coefficient is less than 0.25¢/MWt. Neither condition is expected to occur during the evolution to a ternary-fuel core; the average coefficient is expected to increase by about 30% and the smallest average coefficient ever measured for EBR-II was 66% larger than the 0.25¢/MWt limit. Thus while no measurement of the prompt coefficient to meet the Tech. Spec. requirement is anticipated, the coefficient will be evaluated every run, since it provides a measure of the prompt (fuel and cladding) temperature feedback which alone can serve to limit power in response to near-step insertion of reactivity.

Flux level measurements will be performed to provide an indication of how the neutron flux levels are changing as ternary fuel is introduced. The core average Σ_f will be lower by 15% in the ternary core and the power level is proportional to the integral of the neutron flux times Σ_f, hence the neutron flux level for a given power level is expected to rise by 15% in the driver region.

6.5.3 Analysis

Several of the parameters measured in of the core neutronics surveillance program are routinely calculated. In particular, calculated or predicted values are required for the reactivity effect of all loading changes, as well as estimated critical rod positions for all proposed EBR-II configurations. Several analysis methods can be used to predict substitution worths. They include first-order perturbation theory (through the use of reactivity worth tables) and eigenvalue difference calculations based on three-dimensional (hexagonal-Z) models with either DIF3D nodal diffusion theory or VIM continuous-energy Monte Carlo [6.69]. Several recent investigations of predictions of critical control rod position for EBR-II startups have concluded the three-dimensional nodal diffusion theory eigenvalue approach can be relied on with considerable confidence [6.70, 6.71]. During the transition to the Mark-V core and the equilibrium Mark-V core, various neutronic methodologies will be utilized to predict the reactivity behavior of the EBR-II reactor. In addition, the calculated values will be compared against the measured values per procedures.

6.6 Summary

In conclusion, two core loading configurations were considered in the physics analysis of U-20Pu-10Zr fuel: A six-row and a six-plus-row configuration. (The six-plus-row loading had 18 fueled subassemblies, out of a possible 36 subassemblies, in row 7.) These configurations reflect the range of loadings used in EBR-II operations. (The six-plus-row loading configuration is representative of current EBR-II loadings.) In the six-row core the structural material was assumed to be HT9, whereas in the six-plus-row loading the structural material was assumed to be 316SS. (Whereas structural material type, whether HT9 or 316SS, will affect the mechanical properties of a loading, it does not significantly affect the physics properties of a loading.) Irrespective of which loading configuration is considered, the two effects that standout when a ternary fueled loading is compared with the equivalent binary fueled loading are: (1) beta (the delayed neutron fraction) is smaller, and (2), the flux (both fast and total) is higher. The overall system beta is a weighted average of the betas of all the fissionable materials. Since beta for ^{239}Pu is smaller than the beta for ^{235}U, the system beta is smaller for a ternary fueled core relative to the beta for the equivalent binary fueled core. A smaller beta means control- and safety-rod worths in terms of dollars will increase (given equivalent rods), thereby possibly approaching the limit for EBR-II Technical Specification maximum rod worth. The flux is higher in a ternary fueled core because the higher worth of ^{239}Pu (relative to ^{235}U) leads to less fissile core mass (for the same eigenvalue); therefore the flux has to increase to maintain a given power level. Higher fluxes mean that there will be higher powers in binary-fueled control/safety-rods and in blanket regions. Higher fast fluxes also imply swelling effects will appear earlier in structural components. Therefore higher flux levels may have thermal and material implications on item (control/safety-rod, blanket, structural component, etc.) lifetime.

Depletion characteristics of the Mark-V core were also studied. The burnup reactivity swing was seen to be ~28% greater for the equilibrium Mark-V ternary core relative to the Mark-III binary core. The reactivity effect of 1.5 w/o ^{241}Am (replacing U or ^{241}Pu) in the Mark-V feedstock is very small. Addition of cadmium (up to 1 w/o) to the ternary Mark-V fuel has negligible reactivity effects. The burnup reactivity swing for the Mark-VA core is very similar to other ternary-fueled Mark-V cores. However, the higher fuel volume fraction raises the eigenvalue by ~3.5% δk, thereby requiring a reduction in the number of driver subassemblies.

The reactivity differences observed in these parametric depletion studies are small enough such that the current enrichment specifications are valid. The reactivity differences can be accounted for or adjusted by fuel management strategies. The buildup of higher actinides with recycle of the ternary Mark-V fuel is small.

When comparing the smaller core loading with the larger core loading configuration (given the same enrichment) it was seen that the peak coolant mixed-mean outlet temperature for the hottest driver subassemblies are similar. (The hottest driver in the larger core had a smaller power but the subassembly flow rate was also reduced.) In the larger core, the average driver power per subassembly was smaller (relative to the smaller configuration) in the inner rows: however, the average driver power per assembly was similar in the outer rows. Moreover, in the larger core loading configuration, the flux, and therefore the power, is reduced in the binary-fueled control/safety-rods and the blanket regions.

Finally, during the transition from a binary core to a ternary core beta and flux changes will be a function of the core loading configuration. Moreover, even if the loading configuration is constant for the transition (i.e., ternary-fueled drivers exchanged for a binary-fueled drivers in the same loading configuration), the powers and corresponding temperatures for a standard Mark-III U-10Zr-fueled and Mark-V U-20Pu-10Zr-fueled subassembly will be different depending on mass of each fuel-type present in the loading. (Initially, a ternary-fueled Mark-V subassembly in a binary-fueled Mark-III environment will be underpowered, whereas a binary-fueled Mark-III subassembly in a ternary-fueled Mark-V environment will be overpowered.)

As a result of these changes the feedback coefficients in cents will increase, generally by 20% to 40% in a complete ternary core. This tends to improve safety for protected transients because it retards the power rise before the scram takes effect. Peak temperatures in unprotected loss-of-flow and loss-of-normal-power events should also be reduced. Except for the power coefficient contribution from low burnup (<2 at. %) fuel, feedback coefficient ratios change less than 10% and more often decrease than increase. The effect on asymptotic temperatures in unprotected accidents (outside the scope of the safety analysis) could be slightly adverse; this could be significant for transient overpower but not for loss of heat sink, loss of flow and loss of normal power - asymptotic temperatures for these are very far from safety limits. Overall, then, the

feedback changes tend to have a beneficial effect on safety.

Section 6 References

6.1 D. Meneghetti, W. P. Keeney, R. O. Vosburgh, D. G. Stenstrum, K. E. Phillips, and J. M. Gasidlo, "Depleted-Uranium, Nickel, and Steel-Reflected EBR-II Critical Assemblies on ZPR-3--Experiments and Calculations," Trans. Am. Nucl. Soc. 13 (2), p. 733 (November 1970).

6.2 D. Meneghetti, W. P. Keeney, R. O. Vosburgh, G. G, Simons, D. G. Stenstrom, K. E. Phillips, and J. M. Gasidlo, "Experiments and Analyses of Heterogeneous Cores and Neutron Spectra in EBR-II Critical Assemblies on ZPR-3," Trans. Am. Nucl. Soc. 14 (1), p. 20 (June, 1971).

6.3 D. Meneghetti and D. G. Stenstrom, "Radial and Axial Reaction-rate Traverses for ZPR-3 Assembly 60," ANL-7688, 137 (April-May 1970).

6.4 D. Meneghetti, D. G. Stenstrom, and K. E. Phillips, "Radial and Axial Reactor Rate Traverses for ZPR-3 Assembly 61," ANL-7726, 73 (July 1970).

6.5 D. Meneghetti, D. G. Stenstrom, and K. E. Phillips, "Radial Reaction-Rate Traverses in ZPR-3 Assembly 62," ANL-7742, 87 (September 1970).

6.6 D. Meneghetti, K. E. Phillips, and D. G. Stenstrom, "Radial Reaction-Rate Traverses in ZPR-3 Assembly 62," ANL-7753, 89 (October 1970)

6.7 D. Meneghetti, K. E. Phillips, and D. G. Stenstrom, "Axial Reaction-Rate Traverses in ZPR-3 Assembly 62," ANL-7765, 48 (December 1970).

6.8 D. G. Stenstrom and D. Meneghetti, "Radial Reaction-Rate Traverses for ZPR-3 Assemblies 63B and 63C," ANL-7825, 1.70 (April-May 1971).

6.9 D. G. Stenstrom and D. Meneghetti, "Radial Reaction-Rate Traverses for ZPR-3 Assembly 63A," ANL-7833, 1.27 (June 1971).

6.10 D. G. Stenstrom and D. Meneghetti, "Radial Reaction-Rate Traverses for ZPR-3 Assembly 63B," ANL-7854, 1.23 (August 1971).

6.11 D. Meneghetti and K. E. Phillips, "Central Fission Ratios for ZPR-3 Assembly 62," ANL-7765, p. 48 (December 1970).

6.12 D. Meneghetti and K. E. Phillips, "Analysis of Spectrally Sensitive Foils in Depleted Uranium, Nickel, and Steel-reflected EBR-II Criticals," Trans. Am. Nucl. Soc. 15 (1), p. 539 (June 1972).

6.13 D. Meneghetti and W. B. Loewenstein, "EBR-II Physics Experience," Proc. of Int. Symp. on Physics of Fast Reactors, Vol. I, 175, Tokyo (October 1973).

6.14 D. Meneghetti and W. B. Loewenstein, "EBR-II Irradiation Physics," Topical Meeting on New Developments in Reactor Physics and Shielding, CONF-720901, Book 2, 105 (September 1972).

6.15 D. Meneghetti and K. E. Phillips, "Comparison of 29-group Calculated Spectra with Experimental Spectra in ZPR-3 Assembly 61," ANL-7753, 90 (October 1970).

6.16 D. G. Stenstrom, "Calculated Radial Gamma-deposition Profiles for ZPR-3 Assemblies 60, 61, and 62," ANL-RDP-8, 1.25 (August 1972).

6.17 D. G. Stenstrom and D. Meneghetti, "Axial Gamma - Deposition Profiles for ZPR-3 Assemblies 60, 61, and 62," ANL-7783, 46 (February 1971).

6.18 D. G. Stenstrom, D. Meneghetti, and K. E. Phillips, "Radial Gamma-Deposition Profiles for ZPR-3 Assembly 63A," ANL-7833, 1.28 (June 1971).

6.19 B. R. Sehgal and R. H. Rempert, "Analysis of Dosimetry Measurements in EBR-II," Nucl. Tech. 25 (2), pp. 390-405 (February 1975).

6.20 N. D. Dudey, D. Meneghetti, R. R. Heinrich, and R. H. Rempert, "Measurement and Calculation of Integral Heavy-element Cross-section Ratios in the Fast Breeder Reactor EBR-II," Nucl. Sci. Eng. 53 (1), pp. 9-26 (January 1974).

6.21 D. Meneghetti, E. R. Ebersole, and P. Walker, "Analysis of Burnups in EBR-II Driver-Fuel Elements," Nucl. Tech. 25 (2), pp. 406-415 (February 1975).

6.22 D. A. Kucera and D. Meneghetti, "Calculated Burnups and Fluences for Experimental Fuel Elements Irradiated in EBR-II Runs 5-55B," ANL-76-89, (October 1976).

6.23 D. Meneghetti, E. R. Ebersole, D. A. Kucera, and R. H. Rempert, "Analysis of Blanket-pin Burnups for Depleted-uranium-reflected EBR-II Configurations," Proc. 4th ASTM-EURATOM Symp. on Reactor Dosimetry, Gaithersubrg, MD, March 22-26, 1982, F.B.K. Kam, Ed., NUREG/CP-0029, Vol. 1, pp. 219-227 (July 1982).

6.24 F. C. Franklin, E. R. Ebersole, and R. R. Heinrich, "Analyses of EBR-II Low-Power Dosimetry Run 78C," ANL-77-76 (December 1977).

6.25 D. Meneghetti, E. R. Ebersole, and R. H. Rempert, "Analysis of EBR-II Blanket Dosimetry," Dosimetry Methods for Fuels, Cladding and Structural Materials, EUR 6813, Vol. 1, pp. 580-588, Commission of the European Communities, Luxembourg (1980).

6.26 F. R. Mynatt, "DOT, A Two-Dimensional Discrete-Ordinate Transport Code," K-1694, Radiation Shielding Information Center, Oak Ridge National Laboratory 1970.

6.27 D. Meneghetti and K. E. Phillips, Reactor Development Program Progress Report, ANL-7900, pp. 140-143, Argonne National Laboratory, December, 1971.

6.28 D. C. Cutforth, et. al., "BURNOUT - Software to Calculate Fuel Pin Depletion in the EBR-II Core," June 1991.

6.29 B. J. Toppel, H. J. Rago, and D. M. O'Shea, "MC^2, A Code to Calculate Multigroup Cross Sections," ANL-7318, Argonne National Laboratory, 1967.

6.30 W. E. Ford, III, and D. H. Wallace, "POPOP4, A Code for Converting Gamma-Ray Spectra to Secondary Gamma-Ray Production Cross Sections," CTC-12, Computer Technology Center, Oak Ridge National Laboratory 1969.

6.31 W. E. Ford, III, "The POPOP4 Library of Neutron-Induced Secondary Gamma-Ray Yield and Cross Section Data,"CTC-42, Computer Technology Center, Oak Ridge National Laboratory 1970.

6.32 J. R. Knight, and F. R. Mynatt, "MUG, A Program for Generating Multigroup Photon Cross Sections," CTC-17, Computer Technology Center, Oak Ridge National Laboratory 1970.

6.33 L. B. Miller, and R. E. Jarka, "The Distribution of Gamma Energy Deposition in a Fast Reactor," Trans. Am. Nucl. Soc. 13 (2), p. 831, November 1970.

6.34 Argonne National Laboratory, unpublished information (1990).

6.35 D. A. Kucera, Argonne National Laboratory, unpublished information (1977).

6.36 A. Gopalakrishnan, and J .L. Gillette, "EBRFLOW-A Computer Program for Predicting the Coolant Flow Distribution in the Experimental Breeder Reactor II," Nucl. Technol. 17(3), pp. 205-216, March 1973.

6.37 L. J. Koch, et al., Hazard Summary Report, Experimental Breeder Reactor II (EBR-II), ANL-5719, May 1957 (Appendix D, page 214-217).

6.38 "The Experimental Breeder Reactor-II Inherent Safety Demonstration," Nuclear Engineering and Design, Vol. 101, No. 1, April 1987.

6.39 D. Meneghetti, and D. A. Kucera, "Comparisons of PRD Components for Various EBR-II Configurations," Ann. Nucl. Energy, 14, No. 9, pp. 473-480, Sept. 1987.

6.40 D. Meneghetti, and D. A. Kucera, "Delineations of Power, Power-to-Flow and Inlet-Temperature Feedback Components of EBR-II," Ann. Nucl. Energy, 17, No. 1, pp. 19-26, Jan. 1990.

6.41 K. N. Grimm, and D. Meneghetti, "Time Constants and Feedback Transfer Functions of EBR-II Subassembly Types," Ann. Nucl. Energy, 14, No. 9, pp. 481-487, Sept. 1987.

6.42 D. Meneghetti, and D. A. Kucera, "Calculation of Temperature Coefficients of Reactivity for EBR-II Kinetic Analyses," Ann. Nucl. Energy, 14, No. 12, pp. 663-671, Dec. 1987.

6.43 F. S. Kirn, and W. B. Loewenstein, EBR-II Wet Critical Experiment, ANL-6864, October 1964.

6.44 D. Meneghetti, and D. A. Kucera, "EBRPOCO - A Program to Calculate Detailed Contributions of Power Reactivity Components in EBR-II," Proceedings of the International Topical Meeting on Advances in Mathematical Methods for the Solution of Nuclear Engineering Problems, Hilton International Munchen, April 27-29, 1981 (Vol. 2).

6.45 T. B. Fowler, and D. R. Vondy, "Nuclear Reactor Core Analysis Code: CITATION," ORNL-TM-2496, Oak Ridge National Laboratory, 1970.

6.46 H. A. Larson, Phyllis Walker, and D. Meneghetti, "EBR-II BURNUP AND FLUENCE HISTORY I, Part I: Method and Codes," ANL/EBR-084, Argonne National Laboratory, May 1974.

6.47 H. A. Larson, Phyllis Walker, J. E. Sullivan, K. E. Phillips, and D. Meneghetti, "EBR-II BURNUP AND FLUENCE HISTORY I, Part 2: Calculations," ANL/EBR-085, Argonne National Laboratory, May 1974.

6.48 R. D. McKnight, "Validation of the REBUS-3/RCT Methodologies for EBR-II Core-Follow Analysis," Proc. of Topical Meeting on Advances in Reactor Physics, Charleston, SC, March 8-11, 1992, Vol. 2, pp. 69-80 (1992); also Argonne National Laboratory Report ANL-IFR-153 (Sept. 1991).

6.49 R. Villarreal and M. T. Laug, Argonne National Laboratory, unpublished information (1987).

6.50 B. J. Toppel, "A User's Guide to the REBUS-3 Fuel Cycle Analysis Capability," Argonne National Laboratory Report ANL-83-2 (March 1983).

6.51 W. S. Yang, P. J. Finck, and H. Khalil, "Reconstruction of Pin Burnup Characteristics from Nodal Calculations in Hexagonal Geometry," Proc. of Intl. Conf. on the Physics of Reactors Operation, Design and Computation, Marseille, France, Vol. 2, VIII-22 (April 23-27, 1990).

6.52 R. D. Lawrence, "The DIF3D Nodal Neutronics Option for Two- and Three-Dimensional Diffusion Theory Calculations in Hexagonal Geometry," Argonne National Laboratory Report ANL-83-1 (March 1983).

6.53 K. E. Phillips, Argonne National Laboratory, unpublished information (1986).

6.54 H. P. Planchon, D. L. Porter and W. H. Perry, Argonne National Laboratory, unpublished information (1990).

6.55 B. R. Seidel, Argonne National Laboratory, unpublished information (1990).

6.56 D. Meneghetti and K. E. Phillips, Argonne National Laboratory, unpublished information (1986).

6.57 K. N. Grimm and K. E. Phillips, Argonne National Laboratory, unpublished information (1991).

6.58 K. N. Grimm, Argonne National Laboratory, unpublished information (1991).

6.59 D. Meneghetti and D. A. Kucera, Argonne National Laboratory, unpublished information (1991).

6.60 D. Meneghetti and D. A. Kucera, Argonne National Laboratory, unpublished information (1991).

6.61 D. Meneghetti and D. A. Kucera, Argonne National Laboratory, unpublished information.

6.62 H. P. Planchon, J. I. Sackett, G. H. Golden, and R. H. Sevy, Nucl. Eng. Des. 101, 75 (1987).

6.63 D. Meneghetti and D. A. Kucera, Ann. Nucl. Energy, Vol. 14, No. 12, 663 (1987).

6.64 R. D. McKnight, Argonne National Laboratory, unpublished information (1992).

6.65 G. L. Hofman, R. G. Pahl, C. E. Lahm, and D. L. Porter, "Swelling Behavior of U-Pu-Zr-Fuel," Metallurgical Transactions A, Volume 21A, pp. 517-528, March 1990.

6.66 R. B. Vilim, Argonne National Laboratory, unpublished information (1994).

6.67 R. W. Brock and R. B. Vilim, "Measurement of Delayed Neutron Relative Yields from a Rod Drop Flux Die-Away," ANL-IFR-216 (November 1993).

6.68 R. B. Vilim and S. E. Aumeier, "Assessment of Non-Obtrusive Methods for Verifying Demonstrably Safe Reactor Response," ANL-IFR-224 (February 1994).

6.69 R. N. Blomquist, R. M. Lell, and E. M. Gelbard, "VIM - A Continuous Energy Monte Carlo Code at ANL," ORNL/RSIC-44, April 21-23, 1980.

6.70 R. W. Schaefer, Argonne National Laboratory, unpublished information (1992).

6.71 P. J. Finck, Argonne National Laboratory, unpublished information (1992).

7 DUTY CYCLE AND CATEGORIZATION OF EVENTS

The duty cycle presented in this section is defined for the life of the Mark-V/Mark-VA fueled subassemblies. The duty cycle selection and event categorization of normal and off-normal events are based on EBR-II operational experience, the duty cycle used traditionally, engineering judgement, and information obtained from the probabilistic risk assessment (PRA) analysis of EBR-II (Ref. 7.1). The events are classified into the traditional five categories; they are the normal, the anticipated, the unlikely, the extremely unlikely, and the beyond design basis events. The analysis is performed in the following steps:

(1) Evaluate EBR-II operation history and existing classification of events.
(2) Determine equipment failure frequency and probability of failure based on the EBR-II PRA.
(3) List all off-normal events needed for analysis and categorize them based on frequency of occurrence and judgement.
(4) Group events based on similarity and frequency.
(5) Select the "umbrella" transient in each group based on severity of fuel damage and determine number of duty cycles in each group.

A safety analysis is then performed on the umbrella transients in the normal, anticipated, unlikely, and extremely unlikely categories. This analysis is described in detail in Secs. 9.4 through 9.8.

7.1 Operation History and Equipment Failure Mechanism

The number of events in the duty cycle expected for the life of fuel is based on the reactor operation history and the expected operating conditions.

The off-normal transients are caused by either equipment failure or human error. In the EBR-II PRA analysis [7.1], the frequencies and probabilities of single and multiple equipment malfunctions including human error have been estimated. This information is used to supplement

engineering judgement and categorize the events.

The loss of flow (LOF) in the primary system has been historically a major concern in the off-normal transients, and in order to understand the failure modes of the primary pumps and the differences between the resulting flow transients, the operation of the primary pump is described below. The primary coolant in the reactor is powered by two primary pumping units. Electrical power to the two main pumps is supplied by means of a variable speed motor-generator (M-G) set for each unit. As shown in the schematic, Figure 7-1, electrical power is supplied to each M-G set via two pairs of circuit breakers, i.e., the 2400-volt breakers for the M-G motors and the 110-volt breakers for the eddy-current clutches. An additional pair of breakers connects the generator outputs to provide protection, in traditional fashion, to the motors and/or pumps.

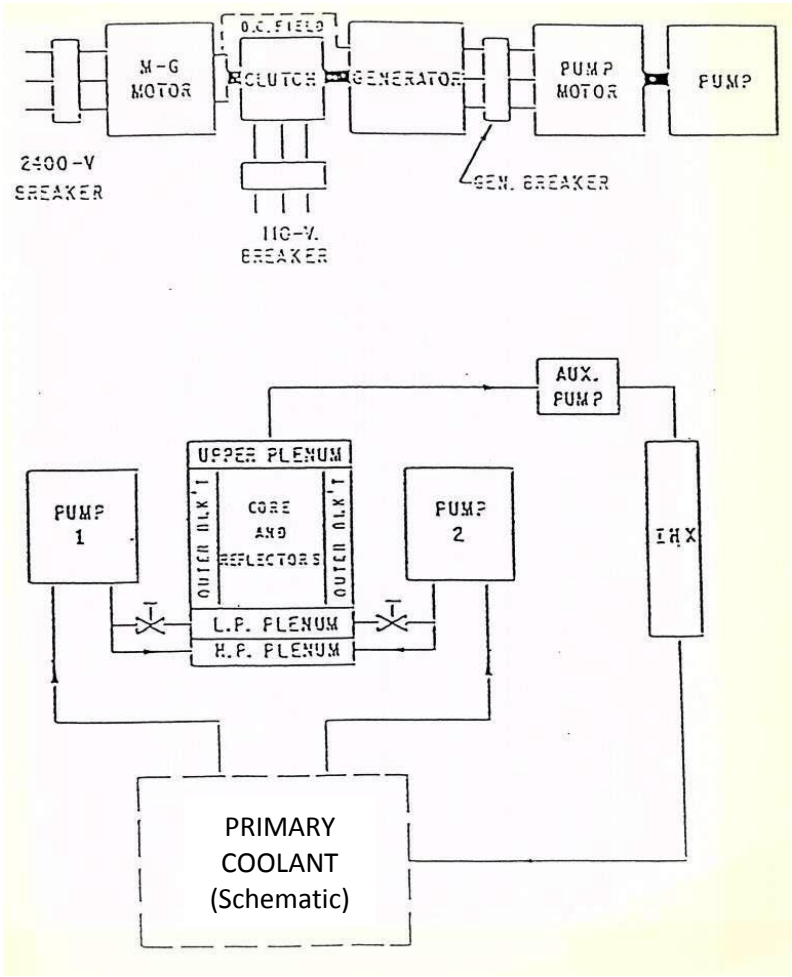

Figure 7-1 Schematic Representation of EBR-II Primary Pumps

The loss of pumping power due to electrical-mechanical failure can be caused in a variety of different ways; by the opening of the M-G input breaker, the M-G output (generator) breaker, or the clutch breaker. The LOF could also be caused by mechanical failure in the pump itself leading to pump seizure or shaft binding; the coastdown associated with pump seizure is rapid, while the coastdown of shaft binding is considerably slower than that of the M-G input breaker trip and is therefore subsumed into that category. The characteristics of primary flow coastdown due to breaker trips and seizure are given in Figure 7-2.

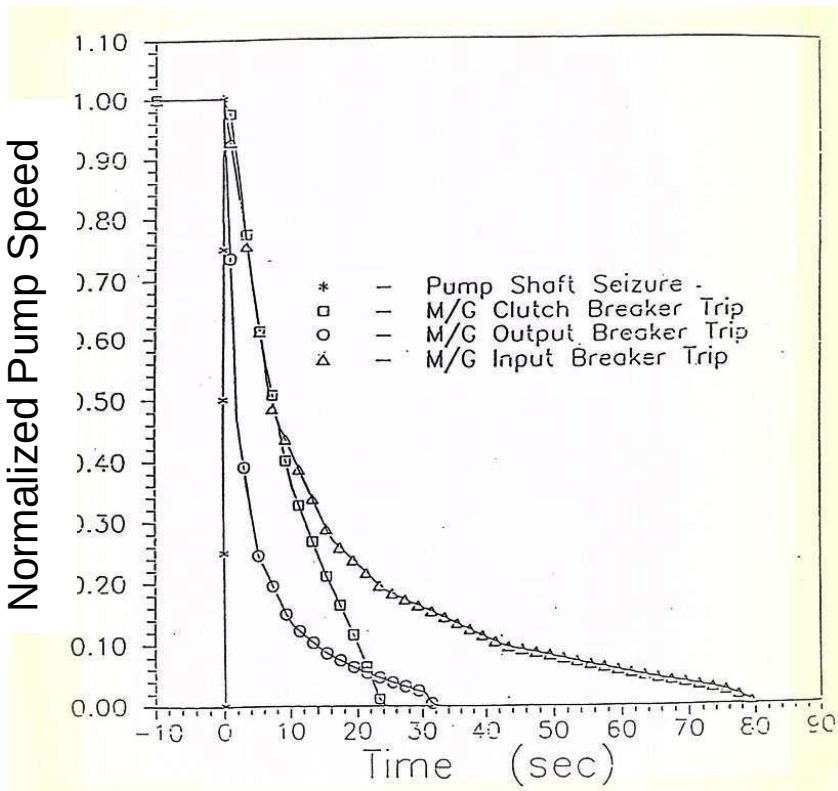

Figure 7-2 Pump Coastdown in EBR-II

The failure mechanisms of control rods, primary pump and secondary pump runouts, the loss of secondary pump and the balance of plant, and the plant protection system (PPS) failures are described in detail in Ref. 7.1.

7.2 Equipment Failure Probability

The probabilistic assessment of plant equipment failures and malfunctions for events selected in the present analysis is given in Table 7-1. Events A-1 through A-17 are initiating

events; these occur with a characteristic expected frequency which is presented in Table 7-1 as a frequency per year. Given the occurrence of one of the initiating events, a demand will be made on the plant protective system. This demand may result in one of the types of equipment failures listed as items A-18 through A-22. The conditional probability of equipment failure once a demand has been made is given in Table 7-1 for events A-18 through A-22. The values of frequency per year for initiating events and probability of failure for plant protective system equipment are based on the results of the EBR-II PRA. If the plant responses for two events are identical but the events have different frequencies due to mode of event initiation, then the event with higher frequency is considered in the table. For instance, case A-1 in the table is a LOF event, in which the loss of power of both pumps is caused by M-G input breaker trips. This event can be initiated by either loss-of-normal power or by equipment failures, and their corresponding frequencies are 10^{-1} and 2.2×10^{-4} per year, respectively. In the table the value appropriate to loss-of-normal power is used. Not all distinct failure mechanisms for the primary pumps are detailed in Table 7-1; the combination of events is based on frequency, similarity, severity, and engineering judgement. For instance, in the loss of single pumping power event, the clutch breaker trip is selected because of its high frequency, and the rest of the events are subsumed into the single pump seizure event as the most severe. In the two-pump failure events, there are twenty-five event combinations, among which six transients are considered in the analysis as tabulated in Table 7-1. In the table the events with frequencies less than 10^{-6}/year are not considered. It should be noted that the frequency of loss of both primary pumps is derived based on the frequency of single pump component failure, and common cause. The simultaneous pump failure was defined as two pump failures occurring within six minutes of each other. When a plant factor of 0.82 is considered, then the probability is 1.39×10^{-5}/yr. The methodology in the determination of failure frequency is described in detail in Ref. 7.1.

7.3 Off-normal Events and Categorization

The off-normal events and the corresponding frequencies of occurrences caused by single and multiple equipment failures are given in Table 7-2 based on Table 7-1 results. The events are classified into five categories based on frequency of occurrence, f, recommended in Ref. 7.2, in which $f \geq 1$ is normal operation; $1 > f \geq 10^{-2}$ is an anticipated event; $10^{-2} > f \geq 10^{-4}$ is an unlikely

event; $10^{-4} > f \geq 10^{-6}$ is an extremely unlikely event; and $f < 10^{-6}$ is a beyond design base event.

Table 7-1 Probabilities of Equipment Failures

Identification	Description of Failure Mode	Frequency Per Year	Probability
A - 1	Loss of pumping power of both pumps due to M-G input breaker (BK) trips caused by loss of normal power	10^{-1}	
A - 2	Loss of pumping power of both pumps due to clutch BK trips	4.7×10^{-3}	
A - 3	Loss of pumping power of both pumps due to M-G output BK trips	2.2×10^{-4}	
A - 4	Loss of pumping power of both pumps due to M-G input BK and clutch BK trips	1.1×10^{-4}	
A - 5	Loss of pumping power of both pumps due to M-G output BK and clutch BK trips	1.4×10^{-4}	
A - 6	Loss of pumping power of one pump due to clutch BK trip and loss of flow of the second pump due to pump seizure	6.6×10^{-6}	
A - 7	Loss of pumping power of a single pump due to M-G output BK trip	8.3×10^{-1}	
A - 8	Loss of flow due to a single pump seizure	2.7×10^{-2}	
A - 9	Reactivity insertion due to a single control rod (C.R.) runout	3.3×10^{-2}	
A - 10	Reactivity insertion due to double C.R. runout	2.2×10^{-3}	
A - 11	Single C.R. runout with a maximum reactivity insertion of 20¢	3.0×10^{-2}	
A - 12	Single C.R. runout with a maximum reactivity insertion of 60¢	3.1×10^{-3}	
A - 13	Loss of balance of plant caused by equipment failure of any kind	3.7×10^{-1}	
A - 14	Primary pump runout to its full capacity	3.0×10^{-1}	
A - 15	Secondary pump runout to its full capacity	3.3×10^{-2}	
A - 16	Completely loss of secondary flow	6.3×10^{-1}	
A - 17	Loss of steam due to large steam leak	10^{-1}	
A - 18	Failure of reactor scram due to control rod and safety rod (S.R.) jam		4.5×10^{-6}
A - 19	Failure of SOT trip function		2.5×10^{-2}
A - 20	Failure of flow trip function		1.8×10^{-7}
A - 21	Failure of power trip function		3.6×10^{-6}
A - 22	Single control rod jam during scram		2.7×10^{-4}

The five categories are the same ones used traditionally in EBR-II event categorization; however, the traditional approach did not identify boundaries between categories so precisely, and estimation of frequency of occurrence was based on a combination of EBR-II operational experience and engineering judgment, rather than on the highly detailed analyses of PRA. In general, the traditional classification philosophy categorized an event as anticipated if it involved a single equipment failure, as unlikely if it involved two failures, as extremely unlikely if it involved three failures, and as beyond design basis if it involved four or more failures. An exception to this philosophy is classification of single pump seizure as an unlikely event.

In some cases, the approach of Ref. 7.2 may assign an event to a different category than the one to which it has traditionally been assigned at EBR-II; when this occurs, the traditional categorization is used in the present report if an evaluation of the event indicates that the PRA-based categorization is overly conservative. An example is the original classification of the seizure of one pump as an unlikely event; the PRA adopted a value of 2.7×10^{-2} yr^{-1} for seizure, but this arose due to a conservative approach to treating the various binding events. There have been no pump seizure events at EBR-II, and classification of pump seizure as unlikely is retained. In the frequency analysis and categorization of events B-23, 25, 27, 29, and 31 the possibility of operator intervention is not considered, and the classification is conservative. B-33 and B-34 are reactivity insertion events during reactor startup. In B-33 the reactor is tripped by the primary protection function, the period trip, and is classified as an anticipated event. It is assumed in B-34 that the period trip function is failed and the reactor is tripped by the backup protection function, the power-level trip. The event is thus categorized as an unlikely event based upon the traditional classification philosophy. Event B-35 involves an increase in power- to-flow ratio to anywhere between 1.0 and 1.15 due either to a drift upwards in power or a drift downwards in flow. The drift goes unnoticed due to operator inattention, plus, at sufficiently high power/flow values, failure of the power and SOT alarms. Event B-35 is categorized as anticipated based upon the traditional classification philosophy.

Table 7-2 Categorization of Events Based on Frequency of Occurrence

Identification	Description of Events	Annual Probability	Probability of Scram Failure	Combined Annual Probability	Classification of Events
B - 1	A-1 and the reactor is scrammed by flow trip	10^{-1}	N/A	10^{-1}	Anticipated
B - 2	A-2 and the reactor is scrammed by flow trip	4.7×10^{-3}	N/A	4.7×10^{-3}	Unlikely
B - 3	A-3 and the reactor is scrammed by flow trip	2.2×10^{-4}	N/A	2.2×10^{-4}	Unlikely
B - 4	A-4 and the reactor is scrammed by flow trip	1.1×10^{-4}	N/A	1.1×10^{-4}	Unlikely
B - 5	A-5 and the reactor is scrammed by flow trip	1.4×10^{-4}	N/A	1.4×10^{-4}	Unlikely
B - 6	A-6 and the reactor is scrammed by flow trip	6.6×10^{-6}	N/A	6.6×10^{-6}	Extremely Unlikely
B - 7	A-7 and the reactor is scrammed by flow trip	8.3×10^{-1}	N/A	8.3×10^{-1}	Anticipated
B - 8	A-8 and the reactor is scrammed by flow trip	2.7×10^{-2}	N/A	2.7×10^{-2}	Unlikely
B - 9	Unprotected LOF- A combination of A-1 and A-18	10^{-1}	4.5×10^{-6}	4.5×10^{-7}	BDBE
B - 10	Unprotected LOF- A combination of A-2 and A-18	4.7×10^{-3}	4.5×10^{-6}	2.1×10^{-8}	BDBE
B - 11	Unprotected LOF- A combination of A-3 and A-18	2.2×10^{-4}	4.5×10^{-6}	9.9×10^{-10}	BDBE
B - 12	Unprotected LOF- A combination of A-4 and A-18	1.1×10^{-4}	4.5×10^{-6}	5.0×10^{-10}	BDBE
B - 13	Unprotected LOF- A combination of A-5 and A-18	1.4×10^{-4}	4.5×10^{-6}	6.3×10^{-10}	BDBE
B - 14	Unprotected LOF- A combination of A-6 and A-18	6.6×10^{-6}	4.5×10^{-6}	3.0×10^{-11}	BDBE
B - 15	Unprotected LOF- A combination of A-7 and A-18	0.83	4.5×10^{-6}	3.7×10^{-6}	Extremely Unlikely
B - 16	Unprotected LOF- A combination of A-8 and A-18	2.7×10^{-2}	4.5×10^{-6}	1.2×10^{-7}	BDBE
B - 17	A-9 and the reactor is scrammed by power trip	3.3×10^{-2}	N/A	3.3×10^{-2}	Anticipated
B - 18	A-10 and the reactor is scrammed by power trip	2.2×10^{-3}	N/A	2.2×10^{-3}	Unlikely
B - 19	A-9 and failure of power trip function. The reactor is scrammed by SOT trip (A-9 and A-21)	3.3×10^{-2}	3.6×10^{-6}	1.2×10^{-7}	BDBE

Identification	Description of Events	Annual Probability	Probability of Scram Failure	Combined Annual Probability	Classification of Events
B - 20	Unprotected TOP due to single C. R. runout with a maximum reactivity insertion of 20¢ (A-11 and A-18)	3.0×10^{-2}	4.5×10^{-6}	1.4×10^{-7}	BDBE
B - 21	Unprotected TOP due to single C. R. runout with a maximum reactivity insertion of 60¢ (A-12 and A-18)	3.1×10^{-3}	4.5×10^{-6}	1.4×10^{-8}	BDBE
B - 22	A-13 and the reactor is manually scrammed	3.7×10^{-1}	N/A	3.7×10^{-1}	Anticipated
B - 23	Unprotected loss of balance of plant (A-13 and A-18)	3.7×10^{-1}	4.5×10^{-6}	1.7×10^{-6}	Extremely Unlikely
B - 24	A-14 and the reactor is manually scrammed	3.0×10^{-1}	N/A	3.0×10^{-1}	Anticipated
B - 25	Unprotected primary pump runout (A-14 and A-18)	3.0×10^{-1}	4.5×10^{-6}	1.4×10^{-6}	Extremely Unlikely
B - 26	A-15 and the reactor is manually scrammed	3.3×10^{-2}	N/A	3.3×10^{-2}	Anticipated
B - 27	Unprotected secondary pump runout (A-15 and A-18)	3.3×10^{-2}	4.5×10^{-6}	1.5×10^{-7}	BDBE
B - 28	A-16 and the reactor is manually scrammed	6.3×10^{-1}	N/A	6.3×10^{-1}	Anticipated
B - 29	Unprotected loss of secondary flow (A-16 and A-18)	6.3×10^{-1}	4.5×10^{-6}	2.8×10^{-6}	Extremely Unlikely
B - 30	A-17 and the reactor is manually scrammed	10^{-1}	N/A	10^{-1}	Anticipated
B - 31	Unprotected loss of steam (A-17 and A-18)	10^{-1}	4.5×10^{-6}	4.5×10^{-7}	BDBE
B - 32	A-2 and a single high worth control rod jam	4.7×10^{-3}	2.7×10^{-4}	1.27×10^{-6}	Extremely Unlikely
B - 33	Reactivity insertion during reactor startup and the reactor is tripped by the period trip	--	--	--	Anticipated
B - 34	Reactivity insertion during reactor startup and the reactor is tripped by the power-level trip	--	--	--	Unlikely
B - 35	Power/flow ratio increase due to drift upwards in power or a drift downwards in flow	--	--	--	Anticipated

7.4 Selection of "Umbrella" Transients

The duty cycle events are summarized in Table 7-3, in which the operation life of the Mark-V fuel with a burnup of 10 at. % is taken to be two years. In the table, the transients in the same category and with similar thermal behavior are represented by the 'umbrella' transient, which is the most severe transient in the group. The severity of the transients in the group was determined by analysis using the SASSYS/EBR-II model [7.3]. The letters N, AN, UN, EU and BD in the table denote normal, anticipated (operational incident), unlikely (minor incident) extremely unlikely (major incident), and beyond design basis events, respectively.

An increase in the burnup limit, and therefore in the life of the fuel, would increase the number of duty cycles in the normal events. The same would be true if the operation of EBR-II were to change to include shorter runs, with more runs per year. However, as discussed in Sec. 9.7, damage during events N-1 through N-4 is no greater than damage experienced during normal operation, and so a change in the number of duty cycles for these events does not contribute significantly to fuel damage. The duty cycle values for these events should be considered simply representative numbers based on past operating experience; from the standpoint of fuel damage, an arbitrary number of such transients can be allowed.

In the case of off-normal events with a single duty cycle, an increase in fuel life does not necessarily imply an increase in the number of duty cycles, since the expected frequency of most of these events is much less than once in two years, and so the number of duty cycles throughout the life of the fuel would remain at one. Of the off-normal events for which an increase in fuel life would result in an increase in the number of duty cycles, all are mild and result in no significant damage, and so an increase in the number of duty cycles would have no impact on the conclusions of the safety analysis.

7.4.1 Normal Operation

In the normal operation category there are four events: inadvertent reactor scram from full power (N-1), anticipatory reactor shutdown (N-2), normal reactor shutdown (N-3) and normal startup (N-4). Based on EBR-II operation history the duty cycles of N-1, N-2 and N-3 are 4, 4

and 8 times per year, respectively, and these values are conservative. Thus, there are 16 N-4 duty cycles per year resulting from events N-1 to N-3. If it is conservatively assumed that there are 4 off-normal events per year that require reactor restart, then the total number of duty cycles of the N-4 event is 20. The duty cycles in Table 7-3 are for a two-year operation time, which is equivalent to the life of the fuel. It should be noted that the numbers of duty cycles in Table 7-3 do not include those which might be caused by future testing programs. The safety of such tests will be assessed on a test by test basis. Reactor temperatures of transients N-1 to N-4 will not exceed the normal reactor operating temperature; the main concern is the fatigue damage of the subassembly due to thermal stresses in the fuel-cladding, the hex duct, the upper tubesheet of the IHX and parts of the secondary sodium system caused by sudden temperature changes during reactor scram.

Table 7-3 Event Categorization and Duty Cycles Through Life of the Fuel

Identification	**Description of Events**	**"Umbrella" Transient to Envelope Event in this Group**	**No. of Duty Cycles Through Life of the Fuel**	
N - 1	Inadvertent reactor scram	Reactor scram from 100% power and flow conditions	8†	
N - 2	Anticipatory reactor shutdown	Reactor shutdown from 100% power and flow conditions	8†	
N - 3	Normal reactor shutdown	Reactor shutdown from 100% power and flow conditions	16†	
N - 4	Normal reactor startup	Reactor power increases from 0 to 100% power	40†	
AN - 1	Protected LOF due to a single primary pump failure	A single pump M-G output breaker trip and the reactor is scrammed by flow trip	7	
AN - 2	Protected LOF due to failure of both pumps	LOF caused by M-G input breaker trips and the reactor is scrammed by flow trip	1	
AN - 3	Reactivity insertion due to a single control rod runout	Event is initiated at 100 and/or 40 power conditions and the reactor scrammed by power trip	1	*A
AN - 4	Protected reactivity insertion during reactor startup	The reactor is scrammed by the period trip	1	*A
AN - 5	Slow power/flow ratio increase	Power/flow ratio increase due to a drift upwards in power or a drift downwards in flow	1	
AN - 6	Protected TOP due to primary pump runout	Primary pump runout to its full capacity and the reactor is scrammed by power trip	1	
AN - 7	Loss of balance of plant and loss of secondary flow	Loss of heat sink and the reactor is manually scrammed	2	

Identification	Description of Events	"Umbrella" Transient to Envelope Event in this Group	No. of Duty Cycles Through Life of the Fuel	
AN - 8	Large steam leak due to pipe break or rupture	Loss of steam pressure and the reactor is manually scrammed	1	
AN - 9	Protected TOP due to secondary pump runout	Secondary pump runout to its full capacity and the reactor is manually scrammed	2	
UN - 1	Protected LOF due to failure of both pumps	LOF due to clutch breaker trips of both pumps and the reactor is scrammed by flow trip	1	*A
UN - 2	Protected LOF due to failure of both pumps	LOF due to seizure of one pump and clutch breaker trip of another pump. The reactor is scrammed by flow trip	1	*U
UN - 3	A single control rod runout with delayed reactor scram	A single control rod runout and a failure of power trip function. The reactor is scrammed by SOT trip	1	*U
UN - 4	Protected reactivity insertion due to double control rod runout	Two control rods runout simultaneously and the reactor is scrammed by power trip	1	
UN -5	Reactivity insertion during reactor startup with delayed reactor scram	Failure of period trip and the reactor is scrammed by power-level trip	1	*U
EU - 1	LOF and jam of single control rod	UN-1 and stuck control rod	1	*E
BD - 1	LOFWS	Unprotected LOF due to M-G input breaker trips of both pumps	1	
BD - 2	TOPWS	Unprotected reactivity insertion due to a single C.R. runout. The maximum reactivity insertion is 20¢	1	
BD - 3	LOHSWS	Completely loss of heat sink initiated at 100% power and flow conditions	1	
BD - 4	Loss of steam pressure without scram	Unprotected loss of steam pressure at 100% power and flow conditions	1	

*A Anticipated event considered in current EBR-II T.S.
*U Unlikely event considered in current EBR-II T.S.
*E Extremely Unlikely event considered in current EBR-II T.S.

Note that event UN-1 is classed as unlikely in contrast to the existing EBR-II T.S. classification of anticipated. This is because of a plant modification to separate the clutch power supplies so that two separate faults are required for this event.

† Representative numbers of events

7.4.2 Anticipated Events

It is noted in Table 7-1 that the frequency of a single pump failure due to a M-G output breaker trip is given as 0.83/year, event A-7. This transient covers the single-pump-failure

transients due to other causes such as a clutch breaker trip, and other electrical-mechanical failures of a single pump and is traditionally considered as an anticipated event. The EBR-II PRA used the observed frequency of such events, i.e. .15 per year for this event, but .83 per year for all electromechanical failures. This event is therefore categorized as an anticipated event in the present analysis and is represented by the "umbrella" transient, AN-1, which is a protected LOF event caused by a single pump M-G output breaker trip. AN-1 bounds all LOF events due to single pump failure events except pump seizure, which is classified separately as an unlikely event. The number of duty cycles in AN-1 was based upon PRA analysis [7.1], and the number is extremely conservative when compared with EBR-II operation experience.

AN-2 is a LOF event caused by simultaneous M-G input breaker trips of both primary pumps. The AN-1 and AN-2 events are not currently considered in the EBR-II T.S.. In the current EBR-II T.S. the anticipated LOF is represented by a double-pump LOF due to clutch breaker trip. The loss of clutch breaker power of both pumps was caused by loss of constant power (LOCP) supply, which has the same failure frequency as that of AN-2 (10^{-1}/year). A plant modification to separate the clutch power supplies to the primary pumps will be completed in 1994; as a result, the failure frequency of this event is reduced to the level of an unlikely event, as shown by the risk analysis of Ref. 7.4.Therefore, the double clutch breaker trip is classified as unlikely event UN-1 in the Mark-V safety analysis.

The reactivity insertion event, AN-3, is classified in the T.S. as an anticipated event. Parametric study on the effect of initial power to the fuel pin temperature was performed to include the reactor startup conditions. Analytical results indicate that the fuel pin temperature increases slightly with the decrease of initial power. During reactor startup in EBR-II, the period trip function is in place to protect control-rod runout at power below 25 MWt (40%) power conditions. In the present analysis, this event is considered to be initiated at 40% power conditions. AN-4 is a reactivity insertion event occurring during reactor startup, and the reactor is scrammed by the period trip. AN-5 is an event in which the power/flow ratio increases slowly due either to a drift upwards in power or a drift downwards in flow. The drift in power is assumed to stay below the power trip setting, and the drift in flow is assumed to stay above the flow trip setting. This event has not been included in the PRA analysis.

In the primary pump runout event of case AN-6, the reactor temperature will be below the normal reactor operating temperature whether or not the reactor is scrammed by the overpower trip function. The main concern in this event would be the pressure increase during primary pump runout, which may cause additional fatigue and creep damage of the hex duct; this effect has been considered in the structural analysis of the hex duct. The loss of balance of plant and loss of secondary flow events (B-22 and B-28 in Table 7-2) are enveloped by the "umbrella" transient AN-7, which is a loss of heat sink event. AN-7 is a mild transient as demonstrated by the loss-of-heat-sink without scram (LOHSWS) test in Ref. 7.5, and the peak reactor temperature is about the same as the reactor normal operating temperature. The loss of steam event, AN-8, is caused by steam pipe failure. Plant response to this transient depends upon the plant control system. In EBR-II the initial pressure regulator (IPR) is used to maintain constant pressure. As steam leakage is initiated, the IPR tends to close the turbine admission valve (TAV) in order to maintain constant pressure, and the reactor power remains at the initial value although turbine output is reduced. However, in the event the IPR fails to maintain constant pressure due to large steam leakage, the steam pressure will decrease, which causes steam, IHX secondary sodium, and reactor inlet temperatures to drop, and reactor power to increase. In this event, the reactor will be scrammed by the power trip. The thermal transient is again very mild. The secondary pump runout event, AN-9, is also a very mild transient. Increase of secondary flow causes reactor inlet temperature to decrease and reactor power to increase. The capacity of the secondary pump is 6000 gpm, and the reactor power will be increased by 7.5% for a complete secondary pump runout event. The final reactor temperature will not be much higher than that of the normal operation condition.

7.4.3 Unlikely Events

Among the unlikely LOF events, loss of pumping power of both pumps due to the clutch breaker trips, UN-1, represents the most severe transient in this category and bounds all protected LOF transients due to power loss to both pumps caused by simultaneous trips of 1) M-G input and clutch breakers, 2) M-G output and clutch breakers, or 3) both M-G output breakers. The system response to these transients was determined from SASSYS/EBR-II code calculations, and the clutch breaker trip is the most severe. UN-2 is a LOF event caused by one pump seizure and loss of power of another pump due to clutch breaker trip. This event envelopes the single pump

seizure event and has a frequency of 6.6 x 10^{-6} per year based on PRA results, and should strictly be classified as an extremely unlikely event. However, this event is included as an unlikely event in the present report in order to be consistent with the current T. S.. UN-3 is a single C.R. runout event combined with a failure of the power trip function; in this case, the reactor is scrammed by the SOT trip. This event is again classified as an unlikely event in order to be consistent with the current T.S., although the frequency of occurrence is 1.1 x 10^{-7}/year. The protected double C.R. runout event, UN-4, is not considered in the existing T.S.. In this event, two control rods are assumed to run out simultaneously, and the reactor is scrammed by the power trip. UN-5 is a reactivity insertion event during reactor startup, in which the reactor is scrammed by the backup power-level trip function assuming the failure of the period trip function.

7.4.4 Extremely Unlikely Events

If events were classified based on frequency of occurrence as defined in Section 7.3, the events in the extremely unlikely category would be the unprotected LOF due to loss of power of a single pump, the unprotected loss of balance of plant and UN-1 with a stuck control rod (B-15, B-23 and B-32 in Table 7-2). Traditionally, the unprotected events are classified as BDBE's; we therefore consider these transients as BDBE's in the present analysis. The only event remaining in this category is UN-1 with the addition of a stuck high worth control rod, designated EU-1.

7.4.5 Beyond Design Basis Events

Four unprotected events are considered in the beyond design basis events (BDBE) category to represent four types of unprotected transients; the loss of flow without scram (LOFWS), the loss of heat sink without scram (LOHSWS), the transient overpower without scram (TOPWS) and the loss of steam pressure without scram event. BD-1 is a LOFWS event, and the flow coastdown of both pumps is caused by M-G input breaker trips due to loss of normal power. This "umbrella" transient bounds all unprotected LOF transients caused by single pump failures. BD-2 is a TOPWS event, in which the reactivity insertion is caused by a single control rod runout and has a maximum reactivity insertion of 20¢. For the event where the maximum reactivity insertion reaches 60¢, the frequency of occurrence will be an order of magnitude less, and so this event need not be considered in the BDBE analysis. The LOHSWS event, BD-3, is a very mild transient; as a matter of fact, during a loss of heat sink transient the reactor power and temperature will not

reach their corresponding power and sodium outlet temperature trip settings, respectively. BD-4 is the unprotected AN-7 event, in which the reactor power increases until the steam pressure reaches atmospheric pressure or the secondary sodium IHX inlet temperature reaches the sodium solidus temperature.

Thermal-hydraulic behavior of BDBE's are not analyzed in the present SAR, because they are not EBR-II design basis events. They are included here for future reference.

7.5 Summary of Transients for Thermal-Hydraulic Analysis

In the safety analysis of the Mark-V fuel, only events which are important in terms of temperature and cladding damage are selected for thermal-hydraulic and fuel pin damage analysis. Based on Table 7-3, discussion in Section 7.4, and scoping analyses, the transients considered for safety analysis are given below:

A. <u>Anticipated Events</u>

- LOF due to M-G output breaker trip of a primary pump, with the reactor scrammed by the primary flow trip (AN-1).
- LOF due to M-G input breaker trips of both pumps caused by loss of normal power, with the reactor scrammed by the primary flow trip (AN-2).
- Reactivity insertion due to a single control rod runout, and the reactor is scrammed by power trip. The event is initiated at reactor power of 40% (AN-3).
- Reactivity insertion during startup, the reactor is scrammed by the period trip (AN-4).
- Power/flow ratio rises due to a drift upwards in power or a drift downwards in flow (AN-5).

B. <u>Unlikely Events</u>

- LOF due to clutch breaker trips of both pumps, with the reactor scrammed by the

primary flow trip (UN-1).

- LOF due to clutch breaker trip of one pump and seizure of another pump. The reactor is scrammed by the primary flow trip (UN-2).

- Reactivity insertion due to a single control rod runout, and a failure of power trip function. The event is initiated at 40% power condition, and the reactor is scrammed by the secondary SOT trip (UN-3).

- Reactivity insertion due to simultaneous runout of two control rods. The event is initiated at 40% power condition, and the reactor is scrammed by power trip (UN-4).

- Reactivity insertion during reactor startup, the reactor is scrammed by the power-level trip (UN-5).

C. <u>Extremely Unlikely Events</u>

- LOF due to clutch breaker trip of both pumps, reactor scram by flow trip with one high-worth control rod stuck (EU-1).

7.6 Input Descriptions for Off-Normal Event Analysis

The six-row and the six-plus-row core loading conditions (see Sections 6.2.1.1 and 6.2.1.2) have both been considered for Mark-V and Mark-VA safety analysis. The total flow of the pumps and through subassemblies of the two reactor core loadings are identical, and they are 9340 and 8880 gpm, respectively. There is a 10.0 gpm leakage at the pump disconnects, a 25.0 gpm leakage at the low-plenum throttle valves and a 425 gpm leakage at the high-pressure plenum, in which 305 gpm leak downward and 120 gpm leak upward through the by-pass thimbles of the control rods. The pressure drops from the high- and the low-pressure plenums to the upper plenum are 44.0 and 12.2 psi, respectively for the six-row core, and are 40.5 and 11.4 psi, respectively for the six-plus-row core. The total power generated by all subassemblies is 62.5 MWt for both types of reactor core loadings. The hydraulic conditions are summarized in Table 7-4 and compared to similar Mark-II and Mark-III cores.

Table 7-4 Comparison of Hydraulic Characteristics of Various EBR-II Cores

Core Subassembly Type	Mark-II	Mark-III	Mark-V 6-Row	Mark-V 6+Row
Pressure				
High Pressure Plenum - Upper Plenum, psi	40.7	44.0	44.0	40.5
Low Pressure Plenum - Upper Plenum, psi	11.4	12.2	12.2	11.4
Flow				
Total, gpm[a]	9340	9340	9340	9340
High Pressure Plenum Subassemblies, gpm	7417	7364	7363	7420
Low Pressure Plenum Subassemblies, gpm	1463	1576	1517	1460
Subassembly, gpm				
Row 1	-	-	138	132
Row 2	143	135	135	129
Row 3	123	119	119	114
Row 4	94.7	93.3	93.2	89.4
Row 5	-	-	78.7	75.3
Row 6	68.5	67.8	67.8	65.0
Row 6 (High Flow)	74.2	76.0	76.0	72.8
Row 7	-	-	-	65.4

[a]Multiply gpm by 0.0483 to obtain L/s.

In the transient predictions of the off-normal events, the transients are assumed to be initiated at 105% normal power and 100% normal flow conditions. It was found that rod insertion events from 40% power were more severe and this initial condition was used where appropriate. Startup events are initiated at 62.5 Wth. The power, flow, SOT and period trip settings are set at 115% power, 88% flow, 115% ΔT, and 17s, respectively. The shutdown reactivity of 3.7$ is used in all calculations. These values represent the Limiting-Safety-System Settings (LS[3]).

In the LOF calculations, the primary pump coastdown data in Figure 7-1 are employed. The auxiliary pump is assumed to be off during all LOF events, and the flow in the reactor is due to natural convection only after a loss of flow. The secondary pump is tripped 6 seconds after reactor scram in all LOF events except the loss of normal power event of AN-2, in which case the secondary pump is tripped as soon as the reactor is scrammed. The secondary pump is an E-M pump, and the flow is modeled as stopping immediately once the pump is tripped.

In the TOP calculations, the reactor power is driven by reactivity insertion rates for single and double control-rod runouts which are 1 and 2¢/s, respectively. The overpower setting is the primary trip function, while the SOT setting serves as the secondary trip function.

The delayed neutron fraction for the Mark-III and the Mark-V reactor cores are 0.0067 and 0.0053, respectively. The β_{eff} value is expected to be between the two values for the transition core. In the present analysis the β_{eff} of 0.0053 is used for the transient predictions. The effects of β_{eff} on fuel pin temperature and damage have been studied for the protected off-normal events [7.6]; the results indicate that for the range of β_{eff} values considered (0.0053 to 0.0067), the β_{eff} has an insignificant effect on the fuel pin temperature and cladding damage, and so the safety analysis is valid for transition cores as well as for cores made up entirely of Mark-V fuel. This issue is discussed further in Sec. 10.5.

The power, flow and power-to-flow ratio histories for all considered events are given in Appendix C.

Section 7 References

7.1 D. J. Hill, W. A. Ragland and J. Roglans-Ribas, "EBR-II Level 1 Probabilistic Risk Assessment," Revision 2, June 30, 1991, Argonne National Laboratory.

7.2 R. R. Landry, T. L. King and J. N. Wilson, "Draft Preapplication Safety Evaluation Report for Power Reactor Inherently Safe Liquid Metal Reactor," NUREG-1368, September 1989.

7.3 J. P. Herzog, "SASSYS Validation with the EBR-II Shutdown Heat Removal Tests", Fifth Proceeding of Nuclear Thermal Hydraulics, winter meeting, November 26-30, 1989, San Francisco, California.

7.4 J. Roglans and L. K. Chang, Argonne National Laboratory, unpublished information (1994).

7.5 E. E. Feldman, et al., "EBR-II Unprotected Loss-of-heat-sink Predictions and Preliminary Test Results," Nuclear and Engineering Design 101, 1987.

7.6 T. C. Hung, Argonne National Laboratory, unpublished information (1991).

8 STRUCTURAL ANALYSIS OF SUBASSEMBLY DUCTS

8.1 Introduction

During steady state irradiation in EBR-II there are five areas of operational concerns that relate directly to the structural integrity of the Mark-V fuel subassembly duct, namely duct dilation, subassembly bowing, bundle-duct interaction, weld integrity, and intersubassembly thermal gradients induced by operating transients. None of these areas has an impact on reactor safety; nonetheless, all have been analyzed to investigate possible higher fluence limits and HT9 performance and to identify any sudden changes in performance which the Mark-V and Mark-VA subassemblies might be approaching in the modified core environment.

Duct dilation is an important operational issue and is limited to 40 mils (0.1 cm) in EBR-II. Permanent deformation of the duct is primarily caused by irradiation-enhanced creep and swelling. Excessive dilation may jeopardize subassembly removal, and, in EBR-II, it may also cause difficulty placing the subassembly in the storage basket. Excessive thermal bowing makes it necessary to use a large pulling force during fuel handling, and as a result, the potential for weld failures at connections between duct and preassemblies exists. When bowing is coupled with excessive dilation, a large amount of friction between neighboring subassemblies results, and again a large pulling force is required for subassembly removal. The radial thermal gradient caused by intersubassembly heat transfer must be evaluated to assess the fatigue damage of the duct during transient operation.

The present analyses involve both analytical and computer-assisted approaches. Due to the complexity of geometry and loading history, the duct dilation, subassembly bowing and bundle-duct interaction problems are analyzed by the computer codes ANSYS [8.1] and BOW-V [8.2]. Evaluation of the duct structural integrity is carried out according to the safety design criteria listed in Section 2.2. The following sections describe the loading conditions and analysis methods used to evaluate the structural integrity of the duct.

8.2 Loading on the Duct

The duct is subjected to mechanical, thermal, and subassembly interaction loadings. The mechanical loading is primarily caused by pressure difference between flow inside the duct and the stagnant sodium outside the duct. The pressure loading depends on pressure drop in the fuel bundle, and it is a function of axial location. In EBR-II the pressure loading is generally higher for the inner-row subassemblies than that for the outer-row subassemblies because of higher flow rates in the inner rows. The pressure loadings of subassembly ducts were given in Ref. 8.3 for a Mark-III core. Since Mark-III and Mark-V subassemblies have identical geometry, pressure drops in Mark-III and Mark-V fuel bundles are expected to be the same. The flow in the row 2 subassembly of the Mark-III core in Ref. 8.3 is similar to that of row 1 and row 2 subassemblies of the Mark-V core. The row 2 subassembly was chosen for structural analysis because pressure within this subassembly is relatively high. The pressures within the row 2 subassembly at the bottom, the middle and the top of the fuel are 32, 26 and 7 psi (221, 180 and 48 kpa), respectively.

Thermal loading in the duct is induced by the temperature gradient across the thickness of the duct wall due to temperature differences between adjacent subassemblies. Due to a thermal fatigue concern for the EBR-II holddown fingers, the difference between the exit coolant temperature of a subassembly and the average exit coolant temperature of the six adjacent subassemblies is limited to 100°F (56°C) in normal reactor operation. An upper bound on the temperature gradient across the duct can be set by assuming an inlet coolant temperature of 700°F (371°C) and a peak hot-channel coolant temperature of 1070°F (560°C), which bounds the Tech. Spec. limiting peak pin coolant temperature for either Mark-V or Mark-VA fuel and corresponds to an average outlet temperature of 994°F (534°C), assuming a peaking factor of 1.26 (see Sec. 9.3 for a discussion on selection of a peaking factor). It has been estimated that overcooling of the pins along the edge of the subassembly causes the inner duct temperature to be about 24°F (13°C) lower than the average outlet temperature, giving an inner duct temperature of 970°F (521°C). Examination of run reports indicates that the coldest subassembly in the core has an edge temperature of about 740°F (393°C). If it is assumed that the hottest and coldest subassemblies are adjacent to one another, then the maximum temperature difference radially between these two subassemblies is 230°F (128°C), and this is the value used in the structural analysis discussed

below. This temperature difference estimate is highly conservative, since it neglects the effect of intersubassembly heat transfer.

The subassembly interaction loading caused by thermal bowing of subassemblies has been investigated in Ref. 8.6, which indicated that for the worst-case scenario the maximum force between subassemblies is about 222.4N (50 lb_f). The possibility of bundle-duct interaction is investigated in Sec. 8.3.

8.3 Structural Analysis

The structural analysis of the duct addressed irradiation-induced dilation, thermal bowing, fuel-bundle-duct interaction, welding between the duct and the radiation shield, cross-the-duct-wall thermal gradient, and the effect of a pressure increase due to runout of the primary pumps. The first, second, and fifth issues were analyzed with computer codes, and the rest were evaluated analytically. The analyses are summarized below:

(1) Duct Dilation

The 2-D ANSYS model was used to analyze the duct dilation for the Mark-V driver fuel subassembly. A typical Mark-V driver subassembly of 61 pins in row 2 was analyzed. Duct dilation is induced by a combination of fluence, duct wall temperature and coolant pressure. Since profilometry measurements of EBR-II driver subassemblies have consistently shown that the worst dilation occurs at the core midplane, duct dilations at that elevation were considered. The average sodium outlet temperature of the limiting row 2 subassembly is about 894°F (479°C), which corresponds to a core midplane duct wall temperature of about 788°F (420°C). As stated in Sec. 8.2, the pressure loading at the fuel midplane is 26 psi (0.18 MPa) for this subassembly. Therefore, a duct wall temperature of 788°F (420°C) and a pressure loading of 26 psi (0.18 MPa) were assumed in the duct dilation analysis [8.3]. The average high energy flux in row 2 is 2.72×10^{15} n/cm^2-sec which corresponds to a fluence per at. % of $1.024 \times 10^{22} n/cm^2$. The peak fluence per at. % is 1.065×10^{22} n/cm^2 in row 2, and this fluence was used for the analysis. It was noted that for the same burnup the fluence produced by the Mark-V core is about 5% more than that by the Mark-III core.

The 2-D finite-element model described in Section 4.6 was used to predict the duct dilation. The gap between ducts is 0.712 mm (28 mils), not including the button. There is a 0.356 mm (14 mil) button located on the duct at the core midplane, and point contact between ducts is made at the buttons as soon as the subassemblies are loaded into the reactor. Thus, duct-to-duct contact is initiated at the core midplane and is propagated in the axial direction as fluence increases. However, only a small lengthwise portion of the duct is in contact throughout the life of the subassembly.

The analysis indicated that the maximum diametral dilation for HT9 duct is 0.653 mm (25.7 mils) at 15 at. % and 0.813 mm (32 mils) for 12% CW 316SS duct at 10 at. % burnup. When uncertainty factors of 1.6 and 1.43 were applied to the swelling correlations of HT9 and 316SS, respectively [8.4, 8.5], the maximum dilations (flat-to-flat) for HT9 and 316SS became 0.68 mm (26.75 mils) and 0.918 mm (36.14 mils), respectively. None of the duct dilation values exceeded the storage basket limit of 1.016 mm (40 mils) discussed in Section 2.2.3, so the design criterion is satisfied. It was noted in the present analysis that the application of uncertainty factors on the HT9/316SS creep correlations has little effect on the duct dilation because the creep dilation is limited by the gap size and is constrained by the neighboring subassembly ducts.

(2) Duct Bowing

A thermal bowing study of Mark-V subassemblies was performed and is described in detail in Ref. 8.6. The purpose of this study was to provide bounds on the interaction forces between subassemblies which are caused by thermal bowing. Six hypothetical subassembly thermal loading conditions were considered in order to cover all possible bowing variations in the reactor. The BOW-V computer code [8.2] was employed for the calculation. The effects of creep and irradiation swelling were neglected. This was justified by a preliminary bowing analysis which indicated that stress due to bowing was low due to a very low subassembly interaction force, and so creep could be neglected. Since only a minor flux tilting of less than 10% of the average value occurs across opposite flats, the effect of irradiation swelling could also be neglected. The two duct locations which experience interaction loads as a result of bowing are at the top and at the button of

the subassembly. The maximum interaction loads occurring at the top are 47.6 N (10.6 lb_f) and 97.5 N (21.9 lb_f), respectively, for HT9 and 20% CW 316. The corresponding loads occurring at the button are 118.3 N (26.6 lb_f) and 244.6 N (55 lb_f). These loads are less than 10% of the maximum force exerted by the fuel handling system and so are of no concern.

(3) Fuel-Bundle-Duct Interaction

The prospective fuel-bundle-duct interactions (BDI) were examined for subassemblies of two different designs; Mark-V and Mark-VA [8.7]. For both designs, the BDI evaluations of Ref. 8.7 assumed a 316SS duct. Bundle-duct interaction between a Mark-V bundle and an HT-9 duct is discussed at the end of this section. The Mark-VA design is more apt to have BDI at high burnups due to a higher thermal expansion coefficient and higher creep and swelling rates for the 316SS cladding. The analysis considered the BDI behavior in terms of the clearance (gap) between fuel bundle and hex duct as a function of burnup, coolant pressure and metal temperature. Axial gap distributions for each design were calculated for subassemblies located in row 2 and row 6 to cover the spatial variance over the core. To envelope the worst scenario of fuel bundle expansion, the plenum pressure at the maximum burnup was assumed to act on the cladding throughout the pin life. The gap variations for the Mark-V/316SS duct and Mark-VA/316SS duct designs are shown in Figure 8-1 through Figure 8-4, in which the change of clearance from an initial value of 1.21 mm (47.76 mils) is presented both at the beginning of life (BOL) and at the end of life (EOL), at 10 at. % burnup. The 1.21 mm (47.76 mils) clearance (not including the wire wrap) denotes the nominal gap between the cladding at the outer row of the bundle and the inner surface of the duct. When the wire wrap is considered, the minimum clearance reduces to 0.132 mm (5.2 mils). The wire wrap spirals in and out of the nominal clearance, varying the gap between the bundle and the duct. Also, at any elevation, the gap is narrower at one flat and wider at the opposite flat of the duct due to wire wrap positioning. Consequently, when the bundle expands and touches one flat of the duct during irradiation, the wire wrap contact pressure is relieved through bending or translating the fuel pins toward the opposite flat, where the wider gap accommodates the motion. Therefore the duct wall is not sufficiently loaded to cause noticeable BDI. If

the wider gap is also closed by the overly dilated bundle through creep or swelling at high burnup, solid contact between duct and bundle will occur on all flats and severe BDI will result. This phenomenon has been observed in the destructive examination of subassemblies in EBR-II. There has never been any example of BDI for 316SS duct at 10 at. % burnup, even though the fuel pins exhibit a waving profile. However, traces of BDI on the duct wall have been observed at 15 at. % or higher burnup.

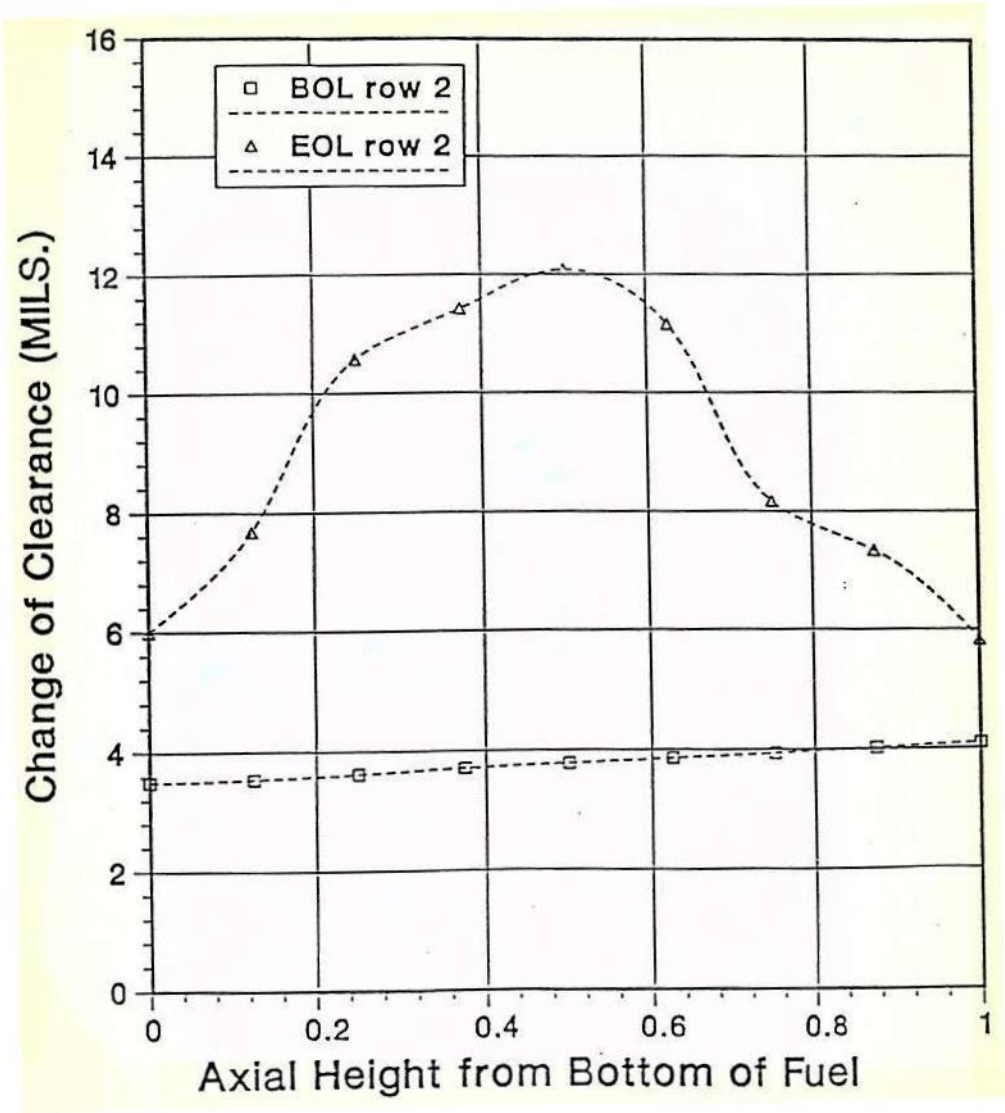

Figure 8-1 Gap Variation of Mark-V/316SS Duct Subassembly in Row 2

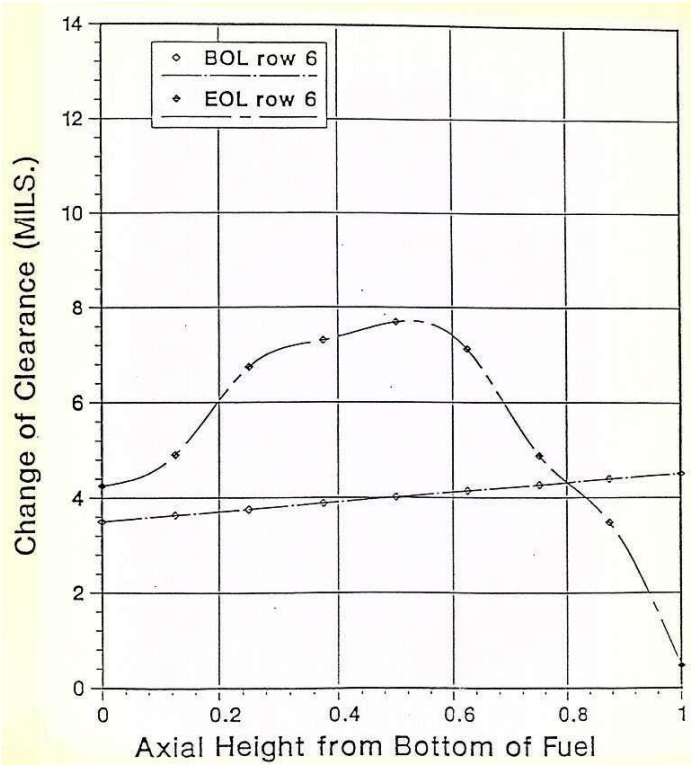

Figure 8-2 Gap Variation of Mark-V/316SS Duct Subassembly in Row 6

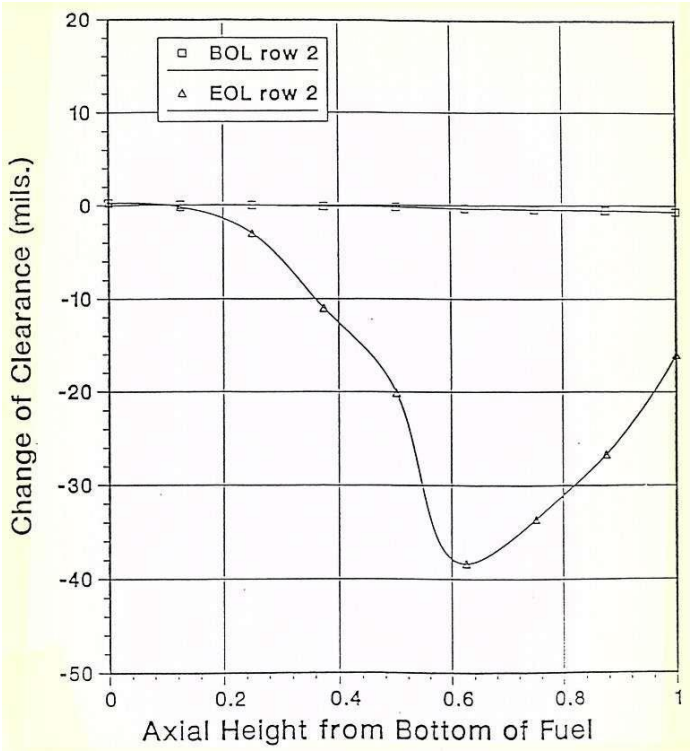

Figure 8-3 Gap Variation of Mark-VA/316SS Duct Subassembly in Row 2

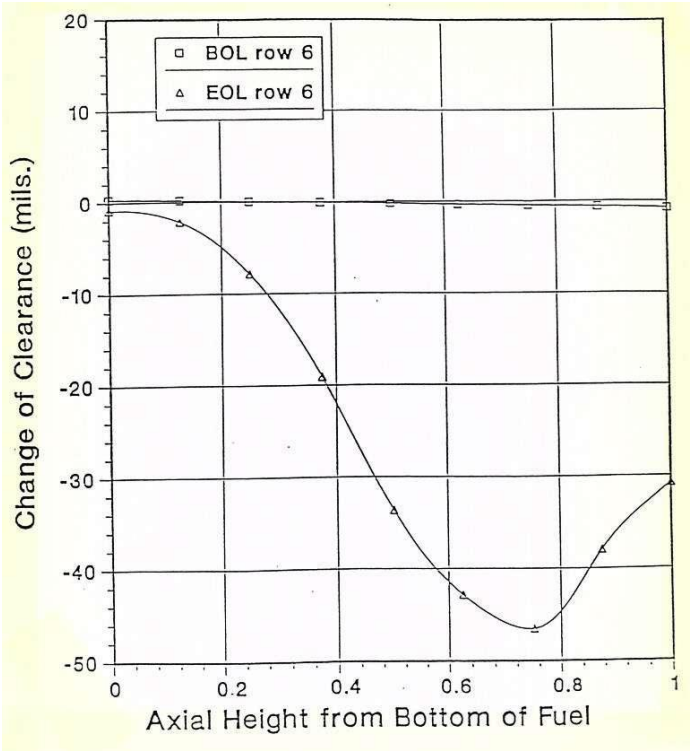

Figure 8-4 Gap Variation of Mark-VA/316SS Duct Subassembly in Row 6

As indicated in Figure 8-1 and Figure 8-2, the clearance at the core midplane of the Mark-V design is enlarged by a maximum of 12 mils (0.03 cm) at row 2 and 7.2 mils (0.018 cm) at row 6, which reduces the possibility of BDI. For the Mark-VA design the clearance shrinks, and the maximum shrinkage amounts to 38 mils (0.097 cm) at row 2 and 46 mils (0.117 cm) at row 6. It can be seen from the figures that the maximum gap change is less than the original clearance between bundle and duct, thus BDI will not occur within the targeted 10 at. % burnup. In the analyses the uncertainty in the duct dimension caused by the manufacturing tolerances was considered.

At 10 at. % burnup, the maximum expansion of a Mark-V bundle occurs at the top of the fuel and is 15 mils (.038 cm) for a row 2 subassembly and 19 mils (.048 cm) for a row 6 subassembly, according to the structural evaluations performed for Ref. 8.7. These are both less than the initial clearance between the bundle and the duct, and so no BDI would occur between a Mark-V bundle and an HT-9 duct, even neglecting any expansion of the HT-9 duct, over the design life of the subassembly.

When a Mark-V fuel bundle is contained in a 316SS duct, the gap between bundle and duct increases, and the peak pin fuel temperature will increase due to diversion of flow from the center of the bundle. The thermal-hydraulic effects of this gap increase are discussed in Sec. 9.9. The BDI behavior of a Mark-VA fuel bundle in an HT9 duct was not addressed in this section, since the HT9 duct will be used only with Mark-V fuel (which has HT9 cladding).

(4) Duct Connections

Two types of duct connections are employed in the Mark-V subassemblies; fillet welds for 316SS duct and mechanical screws for HT9 duct. All the connections are located at the junctions of the radiation shields and end adapters, which are 3-4 inches (7-10 cm) away from the core. As a result, there are no significant thermal or pressure loads exerted on the connections, and the only major load comes from subassembly handling.

Analytical investigation [8.8] of the welded connection indicated a maximum loading capacity of 14,991 N (3370 lb_f), which is more than the current requirement of 2,891 N (650 lb_f) in the EBR-II test specification.

The six mechanical screws connecting the HT9 duct wall to the irradiation shield are made from 17-4 PH, condition H-900 stainless steel. The screw has a diameter of 0.9525 cm (0.375 in.) and is concentric, with a hexagonal hole 0.488 cm (0.192 in) in diameter (Figure 3-3). It is located at the middle of each duct flat that connects the HT9 hex collar next to the top or bottom end fixture. During subassembly handling the direct pulling force on the top end fixture will be transmitted to the duct wall by the six screws. The load will transmit to the collar through bearing, and then to the screw through shear and finally to the wall through bearing again [8.9]. The allowable shear and bearing stresses of the connecting parts are 0.4 σ_y and 0.9 σ_y, respectively, as listed in the section "Rule for Design of Linear Support" of Ref. 8.10. Yield stresses at an irradiation temperature of 500°C are available in Ref. 8.5. According to Ref. 8.5, the yield stress of HT9 at 500°C varies between 450 MPa (65.3 ksi) and 500 MPa (72.5 ksi). The former is valid for unirradiated HT9, and the later applies to HT9 irradiated up to 20 x 10^{22} n/cm^2. The 17-4 PH

martensitic steel has a very high yield stress of 1227 MPa (178 ksi) at 500°C. During subassembly handling, the temperature is371°C and the use of the above yield stresses for structural evaluation is conservative. The two critical areas along the stress path are the bearing area of 0.0968 cm^2 (0.015 in^2) between the duct wall and the screw and the shear cross-sectional area of the screw, 0.507 cm^2 (0.0786 in^2). Therefore the loading capacity of the connector is limited by the bearing between the screw and the HT9 duct, since this is the smaller of the two critical areas. The analysis indicated that the minimum allowable loading capacity on the six screws is 23,576 N (5300 lb_f), which is considerably higher than the load limit of 2891 N (650 lb_f) in fuel handling.

(5) Intersubassembly Thermal Gradient

During steady state irradiation, the temperature difference across the duct wall due to intersubassembly heat transfer, ΔT_w, is closely related to the difference in average coolant temperature between adjacent subassemblies, ΔT_c. In EBR-II it would be impractical to examine all subassembly pairs to find the maximum ΔT_w. To envelope all possible cases, a worst combination of the hottest driver subassembly next to the coldest dummy subassembly was assumed. The maximum ΔT_c in this case may reach 128°C (230°F) at full reactor power and at the top of the subassemblies. Three thermal transients, namely TOP events UN-3 and UN-4 and LOF event UN-1, were considered for this analysis. The resulting computed coolant outlet temperatures from the ducts were taken as the forcing functions for the ΔT_w calculation, and the THTB Code [8.11] was employed to investigate the transient temperature difference across the duct wall. Figures 8.5 to 8.7 display the results. It was conservatively assumed in the analysis that the cold subassembly remains at the initial temperature of 740°F (393°C) throughout the transient. During full power steady state, the ΔT_w is 50°C (90°F), Figure 8-7, while at 40% of normal power it is 20°C, Figure 8-5 and Figure 8-6. For the thermal transients, this ΔT_w is raised to maximum values of 106°C (191°F) for the LOF case and 60°C (108°F) for the TOP cases as shown in Figure 8-5 to Figure 8-8. The flexural stress in the duct can be estimated as:

$$\sigma_{max} = E\alpha\Delta T_w/2(1-\nu)$$

where E and α are Young's Modulus and the linear thermal expansion coefficient, respectively, and ν is the Poisson's ratio. The maximum flexural stresses during steady state operation will reach 99.4 MPa for 12% CW 316SS and 64.2 MPa for HT9. Thus the thermal gradient effect is more pronounced for 12% CW 316SS. This is because the 316SS has a higher thermal expansion coefficient than that of HT9. The flexural stresses will rise to 210.7 MPa and 136.1 MPa respectively during the LOF transient.

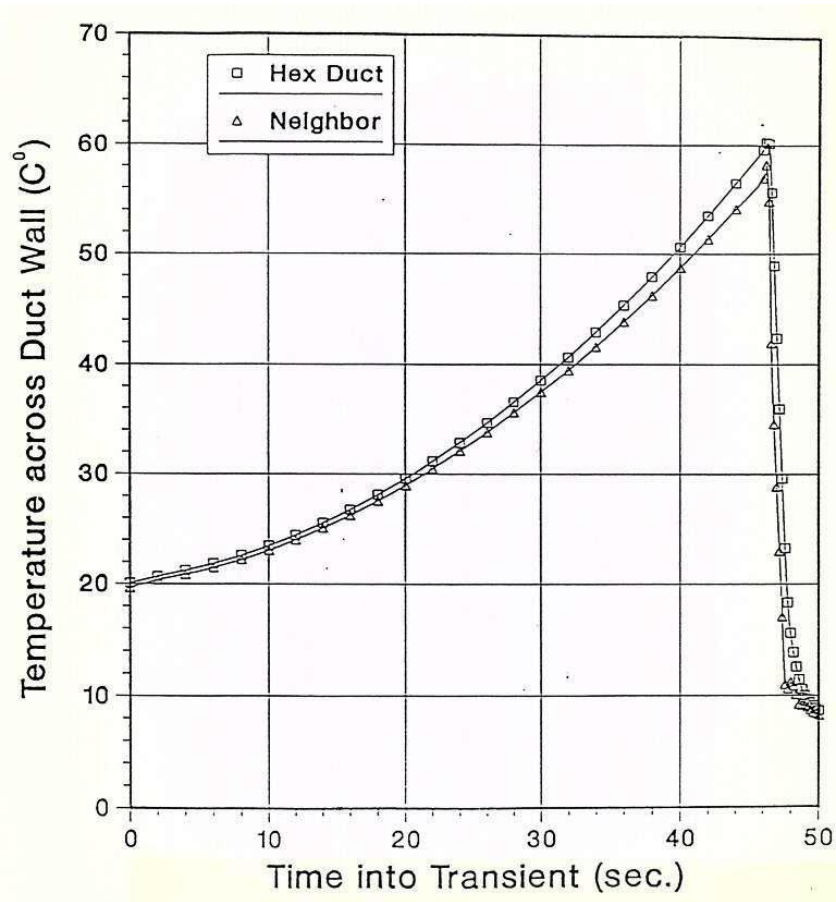

Figure 8-5 Temperature Difference Across Duct Walls of Adjacent Subassemblies During an Unlikely Transient Overpower Event (UN-3)

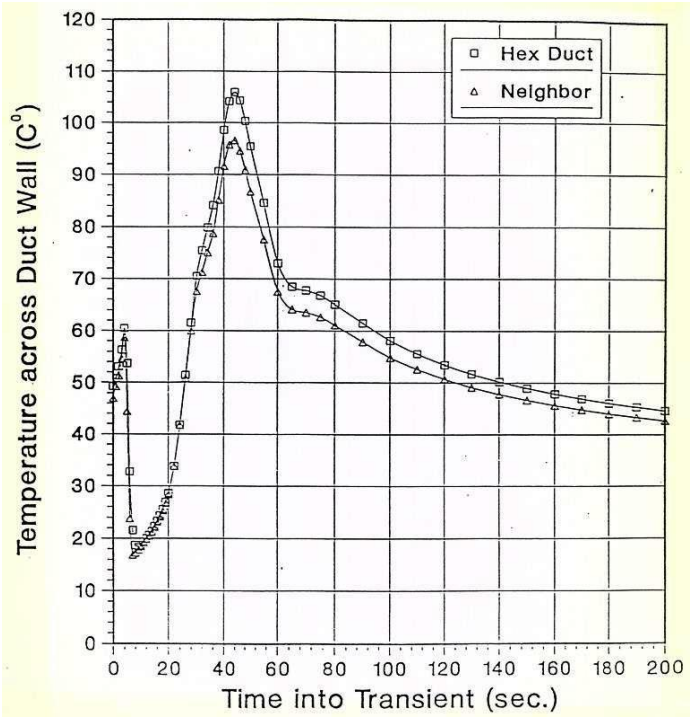

Figure 8-6 Temperature Difference Across Duct Walls of Adjacent Subassemblies During an Unlikely Transient Overpower Event (UN-4)

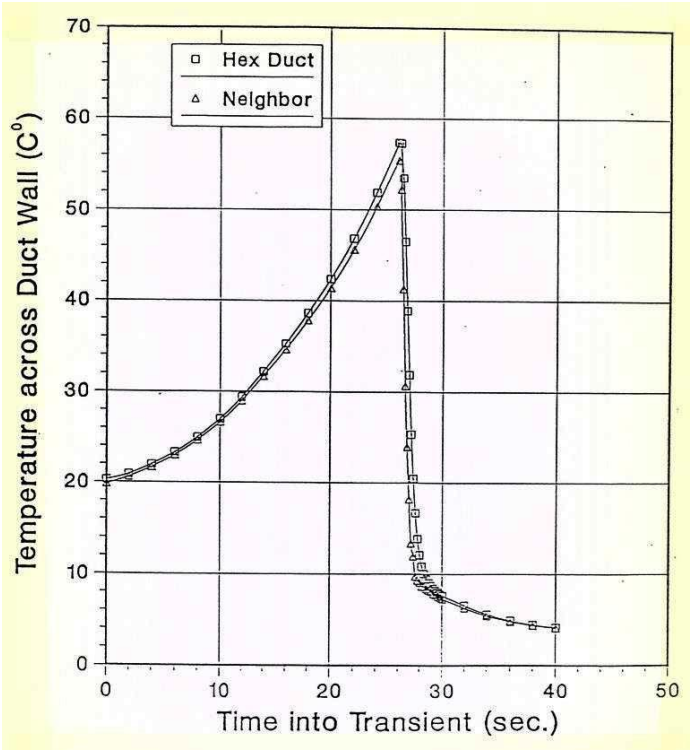

Figure 8-7 Temperature Difference Across Duct Walls of Adjacent Subassemblies During an Unlikely Loss-of-Flow Event (UN-1)

(6) Pressure Increase for Primary-Pump Runout Event

The two primary pumps, which have a combined delivery capacity of 580 kg/s, deliver a flow of 485 kg/s at a power of 62.5 MWt. During a primary-pump runout event, the flow in the subassembly will be increased by 20% from its normal operating condition, and the corresponding pressure on the hex duct is increased by 45% (the pressure change is proportional to the square of the flow). The maximum pressure loading occurs at a row-2 subassembly, and this subassembly is considered in the present analysis. When pressure loading is increased by 45% on the hex duct, the P_m and (P_L + P_b) (defined in Sec. 2.2.1) for 316SS and HT9 duct are identical and have the values 33.9 and 126.7MPa, respectively. The peak (P_L + P_b + Q) for 316SS and HT9 are 153 and 135 MPa, respectively.

8.4 Structural Evaluation

The above structural analyses have been chosen to be conservative. They envelope the deformation, stress and strain states under all loading conditions. The structural integrity is evaluated against the safety design criteria discussed in Section 2.2, and the results are summarized in Table 8-1. Five aspects of the detailed structural evaluation are discussed below:

(1) Deformation:

The design criteria for operation limits impose a duct dilation limit of 1.016 mm (40 mils). This limit was established to meet the storage basket restriction. The analysis has indicated that the maximum dilations are 0.918 mm (36.1 mils) for the 12% CW 316SS duct and 0.68 mm (26.8 mils) for the HT9 duct. It should be noted that dilations of HT9 and 316SS ducts were calculated based on fluences of 1.598 x 10^{23} n/cm^2 (15 at. % burnup) and 1.065 x 10^{23} n/cm^2 (10 at. % burnup), respectively. In both cases the maximum dilations do not exceed the limit of 1.016 mm (40 mils) for the target burnups. Consequently, the deformation requirement is satisfied.

(2) Stress and Strain

In the evaluation of primary stresses, the predicted primary stress limits are either based on

1.66 S_y or S_u, whichever is less, as indicated in Sec. 2.2.1. For 316SS and HT9, S_u is always less than 1.66 S_y for temperature and fluence ranges considered in the analysis, and S_u is therefore used as the basis for the structural evaluation. Also, the shape factor K is taken to be 1.0 since S_y/S_u is greater than 0.6 [8.12].

Table 8-1 Summary of Duct Structural Evaluation

Items	Criteria	Design or Operation Limits	Maximum Predicted Values	Comments
Steady-State Duct Stresses, MPa	2.2.1	P_m, $P_b + P_L \leq 385$ (316SS) ≤ 380 (HT9) $P_b + P_L + Q \leq 400$ (316SS) ≤ 365 (HT9)	$P_m = 23.4$ $P_b + P_L = 87.4$ $P_b + P_L + Q = 121$ (316SS) $= 103$ (HT9)	Design criteria are satisfied
UN-1 Duct Stresses, MPa	2.2.1	P_m, $P_b + P_L \leq 385$ (316SS) ≤ 380 (HT9) $P_b + P_L + Q \leq 246$ (316SS) ≤ 162 (HT9)	$P_m = 23.4$ $P_b + P_L = 87.4$ $P_b + P_c + Q = 230$ (316SS) $= 155$ (HT9)	Conservative thermal boundary conditions were applied in the analysis
Primary pump runout event duct stresses, MPa	2.2.1	P_m, $P_b + P_L \leq 385$ (316SS) ≤ 380 (HT9) $P_b + P_L + Q \leq 400$ (316SS) ≤ 365 (HT9)	$P_m = 33.9$ $P_b + P_L = 127$ $P_b + P_L + Q = 153$ (316SS) $= 135$ (HT9)	Design criteria are satisfied
Creep and fatigue damage, β	2.2.2	$\beta \leq 0.1$	$\beta = 0.001$ (316SS) $= 0.0002$ (HT9)	Design criterion is satisfied
Pulling force F, Newtons	2.2.3	$F \leq 2891$	Load Capacity = 14991 (316SS) 23576 (HT9)	The operation limit is less than the theoretical limit
Duct Dilation ΔD, mil (cm)	2.2.3	$\Delta D = 40$ (0.1016)	$\Delta D = 36$ (0.092) (316SS) $= 27$ (0.068) (HT9)	The predicted ΔD's are for the duct general performance
Strain at weld for 316SS duct, $\in$	2.2.5	$\in \leq 0.5\%$	$\in = 0.0139\%$	Design criterion is satisfied
Embrittlement of HT9 Duct, K_I, MPa $\sqrt{m}$	2.2.4	$K_I \leq 28$	$K_I = 1.9$	Design criterion is satisfied

The pressure and the thermal loading of the subassembly ducts both vary with the duct axial location and do not reach their respective maxima at the same location (e.g., at the bottom of the subassembly the pressure is at the maximum but the thermal loading is low). Therefore, the sum of the primary and secondary stresses must be evaluated over the entire

length of the subassembly in order to locate the peak value of the sum for evaluation of limit (3) of criterion 2.2.1. Furthermore, S_u is a function of both temperature and fluence, as shown in Figure 8-8 and Figure 8-9 [8.5]. In the structural evaluation the worst-case scenarios are considered.

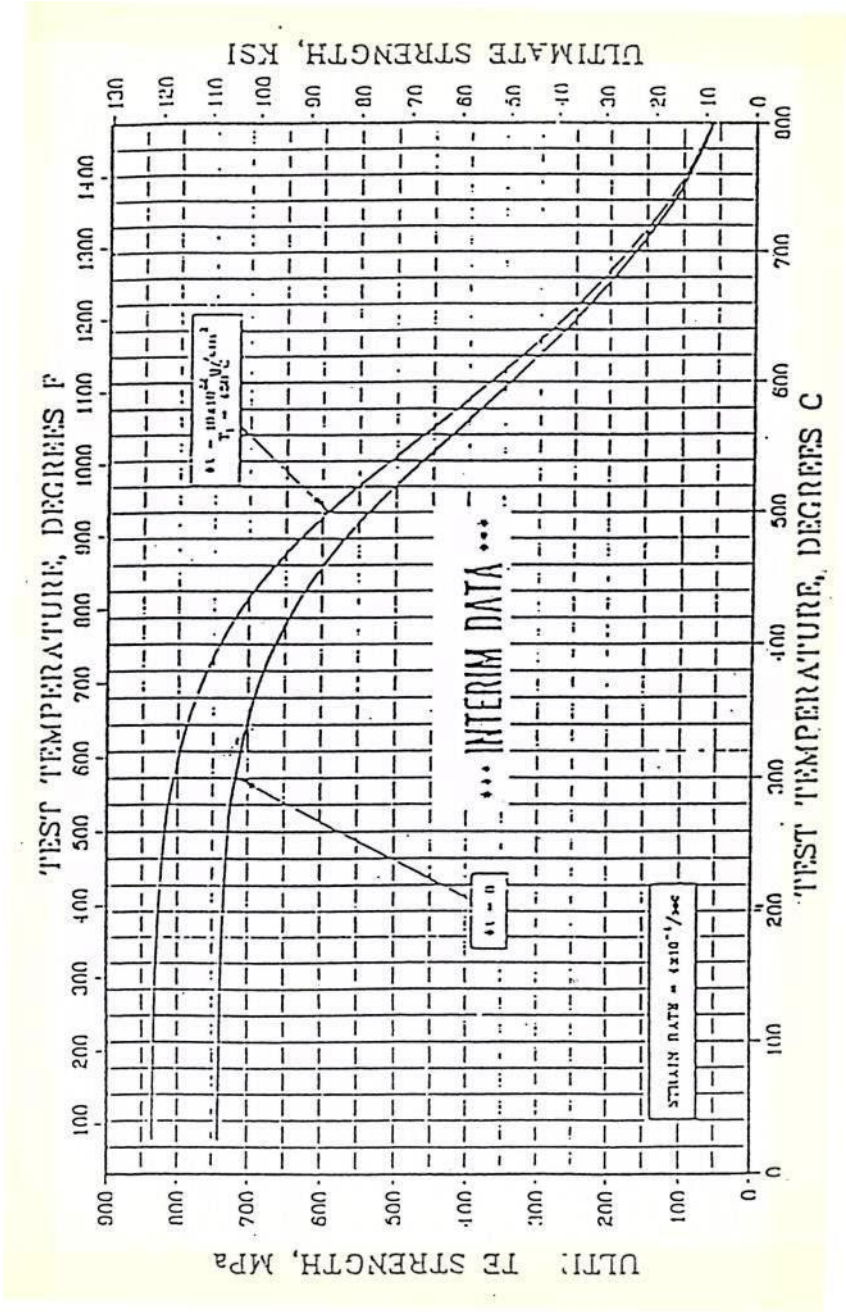

Figure 8-8 Ultimate Strength of HT9 (from Ref. 8.5)

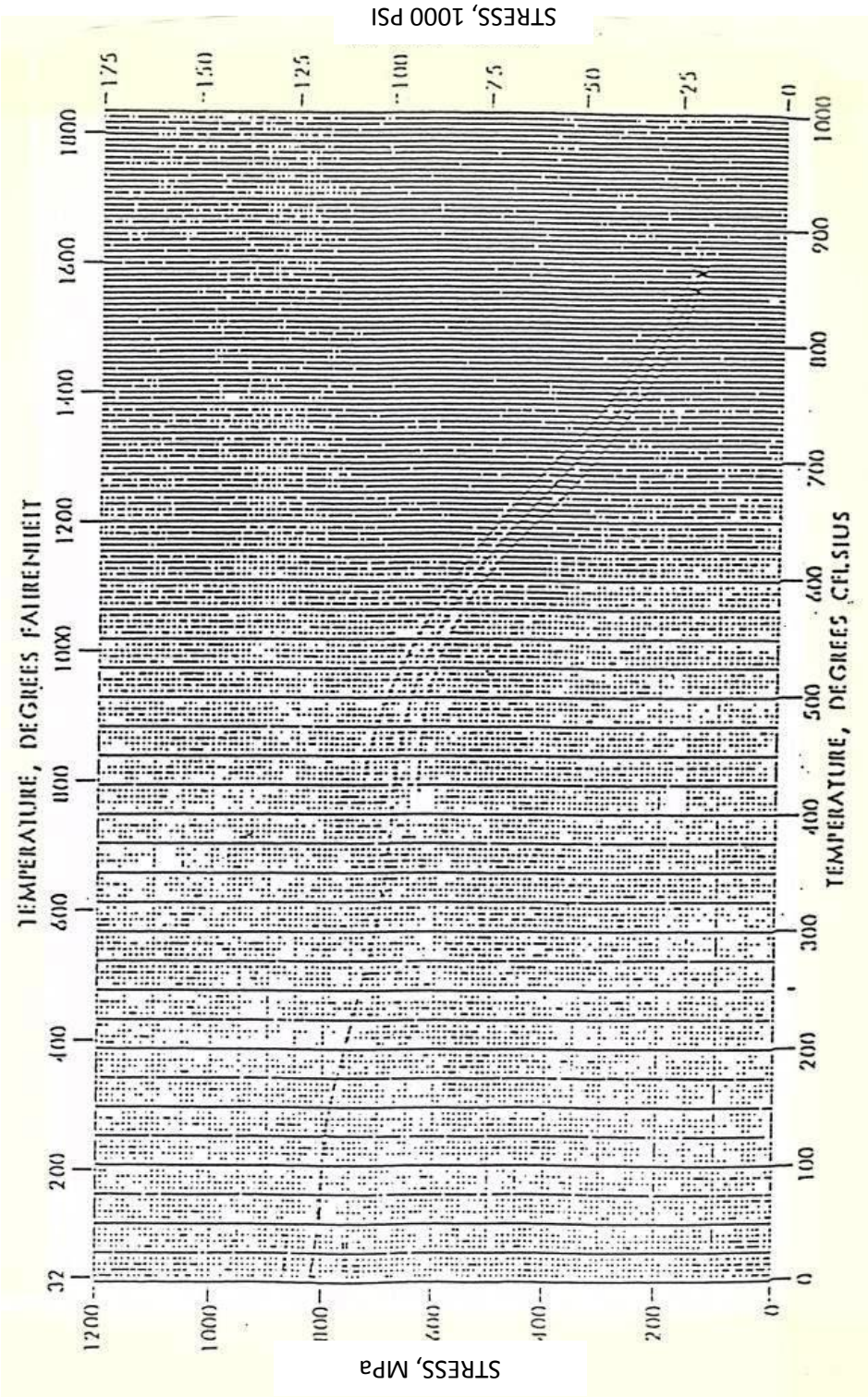

Figure 8-9 Ultimate Strength of Irradiated 20% CW 316SS (from Ref. 8.5)

(i) Steady-State Normal Operation

The subassemblies in rows 1 and 2 have the highest pressure loading, and the row-2 duct is considered in the present evaluation. The peak P_m and $(P_L + P_b)$ were found to be 23.4 and 87.4 MPa, respectively, occurring at the fuel bottom location, while the peak $((P_L + P_b) + Q)$ was found to be 121 MPa for 316SS and 103 MPa for HT9, occurring at the core midplane. The duct temperatures at the bottom and midplane of the core are about 371°C (700°F) and 445° (833°F), respectively, and the corresponding ultimate stresses are 700 and 660 MPa for unirradiated 316SS, and 690 and 610 MPa for unirradiated HT9, respectively. For level A service, α and χ in Section 2.2.1 are 0.55 and 0.6, respectively. The strain of either 316SS or HT9 duct is less than 1%. Criterion (3)(ii) of Sec. 2.2.1 is used for the evaluation. It can be seen that the predicted maximum P_m, $(P_L + P_b)$, and $((P_L + P_b) + Q)$ are considerably less than the allowable values for either the 316SS or the HT9 duct.

(ii) Off-Normal Transients

Results from Section 8-3 indicate that UN-1 represents the most severe thermal transient, while the primary pump runout event is the only transient that increases the pressure loading on the duct.

(A) UN-1 Loss-of-Flow Event

Although UN-1 is an unlikely event and should therefore be evaluated under Level B service limits (according to the service classification presented in Sec. 2.2), it was evaluated under Level A limits in order to assure that the evaluation bounds any anticipated LOF events as well. Therefore, the maximum primary stresses of this transient are identical to those obtained for the steady-state condition. The maximum primary-plus-secondary stresses are 230 and 155 MPa for 316SS and HT9 ducts, respectively, and occur at the top of the fuel. The material temperature at the top of the fuel is about 640°C (1185°F), and the corresponding ultimate stresses for 316SS and HT9 are 410 MPa (for a fluence of 10^{23} n/cm^2) and 270 MPa (unirradiated), respectively. It can be seen that the primary-plus-secondary stress

criterion is satisfied for both 316SS and HT9, even with the conservative assumptions applied on thermal environment and boundary conditions in the analysis.

(B) Primary Pump Runout Event

During this event, the pressure loading is increased by 45% from the steady-state condition. As a result, the primary stresses are increased by 45%. The maximum primary membrane and local membrane-plus-bending stresses are 33.9 and 126.7 MPa, respectively, and they occur at the bottom of the fuel. The maximum primary-plus-secondary stresses occur at the core midplane, and they are 153 MPa for the 316SS and 135 MPa for the HT9. These stresses are less than 0.55 S_u or 0.6 S_u in Section 2.2.1, so the design criteria are satisfied.

(3) Welding

Since the welds are located away from the core, the irradiation-induced creep or swelling is negligible. In fact, the fluence at the welds is less than 10% of the peak midplane value for all reactor locations. The membrane stress of the duct under coolant pressure is negligible due to the bulky neutron shield which supports the duct and reduces stress to nil. A nominal swelling strain of 0.03283% is estimated conservatively at 550°C and 2.0×10^{22} n/cm^2 for 316SS. In the case of HT9 there is virtually no swelling strain at all under the above fluence and temperature. Thus the accumulated inelastic strain in the welds is negligible. The only significant loading on the welds would be the handling load. EBR-II field load testing on subassemblies indicated that a 8,896 N (2000 lb_f) load would not fail the welds. Analysis shows a 14,991 N (3370 lb_f) capacity for the welds. Thus the welding has a large margin over the pulling load limit of 2,891 N (650 lb_f) in the Operating Instructions.

(4) Creep and Fatigue Damage:

The only fatigue damage to the duct is caused by the LOF and TOP transients of the reactor. These transients do not constitute more than 20 cycles throughout the life of the

subassembly. Since the maxima of the stress range are 210.7 MPa for 20% CW 316SS and 136.1 MPa for HT9, the corresponding elastic strain range is less than 0.15%. The allowable number of fatigue cycles for 316SS and HT9 is $2x10^4$ and $1x10^5$ cycles, respectively, and the corresponding fatigue damages are $1.0x10^{-3}$ and $2.0x10^{-4}$, respectively, assuming a total of 20 duty cycles through the life of the duct. The duct creep damage was evaluated with the stress rupture time formulation developed for cylindrical tubing. This formulation is conservative when applied to the duct, since tube rupture is caused by primary membrane stress alone, whereas the duct evaluation computes stress rupture time based on local membrane plus bending stresses. When the temperature of HT9 and 316SS is below 427°C, the creep damage can be neglected. The creep damage fraction during transients is less than $1.0x10^{-5}$, which is negligible. Thus the total damage fractions for 316SS at 10 at. % and HT9 at 15 at. % are 0.1% and 0.02% respectively. The duct is therefore able to withstand the operational transients safely throughout the design life.

(5) Embrittlement Evaluation of the HT9 Duct

The tempered martensitic structure of HT9 is known to undergo a transition from ductile failure to brittle failure at a particular ductile-brittle transition temperature (DBTT), and fracture analysis is required when loads are applied at a temperature lower than the DBTT. In Section 2.2.4, "Non-Ductile Failure Protection", it was proposed that the maximum temperature for brittle fracture for HT9 duct irradiated at 360°C be increased 33°C above the DBTT of 180°C in order to reach the upper shelf fracture energy. Thus HT9 duct under 213°C could fail with a brittle fracture. In the reactor as well as the Fuel Unloading Machine (FUM), the duct temperature is above the DBTT. However, when in the Inter-Building Coffin (IBC), the argon inlet temperature is about 49°C, while the temperature rise is usually between 65 to 95°C, but is limited to 277°C. It is possible for the duct to fall below the DBTT. There is no operational limit on the fuel handling load in the IBC; however, the load must be lower than the test load of 8896 N (2000 lb_f). This load was employed in the structural evaluation. In the brittle fracture failure analysis of the duct, an initial flaw with a rectangular notch is assumed, and the depth of the notch is assumed

to be 1/4 of the wall thickness [8.13]. The stress intensity factor is expressed as

$$K_I = \sigma_T \sqrt{\pi a}\ F_1(a/b)\ ,$$

where "a" is the crack depth, "b" is the wall thickness, σ_T is the nominal uniformly distributed stress, and F_1 is the shape factor of the crack. F_1 is a function of a/b and was found to be 0.98 based on Ref. 8.13. σ_T was found to be 45 MPa (6.54 ksi) due to a handling load of 8896 N (2000 lb_f) when a and b are 0.01 and 0.04 inches (0.025 and 0.1 cm), respectively. The stress intensity factor K_I was found to be 1.91 MPa $\sqrt{m}$ (1.74 ksi $\sqrt{in}$, which is considerably less than the critical stress intensity of 28 MPa $\sqrt{m}$ around the crack tip, as given in Ref. 8.14. Therefore, the DBTT of the HT9 duct will not cause fuel handling problems in the IBC.

8.5 Conclusions

Structural evaluation of the duct is summarized in Table 8-1. These results indicate that the design criteria are met. Dilation behavior of both HT9 and 316SS ducts shows that duct dilations are below the operation limit of 1.016 mm (40 mils) for 15 and 10 at. % burnups, respectively.

Section 8 References

8.1. Swanson Analysis Systems, Inc., Houston, Pennsylvania, "ANSYS Engineering Analysis System, Rev. 4.4."

8.2. D. A. Kucera and D. Mohr, "BOW-V: A CDC-3600 Program to Calculate the Equilibrium Configurations of Thermally Bowed Reactor Core," ANL/EBR-014, January 1970.

8.3. J. F. Koenig, Argonne National Laboratory, unpublished information (1990).

8.4. G. L. Hofman, et al., "Metallic Fuels Handbook," Argonne National Laboratory, ANL-IFR-29 (November 1985).

8.5. Nuclear Systems Materials Handbook, TID 26666, Rev. 37, Sept. 1988.

8.6. L. K. Chang, Argonne National Laboratory, unpublished information (1990).

8.7. L. K. Chang, M. J. Lee and J. Y. Ku, Argonne National Laboratory, unpublished information (1991).

8.8. R. C. Brubaker, Argonne National Laboratory, unpublished information (1988).

8.9. D. H. Thompson, Argonne National Laboratory, unpublished information (1993).

8.10. ASME Boiler and Pressure Vessel Code, Section III, Class 1 Components in Elevated Temperature Service, Case N-47-28, July 27, 1988.

8.11. G.L. Stephens and D. G. Campbell, "Program THTB, for Analysis of General Heat Transfer System," General Electric No R60FPD647, April 1961.

8.12. "Structural Design Guideline for FBR Core Components - Structural Design Criteria," RDT F9-7, Draft, August 1978.

8.13. Hiroshi Tada, etc. "The Stress Analysis of Cracks Handbook", Del Research Corporation, Hellertown, PA, 1973.

8.14. F. H. Huang, "Effect of Irradiation on the Fracture Behavior and Tensile Properties of an HT9 Duct," Westinghouse Hanford Company Report WHC-SP-0454, May 1989.

9 THERMAL-HYDRAULIC SAFETY ANALYSIS

9.1 Introduction

Calculations evaluating the performance of Mark-V and Mark-VA fuel have been assembled and are presented in this chapter. This analysis serves as the technical basis for converting the current EBR-II core into a ternary-fueled (U-Pu-Zr) core. Specifically, the aim of the analysis is to:

1) Establish limiting conditions (power, temperature and burnup) for operation of the fuel. The analysis must consider operational necessity as well as material limitation.
2) Show that the fuel meets the design requirements defined in Sec. 2.0 when evaluated for normal operation and all off-normal events in the duty cycle defined in Sec. 7.0. The evaluations are conducted from the limiting conditions for operation; consider all thermal, hydraulic and nuclear uncertainties as defined in Sec. 4.6, and assume the Reactor Shutdown System is operating at limiting safety system settings.

In the end, the conclusion that the analysis must support is: The Mark-V fuel, when operated at the extreme operational limits, will meet all safety-related design requirements. The analysis, then, is the basis for the Safety Limits, the Limiting Conditions for Operation, and the Limiting Safety System Settings specified in the EBR-II Technical Safety Requirements.

The calculational sequence used for the analysis is shown in Table 9-1. First, the subassembly powers, flows, flux levels, and other quantities are calculated for the representative small and large cores (six and six-plus rows) defined in Secs. 6.2.1.1 and 6.2.1.2 using the standard neutron and core flow methods described in Sec. 6.1.2. The key results are steady-state power, flow, and coolant bulk temperature rise for each subassembly. These results allow identification of the hottest subassembly in each row and provide powers and flows for detailed analysis of these limiting subassemblies. Detailed steady-state temperature calculations of the hottest subassembly in each row are calculated with SUPERENERGY-2 [9.1] in order to define the maximum pin conditions for mechanical analysis. A by-product of the SUPERENERGY-2

analysis is the peaking factor, defined as the ratio between the hottest subchannel sodium temperature rise and the average bulk sodium subassembly temperature rise. This thermal hydraulic calculation is carried out for the pins at beginning-of-life (BOL), which is the hottest condition, and corresponds to the methods applied in EBR-II experimental subassembly analysis. The results of the SUPERENERGY-2 analysis are described in Section 9.3.

Table 9-1 Design and Safety Calculational Sequence

Code	Nature of Calculation	Analysis	Output	Comment	
EBRFLOW SUBPOWR	Steady State Power and Flow	Nominal Reference Cores Thermal Conditions	• Subassembly Temperature Rise	Run Report Methodology	Design
SUPERENERGY-2	Steady-State Power and Flow	Fuel pin thermal condition at BOL of the hottest subassembly in each row	• Limiting Conditions in Reference Cores • Peaking Factor	Experiment Design Methodology	Design Sec 9.3
LIFE-METAL	Steady-State Flow; Quasi-Steady Power	Fuel pin thermal-mechanical	• Expected Behavior of Mark-V and -VA fuel in reference cores	Reference Fuel Performance Code for IFR Program	Design Sec. 9.4
LIFE-METAL	Steady-State Flow; Quasi-Steady Power	Fuel pin thermal-mechanical Parametric	• Irradiation temperature and burnup limits • Initial conditions for transient analysis	Reference Fuel Performance Code for IFR Program	Design Sec. 9.5 and Safety Sec. 9.6
SASSYS	Transient Power and Flow	Fuel pin transient thermal mechanical analysis	• Temperature and burnup limits via performance requirements	Reference thermal hydraulic code for IFR Program	Safety Sec. 9.7
Not Applicable*	Steady-State Power and Flow	Use uncertainties to set subassembly subchannel temperature limit	• Tech. Spec. Limits on Subchannel temperature		Safety Sec 9.8

*Safety evaluation based on design criteria.

The identified highest power and temperature fuel pins are then analyzed by the fuel pin mechanical code LIFE-METAL [9.2] to describe the expected behavior of Mark-V and Mark-VA fuel pins in the reference core loadings in EBR-II. The LIFE-METAL results are described in Section 9.4.

At this point in the analysis the measures of fuel pin performance (i.e., temperatures; cladding stress, strain, and wastage; and cladding damage) at the maximum conditions of the reference core loadings have been calculated and shown to meet the appropriate design criteria. This analysis corresponds to a design or reference analysis and does not define limits upon burnup or irradiation temperature that steady-state fuel pin performance issues impose.

The burnup and irradiation temperature limits are then defined by a separate parametric analysis (sensitivity study), once again using LIFE-METAL, Sec. 9.5. Initial conditions for transient thermal analysis are defined based upon the results of these calculations, Section 9.6. The uncertainty factors derived in Sec. 4.6 are used in a SASSYS [9.3] thermal hydraulic analysis to derive the subassembly subchannel temperatures which become the Technical Specification limits actually imposed, together with a burnup limit. SASSYS is then utilized to perform a full transient thermal-hydraulic and fuel pin mechanical analysis at the limiting conditions, including all uncertainties described in Section 4.6, and the burnup and irradiation temperature limits confirmed, or modified if necessary, based upon the criteria described in Section 2.1.4. This analysis is described in Section 9.7. The results of the LIFE-METAL and SASSYS analyses are then used in Section 9.8 to verify that all of the design criteria of Sections 2.1.4 and 9.2 are met.

The SASSYS calculations are performed using a combination of worst case conditions to bound the actual pin condition for all the time in reactor. Specifically,

(1) The gas pressure and clad wastage are based upon 10 at. % burnup,
(2) The fuel conductivity is chosen at the minimum expected (i.e., appropriate to 2 at. % burnup), the fuel solidus is based upon the minimum Zr content zone observed (2 wt.%),
(3) The eutectic threshold temperature is selected to be 650°C, i.e., appropriate for unrecycled fuel at burnups of greater than 10 at. % to ensure the effect of fission product carryover in recycled fuel is bounded.

This selection of conditions ensures that the conclusions drawn from the SASSYS analysis will apply to all irradiation conditions anticipated for Mark-V and Mark-VA fueled subassemblies, including those manufactured with recycled fuel.

9.2 Operational Limits

In specifying the conditions under which a fuel type is to be approved for use in EBR-II a number of different limits are applied. First, there are Safety Limits which are limits that protect the integrity of barriers to uncontrolled radiation release. In this case the barrier in question is the fuel pin cladding. The next type of limit is the Limiting Safety System Setting, (LSSS or LS^3), which gives the settings for automatic protective devices that monitor variables having significant safety functions. The LS^3 in this case are the 15% overpower, 12% underflow, 15% over temperature rise, and 17s period trip settings defined in the Technical Specifications. These must be independent of the fuel type because any of the approved driver fuel could, in principle, be in any core position at any time. Finally, there are Limiting Conditions for Operation, (LCO), which are conditions on equipment and technical characteristics of the plant required to ensure safe facility operation.

If a safety limit is exceeded, it must be demonstrated that a plant can still be brought to a safe and stable condition and maintained in that condition. Safety limits do not necessarily provide values against which monitored process parameters can be evaluated during operation; LS^3 and LCO's serve that function.

The fuel design criteria evaluate cladding damage using a cumulative damage methodology which explicitly accounts for the effect of time dependence of eutectic penetration and strain. The design criteria are predicated upon one fuel failure per core, which requires restricting the cumulative damage function (CDF) to 5% during normal operation and 10% accumulated over all anticipated design basis events plus the single most damaging unlikely event (see Sec. 2.1.4). To be consistent with the fuel design methodology, the fuel safety limit should also be expressed as a limit on the CDF. The limit which has been selected is that the CDF shall not exceed 1.0 for the limiting driver fuel pins.

A limit of CDF of 1.0 assures that the core is coolable and thus it can be demonstrated that the plant can be brought to a safe and stable condition. Assurance of core coolability at a CDF of 1.0 is indicated by the following argument. A CDF of 1.0 on the limiting fuel pins indicates a failure probability for these pins of 50%. As can be seen from the SUPERENERGY-2 results

presented in Sec. 9.3 and Appendix B, overcooling of the outer rows of pins in a subassembly and power and flow variations within the inner rows constrain the number of pins which operate at limiting conditions to less than 25% of the pins in the limiting subassemblies. At a CDF of 1.0, only half of these pins, or about 10% of the subassembly, will fail and these failures will be in the inner rows of pins of the subassembly. Since metallic fuel cladding breaches are of the pinhole type, they are benign with respect to blockage formation (see Secs. 5.2.2, 5.2.3, 5.2.4), and so neither pin-to-pin failure propagation within a subassembly nor failure propagation between subassemblies is indicated. Therefore, even in the highly improbable case of reaching a CDF of 1.0 in the limiting fuel pins, core coolability would still be maintained and uncontrolled radiation release would be avoided.

The coolant temperature LCOs in Rev. 47 of the EBR-II Technical Specifications are:

Reactor Outlet Temperature	892°F
Bulk Sodium Temperature	580-730°F
Local Coolant Channel Temperature	1050°F Mark-II 1040°F Mark-III and Mark-IIIA

The coolant channel temperature LCO's above are based upon avoidance of clad breach. As was described in Section 2.1.3, the solidus temperature in the low-Zr fuel zones of the Mark-V fuel is much lower than the solidus temperature of U-10Zr fuel, and the supporting LCOs for the Mark-V fuel have to also consider the requirement to avoid bulk fuel melting. This was considered for earlier fuel types, but the fuel-clad interface temperature was determined to be the limiting parameter and so no LCO specific to fuel melting was implemented.

As mentioned above, in reactor operation it is required that the subassembly temperatures are constrained by a specific LCO in the Technical Specifications (T.S.) which limits the peak sodium temperature rise of the subassembly for steady-state 100% power and flow condition. This temperature limit is customarily referred to as the hot channel temperature limit in EBR-II and assumes a reactor inlet temperature of 700°F. In order to accommodate core and blanket changes which shift power and flow from one region of the reactor to another, LCO's on subassembly power have also been added. Finally, a requirement that reactor coolant inlet temperature be maintained from 10°F below the authorized bulk sodium temperature up to 730°F

has been added as a LCO.

The Mark-V and -VA temperature and power limits are determined row by row by evaluation of the design criteria provided in Sec. 2.1.4 for both steady-state and transient operation of the plant, including off-normal events. In the present analysis, potential values for the T.S. limiting temperatures and powers are first determined by the steady-state analysis. The steady-state limiting values are determined by the condition that the fuel should be able to operate to its burnup limit at the boundary of normal operation (105% of normal power). These tentative limiting conditions of operation are then used to predict thermal transient behavior as well as fuel performance for off-normal conditions including parametric study at the bounds of the inlet temperature LCO (see Sec. 10.6). If the design criteria cannot be satisfied for the proposed T.S. limiting temperatures and powers during off-normal transients, then the T.S. limiting values are adjusted. Similar analyses are performed to verify that Mark-III and -IIIA fuels meet the design criteria when operating at the LCO's developed for Mark-VA fuel (see Sec. 10.3). This approach is also used to develop LCO's for Mark-IIC (safety rod) and Mark-IICS (control rod) subassemblies which are consistent with the design criteria (see Sec. 10.13).

9.3 Steady-State Thermal Analysis

The steady-state thermal analysis of the Mark-V and Mark-VA fuel pins has been performed using the SUPERENERGY-2 code, in which inter-subassembly heat transfer is neglected. The thermal performance of the Mark-V and Mark-VA fuel pins was calculated for the 6-row core conditions, as described in Section 6.2. In both loading conditions, fresh fueled Mark-V/Mark-VA fueled subassemblies are considered. The analysis was performed for the hottest subassembly in each row. The goals of the analysis are:

(1) To show that, during normal operation at beginning of life, the temperatures of fuel, safety and control rods are acceptable.
(2) To determine a row by row coolant peaking factor.
(3) To provide a benchmark for thermal analysis using LIFE-METAL.

9.3.1 Thermal Analysis of Reference Mark-V Fueled Subassemblies

The maximum temperatures in a core containing HT9-clad Mark-V fuel pins, have been

calculated. The subassemblies analyzed were taken from the 6-row core described in Section 6.2. The powers are summarized in Table 9-2 along with the subassembly flow rates at a core pressure loss of ~44 psi. The fuel pin temperatures were calculated using the SUPERENERGY-2 [9.1] program with the subassembly flow distribution given by the Cheng-Todreas model [9.4].

Table 9-2 Mark-V or Mark-VA Fuel Pins, U-20Pu-10Zr Fuel – HT9 Clad, Hottest Subassembly Power and Flow Rate

Location	Power kW	Flow gpm*
1A1	530.0	75.36
2F1	983.5	134.9
3A1 (Safety Rod)	666.2	98.64
3E2	939.5	119.3
4E2	844.8	93.24
5B3 (Control Rod)	540.5	64.16
5E2	390.0	59.16
6E3 (Increased Flow)	646.9	75.98
6F1 (Normal Flow)	581.3	67.78

*At 800°F and 44 psi ΔP

The detailed pin by pin results are given in Appendix B, together with a discussion of the analysis. The analysis is appropriate to beginning-of-life conditions because the thermal conductivity of the fuel is that appropriate to the unswollen fuel, which is only relevant at the beginning-of-life. The maximum condition in each subassembly is summarized in Table 9-3. It should be noted that the peak temperatures do not always occur at the same axial elevation. The safety and control rods will continue to use the Mark-IIC and Mark-IICS pins with U-10Zr. Because of the increased flux level, the control and safety rod powers and temperatures will increase from current levels, and therefore the peak temperatures of these subassemblies are included in Table 9-3. The peak temperature condition for each pin in the subassembly is summarized in Appendix B for the highest power subassembly in each row. The pin arrangement and pin number identifications in a subassembly are also given in Appendix B.

9.3.2 Thermal Analysis of Reference Mark-VA Core Fueled Subassemblies

The maximum temperatures in a core containing 316 stainless steel clad, Mark-VA fuel pins have been calculated. The core analyzed was again the 6-row core described in Section 6.2. The maximum subassembly row powers are given in Table 9-4 along with the subassembly flow rates. The radial power gradient in the subassembly was based on the BURNT program for a similar core. The fuel pin temperatures were calculated using the SUPERENERGY-2 [9.1] program with the subassembly flow distribution according to the Cheng-Todreas MIT model [9.4].

Table 9-3 Maximum Conditions in Mark-V Subassemblies and Mark-II Control and Safety Rods, Beginning-of-Life Conditions, 6-Row Core

U-20Pu-10Zr Unswollen Fuel Mark-V Fueled Subassemblies

		Peak Temperatures				
		Coolant	Clad Inside	Fuel Centerline	Bundle Average Flow Temperature	Peaking Factor
Location	Peak kW/ft	F C	F C	F C	F C	
1A1	16.19	928. - 498.	1017. - 547.	1353. - 734.	885. - 474.	1.23
2F1	15.37	936. - 502.	1016. - 547.	1330. - 721.	891. - 477.	1.24
3E2	15.02	957. - 514.	1033. - 556.	1329. - 721.	907. - 486.	1.24
4E2	13.79	994. - 534.	1063. - 573.	1320. - 715.	938. - 503.	1.24
5E2	12.80	917. - 492.	984. - 529.	1246. - 674.	873. - 467.	1.25
6E3	10.61	977. - 525.	1029. - 554.	1228. - 665.	923. - 495.	1.24
6F1	9.36	975. - 524.	1021. - 550.	1197. - 647.	925. - 496.	1.22

U-10Zr Unswollen Fuel, Mark-IIC Fueled Control and Safety Rod Assemblies

		Peak Temperatures				
		Coolant	Clad Inside	Fuel Centerline	Bundle Average Flow Temperature	Peaking Factor
Location	Peak kW/ft	F C	F C	F C	F C	
1A1	10.38	916. - 491.	992.- 533.	1151. - 622.	854. - 457.	1.40
2F1	8.60	979. - 526.	1040. - 560.	1167. - 631.	892. - 478.	1.45

The maximum condition in each subassembly is summarized in Table 9-4. (It should be noted that the peak temperatures do not always occur at the same axial elevation). The peak temperature condition for each pin in the subassembly is summarized in Appendix B for the highest power subassembly in each row. The pin arrangement and pin number identifications in a subassembly are also given in Appendix B.

Table 9-4 Maximum Conditions in Mark-VA Subassemblies,
Beginning-of-Life Conditions, 6-Plus-Row Core

U-20Pu-10Zr/316SS Clad Unswollen Fuel

		Peak Temperatures				
Location	Peak kW/ft	Coolant F C	Clad Inside F C	Fuel Centerline F C	Bundle Average Flow Temperature F C	Peaking Factor
1A1	16.19	928. - 498.	1019. - 548.	1358. - 737.	885. - 474.	1.23
2F1	15.37	936. - 502.	1017. - 547.	1333. - 723.	891. - 477.	1.24
3E2	15.02	957. - 514.	1034. - 557.	1332. - 722.	907. - 486.	1.24
4E2	13.79	994. - 534.	1062. - 572.	1320. - 716.	938. - 503.	1.24
5E2	12.80	917. - 492.	986. - 530.	1249. - 676.	873. - 467.	1.25
6E3	10.61	977. - 525.	1029. - 554.	1229. - 665.	923. - 495.	1.24
6F1	9.36	975. - 524.	1021. - 550.	1198. - 647.	925. - 496.	1.22

The subassembly coolant peaking factor of 1.26 used throughout the Mark-V safety case can be derived from the SUPERENERGY-2 analysis. Assuming an inlet temperature of 700°F, peaking factors for the limiting subassembly in each row can be computed from the ratio of the peak temperature rise and the average temperature rise along the subassembly. Table 9-3 and Table 9-4 list peaking factors for the limiting subassemblies, along with the peak and average coolant temperatures. It is clear that the peaking factors do not vary much by row. They are also consistent with the ratio of the interior pin flow area (0.00017037 m^2/pin) to the subassembly average pin flow area (0.0000139 m^2/pin) used by SUPERENERGY-2, which is 1.22. Since the interior region velocity and the subassembly average velocity used by SUPERENERGY-2 are nearly the same, and since density does not vary much across the subassembly. the ratio of the

areas should be representative of peaking attributable to variation in flow per pin. This would indicate that power skew plays a fairly minor role in the peaking factor. Note that the peaking factors in Table 9-3 and Table 9-4 are all consistent with the peaking factors given for the corresponding subassemblies in the Mark-III safety case.

Since the value 1.26 bounds the coolant peaking factors computed row by row using SUPERENERGY-2, this was the value applied throughout the core.

Table 9-3 and Table 9-4 also show that in normal operation there is a large margin to fuel/clad eutectic and fuel melting in the hottest subchannels at beginning-of-life conditions.

9.4 Thermal and Mechanical Steady-State Fuel Performance Analysis Using LIFE-METAL

The steady-state fuel analysis was done with the LIFE-METAL code to determine the capabilities and limitations of the fuel for a variety of powers, flows, and fuel burnups that could exist during duty cycle operation.

Analysis cases were done at rated reactor conditions (100% power), at the upper limit of normal operation (105% power), and at the upper limit of automatic protection (115% power trip). Conditions for two cores were studied - the small six-row core and a larger six-plus row core. These cores represent extremes realized in past practice. The calculations considered uncertainties in power, flow and material properties.

9.4.1 Thermal Analysis

The LIFE-METAL thermal analysis allows for temperature dependent fuel and cladding thermal conductivity, the effects of U, Pu, and Zr radial redistribution on thermal conductivity and volumetric heat generation, and feedback to the thermal analysis due to fuel and cladding deformation and fission-gas porosity. The results of the SUPERENERGY-2 calculations were used to select pins for detailed LIFE-METAL thermal analysis. Table 9-5 summarizes the Mark-V and Mark-VA cases chosen to yield the highest fuel and cladding temperatures, with an additional Mark-VA case for the highest fast flux because of the stainless steel swelling issue. These cases are also used for the cladding stress, strain, deformation, and lifetime analyses. For

all of the cases, a peak-to-average fast flux and power ratio of 1.12 was used consistent with the SUPENERGY-2 assumptions. The power reduction with burnup was taken as 1.67%/ at. % based on results of ORIGEN [9.5] calculations. Also, the low Zr zone was assumed to have a Zr content of 2 wt.% and to be located at a normalized radial position of $0.3 \leq r/r_o \leq 0.5$.

Table 9-5 Mark-V and Mark-VA Cases for LIFE-METAL Analysis

Design	**Case Type**	**Case ID**	**Peak Fast Flux, 10^{15} n/cm^2-s**	**Peak Linear Heat Rate, kW/ft**	**Coolant Outlet Temp., °C (°F)**
Mark-V	Peak Fuel Temperature	V-PFT	3.17	15.64	502 (935)
		V-PFTU-5op	3.56	18.11	527 (981)
		V-PFTU-15op	3.90	19.84	542 (1008)
	Peak Clad Temperature	V-PCT	2.61	14.00	537 (999)
		V-PCTU-5op	2.93	16.21	569 (1057)
		V-PCTU-15op	3.21	17.75	588 (1091)
Mark-VA	Peak Fast Flux	VA-PFL	2.40	12.43	479 (895)
		VA-PFLU-5op	2.69	14.40	501 (933)
		VA-PFLU-15op	2.95	15.77	513 (955)
	Peak Fuel Temperature	VA-PFT	2.22	12.24	522 (972)
		VA-PFTU-5op	2.49	14.18	552 (1026)
		VA-PFTU-15op	2.73	15.53	569 (1057)
	Peak Clad Temperature	VA-PCT	2.01	11.15	537 (998)
		VA-PCTU-5op	2.26	12.91	569 (1057)
		VA-PCTU-15op	2.48	14.14	588 (1091)

Cases V-PFT (Mark-V peak fuel temperature), V-PCT (Mark-V peak cladding temperature), VA-PFL (Mark-VA peak fast flux), VA-PFT (Mark-VA peak fuel temperature), and VA-PCT (Mark-VA peak cladding temperature) represent cases at 100% power and flow with no uncertainties and correspond to the SUPERENERGY-2 calculations in Section 9.3. Case V-PFT corresponds to the 1A1 case in Table 9-3. The maximum heat rating (15.64 kW/ft) and coolant outlet temperature (939°F) for this case correspond to pin #31 in subassembly 1A1, see Appendix B. Case V-PCT corresponds to the 4E2 position (Table 9-3). By using the subassembly peak linear heat rating (14.0 kW/ft) and the peak coolant outlet temperature (999°F), all pins are bounded by this case which is a combination of the power from pin #1 and coolant outlet temperature for pin #21. Notice that the PICT for location 5E4 (1070°F) is essentially the

same as for location 4E2 (1069°F). The reason that the higher-power (14.0 kW/ft) 4E2 pin was selected to bound all Mark-V PICT cases is that when uncertainties and the 5% direct overpower are applied to this case, the resulting PICT value is higher than it would be for the lower-power (12.3 kW/ft) 5E4 pin. For the Mark-VA cases, Table 9-4 was used to bound the peak fluence (pin #31 from 1A1), the peak fuel temperature (power for pin #1 and coolant temperature for pin #14 from 4E2) and the peak cladding temperature (power for pin #35 and coolant temperature for pin #32 from 5A4).

The second set of cases shown in Table 9-5 (V-PFTU-5op, V-PCTU-5op, VA-PFLU-5op, VA-PFTU-5op, and VA-PCTU-5op) correspond to the first set with the addition of uncertainties in operating conditions, fabrication variables and material properties along with a direct 5% overpower. The set corresponds to the operational requirements specified in Section 2.1.2 and is designed to operate within the design criteria for the life (10 at. %) of the fuel. The uncertainties are taken from Section 4.5. However, because LIFE-METAL is a deterministic code and uncertainties are statistical in nature, "equivalent-deterministic" factors were defined to give the correct fuel and cladding maximum temperatures based on a statistical uncertainty analysis. The logic of this analysis is as follows. Let T_{in} be the coolant inlet temperature, T_{cm} be the peak cladding temperature, and T_{fm} be the peak fuel temperature and $\Delta T_c = T_{cm} - T_{in}$ and $\Delta T_f = T_{fm} - T_{in}$. To be consistent with the statistical uncertainty analysis, the LIFE-METAL ΔT_c should increase by a factor of 1.13 due to uncertainties and the ΔT_f should increase by a factor of 1.21 due to uncertainties. To accomplish these results, the power was increased by 10.1%, the flow was reduced by 8.6%, and the fuel thermal conductivity was reduced by 15%. In addition, the fast flux was increased by 7% for the purpose of determining end-of-life cladding strains. After making these changes and checking the results, the power was then increased by 5% to give the required operational conditions.

The values for the adjustments in power, flow, fuel thermal conductivity, and flux were determined as follows. The uncertainty of 7% in fast flux is the value given for this parameter in `Table 4-4` through `Table 4-7` of Section 4.5.4.2. The uncertainty of 8.6% in flow is taken as the direct flow uncertainty factor for transient analysis given in Section 0. If the uncertainty in power is set to 10.1% and these three factors are applied to the nominal cases in Table 9-5, the peak cladding temperatures in cases V-PCT and VA-PCT are consistent with the cladding hot

channel factor of 1.134 derived statistically in Section 4.5.4.2.2. The 15% uncertainty in fuel thermal conductivity is the value which, when applied along with the above uncertainties on flux, flow, and power to the nominal cases, results in peak fuel temperatures in cases V-PFT and VA-PFT which are consistent with those obtained using the fuel hot channel factor of 1.214 derived in Section 4.5.4.2.1.

The final set of cases in Table 9-5 (V-PFTU-15op, V-PCTU-15op, VA-PFLU-15op, VA-PFTU-15op, and VA-PCTU-15op) are identical to the previous cases except that the power is increased by 15% rather than 5%. These cases are designed to determine if the calculated peak fuel temperature in the low Zr zone is within limits at the power LSSS (≤ 1040°C solidus temperature) and to determine the allowable time to be operated at 115% power condition. While lifetime calculations are also performed for these cases, the pins are not required to survive the 10 at. % goal burnup at these conditions.

The results from the LIFE-METAL thermal analyses are shown in Table 9-6 for the cases described in Table 9-5. For the cases (V-PFT and VA-PFL) without uncertainties and overpowers which used the SUPERENERGY-2 pin powers and coolant outlet temperatures directly, the LIFE-METAL results can be compared directly with the SUPERENERGY-2 results from Section 9.3. The peak cladding temperatures occur at the beginning of life (BOL) at the top of the fuel column. The LIFE-METAL results agree with the SUPERENERGY peak cladding outer-diameter temperature for Mark-V and Mark-VA pin #31 in 1A1 to within 1°C. This suggests that the film heat transfer coefficients are consistent. However, the LIFE-METAL PICT values are 7°C lower than the SUPERENERGY value for the HT9 Mark-V cladding and 3°C lower for the 316SS Mark-VA cladding. For HT9 the primary difference is in the thermal conductivity. LIFE-METAL uses a thermal conductivity value (29 W/m-K) recommended in Refs. 9.6 and 9.7 while SUPERENERGY uses the more recent correlation (26.1 W/m-K average conductivity in the range of 500-550°C) in the Metallic Fuels Handbook [9.8]. A secondary difference is that LIFE-METAL subtracts the OD scratch allowance (0.5 mils) from the cladding thickness in performing the thermal analysis.

The maximum fuel surface temperatures calculated by LIFE-METAL are 9°C lower than SUPERENERGY for the Mark-V 1A1 pin #31 and 5°C lower for the corresponding Mark-

VA case. Most of this difference is due to the difference in the cladding ID temperature calculation. Finally, the peak fuel temperature calculated by LIFE-METAL is 19°C lower than SUPERENERGY for Mark-V and 14°C lower for Mark-VA. Less than half of this difference is due to the cladding ID temperature calculation. The remaining difference is that SUPERENERGY uses the overly pessimistic Metallic Fuels Handbook fuel thermal conductivity, while LIFE-METAL uses a correlation which is a much better fit to the U-Pu-Zr data. Thus, SUPERENERGY does a better calculation of cladding ID temperature, while LIFE-METAL does a better calculation of temperature increase across the fuel radius.

Table 9-6 LIFE-METAL Results for the Mark-V and Mark-VA Calculations

Design	**Case Type**	**Case ID**	**Peak Clad. Temp., °C(°F)**	**Peak BOL Fuel Temp. °C (°F)**	**Peak Lifetime Fuel Temp. in Low Zr Zone, °C (°F)**
Mark-V	Peak Fuel Temperature	V-PFT	540 (1004)	708 (1307)	803 (1478)
		V-PFTU-5op	572 (1061)	791 (1456)	919 (1687)
		V-PFTU-15op	591 (1096)	828 (1522)	962 (1763)
	Peak Cladding Temperature	V-PCT	573 (1063)	708 (1307)	790 (1454)
		V-PCTU-5op	611 (1131)	789 (1452)	895 (1643)
		V-PCTU-15op	634 (1172)	826 (1518)	935 (1715)
Mark-VA	Peak Fast Flux	VA-PFL	513 (955)	652 (1206)	730 (1346)
		VA-PFLU-5op	539 (1002)	721 (1330)	828 (1522)
		VA-PFLU-15op	555 (1030)	751 (1384)	865 (1589)
	Peak Fuel Temperature	VA-PFT	555 (1032)	677 (1250)	750 (1383)
		VA-PFTU-5op	590 (1094)	749 (1380)	846 (1554)
		VA-PFTU-15op	611 (1131)	782 (1439)	880 (1617)
	Peak Cladding Temperature	VA-PCT	567 (1053)	671 (1240)	735 (1355)
		VA-PCTU-5op	604 (1120)	741 (1366)	825 (1517)
		VA-PCTU-15op	626 (1159)	774 (1425)	861 (1581)

The peak Mark-V cladding temperature is 611°C for the case which includes all uncertainties plus 5% overpower, which is below the 650°C limit. Likewise, the analogous Mark-VA case has a calculated peak cladding temperature of 604°C which is also below the 650°C limit. The peak fuel temperatures in the low Zr zone for Mark-V (962°C) and Mark-VA 880°C) are well below the solidus limit (1040°C) at 15% overpower, including uncertainties. Thus, LIFE-METAL calculations support the Mark-V and Mark-VA designs with regard to thermal

performance.

The maximum fuel centerline and low-Zr-zone temperatures are calculated to occur at a normalized axial location along the fuel column of $0.5 \leq x/L_o \leq 0.7$, and to occur in the burnup range of 1-2 at. % depending on pin power and coolant temperature rise. The radial distribution of Zr, along with the corresponding fuel solidus and liquidus temperatures, used for the calculations (Table 9-7) is typical of what has been observed in high power pins for this range ($0.5 \leq x/L_o \leq 0.7$) of axial locations. However, as shown in Figure 5-5, it is possible for lower power pins to have the low Zr zone at the fuel centerline in the upper part ($x/L_o \geq 0.88$) of the fuel column. Although this is not a "probable" distribution for a high-power pin, it is prudent to examine the effects of such a "low-power" Zr distribution on the thermal results. Thus, the highest power cases were rerun with the low-power Zr distribution assumed to exist at $0.7 \leq x/L_o \leq 1.0$ along the fuel column. The results are displayed in Table 9-7.

Table 9-7 Radial distributions for Zr weight fraction W_z and solidus (T_s) and liquidus (T_l) temperatures

Distributions	**Ring No.**	**W_z, Wt. %**	**T_s, °C**	**T_l, °C**	**T_s - T_{fm}, °C**	
					Mark-V	**Mark-VA**
Most-probable ($0 \leq x/Lo \leq 1$)	1	25	1290	1490	291	378
	2-3	2	1040	1100	78	160
	4	4	1060	1160	154	223
	5-10	11	1130	1330	257	318
	11	13	1150	1360	508	505
	12	15	1170	1390	560	547
Low-power ($0.7 \leq x/Lo \leq 1$)	1	1.1	1030	1070	24	102
	2	5.0	1080	1190	105	177
	3	7.5	1100	1260	158	223
	4-12	12.6	1150	1360	242	301

Distributions are for the most-probable and low-power distributions based on data. Rings are equal volume starting at the fuel centerline. Also shown are the LIFE-METAL-calculated difference between T_s and the maximum fuel temperature (T_{fm}) in each zone for the Mark-V and Mark-VA 115% overpower (with uncertainties) cases.

For the most probable Zr distribution, the maximum calculated fuel temperatures in the low Zr zones of Mark-V and Mark-VA 115% power cases are 77 and 159°C, respectively, below the fuel solidus temperatures. For the low power Zr distribution, these margins are reduced to 24 and 102°C for Mark-V and Mark-VA respectively. Therefore, even if a low Zr zone were to form at the fuel centerline for $0.7 \leq x/L_o \leq 1.0$, the fuel melting requirement would be met for both Mark-V and Mark-VA.

9.4.2 Wastage

LIFE-METAL has provisions for reducing the cladding thickness from its nominal value due to inner-diameter (ID) and outer-diameter (OD) fabrication tolerances and scratches; due to OD sodium/cladding corrosion, decarbonization, and intergranular attack; and due to ID fuel/cladding chemical or metallurgical interaction (FCCI). For both Mark-V (HT9) and Mark-VA (316SS) claddings, ID FCCI is characterized by fission product (FP) diffusion into the cladding and some cladding constituent (e.g. Fe, Ni, C, etc.) diffusion to the fuel. The fission-product-rich cladding layer tends to be very brittle (high microhardness) and cracked. Thus, it cannot be relied upon as a load-bearing cladding layer.

Let δ_o and δ_i be the cladding thicknesses (in mils) to be removed from the cladding OD and ID, respectively, for the purposes of the structural analysis. In the LIFE-METAL approach, δ_o is removed from the cladding OD for both the thermal and mechanical analysis. This is reasonable in that it is assumed that the dominant contribution to δ_o is corrosion. In the case of ID wastage, δ_i defines a cladding thickness layer which is present both for the thermal analysis and for determining fuel/cladding gap closure. However, the shear modulus is reduced by a factor of 10 and the creep rate of this layer is increased by a factor of 100 to make this fission product rich layer essentially non-load-bearing. It simply transmits the gas pressure or fuel/cladding mechanical interaction (FCMI) interface stress unabated to the intact base cladding.

Based on the discussion in Section 2.1.3, it is recommended that a tolerance/scratch allowance of 0.5 mils be used for both the cladding ID and OD. Also, given the fact that temperature and operating conditions change with time, it is recommended that δ_o and δ_i be determined from rate laws:

$$\delta_o = 0.5 + \int_0^t \dot{\delta}_o dt, \text{ mils} \tag{9.4-1}$$

and

$$\delta_i = 0.5 + \int_0^t \dot{\delta}_i dt, \text{ mils} \tag{9.4-2}$$

The δ_o functional form and parameters are determined from cladding properties and presented in Section A.4.

Appendix A describes two approaches to determining a wastage rate correlation. The first is a best-fit correlation, which is a best fit to the FCCI zone thicknesses measured for X441 and X447. This approach ignores the carbon depletion layer. It results in good peak strain predictions and good failure statistics for X447, but it predicts a low CDF and does not provide a bound on the data. The second approach, called the "design" or "Mark-V fit" correlation, uses a high enough wastage rate to bound the measured peak strains and the failure statistics based on a thermal creep strain criterion, while providing a wastage zone prediction in between the average peak FCCI zone and the average peak FCCI plus carbon-depleted zone. This second correlation treats about 80% of the carbon-depleted zone as wastage.

The rate correlation for corrosion formation (δ_i) at the cladding ID is assumed to be of the diffusional form. Figure A-11 shows the agreement between the "best-fit" and "Mark-V fit" HT9 correlations and the HT9/U-19Pu-10Zr and HT9/U-10Zr FCCI data in terms of an Arrhenius plot. The "best-fit" equation is derived by correlating local wastage at a particular axial location with the local cladding ID temperature at this location. The agreement between predicted and measured local FCCI zone is shown directly in Figure A-12. For design analysis purposes, it was found to be more prudent to correlate the maximum observed FCCI zone (occurring within $0.7 \leq x/L_o \leq 1.0$) with the maximum cladding ID temperature (occurring at $x/L_o=1.0$). This "Mark-V fit" is shown in the Arrhenius plot of Figure A-11 and is compared directly to the peak FCCI zone (FP) measured, as well as the combined FCCI and carbon-depleted (CD) zone, in Figure A-13. With regard to burnup (≤11 at. %) and peak cladding inner temperature (≤657°C), the data base brackets all of the Mark-V design cases. The primary source of uncertainty is in the use of the high temperature HT9/U-10Zr data to model the Mark-V HT9/U-20Pu-10Zr fuel pin. No high temperature HT9/ternary data are available to support this approach.

Because of the abundance of D9 FCCI data, as compared to 316SS data, the D9/U-19Pu-10Zr data were used to determine a best-fit to the local data. This "best-fit" correlation is compared to the D9/U-19Pu-10Zr data, as well as the limited 316SS/U-19Pu-10Zr and D9/U-10Zr data, in the Arrhenius plot of Figure A-14. The direct comparisons between predicted and measured local wastage and predicted and measured peak wastage are shown, respectively, in Figure A-15 and Figure A-16. For D9/U-19Pu-10Zr, the "best-fit" correlation gave the best agreement for both local wastage and peak wastage. However, the correlation predicted a peak wastage which is ~80% too high for the 316SS/U-19Pu-10Zr pin (T581) examined. In selecting the design correlation for Mark-VA analysis, the D9 correlation was scaled downward to give the best agreement between predicted and measured peak wastage for T581. Both correlations are compared to the T581 data in Figure A-17. The major uncertainty in this work is the extrapolation from the 316SS data base of Peak Inner Cladding Temperature (PICT) ≤ 590°C to the 650°C limit of the design range. Recent data for D9/U-10Zr with PICT=629°C indicate that the extrapolation gives a conservative upper bound on the peak wastage data.

Using Eqs. A.4-3 through A.4-11, the LIFE-METAL peak (x/L_o = 1.0), end-of-life (EOL) wastage predictions for the cases in Table 9-5 are shown in Table 9-8. The nominal cases (V-PFT, V-PCT, VA-PFL, VA-PFT, and VA-PCT) were run for a peak end-of-life burnup of 10 at. %. The remaining cases were run for the same times (400 to 450 full power days for Mark-V and 535 to 600 full power days for Mark-VA). Thus, the end-of-life burnups for the 5% and 15% overpower cases are higher than 10 at. % for the cases in Table 9-8. The corresponding CDF values and the limiting burnups for these cases are given in Section 9.4.4.

9.4.3 Stress

LIFE-METAL considers two main sources of stress on the cladding: gas pressure loading and fuel-cladding mechanical interaction (FCMI). The gas pressure (i.e., plenum pressure) loading is a rather straightforward prediction based on plenum volume, moles of gas released to the plenum, and plenum temperature. Based on data from similar high-power pins, ~ 80% of the gas generated in the fuel is released to the plenum after a transition period of up to ~ 5 at. % burnup. Thus, LIFE-METAL predictions for gas pressure can be, and have been, validated directly to data. With regard to FCMI, cladding diametral strain profiles are measured for irradiated fuel pins, and

the difference between total measured cladding strain and calculated cladding strain due to swelling and gas pressure is attributed to FCMI. Fuel swelling and creep parameters are adjusted to give a reasonably good fit to measured peak cladding strains and cladding strain axial profiles. Figure 4.1 shows the results of this exercise for U-19Pu-10Zr pins with HT9 and D9 cladding. In general, the cases are predicted within the certainty of the data up to 12 at. % burnup.

Table 9-8 End-of-Life Wastage Values for LIFE-METAL Cases

Design	**Case**	**EOL Wastage, µm (mils)**		
		ID	**OD**	**Total**
Mark-V	V-PFT	37 (1.44)	13(0.51)	50(2.0)
	V-PFTU-5op	53 (2.07)	13(0.52)	66(2.6)
	V-PFTU-15op	66 (2.61)	13(0.53)	80(3.1)
	V-PCT	57 (2.24)	13(0.53)	70(2.8)
	V-PCTU-5op	91 (3.59)	14(0.56)	105(4.2)
	V-PCTU-15op	120 (4.72)	17(0.67)	137(5.4)
Mark-VA	VA-PFL	25 (1.00)	13(0.50)	38(1.5)
	VA-PFLU-5op	35 (1.40)	13(0.51)	49(1.9)
	VA-PFLU-15op	45 (1.75)	13(0.51)	57(2.3)
	VA-PFT	47 (1.85)	13(0.51)	60(2.4)
	VA-PFTU-5op	83 (3.28)	13(0.53)	97(3.8)
	VA-PFTU-15op	117 (4.60)	14(0.54)	130(5.1)
	VA-PCT	59 (2.34)	13(0.52)	73(2.9)
	VA-PCTU-5op	112 (4.40)	14(0.54)	123(5.0)
	VA-PCTU-15op	154 (6.07)	16(0.64)	173(6.8)

The design criteria call for the wall-averaged hoop stress, $\bar{\sigma}_H$, due to gas pressure loading, to be less than 150 MPa for both HT9 and 316SS. The cases in Table 9-5 were reviewed to determine the maximum gas pressures, maximum interface pressures (FCMI and gas pressure), and maximum $\bar{\sigma}_H$. The results are presented in Table 9-9. In all cases the maximum plenum pressure (P_p), the maximum fuel-cladding interface pressure (P_{fc}) and the maximum cladding midwall hoop stress occur at the end-of-life with the fuel pin at full power. All of the peak $\bar{\sigma}_H$ values satisfy the design criterion for all cases for both plenum pressure loading and FCMI loading.

Based on LIFE-METAL sensitivity studies with 85% smear-density pins from X441 [9.9], it appears that LIFE-METAL gives a higher rate of FCMI and cladding strain increase with burnup than the data indicate. This is due primarily to the solid fission product swelling rate (1.62

vol.%/at. % vs. the 1.34 vol. %/at. % recommended in Section A.5) used for the Mark-V and Mark-VA calculations. Thus the P_{fc} and $\bar{\sigma}_H$ values in Table 9-9 should be viewed as upper bound values. The axial location of these peak $\bar{\sigma}_H$ values is in the lower third of the fuel column which is relatively cold. Thus, while the large FCMI values contribute somewhat to total diametral strain, their contribution to peak cladding thermal strain and cumulative damage fraction are negligible. The top of the fuel column, which has the highest cladding temperature and suffers the most damage, tends to be loaded by plenum pressure only. The end-of-life $\bar{\sigma}_H$ axial distributions for the Mark-V and Mark-VA operational requirement cases with the highest cladding temperatures (V-PCTU-5op and VA-PCTU-5op) are shown in Figure 9-1. Clearly, gas pressure loading dominates over the top half of the fuel column where the cladding is hottest.

Table 9-9 Maximum Gas Pressure (P_p), Interface Pressures (P_{fc}) and Mid-wall Cladding Hoop Stresses $\bar{\sigma}_H$ for the LIFE-METAL Cases in Table 9-5

Design	**Case**	**P_p, MPa**	**P_{fc}, MPa**	**$\bar{\sigma}_H$, MPa***	
				Due to P_p	**Due to P_{fc}**
Mark-V	V-PFT	7.3	17.1	45	99
	V-PFTU-5op	9.0	19.3	57	112
	V-PFTU-15op	10.1	22.2	66	129
	V-PCT	7.7	16.7	49	96
	V-PCTU-5op	9.5	19.0	68	110
	V-PCTU-15op	10.6	21.9	84	128
Mark-VA	VA-PFL	7.1	13.1	52	95
	VA-PFLU-5op	8.4	14.2	64	104
	VA-PFLU-15op	9.2	16.5	73	121
	VA-PFT	7.5	12.6	59	91
	VA-PFTU-5op	8.8	14.6	81	106
	VA-PFTU-15op	9.6	16.4	101	120
	VA-PCT	7.6	12.1	63	87
	VA-PCTU-5op	8.9	14.3	92	103
	VA-PCTU-15op	9.6	16.5	125	120

*The design limit is $\bar{\sigma}_H$ (due to P_p) < 150 MPa.

The cladding total strain profiles are shown in Figure 9-2 for these two cases. For the Mark-VA case, stress-free swelling dominates and FCMI contributes little to the total cladding strain. For the Mark-V case, swelling is negligible and gas-pressure and FCMI loading determine the total strain profile.

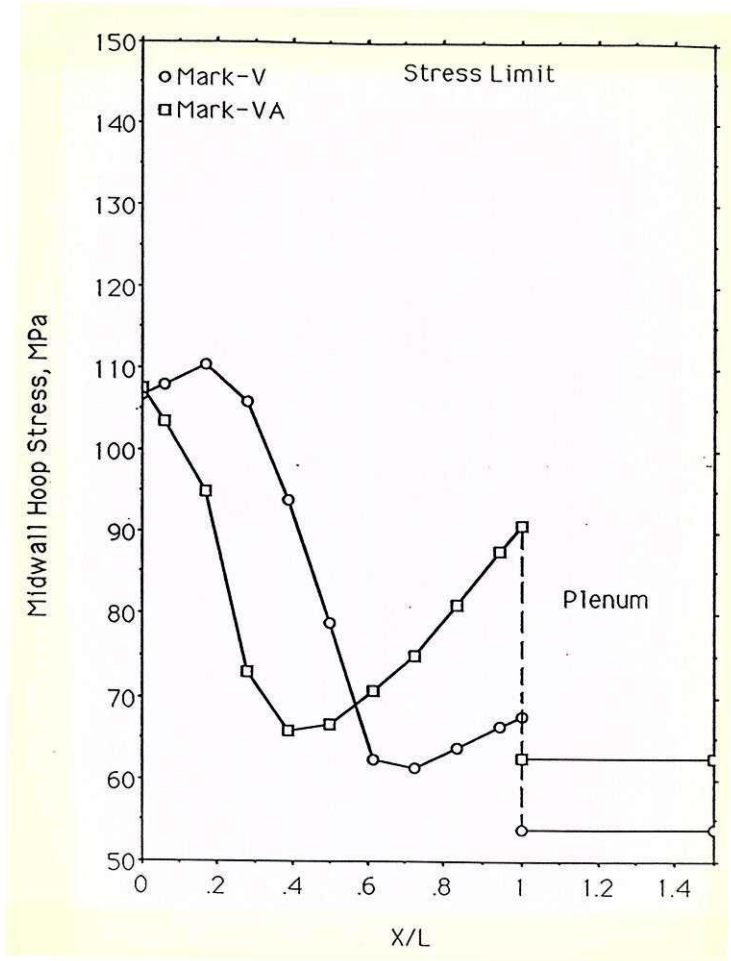

Figure 9-1 Mark-V and Mark-VA Cladding Midwall EOL Hoop Stress for 5% Overpower

9.4.4 Cladding Damage

Cumulative damage limits in terms of time to rupture and thermal creep strain are imposed on Mark-V and Mark-VA operation. The cumulative damage function (CDF) based on rupture time is limited to 0.05 while the thermal creep strain (TCS) is limited to 1% for Mark-V and 0.2% for Mark-VA. Table 9-10 summarizes the EOL thermal creep strain and CDF values for all of the cases in Table 9-5. Also included are the peak irradiation creep strains and the peak diametral strain. For all of these cases the maximum damage is at the top of the fuel column which is loaded by plenum pressure alone. The peak irradiation creep and total strains occur closer to midplane ($0.3 < x/L < 0.7$).

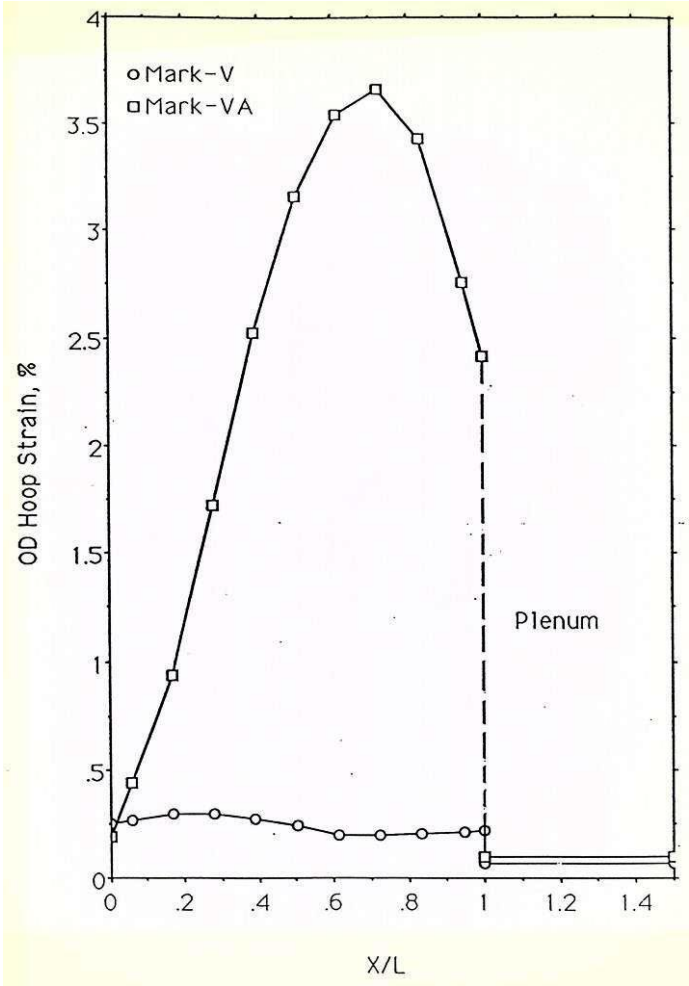

Figure 9-2 Mark-V and Mark-VA Cladding EOL Diametral Strain for 5% Overpower

9.4.5 Summary of Expected Behavior of Mark-V and Mark-VA Fuel in the Reference Cores

In terms of CDF and TCS, all cases meet the design criteria, up to 10 at. % burnup. The total strains for the HT9 cases are moderate and would cause no concerns with regard to pin-duct interaction. The 316SS Mark-VA cases have larger strains due to higher irradiation creep and swelling strain rates. However, even strains this high would not induce significant pin-duct interaction because of the duct swelling. The lifetime of 316SS subassemblies is more limited by duct dilation than by fuel pin deformation.

9.5 Fuel Performance Sensitivity Analysis

Thermal and cladding damage analyses were performed to determine the T.S. limiting

subassembly temperature of Mark-V and Mark-VA fuels such that steady-state design safety criteria in Section 2.1.4 are satisfied. Once these steady-state limits are established, transient performance must be addressed, see Section 9.6. The safety parameters to be considered in the design criteria for steady-state operation are cladding stress and strain, CDF, and temperatures of fuel, cladding and sodium. Parametric studies were performed to determine the allowable subassembly temperatures, which reflect the maximum reactor power allowed. LIFE-METAL was used to determine the temperature limit of the fuel pin, which satisfies for both Mark-V and Mark-VA

(1) the CDF design constraint (CDF <0.05),

(2) the thermal strain constraint (<1% for HT9 and <0.2% for 316SS), and

(3) the hoop stress constraint (<150 MPa) up to 10 at. % burnup for both Mark-V and Mark-VA fuels.

Table 9-10 Summary of End-of-Life Strains and Cumulative Damage Fractions for Mark-V and Mark-VA Cases

Design	**Case**	**CDF[1]**	**TCS[2], %**	**ICS[3], %**	**($\Delta D/D_o$)[4], %**	**Bu. at. %***
Mark-V	V-PFT	1.14E-9	0.019	0.262	0.278	10.0
	V-PFTU-5op	2.16E-7	0.034	0.309	0.330	11.4
	V-PFTU-15op	3.07E-6	0.048	0.378	0.407	12.4
	V-PCT	2.17E-7	0.034	0.232	0.249	10.0
	V-PCTU-5op	5.08E-5	0.071	0.277	0.298	11.5
	V-PCTU-15op	1.05E-3	0.126	0.339	0.365	12.4
Mark-VA	VA-PFL	9.25E-5	0.000	0.447	1.734	10.0
	VA-PFLU-5op	4.46E-4	0.003	0.586	2.705	11.4
	VA-PFLU-15op	1.08E-3	0.008	0.827	3.628	12.4
	VA-PFT	8.89E-4	0.008	0.479	2.064	10.0
	VA-PFTU-5op	6.54E-3	0.080	0.911	3.362	11.5
	VA-PFTU-15op	2.26E-2	0.157	1.441	4.705	12.4
	VA-PCT	1.89E-3	0.026	0.521	2.167	10.0
	VA-PCTU-5op	1.75E-2	0.149	1.087	3.659	11.4
	VA-PCTU-15op	5.00E-2	0.177	1.229	3.691	10.7

* Nominal calculations run to 10% burnup - all other (except VA-PCTU-15op) run for same irradiation time and hence higher burnup.

[1]Cumulative Damage Function

[2]Thermal Creep Strain

[3]Irradiation Creep Strain

[4]Total Strain

By limiting the design lifetime based upon these constraints, the maximum allowable fuel burnup becomes a function of peak inner cladding temperature (PICT).

LIFE-METAL results are given in Table 9-11 and Figure 9-3. The eutectic penetration model has not been included in these calculations, so the HT9 results above 650°C may be too optimistic. For a given cladding temperature, the Mark-V fuel can reach a higher burnup than that of the Mark-VA fuel. This is because the predicted FCCI cladding wastage is lower while the cladding is thicker for Mark-V fuel (18 mils vs. 15 mils). The insensitivity of the Mark-V results for a PICT < 640°C (1184°F) is because the thermal creep strain limit of 1% is exceeded just below the core midplane at ~21 at. % burnup due to FCMI. In the temperature range of 640°C (1184°F) to 645°C (1193°F), the maximum CDF and TCS values still occur below the core midplane, but the hoop stress constraint at x/L_o=1.0 is exceeded at 19-20 at. % burnup slightly ahead of the time that TCS exceeds 1% below core-midplane. For PICT ≥ 650°C (1202°F), design lifetime is determined by CDF reaching 0.05 at the top of the fuel column due to wastage-thinned cladding and fission gas pressure. In the case of Mark-VA, all of the cases are limited by CDF ≤ 0.05 at the top of the fuel column.

Based on Table 9-11, it is clear that the Mark-V interim target fuel burnup of 10 at. % is achievable within the design constraints for PICT ≤ 650°C. While the sensitivity study indicates that this burnup could also be achieved with PICT < 665°C, it would not be prudent to utilize this high a temperature because of the possibility of eutectic penetration for PICT>650°C. For Mark-VA with thinner cladding and a higher wastage rate, it is necessary to restrict PICT ≤ 627°C (1161°F) in order to achieve 10 at. % burnup within the limitations imposed by the design constraints.

The LIFE-METAL results at 10 at. % burnup for the PICT = 650°C case are of special interest as the EOL steady-state conditions form part of the basis for the initial conditions for the transient analysis. The total cladding OD and ID peak wastages are predicted to be 1.0 and 6.1, respectively, at x/L=1.0. Thus, the effective load bearing thickness for transient analyses is 10.9 mils. This corresponds to a mid-wall hoop stress of 77.2 MPa at the EOL plenum pressure of 8.41 MPa. The peak cladding diametral strain ($\Delta D/D_o$), thermal creep strain (TCS) and cumulative damage function (CDF) are predicted to be 0.439%, 0.203%, and 7.30×10^{-3},

respectively.

Table 9-11 Summary of Sensitivity Study for Lifetime vs. Peak Inner Cladding Temperature (PICT) for Mark-V and Mark-VA Cases

Design	Parameter (Peak)	PICT, °C[a]									
		610	620	630	640	645	650	655	660	665	670
Mark-V	Bu, at. %	-	21.03	21.01	19.78	18.78	16.09	13.03	11.06	9.61	8.40
	CDF	-	0.044	0.045	0.020	0.036	0.0501*	0.050*	0.050*	0.050*	0.050*
	TCS, %	-	1.00*	1.00*	0.85	0.68	0.55	0.51	0.49	0.47	0.46
	$\Delta D/D_o$, %	-	3.93	3.87	3.01	2.37	1.18	0.97	0.86	0.80	0.76
	Stress, MPa[b]	-	134	145	150*	150*	135	112	97	86	76
	Wastage, Mils	-	5.88	6.69	7.52	7.91	8.13	8.20	8.33	8.48	8.61
Mark-VA	Bu, at. %	14.64	11.79	9.48	7.67	6.90	6.19	5.57	-	-	-
	CDF	0.05*	0.050*	0.050*	0.050*	0.050*	0.050*	0.050*	-	-	-
	TCS, %	0.16	0.17	0.16	0.15	0.15	0.15	0.14	-	-	-
	$\Delta D/D_o$, %	7.25	4.89	3.00	1.72	1.28	0.94	0.69	-	-	-
	Stress, MPa	126	112	101	92	89	85	82	-	-	-
	Wastage, Mils	5.73	6.43	7.20	8.00	8.42	8.83	9.26	-	-	-

[a]The values listed are nominal goal values for each run. More precise calculated values are: 620.2, 630.3, 640.4, 645.4, 650.5, 655.5, 660.6, 665.6, and 670.7 for Mark-V; and 609.8, 619.7, 629.7, 639.6. 644.6, 649.5, and 654.5°C for Mark-VA.

[b]Due to plenum pressure

*Design criterion value (shaded boxes)

For the Mark-VA initial conditions for transient analysis, the information can be obtained either directly or by interpolation from Table 9-11. However, for convenience, an extra case was run at PICT=627°C to 10 at. % burnup. The peak OD and ID wastages were predicted to be 0.73 and 6.26 mils, respectively, at x/L=1.0. This gives an effective minimum cladding thickness of 8.0 mils. The peak values of mid-wall hoop stress (105 MPa), TCS (0.16%) and CDF (0.050) are also predicted to occur at x/L=1.0. The peak $\Delta D/D_o$ (3.47%) occurs at x/L=0.611. The EOL plenum pressure is 7.9 MPa. For the Mark-VA fuel with a PICT=650°C in Table 9-11, the relevant values are listed directly. The corresponding plenum pressure is 5.1 MPa.

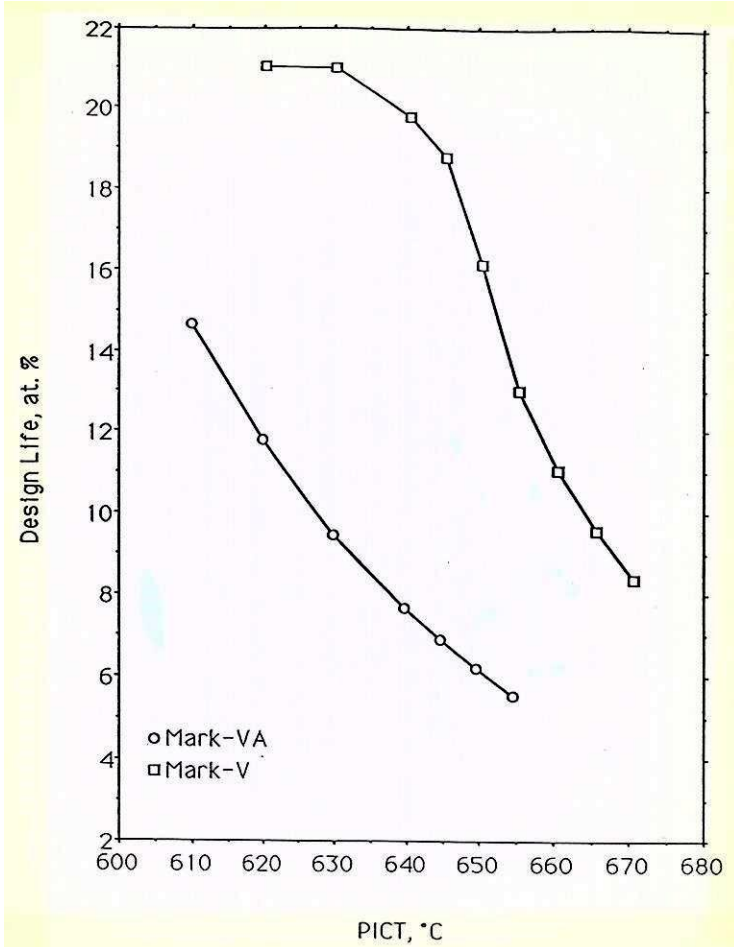

Figure 9-3 LIFE-METAL Predictions of Mark-V and Mark-VA Design Lifetimes vs. PICT

The above analysis assumed nominal cladding thicknesses. To determine the effect of manufacturing tolerances on the results, a sensitivity study [9.10] of the impact of cladding thickness on the design burnup limit has been performed. This study combined uncertainties in wall thickness and scratch allowance additively, rather than statistically, which is conservative. The results of this study indicate negligible impact on the burnup limit for a 3σ uncertainty in wall thickness. If, instead, the burnup limit is fixed at 10 at. %, an interpolation of results from [9.10] and Table 9-11 indicate that the limiting PICT for Mark-VA fuel would be reduced by only 0.3°C. The change in PICT would be even less if tolerances in wall thickness and the scratch allowance were combined statistically. This is a negligible change in PICT, and so the results of the fuel performance sensitivity are unchanged by inclusion of manufacturing tolerances.

9.6 Determination of Limiting Initial Conditions for Transient Analysis

Analysis of off-normal events begins with determining the steady-state conditions which limit peak subassembly power and power/flow ratio. Power/flow ratio is directly proportional to the coolant temperature difference axially across the subassembly, and so if a core inlet temperature of 700°F is assumed, the limit on power/flow ratio can be expressed as a T. S. limiting coolant outlet temperature. For a given subassembly flow and flow distribution radially across the subassembly, the limiting power is determined based on the limits on fuel temperature, steady-state cladding temperature, and transient cladding damage. The power and power/flow ratio are thus determined and establish a local coolant temperature Limiting Condition for Operation (LCO).

Table 9-12 summarizes the limiting conditions for Mark-V and Mark-VA fuel based upon the steady-state sensitivity analysis to 10 at. % burnup which was presented in Section 9.5, and this forms the basis for derivation of the local coolant temperature LCO's for inclusion in the Technical Specifications. It is necessary that the LCO's guarantee that the fuel temperature is limited by the fuel solidus temperature and that the Peak Inner Cladding Temperature (PICT) is limited to 650°C (1202°F) and 627°C (1161°F) for Mark-V and Mark-VA fuel, respectively, but these are not sufficient conditions. The transient performance of the fuel must also be evaluated and compared to the design criteria which have been summarized in Section 9.2. Table 9-12 also gives the extremal values of the key physical quantities (e.g., wastage) which are required as initial conditions for the transient analysis, together with the burnup at which they occur. These physical quantities are applied to the transient analysis irrespective of burnup, to ensure a bounding treatment of relevant phenomena for transient analysis.

Selection of a fuel solidus temperature must account for the fact that the ternary fuel composition does not remain uniform. The fuel tends to redistribute Zr and form three zones based on Zr weight fraction. These three zones are referred to as the inner, the intermediate, and the outer zones. If the outer radius of the fuel is denoted by r, then the intermediate zone is between 0.3r and 0.5r. The intermediate zone has a low Zr fraction and, consequently, a solidus temperature that is considerably lower than that of the other two zones. Therefore, the limit requiring the fuel temperature to stay below the fuel solidus temperature is set at 1041°C, the

solidus temperature of the intermediate zone.

Table 9-12 Limiting Conditions and Associated Physical Quantities for Mark-V and Mark-VA Fuel Based Upon Steady State Sensitivity Analysis to 10 at. % Burnup

	Mark-V	**Mark-VA**
PICT	650°C (BOL)	627°C (BOL)
Wastage	7.1 mils (EOL)	7.0 mils (EOL)
Plenum Pressure	8.4 MPa (EOL)	7.9 MPa (EOL)
Fuel Thermal Conductivity	50% nominal (2 at. % BU)	50% nominal (2 at. % BU)
Fuel Solidus Temperature	1041°C (EOL)	1041°C (EOL)
Inside Radius of Intermediate Zone for High-Power Fuel	0.3r	0.3r

Fuel temperature primarily depends on power, while the cladding temperature is a strong function of power/flow ratio. In EBR-II, the power of inner-row subassemblies is in general higher than that of the outer-row subassemblies, while power/flow ratio is higher in the outer-row subassemblies. Therefore, in the case of the Mark-V design, the steady-state temperatures of inner-row subassemblies are limited by the low solidus temperature in the fuel intermediate zone, while the outer-row subassembly temperatures are limited by the fuel-cladding eutectic liquefaction temperature. In the Mark-VA design, the cladding temperature limit is set by FCCI and is sufficiently lower than the eutectic liquefaction threshold that, even in the inner rows, the cladding temperature limit is reached at a lower coolant ΔT than is the fuel solidus temperature, and so the steady-state temperatures of subassemblies in both inner and outer rows are limited by the steady-state cladding temperature limit.

Since, according to the design criteria described in Sections 2.1.4 and 9.2, fuel solidus temperature is a limiting condition during both steady-state operation and off-normal transients, the limiting subassembly temperatures must be set so that this criterion is met during off-normal transients, as well as under the steady-state conditions described above. Off-normal transient analysis indicates that the outer row Mark-V and Mark-VA subassembly temperatures are limited by the steady-state design safety criteria, as expressed by the inner cladding temperature limits.

However, the inner three rows are limited by the fuel solidus temperature at a limiting power that would be reached during the transient overpower event UN-3, which is a single control rod runout in which the reactor is scrammed by the SOT trip function. If the reactor inlet temperature should vary below 700°F, the limiting power in the inner three rows is further reduced, and, in the case of Mark-V fuel, the fourth row will also be limited by the fuel solidus temperature. Since it is desired to allow an operating band on reactor inlet temperature of ±10°F, the limiting powers are those at which no fuel melting results if the UN-3 transient occurs at an inlet temperature of 690°F.

For the same power and flow conditions, the peak fuel temperature of the Mark-V fuel is higher than that of the Mark-VA fuel. However, the peak temperature difference between the two fuels is small in the low-Zr zone.

Because the factors which limit temperature vary from row to row, as well as between the two fuel designs, subassembly temperature limits must be derived for each design on a row-by-row basis. The temperature limit for each row must be independent of the core loading conditions. Currently, two core loadings are being considered: the 6-row and the 6-plus row. Therefore, both designs must be evaluated for both loadings in order to derive a single limit in each row for each design.

The temperature limits of both Mark-V and Mark-VA fueled subassemblies for steady-state operation with a reactor inlet temperature of 700°F and for the UN-3 transient with a reactor inlet temperature of 690°F were determined using the SASSYS code, and the results are tabulated in Table 9-13 for Mark-V fuel in the 6-row core, in Table 9-14 for Mark-V fuel in the 6-plus core, in Table 9-15 for Mark-VA fuel in the 6-row core, and in Table 9-16 for Mark-VA fuel in the 6-plus core. In all cases, the fuel temperature calculations have been based on a burnup of 2 at. %, where the fuel thermal conductivity is a minimum, so that the resulting fuel temperature is conservative. The hottest pin in each subassembly was analyzed using the SASSYS single-pin model to predict the thermal performance of the fuel pin. Since intersubassembly heat transfer is neglected in the single-pin model, the results of the thermal analysis are conservative. A peaking factor of 1.26 was used with the single-pin model to simulate the hottest pin in the subassembly. This factor bounds the peaking factors (peak-to-average coolant ΔT) which can be extracted for each row from the SUPERENERGY-2 analysis discussed in Section 9.3 and is identical to that used for Mark-III

and Mark-IIIA fuels. For the transient analysis, the design safety parameters of cladding strain, CDF, and eutectic penetration were calculated using the DEFORM-5 model [9.11] in SASSYS. Calculations were made for the driver subassemblies listed in Table 9-2 and Table 9-4. Note that two subassemblies in row 6 were evaluated: an increased flow subassembly, and a normal flow subassembly (listed in Table 9-13 - Table 9-16 as 6H and 6L, respectively).

Table 9-13 Limiting Conditions for Mark-V Fueled Subassemblies in the 6-Row Core

Row No.	Flow Rate (gpm/SA)	ΔT (°F)	Tech.Spec. Limit Coolant Subchannel Outlet Temp. (°F)**	Power Limit (kW/SA)	Fuel Temperature		Clad Temperature	
					Peak Transient (UN-3)†	Margin to Solidus (1041°C)	Peak Steady-State**	Margin to Eutectic (650°C)
1	138	239	939	989	***1041°C (1905°F)**	**0°C (1°F)**	583°C (1082°F)	67°C (120°F)
2	135	243	943	985	***1040°C (1905°F)**	**1°C (1°F)**	586°C (1087°F)	64°C (115°F)
3	119	269	969	965	***1040°C (1904°F)**	**1°C (2°F)**	602°C (1116°F)	48°C (86°F)
4	93	328	1028	917	***1039°C (1903°F)**	**2°C (3°F)**	638°C (1180°F)	12°C (22°F)
5	79	354	1054	835	1011°C (1851°F)	30°C (55°F)	***650°C (1202°F)**	**0°C (0°F)**
6H	76	356	1056	811	1000°C (1832°F)	41°C (74°F)	***650°C (1202°F)**	**0°C (0°F)**
6L	68	363	1063	738	967°C (1773°F)	74°C (133°F)	***650°C (1202°F)**	**0°C (0°F)**

*The power limits and the Tech. Spec. coolant subchannel temperatures are established by these temperatures, which approach design criterion 3.0 (fuel temperature below melting) in rows 1-4 and criterion 4.0 (steady-state cladding temperature below the eutectic) in rows 5 and 6.

**Based on 700°F reactor inlet temperature.

†For 690°F reactor inlet temperature.

Table 9-14 Limiting Conditions for Mark-V Fueled Subassemblies in the 6-Plus-Row Core

Row No.	Flow Rate (gpm/SA)	ΔT (°F)	Tech. Spec. Limit Coolant Subchannel Outlet Temp. (°F)**	Power Limit (kW/SA)	Fuel Temperature		Clad Temperature	
					Peak Transient (UN-3)†	Margin to Solidus (1041°C)	Peak Steady-State**	Margin to Eutectic (650°C)
1	132	246	946	976	***1041°C (1905°F)**	**0°C (1°F)**	587°C (1089°F)	63°C (117°F)
2	129	250	950	971	***1040°C (1904°F)**	**1°C (2°F)**	590°C (1094°F)	60°C (112°F)
3	114	278	978	952	***1040°C (1904°F)**	**1°C (1°F)**	607°C (1124°F)	43°C (82°F)
4	89	337	1037	903	***1040°C (1904°F)**	**1°C (2°F)**	643°C 1190°F)	7°C (12°F)
5	75	356	1056	806	1002°C (1835°F)	39°C (71°F)	***650°C (1202°F)**	**0°C (0°F)**
6H	73	359	1059	782	991°C (1816°F)	50°C (90°F)	***650°C (1202°F)**	**0°C (0°F)**
6L, 7	65	365	1065	712	959°C (1758°F)	82°C (148°F)	***650°C (1202°F)**	**0°C (0°F)**

*The power limits and the Tech. Spec. coolant subchannel temperatures are established by these temperatures, which approach design criterion 3.0 (fuel temperature below melting) in rows 1-4 and the limit for steady-state cladding temperature (established in Sec. 9.5) in rows 5-7.

**Based on 700°F reactor inlet temperature.

†For 690°F reactor inlet temperature.

A comparison of Table 9-13 and Table 9-14 shows that the limiting outlet temperatures for each row are lower for the 6-row core than for the 6-plus core, and therefore the 6-row core provides the limiting case for Mark-V fuel. The same is true for Mark-VA fuel, as seen by comparing Table 9-15 and Table 9-16. This situation reflects the fact that the power/flow ratio in the T. S. limiting subassemblies is higher in the larger, 6-plus core, in which subassembly flows are lower than in the 6-row core. In the inner rows, which are limited by fuel solidus temperature, power is the primary limiting condition, and the smaller flow in the 6-plus core has little effect on the peak fuel temperature for similar subassembly powers in the two loadings. In the outer four rows, which are limited by cladding temperature, power/flow ratio is the primary limiting condition. If power/flow ratio were the only limiting factor, the limiting outlet temperatures would be the same for both loadings in these rows. However, power does contribute a secondary effect, so that for a lower flow, the power/flow ratio must be increased slightly in order to maintain

the same cladding temperature. This difference in limiting conditions between the inner and outer rows is easily seen from Table 9-13 - Table 9-16, which show limiting outlet temperatures in the two loadings to be within a few degrees Celsius of each other in the outer rows (reflecting that cladding temperature is limiting and so power/flow ratio does not differ much between the two loadings) but separated by about 10°C in the inner rows (reflecting that fuel temperature is limiting and so power, rather than power/flow ratio, stays nearly the same between the two loadings).

Table 9-15 Limiting Conditions for Mark-VA Fueled Subassemblies in the 6-Row Core

Row No.	**Flow Rate (gpm/SA)**	**ΔT (°F)**	**Tech.Spec. Limit Coolant Subchannel Outlet Temp. (°F)****	**Power Limit (kW/SA)**	**Fuel Temperature**		**Clad Temperature**	
					Peak Transient (UN-3)†	**Margin to Solidus (1041°C)**	**Peak Steady-State****	**Margin to Maximum (627°C)**
1	138	240	940	992	***1040°C (1904°F)**	**1°C (2°F)**	584°C (1083°F)	43°C (78°F)
2	135	244	944	989	***1040°C (1904°F)**	**1°C (2°F)**	587°C (1088°F)	40°C (73°F)
3	119	271	971	970	***1040°C (1904°F)**	**1°C (2°F)**	602°C (1116°F)	25°C (45°F)
4	93	314	1014	879	1011°C (1852°F)	30°C (54°F)	***625°C (1157°F)**	**2°C (4°F)**
5	79	324	1024	765	958°C (1756°F)	83°C (150°F)	***625°C (1157°F)**	**2°C (4°F)**
6H	76	327	1027	746	950°C (1742°F)	91°C (164°F)	***626°C (1159°F)**	**1°C (2°F)**
6L	68	334	1034	679	918°C (1685°F)	123°C (221°F)	***626°C (1159°F)**	**1°C (2°F)**

*The power limits and the Tech. Spec. coolant subchannel temperatures are established by these temperatures, which approach design criterion 3.0 (fuel temperature below melting) in rows 1-3 and the limit for steady-state cladding temperature (established in Sec. 9.5) in rows 4-6

**Based on 700°F reactor inlet temperature.

†For 690°F reactor inlet temperature.

In addition to LCO's row by row on local coolant temperatures, it is necessary to specify limits on subassembly power row by row. These limits are needed to accommodate the planned replacement of the outer blanket depleted uranium subassemblies with stainless steel reflectors. One effect of this process will be a systematic shift of power and flow to the core region. This

shift must be done with local power limits imposed for two reasons. First, fuel temperature is strongly dependent on local power and is only weakly affected by coolant temperature. The inner row subassemblies are limited by fuel melting, and so coolant temperature limits alone are not sufficient to guarantee that fuel does not melt; power in these subassemblies must also be limited. Second, if fixed limits on subassembly outlet temperatures are imposed, any increase in subassembly power will increase the peak inner cladding temperature, thereby increasing cladding damage, and so in the outer rows, which are limited by steady-state cladding damage, coolant temperature limits are again not sufficient; power must be limited also.

Table 9-16 Limiting Conditions for Mark-VA Fueled Subassemblies in the 6-Plus-Row Core

Row No.	**Flow Rate (gpm/SA)**	**ΔT (°F)**	**Tech.Spec. Limit Coolant Subchannel Outlet Temp. (°F)****	**Power Limit (kW/SA)**	**Fuel Temperature**		**Clad Temperature**	
					Peak Transient (UN-3)†	**Margin to Solidus (1041°C)**	**Peak Steady-State****	**Margin to Maximum (627°C)**
1	132	247	947	980	***1040°C (1904°F)**	**1°C (2°F)**	588°C (1090°F)	39°C (71°F)
2	129	252	952	976	***1040°C (1904°F)**	**1°C (2°F)**	591°C (1095°F)	36°C (66°F)
3	114	279	979	957	***1040°C (1903°F)**	**1°C (3°F)**	607°C (1125°F)	20°C (36°F)
4	89	318	1018	853	1003°C (1837°F)	38°C (69°F)	***626°C (1159°F)**	**1°C (2°F)**
5	75	328	1028	742	951°C (1744°F)	90°C (162°F)	***626°C (1159°F)**	**1°C (2°F)**
6H	73	330	1030	721	941°C (1726°F)	100°C (180°F)	***626°C (1159°F)**	**1°C (2°F)**
6L, 7	65	336	1036	655	910°C (1670°F)	131°C (236°F)	***626°C (1159°F)**	**1°C (2°F)**

*The power limits and the Tech. Spec. coolant subchannel temperatures are established by these temperatures, which approach design criterion 3.0 (fuel temperature below melting) in rows 1-3 and the limit for steady-state cladding temperature established in Sec. 9.5) in rows 4-7.

**Based on 700°F reactor inlet temperature.

†For 690°F reactor inlet temperature.

Initially, the local coolant temperature limits and power limits will be as indicated in Table 9-13 through Table 9-16 (with the limits for rows 1-6 coming from Table 9-13 and Table 9-15 and the limits for row 7 coming from Table 9-14 and Table 9-16), and these values are constraining

for all cores. However, as power and flow are shifted to the core region as blanket subassemblies are replaced by reflectors, the current limits will reduce the flexibility of core design. Note, though, that, in the outer rows, these are excessively conservative limits, since at the limiting powers, the fuel is well below melting. If flow is shifted to the outer rows, the outer row limiting powers could be increased up to the point of reaching fuel melting if the coolant temperature limits were lowered to keep the peak inside cladding temperature at the limiting value. During the blanket replacement process, the option of allowing higher limiting powers in the outer rows by reducing the corresponding limiting coolant temperatures will be exercised if needed to avoid unnecessarily restricting core design and reactor operation.

The steady-state thermal and safety analyses indicated that, for a plenum gas pressure corresponding to a burnup of 10 at. %, a fuel thermal conductivity corresponding to 2 at. % burnup, and a reactor inlet temperature of 690°F or 700°F, whichever is more severe, the design safety criteria were satisfied for the subassembly temperature limits tabulated in Table 9-13 - Table 9-16. Since the 6-row core is the limiting case for both fuel types, it was used as the basis for the off-normal transient safety analysis. Thus, the subassembly temperature limits in Table 9-13 and Table 9-15 were used as the initial conditions for Mark-V and Mark-VA transient cladding damage calculations. The results of these calculations were used to check that design criteria 3.0 and 6.0 through 9.0 of Table 2-1 and Table 2-2 were met for Mark-V and Mark-VA fuel, respectively. The calculations were performed with the SASSYS code, and the design safety parameters of cladding strain, CDF, and eutectic penetration were calculated with the DEFORM-5 model in SASSYS, as discussed above with regard to the UN-3 event analysis. In addition, the peak fuel temperature in the intermediate zone and the coolant temperature were monitored, to assure that both remained within the safety limits. The single-pin model described above was used to model the hottest subassembly in each row.

In the steady-state calculations for both types of subassembly, the overall steady-state uncertainty factors (1.21 for fuel and 1.13 for cladding) derived in Section 4.6.4 were applied to the peak temperature in the low-Zr fuel intermediate zone and to the inner cladding temperature. The steady-state uncertainty factors are:

(1) Fuel 1.21,

(2) Cladding 1.13.

In the transient analyses, the transient uncertainty factors described in Section 4.6.5 were used. These include separate uncertainty factors for

(1) Power	1.07,
(2) Flow	1.06,
(3) Film coefficient	1.13,
(4) Cladding conductivity	1.05,
(5) Fuel conductivity	1.21.

These factors were derived so as to be consistent at the start of the transient with the steady-state uncertainty factors on fuel and cladding temperatures. Steady-state peak radial fuel temperature distributions for the row 1 subassembly at both nominal conditions and with uncertainties are given in Figure 9-4 for Mark-V fuel and in Figure 9-5 for Mark-VA fuel. These distributions were calculated at 5% overpower, i.e., at the boundary of normal operation.

Wastage was treated as loss of material strength while maintaining thermal properties. The DEFORM-5 model was modified to accommodate this treatment of wastage. The steady-state wastages of the limiting fuel pins are 6.1 mils on the inner surface and 1.0 mil on the outer surface for Mark-V fuel and 6.26 mils on the inner surface and 0.73 mils on the outer surface for Mark-VA fuel, as stated at the end of Section 9.5.

As discussed in Section 9.5, eutectic formation was not included in the steady-state analysis due to the low PICT of both the Mark-V (650°C) and Mark-VA (627°C) designs. Eutectic formation does occur in the off-normal transients and is included in the SASSYS calculation through the DEFORM-5 module. The eutectic penetration rate calculation in DEFORM-5 was based upon the ANL correlation (see Appendix A).

9.7 Safety Analysis

Transient analyses were performed using SASSYS for all the transients discussed in Section 7.5 except AN-5, which was analyzed with the LIFE-METAL code. These events are significant in terms of cladding temperature and damage. These include both loss-of-flow and

transient overpower events, all initiated at full flow. All loss-of-flow events were evaluated at 105% nominal power (65.625 MW). Scoping analyses of the protected TOP events (other than startup events) over a range of initial powers between 40% and 105% of normal power indicated that the damage is most severe when the transient is initiated at 40% of normal power (25 MW), and so TOP events other than startup events were initiated at 25 MW.

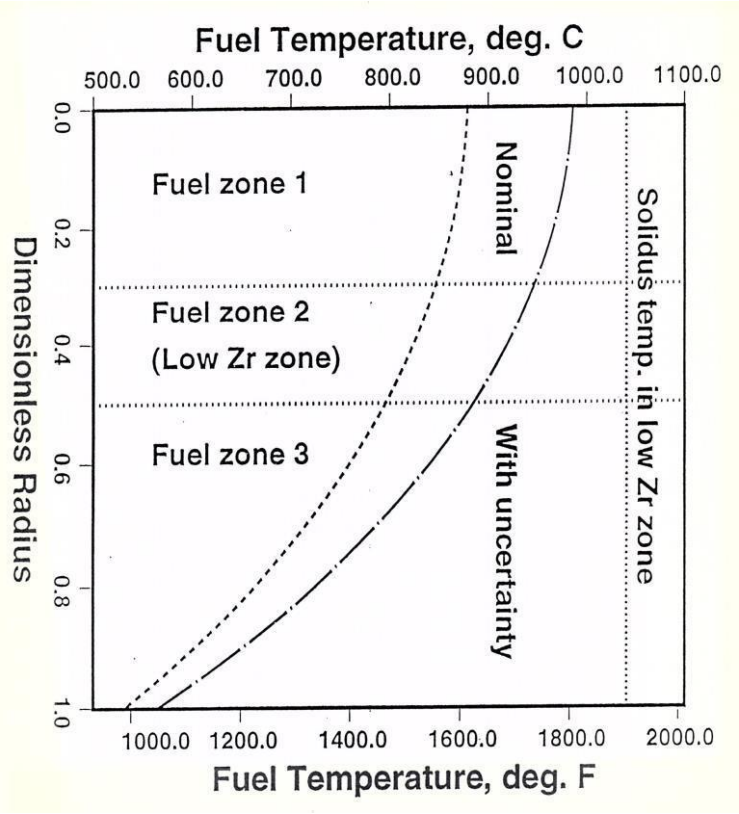

Figure 9-4 Fuel Temperature Radial Configuration Across the Hottest Pin of the T. S. Limiting Mark-V Fueled Subassembly in Row 1 at 105% Power in a Six-Row Core

All events were analyzed for all the driver subassemblies listed in Table 9-2 and Table 9-4. The power limits shown in Table 9-13 - Table 9-16 are the steady-state powers which, when applied with the flow rates shown, give the peak steady-state cladding temperatures listed. These are the powers used as starting conditions at 105% nominal power for the LOF off-normal transients. When multiplied by 40/105 = 0.38, they are the steady-state powers for the TOP off-normal transients which begin at 40% nominal power and give the peak transient fuel temperatures listed for the UN-3 event.

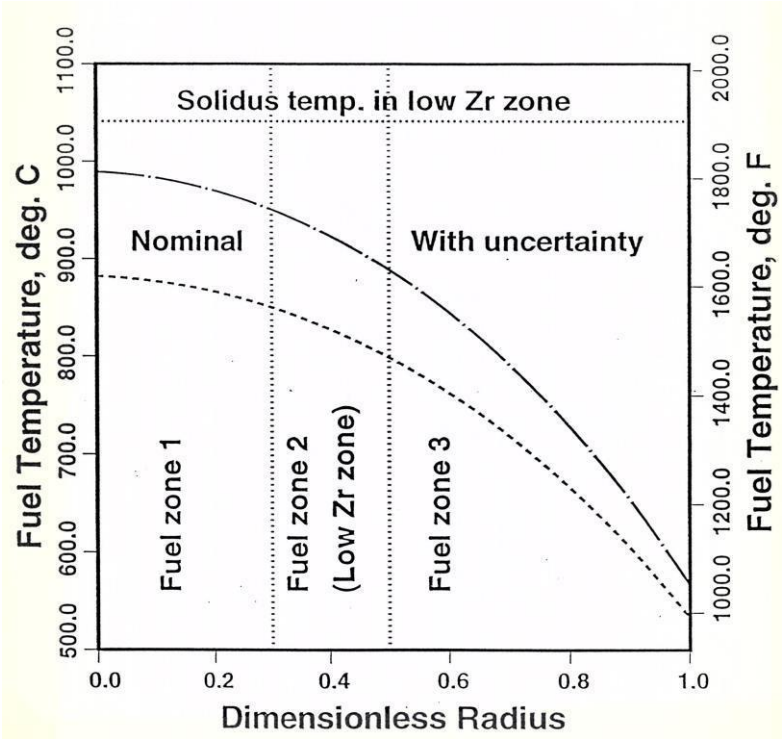

Figure 9-5 Fuel Temperature Radial Configuration Across the Hottest Pin of the T. S. Limiting Mark-VA Fueled Subassembly in Row 1 at 105% Power in a Six-Row Core

In the current EBR-II operation, when loss of primary flow occurs, the auxiliary pump will provide either 5% or 3.3% of normal flow, depending on whether the power to the pump is supplied by diesel generator or by battery. In the present analysis, the auxiliary pump is assumed inoperative in all LOF events, so that the failure of the auxiliary pump is not a safety issue. This assumption incorporates considerable conservatism into the temperature predictions for this analysis when compared with previous studies of Mark-III and Mark-IIIA fuels for similar transients.

The following limits and conditions were used in the analysis:

- Nominal power 62.5 MWt

  Initial power for loss-of-flow events is 105% nominal power. 65.625 MWt

  Initial power for transient overpower events is 40% nominal power. 25 MWt

  Initial power for starup events is 10^{-6} nominal power. 62.5 Wt
- Transient Uncertainty factors:

  Power 1.07

Flow	1.06
Film heat transfer coefficient	1.13
Cladding conductivity	1.05
Fuel conductivity	1.21

- The fuel conductivity is chosen as the minimum expected (i.e., appropriate to 2 at. % burnup)
- The gas pressure and clad wastage are based upon 10 at. % burnup
- The fuel solidus is based upon the minimum Zr content zone observed (2 wt.%)
- Secondary pump tripped 6 s after scram, unless the initiator is a loss of normal power.

Specifications for the off-normal event analyses, together with tables and plots of normalized power, normalized flow, and power-to-flow ratio, are given for all SASSYS off-normal transient analyses in Appendix C.

9.7.1 Normal Events

Normal events N-1 through N-4, discussed in Section 7.4.1, do not experience cladding temperatures higher than those of normal operation, and so these events are covered by the LIFE-METAL analysis of normal operation discussed in Section 9.4. The predicted CDF, stress, and strain of events N-1 through N-4 are considerably below the design criteria listed in Table 2-1 and Table 2-2 for normal operation.

9.7.2 Anticipated Events

Transients AN-1 through AN-4 of Section 7.5 were simulated with the SASSYS code. Transient AN-5 was evaluated with the LIFE-METAL code. These calculations were used to confirm that, for the significant anticipated events, the transient design criteria of Table 2-1 and Table 2-2 were met for Mark-V and Mark-VA fuel, respectively. Based on these criteria, the key design safety parameters to monitor during the transients are peak intermediate zone fuel temperature (criterion 3.0, no fuel melting), peak sodium temperature (criterion 9.0, no sodium boiling, to assure core coolability), cladding eutectic penetration during the transient (criterion 6.0, cumulative eutectic penetration below 5%), cumulative damage function at the end of the transient (criterion 7.0, CDF for all occurrences of all anticipated events, plus the worst unlikely event, below 0.1), and maximum cladding strain (criterion 8.0, total plastic hoop strain for all occurrences

of all anticipated events, plus the worst unlikely event, below 1% for Mark-V fuel and below 0.1% for Mark-VA fuel). With the exception of the peak sodium temperature, these parameters, plus the peak inner cladding temperature and the minimum saturation temperature, are summarized for all anticipated events in Table 9-17 for Mark-V fuel and in Table 9-18 for Mark-VA fuel. The peak sodium temperature is omitted because it is bounded by the peak inner cladding temperature, and so it is sufficient to compare the peak inner cladding temperature to the minimum sodium saturation temperature in order to guarantee that criterion 9.0 is met. Satisfaction of criteria 3.0 and 9.0 can be evaluated independently for each event; to ensure that criteria 6.0, 7.0 and 8.0 are met, results from all off-normal transients must be considered. This is done in Section 9.7.

For a given transient, cladding damage is more severe in the outer rows than in the inner rows, since cladding and sodium temperatures are higher in the outer rows (producing higher pin plenum pressures) and the time, if any, spent above the eutectic temperature is longer. The largest values of CDF, eutectic penetration, and strain occur in the row 6 normal flow subassembly, as does the lowest value of the saturation temperature. On the other hand, the rows in which the highest fuel and cladding temperatures occur vary with the transient. For the same transient, the row in which the peak cladding temperature occurs sometimes varies between the two fuel types, since the limiting cladding temperature is lower for Mark-VA fuel than for Mark-V fuel, and so the limiting powers (and, therefore, the initial fuel temperatures) in rows 4-6 are considerably lower for Mark-VA fuel than for Mark-V. Therefore, Table 9-17 and Table 9-18 indicate the rows in which the peak intermediate zone fuel and peak inner cladding temperatures reach their maxima for each transient.

9.7.2.1 Protected Loss of a Single Pump, AN-1

In this transient, which is initiated from 105% nominal power and full flow, one pump suffers a loss of flow due to a M-G output breaker trip, with the pump coasting down (pump speed going from 100% to 0) in about 32 seconds. The reactor scrams on flow, which is the primary trip in this situation. The behavior of the peak intermediate zone fuel, peak inner cladding, and peak sodium temperatures in the hottest pin in the row 6 normal flow subassembly is indicated in Figure 9-6 for Mark-V fuel and in Figure 9-7 for Mark-VA fuel. All temperature plots include uncertainties. In both cases, the temperatures reach their maxima at the time of scram, then drop off sharply and stabilize by about 100 seconds. The SASSYS analysis shows similar behavior in

the other rows.

Table 9-17 Mark-V Fuel Safety Parameters for Anticipated Events

	Event	Peak Fuel Temp. in Low Zr Zone (Criterion 3.0†)	Peak Clad Temp. (Criterion 9.0†)	Minimum Saturation Temp.* (Criterion 9.0†)	CDF* (Criterion 7.0†)	Eutectic Penetration (%)* (Criterion 6.0†)	Clad Strain (%)* (Criterion 8.0†)
LOF Events	AN-1 (Output Breaker Trip of One Primary Pump)	965°C (1769°F) (Row 4)	727°C (1341°F) (Row 5)	929°C (1705°F)	2.0×10^{-4}	1.3×10^{-3}	2.2×10^{-3}
	AN-2 (Input Breaker Trip of Both Primary Pumps)	952 °C (1745°F) (Row 4)	685°C (1264°F) (Row 6H)	909°C (1669°F)	4.8×10^{-4}	5.2×10^{-4}	3.9×10^{-3}
TOP Events	AN-3 (Single Rod Ru-nout (0.01$/s), Power Trip)	986°C (1807°F) (Row 1)	663°C (1225°F) (Row 5)	976°C (1790°F)	3.0×10^{-5}	0.0	2.6×10^{-4}
	AN-4 (Single Rod Runout (0.01$/s) at Startup, Period Trip)	371°C (700°F)	371°C (700°F)	971°C (1779°F)	$<10^{-6}$	0.0	$<10^{-6}$
	AN-5 (Power/flow Ratio Rises Due to a Drift Upwards in Power or a Drift Downwards in Flow)	979°C (1795°F) (Row 1)	677°C (1251°F) (Row 6L)	970°C (1779°F)	$<10^{-6}$	2.5	1.2×10^{-3}

*These values occur in the row 6 normal flow subassembly 6F1 (designated row 6L). All values in the table include uncertainties.

†Design Criteria:

3.0 There shall be no bulk fuel melting in anticipated or unlikely transients.

6.0 The cumulative cladding eutectic penetration for anticipated events, the single most damaging unlikely event, and the extremely unlikely event is limited to 5% of the wall thickness.

7.0 The accumulated CDF for anticipated events and the single most damaging unlikely event is limited to 0.1.

8.0 The cumulative hoop strain resulting from anticipated events and the single most damaging unlikely event, through the life of the fuel, is limited to 1% for HT9.

9.0 There shall be no sodium boiling in anticipated, unlikely or extremely unlikely transients.

Table 9-18 Mark-VA Fuel Safety Parameters for Anticipated Events

	Event	Peak Fuel Temp. in Low Zr Zone (Criterion 3.0†)	Peak Clad Temp. (Criterion 9.0†)	Minimum Saturation Temp.* (Criterion 9.0†)	CDF* (Criterion 7.0†)	Eutectic Penetration (%)* (Criterion 6.0†)	Clad Strain (%)* (Criterion 8.0†)
LOF Events	AN-1 (Output Breaker Trip of One Primary Pump)	950°C (1742°F) (Row 3)	698°C (1288°F) (Row 4)	929°C (1705°F)	3.1×10^{-5}	5.4×10^{-4}	2.3×10^{-6}
	AN-2 (Input Breaker Trip of Both Primary Pumps)	949°C (1740°F) (Row 1)	657°C (1214°F) (Row 6L)	909°C (1669°F)	2.2×10^{-5}	0.0	3.1×10^{-6}
TOP Events	AN-3 (Single Rod Runout (0.01$/s), Power Trip)	990°C (1815°F) (Row 1)	638°C (1180°F) (Row 4)	976°C (1790°F)	2.8×10^{-6}	0.0	$<10^{-6}$
	AN-4 (Single Rod Runout (0.01$/s) at Startup, Period Trip)	371°C (700°F)	371°C (700°F)	971°C (1779°F)	$<10^{-6}$	0.0	$<10^{-6}$
	AN-5 (Power/flow Ratio Rises Due to a Drift Upwards in Power or a Drift Downwards in Flow)	982°C (1800°F) (Row 1)	651°C (1204°F) (Row 6L)	970°C (1779°F)	7.7×10^{-6}	0.0	4.0×10^{-3}

*These values occur in the row 6 normal flow subassembly 6F1 (designated row 6L). All values in the table include uncertainties.

†Design Criteria:

3.0 There shall be no bulk fuel melting in anticipated or unlikely transients.

6.0 The cumulative cladding eutectic penetration for anticipated events, the single most damaging unlikely event, and the extremely unlikely event is limited to 5% of the wall thickness.

7.0 The accumulated CDF for anticipated events and the single most damaging unlikely event is limited to 0.1.

8.0 The cumulative hoop strain resulting from anticipated events and the single most damaging unlikely event, through the life of the fuel, is limited to 0.1% for 316SS.

9.0 There shall be no sodium boiling in anticipated, unlikely or extremely unlikely transients.

The maximum cladding temperature occurs in row 5 for Mark-V fuel and in row 4 for Mark-VA fuel (by a few degrees), but the pin plenum pressure is a little higher in the row 6 normal flow subassembly (since the sodium in the plenum region above the top of the fuel is hotter due to

higher power/flow ratio in row 6), and so the greatest damage occurs in subassembly 6F1, where the plenum pressure is greatest. The highest fuel temperature occurs in row 4 for Mark-V fuel (a few degrees higher than in rows 1-3) and in row 3 for Mark-VA fuel (again, a few degrees higher than in rows 1 and 2). The fuel temperature curves are for the peak intermediate zone fuel temperature at any point in the fuel pin; the axial location of this temperature varies during the course of the transient. As indicated in Table 9-17 and Table 9-18, fuel temperatures are well below melting and sodium temperatures are well below boiling in both cases.

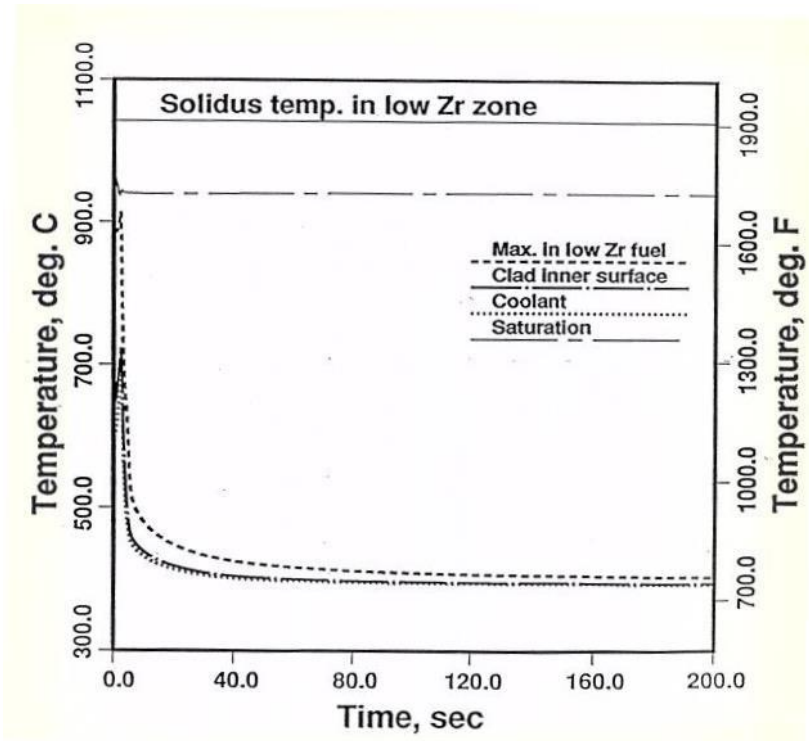

Figure 9-6 Thermal Response of the T. S. Limiting Pin in Row 6L for Mark-V Fuel During a Loss of a Single Pump Event (AN-1), with Uncertainties

9.7.2.2 Protected Loss of Flow Due to Loss of Normal Power, AN-2

Event AN-2 simulates a double M-G input breaker trip from full flow and 105% nominal power due to loss of normal power. The coastdown time is about 80 seconds, and the reactor scrams on the primary trip (flow). Figure 9-8 and Figure 9-9 present, for the row 6 normal flow subassembly hottest pin, the peak intermediate zone fuel temperature, the peak inner cladding temperature, and the peak coolant temperature during the transient for Mark-V fuel and Mark-VA

fuel, respectively, all with uncertainties included.

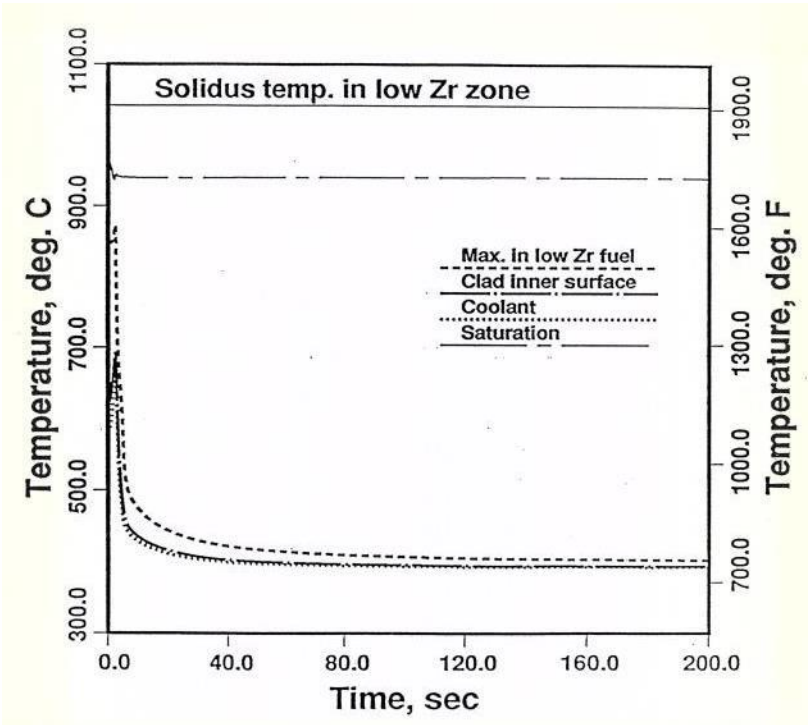

Figure 9-7 Thermal Response of the T. S. Limiting Pin in Row 6L for Mark-VA Fuel During a Loss of a Single Pump Event (AN-1), with Uncertainties

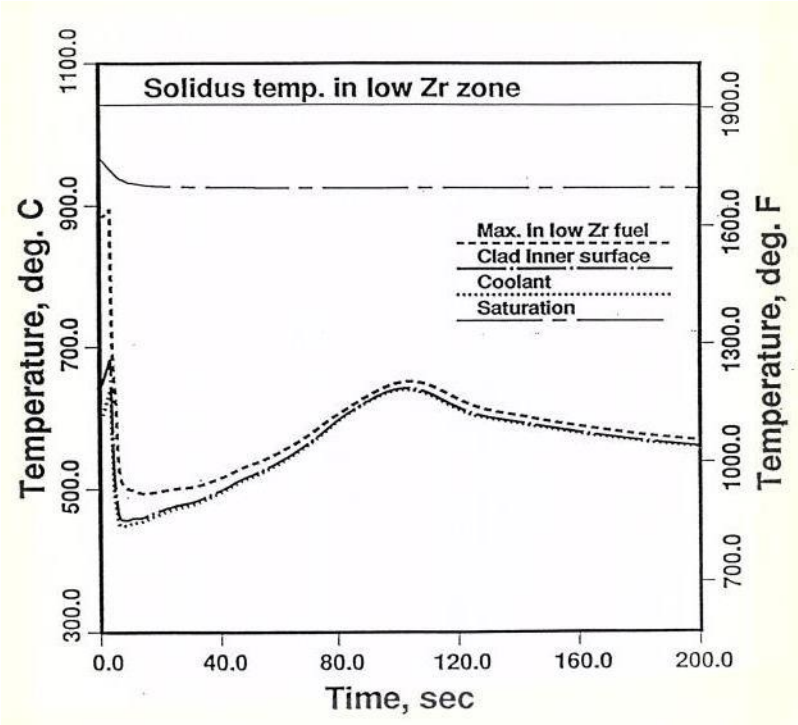

Figure 9-8 Thermal Response of the T. S. Limiting Pin in Row 6L for Mark-V Fuel During a Loss of Flow Due to Loss of Normal Power (AN-2), with Uncertainties

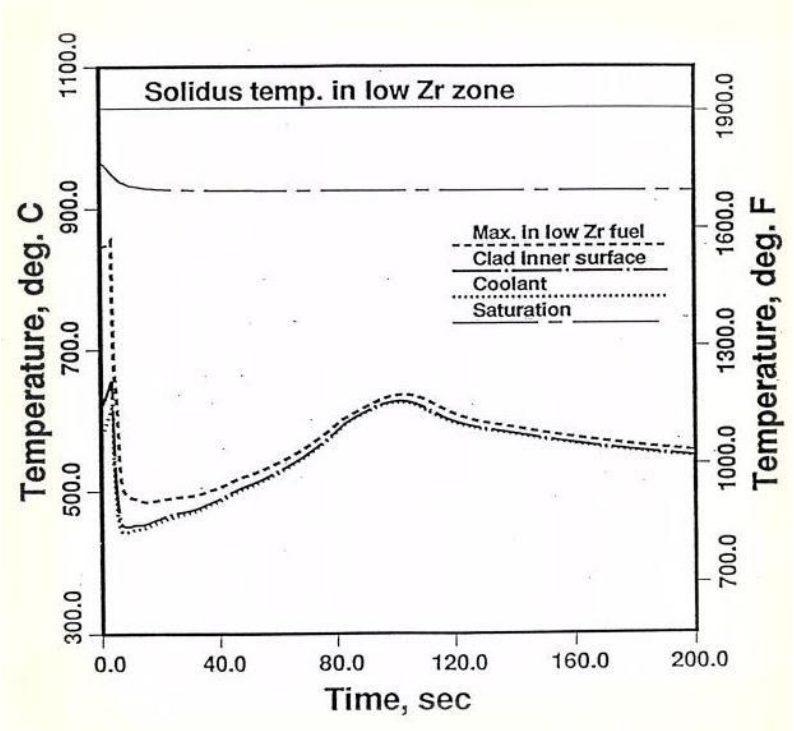

Figure 9-9 Thermal Response of the T. S. Limiting Pin in Row 6L for Mark-VA Fuel During a Loss of Flow Due to Loss of Normal Power (AN-2), with Uncertainties

As in AN-1, the maximum fuel, cladding, and sodium temperatures are reached at the time of scram. Because the coastdown is less severe in AN-2 than it is in AN-1, the temperatures do not shoot up as high in AN-2 as they do during AN-1. The curves exhibit the usual behavior seen in a double pump trip, namely sharp dropoff of temperature as the power drops after the scram, followed by a rise in temperature once the power reaches decay heat level but the flow continues to drop (causing a rise in power/flow ratio), and finally peaking and decline of the temperatures as the flow moves into natural circulation and the decay power gradually decreases. For Mark-V fuel, about 90% of the damage occurs during the second peak; for Mark-VA fuel, the second peak accounts for about 75% of the damage. The damage during the first peak is much less for both fuels than during AN-1, due to the milder coastdown in AN-2. The plenum pressure and cladding temperature in the second temperature peak of the Mark-V pin are high enough to cause more damage in AN-2 than in AN-1; the opposite is true in the Mark-VA pin, where the plenum pressure during the second peak is 7-8% less than it is in the Mark-V pin. This is confirmed by the values of CDF and clad strain shown in Table 9-17 and Table 9-18.

The Mark-V limiting pin in subassembly 6F1 experiences some increase in wastage during AN-2 due to eutectic penetration during the first temperature peak. Although the peak inner cladding temperature in the Mark-VA pin exceeds the eutectic threshold (650°C) during the first temperature peak, the temperature inside the cladding at the wastage interface is less than 650°C, and so no eutectic penetration occurs.

As in AN-1, the fuel stays well below melting and the sodium well below boiling during AN-2 for both fuel types, as indicated in Table 9-17 and Table 9-18.

9.7.2.3 Protected TOP Due to a Single Control Rod Runout, AN-3

This event is initiated by runout of a single control rod at a rate of 0.01$/s, beginning at 40% full power (25 MW) and full reactor flow. The reactor is scrammed by the power trip, which is the primary trip. The peak intermediate zone fuel temperature, peak inner cladding temperature, and peak sodium temperature are plotted for Mark-V fuel in Figure 9-10 for the row 1 hottest pin and in Figure 9-11 for the row 6 normal flow assembly hottest pin. The same parameters are plotted for Mark-VA fuel in Figure 9-12 for the row 1 hottest pin and in Figure 9-13 for the row 6 normal flow assembly hottest pin. All plots include uncertainties. The highest intermediate zone fuel temperature in the reactor during AN-3 occurs in row 1 for both Mark-V and Mark-VA fuels; however, the highest Mark-V fuel temperatures in rows 2-4 are within 2°C of the row 1 temperature, and the same is true of the Mark-VA row 2 and 3 temperatures compared to the row 1 temperature, so the inner rows are all about equally limiting with respect to fuel temperature. Similarly, the hot pins in rows 4, 5, and both row 6 subassemblies all reach nearly the same maximum cladding temperature, both for Mark-V and for Mark-VA fuel.

As shown by the plots, the fuel, cladding, and coolant temperatures rise gradually until the reactor scrams, then drop off sharply and reach equilibrium within 20 seconds or so. The maximum temperatures occur at the time of scram. Nearly all the cladding damage occurs prior to the scram. Table 9-17 and Table 9-18 show that the CDF and strain are both an order of magnitude less for both fuels during AN-3 than during either of the LOF anticipated events. No eutectic penetration occurs in either fuel. Neither the fuel melting limit nor the sodium boiling limit is challenged for either fuel.

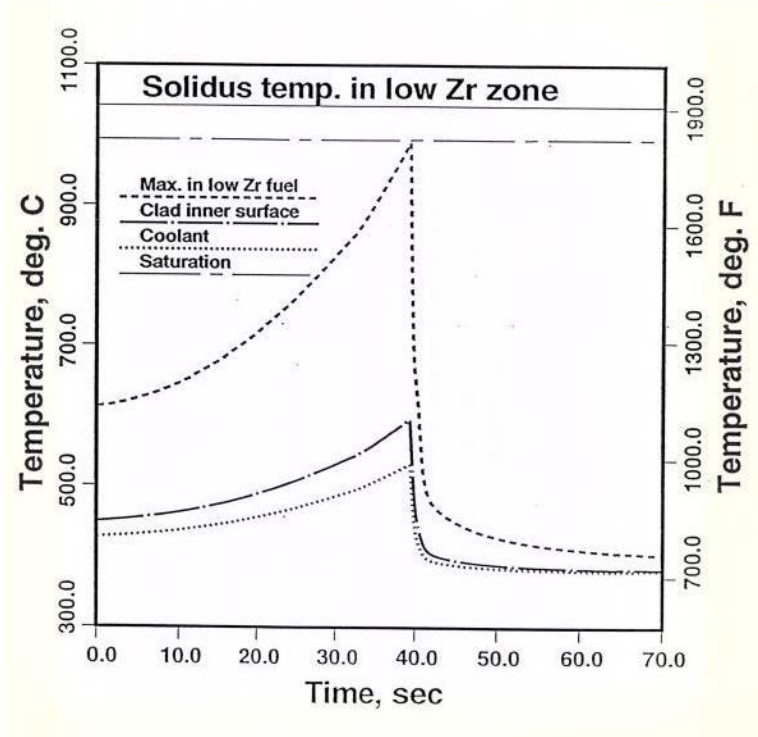

Figure 9-10 Thermal Response of the T. S. Limiting Pin in Row 1 for Mark-V Fuel During a Control Rod Runout Event (AN-3), with Uncertainties

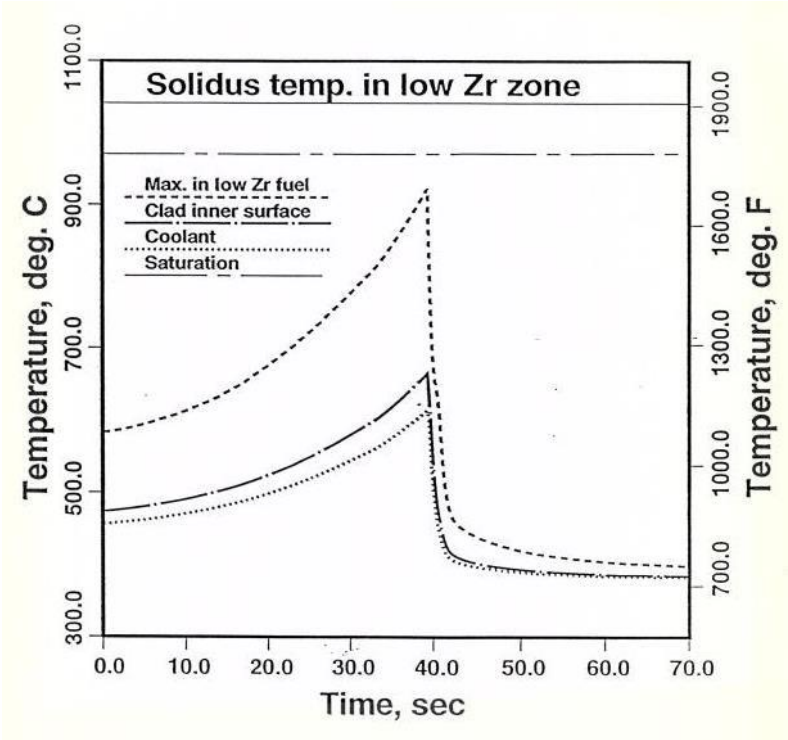

Figure 9-11 Thermal Response of the T. S. Limiting Pin in Row 6L for Mark-V Fuel During a Control Rod Runout Event (AN-3), with Uncertainties

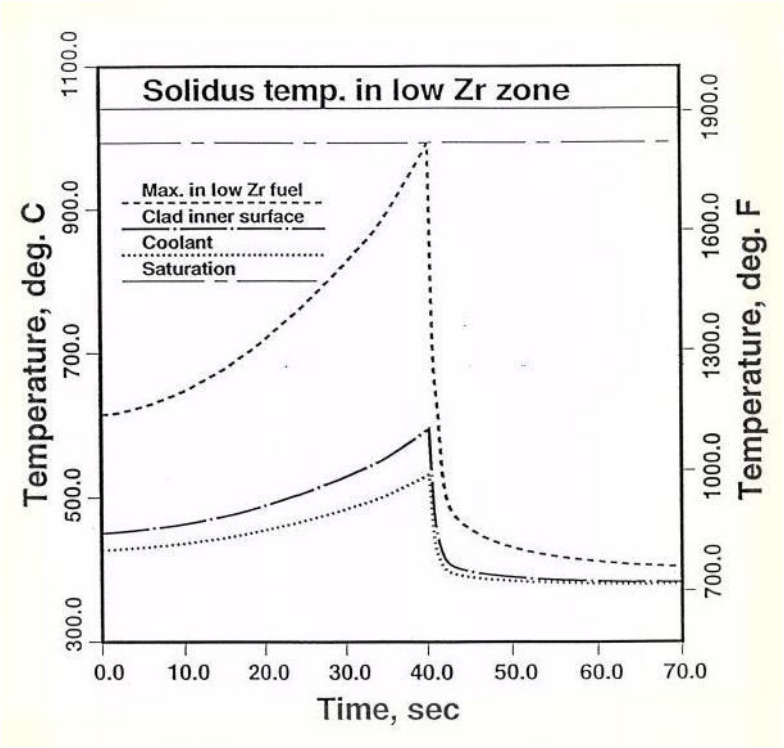

Figure 9-12 Thermal Response of the T. S. Limiting Pin in Row 1 for Mark-VA Fuel During a Control Rod Runout Event (AN-3), with Uncertainties

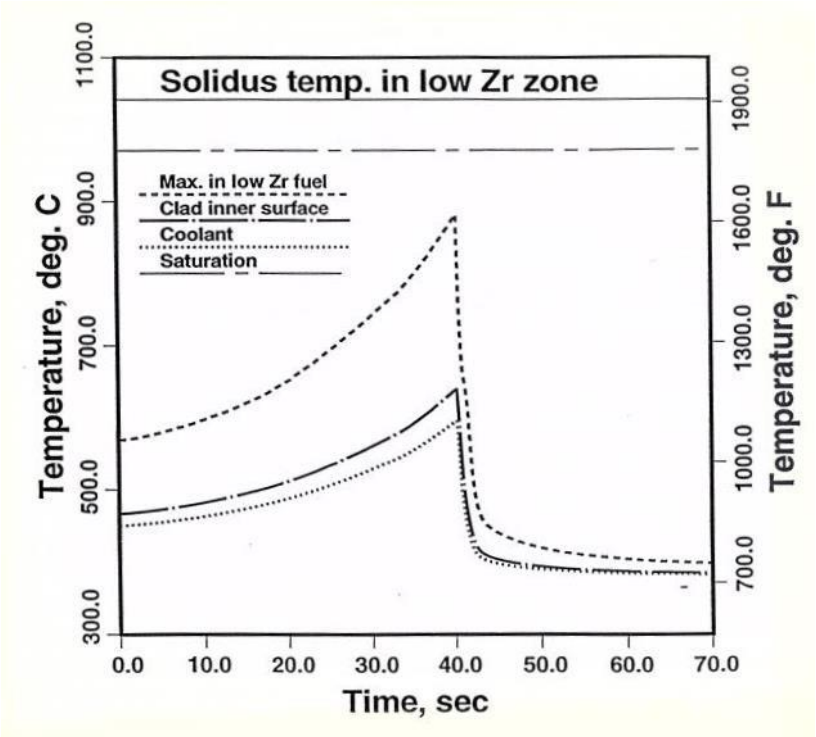

Figure 9-13 Thermal Response of the T. S. Limiting Pin in Row 6L for Mark-VA Fuel During a Control Rod Runout Event (AN-3), with Uncertainties

9.7.2.4 Protected TOP During Reactor Startup, AN-4

Below 25 MW, the period trip becomes the primary trip function, and off-normal transient behavior changes. To investigate this area, several off-normal transients were run from startup conditions (full flow, 62.5 W, reactor uniformly at 700°F). Only one of these can be categorized as an anticipated event -- a single rod runout at 0.01$/s, in which the reactor is scrammed by the period trip. The SASSYS period trip model predicts that the control rods will begin to move at 28.9 seconds, which compares well with the value of 28.5 seconds reported in Ref. 9.12. The scram occurs at about 220 W, so the reactor does not heat up measurably and the fuel, cladding, and sodium stay at 700°F throughout the transient. This transient is really only a test of the modelling of the period trip system and does not challenge any of the design criteria.

9.7.2.5 Limited Operation up to Power/Flow Ratio of 1.15, AN-5

Anticipated transient event AN-5 considers the effect of an increase in the power/flow ratio due either to a drift upward of the power while maintaining full flow or a drift downward of the flow while maintaining full power. The drift of power is assumed to stay below the power trip setting of 115%, and the drift in flow is assumed to stay above the flow trip setting of 88%. The power/flow ratio therefore does not exceed 1.15.

LIFE-METAL was used to analyze this transient. The subassembly powers and outlet temperatures of Table 9-13 and Table 9-15 provided the initial conditions for the Mark-V and Mark-VA calculations, respectively. The fuel was assumed to be recycled fuel at beginning-of-life conditions (BOL). These assumptions were made based on results of scoping calculations between 0 and 10 at. % burnup which were performed with LIFE-METAL. These indicated that, for Mark-V fuel (for which the limiting steady-state peak inner cladding temperature is the eutectic liquefaction temperature), eutectic penetration is the limiting design criterion for this type of transient at BOL, when cladding temperatures are highest. The most rapid eutectic penetration occurs for recycled fuel, since the lanthanides in the recycled fuel assist in eutectic penetration. Thus, the conditions assumed for AN-5 are the worst conditions under which the transient can occur for Mark-V fuel.

The LIFE-METAL analysis investigated the time required to reach the eutectic penetration limit of 5% (design criterion 6.0) as a function of power/flow ratio if it is assumed that the power

drifts upward and the flow remains constant. The results for Mark-V fuel are presented in Figure 9-14. These indicate that, below 5% overpower, criterion 6.0 is never reached, while between 5% and 15% overpower, the time at which the criterion is reached is a monotonically decreasing function of overpower ranging from 6 hours just above 5% overpower to 2.1 hours at 115% overpower. For Mark-VA fuel (for which the limiting steady-state peak inner cladding temperature is set by fuel-cladding chemical interaction and is 23°C (41°F) below the eutectic liquefaction temperature), eutectic liquefaction does not occur until past 15% overpower.

Since eutectic penetration is driven by cladding temperature and cladding temperature increases with power if power/flow ratio is held constant, eutectic penetration rate increases with power for a given power/flow ratio. Therefore, the LIFE-METAL results just described for overpowers up to 15% bound the corresponding curve of time to reach 5% eutectic penetration as a function of power/flow ratio if the flow drifts downward while full power is maintained.

The other design parameters are far from challenging limiting values in transients which fall within the AN-5 event envelope. To demonstrate this, all design parameter values were evaluated for the most severe case in the envelope, a drift in power to 115%. Parameters were evaluated after one hour at 115% power. These values are summarized in Table 9-17 for Mark-V fuel and in Table 9-18 for Mark-VA fuel. All design criteria are met, with a substantial amount of eutectic penetration predicted in the Mark-V fuel, consistent with the results in Figure 9-14. For Mark-VA fuel, the results in Table 9-18 indicate that the transient is completely benign.

9.7.3 Unlikely Events

Events UN-1 through UN-5 of Section 7.5 were evaluated with SASSYS in the same fashion as for the anticipated events. These include two loss-of-flow transients (UN-1 and UN-2), two TOP events from 40% power (UN-3 and UN-4), and three reactivity insertion transients from startup conditions, all of which are grouped under the label UN-5. Table 9-19 and Table 9-20 summarize the key safety parameters for all of these unlikely events.

9.7.3.1 Protected LOF Due to Double Clutch Breaker Trip, UN-1

During UN-1, both primary pumps coast down from full flow and 105% nominal reactor power due to simultaneous clutch breaker trips, and the reactor scrams on the primary trip

(flow). Until recently, this event was classified as an anticipated transient because there was a cross-connection between the uninterruptible power supply units for the two pumps, which introduced a common cause failure mode between the clutch mechanisms of the two pumps. This cross-connection is being removed, however, and so the double clutch breaker trip of the primary pumps has become an unlikely event. A clutch breaker trip coastdown proceeds more quickly than either the input or the output breaker coastdown, with primary pump 1 coasting down in about 23 seconds and primary pump 2 in about 25 seconds.

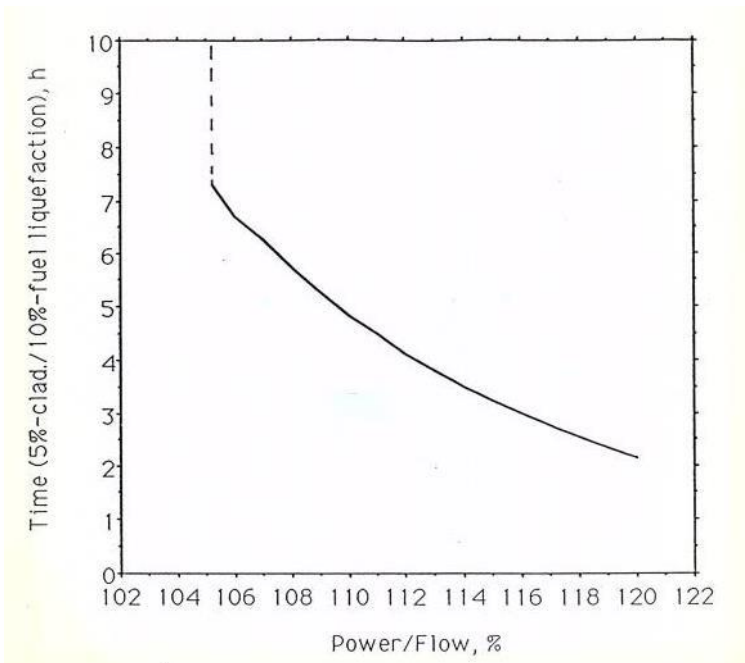

Figure 9-14 Lower Bound on Time to Reach 5%-Clad/10%-Fuel Liquefaction for Mark-V Fuel

Figure 9-15 and Figure 9-16 show the progression in the hottest pin of the row 6 normal flow subassembly of the peak intermediate zone fuel temperature, the peak inner cladding temperature, and the peak coolant temperature during the transient for Mark-V fuel and Mark-VA fuel, respectively, with uncertainties included. These plots exhibit the same double peak behavior as was observed during AN-2, the double input breaker trip transient (see Figure 9-8 and Figure 9-9). However, the more rapid coastdown during UN-1 causes the temperatures to reach higher values and to reach the top of the second peak much more rapidly. Peak pin plenum pressures for both fuel types are about 12% higher than during AN-2, and cladding and sodium

temperatures are significantly higher during the second peak than during the first, which was not the case in AN-2. Virtually all the cladding damage occurs during the second peak after the cladding temperature has passed the eutectic temperature. Damage is, of course, much greater for both fuels during UN-1 than during AN-2 (compare Table 9-19 and Table 9-20 to Table 9-17 and Table 9-18) and is significantly higher in the Mark-V fuel due to the higher powers allowed in the outer row subassemblies. No fuel melting or sodium boiling occurs in either fuel design.

9.7.3.2 Protected LOF Due to Seizure of One Pump and Clutch Breaker Trip of One Pump, UN-2

This transient is identical to UN-1 except that one of the primary pumps seizes instead of coasting down from a clutch breaker trip. The temperature plots of Figure 9-17 and Figure 9-18 show the progression of the transient in the row 6 normal flow assembly hot pin for Mark-V and Mark-VA fuel, respectively. Because the overall loss of flow is more rapid than in UN-1, temperatures rise much more rapidly (compare with the plots in Figure 9-15 and Figure 9-16) and reach higher values by the time the reactor trips. The higher sodium temperature in UN-2 produces greater buoyancy and a higher natural circulation flow during the second temperature peak, with the result that the temperatures do not climb as high during the second peak as in UN-1. As shown in Table 9-19 and Table 9-20, cladding damage is less during UN-2 than during UN-1 for both fuels. There is a comfortable margin to both fuel melting and sodium boiling.

9.7.3.3 Protected TOP Due to a Single Control Rod Runout with Delayed Reactor Scram, UN-3

Event UN-3 is identical to AN-3 except that the primary trip is assumed to fail and the reactor scrams on the TOP trip. This allows the rod runout to continue for about 1.5 seconds longer. Plots for the row 1 hot pin (which has the highest fuel temperature) are given in Figure 9-19, while plots for the row 6 normal flow hot pin (which suffers the greatest cladding damage) are in Figure 9-20, both for Mark-V fuel, including uncertainties. Corresponding curves are presented for Mark-VA fuel in `Figure 9-21` (row 1) and `Figure 9-22` (row 6L). These plots are nearly identical to those for AN-3 in Figure 9-10 through Figure 9-13; the temperatures are simply a few degrees higher. As can be seen from Table 9-19 and Table 9-20, cladding damage is somewhat greater than in AN-3 but considerably below that encountered in either UN-1 or UN-2 for either fuel. The sodium remains well below boiling. The analysis of UN-3 for

this section was performed at a reactor inlet temperature of 700°F, rather than 690°F, for consistency with the analyses of the other transients, and so the peak fuel temperatures in Figure 9-19 and Figure 9-21 fall about 20K short of the solidus temperature. For a detailed discussion on the effects on the off-normal transients of varying reactor inlet temperature, see Sec. 10.6.

Table 9-19 Mark-V Fuel Safety Parameters for Unlikely Events

	Event	**Peak Fuel Temp. in Low Zr Zone (Criterion 3.0†)**	**Peak Clad Temp. (Criterion 9.0†)**	**Minimum Saturation Temp.* (Criterion 9.0†)**	**CDF* (Criterion 7.0†)**	**Eutectic Penetration (%)* (Criterion 6.0†)**	**Clad Strain (%)* (Criterion 8.0†)**
LOF Events	UN-1 (Clutch Breaker Trip of Both Primary Pumps)	953°C (1747°F) (Row 4)	745°C (1373°F) (Row 6L)	909°C (1668°F)	$1.6x10^{-2}$	$3.4x10^{-2}$	$1.7x10^{-1}$
	UN-2 (Clutch Breaker Trip of One Pump, Seizure of One Pump)	990°C (1814°F) (Row 4)	785°C (1444°F) (Row 5)	869°C (1595°F)	$4.6x10^{-3}$	$5.0x10^{-2}$	$1.6x10^{-2}$
TOP Events	UN-3 (Single Rod Runout (0.01$/s), SOT Trip)	1019°C (1866°F) (Row 1)	681°C (1257°F) (Row 5)	976°C (1789°F)	$6.2x10^{-5}$	$3.7x10^{-4}$	$5.6x10^{-4}$
	UN-4 (Double Rod Runout (0.02$/s), Power Trip)	983°C (1802°F) (Row 1)	659°C (1218°F) (Row 5)	976°C (1789°F)	$1.5x10^{-5}$	0.0	$1.4x10^{-4}$
	UN-5 (Single Rod Runout (0.01$/s) at Startup, Power Trip)	978°C (1793°F) (Row 1)	652°C (1206°F) (Row 5)	976°C (1788°F)	$4.7x10^{-6}$	0.0	$4.4x10^{-5}$

*These values occur in the row 6 normal flow subassembly 6F1 (designated row 6L). All values in the table include uncertainties, and all transients were run with a reactor inlet temperature of 700°F.

†Design Criteria:

3.0 There shall be no bulk fuel melting in anticipated or unlikely transients.

6.0 The cumulative cladding eutectic penetration for anticipated events, the single most damaging unlikely event, and the extremely unlikely event is limited to 5% of the wall thickness.

7.0 The accumulated CDF for anticipated events and the single most damaging unlikely event is limited to 0.1.

8.0 The cumulative hoop strain resulting from anticipated events and the single most damaging unlikely event, through the life of the fuel, is limited to 1% for HT9.

9.0 There shall be no sodium boiling in anticipated, unlikely or extremely unlikely transients.

Table 9-20 Mark-VA Fuel Safety Parameters for Unlikely Events

	Event	Peak Fuel Temp. in Low Zr Zone (Criterion 3.0†)	Peak Clad Temp. (Criterion 9.0†)	Minimum Saturation Temp.* (Criterion 9.0†)	CDF* (Criterion 7.0†)	Eutectic Penetration (%)* (Criterion 6.0†)	Clad Strain (%)* (Criterion 8.0†)
LOF Events	UN-1 (Clutch Breaker Trip of Both Primary Pumps)	949°C (1740°F) (Row 1)	725°C (1337°F) (Row 6L)	909°C (1688°F)	$1.2x10^{-3}$	$2.2x10^{-2}$	$2.6x10^{-4}$
	UN-2 (Clutch Breaker Trip of One Pump, Seizure of One Pump)	966°C (1772°F) (Row 3)	754°C (1390°F) (Row 4)	869°C (1595°F)	$4.9x10^{-4}$	$8.9x10^{-3}$	$6.5x10^{-5}$
TOP Events	UN-3 (Single Rod Runout (0.01$/s), SOT Trip)	1020°C (1867°F) (Row 1)	652°C (1205°F) (Row 4)	976°C (1789°F)	$5.8x10^{-6}$	.0	$<10^{-6}$
	UN-4 (Double Rod Runout (0.02$/s), Power Trip)	987°C (1809°F) (Row 1)	635°C (1175°F) (Row 4)	976°C (1789°F)	$1.7x10^{-6}$	0.0	$<10^{-6}$
	UN-5 (Single Rod Runout (0.01$/s) at Startup, Power Trip)	982°C (1799°F) (Row 1)	631°C (1167°F) (Row 4)	976°C (1788°F)	$<10^{-6}$	0.0	$<10^{-6}$

*These values occur in the row 6 normal flow subassembly 6F1 (designated row 6L). All values in the table include uncertainties, and all transients were run with a reactor inlet temperature of 700°F.

†Design Criteria:

3.0 There shall be no bulk fuel melting in anticipated or unlikely transients.

6.0 The cumulative cladding eutectic penetration for anticipated events, the single most damaging unlikely event, and the extremely unlikely event is limited to 5% of the wall thickness.

7.0 The accumulated CDF for anticipated events and the single most damaging unlikely event is limited to 0.1.

8.0 The cumulative hoop strain resulting from anticipated events and the single most damaging unlikely event, through the life of the fuel, is limited to 0.1% for 316SS.

9.0 There shall be no sodium boiling in anticipated, unlikely or extremely unlikely transients.

9.7.3.4 Protected TOP Due to Double Control Rod Runout, UN-4

This event is identical to AN-3 except that two rods are withdrawn at a rate of 0.01$/s, so the combined reactivity insertion is 0.02$/s. For Mark-V fuel, curves for the hottest pin temperatures in row 1 are given in Figure 9-23 and are given in Figure 9-24 for the row

6 normal flow subassembly. For Mark-VA fuel, temperatures are plotted for the row 1 hottest pin temperatures in Figure 9-25 and in Figure 9-26 for the row 6 normal flow subassembly pin. These plots look much like the curves for AN-3 (Figure 9-10 through Figure 9-13), but compressed into about half the time span. A comparison of Table 9-19 and Table 9-20 to Table 9-17 and Table 9-18 indicates that temperatures are slightly lower for UN-4 than for AN-3 and that cladding damage is less. Fuel temperature and sodium temperature are both well below the design criteria.

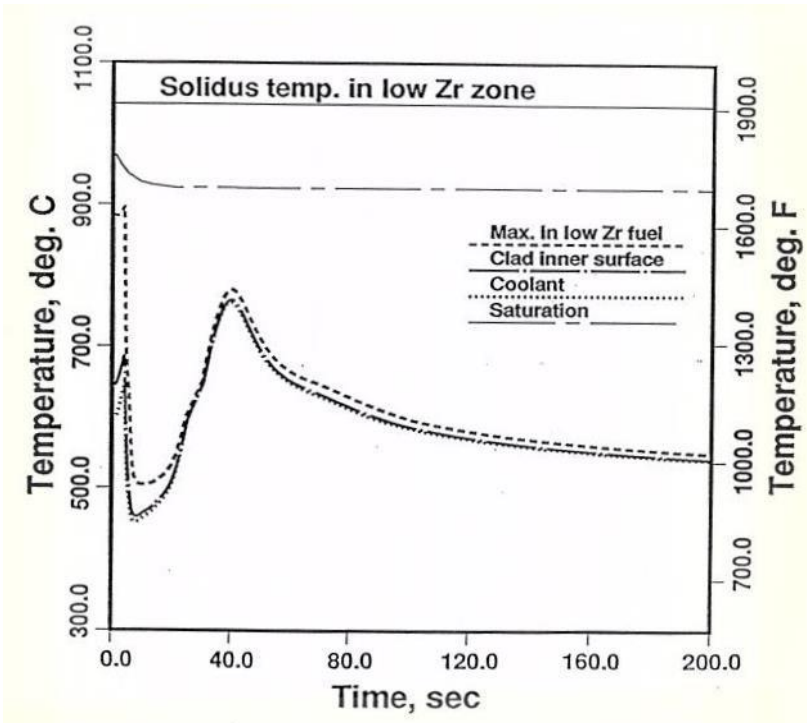

Figure 9-15 Thermal Response of the T. S. Limiting Pin in Row 6L for Mark-V Fuel During a Loss of Flow Due to a Double Clutch Breaker Trip Event (UN-1), with Uncertainties

9.7.3.5 Protected TOP During Reactor Startup with Delayed Reactor Scram, UN-5

Transient UN-5 is initiated in the same way as the anticipated startup event, AN-4. However, in UN-5, the period trip is assumed to fail, so that instead of a reactor scram while the reactor is at inlet temperature conditions throughout, as occurs in AN-4, the UN-5 transient runs until the reactor is scrammed when the power trip setpoint is exceeded. Thus the rod runout must drive the reactor all the way from 62.5 W to almost 72 MW. Figure 9-27 (row 1) and Figure 9-28 (row 6L) show the progression of the Mark-V fuel temperatures during the transient, and Figure 9-29 (row 1) and Figure 9-30 (row 6L) show the corresponding

plots for Mark-VA fuel. The reactor stays at 700°F for about one minute, then begins to heat up rapidly and scrams at about 79 seconds. Temperatures and cladding damage are comparable to those in UN-4. No fuel melting or sodium boiling occur.

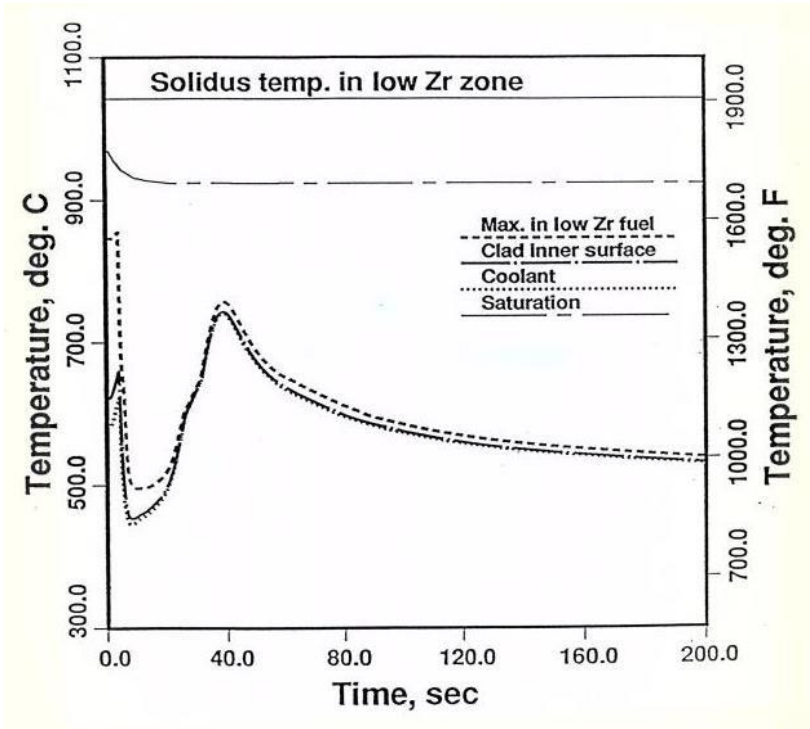

Figure 9-16 Thermal Response of the T. S. Limiting Pin in Row 6L for Mark-VA Fuel During a Loss of Flow Due to a Double Clutch Breaker Trip Event (UN-1), with Uncertainties

In addition to UN-5, two other unlikely startup events were examined. Both events were assumed to scram on period trip. In the first, a double rod runout such as was evaluated in UN-4 was performed from startup. The reactor scrammed at 14.4 seconds, with no change in temperature. In the second event, the transient was initiated by a 0.5$ step reactivity insertion. The reactor scrammed at 1.4 seconds, again with no change in temperature.

9.7.4 Extremely Unlikely Events

Section 7.5 discusses only one event in this category: event EU-1, which is the double clutch breaker trip of UN-1 with the addition of a single high-worth control rod stuck during reactor scram. The stuck control rod is assumed to have the highest possible worth (1.3$), and the shutdown reactivity is conservatively taken to be 2.34$, the value traditionally used in EBR-II

safety analyses which involve one stuck rod. Because this is an extremely unlikely event, the only criteria which must be met are that the sodium stay below boiling and the cladding eutectic penetration not cause the cumulative penetration over all off-normal events to exceed 5% of wall thickness.

Peak temperatures (with uncertainties) in the fuel intermediate zone, the inner cladding surface, and the sodium are displayed for the hottest pin in the row 6 normal flow subassembly in Figure 9-31 for Mark-V fuel and in Figure 9-32 for Mark-VA fuel. These are qualitatively similar to the plots for transient UN-1 (Figure 9-15 and Figure 9-16). However, the second peak occurs a few seconds earlier in EU-1, and the temperatures rise considerably higher during the second peak of EU-1 than was the case for UN-1. Despite the severity of this transient, the fuel stays well below the solidus point and the sodium keeps well below boiling, even at the top of the second peak. Maximum cladding eutectic penetration is 0.14% for Mark-V fuel and 0.09% for Mark-VA fuel.

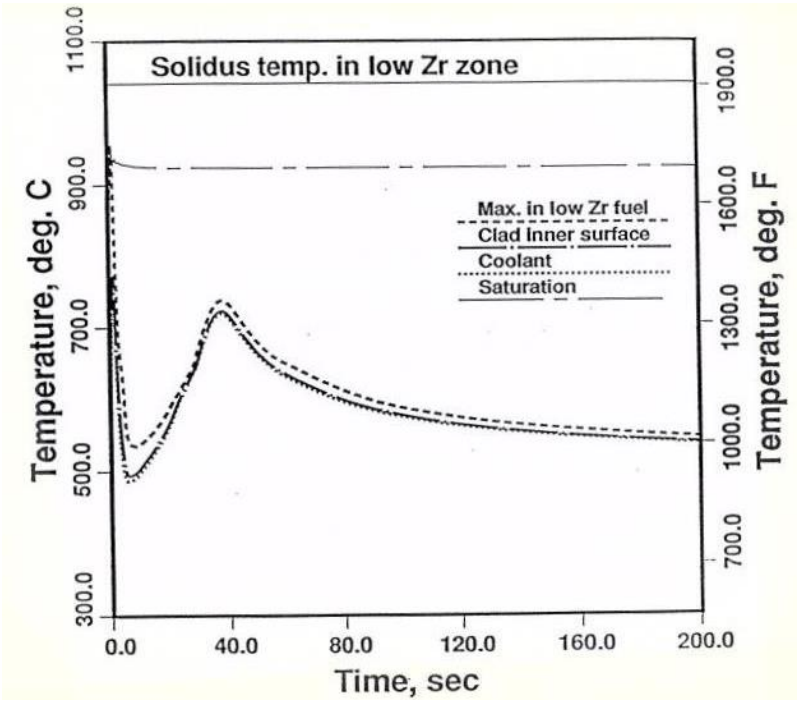

Figure 9-17 Thermal Response of the T. S. Limiting Pin in Row 6L for Mark-V Fuel During a Loss of Flow Due to Seizure of One Pump and Clutch Breaker Trip of One Pump (UN-2), with Uncertainties

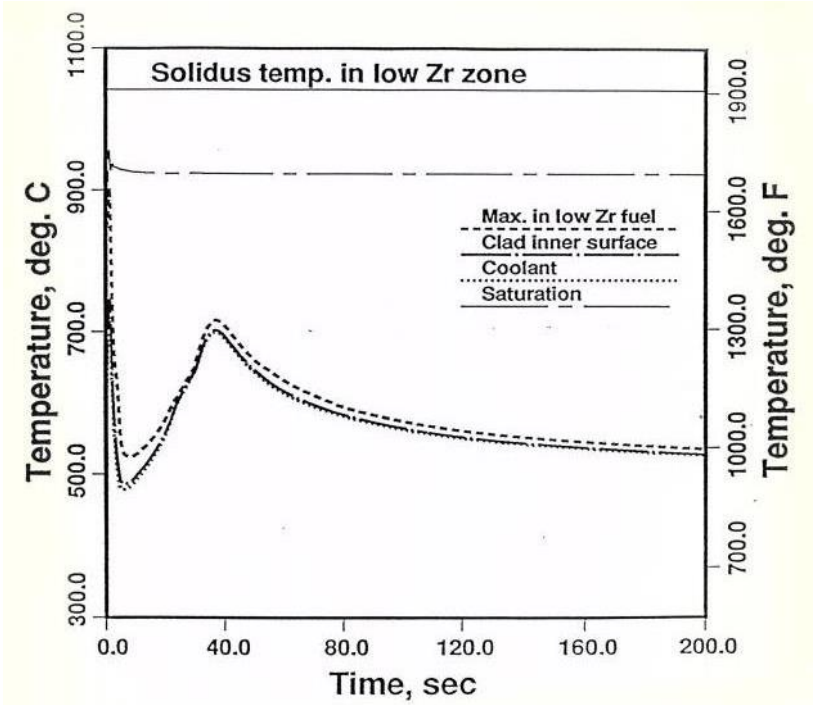

Figure 9-18 Thermal Response of the T. S. Limiting Pin in Row 6L for Mark-VA Fuel During a Loss of Flow Due to Seizure of One Pump and Clutch Breaker Trip of One Pump (UN-2), with Uncertainties

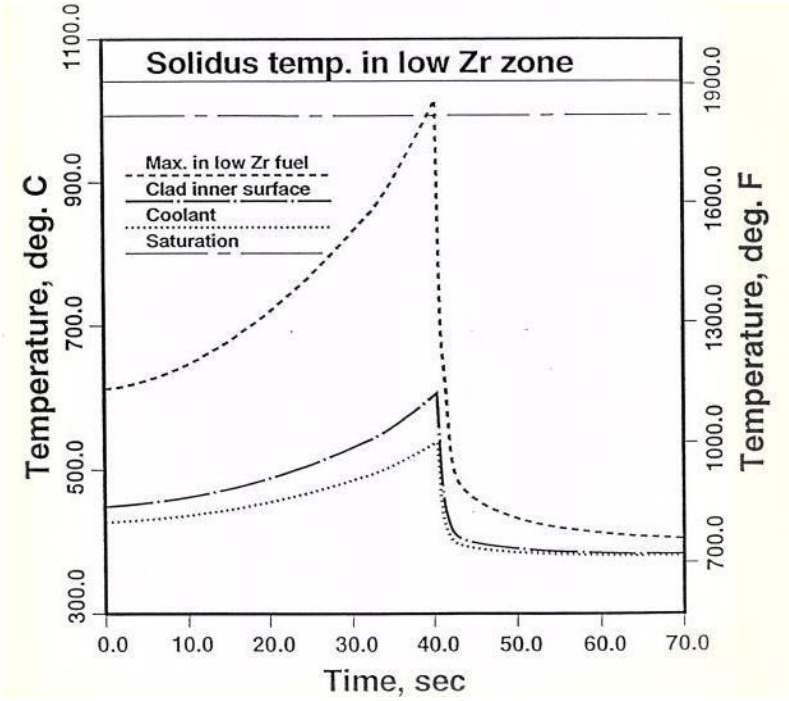

Figure 9-19 Thermal Response of the T. S. Limiting Pin in Row 1 for Mark-V Fuel During a Control Rod Runout with Delayed Scram (UN-3), with Uncertainties

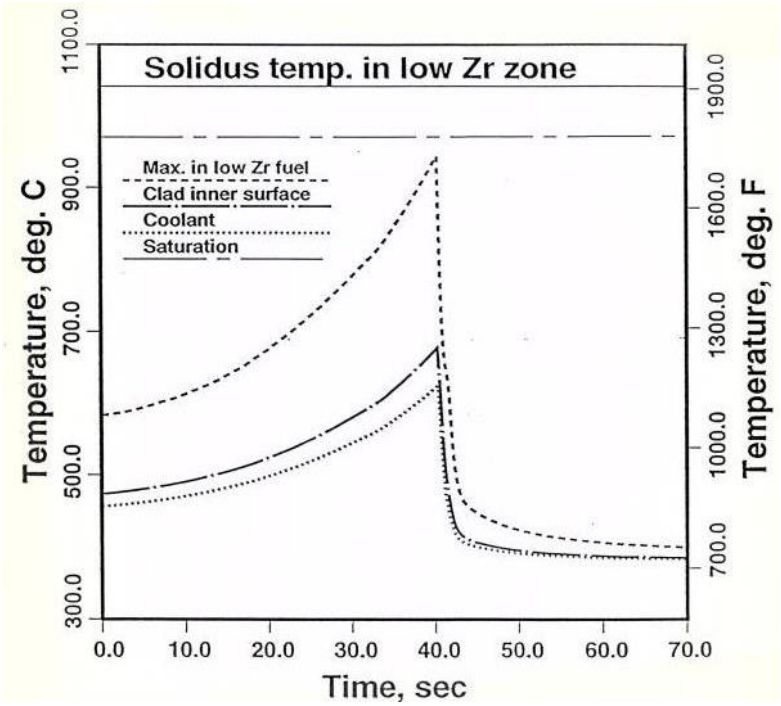

Figure 9-20 Thermal Response of the T. S. Limiting Pin in Row 6L for Mark-V Fuel During a Control Rod Runout with Delayed Scram (UN-3), with Uncertainties

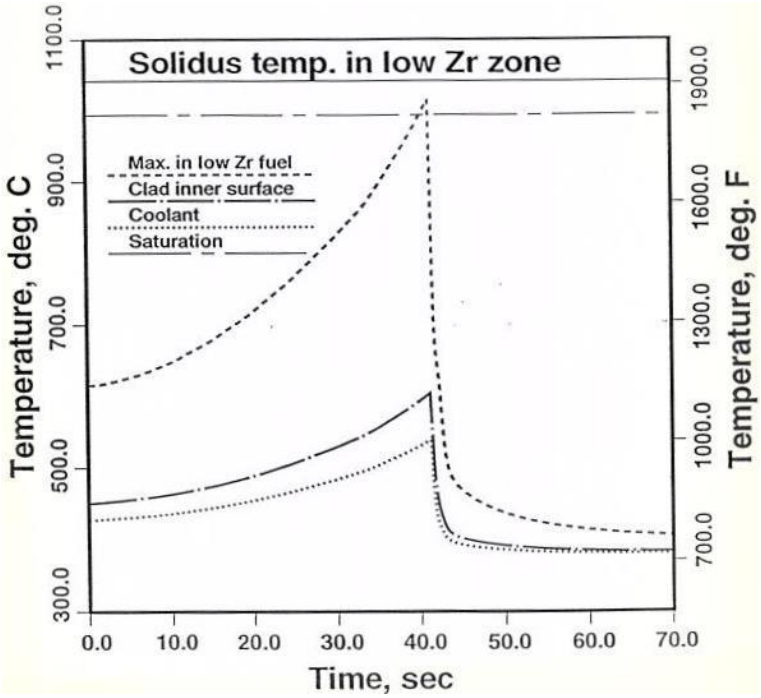

Figure 9-21 Thermal Response of the T. S. Limiting Pin in Row 1 for Mark-VA Fuel During a Control Rod Runout with Delayed Scram (UN-3), with Uncertainties

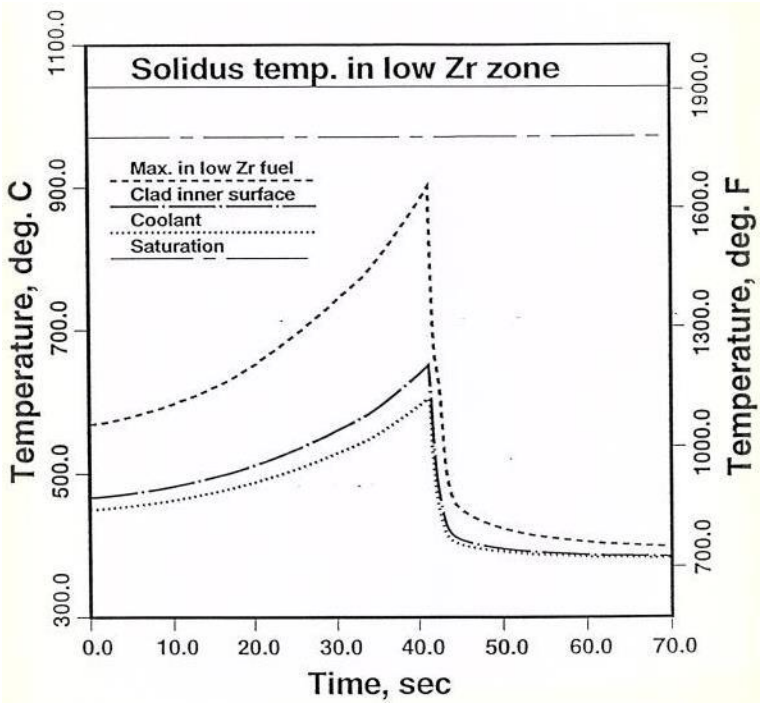

Figure 9-22 Thermal Response of the T. S. Limiting Pin in Row 6L for Mark-VA Fuel During a Control Rod Runout with Delayed Scram (UN-3), with Uncertainties

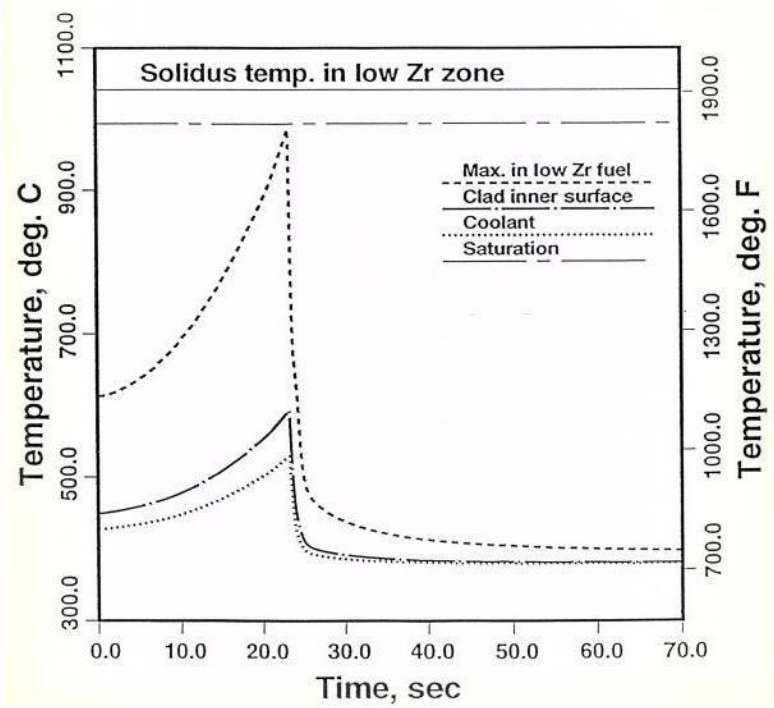

Figure 9-23 Thermal Response of the T. S. Limiting Pin in Row 1 for Mark-V Fuel During a Double Rod Runout Event (UN-4), with Uncertainties

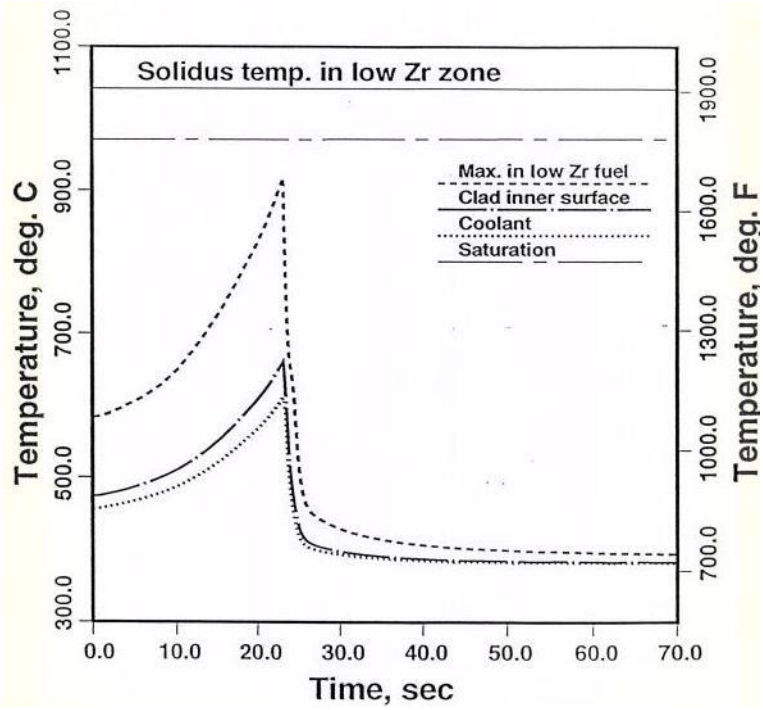

Figure 9-24 Thermal Response of the T. S. Limiting Pin in Row 6L for Mark-V Fuel During a Double Rod Runout Event (UN-4), with Uncertainties

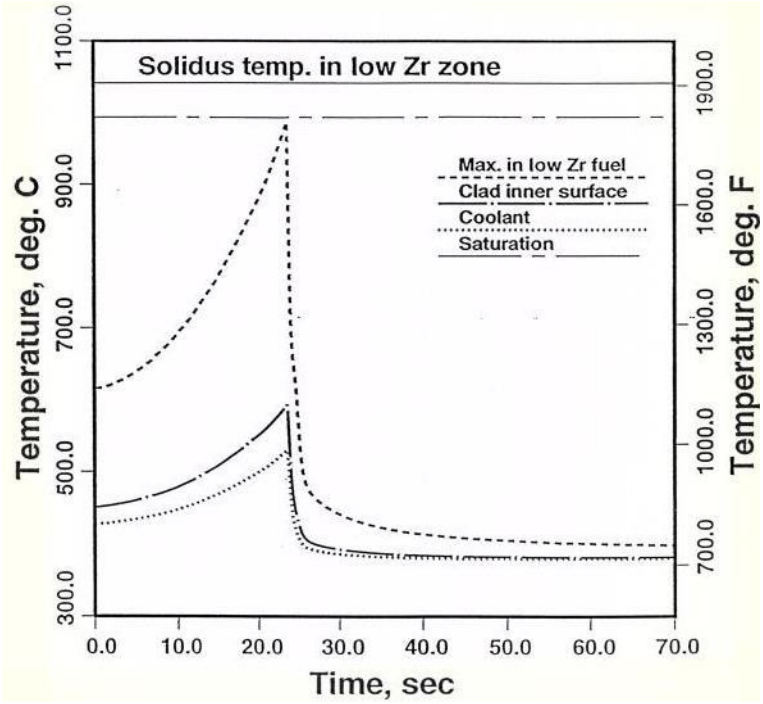

Figure 9-25 Thermal Response of the T. S. Limiting Pin in Row 1 for Mark-VA Fuel During a Double Rod Runout Event (UN-4), with Uncertainties

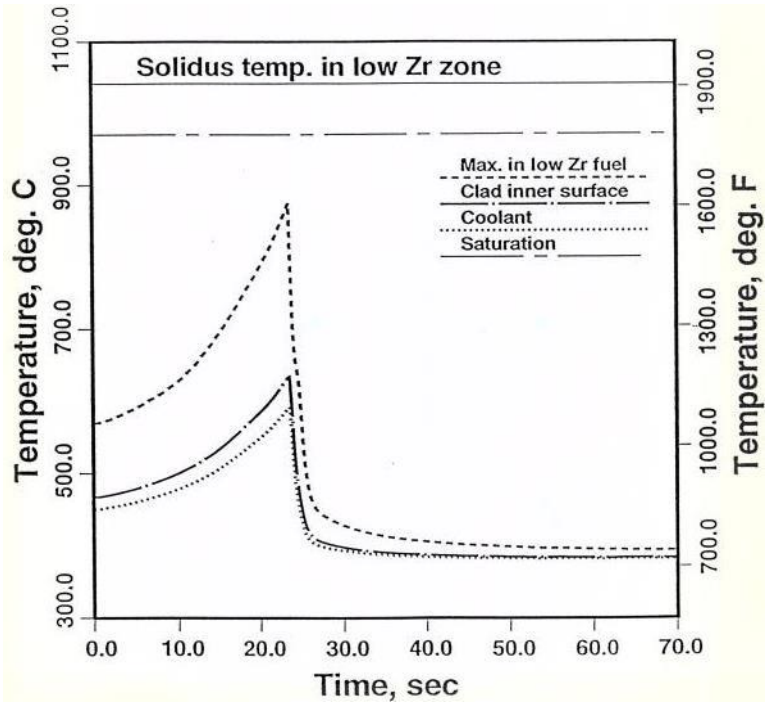

Figure 9-26 Thermal Response of the T. S. Limiting Pin in Row 6L for Mark-VA Fuel During a Double Rod Runout Event (UN-4), with Uncertainties

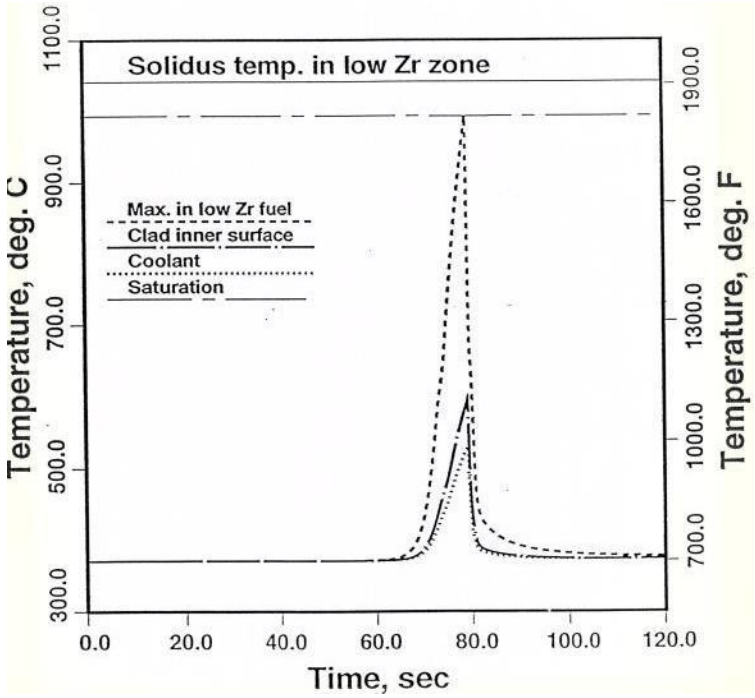

Figure 9-27 Thermal Response of the T. S. Limiting Pin in Row 1 for Mark-V Fuel During a Protected TOP During Reactor Startup with Delayed Reactor Scram (UN-5), with Uncertainties

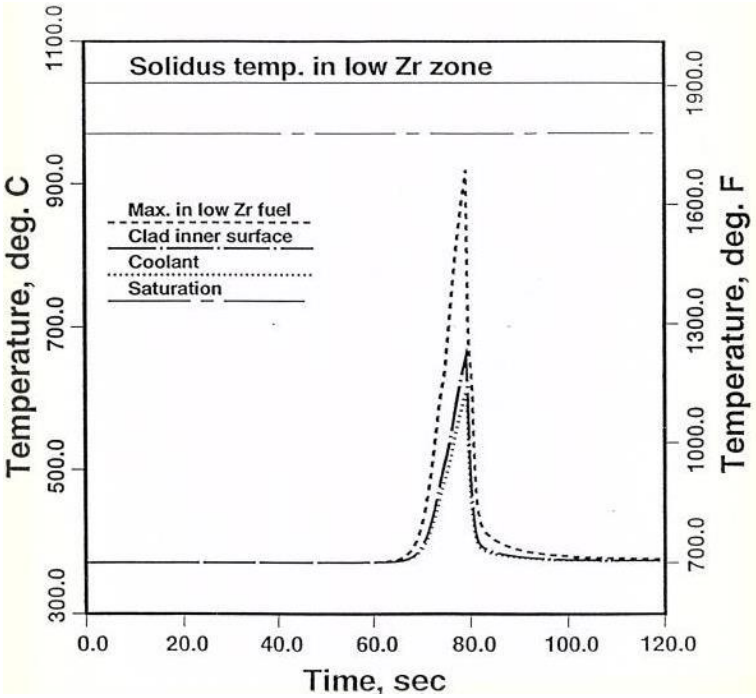

Figure 9-28 Thermal Response of the T. S. Limiting Pin in Row 6L for Mark-V Fuel During a Protected TOP During Reactor Startup with Delayed Reactor Scram (UN-5), with Uncertainties

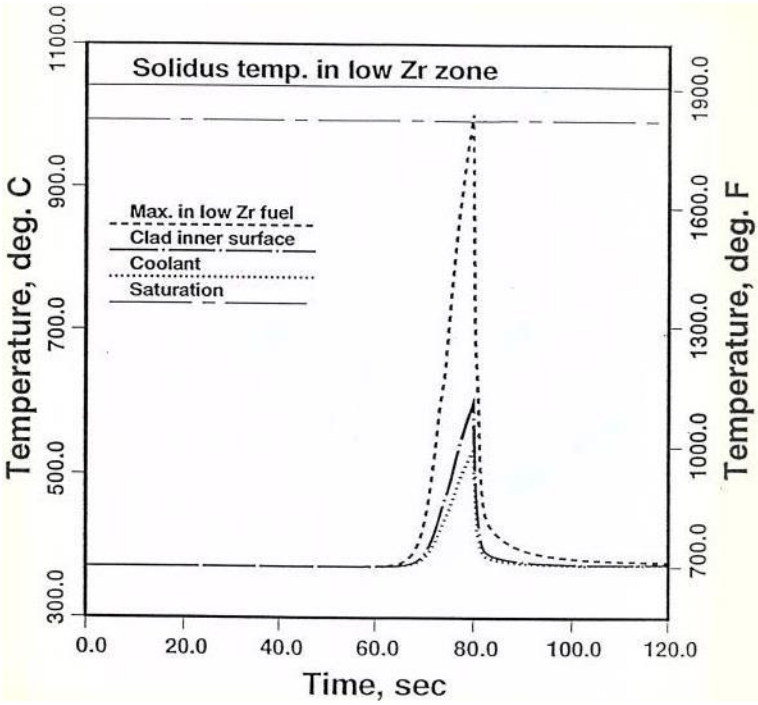

Figure 9-29 Thermal Response of the T. S. Limiting Pin in Row 1 for Mark-VA Fuel During a Protected TOP During Reactor Startup with Delayed Reactor Scram (UN-5), with Uncertainties

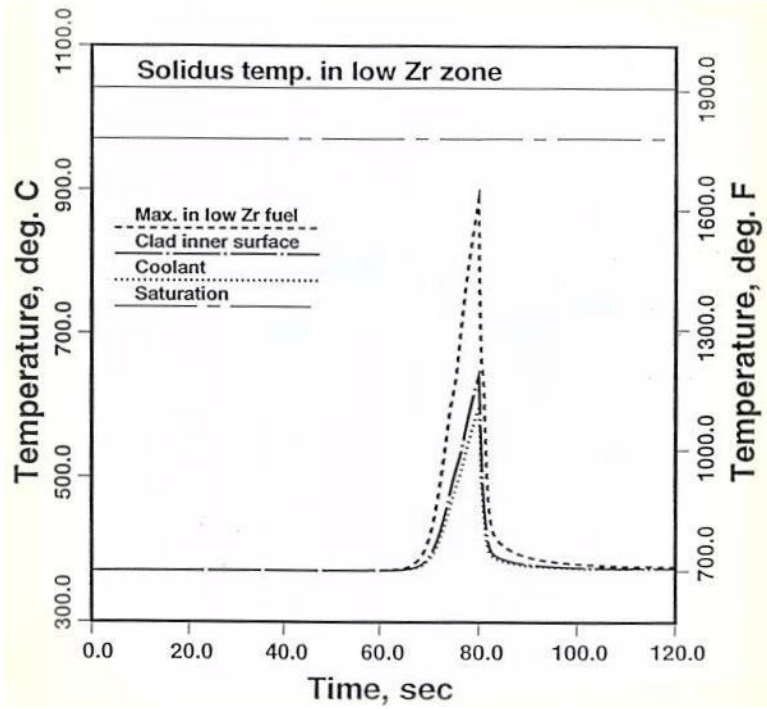

Figure 9-30 Thermal Response of the T. S. Limiting Pin in Row 6L for Mark-VA Fuel During a Protected TOP During Reactor Startup with Delayed Reactor Scram (UN-5), with Uncertainties

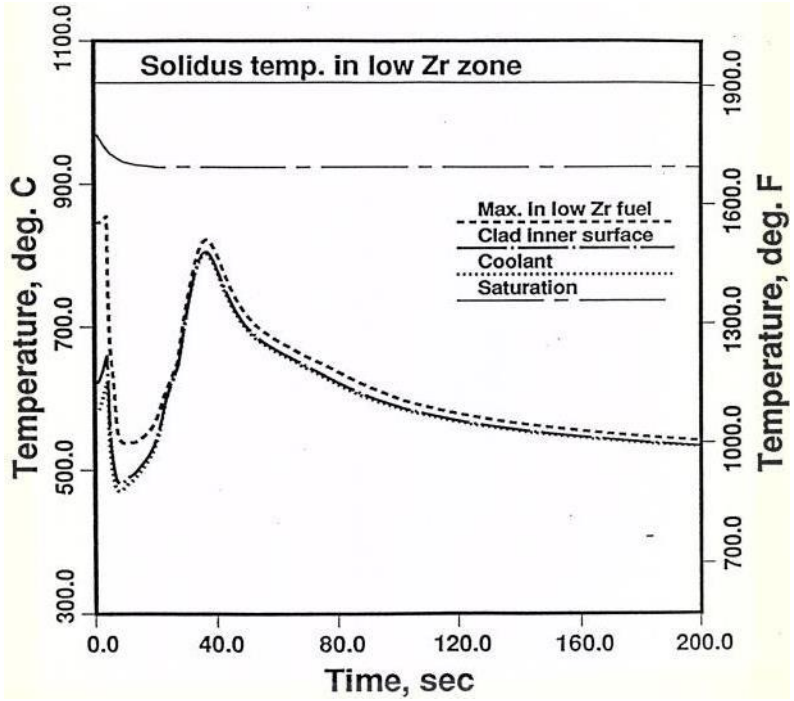

Figure 9-31 Thermal Response of the T. S. Limiting Pin in Row 6L for Mark-V Fuel During a Loss of Flow Due to a Double Clutch Breaker Trip Event with One Stuck Rod (EU-1), with Uncertainties

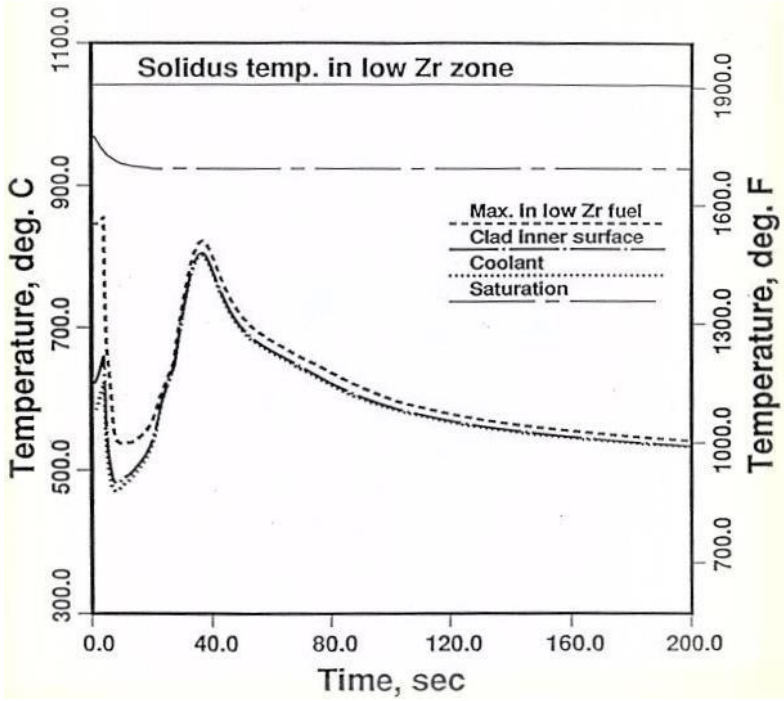

Figure 9-32 Thermal Response of the T. S. Limiting Pin in Row 6L for Mark-VA Fuel During a Loss of Flow Due to a Double Clutch Breaker Trip Event with One Stuck Rod (EU-1), with Uncertainties

9.8 Safety Evaluation

Fuel-cladding integrity and fuel temperature limits are evaluated based on design requirements summarized in Section 9.2 for both Mark-V and Mark-VA fuel, in which normal and anticipated/unlikely conditions are satisfied.

9.8.1 Normal Operation

The events considered in this category include (1) normal steady-state operation with reactor operated between 100 and 105% of normal power condition for the life of the fuel element, and (2) normal transients N-1 to N-4, with the corresponding duty cycles through the life of the fuel pin being as follows:

Identification	Description of Events	Duty Cycles
N-1	Reactor scram from 100% power and flow conditions	8
N-2	Anticipatory reactor shutdown from 100% power and flow conditions	8
N-3	Normal reactor shutdown from 100% power and flow conditions	16
N-4	Reactor power increased from 0 to 100% power	40

9.8.1.1 Mark-V Fuel Pin

The LIFE-METAL computer code was used to predict the Mark-V fuel behavior for various peak cladding temperature conditions as tabulated in Table 9-11, which indicates that at the cladding peak temperature of 650°C (1202°F), the corresponding fuel burnup, CDF, thermal creep strain and hoop stress are 16.1 at. %, 0.05, 0.55% and 135 MPa, respectively. The results indicate that the design safety criteria for steady-state normal operation are satisfied when the burnup is limited to 16.1 at. % for an initial peak cladding temperature of 650°C (1202°F). This temperature is the fuel-cladding eutectic liquefaction temperature as well as the cladding temperature limit for 105% overpower operation condition. Since the target burnup of 10 at. % is considerably less than the calculated 16.1 at. %, the safety criteria of Mark-V fuels are satisfied for steady-state operation.

The T.S. limiting subassembly hot-channel temperatures for reactor operation are given in Table 9-13 for the Mark-V fuel. In Table 9-13, all uncertainties are considered, and the cladding temperatures were calculated based on 105% overpower condition. It should be noted that for both steady-state and transient operations the fuel temperature is limited to the fuel solidus temperature, and the peak fuel temperatures in Table 9-13 are the maximum fuel temperatures in the low-Zr zone for UN-3 TOP conditions, which was identified as having the highest fuel temperature among all steady-state and transient conditions.

Analysis of the N-1, N-2, N-3 and N-4 transients indicates that CDFs and strains of these transients are considerably less than the safety limits for normal operation. It is concluded that during normal operation, the reactor can operate between 100 to 105% power through the life of the fuel pin without cladding failure.

9.8.1.2 Mark-VA Fuel Pin

Mark-VA fuel pin behavior was predicted using the LIFE-METAL code and is tabulated in Table 9-11, which indicates that for a target of 10 at. % burnup the peak cladding temperature is limited to 627°C (1161°F). The corresponding CDF, creep strain and hoop stress at this condition are 0.05, 0.16% and 105 MPa, respectively, and the design safety criteria are satisfied. The cladding damage of Mark-VA fuel is higher when compared with Mark-V fuel, and it is caused by higher FCCI wastage and thinner cladding of the Mark-VA fuel pin. For the T.S. limiting subassembly temperatures given in Table 9-15, the peak cladding temperature (with uncertainties) is below 627°C (1161°F) and the fuel temperature is below the fuel solidus temperature. The design safety criteria for steady-state operation are therefore satisfied.

The CDFs and thermal creep strains for transients N-1 to N-4 were found to be negligible. It is concluded that the reactor can be operated between 100 and 105% power condition without fuel pin failure.

9.8.2 Off-Normal Events

The cumulative values of CDF, strain and eutectic penetration are used as the basis for design evaluation. These values are accumulated through each cycle of operation and have been given in Table 9-17 to Table 9-20 for Mark-V and Mark-VA fuel for each of the anticipated and unlikely events. Values for cladding penetration for the extremely unlikely event are reported in Sec. 9.7.4. The design criteria for all off-normal events are identical except for criterion 8.0 on diametral strain, for which the limit for Mark-V fuel is 1%, whereas the limit for Mark-VA fuel is 0.1%. Events AN-1 to AN-5, UN-1 to UN-5, and EU-1 have been analyzed. The duty cycles for these transients are as follows:

Anticipated Events:

Identification	Description of Events	Duty Cycles
AN-1	A single pump M-G set output breaker trip and the reactor is scrammed by low flow trip.	7
AN-2	LOF caused by M-G set input breaker trips and the reactor is scrammed by low flow trip.	1
AN-3	Reactivity insertion initiated during reactor startup and the reactor is scrammed by period trip.	1
AN-4	Reactivity insertion initiated during reactor startup and the reactor is scrammed by period trip.	1
AN-5	Power/flow ratio rises due to a drift upwards in power or a drift downwards in flow.	1

Unlikely Events:

Identification	Description of Events	Duty Cycles
UN-1	LOF due to M-G set clutch breaker trips of both pumps and the reactor is scrammed by low flow trip.	1
UN-2	LOF due to seizure of one pump and clutch breaker trip of the other pump The reactor is scrammed by low flow trip.	1
UN-3	A single control rod runout and a failure of power trip function. The reactor is scrammed by SOT trip.	1
UN-4	Two control rods runout simultaneously and the reactor is scrammed by power trip.	1
UN-5	Reactivity insertion initiated during reactor startup with failure of period trip and the reactor is scrammed by power trip.	1

Extemely Unlikely Event:

Identification	Description of Events	Duty Cycles
EU-1	LOF due to M-G set clutch breaker trips of both pumps, plus one high-worth control rod sticks during reactor scram. The reactor is scrammed by low flow trip.	1

9.8.2.1 Mark-V Fuel Pin

The accumulated fuel-cladding strain for the off-normal events was found to be 0.19%, which is much less than the allowable value of 1%; the cumulative eutectic penetration of the cladding throughout all anticipated events plus the single most damaging unlikely and the single most damaging extremely unlikely transients is 2.68%, less than the 5% allowed by the design requirement; the fuel-cladding CDF for the anticipated and unlikely transients was found to be 0.018, much less than 0.1; so in all cases the design requirements are satisfied.

9.8.2.2 Mark-VA Fuel Pin

The data tabulated in Table 9-18 and Table 9-20 indicate that the accumulated strain and eutectic penetration of the fuel-cladding were found to be 0.00433% and 0.12%, respectively, and are considerably less than their corresponding allowable values of 0.1% and 5%; the CDF of the 316SS cladding was found to be 0.0014, much less than the allowable value of 0.1; so in all respects the design criteria are satisfied.

Safety evaluations of Mark-V and VA fuel have demonstrated that the design criteria are satisfied for steady-state normal and off-normal transient operations.

9.9 Discussion and Conclusions

The analysis presented in this section has utilized a standard, conservative, 3σ, methodology to derive the limiting subassembly subchannel temperature. The methodology involves use of fuel and clad temperature uncertainty factors and conservative material properties including fuel redistribution and its effect on fuel thermal conductivity and solidus temperature.

The first analysis used SUPERENERGY-2 to evaluate the local subchannel temperature distributions in typical subassemblies in each row of the core for both the 6-row and 6-plus-row configurations, Appendix B. These results are for beginning-of-life conditions. The peak coolant temperatures are found to occur in the row 5 subassemblies in both core configurations.

The second analysis presented gives results of LIFE-METAL calculations of the performance of the elements with 10 at. % burnup and highest fuel-clad interface temperatures attainable. These design calculations are repeated with uncertainties and also with uncertainties

and the overpower factor of 5%. Since LIFE-METAL has been validated against the closely allied X441 experiment [9.9], there is good support for these calculations.

In Section 9.5 LIFE-METAL is used to perform a sensitivity study and derive initial Limiting Conditions of Operation (LCO's) for the Mark-V and Mark-VA fueled subassemblies based upon requirements for steady-state operation. These limits are then used in a scoping transient analysis of the full duty cycle and the LCOs reduced if any criteria are not met in the transient analysis, Sec. 9.5. The limiting conditions of operation for Mark-V and Mark-VA fueled subassemblies derived from results presented in Sections 9.5 and 9.6 are summarized in Table 9-21.

Table 9-21 LCOs for Mark-V and Mark-VA Fuels

Row No.	Mark-V		Mark-VA	
	Hot Channel Coolant Temperature °F (°C)	Power Limit (Kw/SA)	Hot Channel Coolant Temperature °F (°C)	Power Limit (Kw/SA)
1	939 (504)[2]	989[2]	940 (504)[2]	992[2]
2	943 (506)[2]	985[2]	944 (507)[2]	989[2]
3	969 (521)[2]	965[2]	971 (522)[2]	970[2]
4	1028 (553)[1]	917[1]	1014 (546)[3]	879[3]
5	1054 (568)[1]	835[1]	1024 (551)[3]	765[3]
6H	1056 (569)[1]	811[1]	1027 (553)[3]	746[3]
6L	1063 (573)[1]	738[1]	1034 (557)[3]	679[3]
7	1065 (574)[1]	712[1]	1036 (558)[3]	655[3]

Limiting Phenomena
1 Fuel-Clad eutectic formation
2 Ternary fuel melting
3 CDF

Once the LCO's are determined, they are applied to a transient analysis of the full duty cycle, described in Sec. 9.7. Section 9.8 summarizes the results of these analyses and compares them to the design criteria. It has been found that for both fuels the inner row subassemblies are limited by the possibility of fuel melting in the protected slow TOP scenarios. In the worst case, when the TOP is terminated by the SOT trip (the UN-3 transient occurring at a reactor inlet

temperature of 690°F (see Section 10.6)), the power reaches about 1.28 times nominal before scram is initiated, which is thermally equivalent to a steady state of 1.28 times nominal. The outer row subassemblies are limited by fuel/clad eutectic threshold temperature.

The uncertainties of the fuel solidus temperature, the fuel-cladding eutectic liquefaction threshold temperature, cladding damage, and thermal conductivity of the fuel are partially responsible for the low T.S. limiting subassembly temperatures presented in Section 9.6. It is felt that when more test data on fuel properties and FCCI wastage data are available, and fuel-cladding interaction behavior is better characterized, the proposed T.S. temperature limits can be increased. The T.S. temperatures of the inner-row subassemblies are limited by the fuel solidus temperature. In the present analysis, the T.S. limiting temperatures were determined based on thermal properties of the fuel at 2 at. % burnup, at which the thermal conductivity is the lowest, and the fuel temperature is the highest.

In the transient safety analysis, the worst-condition scenario is assumed, in which the 10 at. % burnup fuel is considered when the cladding damage is the primary concern, while the fuel is assumed to be 2 at. % when the study is focused on the possibility of fuel melting during a TOP event. In both cases, the T.S. limiting subassembly temperature was used for the safety analysis. The analysis is conservative since the T.S. temperatures are based on the power of fresh fuel, and the power decreases with the increase of burnup.

The claddings of Mark-V and Mark-VA fuel pins are made of HT9 and 316SS, respectively. Mark-V fuel may be contained in either HT9 or 316SS ducts; Mark-VA pins wil be contained only in 316SS ducts. Due to differences of creep, swelling and thermal expansion between cladding and duct, the gap between fuel bundle and hex duct in the reactor varies from its configuration at ambient temperature, and the variation is a function of temperature, pressure and irradiation conditions of fuel pins and the duct. The effects of gap change on the thermal-hydraulics of the subassembly have been studied for Mark-V and Mark-VA subassemblies in row 2 and row 6 positions in Ref. 9.13. The analysis indicates that the gap variations between bundle and duct will not affect the conclusions of this safety analysis.

Section 9 References

9.1 K. L. Basehore and N. E. Todreas, "SUPERENERGY-2: A Multiassembly, Steady-State Computer Code for LMFBR Core Thermal-Hydraulic Analysis," PNL-3379, COO-2245-57TR (August 1980).

9.2 M. C. Billone, Y. Y. Liu, E. E. Gruber, T. H. Hughes, and J. M. Kramer, "Status of Fuel Element Modeling Codes for Metallic Fuels", Proc. ANS International Conference on Reliable Fuels for Liquid Metal Reactors, September 7-11, 1986, p. 5-77.

9.3 J. E. Cahalan and T. Y. C. Wei, "Modeling Developments for the SAS4A and SASSYS Computer Codes," Proceedings of the 1990 International Fast Reactor Safety Meeting (Snowbird, Utah, August 12-16, 1990), American Nuclear Society, II:123 (1990).

9.4 S. K. Cheng and N. E. Todreas, "Hydrodynamics Models and Correlations for Bare and Wire Wrapped Hexagonal Rod Bundles - Bundle Friction Factors, Subchannel Friction Factors, and Mixing Parameters," Nuclear Engineering and Design (1986) 227-251.

9.5 M. J. Bell, "ORIGEN-ORNL Isotope Generation and Depletion Code", ORNL-4628, May 1973.

9.6 Alloy Properties Databook, HEDL-TC-293, Rev. 5.

9.7 "Physical and Mechanical Properties of Alloy HT9," Design Analysis of the Core Demonstration Experiment, HEDL-TC-2895.

9.8 G. L. Hofman, et al., "Metallic Fuels Handbook," Argonne National Laboratory, ANL-IFR-29 (November 1985).

9.9 M. C. Billone, Argonne National Laboratory, unpublished information (1992).

9.10 M. C. Billone, Argonne National Laboratory, unpublished information (1994).

9.11 K. J. Miles, Jr. "Metal Fuel Safety Performance," Proceedings International Topical Meeting on Safety on Next Generation Power Reactors, Seattle Washington, May 1-5, 1988.

9.12 E. M. Dean and J. I. Sackett, "Response of EBR-II to Reactivity Insertion," ANL-75-41,

March 1978.

9.13 L. K. Chang, M. J. Lee and J. Y. Ku, Argonne National Laboratory, unpublished information (1991).

10 ANCILLARY ISSUES

10.1 Containment Design Basis

The existing design basis for the containment has been described in ANL-76-33 [10.1]. The calculations described therein utilize a hypothetical accident to bound all the credible accidents. This accident hypothesizes complete disruption of the whole core including the radial blanket subassemblies, which contain significant amounts of plutonium. Single subassembly actinide release consequences are bounded by the whole-core accident case because single subassembly actinide inventories are only about 1% of the whole-core inventories [10.2]. Even if all the available actinides were released according to the accepted release fractions, the resulting Pu dose contribution would be a small fraction of the applied dose limit; hence, the whole-core accident is clearly bounding. The addition of plutonium to the core driver subassemblies will increase the amount of plutonium in the core. Therefore the calculations of ANL-76-33 have been updated to reflect the larger inventory. The analysis has been described in [10.3] and the results are described below.

In order to determine the radiological consequences of utilizing larger inventories of plutonium and americium in the Mark V fuel a dose calculation must be performed. The dose calculation is based on a conservative representation of a Mark V EBR-II core. It is assumed that the 637 reactor subassembly (S/A) locations are loaded as follows:

S/A Type	Number of S/As
binary	14
ternary	100
reflector	157
blanket	366

The radionuclide inventory developed for the ternary subassemblies is based on a prototypical Mark-V subassembly operating at 0.88 MWt to an average heavy metal burnup of 10 at. %. The ternary radionuclide inventory is based on equilibrium depletion calculations with the

recycling of actinides incorporated to represent the long-term buildup of higher actinides, per Table 6-9. This assumption bounds the inventory for Mark-V fuel at 10 at. % burnup because of the large quantities of fission products. The radionuclide inventory developed for the binary subassemblies is based on a typical Mark-III subassembly operating at a constant power level of 0.772 MWt and irradiated to a peak discharge burnup of 10 at. %. The radionuclide inventory for blanket subassemblies is based on a projected "40-year" plant operating life. The radionuclide inventory for the reflector subassemblies was not included in the analysis because they are comprised primarily of structural materials which would not contribute significantly to the dose. This representation bounds the inventory expected over the 40-year life of EBR-II.

The dose calculations were performed in a manner consistent with the modeling assumptions of ANL-76-33 [10.1]. However, instead of using a critical organ dose as a measure of consequences, the currently accepted Effective Dose Equivalent (EDE) was evaluated in order to compare with the whole-body dose criteria from 10CFR100 [10.4]. This approach has the advantage of incorporating the integral effects of a multitude of radionuclides plus consideration of multiple dose pathways on the whole body. The dose pathways considered in the analysis included inhalation and external air immersion mechanisms. The analysis described in [10.3] also reconstitutes the original calculations to ensure consistency between the original and currently recommended methodologies.

For the bounding accident scenario modeled, it was assumed that the core disruption releases noble gases (100%), halogens (25% or 50%), solid fission products (1%), and plutonium/americium (0.025%) to the containment atmosphere. These inventories are assumed to leak through the containment at the design leakage rate of 0.2 vol%/day. Two halogen release fractions (25% and 50%) were considered to indicate the sensitivity of overall dose to iodine release assumptions. The plutonium/americium release fraction was chosen to be identical to the respirable aerosol release fraction assumed in the Fuel Cycle Facility FSAR [10.5] accident analyses, which is based on fuel oxidation in air and plateout on reactor internals [10.6]. The resulting plutonium and americium inventory based on these conservative assumptions and release fractions is as follows:

Nuclide	Reactor Inventory (kCi)	Respirable Aerosol Released (Ci)
Pu-238	33.9	8.47
Pu-239	12.9	3.22
Pu-240	7.0	1.74
Pu-241	372.0	93.0
Pu-243	53.5	13.4
Am-241	8.2	2.04

This plutonium inventory corresponds to a total mass of 250 kg in the reactor and 62.5 g released as a respirable aerosol to the containment atmosphere. Similarly, the americium inventory corresponds to a total mass of 2.8 kg in the reactor and 0.7 g released as a respirable aerosol. The original analysis considered 200 kg of plutonium and no americium.

Based on the above source terms and leakage assumptions, ANL-W site specific meteorology and current dose commitment factors, the 2-hour and 30-day EDE values were computed at the Exclusion Zone (600 meters) and Low Population Zone (1600 meters), respectively. The calculated doses (EDE) are summarized below for the 25% and 50% iodine release scenarios:

Boundary	25% I Release (Rems)	50% I Release (Rems)
Exclusion Zone (2-hours)	2.8	4.2
Low Population Zone (30-days)	14.7	19.2

These doses are less than the 10CFR100 limit of 25 Rems to the whole body for either boundary. Although the dose is sensitive to assumptions with regard to iodine release fraction the variation in resulting doses is sufficiently small that 10CFR100 criteria are still met with ample margin. Therefore, it is concluded that substantial margin is maintained between the indicated federal dose criteria and the calculated doses even in view of the conservative modeling assumptions cited

above. Hence, the use of larger plutonium/americium inventories in the Mark-V core is acceptable with respect to relevant dose criteria, and the existing design basis is preserved.

10.2 Local Faults

A traditional concern for LMRs is the issue usually referred to as local faults which is concerned with the failure of one fuel pin, or damage to one subassembly, the local fault, propagating to other parts of the core and leading to widespread core damage. This issue has been addressed in detail for Mark-II fuel in [10.7]. Three different considerations were identified:

(1) LOF and TOP events that immediately affect the whole core

(2) Whole subassembly faults

and (3) Single element faults

The first category of events is protected by PPS action and this capability is unchanged in the Mark-V fueled cores and therefore the arguments presented in Ref. 10.7 remain valid. The second and third categories of events are no more likely to occur in Mark-V fuel than for other subassemblies, nor are the consequences of these events more severe for a Mark-V core. Therefore, the EBR-II position on local faults is not affected by use of the Mark-V and Mark-VA designs.

10.3 Mark-III and Mark-IIIA Fueled Subassemblies

During the transition from a fully Mark-III core to a fully Mark-V core, EBR-II will be operated with cores which combine Mark-III and Mark-IIIA subassemblies with Mark-V and/or Mark-VA subassemblies. These cores must be operated under Limiting Conditions for Operation (LCO's) which adequately constrain all subassemblies so as to meet the design criteria described in Section 2.1.4. Such LCO's were established for Mark-V and Mark-VA fuel in Section 9.6. It remains to evaluate the behavior of Mark-III and Mark-IIIA fuel during the duty cycle events of the Mark-V safety case when constrained by the assumptions of Section 9.6. The design criteria established for Mark-V/VA fuel are also valid for Mark III/IIIA fuel, since the database from which the criteria were developed includes measurements on Mark-III and Mark-IIIA pins [10.8].

To this end, a detailed analysis of the performance of Mark-III and Mark-IIIA fuels operating within the constraints of the Mark-V safety case has been carried out using the SASSYS code. Since the cladding materials of Mark-III and Mark-IIIA fuels are D9 and 316SS, respectively, both fuels were operated under the LCO's established for Mark-VA fuel, which is also clad in 316SS. Pin dimensions for Mark-III and Mark-IIIA fuels are the same as for Mark-VA fuel. Because the solidus temperature of U-10Zr (the fuel used in Mark-III and Mark-IIIA pins) is considerably higher than that of the depleted zirconium region of irradiated U-20Pu-10Zr (1234°C vs. 1041°C), coupled with higher thermal conductivity in U-10Zr than in U-20Pu-10Zr, the LCO's established to keep Mark-VA fuel below the solidus point will clearly prevent Mark-III and Mark-IIIA pins from melting. Therefore, the only concern is cladding damage. Since the bulk of the cladding damage occurs during the LOF events, only these events have been examined for Mark-III and Mark-IIIA fuel.

The results of the analysis are summarized in Table 10-1 for Mark-III fuel and in Table 10-2 for Mark-IIIA fuel. Since D9 and 316SS behave very similarly, the results are nearly identical for the two fuels. The peak fuel temperatures listed in the two tables are the maximum fuel pin centerline temperatures achieved during the transients. Because the thermal conductivity of U-10Zr is significantly higher than that of U-20Pu-10Zr, the peak centerline temperatures in Mark-III and Mark-IIIA pins are considerably lower than the peak fuel temperatures in the low zirconium zone given in Table 9-18 and Table 9-20 for Mark-VA fuel during the same events. The peak cladding temperatures are all well below the minimum saturation temperatures for all events, so the sodium remains far from boiling. Comparing the CDF, eutectic penetration, and strain values listed in Table 10-1 and Table 10-2 to the values for Mark-VA fuel in Table 9-18 and Table 9-20 for the corresponding events indicates about the same damage in Mark-III and Mark-IIIA fuels as in Mark-VA pins, so the accumulated values over all events fall well within the design criteria.

The fluence-to-burnup ratio will also change as the core changes from Mark-III/IIIA fuel to Mark-V/VA fuel. Analysis of Sections 4 and 8 has shown that the Mark-III and Mark-IIIA subassemblies can attain the fluence equivalent of the original 10 at. % burnup limit, which corresponds to a fluence of 1.065×10^{23} n/cm^2.

Table 10-1 Mark-III Fuel Safety Parameters for LOF Events

Event	Peak Fuel Temp.	Peak Clad Temp.	Minimum Saturation Temp.*	CDF*	Eutectic Penetration (%)*	Clad Strain (%)*
AN-1 (Output Breaker Trip of One Primary Pump)	877°C (1611°F) (Row 3)	696°C (1286°F) (Row 4)	929°C (1705°F)	2.9×10^{-5}	4.9×10^{-4}	2.2×10^{-6}
AN-2 (Input Breaker Trip of Both Primary Pumps)	868°C (1594°F) (Row 3)	656°C (1213°F) (Row 6L)	909°C (1669°F)	2.2×10^{-5}	0.0	3.2×10^{-6}
UN-1 (Clutch Breaker Trip of Both Primary Pumps)	869°C (1596°F) (Row 3)	728°C (1342°F) (Row 6L)	909°C (1668°F)	1.4×10^{-3}	2.4×10^{-2}	3.0×10^{-4}
UN-2 (Clutch Breaker Trip of One Pump, Seizure of One Pump)	910°C (1670°F) (Row 4)	752°C (1386°F) (Row 4)	869°C (1595°F)	4.7×10^{-4}	9.1×10^{-3}	6.3×10^{-5}
EU-1 (Clutch Breaker Trip of Both Primary Pumps, Plus One Stuck Control Rod)	869°C (1596°F) (Row 3)	782 °C (1440°F) (Row 6L)	909°C (1668°F)	--	9.4×10^{-2}	--

*These values occur in the row 6 normal flow subassembly, 6L.
All values in the table include uncertainties.

In conclusion, then, Mark-III and Mark-IIIA subassemblies can operate within the design criteria when constrained by the LCO's for Mark-VA fuel.

10.4 Safety Considerations for Blanket Fuel

Blanket subassemblies consist of 19 fuel pins arranged in three rows and are located in rows 11 to 16 in the reactor. Depleted-uranium fuel is used in blanket fuel pins. Blanket pins use 304SS cladding with an outside diameter of 0.493 in. (1.25 cm) and a thickness of 0.018 in. (0.046 cm). The pin is sodium-bonded to the cladding, and an argon-helium mixture is used in the gas plenum. The T.S. burnup limit of blanket subassemblies is 0.5 at. %. There are standard and high-flow blankets.

Table 10-2 Mark-IIIA Fuel Safety Parameters for LOF Events

Event	Peak Fuel Temp.	Peak Clad Temp.	Minimum Saturation Temp.*	CDF*	Eutectic Penetration (%)*	Clad Strain (%)*
AN-1 (Output Breaker Trip of One Primary Pump)	877°C (1611°F) (Row 3)	696°C (1285°F) (Row 4)	929°C (1705°F)	2.8×10^{-5}	4.9×10^{-4}	2.1×10^{-6}
AN-2 (Input Breaker Trip of Both Primary Pumps)	868°C (1594°F) (Row 3)	656°C (1213°F) (Row 6L)	909°C (1669°F)	2.2×10^{-5}	0.0	3.2×10^{-6}
UN-1 (Clutch Breaker Trip of Both Primary Pumps)	869°C (1599°F) (Row 3)	728°C (1342°F) (Row 6L)	909°C (1669°F)	1.4×10^{-3}	2.4×10^{-2}	3.0×10^{-4}
UN-2 (Clutch Breaker Trip of One Pump, Seizure of One Pump)	910°C (1670°F) (Row 4)	752°C (1386°F) (Row 4)	868°C (1595°F)	4.7×10^{-4}	9.1×10^{-3}	6.3×10^{-5}
EU-1 (Clutch Breaker Trip of Both Primary Pumps, Plus One Stuck Control Rod)	869°C (1595°F) (Row 3)	782°C (1440°F) (Row 6L)	909°C (1668°F)	--	9.4×10^{-2}	--

*These values occur in the row 6 normal flow subassembly, 6L.
All values in the table include uncertainties.

The current safety criteria for the blanket subassembly are based on fuel-cladding liquefaction temperature and driver fuel operation experience and are given below:

* For anticipated events the fuel-cladding remains below the liquefaction temperature.
* For unlikely events the fuel-cladding temperature is allowed to be between the liquefaction temperature and 1500°F (816°C) for no more than 60 seconds.

Until now, a fuel-cladding liquefaction temperature of 1292°F (700°C) has been used for the blanket. However, as discussed in Ref. 10.8, this value is appropriate to steady-state operation and is overly conservative when applied to transient events. Reference 10.7

recommends a transient limit of 1337°F (725°C) on blanket liquefaction temperature, which is still conservative. Therefore, this study assumes a steady-state liquefaction temperature limit of 1292°F and a transient limit of 1337°F for the blanket.

Thermal-hydraulic analysis of off-normal transients in Ref. 10.9 indicates that, due to the relatively large heat capacitance of the blanket, thermal responses during loss-of-flow (LOF) events are so slow that, if the cladding temperature exceeds the liquefaction temperature during an unlikely event, it will remain above the liquefaction temperature for more than 60 seconds. Therefore, as a practical matter, the fuel-cladding temperature must remain below the transient liquefaction temperature limit for both anticipated and unlikely events.

Several safety analyses of blanket subassemblies have been performed over the years. In the parametric study documented in Ref. 10.9, unlikely LOF event UN-2 (seizure of one primary pump and clutch breaker trip of the other primary pump) was identified as the protected transient which resulted in greatest damage to blanket subassemblies. The present Tech. Spec. blanket hot-channel sodium outlet temperature limit of 1140°F (616°C) for normal operation corresponds to achieving a peak cladding temperature (including uncertainties) during UN-2 just below the steady-state liquefaction temperature of 1292°F, assuming the auxiliary pump provides 5% of the nominal reactor flow once the primary pumps are inoperative. Reference 10.9 used a single-pin model and performed the heat transfer analysis with the THTB code. The analysis in Ref. 10.9 is very conservative.

Since the analysis of Ref. 10.9 was performed, there has been a movement away from reliance on the auxiliary pump. At present, the requirement on the auxiliary pump capacity is only 3.3%, and the Mark-V safety case takes no credit for the auxiliary pump. The need therefore arose to revisit the analysis of Ref. 10.9 and update it to reduced auxiliary pump capacity, as well as taking advantage of current analysis tools. To this end, two studies were performed. In one [10.10], the NATDEMO code was used to evaluate the UN-2 transient with either 3.3% auxiliary pump capacity or the auxiliary pump turned off. The analysis used a single-pin model and so neglected intrasubassembly heat transfer; however, the effect of natural circulation was considered. The NATDEMO results indicated that, if the auxiliary pump provides 3.3% of the nominal flow, the peak UN-2 cladding temperature is below 1292°F, whereas if the auxiliary pump

is turned off, the peak UN-2 cladding temperature is 1301°F (705°C) for standard-flow blanket subassemblies and 1336°F (724°C) for high-flow blankets. Thus, the safety criterion is just barely met when the transient liquefaction temperature limit is assumed.

The other analysis [10.11], using the SASSYS code, employed a multiple-pin model in order to account for intrasubassembly heat transfer. The auxiliary pump was assumed to be off. The results of the analysis indicate that the peak coolant temperature is the initial coolant temperature, and so a hot-channel coolant temperature limit of 1140°F is adequate for UN-2 even without the auxiliary pump. Because the SASSYS analysis includes the effects of intrasubassembly heat transfer, the SASSYS results differ qualitatively from those of Refs. 10.9 and 10.10, which predict a rise in blanket coolant temperature during UN-2. The analysis of Ref. 10.11 also indicates that UN-2 is not the most severe event for blanket subassemblies and that, in general, rapid loss of flow is less severe for the blanket than quasi-static operation. This finding has led to identification of the following three events as the limiting transients for blanket analysis:

(A) LOF Due to Shaft Binding of a Single Pump

This slow LOF is tripped by the flow trip, which is set at 88% of full flow. For a reactor inlet temperature of 700°F (371°C), the nominal hot-channel ΔT at full flow is 440°F (244°C). When an uncertainty factor of 1.21 is applied [Ref. 10.9], ΔT is 532°F (440°F x 1.21 or 296°C) with uncertainty. For this LOF event the peak coolant ΔT with uncertainty is found to be 605°F (532°F/0.88 or 336°C), which corresponds to a coolant temperature of 1305°F (707°C), which is below the liquefaction temperature of 1337°F (725°C). The calculated temperature is conservative because it was calculated neglecting the fact that the reactor power decreases as the flow drops due to reactivity feedback. The cladding temperature would be only a few degrees higher than the coolant temperature, since the blanket flow is so low.

(B) Power Drifting Event AN-5

Event AN-5 postulates that, due to operator inattention and failure of the overpower

warning system, the reactor power could drift near 115% of nominal power and remain there for a period of time. In the proposed T.S., the time is limited to 2.1 hours based on LIFE-METAL Mark-V driver fuel analysis (see Sec. 9.7.2.5). At 15% overpower, the peak coolant temperature with uncertainty is 1312°F (700°F + (532°F x 1.15), or 711°C), which is well below the transient liquefaction temperature.

(C) Limiting Conditions for Operation (LCO)

Reactor operation at 105% of nominal power is defined as the overpower LCO. The LCO hot-channel peak coolant temperature is 1259°F ((700°F + (532°F x 1.05), or 682°C), which is much less than the steady-state liquefaction temperature, so the design criterion is satisfied.

It is concluded that when the correct transient liquefaction temperature is used for design and safety analysis, the blanket satisfies the design criteria for the limiting transients.

10.5 The Effect of β_{eff} on the Safety Case

The delayed neutron fraction (β_{eff}) for the binary (Mark-I through -IV) and ternary (Mark-V) fueled reactor cores are 0.0067 and 0.0053 respectively. The present report addresses the safety considerations of the transition core, in which a small number of Mark-V fuel subassemblies will replace the Mark-III fuel subassemblies initially, and the replacement will be gradually increased until the whole core is converted to the Mark-V fuel. In the transition, the β_{eff} will therefore gradually decrease from 0.0067 to 0.0053. The effects of reactivity feedbacks on the safety analysis, reactor operation and fuel handling are discussed below.

In the off-normal transient analyses a β_{eff} of 0.0053 was used for thermal-hydraulic predictions of the protected off-normal events. The effects of β_{eff} on fuel pin temperatures and cladding damage have been investigated for off-normal transients, and the impact of β_{eff} on LOF (UN-1) and TOP (UN-3) transients was studied in detail. The analysis indicates that the effects of β_{eff} (0.0067 vs. 0.0053) on both fuel pin temperature and cumulative damage function (CDF) are small for the LOF event when the same shutdown reactivity of 3.70$ was employed. If the

shutdown reactivity is increased above 3.7$ to correctly account for the lower β_{eff} in Mark-V fuel, the CDF is reduced. The main concern of the TOP transient is the fuel temperature. If the reactivity insertion rate is adjusted to be consistent with β_{eff} (from 0.01 $/s for β_{eff} = 0.0053 to 0.0079 $/s for β_{eff} = 0.0067), then peak fuel temperature is essentially invariant with respect to β_{eff}.

For a startup accident, a period trip of 17 s was chosen for Mark-II, -III cores for effective protection, in addition to power level trips, over the range for which SOT trips would not be effective. Reducing β_{eff} slows the rate of increase of the rate of power rise and delays the time at which the period trip scrams the reactor, but the temperatures at the time of the trip are essentially independent of β_{eff} if the reactivity insertion rate is adjusted to be consistent with β_{eff}, and so the period trip of 17 s provides adequate protection. When the rate of power increase is low, the SOT trip is able to provide protection as the period trip becomes less effective. Therefore the existing period trip affords acceptable protection. In conclusion, the variation of β_{eff} has insignificant impact on the off-normal transient analyses.

The Technical Specifications requirements relating to reactivity for the <u>operate mode</u> are as follows:

(1)	Shutdown Reactivity	≥ 3.70 $,
(2)	Maximum worth of one control rod	≤ 1.30 $,
(3)	Maximum worth of ACRDS rod	≤ 1.30 $ in slow speed mode,
(4)	Average Power Coefficient	< -0.0017 $/MW,
(5)	Prompt Power Coefficient	< -0.0007 $/MW.

These limits will be preserved intact during the transition to the ternary core. As β_{eff} decreases it will become easier to meet requirements (1), (4) and (5). Requirements (2) and (3) will become progressively more difficult to meet as the conversion progresses. However, as long as they are met, the core will be inside the bounds of this safety analysis because all protected transients assumed 3.70 $ of shutdown reactivity, except EU-1 in which one rod was assumed to be stuck.

The Technical Specifications requirements for the <u>fuel-handling mode</u> are as follows:

(1)	Total Shutdown Worth	≥ 4.0 $,
(2)	Subassembly Replacement Worth	≤ 2.50 $,
(3)	Minimum Subcriticality	≥ 5.0 $ if replacement worth ≥ 1.80 $.

Total Shutdown Worth and Minimum Subcriticality are used in equivalent fashion in the Technical Specifications. Maintenance of these limits will preserve the safety posture of EBR-II where they represent margins for error and the unit of reactivity is not relevant. In practice the second requirement will restrict the exchanges that can be made to a smaller replacement worth, in absolute reactivity units. This will tend to enhance the safety because requirement (3) will be invoked more often.

The total shutdown worth requirement of 4.0 $ is based upon an extremely unlikely fault with inadvertent replacements of two zero-worth subassemblies with driver subassemblies. Maintenance of the existing 1.80 $ limit will ensure that the 4.0 $ affords appropriate protection.

There is a <u>surveillance requirement</u> that allows the requirement for control and safety-rod worth measurements to be waived for "approved experiments or operation for which estimated control-and safety-rod worths are well established and clearly do not violate stated limiting conditions for operation". This might occur, for example, if any run were to have a core essentially identical to its predecessor. The conditions applied are,

(1)	Shutdown Reactivity	≥ 4.20 $
(2)	Maximum Worth of One Rod	≤ 1.00 $

The second condition will become increasingly difficult to satisfy and so this exception will be taken increasingly less often which, while an operational burden, will enhance surveillance of rod worths. In addition, in a core with a changing β_{eff}, the basic premise of having well-established rod worths may well not be met. Therefore maintenance of this limit is sufficient to preserve the safety envelope of EBR-II.

When a fuel subassembly is moved from the storage basket to the Fuel Unloading Machine (FUM) and Interbuilding Coffin (IBC), the fuel subassembly is cooled by argon to remove the heat generated by decay power. The change of β_{eff} has no significant effect on the decay heat, so the

temperatures in the FUM and IBC of Mark-V/VA subassemblies are expected to be the same as those of Mark-III/IIIA subassemblies. See Sec. 10.12 for a discussion of other considerations in transferring Mark-V/VA subassemblies.

10.6 The Effect of Reactor Inlet Temperature on the Safety Case

EBR-II normally operates at a reactor inlet temperature of 700°F (371°C), maintained to within ±2°F (±1°C). This is the inlet temperature assumed in the definition of the T. S. limit coolant subchannel outlet temperatures discussed in Section 9.6. There are, however, instances in which the reactor inlet temperature is not 700°F, and so the effect of inlet temperature variation on the off-normal transient results discussed in Section 9.7 needs to be evaluated.

Inlet temperatures other than 700°F may occur for any of the following reasons:

1. A drift in the inlet temperature that goes unnoticed by the operators.
2. Intentional inlet temperature reduction for programmatic reasons.
3. Inlet temperature variation during a transient.

Situation 2 differs significantly from situations 1 and 3 in the protection offered by the subassembly outlet temperature (SOT) trip. The Tech. Specs. require that the trip be set to a temperature which is 115% of the measured subassembly coolant temperature rise above the reactor inlet temperature at the maximum authorized reactor power. Thus, if the inlet temperature is intentionally lowered (as was the case in the SHRT tests) the trip setpoint is also lowered. This is the case in situation 2, but not in situations 1 and 3. In these instances, the setpoint is consistent with an initial inlet temperature of 700°F, but the inlet temperature deviates from the initial value; if the inlet temperature has dropped below 700°F, the level of protection offered by the SOT trip will have been reduced.

The current EBR-II Tech. Specs. require only that the reactor inlet temperature be between 580°F (304°C) and 730°F (388°C). In practice, although the reactor has on occasion been operated for transient tests with the initial inlet temperature set significantly below 700°F, it is never operated with the steady-state inlet temperature set above 700°F. A scram alarm is set to trip if the inlet temperature reaches 710°F (377°C), so even during a transient test, the inlet

temperature never approaches the upper bound of 730°F. This upper bound, then, is not an actual operating limit; it is the maximum temperature which could occur in the event of a total loss of secondary cooling if the Tech. Spec. time limit of 25 s elapsed before protective action occurred.

Normal operating practice tries to keep the inlet temperature as steady as possible, ideally to within 2°F of the nominal value. However, it is necessary to provide room for operation with a somewhat greater margin of error in order to allow for all probable situations. An operating band of ±10°F (±6°C) has been selected, which implies that the design criteria must be met for all off-normal transients occurring over this band of inlet temperature variation.

The effects of inlet temperature variation on the safety analysis must therefore be considered under three sets of conditions:

1. Operation in the band between 690°F (366°C) and 710°F (377°C), with the SOT trip setpoint set as though the inlet temperature were 700°F (371°C) (allowing an error margin of ±10°F (±6°C)).
2. Operation with the inlet temperature intentionally reduced below 700°F (371°C), with the trip setpoint set consistent with the lowered inlet temperature. The lower limit of this range is 580°F (304°C).
3. Operation up to 730°F (388°C) as a result of the inlet temperature rising during a transient. The SOT trip setpoint is consistent with an inlet temperature of 700°F (371°C).

Four of the safety case transients were selected for detailed inlet temperature parametric study: AN-3 (single rod runout terminated by power trip), UN-1 (clutch breaker trip of both primary pumps), UN-3 (single rod runout terminated by SOT trip), and UN-5 (single rod runout at startup terminated by power trip). These four are the transients which come closest to exceeding one or more of the design criteria, and they are therefore the transients most likely to exceed those criteria due to change in inlet temperature.

Consider first operation between 690°F and 700°F. Transients which scram on power or flow trips (AN-3, UN-1, and UN-5) will scram at the same time regardless of inlet temperature, so

lowering the inlet temperature will lower the peak fuel and cladding temperatures, thereby increasing the margin to fuel melting and reducing cladding damage. In the case of transient UN-3, which scrams on SOT trip, the lower the inlet temperature, the longer the transient will run until scram, since the SOT trip setpoint remains constant while the initial coolant outlet temperature moves further away from the setpoint. The margin to fuel melting is reduced, and cladding damage is increased.

The opposite is true for operation above 700°F. Scram times for the transients which scram on power or flow trips will still be independent of inlet temperature, but now the higher inlet temperature produces higher peak fuel and cladding temperatures, so the margin to fuel melting is reduced and cladding damage is increased. Conversely, the initial coolant outlet temperature in UN-3 now moves closer to the fixed setpoint, so the transient terminates sooner at lower peak fuel and cladding temperatures, thereby increasing the margin to fuel melting and decreasing cladding damage.

These observations are quantified for Mark-V fuel in Table 10-3, which shows safety parameters for the four transients at inlet temperatures of 690°F, 700°F, and 730°F. The same parameters are given in Table 10-4 for Mark-VA fuel. Comparing the values for CDF, eutectic penetration, and clad strain at 730°F to those at 700°F shows an increase in these parameters, but the increase is not sufficient to challenge the transient design criteria. For Mark-V fuel, the CDF for the anticipated and unlikely transients increases to 0.035, the cumulative eutectic penetration increases to 2.81%, and the accumulated fuel-cladding strain increases to 0.4%, while for Mark-VA fuel, the CDF increases to 0.0031, the cumulative eutectic penetration increases to 0.18%, and the accumulated fuel-cladding strain increases to 0.0047%. All these parameters still fall within the design criteria, and so the outer rows remain limited by the steady-state criteria on cladding temperature. The parameter values at the designated inlet temperature operational upper limit of 710°F will fall below those at 730°F, so during normal operation, the outer rows operate well within the design criteria.

Looking at the peak fuel temperatures as a function of inlet temperature indicates that the inner rows are limited by the power that would be reached during UN-3 at an inlet temperature of 690°F. The ΔT's corresponding to these limiting subassembly powers become the

limiting conditions for operation, as discussed in Section 9.6.

Table 10-3 Mark-V Fuel Safety Parameters as a Function of Reactor Inlet Temperature

Transient	T_{inlet} (°F)	Peak Fuel Temperature in Low Zr Zone	CDF	Eutectic Penetration (%)	Clad Strain (%)
UN-3 (Single Rod Runout (0.01 $/s), SOT Trip)	700	1019°C (1866°F)	6.2×10^{-5}	3.7×10^{-4}	5.6×10^{-4}
	690	1041°C (1905°F)	8.3×10^{-5}	6.2×10^{-4}	7.8×10^{-4}
	730	956°C (1752°F)	2.8×10^{-5}	0.0	2.4×10^{-4}
UN-1 (Clutch Breaker Trip of Both Primary Pumps)	700	953°C (1747°F)	1.6×10^{-2}	3.4×10^{-2}	1.7×10^{-1}
	690	946°C (1735°F)	1.2×10^{-2}	2.9×10^{-2}	1.4×10^{-1}
	730	967°C (1773°F)	3.1×10^{-2}	5.5×10^{-2}	3.6×10^{-1}
AN-3 (Single Rod Runout (0.01 $/s), Power Trip)	700	986°C (1807°F)	3.0×10^{-5}	0.0	2.6×10^{-4}
	690	983°C (1801°F)	2.3×10^{-5}	0.0	2.0×10^{-4}
	730	1001°C (1834°F)	7.4×10^{-5}	4.2×10^{-4}	6.7×10^{-4}
UN-5 (Single Rod Runout (0.01 $/s) at Startup, Power Trip)	700	978°C (1792°F)	4.7×10^{-6}	0.0	4.4×10^{-5}
	690	978°C (1793°F)	3.9×10^{-6}	0.0	3.7×10^{-5}
	730	993°C (1819°F)	1.2×10^{-5}	1.2×10^{-4}	8.0×10^{-5}

If inlet temperature is reduced and the SOT trip setpoint is reduced correspondingly, peak fuel temperatures and cladding temperatures are lowered for all transients, and the safety case provides an envelope for safe operation down to the lower limit of 580°F.

In conclusion, then, parametric analysis of reactor inlet temperature shows that the inner rows are limited by event UN-3 occurring at an inlet temperature reduced to the lower bound of the margin of error allowed during normal operation (690°F). The outer rows remain limited by the steady-state cladding temperature design criteria.

Table 10-4 Mark-VA Fuel Safety Parameters as a Function of Reactor Inlet Temperature

Transient	T_{inlet} (°F)	Peak Fuel Temperature in Low Zr Zone	CDF	Eutectic Penetration (%)	Clad Strain (%)
UN-3 (Single Rod Runout (0.01 $/s), SOT Trip)	700	1020°C (1867°F)	5.8×10^{-6}	0.0	$<10^{-6}$
	690	1040°C (1904°F)	7.8×10^{-6}	0.0	$<10^{-6}$
	730	955°C (1751°F)	2.3×10^{-6}	0.0	$<10^{-6}$
UN-1 (Clutch Breaker Trip of Both Primary Pumps)	700	949°C (1740°F)	1.2×10^{-3}	2.2×10^{-2}	2.6×10^{-4}
	690	944°C (1730°F)	9.1×10^{-4}	1.9×10^{-2}	1.9×10^{-4}
	730	962°C (1764°F)	2.5×10^{-3}	3.7×10^{-2}	6.2×10^{-4}
AN-3 (Single Rod Runout (0.01 $/s), Power Trip)	700	990°C (1815°F)	2.8×10^{-6}	0.0	$<10^{-6}$
	690	985°C (1806°F)	2.0×10^{-6}	0.0	$<10^{-6}$
	730	1004°C (1838°F)	7.6×10^{-6}	0.0	$<10^{-6}$
UN-5 (Single Rod Runout (0.01 $/s) at Startup, Power Trip)	700	982°C (1799°F)	$<10^{-6}$	0.0	$<10^{-6}$
	690	982°C (1800°F)	$<10^{-6}$	0.0	$<10^{-6}$
	730	995°C (1823°F)	2.2×10^{-6}	0.0	$<10^{-6}$

10.7 Startup TOP Events

At the low power levels of reactor startup, reactivity feedback is not significant, and the rate of power rise during a TOP event increases rapidly. A short period is therefore reached very quickly, and so the greatest margin of protective action is given by the period trip. The power-level and subassembly-outlet-temperature-level (SOT) trips are far less effective at protecting the reactor at these powers than is the period trip. This was demonstrated in transient events AN-4 and UN-5. Both events are 1 cent/s reactivity insertions initiated at 62.5 W. AN-4 is terminated by the period trip, while UN-5 is terminated by the power-level trip. As discussed in Section 9.7, virtually no temperature increase or damage occurs during AN-4, whereas UN-5 experiences fuel temperatures which approach the solidus point, plus a limited amount of cladding

damage.

As power increases, the maximum possible rate of power rise for a given rate of reactivity insertion decreases due to increased reactivity feedback, and the period trip becomes ineffective. At this point, the reactor is protected only by the power-level and SOT-level trips.

The effectiveness of level trips vs. the period trip has been analyzed for the unlikely event of a double control-rod runout. This event was chosen because the rate of reactivity insertion is fast enough so that the period trip is effective over a significant power range, yet the event is credible, though highly improbable. The transient was evaluated over a range of initial powers (1 MW to 25 MW) for termination by power-level trip, SOT-level trip, and period trip. An inlet temperature of 700°F was assumed.

Looking first at Mark-V fuel, Figure 10-1 shows the peak-inside-cladding temperature as a function of initial power and trip function, and Figure 10-2 shows the corresponding cumulative damage function (CDF) plots. These plots clearly display the increased margin of protective action provided by the period trip at low powers. Cladding damage is small regardless of trip function and is essentially zero when the transient is terminated by the period trip. Figure 10-3 plots fuel temperature as a function of initial power and trip function; the fuel remains well below melting when the period trip terminates the event and exceeds the solidus only if both period trip and power trip fail, which is a beyond-design-basis event. Note that, at this rate of insertion, the period trip becomes ineffective at about 25 MW, i.e., reactivity feedback becomes strong enough to prevent the reactor period from dropping to 17 s.

Figure 10-4 through Figure 10-6 show similar results for Mark-VA fuel. Peak cladding temperatures and CDF are less than for Mark-V fuel, since the Mark-VA fuel steady-state cladding temperature limit is significantly lower than that for Mark-V fuel, as discussed in Section 9.5.

10.8 Duct Dilations of Control, Safety and Blanket Subassemblies

There are two safety and operational concerns with regard to dilation of control and safety subassembly ducts:

(1) Interference between the control/safety subassembly and the thimble, and

(2) Duct dilation larger than the diametral clearance between the duct and the position hole in the storage basket (ΔD_{gap})

The purpose of this section is to address these issues, as well as the issue of dilation in blanket subassemblies.

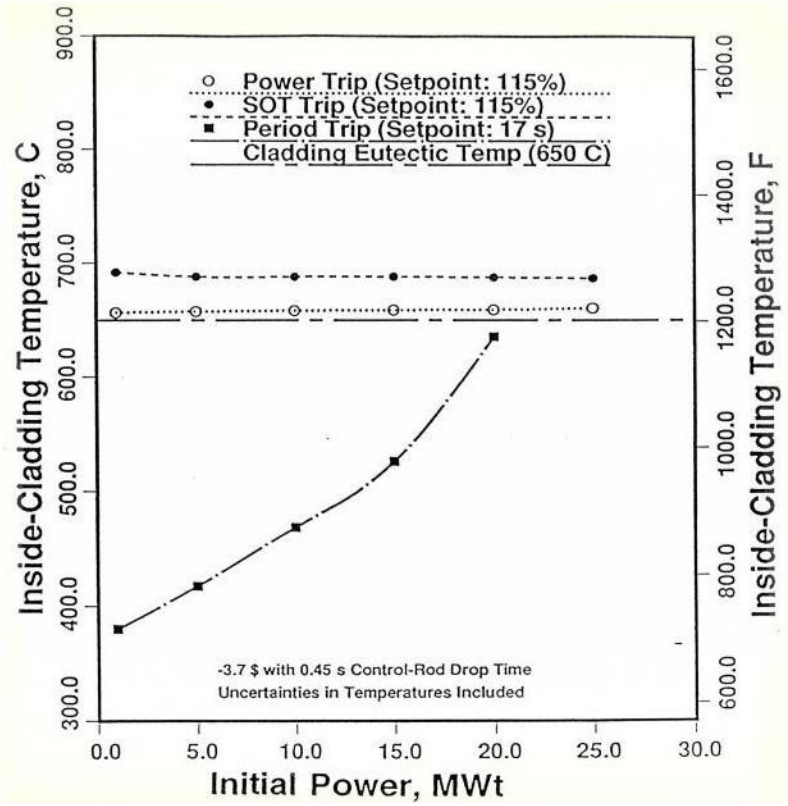

Figure 10-1 Peak Temperature Reached in Cladding of Hottest Mark-V Driver Fuel Pin for Power-Level Trip, SOT Trip, and Period Trip as a Function of Initial Power

Control and safety subassemblies contain 61 Mark-II geometry U-10Zr type pins arranged in 5 rows and are located in rows 5 and 3, respectively. The subassembly duct is made of 316SS, while the thimble duct is made of HT9. Leakage flow is between the subassembly and the thimble ducts. Both ducts are 0.040 (1.02 mm) inches thick, and the outer flat-to-flat distance of the subassembly duct and guide thimble duct are 1.908 in. (48.5 mm) and 2.290 in. (58.2 mm), respectively.

The radial pressure difference across the thimble duct is very small, so creep dilation of the thimble duct can be neglected. Since the thimble duct is made of HT9, it is almost free of

irradiation-induced swelling, and the fluence effect on the thimble duct dilation is negligible.

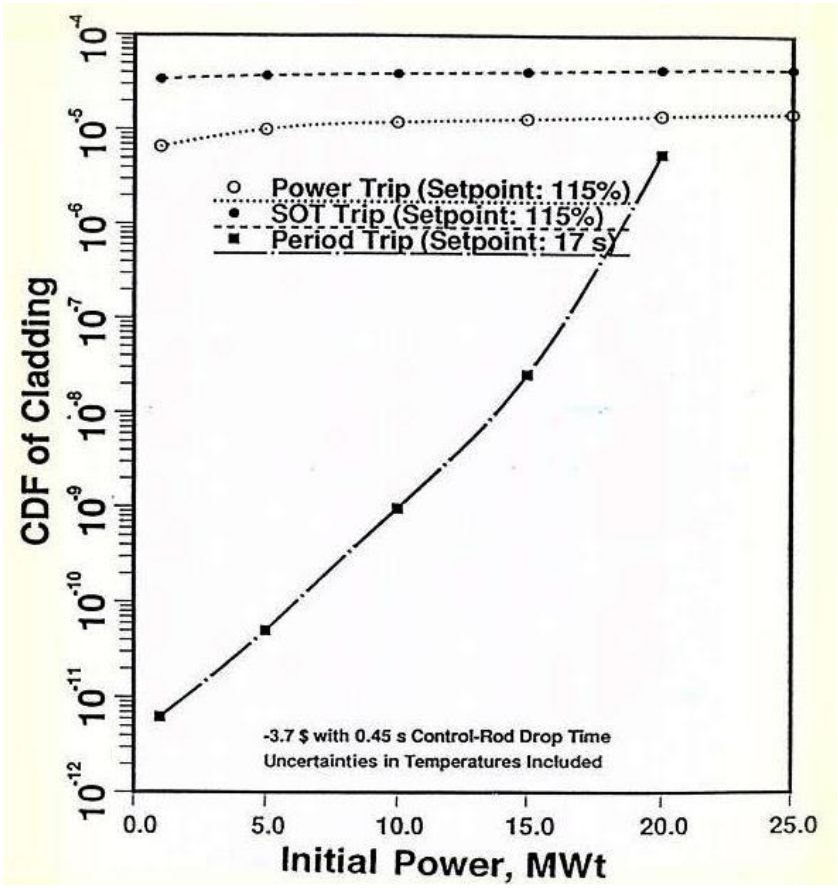

Figure 10-2 CDF of Worst Cladding Damage of Mark-V Driver Fuel Pin for Power-Level Trip, SOT Trip, and Period Trip as a Function of Initial Power

The diametral clearance between the safety-rod subassembly duct and the position hole in the storage basket, ΔD_{gap}, is 0.282 in. (7.16 mm), while the ΔD_{gap} for the control-rod subassembly duct is 0.265 in. (6.73 mm) because of the existence of the guide ring. These clearances are considerably larger than that for the driver subassembly (0.04 in., or 1.04 mm). The gap between the safety/control subassembly duct and the thimble duct is 0.191 in. (4.85 mm), so duct-to-duct interaction is unlikely. Thus, no duct-to-duct interaction should be considered in the dilation analysis.

A dilation analysis in which no duct-to-duct interaction was considered [10.12] was performed for control and safety subassembly ducts using the ANSYS code [10.13]. Dilation of the duct is caused by irradiation/creep-induced deformation and irradiation-induced swelling. Irradiation/creep-induced dilations were predicted in Ref. 10.12 for the following duct size and

thermal and pressure loading conditions:

Duct Temperature = 842°F (450°C)

Pressure = 26 psi (0.18 Mpa)

Outer flat-to-flat distance = 2.29 in. (8.82 cm)

Duct thickness = 0.04 in. (1.02 mm).

The calculation covers burnups up to 14 at. %, which corresponds to a fluence of 1.5 x 10^{23} n/cm^2 and operating time of 4.9 x 10^{7} s (2.2 years) assuming a plant factor of 70%.

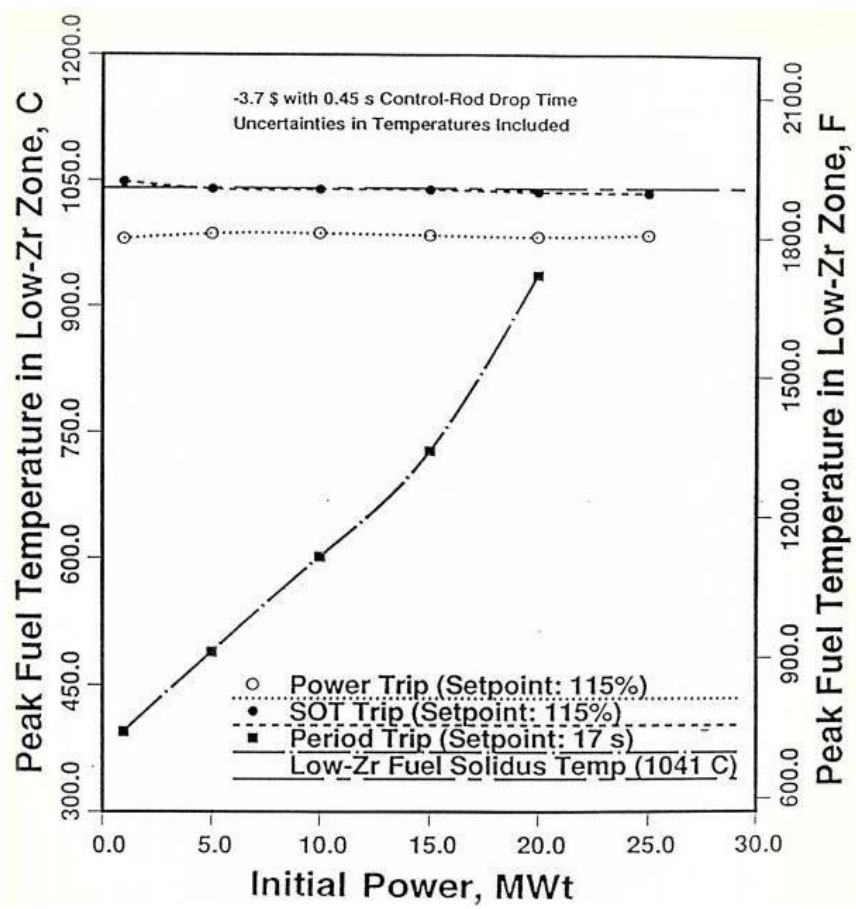

Figure 10-3 Peak Fuel Temperature Reached in Low-Zr Zone of Hottest Mark-V Driver Fuel Pin for Power-Level Trip, SOT Trip, and Period Trip as a Function of Initial Power

EBR-II operation experience indicates that the maximum duct dilation occurs at the core midplane, where the flux is the highest. In the duct dilation analysis, the midplane location is the point of interest.

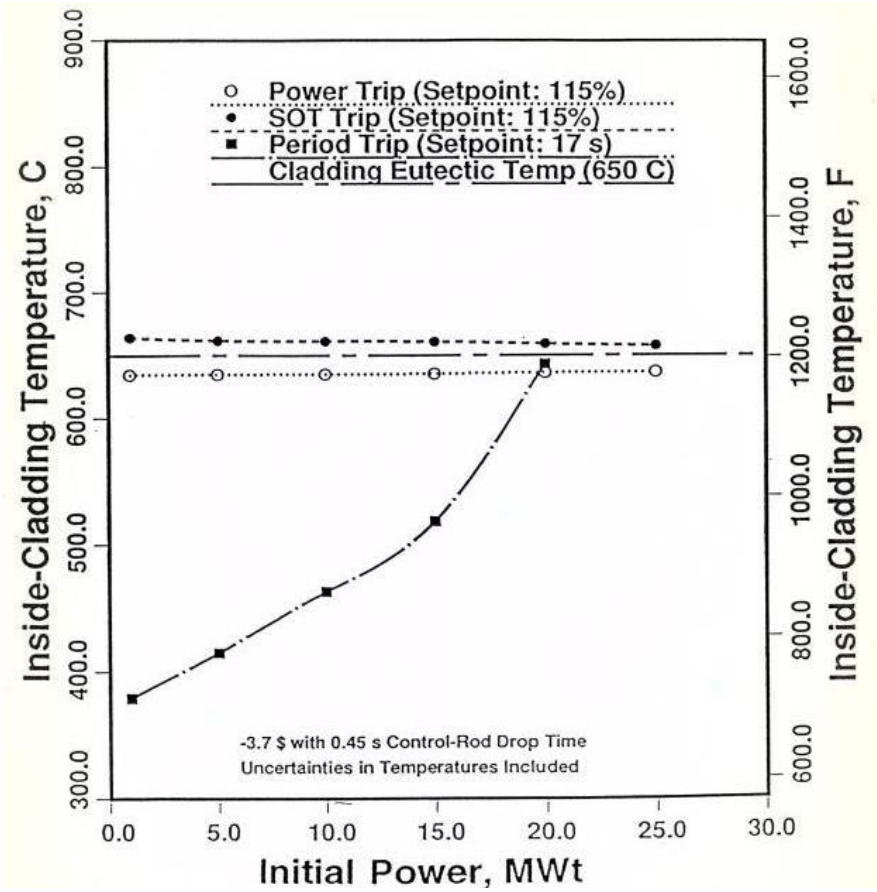

Figure 10-4 Peak Temperature Reached in Cladding of Hottest Mark-VA Driver Fuel Pin for Power-Level Trip, SOT Trip, and Period Trip as a Function of Initial Power

The Tech. Spec. limiting hot-channel temperature is 1050°F (566°C) for both control and safety rods, and the average subassembly outlet temperature is 978°F (526°C), assuming a peaking factor of 1.26. If we conservatively assume that the duct temperature is the same as the average coolant temperature, then at the core midplane, the duct temperature is 840°F (449°C), almost the same temperature used in the analysis of Ref. 10.12.

The fluences of control and safety subassembly ducts are limited to 5.0 x 10^{22} and 6.9 x 10^{22} n/cm^2, respectively, for reactor operation. Using these fluences and the input parameters given above, ANSYS predicts creep-induced diametral dilations of control and safety subassemblies of 31 and 59 mils (0.78 and 1.5 mm), respectively.

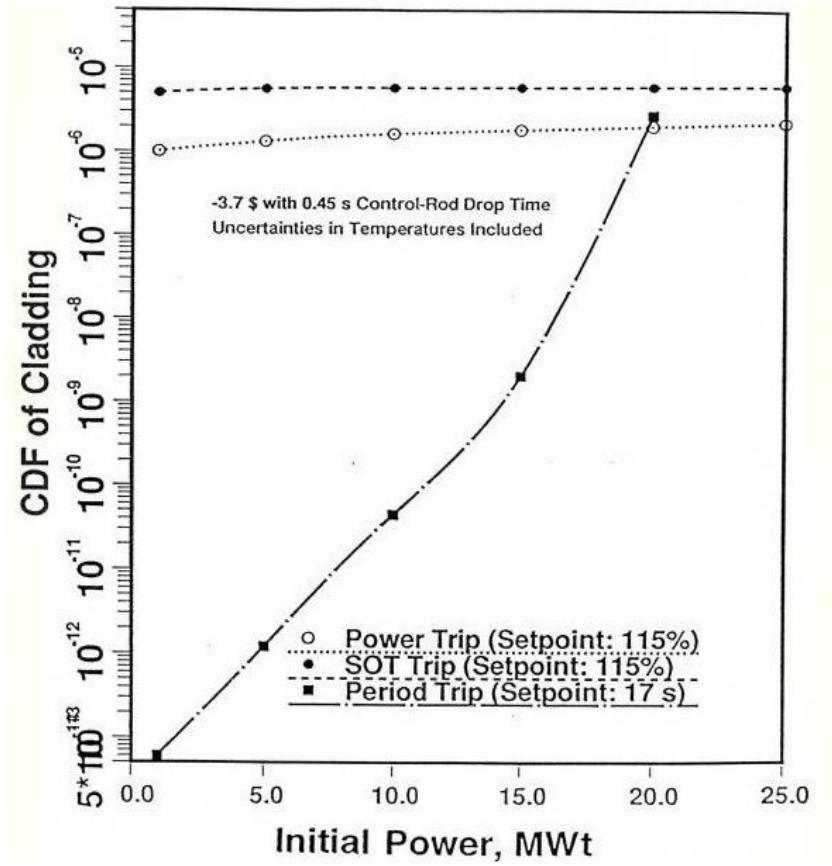

Figure 10-5 CDF of Worst Cladding Damage of Mark-VA Driver Fuel Pin for Power-Level Trip, SOT Trip, and Period Trip as a Function of Initial Power

The total pressure drop of control and safety subassemblies is about 40 psi (0.276 Mpa), so the pressure loading on the duct at the core midplane is less than 40 psi (0.276 Mpa). ANSYS duct dilation calculations in Ref. 10.12 indicate that the dilation is almost linearly proportional to the applied pressure. The boundary conditions of the duct flat are similar to those of a cantilever beam, in which the elastic deformation is proportional to the fourth power of the beam length for a given wall thickness. In the inelastic regime the relationship between the length and deformation is not obvious; however, the deformation increases with increase of the beam length. If we conservatively assume that the pressure loading is 40 psi (0.276 Mpa), then the estimated dilations of the control and safety subassembly ducts are 48 mils (31 mils x (40 psi/26 psi), or 1.22 mm) and 90 mils (59 mils x (40 psi/26 psi), or 2.29 mm), respectively.

Irradiation swelling is a function of fluence and temperature. Diametral dilations of control and safety subassembly ducts due to irradiation swelling were found based on the empirical

equation presented in Ref. 10.14, and they are 1.56 and 5.19 mils (0.04 and 0.13 mm) for control and safety subassembly ducts, respectively. The total dilations for control and safety subassembly ducts are 49.6 (48 + 1.56) and 95.2 (90 + 5.19) mils (1.24 and 2.42 mm), respectively. The predicted dilations are considerably less than the diametrial gap between the subassembly and the thimble (0.382 in., or 9.7 mm) and the ΔD_{gap} for safety (0.282 in. (7.16 mm)) and control (0.265 in. (6.73 mm)) subassemblies. Therefore, it can be concluded that the dilations of control and safety subassemblies will not cause either safety or operation problems.

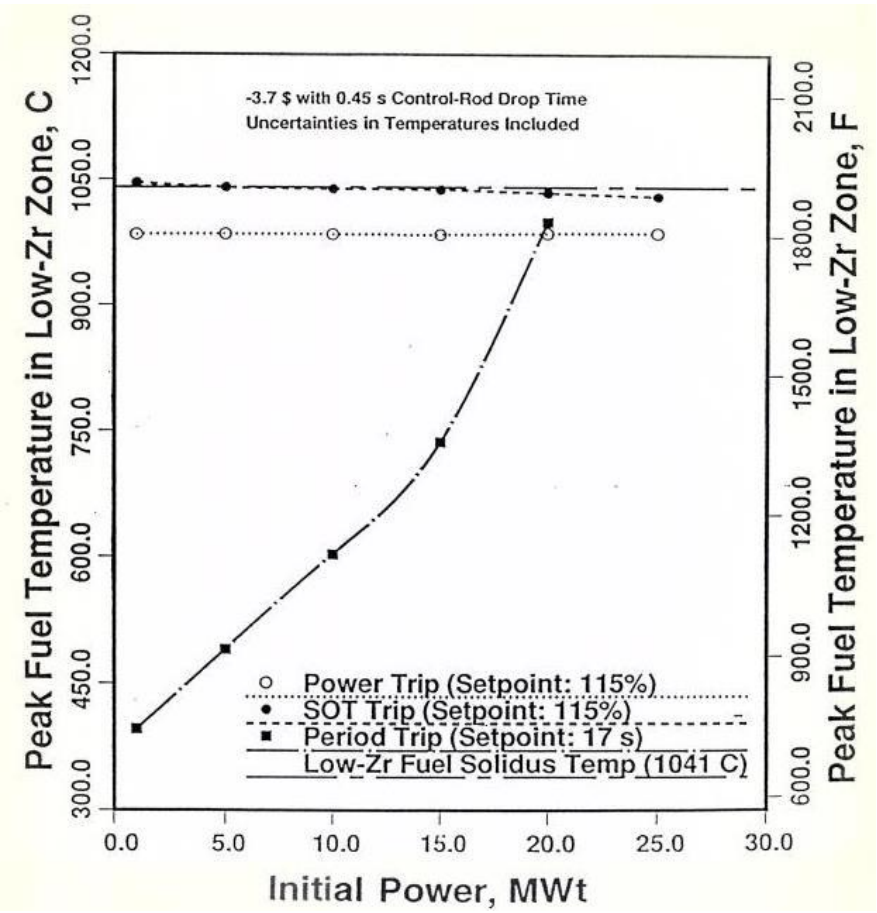

Figure 10-6 Peak Fuel Temperature Reached in Low-Zr Zone of Hottest Mark-VA Driver Fuel Pin for Power-Level Trip, SOT Trip, and Period Trip as a Function of Initial Power

All of the blanket subassemblies in EBR-II are considered to be surveillance subassemblies. One goal of the surveillance program is to determine the allowable Tech. Spec. fluence limit for blanket subassembly ducts. To date, the blanket subassembly ducts have been irradiated to 6.5 x 10^{22} n/cm^2, which corresponds to 0.6 at. % burnup of the blanket fuel, without the duct dilation exceeding the clearance between the duct and the position hole in the storage

basket.

10.9 Bowing of Safety and Control Subassemblies

Control and safety subassemblies are contained in an HT9 guide thimble. The gap between a safety subassembly and the thimble is 0.15 in. (0.38 cm), while the gap between a control subassembly and the thimble is 0.143 in. (0.362 cm). Excessive swelling/thermal-induced bowing and dilation of safety and control subassemblies would cause interaction between the subassemblies and the thimbles and could jeopardize reactor shutdown capability. The current fluence limits imposed on safety (5.0×10^{22} n/cm^2) and control (6.8×10^{22} n/cm^2) subassemblies are based on fuel handling considerations; these limits are set such that a corner-to-corner (inner duct)/flat-to-flat (thimble) interference during rotation will not occur.

Bowing of a subassembly is primarily caused by temperature and fluence differences between opposite flats of the duct. During reactor power maneuvers, control and safety subassemblies are subjected to push or pull action only. A study of EBR-II operation history indicated that the maximum temperature difference between two flats, ΔT, will not exceed 50°F (28°C) for either control or safety subassemblies. A thermal- and swelling-induced bowing analysis [10.15] has been performed in which the subassembly is simulated by a cantilever beam and the axial ΔT distribution is assumed to be linear in the core region. The maximum radial thermal-induced deformation occurred at the top of the subassembly and was found to be 0.087 in. (0.22 cm.)

The evaluation of swelling-induced deformation is based on the burnup limits for safety and control subassemblies of 8.9 and 6.4 at. % burnup, respectively, which correspond to 7.35 and 5.17×10^{22} n/cm^2 in the Mark-V environment. Flux distributions of control and safety subassemblies from EBR-II run information were used, and during reactor normal operation, the temperature rises of control and safety subassemblies were assumed to be 142°F (61°C) and 187°F (86°C), respectively. The maximum swelling-induced deformations were found to be 0.05 in. (0.13 cm) for safety subassemblies and 0.038 in. (0.097 cm) for control subassemblies, occurring at the subassembly top. The dilation of control and safety subassemblies at the subassembly top is negligible, and if it is conservatively assumed that thermal- and swelling- induced deformations

are in the same direction, then the maximum combined radial deformations are 0.137 in. (0.348 cm) and 0.125 in. (0.318 cm) for control and safety subassemblies, respectively. In both cases, the total bowing is less than the gap between the duct and the thimble, and no safety problem is expected.

The exposure limits of safety and control subassemblies will remain at the current values due to operational considerations.

10.10 Adequacy of the Cover Gas Cleanup System (CGCS) for the Mark-V Fuel

The total fission gas inventory generated inside an EBR-II fuel pin is slightly different for binary fuel as compared with ternary fuel, even when both fuel types are operated at the same power level for the same number of effective full-power days (EFPDs). This is because of differences in the cumulative fission yields for the various xenon and krypton isotopes for uranium versus plutonium fissioning.

To evaluate the adequacy of EBR-II's CGCS for operation with Mark-V ternary fuel, calculations were performed of the total xenon and krypton inventories as a function of irradiation time (in EFPDs). The ORIGEN-RA code [10.16] was employed for this investigation. Since the CGCS fission-gas removal capacity is known to be adequate for Mark-III binary fuel, the same computations were performed using Mark-III compositions as input. The same full-power conditions were assumed for both cases.

Results of the investigation are plotted in Figure 10-7 for total xenon, and in Figure 10-8 for total krypton. The results show that for all irradiation times the total fission gas is less for Mark-V ternary fuel than for Mark-III binary fuel. It may be concluded that the EBR-II CGCS will have adequate capacity for operation with Mark-V fuel

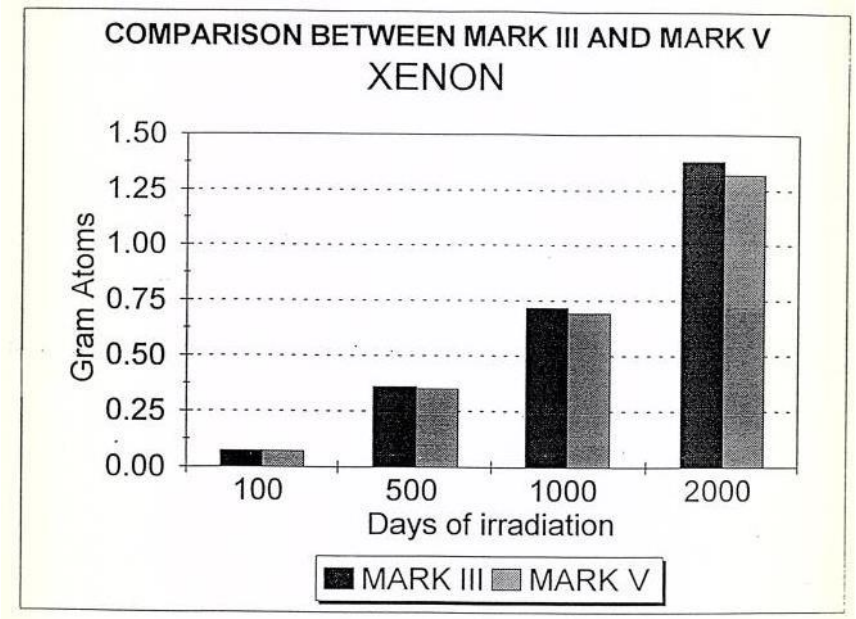

Figure 10-7 Total Xenon Inventory for Mark-III (U-10Zr) and Mark-V (U-20Pu-10Zr) Fuel as a Function of Irradiation Time

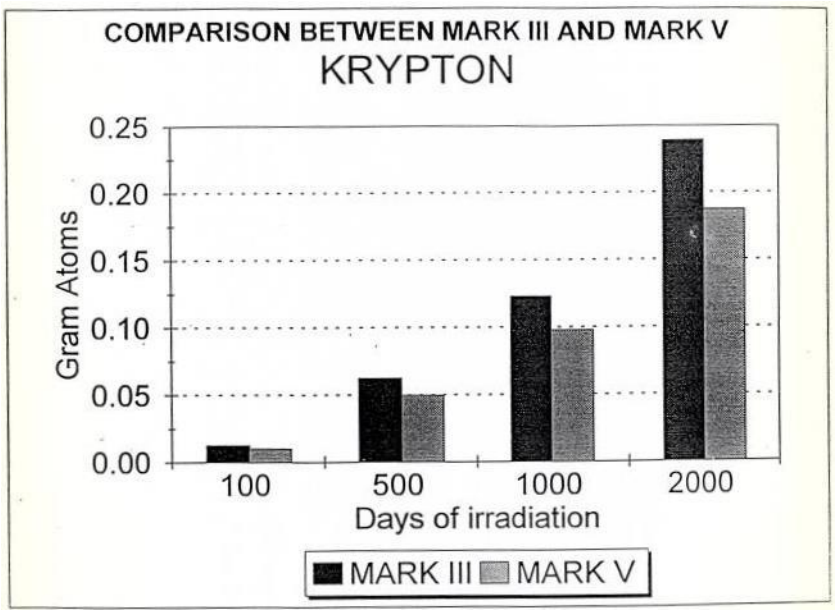

Figure 10-8 Total Krypton Inventory for Mark-III (U-10Zr) and Mark-V (U-20Pu-10Zr) Fuel as a Function of Irradiation Time

10.11 Safety Consideration of Major Components

Thermal and stress analysis of EBR-II major components has been performed in Ref. 10.17 for loss-of-flow (LOF) and transient overpower (TOP) events. The components considered in

Ref. 10.17 include the reactor vessel, the reactor-vessel cover, the intermediate heat exchanger (IHX), the Z-pipe (the pipe between the reactor and the IHX), the superheater, and the secondary piping between the IHX and the superheater. The components beyond the superheater were found to have insignificant structural cyclic damage resulting from off-normal transients, and these components were not considered in the structural analysis as indicated in Ref. 10.17.

When the transients in Ref. 10.17 were compared with the Mark-V transients, it was found that T-3 in Ref. 10.17 is similar to UN-1, while T-7 is more severe than UN-3 in terms of fatigue damage of the components. It should be noted that the fatigue damage of the components considered in this analysis is a function of temperature, the rate of temperature change and the strain range. The analysis indicated that the LOF has insignificant effect on the structural damage, while the most severe structural fatigue damage occurs at the junction between the upper tubesheet and the upper head of the IHX and is caused by reactor scram during the T-7 transient. The fatigue damage at this location was found to be 0.001 per T-7 transient. It was found that prior to 1980 there were 221 reactor scrams [10.17] and between 1980 and 1989 there were 12 reactor scrams [10.18]. All of the previous reactor scram events are less severe than the T-7 transient. If we conservatively assume that the fatigue damage of all previous reactor-scram duty cycles is as severe as that caused by the T-7 transient, and there are a total of 250 reactor scrams by the time the reactor is converted to the Mark-V core, the accumulated damage of the IHX uppersheet would be 0.25. Based on a conservative estimation, the Mark-V fueled core will have four reactor scrams per year, so the reactor can be operated about 180 years after the Mark-V core conversion.

In conclusion the design criteria of EBR-II major components are satisfied for the Mark-V transients.

10.12 Adequacy of Argon Cooling System Fuel Transfer Criteria for Mark-V and Mark-VA Fuels

Fuel transfer criteria have been established [10.19] to ensure that the fuel transfer process in the argon cooling system can be reliably conducted. The criteria for driver subassemblies include: 1) limitation of decay power based on the cooling capacity of the fuel transfer equipment, not upon consideration of maximum permitted subassembly temperature (and therefore

independent of fuel type), 2) limitation of peak cladding temperature to 1000°F (538°C) under normal cooling conditions so as to keep the hottest fuel pin temperature during fuel transfer below the value reached during irradiation, 3) an operational safety limit on cladding surface temperature prior to sodium removal, to limit disturbances from sodium-water chemical reactions (also independent of fuel type), and 4) a requirement that, should a loss of either argon cooling system or inter-building cask cooling occur, the cumulative damage function (CDF) of the cladding of the hottest pin would stay below 1.0 in the first 20 minutes following the loss of flow.

Evaluation of criteria 1) and 3) is independent of fuel type. Criterion 2) is well below the liquefaction temperature of 650°C and therefore falls within the conditions of normal operation evaluated in Sec. 9.5 using the LIFE-METAL code. Criterion 4) simply states that conditions in subassemblies being transferred should be such that, under loss-of-flow conditions, there is less than a 50% probability of failure (CDF=1.0) of the hottest pin. This condition applies just as well to Mark-V/VA fuels as it does to earlier EBR-II fuels. The fuel transfer criteria, then, can be extended to Mark-V/VA fuels with no modifications.

The DECAY [10.20] code determines the minimum amount of time a subassembly must be held in the basket in order to meet the four fuel transfer criteria. DECAY already includes modeling of HT9 and 316SS cladding and of U-20Pu-10Zr fuel, so it can be used as it stands to evaluate both Mark-V and Mark-VA fuel. The CDF calculation performed by DECAY is consistent with that used by the SASSYS code. Therefore, no extensions of DECAY are needed in order to accommodate Mark-V/VA fuels.

10.13 Mark-IIC and Mark-IICS Fueled Subassemblies

The design criteria described in Sec. 2.1.4 establish operating limits for Mark-V/VA and Mark-III/IIIA subassemblies, as discussed in Sections 9.6 and 10.3, respectively. These same criteria also determine operating limits for Mark-IIC (safety rod) and Mark-IICS (control rod) subassemblies. Mark-IIC/CS subassemblies contain five rows of U-10Zr pins clad in 316SS, with pin geometry the same as that in Mark-II driver subassemblies. Since Mark-IIC/CS fuels are of the same fuel and cladding composition as Mark-IIIA fuel, the design criteria which constrain Mark-IIIA operation also apply to Mark-IIC/CS operation.

To establish limiting conditions for operation (LCO's) for control and safety rods, a detailed analysis of the performance of Mark-IIC/CS fuels has been performed, similar to that performed for Mark-VA fuel. The analysis was performed on safety rod subassembly 3A1 and on control rod subassembly 5B3, which are the limiting safety and control subassemblies given in Table 9-2. Subassembly 3A1 was evaluated at a burnup limit of 8.9 at. %, and subassembly 5B3 was evaluated at a burnup limit of 6.4 at. %, which are the limits established in Ref. 10.21 based on hex can bowing. Otherwise, the analysis of the Mark-IIC/CS fuels was identical to those performed for the Mark-V/VA and MarkIII/IIIA fuels, including limiting the peak inside cladding temperature during normal operation to 627°C. Since both safety and control subassemblies are limited to burnups below 10 at. %, this temperature limit could be increased somewhat, as shown in Table 9-12. However, the additional steady-state wastage and higher cladding temperatures that would result would cause the transient damage criteria to be exceeded and would limit the subassembly LCO's below the values resulting from steady-state analysis. Therefore, the temperature limit of 627°C was retained, which is a conservative position.

Because U-10Zr has a considerably higher solidus temperature than does the depleted zirconium region of irradiated U-20Pu-10Zr (1234°C vs. 1041°C) and also has higher thermal conductivity than U-20Pu-10Zr, both control and safety rods are limited by steady-state cladding temperature and not by the peak fuel temperature during the UN-3 overpower transient. For Mark-IIC, the SASSYS steady-state analysis predicts a temperature LCO of 1004°F and a power LCO of 901 kW. For Mark-IICS, the analysis predicts a temperature LCO of 1029°F and a power LCO of 634 kW.

Since fuel melting during the off-normal events of Sec. 7 is not an issue and cladding damage is the only concern, the transients of interest are the loss-of-flow events, during which the bulk of the cladding damage occurs. Table 10-5 presents SASSYS analysis results for the five loss-of-flow events for Mark-IIC fuel, and Table 10-6 presents the results for Mark-IICS fuel. When compared with the CDF, eutectic penetration, and strain results for these same events for Mark-VA fuel (Table 9-18 and Table 9-20), both Mark-IIC and Mark-IICS fuel are predicted to sustain considerably more damage than the limiting Mark-VA drivers (primarily due to the much smaller gas plena, which produce considerably higher gas pressures). However, the accumulated

damage is still within the design criteria.

In conclusion, Mark-IIC and Mark-IICS subassemblies can operate within the design criteria when constrained by the LCO's given above.

Table 10-5 Mark-IIC Fuel Safety Parameters for LOF Events (Row 3)

Event	**Peak Fuel Temp.**	**Peak Clad Temp.**	**Minimum Saturation Temp.**	**CDF**	**Eutectic Penetration (%)**	**Clad Strain (%)**
AN-1 (Output Breaker Trip of One Primary Pump)	822°C (1512°F)	667°C (1233°F)	958°C (1757°F)	1.3×10^{-4}	0.0	8.4×10^{-6}
AN-2 (Input Breaker Trip of Both Primary Pumps)	796°C (1466°F)	625°C (1156°F)	910°C (1669°F)	5.2×10^{-4}	0.0	1.1×10^{-4}
UN-1 (Clutch Breaker Trip of Both Primary Pumps)	798°C (1468°F)	684°C (1262°F)	909°C (1669°F)	5.7×10^{-3}	4.5×10^{-3}	9.5×10^{-4}
UN-2 (Clutch Breaker Trip of One Pump, Seizure of One Pump)	851°C (1563°F)	726 °C (1340°F)	909°C (1669°F)	4.2×10^{-3}	2.5×10^{-3}	5.0×10^{-4}
EU-1 (Clutch Breaker Trip of Both Primary Pumps, Plus One Stuck Control Rod)	798°C (1468°F)	735°C (1355°F)	909°C (1669°F)	--	2.6×10^{-2}	--

All values in the table include uncertainties

Table 10-6 Mark-IICS Fuel Safety Parameters for LOF Events (Row 5)

Event	Peak Fuel Temp.	Peak Clad Temp.	Minimum Saturation Temp.	CDF	Eutectic Penetration (%)	Clad Strain (%)
AN-1 (Output Breaker Trip of One Primary Pump)	773°C (1423°F)	664°C (1227°F)	943°C (1730°F)	2.1×10^{-4}	4.5×10^{-5}	1.5×10^{-5}
AN-2 (Input Breaker Trip of Both Primary Pumps)	744°C (1372°F)	623°C (1153°F)	909°C (1669°F)	4.4×10^{-4}	0.0	8.6×10^{-5}
UN-1 (Clutch Breaker Trip of Both Primary Pumps)	747°C (1376°F)	728°C (1341°F)	909°C (1669°F)	6.2×10^{-2}	1.8×10^{-2}	9.5×10^{-3}
UN-2 (Clutch Breaker Trip of One Pump, Seizure of One Pump)	807°C (1484°F)	719°C (1327°F)	892°C (1638°F)	1.1×10^{-2}	6.2×10^{-3}	1.4×10^{-3}
EU-1 (Clutch Breaker Trip of Both Primary Pumps, Plus One Stuck Control Rod)	778°C (1432°F)	767°C (1413°F)	909°C (1668°F)	--	5.6×10^{-2}	--

All values in the table include uncertainties.

Section 10 References

10.1 C. C. Price et al, "Basis of Criteria for EBR-II Reactor-Containment Isolation", ANL-76-33, Argonne National Laboratory, October 1980.

10.2 J. W. Ahrens, Argonne National Laboratory, unpublished information (1995).

10.3 J. W. Ahrens, Argonne National Laboratory, unpublished information (1995).

10.4 "Reactor Site Criteria", Code of Federal Regulations, Title 10, Part 100, (1962, Revised 1991).

10.5 Fuel Conditioning Facility: Final Safety Analysis Report, Argonne National Laboratory, July 1991.

10.6 J. Mishima and L. C. Schwendiman, "The Amount and Characteristics of Plutonium Made Airborne Under Thermal Stress," Proc. Symp. Health Physics Aspects of Nuclear Facility Siting, P.C. Voilleque and B. R. Baldwin, comps, Eastern Idaho Chapter, Health Physics Society, Idaho Falls, Idaho (1971).

10.7 N. L. Allen et al, "Final Safety Analysis Addenda to Hazards Summary Report, Experimental Breeder Reactor II (EBR-II) Upgrading of Plant Protection System," Volume II, ANL-79-97, June 1980.

10.8 M. C. Billone, Argonne National Laboratory, unpublished information (1994).

10.9 J. F. Koenig, et al, "Effects of Power and Irradiation Behavior on EBR-II Blanket Management", ANL-78-98, September 1979.

10.10 D. Mohr, Argonne National Laboratory, unpublished information (1993).

10.11 Floyd E. Dunn, "Verification and Implications of the Multiple Pin Treatment in SASSYS-1 LMR Systems Analysis Code", ARS 1994 International Meeting on Advanced Reactors Safety, April 17-21, 1994.

10.12 L. K. Chang, Argonne National Laboratory, unpublished information (1994).

10.13 Swanson Analysis System, Inc., Houston, Pennsylvania, "ANSYS Engineering Analysis System, Rev. 4.4".

10.14 Nuclear Systems Materials Handbook (Revision 8), Oak Ridge National Laboratory, TID 26666.

10.15 L. K. Chang, Argonne National Laboratory, unpublished information (1993).

10.16 A. G. Croff, "The ORIGEN-2 Code," RSIC CCC-371, Oak Ridge National Laboratory.

10.17 L. K. Chang, M. J. Lee and J. G. Gale, "Thermal and Stress Analyses of EBR-II Plant Components for the Operational-Reliability-Testing Program," ANL/EBR-118, November 1982.

10.18 D. J. Hill, W. A. Ragland and J. Roglans-Ribas," EBR-II Level I Probabilistic Risk Assessment," Revision 2, June 30, 1991, Argonne National Laboratory.

10.19 R. M. Singer, Argonne National Laboratory, unpublished information (1993).

10.20 R. T. Jensen, Argonne National Laboratory, unpublished information (1993).

10.21 J. F. Koenig, et al., Argonne National Laboratory, unpublished information (1988).

11 SUMMARY

The material presented herein is in support of the changes in EBR-II Technical Specifications required to allow for Mark-V and Mark-VA fueled subassemblies to become driver fuel for EBR-II. The Mark-V and Mark-VA fuels differ from Mark-III and Mark-IV fuels only in the materials used, U-20Pu-10Zr instead of U-10Zr and the remote fabrication in Fuel Cycle Facility.

Initially a peak burnup limit of 10 at. % is proposed for both Mark-V and Mark-VA fueled subassemblies based upon fuel performance analysis described earlier. Both types of fuel may be combined with a 316SS duct, and the limiting phenomena for the 316SS duct are a combination of irradiation-induced swelling and creep, which leads to a limit on fluence of 10.65×10^{22} n/cm^2, the fluence value at which the fuel reaches 10 at. % burnup. Mark-V fuel subassemblies using HT9 duct do not suffer from this limitation. The fluence of 10.65×10^{22} n/cm^2 is an operation limit rather than a safety limit. A surveillance program on the duct dilation is planned to verify the fluence limit.

The case made to support the proposed Technical Specification changes is based upon:

(1) Satisfactory performance history of other U-XPu-10Zr fuel pins with differing cladding materials, (Section 5.0).

(2) A continuing fuel qualification program designed to expand the fuels database and to lead to the introduction of a large number of Mark-V and Mark-VA fueled subassemblies, (Section 4.0).

(3) Detailed thermal-hydraulic, fuel behavioral and structural analyses of the performance of the subassemblies.

There are four considerations which must be accounted for in deriving the operational constraints for these subassemblies:

(1) Zirconium will redistribute, leading to the formation of low-Zr zones in the fuel which have a lower solidus temperature than the nominal composition, (1041°C compared to

1140°C).

(2) Diffusion of lanthanides into cladding leads to steady-state wastage of cladding.

(3) There is experimental evidence that the eutectic threshold temperature may be as low as 650°C for these fuel/clad combinations at high power and high burnups.

(4) With the introduction of plutonium into the core the β_{eff} will change, leading to possibility of changes in transient power histories for a given transient.

These phenomena are accounted for in a conservative manner, and Limiting Conditions for Operation (LCO) are derived for these subassemblies which ensure satisfactory performance.

In contrast many aspects of the core are preserved in the transition from Mark-III fuels to Mark-V and Mark-VA:

(1) The temperature coefficients of reactivity for Mark-V are very close to those for Mark-III cores when expressed in absolute units.

(2) Despite the change in β_{eff} the peak powers in anticipated and unlikely events are changed very little with respect to the Mark-III cores, because of protective system action.

(3) The Mark-III, Mark-IV, Mark-V, and Mark-VA fueled subassemblies are hydraulically identical.

(4) The plenum volumes and fission gas release behavior for Mark-V and Mark-VA are similar to those of the Mark-III design. Therefore, the plenum pressures are similar.

(5) The Limiting Safety System Settings (LS^3) are unchanged at 115% power, 88% flow, 115% coolant outlet temperature rise and 17s period. These apply irrespective of fuel type(s) in the core.

(6) There is no evidence for any phenomena leading to untoward stresses and strains in the cladding apart from gas pressure and limited FCMI. Little or no strain is predicted or observed up to 10 at. % burnup for Mark-V fuel. Higher strains (2-4%) are predicted for Mark-VA fuel due to swelling of the 316SS clad. These swelling strains are not ductility-limited and pose no geometrical problems.

(7) No subassembly structural problems are envisaged.

The limiting conditions of operation for Mark-III, Mark-IIIA, Mark-V, Mark-VA, Mark-

IIC, and Mark-IICS fueled subassemblies are given in Table 11-1 together with an indication of the limiting phenomena.

In deriving these limits the conditions imposed embraced both 6-row and larger cores and therefore there are no constraints on the core configuration other than the LCOs given in Table 11-1.

Table 11-1 LCOs for Mark-IIC, Mark-IICS, Mark-III, Mark-IIIA, Mark-V and Mark-VA Fuels in EBR-II

Row No.	**Mark-V**			**Mark-III, Mark-IIIA, and Mark-VA**		
	Hot Channel Coolant Temperature, °F (°C)	Subassembly Power, kW	Fuel Burnup, at. %	Hot Channel Coolant Temperature, °F (°C)	Subassembly Power, kW	Fuel Burnup, at. %
1	939 (504)[2]	989[2]	10	940[2] (504)[2]	9922	10
2	943 (506)[2]	985[2]	10	944 (507)[2]	989[2]	10
3	969 (521)[2]	965[2]	10	971 (522)[2]	970[2]	10
4	1028 (553)[1]	917[1]	10	1014 (546)[3]	879[2]	10[*]
5	1054 (568)[1]	835[1]	10	1024 (551)[3]	765[3]	10[*]
6H	1056 (569)[1]	811[1]	10	1027 (553)[3]	746[3]	10[*]
6L	1063 (573)[1]	738[1]	10	1034 (557)[3]	679[3]	10[*]
7	1065 (574)[1]	712[1]	10	1036 (558)[3]	655[3]	10[*]
	Mark-IIC			**Mark-IICS**		
3	1004 (540)[3]	901[3]	8.9	--	--	--
5	--	--	--	1029 (554)[3]	634[3]	6.4

Limiting Phenomena:

[1]Fuel-Clad eutectic formation
[2]Ternary fuel melting
[3]CDF

[*]Due to steady-state wastage, either burnup or irradiation temperature must be restricted to keep the CDF within the design limits. In this case, the burnup is set at 10% and peak inside clad temperature restricted to 627°C.

All other LCO's etc. in the Tech. Specs. will be unchanged and used to constrain the transition to a fully Mark-V core.

As part of the process used to present this safety case, guidance was sought from the FFTF FSAR, the CRBR PSAR and the USNRC Standard Review Plan (SRP). Therefore the format and content of the material exceeds that traditionally supplied in support of Tech. Spec. changes. It is the intent that this material can be incorporated into the planned restructured EBR-II Safety Analysis Report (SAR) with minimal editing.

12 QUALITY ASSURANCE

The calculations reported in this document have been performed under the applicable procedures of the various Divisions at Argonne National Laboratory. Reactor Analysis Division is responsible for the calculations of EBR-II Core Physics described in Section 6 and the associated EBRFLOW calculations. Reactor Analysis Division is also responsible for the SUPERENERGY-2 and SASSYS calculations described in Sections 9 and 10 as well as the containment design basis calculations of Section 10.0, using RSAC. Reactor Analysis and Fuels and Engineering Divisions are responsible for the structural modeling of the duct described in Sections 4 and 8, which utilize the structural analysis code ANSYS. Reactor Engineering Division is responsible for the FPIN2 code and any calculations which use FPIN2. Finally Energy Technology Division is responsible for the LIFE-METAL code and calculations, however, the code is developed under the auspices of Fuels and Engineering Division. The calculation information is summarized in Table 12-1.

All the computer codes used are under appropriate configuration control, the actual method of control varies from code to code and division to division but all comply with the applicable Argonne policies.

The quality assurance of the calculations performed in Reactor Analysis Division are governed by the procedures of Reactor Analysis Division as specified in the Reactor Analysis Division Operations Manual [12.1]. Reference 12.2 extracts the pertinent information into a self-contained document specific to the Mark-V Safety Case.

The quality assurance of the FPIN2 calculations performed in the Reactor Engineering Division are governed by the procedures for Category II Computer Codes as specified in the Reactor Engineering Division Policy and Procedures Manual (Reactor Engineering Policy and Procedures Manual, February, 1992).

Table 12-1 Summary of Mark-V/VA Safety Analysis Information

Section	Pages	Figures or Tables	Code	Calculational File or Reference	Description
4.0	4-44 to 4-47	Figure 4-5, Figure 4-6	ANSYS	Detailed analysis and calculations were presented in RA Calculation and Analysis ID No. SRA-059.	Structural models were developed to predict duct dilations, and the models were validated with the measurements.
4.0	4-14 to 4-19	Figure 4-3, Figure 4-4	SASSYS	Analysis and code verification were presented in Ref. 12.3.	EBR-II PPS model was developed and incorporated into SASSYS code. The model was verified by EROS and DSNP calculations.
6.0	6-4 to 6-26	Table 6-1 to Table 6-4	DOT (xy) CITATION (ZZ) SUBPOWER EBRFLOW MC^2 POPOP4 MUG	Calculations were presented in Ref. 12.4, following the calculational procedure in [12.1].	Neutronics and hydraulic analyses of six-row and six-plus-row cores.
6.0	6-26 to 6-31	Table 6-5, Table 6-6	EBRPOCO	All files used in the calculations were documented in Ref. 12.5.	Reactivity feedback analysis.
6.0	6-31 to 6-37	Table 6-7 to Table 6-9	REBUS-3/RCT	Detailed calculations were presented in RA Calculation and Analysis ID No. SRA-058.	Depletion analysis.
8.0	8-10 to 8-13	Figure 8-5 to Figure 8-7	THTB	Detailed calculations were presented in RA Calculation and Analysis ID No. SRA-015.	Transient heat transfer to determine the temperature gradient across the thickness of the duct wall.
8.0	8-3 to 8-10 and 8-13 to 8-20	Figure 8-1 to Figure 8-4, Figure 8-8, Figure 8-9, and Table 8-1	ANSYS	Input of the code and safety evaluation procedure were given in RA Calculation and Analysis ID No. SRA-015.	Finite-element structural analysis models were developed and inelastic duct dilation and stress were predicted using the ANSYS code.

Section	Pages	Figures or Tables	Code	Calculational File or Reference	Description
9.0 and Appendix B	9-6 to 9-10 and B-1 to B-64	Table 9-2 to Table 9-4, B.2 to B.9, and B.11 to B.21	SUPERENERGY-2	Detailed analyses were presented in RA Calculation and Analysis ID No. SRA-016.	Steady state temperature calculations of the hottest subassemblies in each row of the Mark-V (six-row core) and the Mark-VA (six-plus-row core) drivers.
9.0 and Appendix A	9-10 to 9-26 and A-32 to A-43	Figure 9-1 to Figure 9-3, Table 9-5 to Table 9-11, and Figure A-11 to Figure A-17	LIFE-METAL	Calculations were presented in Refs. 12.6 and 12.7. Input for the code and the safety evaluation procedure were given in RA Calculation and Analysis ID No. SRA-056.	Design lifetime analysis of Mark-V and Mark-VA fuel.
9.0 and Appendix C	9-35 to 9-68 and C-1 to C-19	Figure 9-4 to Figure 9-32 and Figure C-1 to Figure C-10 and Table 9-12 to Table 9-21 and Table C-1 to Table C-9	SASSYS LIFE-METAL	Detailed input description and file identification were presented in RA Calculation and Analysis ID No. SRA-051 and SRA-056. Calculations for analysis of event UN-6 (reclassified from AN-4) were presented in Ref. 12.8.	Thermal-hydraulic and neutronic analysis of off-normal transients including normal, anticipated, unlikely and extremely unlikely events.
10.0	10-1 to 10-4	None	RSAC	Analysis was presented in RA Calculation and Analysis ID No. SRA-001 Revision 0.	Containment design basis calculation for ternary fuel.
10.0	10-4 to 10-10	Table 10-1, Table 10-2	SASSYS	Detailed input description and file identification were presented in RA Calculation and Analysis ID No. SRA-051.	Mark-III and -IIIA thermal-hydraulic analysis and safety evaluation.

Section	Pages	Figures or Tables	Code	Calculational File or Reference	Description
10.0	10-10 to 10-13	None	SASSYS	Detailed input description and file identification were presented in RA Calculation and Analysis ID No. SRA-051.	Effect of β_{eff} in the Mark-V safety analysis
10.0	10-13 to 10-17	Table 10-3, Table 10-4	SASSYS	Detailed input description and file identification were presented in RA Calculation and Analysis ID No. SRA-051.	Inlet temperature parametric study
10.0	10-17 to 10-18	Figure 10-1 to Figure 10-6	SASSYS	Calculations were presented in Ref. 12.9.	Startup transient analysis
10.0	10-29 to 10-32	Table 10-5, Table 10-6	SASSYS	Detailed input description and file identification were presented in RA Calculation and Analysis ID No. SRA-051.	Mark-IIC and -IICS thermal-hydraulic analysis and safety evaluation.

The LIFE-METAL code has been developed within the Mechanics of Materials Section of the Energy Technology (ET) Division. While the ET Division does not, as yet, have a final, detailed QA plan for computer software, the Mechanics of Materials Section has a general purpose plan in draft form (Quality Assurance Plan for Mechanics of Materials Section Computer Modeling and Code Development Activities, September 1991). In addition, a detailed QA plan is being drafted for LIFE-METAL, in particular, because its development and application extend beyond the Section and the Division.

The version (1.0) of LIFE-METAL used for all Mark-V and Mark-VA calculations was "frozen" on October 21, 1992, along with the input data files for the 100 fuel pin cases used to validate the code. In addition, a LIFE-METAL Users Group was formed to review all proposed future changes to the models and validation cases. While no changes have been made to Version 1.0 since October 21, 1992, LIFE-METAL has provisions for changing model parameters through the input data file. Two parameters have been changed (and documented) in the steady-state FCCI model for HT9 (Mark-V) and 316SS (Mark-VA) based on new data.

In terms of the specific Mark-V and Mark-VA calculations performed for the Mark-V safety case, the RA approach has been adopted [12.2]. This consists in using the "Calculation and Analysis Coversheet" with a case-by-case listing of the input data deck, the summary output page, and any additional documentation necessary to explain how the values appearing in the Mark-V safety case tables and graphs of LIFE-METAL results were derived from the summary-page output. This documentation is peer reviewed (J. M. Kramer), Section-Manager approved (D. R. Diercks) and stored both in RA and ET. The input data file contains the JCL and the LIFE-METAL input required to run a case. Also, the job name (e.g. V650MV) is identical to the data file stored on WYLBUR. Thus, to rerun a case for traceability and verification, the user merely requests "USE B21068.V650MV" and "RUN NONUM".

Finally, both IFRO Division and Argonne National Laboratory safety review committees provide independent overall safety review. The first level of independent review is through the Experiment Safety Review and Plant Safety Review Groups (ESRG and PSRG) who advise the director of IFRO Division. This document was extensively reviewed at joint meetings of the ESRG/PSRG during 1992 and 1993. The second level of independent review is through the Reactor Safety Review Committee, (RSRC), who advise the Laboratory Director. This document was reviewed by the RSRC in 1993.

Section 12 References

12.1 D. J. Hill, Argonne National Laboratory, unpublished information (1991, 1992).

12.2 D. J. Hill, Argonne National Laboratory, unpublished information (1992).

12.3 J. Ku and T. C. Hung, "SASSYS EBR-II Plant Protection System Model and Model Validation," ANL/FRA-172, October 1992.

12.4 K. N. Grimm and K. E. Phillips, "Subassembly Power, Fluxes, Coolant Rates, Outlet Coolant Temperatures and Reaction Rates for a Prototypical EBR-II Loading with Fresh U-20Pu-10Zr Fuel and SS316 Cladding," unpublished memo, July 3, 1991.

12.5 D. Meneghetti and D. A. Kucera, Argonne National Laboratory, unpublished information

(1991).

12.6 M. C. Billone, Argonne National Laboratory, unpublished information (1993).

12.7 M. C. Billone, Argonne National Laboratory, unpublished information (1993).

12.8 M. C. Billone, Argonne National Laboratory, unpublished information (1993).

12.9 J. Y. Ku, Argonne National Laboratory, unpublished information (1993).

A APPENDIX: ENVIRONMENTAL AND MATERIAL CONSIDERATIONS

This section describes the material properties for fuel, cladding, and duct materials for use in analytical models for various components of fuel pin performance. The intent is to provide descriptions of the behavior of HT9[1] and 12% and 20% cold-worked 316 stainless steels and U-20Pu-10Zr fuel in terms of specific materials properties which can then be used in the performance modeling of fuel pins and fuel subassemblies. The performance modeling of fuel and subassembly components has been presented in the main body of the document. The property descriptions presented here are derived from various sources, including the Metallic Fuels Handbook and the results of specific fuel performance experiments. The description of the in-reactor experiments, and resulting data base, from which fuel behavior models are derived are presented in Sections 4 and 5. The various correlations presented here are given in the units in which they are to be found in the source documents. Where deemed necessary alternatives are given.

A.1. Irradiation-Induced Swelling; Creep Deformation

Deformation of cladding and duct components can occur due to irradiation-induced void swelling or creep induced by both the irradiation and thermal environments. Potential effects include thermal creep damage to the cladding, limiting fuel pin reliability, or reductions in the flow area in the fuel bundle caused by all of the dilation effects, and potentially fuel/bundle interactions. In addition, duct dilation can limit the effective useful lifetime of a driver fuel subassembly, as a 0.040-in. limit to dilation must be maintained to allow handling of the subassembly through the EBR-II storage basket.

[1] HT9 (S42100) is a martensitic stainless steel used for Mark-V cladding, and for some subassembly ducts. T91 and S42200 stainless steel will be used, on a limited basis, for some subassembly ducts. These materials, identical in structure, and very similar in chemical composition, to HT9, perform identically to HT9. This conclusion is based on experimental results presented in Refs. A.1, A.2, A.3, A.4 and A.5.

A.1.1 HT9 Swelling

The swelling of HT9 cladding and ducts will be insignificant for irradiation exposures (neutron fluences) which may reasonably be expected to occur during expected lifetimes of EBR-II driver fuel subassemblies. Insignificant swelling (<0.1% $\Delta V/V_o$) has been observed for HT9 to fast neutron fluences of at least 20 x 10^{22} n/cm^2 (E>0.1 MeV), which corresponds to a peak burnup of more than 10 at. % in EBR-II. The lack of swelling virtually insures that no flow reductions or significant bundle/duct interaction should occur for Mark-V subassemblies.

A.1.2 HT9 Creep

The creep behavior of HT9 can be calculated using the following equations, [A.3]. The creep deformation can be split into components related to that induced purely by the thermal environment and that induced by neutron irradiation.

A creep equation based solely on ex-reactor thermal creep behavior has been developed for predictions above 600°C, where thermal creep often dominates, [A.3], and is effective to 750°C. This equation is represented by $\bar{\epsilon}_T$. The purely irradiation-induced creep is represented as $\bar{\epsilon}_I$ and has the form,

$$\bar{\epsilon}_T = \left[B_o + A \ exp\left(-\frac{Q}{RT}\right)\phi\right]\bar{\sigma}^{1.3} \qquad \text{(A.1-1)}$$

where:

$\bar{\epsilon}_I$ = equivalent strain, %

$\bar{\sigma}$ = equivalent stress, MPa

B_o = 1.83 x 10^{-4}

ϕ = neutron fluence 10^{22} n/cm^2 (E>0.1 MeV)

A = 2.59 x 10^{14}

Q = 73000 cal/gm mole

T = temperature, K

R = 1.987 cal/gm mole K

The thermal creep component, $\bar{\epsilon}_T$, can be calculated using the following equation, (see Ref. A.3).

$$\bar{\epsilon}_T = \bar{\epsilon}_{TP} \ (\text{primary}) + \bar{\epsilon}_{TS} \ (\text{steady} - \text{state}) + \bar{\epsilon}_{TT} \ (\text{tertiary}) \qquad \text{(A.1-2)}$$

where

$$\bar{\varepsilon}_{TP} = \left[C_1 \ exp\left(-\frac{Q_1}{RT}\right)\bar{\sigma} + \ C_2 \ exp\left(-\frac{Q_2}{RT}\right)\bar{\sigma}^4 + \ C_3 \ exp\left(-\frac{Q_3}{RT}\right)\bar{\sigma}^{0.5}\right] \ x \ (1 - exp[-C_4 t])$$

$$\bar{\varepsilon}_{TS} = \left[C_5 \ exp\left(-\frac{Q_4}{RT}\right)\bar{\sigma}^2 + \ C_6 \ exp\left(-\frac{Q_5}{RT}\right)\bar{\sigma}^5\right] t$$

and

$$\bar{\varepsilon}_{TT} = \ C_7 \ exp\left(-\frac{Q_6}{RT}\right)\bar{\sigma}^{10} t^4$$

The rate form at constant temperature and stress is given by $\dot{\bar{\varepsilon}}_T$ as follows:

$$\dot{\bar{\varepsilon}}_T = \ \dot{\bar{\varepsilon}}_{TP} + \ \dot{\bar{\varepsilon}}_{TS} + \ \dot{\bar{\varepsilon}}_{TT} \qquad \text{(A.1-3)}$$

where

$$\dot{\bar{\varepsilon}}_{TP} = \left[C_1 \ exp\left(-\frac{Q_1}{RT}\right)\bar{\sigma} + \ C_2 \ exp\left(-\frac{Q_2}{RT}\right)\bar{\sigma}^4 + \ C_3 \ exp\left(-\frac{Q_3}{RT}\right)\bar{\sigma}^{0.5}\right] C_4 \ \exp(-C_4 \ t)$$

$$\dot{\bar{\varepsilon}}_{TS} = \ C_5 \ exp\left(-\frac{Q_4}{RT}\right)\bar{\sigma}^2 + \ C_6 \ exp\left(-\frac{Q_5}{RT}\right)\bar{\sigma}^5$$

and

$$\dot{\bar{\varepsilon}}_{TT} \ = \ 4C_7 \ exp\left(-\frac{Q_6}{RT}\right)\bar{\sigma}^{10} t^3$$

The values for the constants in these equations are:

C_1 = 13.4
C_2 = 8.43 x 10^{-3}
C_3 = 4.08 x 10^{18}
C_4 = 1.6 x 10^{-6}
C_5 = 1.17 x 10^{9}
C_6 = 8.33 x 10^{9}
C_7 = 9.53 x 10^{21}
Q_1 = 15027
Q_2 = 26451
Q_3 = 89167
Q_4 = 83142
Q_5 = 108276

$Q_6 = 282700$

The definitions for the other terms in these correlations are:

$\bar{\varepsilon}_T$ = equivalent thermal creep strain, %
R = gas constant = 1.987 cal/gm·mole K
t = time in seconds
T = temperature, K
$\bar{\sigma}$ = equivalent stress, MPa
$\dot{\bar{\varepsilon}}_T$ = equivalent thermal creep strain rate, %/s

These equations are valid for the following environment:

temperature range: 350-750°C
stress range: 0-250 MPa

The total creep strain $\bar{\varepsilon}_C$ can be calculated using the summation, $\bar{\varepsilon}_C = \bar{\varepsilon}_I + \bar{\varepsilon}_T$. The second (thermal) term is small for low temperatures and low stresses (<250 MPa, 36 ksi). For high T (625-750°C), thermal creep becomes very important.

A.1.3 Creep and Swelling of 20% and 12% Cold-Worked 316 SS

The creep and swelling properties for 12% cold-worked (CW) 316 ducts have been combined for a conservative exposure limit criterion. The limit of 10^{23} n/cm^2 (E> 0.1 MeV) is based on such an equation, regardless of the reactor row [A.6].

The analyses presented in this document may require component strains to be calculated. Although the existing data base for 12% CW material is limited, the swelling behavior for 12% CW 316SS should be comparable to or a little greater than that for 20% CW 316SS, [A.7], and the irradiation creep is a little less than 20% CW 316SS [A.8]. Reference A.8 presents a guideline for the creep compared to 20% CW 316SS. At 550°C the creep behavior of 12% CW 316 is ~75% of 20% CW 316, and at 400°C the creep behavior is about the same; a linear interpolation can be used. The creep equation in the Nuclear Systems Materials Handbook, Volume 1, Revision 5 was used for the analysis. The effective creep strain, $\bar{\varepsilon}$, for constant stress and temperature conditions can be expressed as

$$\bar{\varepsilon} = A_1[1 - exp(-3\phi)]\bar{\sigma} + A_2(2.78x10^{-4}t)^{0.5}\bar{\sigma}^{4.5} + A_3\left(sinh\frac{\bar{\sigma}}{\sigma_1}\right)^3(2.78x10^{-4}t)^3 + A_4\Phi\bar{\sigma} + 2.2R(T)\Omega^2\bar{\sigma}log_e\left(cosh\frac{\Phi}{\Omega}\right) \quad \text{(A.1-4)}$$

The creep rate, $\dot{\bar{\varepsilon}}$, has the form

$$\dot{\bar{\varepsilon}} = \left\{3A_1\Phi exp(-3\Phi)\bar{\sigma} + 1.390x10^3A_2(2.78x10^{-4}t)^{-0.5}\bar{\sigma}^{4.5} + (2.78x10^3)3A_3\left(sinh\frac{\bar{\sigma}}{\sigma_I}\right)^3(2.78x10^{-4}t)^2 + A_4\Phi\bar{\sigma} + 2.2R(T)\bar{\sigma}\Omega\Phi\left(tanh\frac{\Phi}{\Omega}\right)\right\}x10^{-7} \quad \text{(A.1-5)}$$

where

β	=	$\frac{T-773}{100}$
R(T)	=	exp $[c_o + c_1\beta + c_2\beta^2 + c_3\beta^3 + c_4\beta^4]$
$\bar{\varepsilon}$	=	effective strain expressed in %
$\dot{\bar{\varepsilon}}$	=	effective strain rate expressed in %/s
$\bar{\sigma}$	=	effective stress expressed in MPa
Φ	=	fluence expressed in units of 10^{22} n/cm^2 (E>0.1 MeV)
t	=	time expressed in s
ϕ	=	flux expressed in units of 10^{15} n/cm$^2 \cdot$ s
T	=	temperature expressed in K
σ_I	=	47.0, expressed in units of MPa
A_1	=	134 exp (-9461/T) for biaxial loading
	=	268 exp (-9461/T) for condition of bending
A_2	=	exp (-1.41 - 24,000/T)
A_3	=	exp (77.2 - 95,000/T)
A_4	=	6.26 x 10^{-4}
Ω	=	9.0, expressed in units of 10^{22} n/cm^2
c_o	=	-8,45

$c_1 = 1.70$

$c_2 = 0.805$

$c_3 = -0.721$

$c_4 = -0.482$

The above equations are valid for the temperature range of 370 - 730°C.

The stress-free swelling correlation in the Nuclear Systems Materials Handbook, Volume 1, Revision 8 was used in the structural analyses, and the volumetric swelling strain, δ_o, can be expressed as

$$\delta_O = \frac{\Sigma}{1-\Sigma}, \qquad \text{(A.1-6)}$$

and

$$\Sigma = R\left[\phi t + \frac{1}{\alpha} Ln\left\{\frac{1 + exp[\alpha(\tau - \phi t)]}{1 + exp(\alpha\tau)}\right\}\right]$$

where ϕt = neutron fluence in units of 10^{22} n/cm^2 (E>0.1 MeV);

R is in units of negative fractional density change per 10^{22} n/cm^2

α is in units of $[10^{22}$ n/cm$^2]^{-1}$

τ is in units of 10^{22} n/cm^2 (E>0.1 MeV), and

$R(T) = 0.01\ [\exp(0.497 + 0.795\beta - 0.0948\beta^2 + 0.908\beta^3 - 1.49\beta^4 + 1.3 \exp[-8(\beta-1.35)^2]$

where β = (T - 500)/100 and T is the temperature in °C

α = 0.75.

A.2. Stress Rupture Properties

The most common failure mode for fuel pins is the stress rupture of the cladding, with the stress largely provided by fission gas pressure contained within the fuel pin jacket. Fuel cladding mechanical interaction can provide a secondary source of stress, especially at very high fuel burnup (> 15 at. %) or during an overpower event. Prediction of breach can follow two methods, one related to the expected plastic strain at failure, and one related to the Cumulative Damage Function

(CDF) which relates the time (t_i) under certain stress and temperature conditions to the time-to-rupture (t_r) calculated using stress rupture equations and using those same operating conditions:

$$\mathrm{CDF} = \sum_1^N t_i/t_r \quad \text{or in integral form} \quad = \int_0^t \frac{dt}{t_r} \tag{A.2-1}$$

The stress rupture process can be divided into two regimes, one representing steady-state operating conditions where the stress rupture process occurs by the accumulation of low temperature/low stress creep strain. The other may occur under off-normal operating conditions where stress/temperature conditions could more closely approach conditions of yielding in the cladding material. The following will present the methods used to calculate the time-to-rupture under these various conditions for 20% cold-worked 316SS and normalized-and-tempered HT9 steels. Off-normal conditions may also involve some cladding penetration by the formation of liquid phases between cladding and fuel or fission product components (see Section A.4). If cladding wastage is treated as mere cladding wall thinning, a stress rupture approach to prediction of cladding failure can still be performed.

A.2.1 20% Cold-worked 316SS

A.2.1.1 Steady-state Conditions

The stress rupture correlation for Core 1, 20% cold-worked 316 stainless steel is given by

$$log_{10} t_r = A + \frac{B}{T} + \frac{C}{T} log_{10}\sigma \tag{A.2-2}$$

A	B	C	SEE	
-16.638	+34054	-7113	0.26	(High Stress)
OR* -12.637	+22219	-3591	0.18	(Low Stress)

*Use either the high stress or the low stress equation, depending on which gives the shortest time-to-rupture.

and t_r = hours,

T = K,

σ = MPa,

SEE = Standard Error of Estimate.

A.2.1.2 Transient Conditions

The transient failure correlation based on stress rupture was presented in Ref. [A.9]. The correlation is given below.

$$\ln t_r = A + B \ \ln ln\left(\frac{\sigma^*}{\sigma}\right) + \frac{Q_1}{T} + TRAMP + C \ \ tanh(\Phi t) + 125\left[tanh\left(\frac{\sigma}{550}\right)^{10}\right]\left[1 - tanh\left(\frac{TI}{583} - F\right)^{25}\right]\left[tanh\left(\frac{\Phi t}{2.5}\right)\right] \quad \text{(A.2-3)}$$

$$TRAMP = -0.28 + 1.18 tanh\left[-0.5\left(ln\dot{T}\right) - 1\right]$$

$$\sigma^* = 775 - \left[387.5 \ \ tanh\left(\frac{D - TI}{E}\right)\right] tanh\left(\frac{\Phi t}{2.0}\right) + 125\left[tanh\left(\frac{\sigma}{550}\right)^{10}\right]\left[1 - tanh\left(\frac{TI}{583} - F\right)^{25}\right]\left[tanh\left(\frac{\Phi t}{2.5}\right)\right]$$

where

t_r = time to rupture, hours

σ = hoop stress, MPa (use thin wall formula with midwall tube diameter)

Φt = fluence n/cm^2, E>0.1 MeV, x10^{22}

T = transient temperature, K

TI = steady-state irradiation temperature, K

$\underline{T}$ = transient temperature ramp rate, K/sec

A = -43.06

B = 7.312

C = -1.73

Q_1 = 41339

D = 1000

E = 200

F = 0.438

An alternative method of calculating rupture conditions is related to the comparison of operating conditions to yield conditions and the plastic strains encountered under those conditions [A.9, A.10]. Both types of calculations are used in the FPIN2 and SAS codes to predict transient

performance.

A.2.2 Normalized and Tempered HT9

A.2.2.1 Steady-state Conditions

The stress rupture correlation for steady-state stress rupture of HT9 is that given by

$$\bar{\varepsilon}_T log_{10} t_r = A + \frac{B}{T} + \frac{C}{T} log_{10}\sigma \qquad \text{(A.2-4)}$$

	A	B	C	SEE
High Stress	-32.490	57781	-11800	0.28
Low Stress	-35.173	45858	-5563.1	0.16

where

σ = hoop stress, MPa,

t_r = time to rupture, hrs,

T = temperature, $700 \leq T \leq 1100$ K.

and SEE = standard error of estimate in $\log_{10} t_r$

The choice of high stress coefficients or low stress coefficients should be made to correspond to the equation predicting the shortest time to rupture.

A.2.2.2 Transient Conditions

The transient failure correlation based on stress rupture was presented in Ref. A.11. The correlation is given below.

The Dorn parameter θ is calculated as:

$$\theta = t_r exp\left(\frac{-Q}{RT}\right) \qquad \text{(A.2-5)}$$

$$\ln \theta = A + B \ln \ln \frac{\sigma^*}{\sigma}$$

where

t_R = rupture time (s)

σ = the hoop stress in MPa

σ^* = 730 MPa

T = Transient temperature (K)

Q = 70170 cal/mole

R = 1.987 cal mole · K

with

$$A = -34.8 + tanh\left(\frac{\sigma - 200}{50}\right) + C$$

and

$$B = \frac{12}{1.5 + 0.5 \tanh((\sigma - 200)/50)}$$

where

$$C = -\{0.5\,[1 + \tanh((\sigma - 200)/50)]\}\,[0.75\,[1 + \tanh((\alpha - 58)/17)]\}$$

and α is the heating rate in K/sec.

As with 316 stainless steel, an alternative way to calculate breach is to compare behavior against the yield stress and the strain accumulated during the event. The behavior of HT9 may be more complicated, however, in that above 840°C, HT9 exhibits an alpha-to-gamma ($\alpha \rightarrow \gamma$) phase transformation. The properties of the steel change abruptly when the transformation occurs. An approximation can be used where the flow criterion changes to that of an austenitic stainless steel (316SS for example) for HT9 operating in the gamma phase field. This is done for this type of analysis in the FPIN2 and SAS codes.

A.3. Tensile Properties

The tensile properties of the cladding and duct materials (HT9 and 20, 12% CW 316 stainless steel) are not frequently used for analyses of fuel pin or duct performance during normal operation, as designs are usually such that stresses imposed do not challenge the points where yielding should occur. However, under transient conditions at elevated temperatures the applied stresses can result in general yielding. This behavior is modeled in the FPIN2 and DEFORM-5

codes by using a unified plastic deformation model that includes both rate-independent deformation (classical plasticity) and rate-dependent deformation (creep). The equations describing the generalized plastic flow behavior Type 316 stainless steel and HT9 are in the following sections. The yield strength and ultimate strength of the materials can be calculated from the plastic flow equations by applying them to the geometry of a tensile test. However, for completeness, curves representing fits to yield strength and ultimate strength data are given in Section A.3.3. Also included in Section A.3 are the ductility and fracture toughness of 316SS and HT9 (Sections A.3.4 and A.3.5, respectively).

A.3.1 Generalized Plastic Flow Behavior of 316SS

The deformation behavior of Type 316 Stainless Steel can be described over a broad range of temperature and strain-rate with the set of equations shown below [A.12]. These equations are incorporated in the FPIN2 and DEFORM-5 codes and are used by them in calculations of the strength and deformation of this alloy at temperatures ranging from room temperature to 1400°C under a variety of loading conditions, including thermal-mechanical transients. In this formalism the true equivalent flow stress σ is described by the equation

$$\sigma = \sigma_s - (\sigma_s - \sigma_1)\exp(-\hat{\varepsilon}/\varepsilon_c) \tag{A.3-1}$$

In this equation, σ_1 is yield stress of fully annealed unirradiated material, and σ_s is the saturation value of the flow stress that is asymptotically approached at large values of plastic strain. Ongoing true plastic strain is incorporated in the "hardness" parameter $\hat{\varepsilon}$ as this strain is accumulated. The hardness parameter also contains contributions from prior cold work, irradiation hardening, and softening caused by annealing, all scaled as true plastic strain. Consequently, $\hat{\varepsilon} = 0$ for the fully annealed unirradiated material, and $\hat{\varepsilon} = 0.223$ for 20% cold-worked material. Finally, the value of the parameter ε_c in the Voce equation is determined by the initial hardening rate θ_1 of fully annealed material ($\hat{\varepsilon} = 0$), which by differentiation of the Voce equation is given by

$$\theta_1 = (\sigma_s - \sigma_1)/\varepsilon_c \tag{A.3-2}$$

The initial hardening rate is found to be only temperature dependent through the shear modulus,

so the rate and temperature dependencies of ε_c is obtained from the above equation. Reference A.12 should be sought for details.

The yield stress and saturation flow stress are rate and temperature dependent in accordance with the equations

$$\sigma_s/G = (\sigma_{so}/G)\left\{1 - \exp\left[-\left(\dot{\varepsilon}_p/\dot{\varepsilon}_{os}\right)^{mK}\right]\right\}^{1/K} \tag{A.3-3}$$

$$\sigma_1/G = (\sigma_{1o}/G)\left\{1 - \exp\left[-\left(\dot{\varepsilon}_p/\dot{\varepsilon}_{o1}\right)^{mK}\right]\right\}^{1/K} \tag{A.3-4}$$

where G is the temperature dependent shear modulus, $\dot{\varepsilon}_p$ is the equivalent plastic strain rate, m and K are constants, and σ_{so}, σ_{1o}, $\dot{\varepsilon}_{os}$ and $\dot{\varepsilon}_{o1}$ are temperature dependent functions. The constant m is the rate sensitivity (the reciprocal of the stress-exponent n in a power-law creep equation), and K is a non-physical fitting parameter that governs the sharpness of the transition between rate-dependent flow and rate-independent flow. At a given temperature, in the high strain-rate limit, the equation for the saturation stress reduces to

$$\sigma_s/G = (\sigma_{so}/G) \tag{A.3-5}$$

whereas in the low strain-rate limit, it becomes

$$\sigma_s/G = (\sigma_{so}/G)\left(\dot{\varepsilon}_p/\dot{\varepsilon}_{os}\right)^m, \tag{A.3-6}$$

which reflects the typical power-law creep behavior observed for this material at high temperatures and low strain rates. The equation for the yield stress behaves similarly. The temperature dependencies of σ_{so} and σ_{1o} are in large part eliminated by dividing by G. However, the temperature dependencies of $\dot{\varepsilon}_{os}$ and $\dot{\varepsilon}_{o1}$ reflect the Arrhenius temperature dependence of high-temperature creep in this material:

$$\dot{\varepsilon}_{os} = \dot{\varepsilon}_{oos}\exp(-Q/RT) \tag{A.3-7}$$

$$\dot{\varepsilon}_{o1} = \dot{\varepsilon}_{oo1}\exp(-Q/RT) \tag{A.3-8}$$

where $\dot{\varepsilon}_{oos}$ and $\dot{\varepsilon}_{oo1}$ are constants, and Q, R and T are the creep activation energy, gas constant and absolute temperature, respectively.

The values for the parameters in all of the above equations are:

G	= 92.0 - 4.02x10^{-2}T GPa
θ_1/G	= 3.66x10^{-2}
σ_{1o}/G	= 2.06x10^{-3} + 7.12x10^{-1}/T
σ_{so}/G	= 2.00x10^{-2} - 9.12x10^{-6}T
m	= 0.187 = 1/5.35
Q/R	= 38533 K
$\dot{\varepsilon}_{oos}$	= 1.062x10^{14} s^{-1}
$\dot{\varepsilon}_{oo1}$	= 3.794x10^{12} s^{-1}
K	= 2.0

The combination of the Voce equation and the above strain-rate and temperature laws allows one to generate the complete rate and temperature-dependent true-stress/true-strain curves. The yield stress σ_1 in these equations can be compared to the 0.2% offset yield stress. The ultimate strength, while not specifically denoted in the equations, can be determined by differentiating the Voce equation in accordance with Considere's construction for the true stress σ_u that corresponds to the engineering ultimate strength:

$$\frac{d\sigma}{d\varepsilon}|\varepsilon_{pu} = \theta_1 \exp\left(-\varepsilon_{pu}/\varepsilon_c\right) = \sigma_u \qquad \text{(A.3-9)}$$

where ε_{pu} is the true plastic strain at the ultimate strength, which corresponds to the uniform elongation. Solving the above equation and the Voce equation simultaneously gives σ_u and ε_{pu}.

A.3.2 Generalized Plastic Flow Behavior of HT9

The deformation behavior of the martensitic-ferritic Stainless Steel HT9 can be described over a broad range of temperature and strain-rate with the set of equations shown below [A.13]. These equations are incorporated in the FPIN2 and DEFORM-5 codes and are used by them in

calculations of the strength and ductility of this alloy at temperatures ranging from room temperature to 840°C under a variety of loading conditions, including thermo-mechanical transients. The high-temperature creep behavior is adequately described by an equation of the Dorn power-law form:

$$\dot{\varepsilon}_p/\dot{\varepsilon}_{oos} = (E/\sigma_{so})^n(\sigma_s/E)^n \exp(-Q_c/kT). \qquad \text{(A.3-10)}$$

In this equation, $\dot{\varepsilon}_p$ is the steady-state equivalent creep rate normalized by $\dot{\varepsilon}_{oos}$, a constant; σ_s is the equivalent applied stress in the creep test normalized by the constant σ_{so}; E is the temperature dependent Young's Modulus; Q_c is the creep activation energy; k is Boltzmann's constant, and T is absolute temperature. The temperature dependence of E is expressed as [A.14]:

$$E(T) = 2.12\text{x}10^{11}\ [1.144 - 4.856\text{x}10^{-4}T]\ \text{Pa} \qquad \text{(A.3-11)}$$

The remaining parameters in the creep equation are given by:

$\dot{\varepsilon}_{oos}$	$= 5.1966\text{x}10^{10}\ s^{-1}$
σ_{so}/E	$= 3.956\text{x}10^{-3}$
n	= 2.263
Q_c/k	= 36,739 K

The flow-stress/strain-hardening behavior can be described by an equation of the Voce type:

$$\sigma/E = \sigma_s/E - [(\sigma_s - \sigma_1)/E]\exp(-\varepsilon_p/\varepsilon_c), \qquad \text{(A.3-12)}$$

where σ is the equivalent flow stress at some value of true equivalent plastic strain ε_p, measured from the reference state of as-heat-treated material ($\varepsilon_p = 0$); σ_1 is the yield stress of as-heat-treated material; ε_c is a temperature dependent parameter extracted from the hardening rate at the ultimate strength; and σ_s is the saturation stress or steady-state flow stress, approached at large plastic strain, and assumed compatible with the stress in the above steady-state creep equation. It has been found that assuming that the yield stress $\sigma_1 = 0.8\sigma_s$ throughout allows the generation of flow stress-strain curves that agree well with data. The true stress at the ultimate strength (maximum load) is, after differentiating the above Voce equation, given by:

$$\sigma_u/E = [(\sigma_s - \sigma_1)/\varepsilon_c E]\exp(-\varepsilon_{pu}/\varepsilon_c), \quad \text{(A.3-13)}$$

where ε_{pu} is the true strain at the ultimate strength corresponding to the uniform elongation. Solving, simultaneously, this equation in conjunction with the flow stress equation evaluated at ε_{pu}, the following expression is obtained for the quantity ε_c:

$$\varepsilon_c(T) = 0.12733 - 3.5027\text{x}10^{-4}T + 2.9934\text{x}10^{-7}T^2. \quad \text{(A.3-14)}$$

An equation to model the transition between high-rate, low-temperature, rate independent flow behavior and creep behavior has the form:

$$\sigma_s/E = \sigma_{so}/E\left\{1 - exp\left[\left(\varepsilon_p\, exp(Q_c/kT)/\varepsilon_{oos}\right)^{K/n}\right]\right\}^{1/K}. \quad \text{(A.3-15)}$$

Because of microstructural changes that occur during long-time creep testing of HT9, and the effects they have on flow stress, there is not a smooth transition between short time tensile behavior and creep behavior. However, setting the non-physical fitting parameter K = 0.2, and with all the other parameters set as indicated above, the above equation follows the tensile data quite well, and reduces to the power-law creep equation at very low strain rates.

As noted in Section A.2.2.2, for temperatures above the completion of the γ transformation temperature (960°C), it is assumed in the flow stress model in FPIN2 and DEFORM-5 that the deformation rate for HT9 is the same as that given by the 316 SS equations in Section A.3.1. A simple mixture rule is used to calculate the deformation rates in the α-γ transition region (840° - 960°C).

A.3.3 Yield and Ultimate Tensile Strength

The strength properties of HT9 are presented in Ref. A.15. This document can be referred to in order to obtain various analytical equations to predict yield and tensile strength for a number of conditions. The strength properties are graphically presented in Figure A-1 and Figure A-2.

The strength properties for 20, 12% CW 316SS can be obtained using Reference A.14. The irradiation conditions tend to quickly equalize the mechanical properties, regardless of initial cold-work level. It is therefore recommended that the properties for 20% CW 316SS be used due

to the extensive data base supporting the property correlations. The yield and ultimate tensile strength are graphically shown in Figure A-3 and Figure A-4.

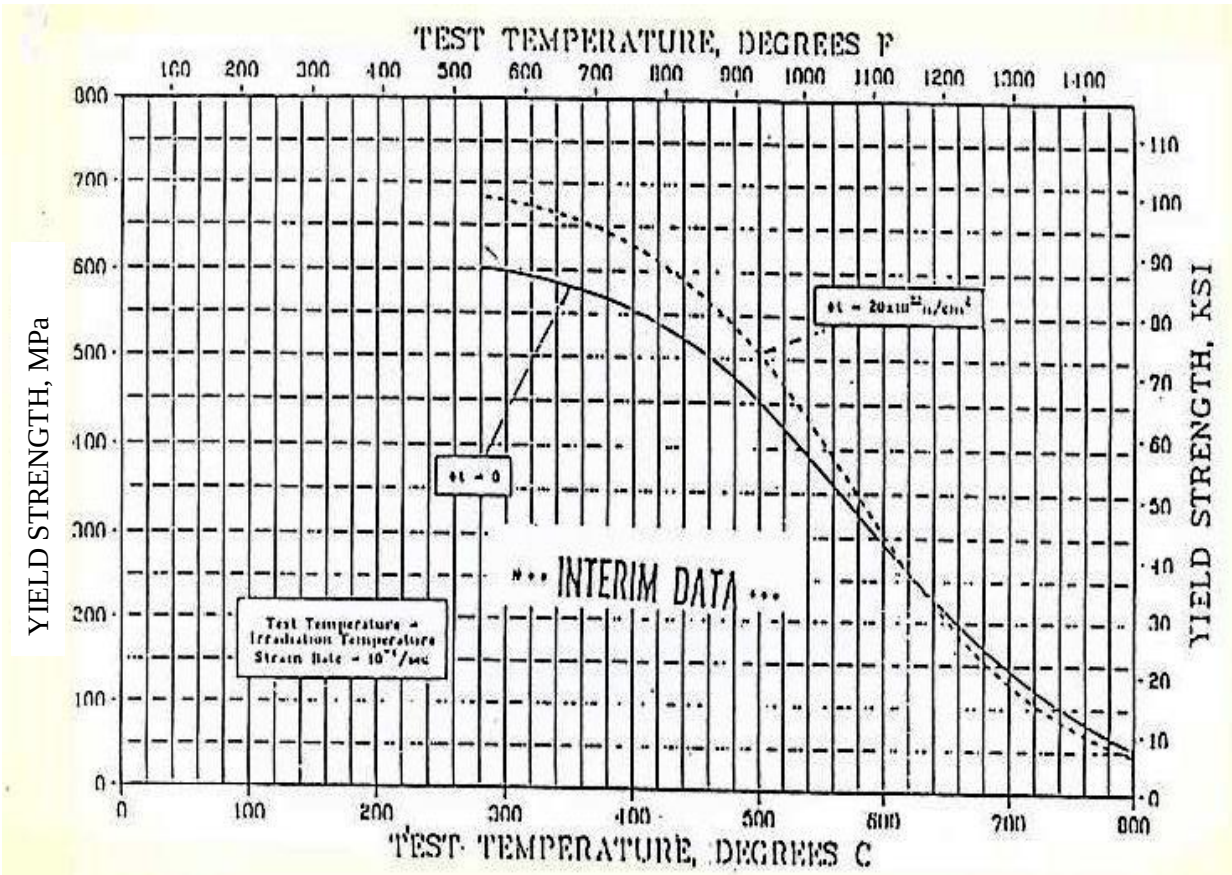

Figure A-1 Yield Strength of HT9 (from Ref. A.15)

The ductility properties of HT9 are presented in Ref. A.15. This document can be referred to in order to obtain various analytical equations of ductility for a number of conditions. The ductility is graphically presented in Figure A-5.

The ductility of 20, 12% CW 316SS can be obtained using Ref. A.14 correlations. The ductility is graphically shown in Figurer A-6.

.

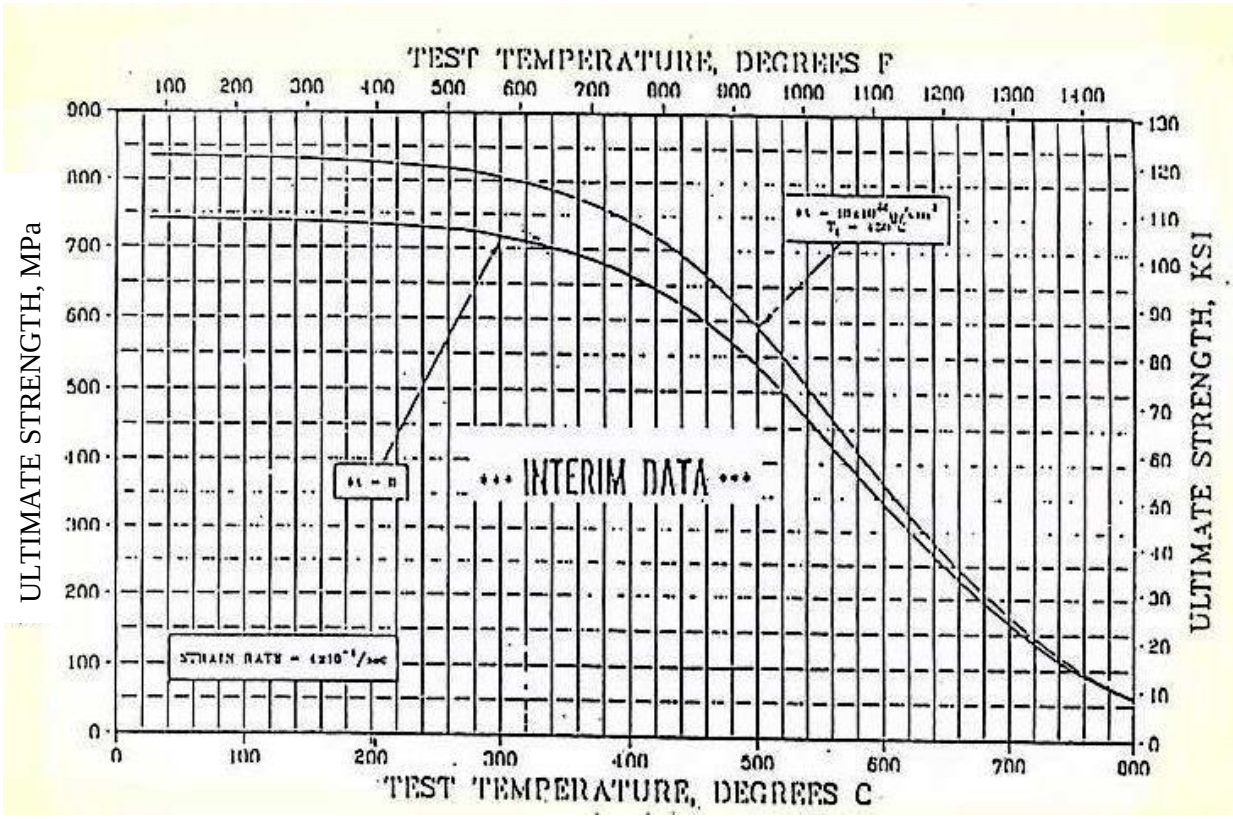

Figure A-2 Ultimate Strength of HT9 (from Ref. A.15)

A.3.5 Fracture Toughness

A guideline for acceptable fracture toughness for the handling of HT9, AISI 422, or T91 ducts is given as $K_{Ic} \geq 0.5\ \sigma_y$ (ksi.in.$^{-1/2}$), [A.16], where σ_y is the yield strength in ksi. There has never been an observed or expected problem with irradiation-induced decreases in fracture toughness with AISI 316 over the exposures allowed for EBR-II ducts, although for most applicable conditions the toughness of irradiated HT9 is superior to irradiated 316SS. The minimum criterion can be used for both duct types.

A.3.5.1 HT9

HT9 is a martensitic stainless steel and therefore undergoes a ductile-to-brittle transition (DBT) upon lowering the test, or operating, temperature. This transition temperature (DBTT) rises with irradiation exposure, especially if the irradiation temperature is very low. The fracture toughness behavior of HT9 is graphically shown in `Figure A-7`, taken from Ref. A.15. The data for the duct material irradiated in FFTF are shown in `Figure A-8` taken from Ref. A.17.

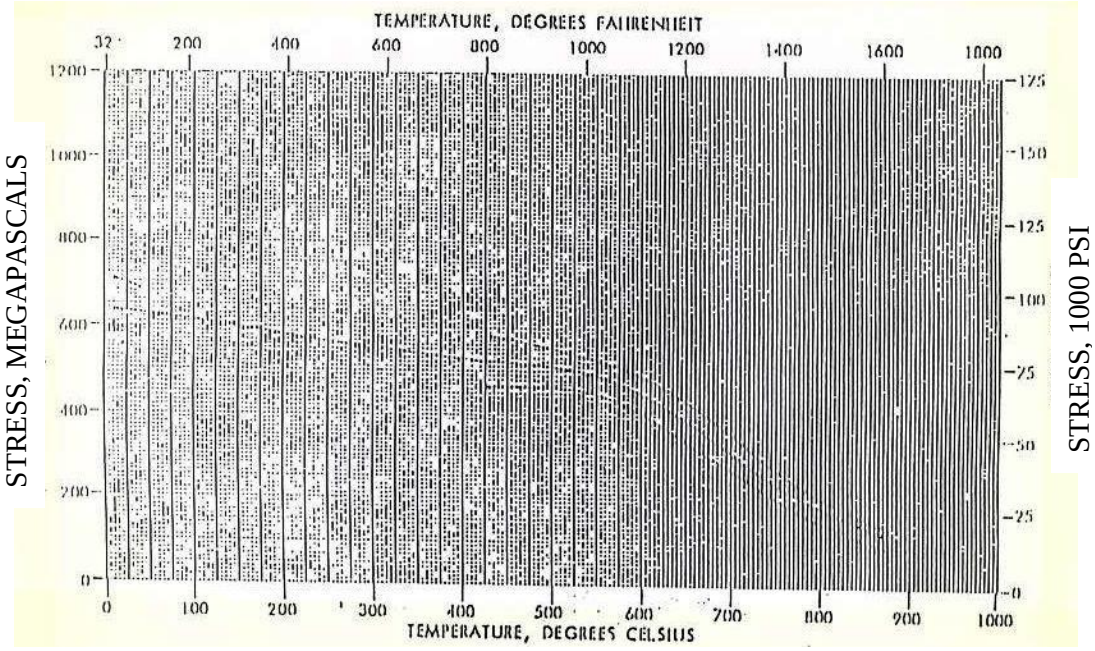

Figure A-3 Yield Strength of 20% CW 316SS (from Ref. A.14)

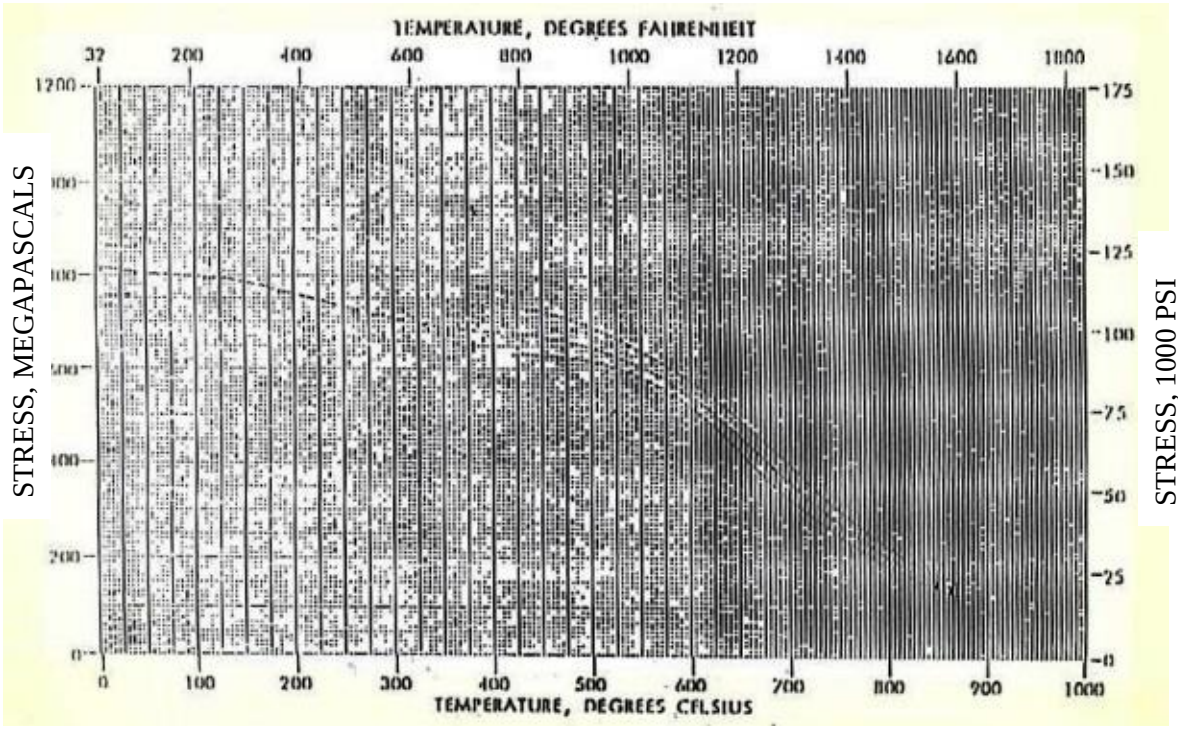

Figure A-4 Ultimate Strength of 20% CW 316SS (from Ref. A.14)

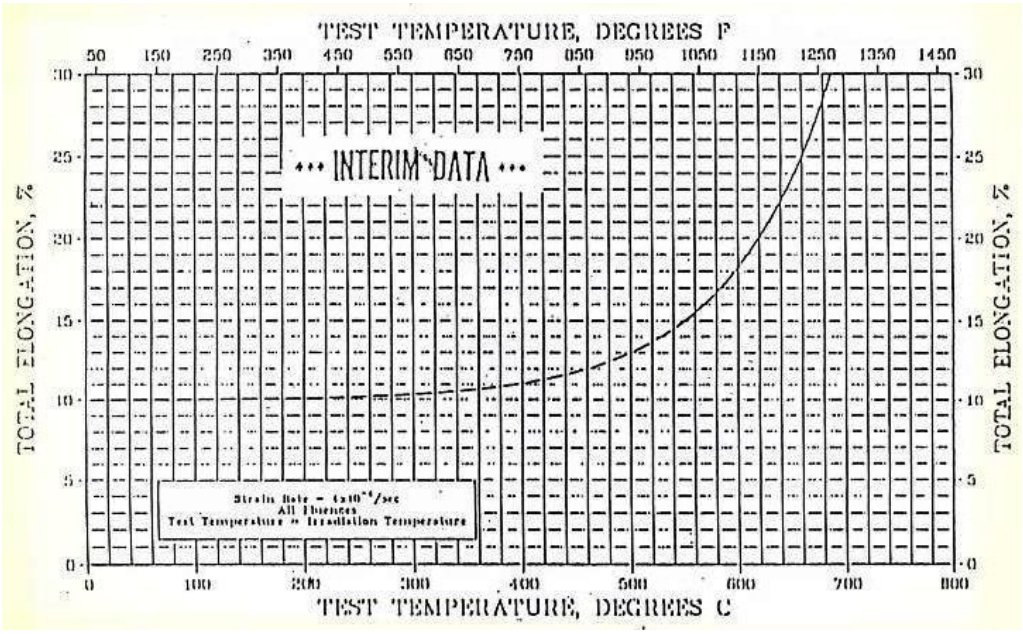

Figure A-5 Ductility of HT9 (from Ref. A.15)

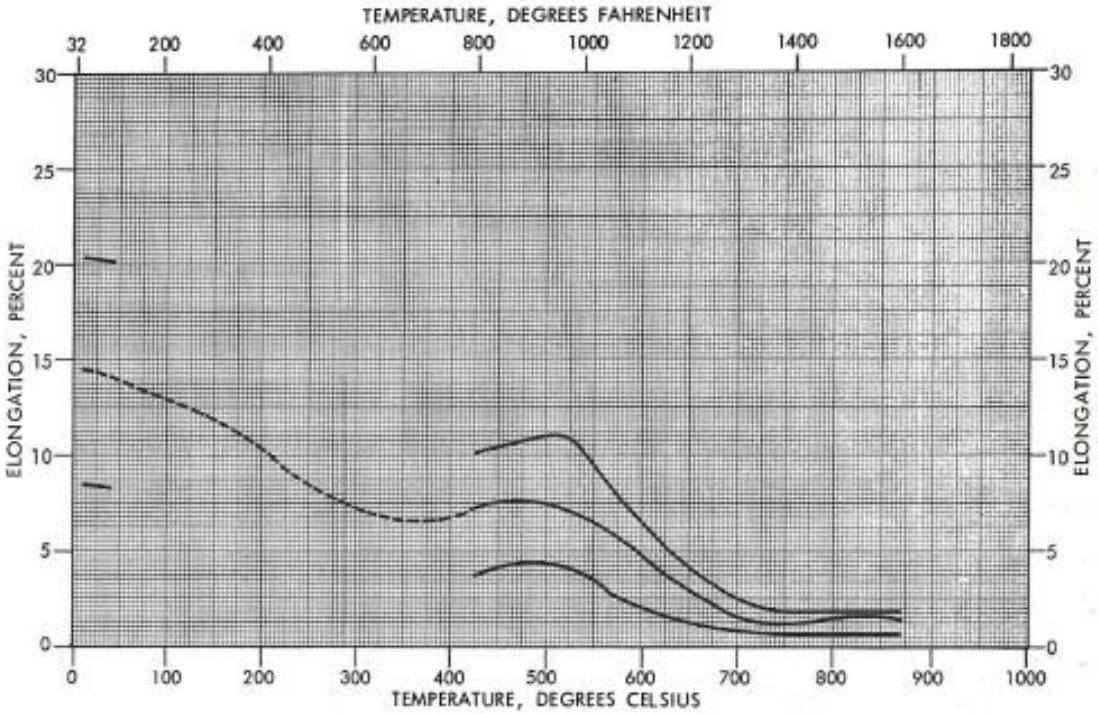

Figure A-6 Ductility of 20% CW 316SS (from Ref. A.14)

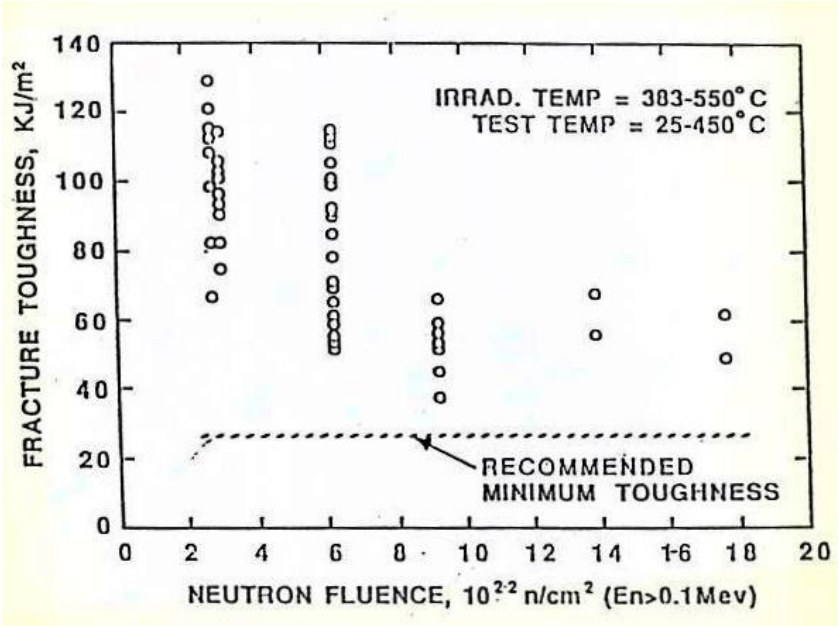

Figure A-7 Fracture Toughness Behavior of Irradiated HT9 (from Ref. A.15)

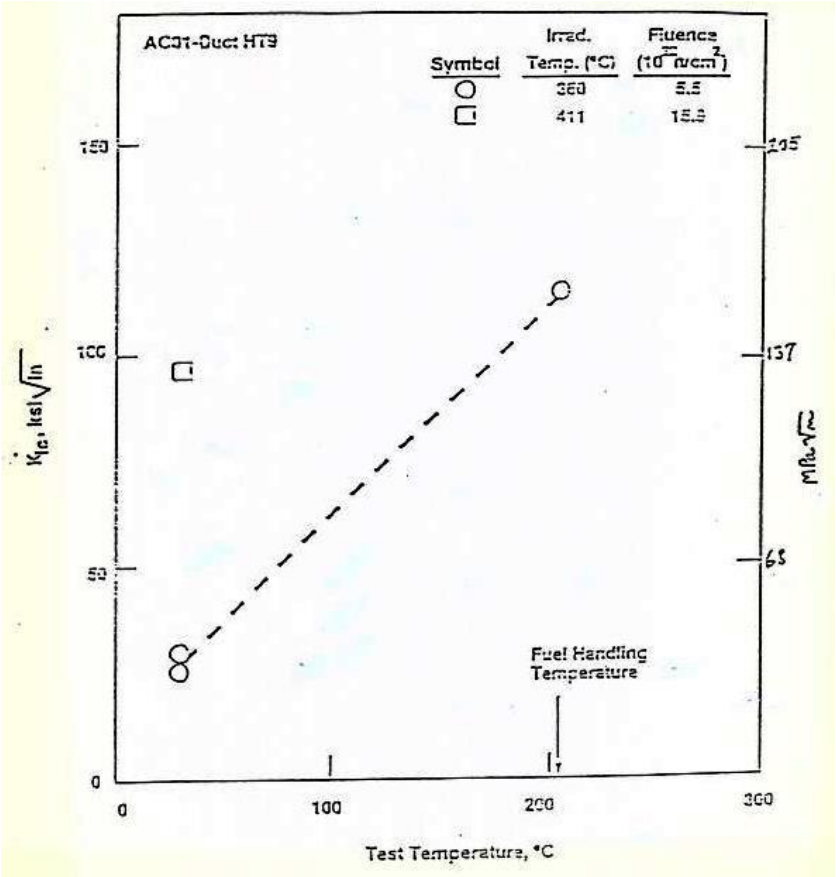

Figure A-8 Temperature Dependence of KIC for the ACO-1 Duct Sample (from Ref. A.17)

Reference A.17 has shown that HT9 FFTF duct material meets the above minimum criteria except for the combination of low temperature irradiation (<400°C) and low temperature handling (~ room temperature). If this behavior were to translate to EBR-II duct geometries then care may be required for hot cell handling but not for in-reactor refueling operations although there are no correlations given to predict the toughness number. An extensive data base concerning fracture toughness properties for HT9 and T91 is given in Refs. A.15 and A.5. Note that the AISI 422 and T91 materials are expected to behave similarly, or with less mechanical property degradation than HT9.

Irradiation of many test fuel pins, including periodic handling for interim examinations, has never shown any indications of problems with the fracture toughness of HT9 cladding. The observation is very supportive of the expectations for benign behavior.

A.3.5.2 Cold-Worked 316 Stainless Steel

The database that exists for 20% CW 316 is used for 12% CW 316 as the irradiation hardening, or softening, tends to equalize the mechanical properties regardless of prior cold-work level, and the higher cold-working provides for lower fracture toughness prior to irradiation. Ref. A.18 showed the fracture toughness behavior of samples from an EBR-II-sized duct (20% CW), irradiated in EBR-II. The data are presented graphically in Figure A-9 and Figure A 10.

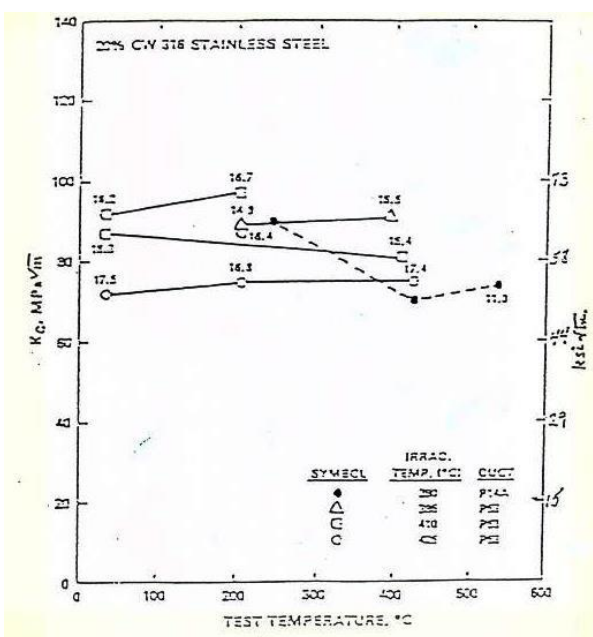

Figure A-9 Effect of Temperature on the K_c of Irradiated 20 CW 316SS (from Ref. A.18)

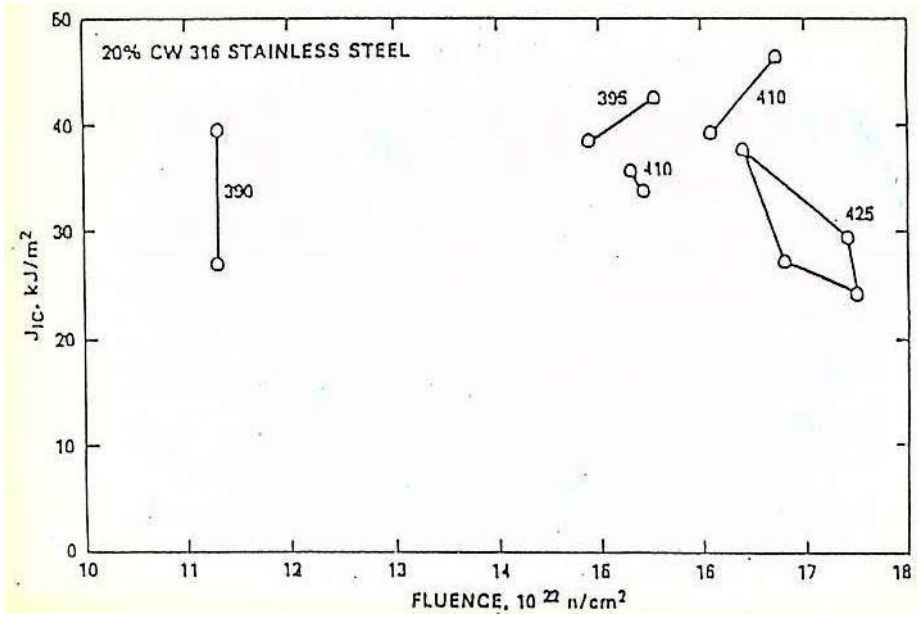

Figure A-10 Effect of Temperature on Fracture Toughness of Irradiated 20 CW 316SS (from Ref. A.18)

A.4. Cladding Wastage

Cladding wastage can be characterized by external loss due to sodium corrosion and internally by interaction with fuel and fission products. These latter effects can further be characterized into steady-state reactions involving only solid phases and effective cladding wastage and reactions during off-normal conditions where liquid phases may form. The following sections provide analytical description of these effects.

A.4.1 Cladding/Coolant Interaction

A.4.1.1 HT9

A minor part of cladding wastage is concerned with chemical interaction of the primary sodium coolant with the HT9 cladding. The suggested [A.19] analytical expression representing the depth to which chemical components in the cladding are lost, which may then weaken the cladding is given by,

$$D = FR_o t + B't^{1/2} + X \qquad \text{(A.4-1)}$$

where

D = total depth of damage, μm

R_o = A exp(-Q/RT), mass loss rate, $mg.dm^{-2}.yr^{-1}$

t = time, years

F = damage factor, 0.021 $\mu m.mg^{-1}\ dm^2$

X = intergranular penetration depth, μm = 0

B′ = ferrite layer growth coefficient, (0.17T - 143.42) μm $yr^{-½}$, for T > 571°C.

Actually, the reference suggests B′ = 0, but carbon depletion has been observed from HT-9 in EBR-II (X447) so the form for 316SS is used instead.

A = constant, $1.76 \times 10^{11}\ mgdm^{-2}yr^{-1}$

Q = activation energy, 36,000 $cal.mol^{-1}$

R = gas constant, 1.987 $cal.mol^{-1}.\ K^{-1}$

T = temperature, K

Another effect which has recently been observed for the martensitic cladding and duct materials is an apparent increased rate of Mn loss. While the current data base is not extensive enough for a definitive identification or analytical description of the effect [A.20], the potential impact is increased transport of ^{54}Mn from the cladding or ducts to other parts of the primary system, thereby potentially making maintenance activities more difficult. A major perturbation in the deposition of ^{54}Mn is not expected, but a surveillance program using deposition samplers will be implemented to track any changes which may occur as the result of core conversion to Mark-V fuel.

A.4.1.2 Cold-Worked 316 Stainless Steel

The corresponding relationship to use for sodium corrosion of 316 stainless steel is,

$$D = FR_o t + B't^{1/2} + X \qquad \text{(A.4-2)}$$

where

D = total depth of damage, μm

R_o = A exp(-Q/RT), mass loss rate, $mg.dm^{-2}.yr^{-1}$

t = time, years

F = damage factor, 0.0125, $\mu m.mg^{-1}\ dm^2$

X = intergranular penetration depth, $(0.22T-192.060)t^{1/2}$ μm

B′ = ferrite layer growth coefficient, (0.17T-143.42) $\mu m\ yr^{-1/2}$

A = constant, $1.76 \times 10^{11}\ mg.dm^{-2}.yr^{-1}$

Q = activation energy, 36,000 $cal.mol^{-1}$

R = gas constant, 1.987 cal. $mol^{-1}\ K^{-1}$

T = temperature, K

In determination of the intergranular penetration depth, X, it should be noted that negative values of X are physically meaningless. Therefore,

set X = 0 for T = 873K

Likewise, a negative value of B′ is not allowed, so that B′ = 0 for T≤ 844 K.

A.4.2 Wastage

LIFE-METAL has provisions for reducing the cladding thickness from its nominal value due to inner-diameter (ID) and outer-diameter (OD) fabrication tolerances and scratches; due to OD sodium/cladding corrosion, decarbonization, and intergranular attack; and due to ID fuel/cladding chemical or metallurgical interaction (FCCI). For both Mark-V (HT9) and Mark-VA (316SS) claddings, ID FCCI is characterized by fission product (FP) diffusion into the cladding and some cladding constituent (e.g. Fe, Ni, Cr, C, etc.) diffusion from the cladding to the fuel. The fission-product-rich cladding layer tends to be very brittle (high microhardness) and cracked. Thus, it cannot be relied upon as a load-bearing cladding layer.

Let δ_o and δ_i be the cladding thicknesses (in mils) to be removed from the cladding OD and ID, respectively, for the purposes of the structural analysis. In the LIFE-METAL approach, δ_o is removed from the cladding OD for both the thermal and mechanical analysis. This is reasonable in that it is assumed that the dominant contribution to δ_o is corrosion. In the case of ID wastage, δ_i defines a cladding thickness layer which is present for both the thermal analysis and for determining fuel/cladding gap closure. However, the shear modulus is reduced by a factor of 10

and the creep rate of this layer is increased by a factor of 100 to make this fission product rich layer essentially non-load-bearing. It simply transmits the gas pressure or fuel/cladding mechanical interaction (FCMI) interface stress unabated to the intact base cladding.

Based on the discussion in Section 2.1.3, it is recommended that a tolerance/scratch allowance of 0.5 mils be used for both the cladding ID and OD. Also, given the fact that temperature and operating conditions change with time, it is recommended that δ_o and δ_i be determined from rate laws:

$$\delta_o = 0.5 + \int_0^t \dot{\delta}_o \, dt, \text{ mils} \tag{A.4-3}$$

and

$$\delta_i = 0.5 + \int_0^t \dot{\delta}_i \, dt, \text{ mils} \tag{A.4-4}$$

The $\dot{\delta}_o$ functional form and parameters are determined from the cladding properties presented in Secs. A.4.1.1 and A.4.1.2. For Mark-VA (316SS), the appropriate equation is

$$\dot{\delta}_o = \exp\left(9.199 - 1.8118 \times 10^4 / T_{co}\right) + 2.1032 \times 10^{-4} (B+C) t^{1/2} \tag{A.4-5}$$

$$B = \max\{0, (0.17 T_{co} - 143.42)\} \tag{A.4-6}$$

$$C = \max\{0, (0.22 T_{co} - 192.06)\} \tag{A.4-7}$$

where T_{co} is cladding OD temperature in K, t is time in hours, and $\dot{\delta}_o$ is in mils/h. For Mark-V (HT9) cladding, the recommended equation is

$$\dot{\delta}_o = \exp\left(9.718 - 1.8118 \times 10^4 / T_{co}\right) + 2.1032 \times 10^{-4} (B+C) t^{1/2} \tag{A.4-8}$$

$$B = \max\{0, (0.17 T_{co} - 143.42)\} \tag{A.4-9}$$

$$C = 0 \tag{A.4-10}$$

Both equations for $\dot{\delta}_o$ (A.4-5 and A.4-8) represent corrosion and ferrite layer growth due to carbon depletion.

The rate correlations for clad ID corrosion are based on steady-state irradiation results and

post irradiation Fuel Behavior Test Apparatus (FBTA) and Whole Pin Furnace (WPF) test results. The D9/U-19Pu-10Zr data base is used as a guide in modeling the Mark-VA cladding (316SS). The HT9/U-19Pu-10Zr data base and the high temperature HT9/U-10Zr data base are used to model Mark-V cladding. For temperatures ≤ 650°C the correlations for $__i$ are assumed to be of the diffusional form

$$\dot{\delta}_1 = 0.5[D_o \exp(-Q/RT_{ci}) + D_{io}\phi]^{0.5} t^{-0.5} \qquad \text{(A.4-11)}$$

where ϕ = neutron fast flux 10^{15} n/cm^2·s, R=1.987x10^{-3} kcal/mol-K, T_{ci} = cladding ID temperature in K, $\dot{\delta}_1$ = wastage rate in mils/h and

HT9 (Best Fit)	HT9 (Design)
D_o = 6.26 x 10^8	D_o = 1.24 x 10^9
Q = 48.227	Q = 48.227
D_{io} = 1.0 x 10^{-7}	D_{io} = 1.0 x 10^{-7}

D9 Best Fit and Design	316SS (Design)
D_o = 4.4 x 10^{13}	D_o = 1.35 x 10^{13}
Q = 63.6	Q = 63.6
D_{io} = 3.57 x 10^{-6}	D_{io} = 1.09 x 10^{-6}

The HT9, D9, and 316SS wastage modeling and results are documented in Refs. A.21 and A.22. Figure A-11 shows the local HT9 data vs. local burnup-averaged temperature in an Arrhenius plot. The vertical axis is the square of the FCCI layer thickness (D_{fp} in mils) divided by time (t_y in effective full power gears), consistent with the diffusion model. The solid line, with a slope corresponding to an activation energy of 48.2 kcal/mole, is a best fit to the local data. The dotted line, labeled Mark-V fit, was derived based on correlating peak observed FCCI zone thickness with peak cladding ID temperature for four pins (U-19Pu-10Zr pins DP16 and DP21 and U-10Zr pins DP70 and DP75). Figure A-12 shows a direct comparison between the predicted and measured local wastage, using the best fit correlation in LIFE-METAL. The scatter is largely due to the non-uniform behavior of FCCI. Figure A-13 shows the direct comparison between the predicted and measured peak FCCI layer for each pin, using the HT9 design correlation. Also shown in Figure A-13 are the data for the combined fission product (FP) plus carbon-depleted

(CD) zone. The three data points at < 3 mils are for lower-temperature (PICT < 600°C) HT9/U-19Pu-10Zr pins. The data points at ≥ 3 mils are for high-temperature (637 ≤ PICT ≤ 658°C) HT9/U-10Zr pins. The fit to the three HT9/U-19Pu-10Zr data points is quite good. For the four HT9/U-10Zr pins, the average prediction (6.9 mils) falls between the average FCCI measurement (4.7 mils) and the average FCCI + CD measurement (6.9 mils). Based on a comparison of predicted and measured peak cladding strain and failure statistics (2/15 failures), it is sufficient to use the HT9 design correlation ($D_o = 1.24 \times 10^9$) to bound the cladding strains and failure statistics without any additional accounting of cladding thinning or weakening due to the carbon-depleted zone.

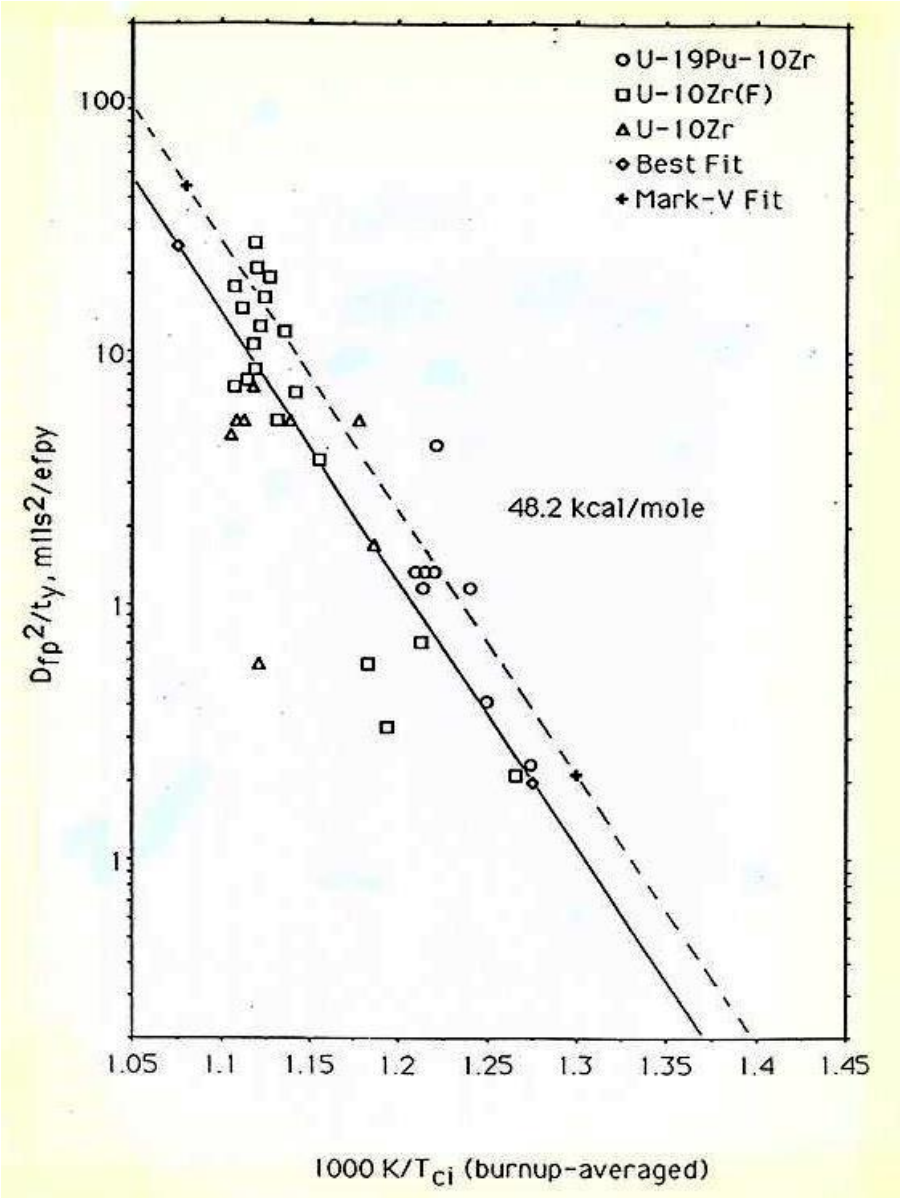

Figure A-11 LIFE-METAL Predictions for HT9/U-19Pu-10Zr and HT9/U-10Zr ID Wastage

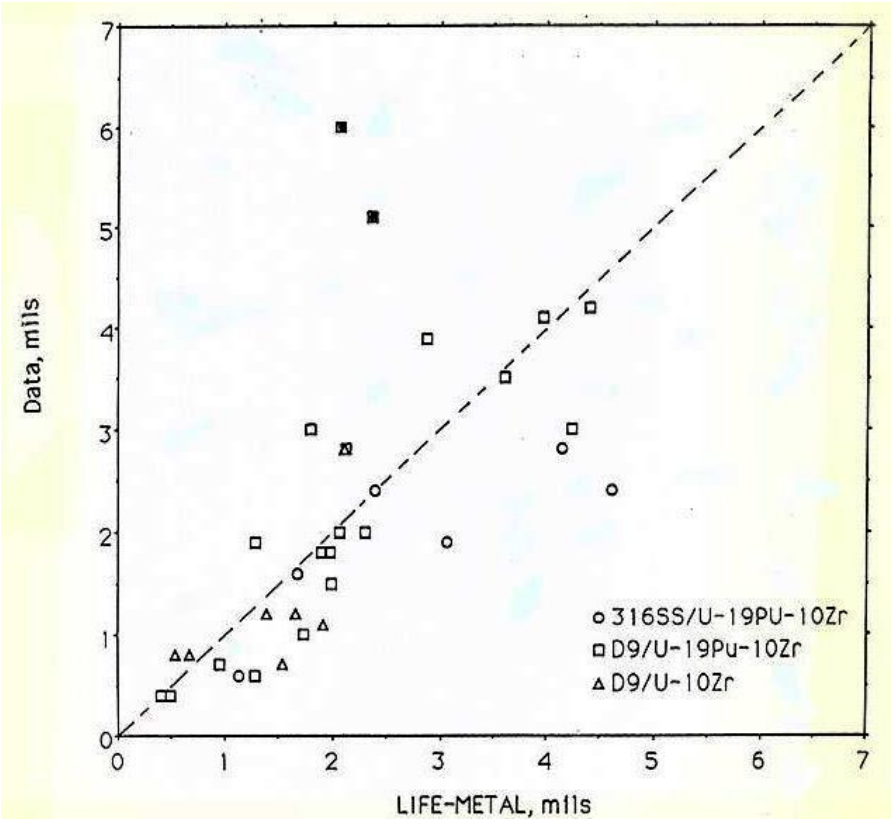

Figure A-12 Predictions vs. Data for 316SS and D9 Local Wastage

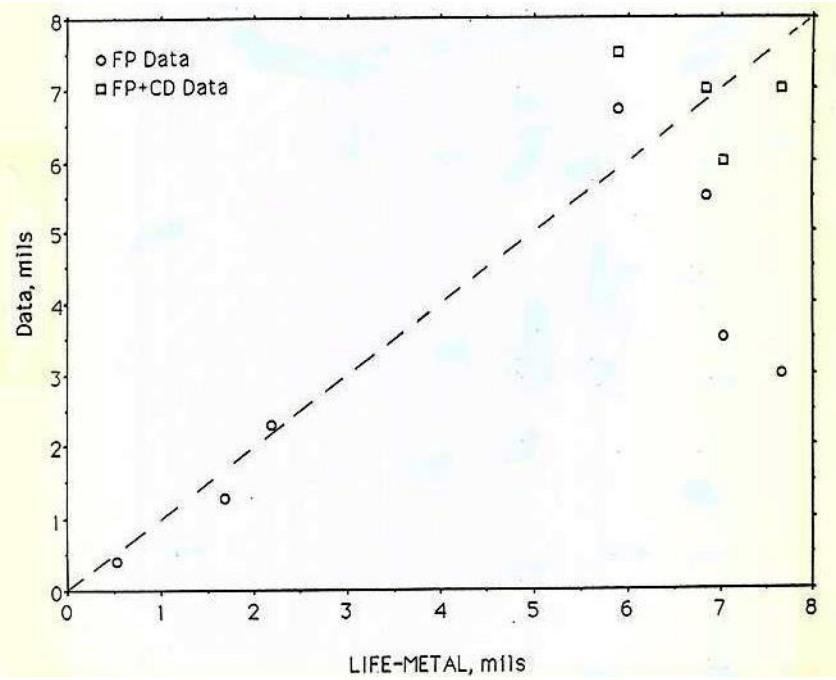

Figure A-13 LIFE-METAL Predictions (with Mark-V Correlation) vs. Data for Peak Wastage in HT9

In the case of D9, a single correlation gave the best fit to both the local FCCI data and the peak (per pin) FCCI data. Figure A-14 shows the Arrhenius plot of the data for D9/U-19Pu-10Zr, D9/U-10Zr, and 316SS/U-19-Pu-10Zr. Direct comparisons between predicted and measured FCCI zone thickness are shown in Figure A-15 (local) and Figure A-16 (peak). From Figure A-16, it is clear that the D9 correlation overpredicts the peak wastage observed for the one 316SS/U-10Pu-10Zr pin examined. Thus, the design correlation for Mark-VA is derived by scaling the D9 correlation to match the peak FCCI zone observed for the 316SS/U-19Pu-10Zr pin TS81. The full profile FCCI data for TS81 are shown in Figure A-17, as well as the results of the D9 correlation and the Mark-VA 316SS correlation.

A.4.3 Eutectic Liquefaction Threshold

The eutectic liquefaction thresholds have been set at 651°C for Mark-V and 661°C for Mark-VA based upon FBTA results described in Section 5. These results are lower bounds to the data at ~11 at. % burnup, which bounds the burnup range sought for Mark-V and Mark-VA fuels. Experiments at lower burnups have shown a higher threshold temperature. No credit was taken for this increase in liquefaction temperature at low burnups in order to allow for fission-product carryover in recycled fuel.

A.4.4 Eutectic Penetration Rate

The safety analyses performed with SASSYS/DEFORM-5 and FPIN2 use the ANL (Bauer-Kramer) correlation for cladding eutectic penetration based upon out-of-reactor tests which measured the erosion of iron samples dipped into various iron-uranium melts. These data agree with earlier dipping test data using uranium-fissium fuel and stainless steel cladding. The dipping test results indicate that the penetration rates are governed by iron and uranium phases and are relatively independent of the fuel or cladding alloy. The data show that the penetration rate r can be correlated to the absolute temperature T (in K) by

1) $\dot{r} = \exp\{22847 - 27624/T\}$ μm/s (A.4-12)

for 650°C ≤ T < 1080°C, and

2) $\dot{r} = 922 + 2.9265(T - 1388) - 0.21522(T - 1388)^2 + 0.001138(T - 1388)^3$ (A.4-13)

for 1080°C ≤ T < 1233°C.

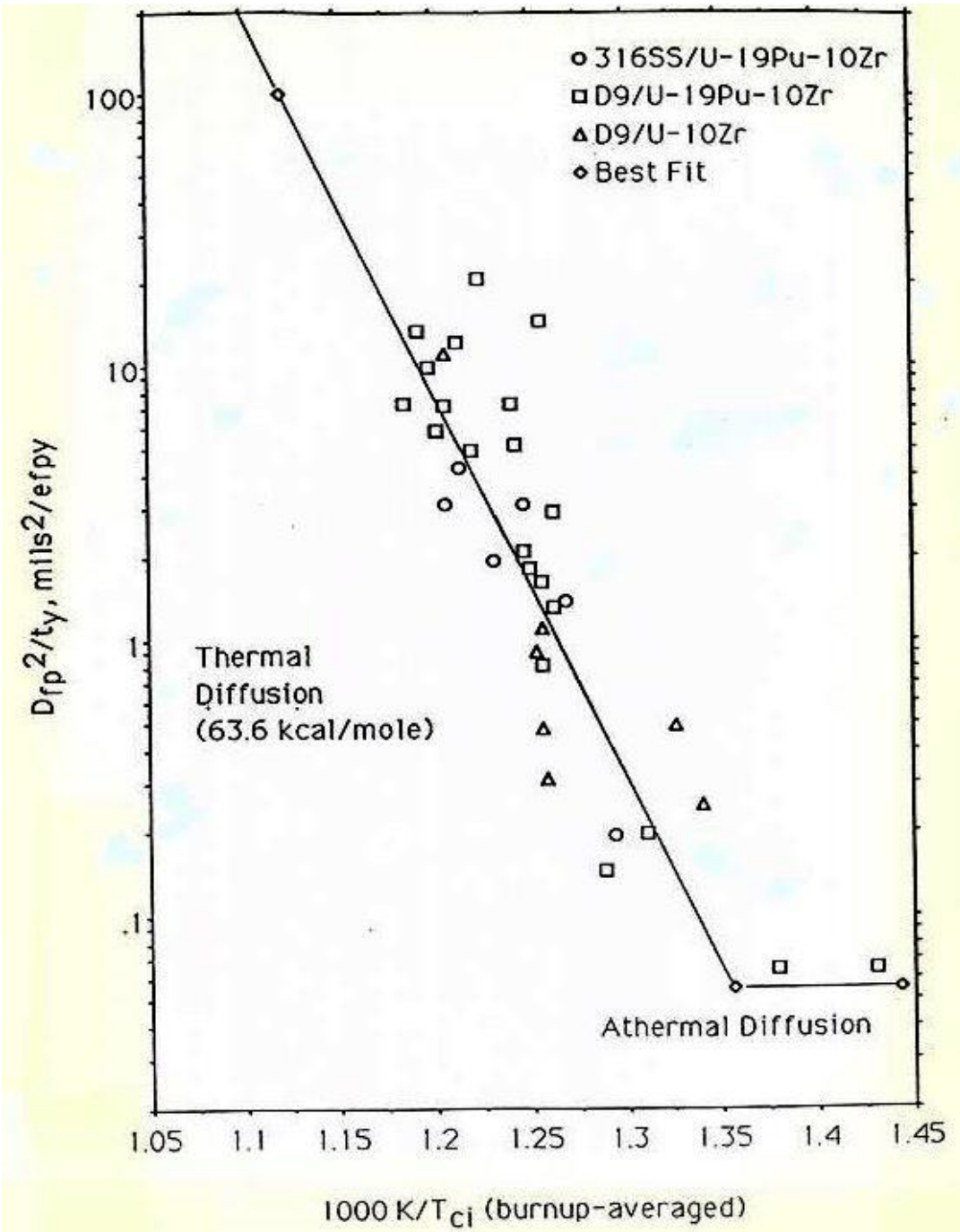

Figure A-14 316SS/D9 Wastage (fission product attack) Data and Correlations

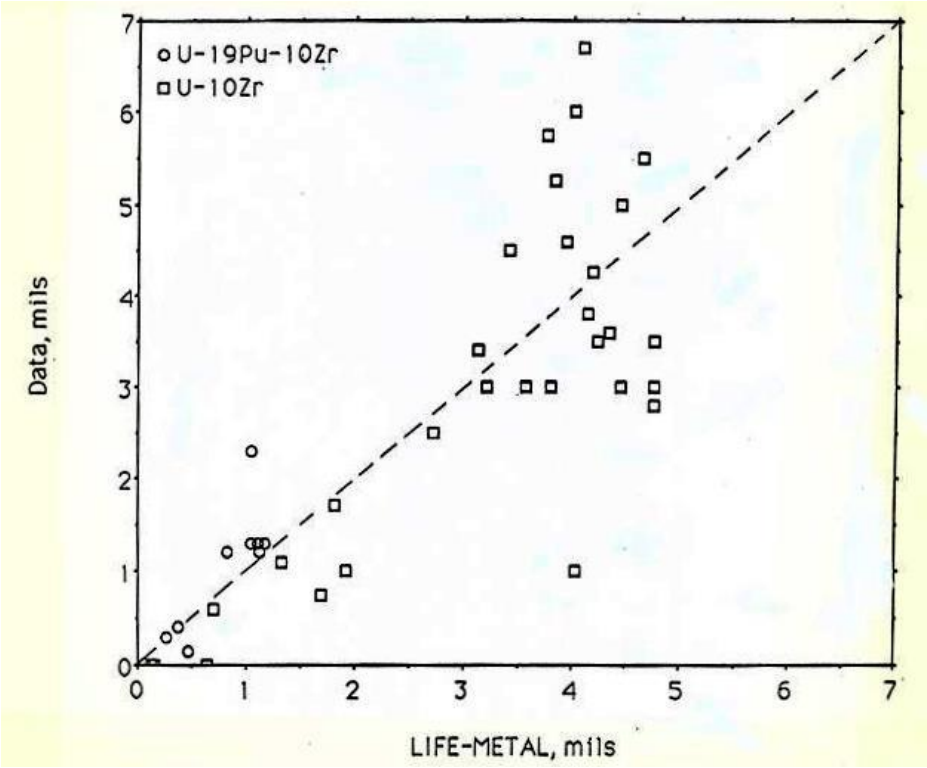

Figure A-15 LIFE-METAL Predictions vs. Data and Local Fission Product Depth in HT9 Cladding

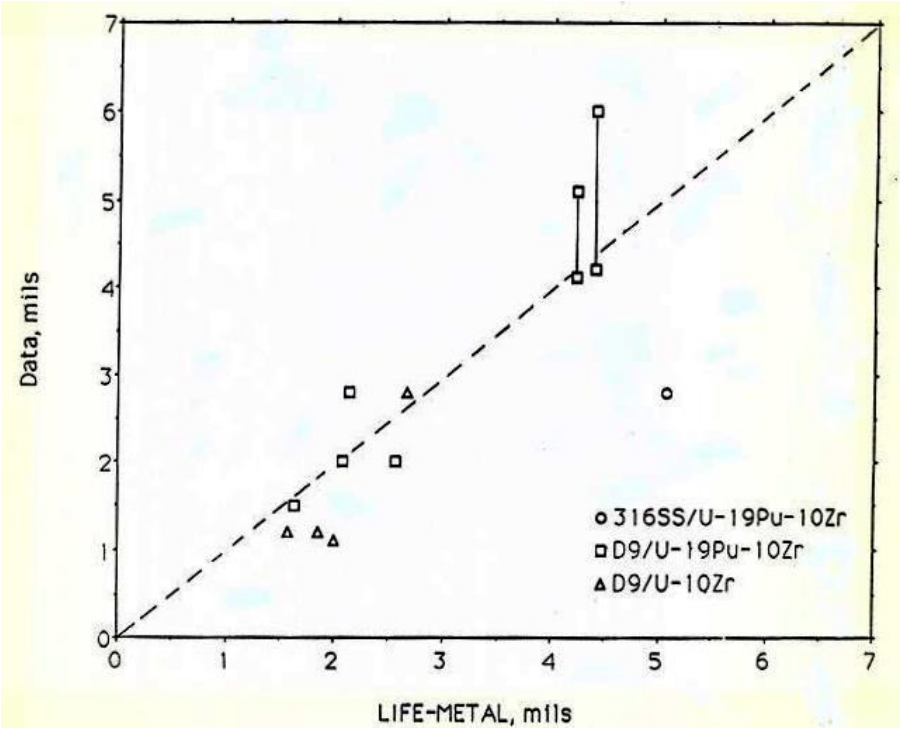

Figure A-16 LIFE-METAL Predictions vs. Data for Peak Wastage in 316SS/D9

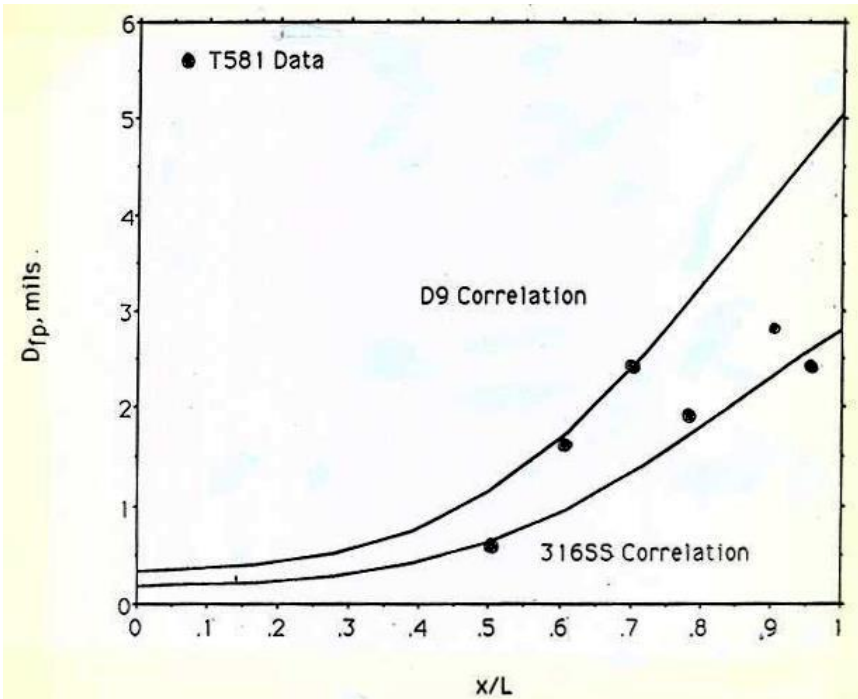

Figure A-17 Comparison of D9 and 316SS ID Fission Product Attack Correlations to T581 316SS/U-19Pu-10Zr Data

As explained in Section 5.2.3, the LIFE-METAL code is used to predict the solid-state ID wastage during normal operating conditions and the Bauer-Kramer correlation (Eq. A.4-12) is used in SASSYS to predict the additional solid/liquid cladding ID wastage due to overheating events. The Bauer-Kramer correlation is to be invoked for $T \geq 650°C$. The additional transient cladding wastage is to be interpreted as liquid for $T \geq T_e$, where $T_e = 651°C$ for Mark-V and 661°C for Mark-VA. In addition, the fraction of fuel which has liquefied is assumed to be twice the fraction of cladding which has liquefied. This methodology has been validated to the data in Table 5-7 and Table 5-8, which include fuel at burnups of 10 at. % or greater and overheating temperatures up to 800°C. The validation consisted of two parts. In the first part, the LIFE-METAL + Bauer-Kramer Correlation predictions for total cladding penetration were compared to the measured total penetration. As shown in Figure 5-11, this approach results in 81% confidence that the predictions for Mark-V will be an upper bound if temperatures without uncertainties are used in the prediction. For the three-sigma temperatures which are used in the safety case, the confidence in an upper bound prediction of total cladding penetration for Mark-V increases to over 99%. In the case of Mark-VA (see Figure 5-12), all data are bounded from above using the nominal temperatures. In the second part of the validation, the predicted fuel liquefaction fractions were

compared to the measured values summarized in Table 5-7 and Table 5-8. Figure 5-13 shows that the use of nominal temperatures in the transient analysis would give a confidence of 57% that the predicted value for Mark-V would be an upper bound. Again, using three-sigma temperatures in the safety analysis increases the confidence level to over 99%. In the case of Mark-VA, all measured fuel liquefaction fractions are bounded from above by the predictions when nominal temperatures are used. The database for Mark-VA is too limited with regard to fuel liquefaction to put a confidence level on these predictions. A high level of confidence could be argued for Mark-VA based on the use of three-sigma upper bound temperatures in the transient analysis.

The validation of the methodology and the Bauer-Kramer correlation of Mark-V and Mark-VA cladding penetration and fuel liquefaction predictions is significant from two perspectives. Firstly, it is a true validation in that none of the data in Table 5-7 and Table 5-8 was used to develop the correlation. Secondly, the proposed methodology and interpretation of predictions are unambiguous, as compared to past descriptions and approaches which sometimes confused total penetration measured after overheating at T > 650°C with incremental or addition penetration, as well as confusing liquid penetration with total penetration.

A.5. Effect of Fuel and Cladding Swelling

HT9 cladding shows insignificant void swelling and therefore cladding swelling has no effect on fuel performance.

The swelling of the fuel slug occurs both axially and radially (see Section 4). The axial swelling, while smaller than the radial component, produces the only notable effect in that it tends to dilute the effective density of fuel in the core. This has been observed in EBR-II where a large number of fresh driver fuel subassemblies are introduced into the core simultaneously. The radial swelling can produce a mechanical effect on the cladding (FCMI) when solid fission products begin to significantly fill the porosity. It has been estimated that the volumetric swelling due to solid and liquid fission products to be in the range of 0.6 to 1.8 vol. %/at. %. LIFE-METAL was then used to obtain a better upper bound by matching cladding strain predictions to data for 85% smear-density cases at 10 at. % peak burnup. The solid fission product swelling rate was increased with the fuel length increase (1.3% axial strain) and the fission gas release fraction (57%) held to the measured values until the predicted cladding diametral strain matched the measured

profile along the length of the pin. The gas bubble contribution was suppressed during this sensitivity study. Good agreement was found for a local swelling rate of 1.34 vol. %/at. %. Thus for FCMI calculations the increase in fuel diametral strain can be expressed as

$$\Delta D/D_o = (0.9872 + 1.3228x10^{-2}b)^{1/2} - 1, \quad \text{(A.5-1)}$$

where b ≥ 3 at. % is the local burnup along the axis of the fuel slug.

The correlation is considered to be an upper bound on solid fission product swelling because the influence of gas-bubble swelling on cladding strain was not considered and the fuel length increase was held to the low value of 1.3%. For lower temperature fuel rods, more of the swelling may be accommodated in length increase than for the high temperature (high power) case considered in the LIFE-METAL work.

The axial swelling behavior is expected to be as described in Section 4, where the swelling over the initial 1-1.5 at. % burnup produces the core dilution effect. Beyond that burnup the fuel has contacted the cladding and additional axial growth is much slower. The initial axial growth can be described by the following equations:

$$\Delta L/L_o\ (\%) = m_1 \times Bu \quad \text{for Bu} \leq 0.75 \text{ at. \%} \quad \text{(A.5-2)}$$

where m_1 = 3.6, and

$$\Delta L/L_o\ (\%) = 2.75 + m_2 \times (Bu - 0.75) \quad \text{for Bu} > 0.75 \text{ at. \%} \quad \text{(A.5-3)}$$

where m_2 = 0.12, and in each case, Bu is the peak burnup (at. %) of the fuel

Note that the database, Figure A-18, contains considerable scatter which can largely be explained by the fuel operating temperature. Outer row pins, colder, swelled more than inner row pins for the experiments.

A.6. Effect of Fuel Constituent Redistribution

A number of U-19Pu-10Zr fuel pins have been examined after irradiation to determine the local concentrations of U, Pu, Zr. Within the accuracy of the measurements, it appears that there is a significant redistribution of U and Zr, while the Pu atoms do not seem to migrate. Locally,

most fuel properties are dependent on the alloy composition. However, sensitivity studies conducted with LIFE-METAL indicate relatively little change in calculated design parameters (centerline fuel temperature, fission gas release, axial strain, and cladding strain) with redistribution. The major parameters which change with redistribution from a safety case viewpoint are the solidus and liquidus temperatures. These temperatures both decrease in a fuel zone as the Zr is depleted through migration. The results of calculations using Pelton's [A.23] model are shown in Figure A-19 as a function of Zr weight fraction for a constant Pu atom fraction corresponding to an initial Pu weight fraction of 20% prior to redistribution.

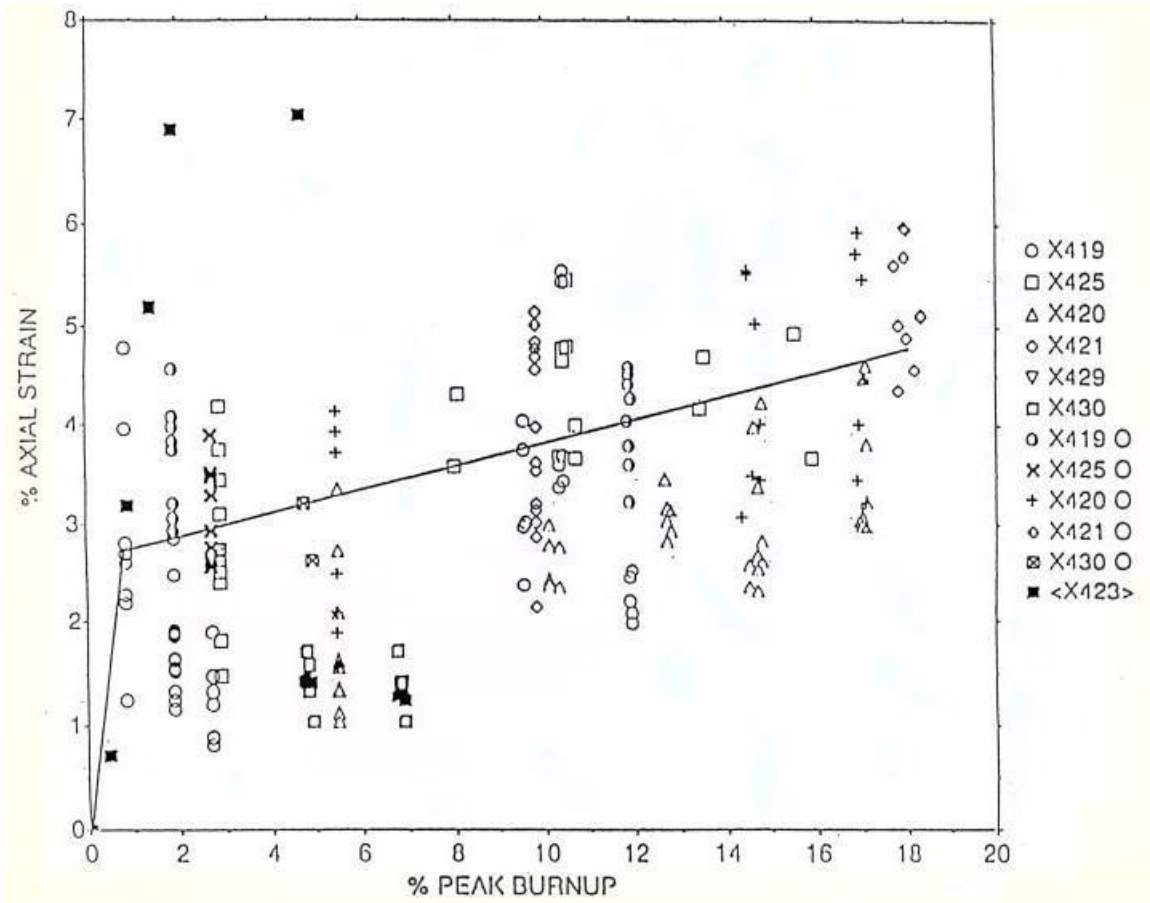

Figure A-18 Swelling Data of U-19Pu-10Zr Fuel

The fuel solidus temperature tends to be a limiting constraint for the higher power fuel pins in the core. Data on similar high-power fuel pins indicate a low Zr (2 wt. %) zone in a ring with normalized radial boundaries of 0.3 to 0.5. Based on Figure A-19, this leads to a minimum solidus temperature across the fuel radius of about 1040°C. At the centerline of such high-power

fuel pins, the Zr content is high (about 25%), the solidus temperature is high (about 1290°C), and fuel melting is not a concern. Thus for the high-power Mark-V fuel pins, a minimum solidus temperature of 1040°C should be used with the corresponding fuel temperature calculated at r/r_o = 0.3. The uncertainty on this solidus is taken as 30°C, giving a lower bound of 1010°C, which corresponds to a U-Pu zone with no Zr. However, the recommended design approach is to use the 1040°C minimum solidus temperature with all of the uncertainties included in the thermal conductivity and operating conditions.

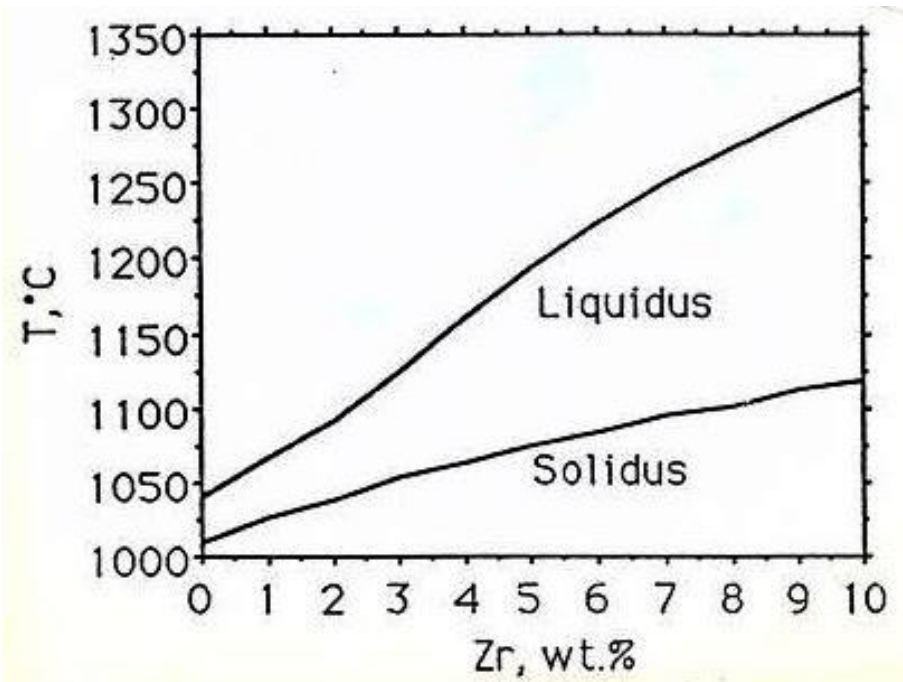

Figure A-19 Solidus/Liquidus Temperatures for Mark-V Fuel (U-20Pu-10Zr) vs. Zr Content

For lower power (< 12 kW/ft) fuel rods at burnups > 5 at. %, a low Zr (1.2 to 8 wt.%) zone has been observed at the center of the fuel slug. While such cases would not limit the Mark-V operation, the results of LIFE-METAL studies investigating the sensitivity of zone location and Zr content are reported in Section 9.4.

A.7. Thermal Properties of Fuel and Cladding

A.7.1 Properties of U-20 wt % Pu-10 wt % Zr

The properties of Mark V fuel, U-20Pu-10Zr, have been taken from the Handbook of Properties of Metallic Fuels [A.24] or more recent updates.

The density of the as-cast fuel is 15.73 g/cm^3 (981 lb/ft^3). The thermal expansion of a similar alloy, U-19Pu-10Zr, is given in the Handbook for heating and cooling.

The solidus temperature is calculated to be 1121°C (2050°F) while the liquidus is 1314°C (2397°F).

A.7.1.1 Enthalpy and Heat Capacity

The enthalpy data are available for U-15Pu-10Zr and should be close to that for U-20Pu-10Zr. Only one solid-solid phase change is considered. The Time-Transformation-Temperature curve is not available so that only equilibrium conditions are considered.

Equations have been fit to the data as given below. The temperature is in K.

<u>α Phase</u> (298 < T < 873K)

$$\Delta H = 19.34\ (T - 298) + 0.0133\ (T^2 - (298)^2)\ \text{J/mole} \qquad \text{(A.7-1)}$$

$$C_p = 19.34 + 0.0266T\ \text{J/mole-K} \qquad \text{(A.7-2)}$$

<u>α-γ Transition</u> (873 ≤ T ≤ 923 K)

$$C_p = 162\ \text{J/mole-K} \qquad \text{(A.7-3)}$$

<u>γ Phase</u> (923 < T < 1379 K)

$$\Delta H = 28000 + 8.752\ (T\text{-}923) + 0.01304\ (T^2 - (923)^2) \qquad \text{(A.7-4)}$$

$$C_p = 8.752 + 0.02608T\ \text{J/mole-K} \qquad \text{(A.7-5)}$$

<u>Solidus-Liquidus</u> (1379 ≤ T ≤ 1588 K)

$$\Delta H = 45600 + 89.95\ (T - 1379)\ \text{J/mole} \qquad \text{(A.7-6)}$$

$$C_p = 89.95\ \text{J/mole-K} \qquad \text{(A.7-7)}$$

<u>Liquid</u> (T > 1588 K)

$$\Delta H = 64440 + 44.4\ (T - 1588)\ \text{J/mole} \qquad \text{(A.7-8)}$$

For unirradiated fuel, the weight is 0.2044 kg/mole

$$C_p = 44.4 \text{ J/mole-K} \tag{A.7-9}$$

The properties are summarized in Table A-1.

Table A-1 Enthalpy and Heat Capacity of Unirradiated U-15Pu-10Zr

	Temperatures			Enthalpy			Heat Capacity		
Phase	°K	°C	°F	J/mole	J/kg	Btu/lb	J/mole-K	J/kg-K	Btu/lb-F
Alpha	298 873	25 600	77 1112	0 20100	0 9830	0.0 42.3	27.3 42.6	133 208	0.0319 0.0497
Alpha-Gamma	873 923	600 650	1112 1202	20100 28000	98300 137000	42.3 58.9	162.0 162.0	793 793	0.189 0.189
Gamma	923 1379	650 1106	1202 2023	28000 45600	137000 223000	58.9 96.0	32.8 44.7	161 219	0.0383 0.0523
Solidus-Liquidus	1379 1588	1106 1315	2033 2399	45600 64400	223000 315000	96.0 136.0	89.9 89.9	440 440	0.105 0.105
Liquid	1588 1788	1315 1515	2399 2759	64000 73300	315000 358000	136.0 154.0	44.4 44.4	217 217	0.0519 0.0519

A.7.1.2 Thermal Conductivity

The thermal conductivity of the unirradiated Mark-V fuel is given by

$$K_o = -8.466 + 5.315 \times 10^{-2}T - 2.075 \times 10^{-5}T^2, \text{ W/m} \cdot \text{K} \tag{A.7-10}$$

where T is in K. As swelling proceeds, the thermal conductivity changes as gas voids develop, as sodium enters the fuel, and as the composition of the fuel changes. For $0 \le Bu < 2$ at. %, where the porosity, P, rapidly increases from 0 to ~0.25 as the fuel swells from 4.27 mm (0.168 in.) to the cladding at 4.93 mm (0.194 in.) diameter in Mark-V fuel and from 4.39 mm (0.173 in.) to the cladding at 5.08 mm (0.2 in.) in Mark-VA fuel,

$$K_{eff}/K_o = (1. - P)/(1. + 1.7P), \tag{A.7-11}$$

$$P = 1. -1/[(1. + \Delta D/D_o)^2 (1. + \Delta L/L_o)], \text{ and}$$

$P = 0.135$ Bu, where ΔD is the diameter increase and ΔL is the fuel length increase.

Minimum value of K_{eff}/K_o at 2 at. % Bu (P ~0.27)

$$K_{eff}/K_o = 0.5 \qquad \text{(A.7-12)}$$

For 2 < Bu < 5 at. % (as sodium enters the fuel)

$$K_{eff}/K_o = 0.5 + 0.0667\ (Bu - 2.) \qquad \text{(A.7-13)}$$

For Bu ≥ 5 at. %

$$K_{eff}/K_o = 0.7 \qquad \text{(A.7-14)}$$

It must be noted that the corrections for volume swelling are based on limited data and may change as more data become available. The initial decrease is due to gas accumulation in the fuel. The increase after 2 at. % is due to sodium ingress. In addition, the thermal conductivity will change due to accumulation of fission products and the changing chemical compositions in the fuel. The reader is referred to the Handbook for these corrections which only become important at higher burnup. The thermal conductivities are summarized in Table A-2 in SI and Imperial units for zero porosity fresh fuel. The effect of irradiation is given in Figure A-20.

A.7.2 Properties of HT9 Cladding

HT9 is a martensitic stainless steel based on Fe-12Cr-1Mo. The properties are [A.14]:

<u>Density</u>

The density of HT9 is given by

$$\rho = 7.778 - 3.07 \times 10^{-4}\ T \qquad \text{(A.7-15)}$$

where ρ is g/cm^3 and T in °C. The equation is valid from 0 to 800°C.

<u>Thermal Expansion</u>

The elongation for the heating of the martensitic phase is given by

$$\Delta L/L_o = -0.16256 + 1.62307 \times 10^{-4}\ T + 1.42357 \times 10^{-6}\ T^2 - 5.50344 \times 10^{-10}\ T^3, \qquad \text{(A.7-16)}$$

where $\Delta L/L_o$ is in % and T in K and is valid from 293 to 1050K. Above 1050K the expansion is complicated by a phase transition. Figure A-21 shows the expansion behavior through the transition [A.25].

Table A-2 Thermal Conductivity of Unirradiated U-20Pu-10Zr

Temperature °C	Thermal Conductivity W/m x K	Temperature °F	Thermal Conductivity Btu/hr x ft x °F
100	8.4	100	3.5
200	12.0	200	4.8
300	15.2	300	5.9
400	17.9	400	7.0
500	20.2	500	8.1
600	22.1	600	9.0
700	23.6	700	9.9
800	24.7	800	10.7
900	25.3	900	11.5
1000	25.6	1000	12.1
1100	25.4	1100	12.7
		1200	13.2
		1300	13.7
		1400	14.0
		1500	14.3
		1600	14.6
		1700	14.7
		1800	14.8
		1900	14.8
		2000	14.7

Heat Capacity

The heat capacity is shown in Table A-3. A phase transformation (martensitic to austenitic) occurs at ~800°C.

Thermal Conductivity

The thermal conductivity of HT9 was measured and fit to the following equations:

$$k = 29.65 - 6.668 \times 10^{-2}\, T + 2.184 \times 10^{-4}\, T^{2} - 2.527 \times 10^{-7}\, T^{3} + 9.621 \times 10^{-11}\, T^{4} \text{ W/m-K} \qquad \text{(A.7-17)}$$

where T is in K. The values are listed in Table A-3.

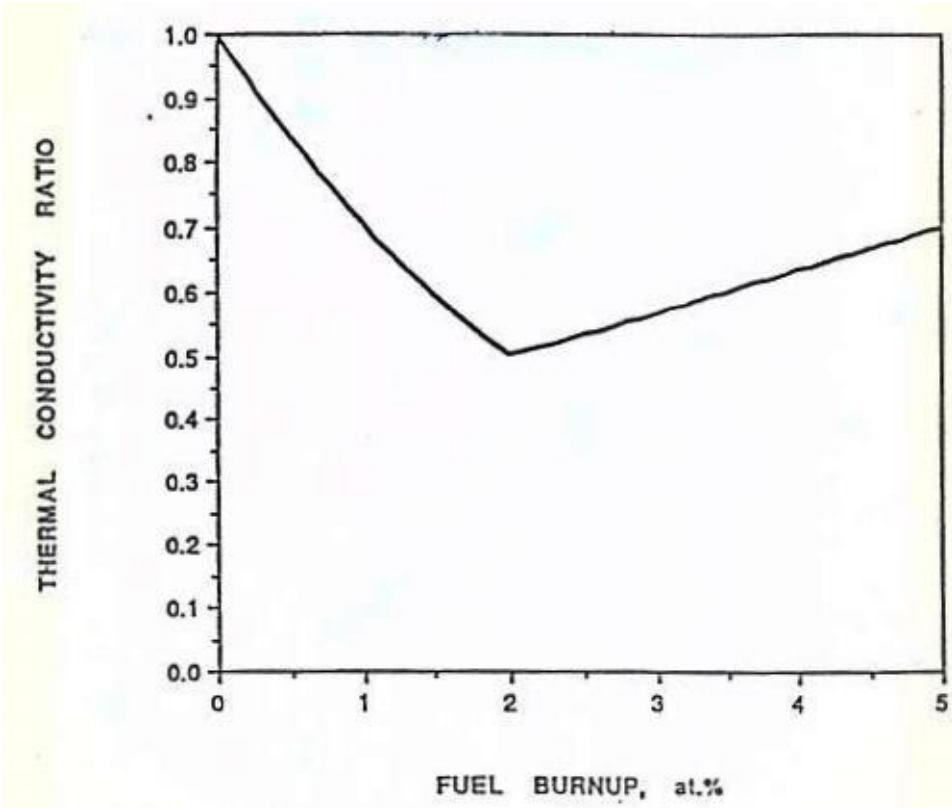

Figure A-20 The Effect of Fuel Burnup on the Thermal Conductivity of the Mark-V Fuel

A.7.3 Properties of 316 Stainless Steel

Type-316 stainless steel is an austenitic steel that has been used as the cladding in the Mark-II and Mark-III fuel pins. The properties are taken from Book 2 of Ref. A.14. The properties are for annealed stainless steel.

<u>Density</u>

The density of 316SS is given by

$$\rho = 498.5886 - 0.0537035\ T\ \text{lb/ft}^3, \qquad \text{(A.7-18)}$$

where T is in °F. The equation is valid from 100 to 1500°F.

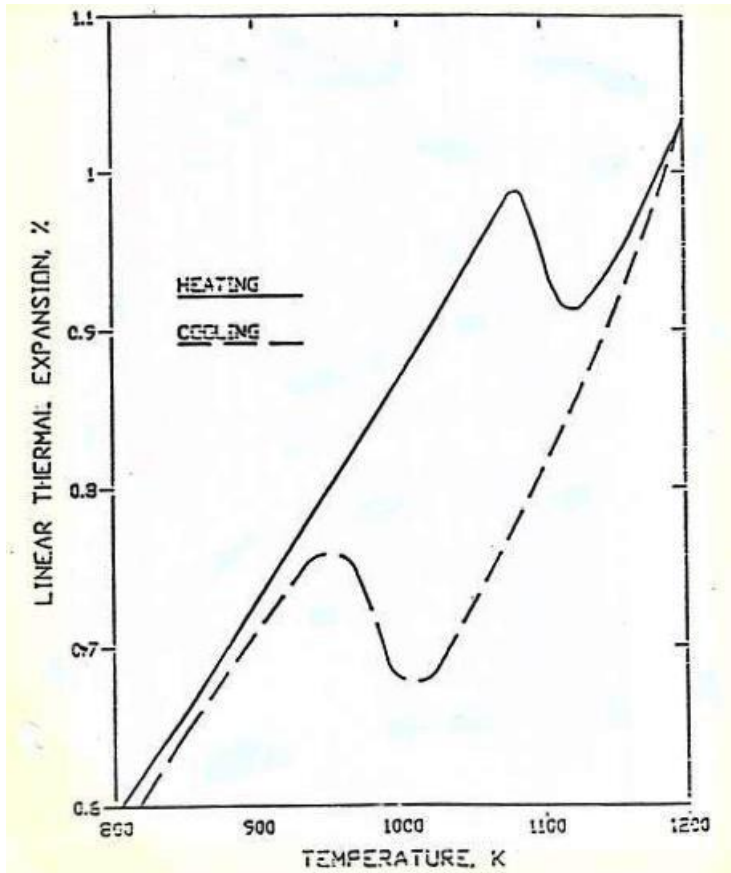

Figure A-21 Thermal Expansion of HT9 (from Ref. A.25)

Thermal Expansion

The mean thermal expansion is given by

$$\Delta L/L_o = -7.407489 \times 10^{-1} + 1.002488 \times 10^{-2}\, T + 2.569491 \times 10^{-6}\, T^2 - 5.029476 \times 10^{-10}\, T^{-3}, \qquad \text{(A.7-19)}$$

where $\Delta L/L_o$ is in in./ft x 10^{-2} and T is in °F.

Heat Capacity

The heat capacity of 316SS is given by:

$$C_p = 1.071939 \times 10^{-1} + 6.034521 \times 10^{-5}\, T - 4.397679 \times 10^{-8}\, T^2 + 1.438572 \times 10^{-11}\, T^3 \qquad \text{(A.7-20)}$$

where C_p is in Btu/lb °F and T in °F. The results are summarized in Table A-4.

Table A-3 Heat Capacity and Thermal Conductivity of HT9

Temperature °C	**Specific Heat J/kg x °C**	**Thermal Conductivity W/m x K**	**Temperature °F**	**Specific Heat Btu/lb x °F**	**Thermal Conductivity Btu/hr x ft x °F**
21	449	23.2	100	0.109	13.5
100	482	23.9	200	0.115	13.8
200	521	25.0	300	0.120	14.1
300	563	26.0	400	0.125	14.5
400	615	26.4	500	0.130	14.8
500	685	26.2	600	0.136	15.1
600	785	25.6	700	0.143	15.2
700	1021	25.0	800	0.151	15.3
725	1210	24.9	900	0.160	15.2
750	863	24.8	1000	0.171	15.1
800	748	24.9	1100	0.185	14.8
816	762	25.0	1200	0.206	14.6
			1300	0.250	14.4
			1340	0.289	14.4
			1400	0.195	14.4
			1500	0.182	14.5

Thermal Conductivity

The thermal conductivity is given by:

$$k = 7.336869 + 5.567335 \times 10^{-3}\, T - 4.511739 \times 10^{-7}\, T^{2} - 1.905863 \times 10^{-11}\, T^{3} \qquad \text{(A.7-21)}$$

where k is in Btu/hr-ft-°F and T is in °F. The results are summarized in Table A-4.

Table A-4 Heat Capacity and Thermal Conductivity of 316 Stainless Steel

Temperature °C	Specific Heat J/kg - K	Thermal Conductivity W/m - K	Temperature °F	Specific Heat Btu/lb - °F	Thermal Conductivity Btu/hr - ft - °F
21	465.6	13.36	70	0.1112	7.724
50	477.0	13.85	100	0.1128	7.889
100	494.7	14.70	200	0.1176	8.432
150	510.0	15.53	300	0.1217	8.966
200	523.2	16.34	400	0.1252	9.490
250	534.5	17.15	500	0.1282	10.01
300	544.3	17.94	600	0.1307	10.51
350	552.8	18.71	700	0.1328	11.01
400	560.3	19.48	800	0.1347	11.49
450	567.0	20.22	900	0.1346	11.97
500	573.1	20.96	1000	0.1395	12.89
600	584.9	22.39	1200	0.1411	13.34
650	591.1	23.08	1300	0.1429	13.77
700	597.8	23.76	1400	0.1450	14.19
750	605.3	24.42	1500	0.1473	14.61
800	613.9	25.07	1600	0.1501	15.01
850	623.8	25.70			

Appendix A References

A.1 C. Martinez and R. J. Puigh, "Interim Report on Pressurized Tube Data from MOTA-1E (Cycle 9)," Westinghouse Hanford Company Report WHC-SP-0227 (January, 1988).

A.2 V. R. Sikka and P. Patriarca, "Data Package for Modified 9Cr-1Mo Alloy," ORNL, Dec. 1983.

A.3 M. L. Hamilton, F. H. Huang, and W. L. Hu, "Mechanical Properties of AISI 422," TC-160-35, Dec. 1982.

A.4 R. J. Puigh and D. S. Gelles, "Irradiation Creep of Ferritic (and other BCC) Alloys," DOE/ER-0313/6, March 1989.

A.5 F. H. Huang and M. L. Hamilton, "The Fracture Toughness Data Base for HT9 and Modified 9Cr-1Mo Irradiated in Several Reactors Up to 100 dpa," DOE/ER-0313/6, March 1989.

A.6 D. L. Porter, "Exposure Guidelines for EBR-II Components," unpublished memo, Oct. 3, 1989.

A.7 D. L. Porter, E. L. Wood, and F. A. Graner, "Influence of the Thermomechanical Treatment and Environmental History on Creep, Swelling and Embrittlement of AISI316 at 400°C and 130 dpa," Effects of Radiation on Materials: 14th International Symposium (Volume II), ASTM STP 10546, N. H. Packan, R. E. Stoller, and A. S. Kramer, Eds., American Society for Testing and Materials, pp. 551-569 (1990) Philadelphia, Pa.

A.8 E. R. Gilbert and D. L. Porter, "Effect of AISI 316SS Cold Work Level on In-reactor Creep," HEDL-TC-160-24 p. 39-45 (1980).

A.9 J. M. Kramer and R. J. DiMelfi, "An Evaluation of Transient Fuel Pin Cladding Failure Criteria for Application to Inherently Safe LMFBR Designs, Argonne National Laboratory Report ANL/RAS 84-6 (March, 1984).

A.10 R. J. DiMelfi and J. M. Kramer, "Cladding Failure Analysis for Advanced Fuel and Cladding Types," Argonne National Laboratory Report ANL-RDP-118, 1.21 (April - September, 1985), "Mechanical Behavior of Fast Reactor Fuel Pin Cladding Subjected to Simulated Overpower Transients," Hanford Engineering Development Laboratory Report HEDL-TME 78-13 (June, 1978).

A.11 M. L. Hamilton and N. S. Cannon, "HT9 Transient Data Base and Failure Correlation," Hanford Engineering Development Laboratory Report HEDL-TC-2681 (March 1985).

A.12 R. J. DiMelfi and J. M. Kramer, J. Nucl. Mater., 89 (1980) 338-347.

A.13 R. J. DiMelfi and J. M. Kramer, Argonne National Laboratory Report ANL-RDP-118, 1985, 1.21-1.26.

A.14 Nuclear Systems Materials Handbook, Oak Ridge National Laboratory Report TID 26666. (Note: Correlations and data used represent the most recent contributions as of October 1991).

A.15 G. D. Johnson, "The Mechanical Properties of Alloy HT9," Westinghouse Hanford

Company Report WHC-SP-0230, Feb. 1988.

A.16 S. Vaidyananthan, Argonne National Laboratory, unpublished information (1981).

A.17 F. H. Huang, "Effect of Irradiation Temperature on the Fracture Behavior and Tensile Properties of a HT9 Duct," Westinghouse Hanford Company Report WHC-SP-0454, May 1989.

A.18 F. H. Huang, "Fracture Behavior of a High-Fluence EBR-II Duct," HEDL-TC-160-40, Jan. - March 1984, p. 173-182.

A.19 Alloy Properties Databook, HEDL-TC-293, Rev. 5.

A.20 G. L. Hofman and W. H. Olson, Argonne National Laboratory, unpublished information (1990).

A.21 M. C. Billone, Argonne National Laboratory, unpublished information (1993).

A.22 M. C. Billone, Argonne National Laboratory, unpublished information (1993).

A.23 L. Leibowitz, E. Veleckis, R. A. Blomquist, and A. D. Pelton, "Solidus and Liquidus Temperatures in the Uranium-Plutonium-Zirconium System," J. Nucl. Maters., 154 (1988) pp.145-153.

A.24 G. L. Hofman, et al., "Metallic Fuels Handbook," Argonne National Laboratory, ANL-IFR-29 (November 1985).

A.25 L. Leibowitz and R. A. Blomquist, "Thermal Conductivity and Thermal Expansion of Stainless Steel D9 and HT9", International Journal of Thermophysics, Vol. 9, no. 5, 873 (1988).

B APPENDIX: REFERENCE CORE LOADINGS AND STEADY-STATE ANALYSIS

B.1. Thermal Analysis of Reference Mark-V Fueled Subassemblies

The maximum temperatures in a core containing HT9-clad, Mark-V fuel pins have been calculated. The subassemblies analyzed were taken from the 6-row core described in Section 6.2. The powers are summarized in Table B-1 along with the subassembly flow rates at a core pressure loss of ~ 44 psi. The radial power gradient in the subassembly was based on the BURNOUT program [B.1]. The fuel pin temperatures were calculated using the SUPERENERGY-2 [B.2] program with the subassembly flow distribution given by the Cheng-Todreas model [B.3]. The coolant-clad film coefficient is taken from [B.4]. The temperatures were calculated for beginning-of-life (BOL) conditions. As irradiation of the fuel occurs, the fuel will swell and expand, radially displacing the bond sodium. Diffusion of the fissile and zirconium materials will also occur. These effects are not modelled and therefore only BOL conditions are given.

The maximum temperature condition in each subassembly is summarized in Table B-2. It should be noted that the peak temperatures do not always occur at the same axial elevation. The pin arrangement and pin number identifications in a 61-pin subassembly are given in Figure B-1. For the highest power subassembly in each row, the peak conditions for each pin in the subassembly are summarized in Table B-3 through Table B-9. Note that the driver subassemblies in rows 1 and 5 are partial drivers, and so Table B-3 and Table B-7 list results for only 31 pins, instead of 61. The safety and control rods will continue to use the Mark-IIC and Mark-IICS pins containing U-10Zr fuel. Because of the increased flux level, the control and safety rod power and temperatures will increase from current levels. The peak temperature of each pin is summarized in Table B-10 and Table B-11.

Table B-1 Mark-V or Mark-VA Fuel Pins, 6-Row Core, U-20Pu-10Zr Fuel – HT9 Clad, Hottest Subassembly Power and Flow Rate

Location	Power, kW	Flow, gpm*
1A1	530.0	75.36
2F1	983.5	134.9
3A1 (Safety Rod)	666.2	98.64
3E2	939.5	119.3
4E2	844.8	93.24
5B3 (Control Rod)	540.5	64.16
5E2	390.0	59.16
6E3 (Increased Flow)	646.9	75.98
6F1 (Normal Flow)	581.3	67.78

*At 800°F and 44 psi ΔP

Table B-2 BOL Peak Powers and Temperatures of Mark-V and Mark-IIC Fueled Subassemblies

U-20Pu-10Zr Unswollen Fuel
Mark-V Fueled Subassemblies

Location	Peak kW/ft	Peak Temperatures								Peaking Factor
		Coolant		Clad Inside		Fuel Centerline		Bundle Average Flow Temperature		
		F	C	F	C	F	C	F	C	
1A1	16.19	928.	498.	1017.	547.	1353.	734.	885.	474.	1.23
2F1	15.37	936.	502.	1016.	547.	1330.	721.	891.	477.	1.24
3E2	15.02	957.	514.	1033.	556.	1329.	721.	907.	486.	1.24
4E2	13.79	994.	534.	1063.	573.	1320.	715.	938.	503.	1.24
5E2	12.80	917.	492.	984.	529.	1246.	674.	873.	467.	1.25
6E3	10.61	977.	525.	1029.	554.	1228.	665.	923.	495.	1.24
6F1	9.36	975.	524.	1021.	550.	1197.	647.	925.	496.	1.22

U-10Zr Unswollen Fuel
Mark-IIC Fueled Control and Safety Rod Assemblies

Location	Peak kW/ft	Peak Temperatures								Peaking Factor
		Coolant		Clad Inside		Fuel Centerline		Bundle Average Flow Temperature		
		F	C	F	C	F	C	F	C	
1A1	10.38	916.	491.	992.	533.	1151.	622.	854.	457.	1.40
2F1	8.60	979.	526.	1040.	560.	1167.	631.	892.	478.	1.45

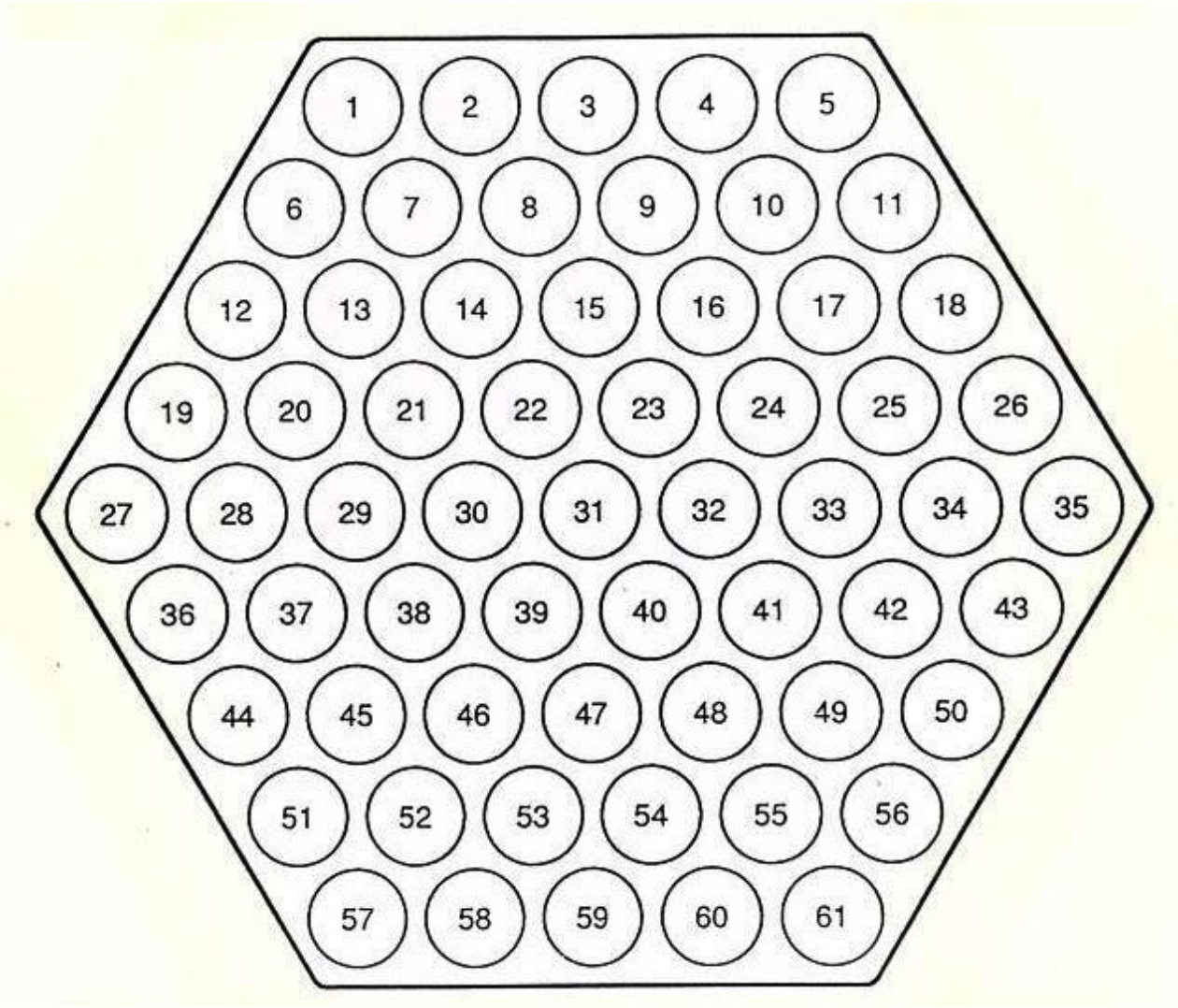

Figure B-1 EBR-II and SUPERENERGY-2 Pin Numbering System of the Mark-V Fuel Pins

Table B-3 Maximum Heat Rating and Temperatures, Mark-V Fuel Pins, Position 1A1, Beginning-of-Life Conditions

		Peak Temperatures				
Pin No. EBR-II	Peak kW/ft	Coolant F C	Clad Outside F C	Clad Inside F C	Fuel Surface F C	Fuel Centerline F C
1	16.09	870. - 466.	891. - 477.	961. - 516.	997. - 536.	1323. - 717.
3	16.09	881. - 472.	901. - 483.	972. - 522.	997. - 536.	1327. - 720.
5	16.04	866. - 463.	887. - 475.	958. - 514.	984. - 529.	1321. - 716.
7	16.09	908. - 486.	928. - 498.	998. - 537.	1024. - 551.	1344. - 729.
9	16.09	914. - 490.	934. - 501.	1004. - 540.	1029. - 554.	1346. - 730.
11	16.04	883. - 473.	904. - 484.	975. - 524.	1000. - 538.	1331. - 722.
13	16.14	913. - 489.	933. - 501.	1004. - 540.	1029. - 554.	1347. - 731.
15	16.14	926. - 497.	945. - 507.	1015. - 546.	1040. - 560.	1351. - 733.
17	16.09	915. - 490.	934. - 501.	1005. - 540.	1030. - 555.	1346. - 730.
19	16.09	872. - 467.	877. - 469.	947. - 508.	973. - 523.	1314. - 712.
21	16.14	924. - 495.	943. - 506.	1013. - 545.	1038. - 559.	1350. - 732.
23	16.14	926. - 497.	945. - 507.	1015. - 546.	1040. - 560.	1351. - 733.
25	16.09	912. - 489.	932. - 500.	1002. - 539.	1027. - 553.	1345. - 729.
27	16.09	866. - 463.	876. - 469.	948. - 509.	974. - 523.	1318. - 714.
29	16.14	924. - 496.	944. - 507.	1014. - 546.	1039. - 560.	1352. - 733.
31	16.19	928. - 498.	947. - 508.	1017. - 547.	1043. - 562.	1353. - 734.
33	16.14	924. - 495.	943. - 506.	1013. - 545.	1038. - 559.	1351. - 733.
35	16.09	866. - 463.	876. - 469.	948. - 509.	974. - 523.	1318. - 714.
37	16.14	912. - 489.	932. - 500.	1003. - 539.	1028. - 553.	1346. - 730.
39	16.14	927. - 497.	945. - 507.	1015. - 546.	1040. - 560.	1351. - 733.
41	16.14	924. - 496.	943. - 506.	1013. - 545.	1038. - 559.	1350. - 732.
43	16.09	872. - 467.	877. - 469.	947. - 509.	973. - 523.	1314. - 712.
45	16.14	915. - 491.	935. - 502.	1006. - 541.	1031. - 555.	1348. - 731.
47	16.19	926. - 497.	946. - 508.	1016. - 547.	1041. - 561.	1353. - 734.
49	16.14	913. - 490.	933. - 501.	1004. - 540.	1029. - 554.	1347. - 731.
51	16.09	883. - 473.	904. - 485.	975. - 524.	1001. - 539.	1332. - 722.
53	16.14	914. - 490.	934. - 501.	1005. - 540.	1030. - 555.	1347. - 731.

Pin No. EBR-II	Peak kW/ft	Peak Temperatures Coolant F C	Clad Outside F C	Clad Inside F C	Fuel Surface F C	Fuel Centerline F C
55	16.14	908. - 487.	928. - 498.	999. - 537.	1025. - 552.	1345. - 730.
57	16.14	867. - 464.	888. - 475.	959. - 515.	985. - 529.	1324. - 718.
59	16.14	882. - 472.	902. - 483.	972. - 522.	998. - 537.	1329. - 720.
61	16.14	871. - 466.	891. - 477.	962. - 517.	988. - 531.	1324. - 718.

Table B-4 Maximum Heat Rating and Temperatures, Mark-V Fuel Pins, Position 2F1, Beginning-of-Life Conditions

		Peak Temperatures									
		Coolant		Clad Outside		Clad Inside		Fuel Surface		Fuel Centerline	
Pin No. EBR-II	Peak kW/ft	F	C	F	C	F	C	F	C	F	C
1	15.31	873.	467.	879.	471.	946.	508.	970.	521.	1292.	700.
2	15.36	879.	471.	895.	479.	961.	516.	985.	530.	1302.	705.
3	15.37	881.	472.	896.	480.	963.	517.	987.	531.	1303.	706.
4	15.36	879.	470.	894.	479.	961.	516.	985.	530.	1302.	705.
5	15.36	872.	467.	879.	471.	946.	508.	970.	521.	1293.	701.
6	15.33	879.	471.	894.	479.	961.	516.	985.	529.	1301.	705.
7	15.34	911.	488.	927.	497.	994.	534.	1017.	547.	1320.	716.
8	15.36	920.	493.	935.	502.	1002.	539.	1025.	552.	1324.	718.
9	15.36	920.	493.	935.	502.	1002.	539.	1026.	552.	1324.	718.
10	15.36	911.	488.	927.	497.	994.	534.	1018.	548.	1321.	716.
11	15.36	878.	470.	894.	479.	961.	516.	985.	529.	1302.	705.
12	15.31	881.	472.	896.	480.	962.	517.	986.	530.	1301.	705.
13	15.33	919.	493.	935.	502.	1001.	538.	1025.	552.	1323.	717.
14	15.34	932.	500.	947.	508.	1013.	545.	1036.	558.	1328.	720.
15	15.36	934.	501.	948.	509.	1014.	546.	1038.	559.	1329.	721.
16	15.36	932.	500.	947.	508.	1013.	545.	1037.	558.	1329.	720.
17	15.34	919.	493.	935.	502.	1001.	538.	1025.	552.	1324.	718.
18	15.34	880.	471.	895.	480.	962.	517.	986.	530.	1302.	705.
19	15.21	879.	471.	893.	479.	959.	515.	983.	528.	1297.	703.
20	15.27	918.	492.	934.	501.	1000.	538.	1024.	551.	1321.	716.
21	15.34	933.	501.	948.	509.	1014.	545.	1037.	558.	1328.	720.
22	15.36	936.	502.	950.	510.	1016.	547.	1039.	560.	1330.	721.
23	15.36	936.	502.	950.	510.	1016.	547.	1039.	560.	1330.	721.
24	15.34	934.	501.	948.	509.	1014.	545.	1037.	559.	1329.	720.
25	15.31	919.	493.	934.	501.	1000.	538.	1024.	551.	1322.	717.
26	15.27	877.	470.	893.	478.	959.	515.	983.	528.	1299.	704.
27	15.10	873.	467.	877.	470.	943.	506.	967.	519.	1285.	696.
28	15.18	909.	487.	925.	496.	990.	532.	1014.	546.	1314.	712.

Pin No. EBR-II	Peak kW/ft	Peak Temperatures: Coolant F	Coolant C	Clad Outside F	Clad Outside C	Clad Inside F	Clad Inside C	Fuel Surface F	Fuel Surface C	Fuel Centerline F	Fuel Centerline C
29	15.22	929.	499.	944.	507.	1009.	543.	1033.	556.	1324.	718.
30	15.30	935.	502.	949.	509.	1015.	546.	1038.	559.	1327.	720.
31	15.36	936.	502.	950.	510.	1016.	546.	1039.	560.	1329.	721.
32	15.31	935.	502.	949.	510.	1015.	546.	1038.	559.	1328.	720.
33	15.27	931.	500.	946.	508.	1011.	544.	1035.	557.	1326.	719.
34	15.22	909.	487.	925.	496.	991.	533.	1015.	546.	1316.	713.
35	15.19	870.	466.	877.	469.	943.	506.	967.	519.	1287.	697.
36	15.05	878.	470.	892.	478.	957.	514.	981.	527.	1292.	700.
37	15.11	917.	491.	932.	500.	997.	536.	1021.	549.	1316.	713.
38	15.19	931.	500.	946.	508.	1011.	544.	1034.	557.	1323.	717.
39	15.22	934.	501.	948.	509.	1013.	545.	1037.	558.	1325.	718.
40	15.24	934.	501.	948.	509.	1014.	545.	1037.	558.	1325.	719.
41	15.24	932.	500.	946.	508.	1012.	544.	1035.	557.	1325.	718.
42	15.19	917.	492.	933.	500.	998.	537.	1022.	550.	1318.	715.
43	15.14	877.	469.	892.	478.	958.	514.	981.	527.	1295.	701.
44	15.02	880.	471.	893.	478.	958.	514.	981.	527.	1291.	700.
45	15.05	916.	491.	931.	499.	996.	535.	1019.	548.	1313.	712.
46	15.10	929.	498.	943.	506.	1008.	542.	1031.	555.	1320.	715.
47	15.14	931.	499.	945.	507.	1010.	543.	1033.	556.	1322.	716.
48	15.13	929.	498.	943.	506.	1008.	542.	1032.	555.	1321.	716.
49	15.11	916.	491.	932.	500.	997.	536.	1020.	549.	1316.	713.
50	15.11	879.	470.	893.	478.	959.	515.	982.	528.	1294.	701.
51	14.93	878.	470.	890.	477.	955.	513.	979.	526.	1288.	698.
52	14.98	906.	486.	922.	494.	987.	530.	1010.	543.	1308.	709.
53	15.02	915.	491.	930.	499.	995.	535.	1018.	548.	1312.	711.
54	15.04	915.	491.	930.	499.	995.	535.	1019.	548.	1313.	712.
55	15.02	907.	486.	923.	495.	988.	531.	1011.	544.	1309.	710.
56	15.01	876.	469.	890.	477.	956.	513.	979.	526.	1290.	699.
57	14.86	871.	466.	875.	468.	939.	504.	963.	517.	1277.	692.
58	14.89	877.	469.	890.	476.	954.	512.	977.	525.	1286.	697.
59	14.93	879.	470.	891.	477.	956.	513.	979.	526.	1288.	698.

Pin No. EBR-II	Peak kW/ft	Peak Temperatures									
		Coolant		Clad Outside		Clad Inside		Fuel Surface		Fuel Centerline	
		F	C	F	C	F	C	F	C	F	C
60	14.93	877.	469.	890.	477.	955.	513.	978.	526.	1288.	698.
61	14.92	870.	466.	875.	468.	940.	504.	963.	517.	1279.	693.

Table B-5 Maximum Heat Rating and Temperatures, Mark-V Fuel Pins, Position 3E2, Beginning-of-Life Conditions

		Peak Temperatures									
		Coolant		Clad Outside		Clad Inside		Fuel Surface		Fuel Centerline	
Pin No. EBR-II	Peak kW/ft	F	C	F	C	F	C	F	C	F	C
1	15.02	887.	475.	895.	479.	960.	515.	983.	528.	1292.	700.
2	14.96	896.	480.	911.	488.	976.	524.	999.	537.	1300.	704.
3	14.93	897.	480.	912.	489.	977.	525.	1000.	538.	1299.	704.
4	14.82	893.	479.	909.	487.	973.	523.	996.	535.	1295.	701.
5	14.71	883.	473.	891.	477.	954.	512.	977.	525.	1281.	694.
6	14.98	896.	480.	912.	489.	977.	525.	1000.	538.	1300.	705.
7	14.93	932.	500.	948.	509.	1012.	544.	1035.	557.	1321.	716.
8	14.89	941.	505.	956.	513.	1020.	549.	1043.	561.	1324.	718.
9	14.82	939.	504.	954.	512.	1018.	548.	1041.	560.	1321.	716.
10	14.71	928.	498.	944.	507.	1007.	542.	1030.	554.	1313.	712.
11	14.60	891.	477.	906.	486.	969.	521.	992.	533.	1287.	697.
12	14.93	898.	481.	913.	490.	978.	525.	1001.	538.	1299.	704.
13	14.89	941.	505.	956.	513.	1020.	549.	1043.	562.	1324.	718.
14	14.86	954.	512.	968.	520.	1032.	556.	1055.	568.	1329.	721.
15	14.80	955.	513.	969.	520.	1032.	556.	1054.	568.	1328.	720.
16	14.70	952.	511.	966.	519.	1029.	554.	1051.	566.	1323.	717.
17	14.60	936.	502.	951.	510.	1014.	545.	1036.	558.	1313.	712.
18	14.50	892.	478.	907.	486.	969.	521.	991.	533.	1284.	696.
19	14.83	896.	480.	911.	488.	975.	524.	998.	536.	1295.	702.
20	14.83	940.	504.	955.	513.	1019.	548.	1041.	561.	1322.	716.
21	14.82	955.	513.	969.	520.	1032.	556.	1055.	568.	1328.	720.
22	14.77	957.	514.	970.	521.	1033.	556.	1056.	569.	1327.	720.
23	14.70	955.	513.	969.	520.	1032.	555.	1054.	568.	1325.	718.
24	14.60	951.	511.	965.	518.	1027.	553.	1049.	565.	1320.	716.
25	14.47	934.	501.	949.	509.	1011.	544.	1033.	556.	1308.	709.
26	14.32	889.	476.	903.	484.	965.	518.	987.	530.	1278.	692.
27	14.74	889.	476.	893.	479.	957.	514.	980.	527.	1283.	695.
28	14.73	929.	498.	945.	507.	1008.	542.	1031.	555.	1314.	712.

Pin No. EBR-II	Peak kW/ft	Peak Temperatures Coolant F C	Clad Outside F C	Clad Inside F C	Fuel Surface F C	Fuel Centerline F C
29	14.71	951. - 511.	965. - 518.	1028. - 553.	1051. - 566.	1324. - 718.
30	14.70	956. - 513.	969. - 520.	1032. - 556.	1054. - 568.	1325. - 718.
31	14.70	955. - 513.	968. - 520.	1031. - 555.	1053. - 567.	1324. - 718.
32	14.55	953. - 512.	966. - 519.	1029. - 554.	1050. - 566.	1319. - 715.
33	14.42	947. - 508.	961. - 516.	1022. - 550.	1044. - 562.	1313. - 712.
34	14.29	922. - 495.	937. - 503.	999. - 537.	1021. - 549.	1298. - 703.
35	14.15	882. - 472.	885. - 474.	946. - 508.	968. - 520.	1262. - 684.
36	14.63	895. - 480.	909. - 487.	972. - 522.	994. - 535.	1289. - 698.
37	14.63	937. - 503.	952. - 511.	1014. - 546.	1037. - 558.	1314. - 712.
38	14.61	951. - 511.	965. - 518.	1028. - 553.	1050. - 565.	1320. - 716.
39	14.55	953. - 512.	966. - 519.	1029. - 554.	1050. - 566.	1319. - 715.
40	14.48	952. - 511.	965. - 518.	1027. - 553.	1048. - 565.	1316. - 714.
41	14.38	948. - 509.	961. - 516.	1023. - 550.	1044. - 562.	1312. - 711.
42	14.25	931. - 499.	945. - 507.	1006. - 541.	1028. - 553.	1301. - 705.
43	14.10	889. - 476.	901. - 483.	962. - 517.	983. - 529.	1270. - 688.
44	14.53	897. - 481.	909. - 487.	972. - 522.	994. - 534.	1286. - 697.
45	14.47	935. - 501.	949. - 510.	1011. - 544.	1033. - 556.	1309. - 709.
46	14.42	947. - 508.	961. - 516.	1023. - 550.	1044. - 562.	1313. - 712.
47	14.37	948. - 509.	961. - 516.	1022. - 550.	1044. - 562.	1311. - 711.
48	14.26	944. - 507.	958. - 514.	1019. - 548.	1040. - 560.	1307. - 708.
49	14.16	930. - 499.	944. - 507.	1005. - 540.	1026. - 552.	1297. - 703.
50	14.07	891. - 477.	902. - 483.	963. - 517.	984. - 529.	1270. - 688.
51	14.34	894. - 479.	905. - 485.	967. - 519.	989. - 532.	1279. - 693.
52	14.29	923. - 495.	938. - 503.	999. - 537.	1022. - 550.	1298. - 703.
53	14.23	931. - 499.	945. - 507.	1006. - 541.	1028. - 553.	1300. - 705.
54	14.16	930. - 499.	944. - 507.	1005. - 540.	1026. - 552.	1297. - 703.
55	14.06	919. - 493.	934. - 501.	995. - 535.	1016. - 547.	1290. - 699.
56	13.96	889. - 476.	899. - 482.	960. - 515.	981. - 527.	1266. - 685.
57	14.15	887. - 475.	888. - 475.	949. - 509.	970. - 521.	1263. - 684.
58	14.10	892. - 478.	902. - 484.	963. - 517.	985. - 529.	1271. - 688.
59	14.05	893. - 479.	903. - 484.	963. - 517.	985. - 529.	1269. - 687.

		Peak Temperatures									
		Coolant		Clad Outside		Clad Inside		Fuel Surface		Fuel Centerline	
Pin No. EBR-II	Peak kW/ft	F	C	F	C	F	C	F	C	F	C
60	13.94	890.	477.	900.	482.	960.	516.	982.	528.	1265.	685.
61	13.84	883.	473.	883.	473.	943.	506.	964.	518.	1253.	678.

Table B-6 Maximum Heat Rating and Temperatures, Mark-V Fuel Pins, Position 4E2, Beginning-of-Life Conditions

		Peak Temperatures									
		Coolant		Clad Outside		Clad Inside		Fuel Surface		Fuel Centerline	
Pin No. EBR-II	Peak kW/ft	F	C	F	C	F	C	F	C	F	C
1	13.79	916.	491.	923.	495.	982.	528.	1003.	539.	1273.	689.
2	13.66	927.	497.	941.	505.	1000.	538.	1021.	549.	1282.	694.
3	13.53	928.	498.	942.	505.	1000.	538.	1020.	549.	1278.	692.
4	13.45	924.	495.	937.	503.	995.	535.	1015.	546.	1274.	690.
5	13.36	911.	488.	916.	491.	973.	523.	993.	534.	1257.	681.
6	13.73	929.	498.	943.	506.	1002.	539.	1023.	550.	1285.	696.
7	13.60	969.	521.	984.	529.	1042.	561.	1063.	573.	1311.	711.
8	13.45	978.	526.	992.	533.	1049.	565.	1070.	576.	1312.	711.
9	13.35	976.	524.	989.	532.	1047.	564.	1067.	575.	1308.	709.
10	13.27	963.	517.	977.	525.	1034.	557.	1054.	568.	1298.	704.
11	13.18	920.	493.	934.	501.	990.	532.	1010.	543.	1264.	685.
12	13.65	931.	499.	945.	507.	1003.	540.	1024.	551.	1283.	695.
13	13.52	979.	526.	993.	534.	1051.	566.	1071.	577.	1315.	713.
14	13.39	993.	534.	1005.	541.	1063.	573.	1083.	584.	1320.	715.
15	13.26	993.	534.	1005.	540.	1061.	572.	1081.	583.	1316.	713.
16	13.17	989.	531.	1001.	538.	1057.	569.	1077.	580.	1311.	710.
17	13.09	971.	522.	984.	529.	1040.	560.	1059.	571.	1298.	703.
18	13.00	920.	493.	933.	501.	989.	532.	1008.	542.	1259.	682.
19	13.56	928.	498.	941.	505.	1000.	538.	1020.	549.	1279.	693.
20	13.44	978.	525.	991.	533.	1049.	565.	1069.	576.	1312.	711.
21	13.31	994.	534.	1005.	541.	1063.	573.	1082.	584.	1317.	714.
22	13.18	994.	534.	1005.	541.	1062.	572.	1081.	583.	1314.	712.
23	13.07	991.	533.	1003.	539.	1059.	570.	1078.	581.	1309.	710.
24	12.98	987.	530.	998.	537.	1054.	568.	1073.	579.	1304.	707.
25	12.92	968.	520.	980.	527.	1036.	558.	1055.	568.	1291.	699.
26	12.87	916.	491.	929.	498.	984.	529.	1003.	539.	1253.	678.
27	13.45	919.	493.	921.	494.	979.	526.	999.	537.	1262.	683.
28	13.34	966.	519.	979.	526.	1037.	558.	1057.	569.	1301.	705.

Pin No. EBR-II	Peak kW/ft	Peak Temperatures Coolant F C	Clad Outside F C	Clad Inside F C	Fuel Surface F C	Fuel Centerline F C
29	13.22	989. - 532.	1001. - 539.	1058. - 570.	1078. - 581.	1313. - 712.
30	13.10	992. - 533.	1003. - 540.	1059. - 571.	1079. - 582.	1310. - 710.
31	12.97	990. - 532.	1001. - 538.	1057. - 569.	1076. - 580.	1306. - 708.
32	12.90	988. - 531.	999. - 537.	1054. - 568.	1073. - 579.	1302. - 706.
33	12.85	982. - 528.	993. - 534.	1049. - 565.	1068. - 575.	1298. - 703.
34	12.79	955. - 513.	968. - 520.	1023. - 550.	1042. - 561.	1280. - 693.
35	12.72	909. - 487.	909. - 487.	963. - 517.	982. - 528.	1235. - 668.
36	13.24	926. - 497.	938. - 503.	995. - 535.	1014. - 546.	1268. - 687.
37	13.13	972. - 522.	985. - 530.	1042. - 561.	1061. - 572.	1300. - 704.
38	13.00	988. - 531.	999. - 537.	1055. - 568.	1074. - 579.	1305. - 707.
39	12.93	988. - 531.	999. - 537.	1055. - 568.	1074. - 579.	1303. - 706.
40	12.87	987. - 530.	998. - 536.	1053. - 567.	1072. - 578.	1300. - 705.
41	12.77	982. - 528.	994. - 534.	1048. - 565.	1067. - 575.	1296. - 702.
42	12.72	964. - 518.	976. - 525.	1031. - 555.	1050. - 565.	1283. - 695.
43	12.66	917. - 492.	927. - 497.	981. - 527.	1000. - 538.	1246. - 674.
44	13.01	928. - 498.	937. - 503.	993. - 534.	1012. - 544.	1261. - 683.
45	12.96	969. - 521.	982. - 528.	1038. - 559.	1057. - 569.	1293. - 700.
46	12.89	983. - 528.	994. - 535.	1050. - 565.	1069. - 576.	1299. - 704.
47	12.83	983. - 528.	994. - 535.	1049. - 565.	1068. - 576.	1298. - 703.
48	12.73	979. - 526.	991. - 533.	1046. - 563.	1065. - 574.	1293. - 701.
49	12.66	963. - 517.	975. - 524.	1030. - 554.	1048. - 565.	1281. - 694.
50	12.58	919. - 493.	928. - 498.	982. - 528.	1000. - 538.	1244. - 673.
51	12.92	925. - 496.	933. - 501.	988. - 531.	1007. - 542.	1256. - 680.
52	12.85	957. - 514.	970. - 521.	1025. - 552.	1044. - 562.	1282. - 695.
53	12.79	965. - 518.	978. - 526.	1033. - 556.	1052. - 567.	1286. - 697.
54	12.72	964. - 518.	976. - 525.	1031. - 555.	1050. - 565.	1283. - 695.
55	12.63	952. - 511.	965. - 518.	1019. - 549.	1038. - 559.	1274. - 690.
56	12.55	917. - 492.	926. - 496.	979. - 526.	998. - 537.	1242. - 672.
57	12.81	917. - 491.	917. - 491.	968. - 520.	987. - 530.	1240. - 671.
58	12.73	922. - 494.	930. - 499.	984. - 529.	1003. - 539.	1249. - 676.

Pin No. EBR-II	Peak kW/ft	Peak Temperatures									
		Coolant		Clad Outside		Clad Inside		Fuel Surface		Fuel Centerline	
		F	C	F	C	F	C	F	C	F	C
59	12.68	923.	495.	930.	499.	985.	529.	1003.	540.	1248.	676.
60	12.59	920.	493.	927.	497.	981.	527.	999.	537.	1244.	673.
61	12.51	911.	489.	911.	489.	961.	516.	980.	527.	1228.	665.

Table B-7 Maximum Heat Rating and Temperatures, Mark-V Fuel Pins, Position 5E2, Beginning-of-Life Conditions

		Peak Temperatures				
		Coolant	Clad Outside	Clad Inside	Fuel Surface	Fuel Centerline
Pin No. EBR-II	Peak kW/ft	F C	F C	F C	F C	F C
1	11.07	858. - 459.	867. - 464.	914. - 490.	931. - 499.	1168. - 631.
3	11.40	867. - 464.	880. - 471.	929. - 498.	946. - 508.	1184. - 640.
5	11.66	859. - 460.	872. - 467.	922. - 494.	940. - 504.	1189. - 643.
7	11.29	886. - 474.	900. - 482.	948. - 509.	965. - 519.	1196. - 647.
9	11.58	896. - 480.	910. - 488.	960. - 516.	977. - 525.	1210. - 654.
11	11.84	874. - 468.	889. - 476.	940. - 505.	958. - 515.	1205. - 652.
13	11.33	891. - 477.	905. - 485.	954. - 512.	971. - 521.	1200. - 649.
15	11.62	908. - 486.	921. - 494.	971. - 522.	988. - 531.	1216. - 658.
17	11.88	903. - 484.	917. - 492.	968. - 520.	986. - 530.	1222. - 661.
19	11.14	856. - 458.	856. - 458.	901. - 483.	917. - 492.	1161. - 627.
21	11.51	903. - 484.	916. - 491.	966. - 519.	983. - 528.	1210. - 655.
23	11.81	911. - 488.	924. - 496.	975. - 524.	992. - 533.	1223. - 662.
25	12.10	903. - 484.	918. - 492.	970. - 521.	988. - 531.	1228. - 665.
27	11.14	850. - 455.	852. - 456.	900. - 482.	917. - 492.	1164. - 629.
29	11.51	903. - 484.	917. - 492.	966. - 519.	984. - 529.	1212. - 655.
31	11.88	914. - 490.	927. - 497.	978. - 526.	996. - 535.	1227. - 664.
33	12.21	916. - 491.	930. - 499.	982. - 528.	1001. - 538.	1239. - 670.
35	12.54	861. - 461.	870. - 466.	925. - 496.	944. - 507.	1215. - 657.
37	11.51	893. - 478.	907. - 486.	956. - 514.	974. - 523.	1206. - 652.
39	11.88	913. - 489.	926. - 497.	977. - 525.	995. - 535.	1226. - 663.
41	12.32	917. - 492.	932. - 500.	984. - 529.	1003. - 539.	1242. - 672.
43	12.65	867. - 464.	871. - 466.	926. - 496.	945. - 507.	1215. - 657.
45	11.70	898. - 481.	913. - 489.	963. - 517.	981. - 527.	1215. - 657.
47	12.14	916. - 491.	930. - 499.	982. - 528.	1000. - 538.	1236. - 669.
49	12.54	910. - 488.	925. - 496.	979. - 526.	998. - 537.	1246. - 674.
51	11.73	869. - 465.	884. - 473.	935. - 502.	953. - 512.	1200. - 649.
53	12.14	905. - 485.	920. - 493.	972. - 522.	990. - 532.	1231. - 666.
55	12.54	905. - 485.	921. - 494.	975. - 524.	994. - 535.	1244. - 673.

Pin No. EBR-II	Peak kW/ft	Peak Temperatures									
		Coolant		Clad Outside		Clad Inside		Fuel Surface		Fuel Centerline	
		F	C	F	C	F	C	F	C	F	C
57	11.95	854.	457.	870.	466.	922.	494.	940.	505.	1198.	648.
59	12.39	874.	468.	889.	476.	943.	506.	962.	517.	1219.	659.
61	12.80	868.	464.	884.	473.	940.	504.	959.	515.	1228.	665.

Table B-8 Maximum Heat Rating and Temperatures, Mark-V Fuel Pins, Position 6E3, Beginning-of-Life Conditions

Pin No. EBR-II	Peak kW/ft	Peak Temperatures				
		Coolant	Clad Outside	Clad Inside	Fuel Surface	Fuel Centerline
		F C	F C	F C	F C	F C
1	10.61	902. - 483.	907. - 486.	952. - 511.	967. - 520.	1177. - 636.
2	10.49	913. - 490.	924. - 496.	969. - 520.	984. - 529.	1187. - 642.
3	10.38	913. - 489.	923. - 495.	968. - 520.	983. - 528.	1184. - 640.
4	10.23	908. - 487.	918. - 492.	962. - 517.	977. - 525.	1177. - 636.
5	10.08	897. - 481.	898. - 481.	941. - 505.	955. - 513.	1156. - 625.
6	10.56	916. - 491.	926. - 497.	971. - 522.	987. - 530.	1191. - 644.
7	10.45	954. - 512.	965. - 518.	1009. - 543.	1025. - 551.	1219. - 659.
8	10.33	962. - 516.	972. - 522.	1016. - 546.	1031. - 555.	1220. - 660.
9	10.19	958. - 515.	968. - 520.	1012. - 544.	1027. - 553.	1214. - 657.
10	10.05	945. - 507.	955. - 513.	998. - 537.	1013. - 545.	1201. - 649.
11	9.90	905. - 485.	914. - 490.	956. - 513.	970. - 521.	1164. - 629.
12	10.51	918. - 492.	928. - 498.	973. - 523.	988. - 531.	1190. - 643.
13	10.39	963. - 517.	973. - 523.	1018. - 548.	1033. - 556.	1223. - 662.
14	10.27	976. - 524.	985. - 529.	1029. - 554.	1044. - 562.	1228. - 665.
15	10.17	975. - 524.	983. - 528.	1027. - 553.	1042. - 561.	1224. - 662.
16	10.01	969. - 521.	978. - 526.	1021. - 549.	1035. - 557.	1216. - 658.
17	9.87	951. - 511.	961. - 516.	1003. - 539.	1017. - 547.	1200. - 649.
18	9.71	906. - 486.	913. - 490.	955. - 513.	969. - 520.	1158. - 626.
19	10.42	915. - 490.	925. - 496.	969. - 521.	984. - 529.	1186. - 641.
20	10.32	962. - 517.	972. - 522.	1016. - 547.	1031. - 555.	1220. - 660.
21	10.23	977. - 525.	985. - 529.	1029. - 554.	1044. - 562.	1227. - 664.
22	10.11	976. - 525.	984. - 529.	1027. - 553.	1042. - 561.	1223. - 662.
23	9.98	973. - 523.	981. - 527.	1023. - 551.	1038. - 559.	1217. - 659.
24	9.83	967. - 520.	976. - 524.	1017. - 547.	1032. - 555.	1210. - 654.
25	9.75	949. - 509.	958. - 514.	999. - 537.	1014. - 545.	1195. - 646.
26	9.67	903. - 484.	910. - 488.	951. - 511.	965. - 518.	1155. - 624.
27	10.32	906. - 485.	906. - 485.	950. - 510.	965. - 518.	1168. - 631.
28	10.23	950. - 510.	961. - 516.	1004. - 540.	1019. - 548.	1210. - 654.

Pin No. EBR-II	Peak kW/ft	Peak Temperatures									
		Coolant		Clad Outside		Clad Inside		Fuel Surface		Fuel Centerline	
		F	C	F	C	F	C	F	C	F	C
29	10.13	972.	522.	981.	527.	1024.	551.	1039.	560.	1222.	661.
30	10.04	975.	524.	983.	528.	1025.	552.	1040.	560.	1220.	660.
31	9.94	973.	523.	981.	527.	1023.	550.	1037.	559.	1216.	658.
32	9.86	970.	521.	978.	525.	1020.	549.	1034.	557.	1212.	655.
33	9.79	963.	517.	972.	522.	1013.	545.	1028.	553.	1206.	652.
34	9.70	937.	503.	947.	509.	989.	531.	1003.	539.	1186.	641.
35	9.62	897.	480.	897.	480.	934.	501.	947.	508.	1140.	616.
36	10.13	913.	489.	921.	494.	965.	518.	979.	526.	1175.	635.
37	10.14	957.	514.	966.	519.	1010.	543.	1024.	551.	1211.	655.
38	9.94	971.	522.	979.	526.	1021.	550.	1036.	558.	1215.	657.
39	9.92	972.	522.	979.	526.	1022.	550.	1036.	558.	1215.	657.
40	9.88	970.	521.	978.	525.	1020.	549.	1034.	557.	1212.	656.
41	9.81	966.	519.	974.	523.	1015.	546.	1030.	554.	1208.	653.
42	9.73	948.	509.	957.	514.	998.	537.	1013.	545.	1194.	645.
43	9.65	904.	485.	910.	488.	951.	511.	965.	518.	1155.	624.
44	9.95	915.	490.	921.	494.	963.	517.	977.	525.	1170.	632.
45	9.92	954.	512.	963.	517.	1005.	541.	1020.	549.	1203.	651.
46	9.90	967.	519.	975.	524.	1017.	547.	1032.	555.	1211.	655.
47	9.88	967.	520.	975.	524.	1017.	547.	1032.	556.	1211.	655.
48	9.81	964.	518.	972.	522.	1014.	546.	1028.	554.	1207.	653.
49	9.75	948.	509.	957.	514.	999.	537.	1013.	545.	1195.	646.
50	9.69	907.	486.	913.	489.	954.	512.	968.	520.	1157.	625.
51	9.90	911.	489.	917.	492.	959.	515.	973.	523.	1166.	630.
52	9.88	942.	506.	952.	511.	994.	535.	1009.	543.	1194.	646.
53	9.86	951.	510.	960.	516.	1002.	539.	1017.	547.	1199.	649.
54	9.81	950.	510.	959.	515.	1001.	538.	1015.	546.	1197.	647.
55	9.75	939.	504.	949.	509.	990.	532.	1004.	540.	1188.	642.
56	9.69	905.	485.	911.	488.	952.	511.	966.	519.	1156.	625.
57	9.86	904.	484.	904.	484.	940.	505.	954.	512.	1150.	621.
58	9.84	909.	487.	914.	490.	956.	513.	970.	521.	1162.	628.
59	9.81	910.	488.	915.	491.	957.	514.	971.	522.	1162.	628.

Pin No. EBR-II	Peak kW/ft	Peak Temperatures									
		Coolant		Clad Outside		Clad Inside		Fuel Surface		Fuel Centerline	
		F	C	F	C	F	C	F	C	F	C
60	9.75	907.	- 486.	912.	- 489.	954.	- 512.	968.	- 520.	1159.	- 626.
61	9.69	900.	- 482.	900.	- 482.	936.	- 502.	949.	- 510.	1143.	- 617.

Table B-9 Maximum Heat Rating and Temperatures, Mark-V Fuel Pins, Position 6F1, Beginning-of-Life Conditions

		Peak Temperatures									
		Coolant		Clad Outside		Clad Inside		Fuel Surface		Fuel Centerline	
Pin No. EBR-II	Peak kW/ft	F	C	F	C	F	C	F	C	F	C
1	9.33	905.	485.	905.	485.	945.	507.	958.	514.	1141.	616.
2	9.34	914.	490.	923.	495.	963.	517.	977.	525.	1157.	625.
3	9.36	916.	491.	925.	496.	965.	518.	979.	526.	1158.	626.
4	9.34	913.	490.	923.	495.	962.	517.	976.	524.	1156.	624.
5	9.32	903.	484.	903.	484.	943.	506.	956.	513.	1140.	615.
6	9.19	913.	489.	922.	494.	961.	516.	974.	523.	1151.	622.
7	9.18	951.	511.	960.	516.	1000.	538.	1013.	545.	1183.	639.
8	9.21	962.	516.	970.	521.	1009.	543.	1023.	551.	1191.	644.
9	9.21	962.	516.	970.	521.	1009.	543.	1023.	551.	1191.	644.
10	9.19	951.	510.	960.	516.	999.	537.	1013.	545.	1183.	640.
11	9.19	911.	488.	920.	493.	959.	515.	972.	522.	1150.	621.
12	9.05	915.	491.	922.	494.	960.	516.	973.	523.	1147.	620.
13	9.06	959.	515.	967.	519.	1005.	541.	1019.	548.	1185.	640.
14	9.08	973.	523.	981.	527.	1019.	549.	1033.	556.	1196.	647.
15	9.08	975.	524.	983.	528.	1021.	549.	1034.	557.	1197.	647.
16	9.07	973.	523.	981.	527.	1019.	548.	1033.	556.	1195.	646.
17	9.06	958.	515.	967.	519.	1005.	541.	1018.	548.	1185.	640.
18	9.04	911.	489.	920.	493.	958.	515.	971.	522.	1146.	619.
19	9.03	913.	489.	919.	493.	957.	514.	970.	521.	1145.	618.
20	8.98	956.	514.	965.	518.	1003.	539.	1016.	547.	1181.	638.
21	8.93	972.	522.	979.	526.	1017.	547.	1030.	555.	1191.	644.
22	8.94	975.	524.	981.	527.	1019.	548.	1032.	556.	1192.	644.
23	8.94	975.	524.	981.	527.	1019.	548.	1032.	556.	1192.	644.
24	8.93	972.	522.	979.	526.	1017.	547.	1030.	555.	1191.	644.
25	8.98	956.	513.	964.	518.	1003.	539.	1016.	547.	1181.	638.
26	9.03	908.	487.	917.	492.	955.	513.	968.	520.	1144.	618.
27	9.01	905.	485.	905.	485.	939.	504.	951.	511.	1129.	609.
28	8.96	946.	508.	954.	512.	993.	534.	1006.	541.	1173.	634.

Pin No. EBR-II	Peak kW/ft	Peak Temperatures: Coolant F C	Clad Outside F C	Clad Inside F C	Fuel Surface F C	Fuel Centerline F C
29	8.92	969. - 520.	976. - 524.	1014. - 545.	1027. - 553.	1188. - 642.
30	8.87	973. - 523.	979. - 526.	1017. - 547.	1030. - 554.	1188. - 642.
31	8.82	973. - 523.	979. - 526.	1016. - 547.	1029. - 554.	1187. - 642.
32	8.87	973. - 523.	979. - 526.	1017. - 547.	1030. - 554.	1189. - 643.
33	8.92	969. - 521.	976. - 525.	1014. - 546.	1027. - 553.	1188. - 642.
34	8.98	945. - 507.	954. - 512.	992. - 534.	1005. - 541.	1173. - 634.
35	9.03	900. - 482.	900. - 482.	937. - 503.	950. - 510.	1128. - 609.
36	8.94	911. - 488.	917. - 491.	955. - 513.	967. - 520.	1141. - 616.
37	8.90	954. - 512.	962. - 517.	1000. - 538.	1013. - 545.	1177. - 636.
38	8.84	969. - 521.	976. - 525.	1014. - 545.	1027. - 553.	1186. - 641.
39	8.83	971. - 522.	978. - 525.	1015. - 546.	1028. - 553.	1187. - 641.
40	8.83	971. - 522.	978. - 526.	1015. - 546.	1028. - 553.	1187. - 641.
41	8.86	969. - 521.	976. - 525.	1014. - 545.	1027. - 553.	1186. - 641.
42	8.83	954. - 512.	962. - 517.	999. - 537.	1012. - 545.	1175. - 635.
43	8.97	908. - 487.	916. - 491.	954. - 512.	967. - 519.	1141. - 616.
44	8.87	913. - 489.	917. - 492.	955. - 513.	968. - 520.	1139. - 615.
45	8.86	953. - 512.	961. - 516.	999. - 537.	1012. - 544.	1175. - 635.
46	8.84	967. - 519.	974. - 523.	1011. - 544.	1024. - 551.	1184. - 640.
47	8.83	968. - 520.	975. - 524.	1013. - 545.	1026. - 552.	1185. - 640.
48	8.85	967. - 519.	974. - 523.	1012. - 544.	1025. - 552.	1185. - 640.
49	8.89	953. - 512.	961. - 516.	999. - 537.	1012. - 544.	1176. - 636.
50	8.92	910. - 488.	917. - 492.	955. - 513.	967. - 520.	1140. - 616.
51	8.87	910. - 488.	915. - 490.	953. - 511.	965. - 518.	1137. - 614.
52	8.86	943. - 506.	951. - 511.	989. - 532.	1002. - 539.	1168. - 631.
53	8.84	952. - 511.	960. - 516.	998. - 537.	1011. - 544.	1174. - 634.
54	8.84	952. - 511.	960. - 516.	998. - 537.	1011. - 544.	1174. - 635.
55	8.88	943. - 506.	952. - 511.	990. - 532.	1002. - 539.	1169. - 631.
56	8.91	907. - 486.	914. - 490.	952. - 511.	965. - 518.	1138. - 615.
57	8.87	902. - 484.	902. - 484.	935. - 501.	947. - 508.	1123. - 606.
58	8.85	908. - 487.	914. - 490.	952. - 511.	964. - 518.	1136. - 614.

Pin No. EBR-II	Peak kW/ft	Peak Temperatures: Coolant F	Coolant C	Clad Outside F	Clad Outside C	Clad Inside F	Clad Inside C	Fuel Surface F	Fuel Surface C	Fuel Centerline F	Fuel Centerline C
59	8.84	910.	488.	916.	491.	953.	512.	966.	519.	1137.	614.
60	8.87	908.	487.	914.	490.	952.	511.	965.	518.	1137.	614.
61	8.90	900.	482.	900.	482.	934.	501.	947.	508.	1123.	606.

Table B-10 Maximum Heat Rating and Temperatures, Safety Rod Mark-IIC Fuel Pins, Position 3A1, Beginning-of-Life-Conditions

		Peak Temperatures				
		Coolant	Clad Outside	Clad Inside	Fuel Surface	Fuel Centerline
Pin No. EBR-II	Peak kW/ft	F C	F C	F C	F C	F C
1	9.84	838. - 448.	856. - 458.	915. - 491.	933. - 500.	1074. - 579.
2	9.92	856. - 458.	874. - 468.	933. - 501.	951. - 510.	1092. - 589.
3	10.01	858. - 459.	876. - 469.	936. - 502.	954. - 512.	1096. - 591.
4	10.08	857. - 458.	876. - 469.	936. - 502.	954. - 512.	1097. - 591.
5	10.15	841. - 450.	860. - 460.	921. - 494.	939. - 504.	1084. - 584.
6	9.76	853. - 456.	871. - 466.	930. - 499.	947. - 508.	1086. - 586.
7	9.94	889. - 476.	907. - 486.	965. - 519.	983. - 528.	1122. - 606.
8	9.99	898. - 481.	916. - 491.	975. - 524.	993. - 534.	1132. - 611.
9	10.01	900. - 482.	917. - 492.	976. - 525.	994. - 535.	1133. - 612.
10	10.19	893. - 479.	912. - 489.	972. - 522.	990. - 532.	1132. - 611.
11	10.27	859. - 460.	878. - 470.	940. - 504.	958. - 514.	1103. - 595.
12	9.82	855. - 457.	873. - 467.	932. - 500.	949. - 509.	1089. - 587.
13	9.89	896. - 480.	914. - 490.	972. - 522.	989. - 532.	1127. - 608.
14	9.98	909. - 487.	926. - 497.	985. - 529.	1003. - 539.	1141. - 616.
15	10.04	912. - 489.	929. - 498.	988. - 531.	1006. - 541.	1145. - 618.
16	10.13	913. - 489.	930. - 499.	989. - 532.	1008. - 542.	1147. - 620.
17	10.28	903. - 484.	921. - 494.	981. - 527.	1000. - 538.	1142. - 617.
18	10.32	861. - 461.	880. - 471.	942. - 505.	960. - 516.	1106. - 597.
19	9.73	853. - 456.	871. - 466.	929. - 498.	946. - 508.	1085. - 585.
20	9.81	895. - 479.	913. - 489.	970. - 521.	988. - 531.	1125. - 607.
21	9.90	909. - 487.	926. - 497.	984. - 529.	1002. - 539.	1139. - 615.
22	9.92	913. - 489.	930. - 499.	988. - 531.	1006. - 541.	1143. - 617.
23	10.12	915. - 491.	932. - 500.	991. - 533.	1010. - 543.	1149. - 621.
24	10.17	915. - 491.	933. - 500.	992. - 533.	1010. - 544.	1150. - 621.
25	10.29	903. - 484.	922. - 494.	982. - 528.	1000. - 538.	1143. - 617.
26	10.36	859. - 459.	878. - 470.	940. - 504.	958. - 515.	1105. - 596.
27	9.75	836. - 447.	854. - 457.	912. - 489.	930. - 499.	1070. - 577.
28	9.79	886. - 475.	904. - 485.	962. - 517.	980. - 526.	1117. - 603.

Pin No. EBR-II	Peak kW/ft	Peak Temperatures				
		Coolant	Clad Outside	Clad Inside	Fuel Surface	Fuel Centerline
		F C	F C	F C	F C	F C
29	9.81	906. - 486.	923. - 495.	981. - 527.	998. - 537.	1134. - 612.
30	9.98	912. - 489.	929. - 498.	987. - 531.	1005. - 541.	1143. - 617.
31	10.05	914. - 490.	931. - 500.	990. - 532.	1008. - 542.	1147. - 619.
32	10.15	916. - 491.	933. - 500.	992. - 533.	1010. - 544.	1150. - 621.
33	10.24	914. - 490.	932. - 500.	991. - 533.	1010. - 543.	1151. - 622.
34	10.25	895. - 479.	913. - 490.	974. - 523.	992. - 533.	1134. - 612.
35	10.38	841. - 450.	861. - 460.	923. - 495.	941. - 505.	1089. - 587.
36	9.76	852. - 455.	870. - 465.	928. - 498.	945. - 507.	1085. - 585.
37	9.86	895. - 479.	913. - 489.	971. - 521.	988. - 531.	1126. - 608.
38	9.94	909. - 487.	926. - 497.	985. - 529.	1002. - 539.	1140. - 616.
39	9.99	912. - 489.	929. - 499.	988. - 531.	1006. - 541.	1144. - 618.
40	10.02	914. - 490.	931. - 499.	989. - 532.	1008. - 542.	1146. - 619.
41	10.07	913. - 490.	931. - 499.	990. - 532.	1008. - 542.	1147. - 619.
42	10.08	901. - 483.	919. - 493.	979. - 526.	997. - 536.	1136. - 614.
43	10.30	858. - 459.	877. - 470.	939. - 504.	957. - 514.	1103. - 595.
44	9.79	854. - 457.	872. - 467.	931. - 499.	948. - 509.	1087. - 586.
45	9.85	895. - 480.	913. - 489.	971. - 522.	988. - 531.	1126. - 608.
46	9.90	908. - 487.	925. - 496.	983. - 528.	1001. - 538.	1138. - 614.
47	9.94	910. - 488.	927. - 497.	986. - 530.	1004. - 540.	1141. - 616.
48	10.04	911. - 488.	928. - 498.	987. - 530.	1005. - 540.	1143. - 617.
49	10.12	900. - 482.	918. - 492.	977. - 525.	996. - 535.	1136. - 613.
50	10.21	858. - 459.	877. - 470.	938. - 503.	956. - 513.	1101. - 594.
51	9.77	853. - 456.	871. - 466.	929. - 498.	946. - 508.	1086. - 585.
52	9.83	887. - 475.	905. - 485.	963. - 517.	980. - 527.	1118. - 603.
53	9.84	896. - 480.	913. - 490.	971. - 522.	989. - 532.	1126. - 608.
54	9.96	97. - 481.	915. - 491.	974. - 523.	991. - 533.	1130. - 610.
55	10.01	890. - 477.	909. - 487.	968. - 520.	985. - 530.	1125. - 607.
56	10.06	855. - 457.	874. - 468.	934. - 501.	952. - 511.	1095. - 590.
57	9.74	835. - 446.	853. - 456.	912. - 489.	929. - 498.	1069. - 576.
58	9.77	852. - 456.	870. - 466.	928. - 498.	946. - 508.	1085. - 585.
59	9.84	855. - 457.	873. - 467.	932. - 500.	949. - 509.	1089. - 587.

Pin No. EBR-II	Peak kW/ft	Peak Temperatures									
		Coolant		Clad Outside		Clad Inside		Fuel Surface		Fuel Centerline	
		F	C	F	C	F	C	F	C	F	C
60	9.97	854.	457.	873.	467.	932.	500.	950.	510.	1092.	589.
61	10.07	838.	448.	856.	458.	917.	492.	935.	501.	1079.	582.

Table B-11 Maximum Heat Rating and Temperatures, Control Rod Mark-IICS Fuel Pins, Position 5B3, Beginning-of-Life-Conditions

		Peak Temperatures				
		Coolant	Clad Outside	Clad Inside	Fuel Surface	Fuel Centerline
Pin No. EBR-II	Peak kW/ft	F C	F C	F C	F C	F C
1	7.78	862. - 461.	877. - 469.	923. - 495.	937. - 503.	1049. - 565.
2	7.78	886. - 475.	902. - 483.	948. - 509.	961. - 516.	1072. - 578.
3	7.85	889. - 476.	904. - 485.	951. - 510.	965. - 518.	1076. - 580.
4	7.83	887. - 475.	902. - 484.	949. - 509.	963. - 517.	1074. - 579.
5	7.87	865. - 463.	881. - 472.	928. - 498.	942. - 505.	1055. - 568.
6	7.78	885. - 474.	900. - 482.	946. - 508.	960. - 515.	1071. - 577.
7	7.82	934. - 501.	949. - 510.	995. - 535.	1009. - 543.	1117. - 603.
8	7.87	947. - 508.	962. - 516.	1007. - 542.	1021. - 550.	1130. - 610.
9	7.93	948. - 509.	963. - 517.	1009. - 543.	1023. - 551.	1132. - 611.
10	7.93	938. - 503.	953. - 512.	999. - 537.	1013. - 545.	1123. - 606.
11	8.03	891. - 477.	907. - 486.	954. - 512.	968. - 520.	1082. - 584.
12	7.89	888. - 476.	904. - 484.	950. - 510.	964. - 518.	1077. - 580.
13	7.87	947. - 508.	962. - 516.	1007. - 542.	1021. - 550.	1130. - 610.
14	7.93	965. - 518.	979. - 526.	1024. - 551.	1039. - 559.	1147. - 619.
15	7.95	968. - 520.	982. - 528.	1028. - 553.	1042. - 561.	1151. - 621.
16	8.00	968. - 520.	982. - 528.	1027. - 553.	1042. - 561.	1151. - 622.
17	8.03	952. - 511.	967. - 519.	1013. - 545.	1028. - 553.	1138. - 615.
18	8.10	895. - 479.	911. - 488.	958. - 515.	973. - 523.	1087. - 586.
19	7.92	887. - 475.	903. - 484.	950. - 510.	964. - 518.	1076. - 580.
20	7.93	949. - 509.	963. - 517.	1009. - 543.	1023. - 551.	1133. - 611.
21	7.96	968. - 520.	982. - 528.	1028. - 553.	1042. - 561.	1151. - 622.
22	8.00	973. - 523.	986. - 530.	1032. - 555.	1047. - 564.	1155. - 624.
23	8.10	974. - 523.	988. - 531.	1034. - 557.	1049. - 565.	1159. - 626.
24	8.09	973. - 523.	987. - 530.	1033. - 556.	1048. - 564.	1158. - 625.
25	8.14	955. - 513.	970. - 521.	1017. - 547.	1032. - 555.	1143. - 617.
26	8.12	894. - 479.	910. - 488.	957. - 514.	972. - 522.	1087. - 586.
27	7.95	863. - 462.	879. - 470.	926. - 497.	940. - 505.	1055. - 568.
28	7.95	938. - 503.	953. - 512.	999. - 537.	1014. - 545.	1124. - 607.

Pin No. EBR-II	Peak kW/ft	Peak Temperatures Coolant F	Coolant C	Clad Outside F	Clad Outside C	Clad Inside F	Clad Inside C	Fuel Surface F	Fuel Surface C	Fuel Centerline F	Fuel Centerline C
29	8.00	966.	519.	980.	527.	1026.	552.	1040.	560.	1150.	621.
30	8.07	974.	523.	988.	531.	1034.	557.	1049.	565.	1159.	626.
31	8.11	976.	525.	990.	532.	1036.	558.	1051.	566.	1161.	627.
32	8.17	977.	525.	991.	533.	1038.	559.	1053.	567.	1164.	629.
33	8.16	974.	523.	988.	531.	1035.	557.	1050.	565.	1161.	627.
34	8.26	946.	508.	962.	517.	1010.	543.	1025.	551.	1138.	615.
35	8.29	871.	466.	888.	475.	937.	503.	952.	511.	1070.	577.
36	8.06	888.	476.	904.	484.	951.	511.	966.	519.	1080.	582.
37	8.08	953.	511.	968.	520.	1014.	546.	1029.	554.	1140.	615.
38	8.14	973.	523.	987.	531.	1034.	557.	1049.	565.	1160.	626.
39	8.19	977.	525.	991.	533.	1038.	559.	1053.	567.	1164.	629.
40	8.17	979.	526.	993.	534.	1040.	560.	1055.	568.	1165.	630.
41	8.31	978.	526.	992.	534.	1040.	560.	1055.	568.	1168.	631.
42	8.23	960.	515.	975.	524.	1022.	550.	1037.	559.	1150.	621.
43	8.39	898.	481.	914.	490.	963.	517.	978.	526.	1097.	591.
44	8.12	893.	478.	909.	487.	957.	514.	971.	522.	1086.	586.
45	8.19	955.	513.	971.	521.	1018.	548.	1033.	556.	1145.	618.
46	8.21	974.	523.	988.	531.	1035.	557.	1050.	566.	1162.	628.
47	8.23	977.	525.	992.	533.	1039.	559.	1054.	568.	1165.	630.
48	8.31	978.	525.	992.	534.	1040.	560.	1055.	568.	1167.	631.
49	8.42	962.	517.	977.	525.	1026.	552.	1041.	561.	1156.	624.
50	8.45	901.	483.	917.	492.	967.	519.	982.	528.	1101.	594.
51	8.24	893.	478.	909.	487.	958.	514.	972.	522.	1089.	587.
52	8.23	946.	508.	961.	516.	1009.	543.	1024.	551.	1137.	614.
53	8.21	959.	515.	974.	523.	1021.	549.	1036.	558.	1148.	620.
54	8.36	961.	516.	976.	525.	1024.	551.	1040.	560.	1154.	623.
55	8.45	951.	510.	967.	519.	1016.	547.	1031.	555.	1147.	619.
56	8.51	898.	481.	915.	491.	965.	518.	980.	527.	1100.	593.
57	8.34	868.	465.	885.	474.	935.	501.	949.	510.	1069.	576.
58	8.40	894.	479.	911.	488.	960.	516.	975.	524.	1094.	590.

Pin No. EBR-II	Peak kW/ft	Peak Temperatures Coolant F	Coolant C	Clad Outside F	Clad Outside C	Clad Inside F	Clad Inside C	Fuel Surface F	Fuel Surface C	Fuel Centerline F	Fuel Centerline C
59	8.34	899.	481.	915.	490.	964.	518.	979.	526.	1096.	591.
60	8.47	898.	481.	915.	491.	965.	518.	980.	527.	1099.	593.
61	8.58	873.	467.	890.	477.	941.	505.	956.	513.	1078.	581.

B.2. Thermal Analysis of Reference Mark-VA Core Fueled Subassemblies

The maximum temperatures in a core containing 316 stainless steel clad, Mark-VA fuel pins have been calculated. The core analyzed was the same 6-row core used in the analysis of Mark-V fuel (Sec. B.1) and is described in Section 6.2. The maximum subassembly powers for each row are given in Table B-1 along with the subassembly flow rates. The radial power gradient in the subassembly was based on the BURNT program [B.1] for a similar core. The fuel pin temperatures were calculated using the SUPERENERGY-2 [B.2] program with the subassembly flow distribution given by the Cheng-Todreas MIT model [B.3]. The coolant-clad film coefficient is taken from [B.4]. The temperatures were calculated for beginning-of-life (BOL) conditions. As irradiation of the fuel occurs, the fuel will swell and expand radially displacing the bond sodium. The fuel swelling decreases the fuel thermal conductivity. Diffusion of the fissile and zirconium materials will also occur. These effects are not modelled and therefore only BOL conditions are given.

The maximum temperature condition in each subassembly is summarized in Table B-12. It should be noted that the peak temperatures do not always occur at the same axial elevation. The peak condition for each pin in the Mark-VA fueled subassembly is summarized in Table B-13 through Table B-19 for the highest power subassembly in each row. Note that the driver subassemblies in rows 1 and 5 are partial drivers, and so Table B-13 and Table B-17 list results for only 31 pins, instead of 61.

The peak coolant temperatures are found in the 6-row core, and it is the row 5 subassembly which gives the hottest coolant temperature. The coolant temperatures are higher in rows 1, 2 and 3 and lower in rows 4, 5, and 6, when compared to the Mark-III and Mark-IIIA analyses,

because of the power shift to the center of the core discussed in Section 6.

Table B-2 also shows that in normal operation there is a large margin to fuel/clad eutectic and fuel melting in the hottest subchannels.

Table B-12 BOL Peak Powers and Temperatures of, Mark-VA Fueled Subassemblies, U-20Pu-10Zr Unswollen Fuel

		Peak Temperatures								
		Coolant		Clad Inside		Fuel Centerline		Bundle Average Flow Temperature		
Location	Peak kW/ft	F	C	F	C	F	C	F	C	Peaking Factor
1A1	16.19	928.	498.	1019.	548.	1358.	737.	885.	474.	1.23
2F1	15.37	936.	502.	1017.	547.	1333.	723.	891.	477.	1.24
3E2	15.02	957.	514.	1034.	557.	1332.	722.	907.	486.	1.24
4E2	13.79	994.	534.	1062.	572.	1320.	716.	938.	503.	1.24
5E2	12.80	917.	492.	986.	530.	1249.	676.	873.	467.	1.25
6E3	10.61	977.	525.	1029.	554.	1229.	665.	923.	495.	1.24
6F1	9.36	975.	524.	1021.	550.	1198.	647.	925.	496.	1.22

Table B-13 Maximum Heat Rating and Temperatures, Mark-VA Fuel Pins, Position 1A1, Beginning-of-Life-Conditions

Pin No. EBR-II	Peak kW/ft	Peak Temperatures				
		Coolant	Clad Outside	Clad Inside	Fuel Surface	Fuel Centerline
		F C	F C	F C	F C	F C
1	16.09	870. - 466.	891. - 477.	965. - 518.	992. - 533.	1329. - 720.
3	16.09	881. - 472.	901. - 483.	975. - 524.	1001. - 538.	1333. - 723.
5	16.04	866. - 463.	887. - 475.	962. - 517.	988. - 531.	1327. - 719.
7	16.09	908. - 486.	928. - 498.	1001. - 538.	1027. - 553.	1348. - 731.
9	16.09	914. - 490.	934. - 501.	1006. - 541.	1032. - 555.	1350. - 732.
11	16.04	883. - 473.	904. - 484.	978. - 525.	1004. - 540.	1336. - 725.
13	16.14	913. - 489.	933. - 501.	1006. - 541.	1032. - 555.	1352. - 733.
15	16.14	926. - 497.	945. - 507.	1017. - 547.	1042. - 561.	1356. - 735.
17	16.09	915. - 490.	934. - 501.	1007. - 542.	1033. - 556.	1351. - 733.
19	16.09	872. - 467.	877. - 469.	952. - 511.	978. - 525.	1321. - 716.
21	16.14	924. - 495.	943. - 506.	1015. - 546.	1040. - 560.	1355. - 735.
23	16.14	926. - 497.	945. - 507.	1017. - 547.	1042. - 561.	1355. - 735.
25	16.09	912. - 489.	932. - 500.	1004. - 540.	1030. - 554.	1349. - 732.
27	16.09	866. - 463.	876. - 469.	952. - 511.	979. - 526.	1324. - 718.
29	16.14	924. - 496.	944. - 507.	1016. - 547.	1042. - 561.	1356. - 736.
31	16.19	928. - 498.	947. - 508.	1019. - 548.	1045. - 563.	1358. - 737.
33	16.14	924. - 495.	943. - 506.	1015. - 546.	1041. - 560.	1355. - 735.
35	16.09	866. - 463.	876. - 469.	952. - 511.	979. - 526.	1324. - 718.
37	16.14	912. - 489.	932. - 500.	1005. - 540.	1031. - 555.	1351. - 733.
39	16.14	927. - 497.	945. - 507.	1017. - 547.	1042. - 561.	1355. - 735.
41	16.14	924. - 496.	943. - 506.	1015. - 546.	1040. - 560.	1355. - 735.
43	16.09	872. - 467.	877. - 469.	952. - 511.	978. - 525.	1321. - 716.
45	16.14	915. - 491.	935. - 502.	1008. - 542.	1034. - 556.	1353. - 734.
47	16.19	926. - 497.	946. - 508.	1017. - 547.	1043. - 562.	1357. - 736.
49	16.14	913. - 490.	933. - 501.	1006. - 541.	1032. - 556.	1352. - 733.
51	16.09	883. - 473.	904. - 485.	979. - 526.	1005. - 541.	1338. - 725.
53	16.14	914. - 490.	934. - 501.	1007. - 542.	1033. - 556.	1352. - 733.
55	16.14	908. - 487.	928. - 498.	1001. - 538.	1027. - 553.	1350. - 732.

Pin No. EBR-II	Peak kW/ft	Peak Temperatures									
		Coolant		Clad Outside		Clad Inside		Fuel Surface		Fuel Centerline	
		F	C	F	C	F	C	F	C	F	C
57	16.14	867.	- 464.	888.	- 475.	963.	- 517.	990.	- 532.	1330.	- 721.
59	16.14	882.	- 472.	902.	- 483.	976.	- 524.	1002.	- 539.	1335.	- 724.
61	16.14	871.	- 466.	891.	- 477.	966.	- 519.	992.	- 534.	1330.	- 721.

Table B-14 Maximum Heat Rating and Temperatures, Mark-VA Fuel Pins, Position 2F1, Beginning-of-Life-Conditions

		Peak Temperatures				
Pin No. EBR-II	Peak kW/ft	Coolant F C	Clad Outside F C	Clad Inside F C	Fuel Surface F C	Fuel Centerline F C
1	15.31	873. - 467.	879. - 471.	950. - 510.	974. - 523.	1298. - 703.
2	15.36	879. - 471.	895. - 479.	965. - 518.	989. - 532.	1307. - 709.
3	15.37	881. - 472.	896. - 480.	966. - 519.	991. - 533.	1308. - 709.
4	15.36	879. - 470.	894. - 479.	965. - 518.	989. - 532.	1308. - 709.
5	15.36	872. - 467.	879. - 471.	950. - 510.	974. - 524.	1299. - 704.
6	15.33	879. - 471.	894. - 479.	964. - 518.	989. - 531.	1306. - 708.
7	15.34	911. - 488.	927. - 497.	996. - 535.	1020. - 549.	1325. - 718.
8	15.36	920. - 493.	935. - 502.	1003. - 540.	1028. - 553.	1328. - 720.
9	15.36	920. - 493.	935. - 502.	1003. - 540.	1028. - 553.	1328. - 720.
10	15.36	911. - 488.	927. - 497.	996. - 535.	1020. - 549.	1325. - 719.
11	15.36	878. - 470.	894. - 479.	964. - 518.	989. - 532.	1307. - 708.
12	15.31	881. - 472.	896. - 480.	965. - 519.	990. - 532.	1306. - 708.
13	15.33	919. - 493.	935. - 502.	1003. - 539.	1027. - 553.	1327. - 720.
14	15.34	932. - 500.	947. - 508.	1014. - 546.	1038. - 559.	1332. - 722.
15	15.36	934. - 501.	948. - 509.	1016. - 546.	1040. - 560.	1333. - 723.
16	15.36	932. - 500.	947. - 508.	1014. - 546.	1038. - 559.	1333. - 723.
17	15.34	919. - 493.	935. - 502.	1003. - 539.	1027. - 553.	1328. - 720.
18	15.34	880. - 471.	895. - 480.	965. - 519.	990. - 532.	1307. - 708.
19	15.21	879. - 471.	893. - 479.	963. - 517.	987. - 530.	1302. - 706.
20	15.27	918. - 492.	934. - 501.	1002. - 539.	1026. - 552.	1325. - 718.
21	15.34	933. - 501.	948. - 509.	1015. - 546.	1039. - 559.	1332. - 722.
22	15.36	936. - 502.	950. - 510.	1017. - 547.	1041. - 561.	1333. - 723.
23	15.36	936. - 502.	950. - 510.	1017. - 547.	1041. - 561.	1333. - 723.
24	15.34	934. - 501.	948. - 509.	1015. - 546.	1039. - 560.	1332. - 722.
25	15.31	919. - 493.	934. - 501.	1002. - 539.	1026. - 552.	1327. - 719.
26	15.27	877. - 470.	893. - 478.	963. - 517.	987. - 531.	1304. - 707.
27	15.10	873. - 467.	877. - 470.	947. - 508.	971. - 522.	1291. - 699.
28	15.18	909. - 487.	925. - 496.	993. - 534.	1017. - 547.	1319. - 715.

Pin No. EBR-II	Peak kW/ft	Peak Temperatures									
		Coolant		Clad Outside		Clad Inside		Fuel Surface		Fuel Centerline	
		F	C	F	C	F	C	F	C	F	C
29	15.22	929.	499.	944.	507.	1011.	544.	1035.	557.	1328.	720.
30	15.30	935.	502.	949.	509.	1016.	547.	1040.	560.	1331.	722.
31	15.36	936.	502.	950.	510.	1017.	547.	1041.	560.	1333.	723.
32	15.31	935.	502.	949.	510.	1016.	547.	1040.	560.	1332.	722.
33	15.27	931.	500.	946.	508.	1013.	545.	1037.	558.	1330.	721.
34	15.22	909.	487.	925.	496.	993.	534.	1018.	548.	1321.	716.
35	15.19	870.	466.	877.	469.	947.	508.	971.	522.	1294.	701.
36	15.05	878.	470.	892.	478.	960.	516.	984.	529.	1298.	703.
37	15.11	917.	491.	932.	500.	999.	537.	1023.	550.	1320.	716.
38	15.19	931.	500.	946.	508.	1012.	544.	1036.	558.	1327.	720.
39	15.22	934.	501.	948.	509.	1015.	546.	1038.	559.	1329.	720.
40	15.24	934.	501.	948.	509.	1015.	546.	1039.	559.	1329.	721.
41	15.24	932.	500.	946.	508.	1013.	545.	1037.	558.	1329.	720.
42	15.19	917.	492.	933.	500.	1000.	538.	1024.	551.	1323.	717.
43	15.14	877.	469.	892.	478.	961.	516.	985.	530.	1300.	705.
44	15.02	880.	471.	893.	478.	961.	516.	985.	530.	1297.	703.
45	15.05	916.	491.	931.	499.	998.	537.	1021.	550.	1318.	714.
46	15.10	929.	498.	43.	506.	1009.	543.	1033.	556.	1324.	718.
47	15.14	931.	499.	945.	507.	1011.	544.	1035.	557.	1326.	719.
48	15.13	929.	498.	943.	506.	1010.	543.	1034.	556.	1325.	718.
49	15.11	916.	491.	932.	500.	999.	537.	1023.	550.	1320.	716.
50	15.11	879.	470.	893.	478.	962.	517.	986.	530.	1300.	704.
51	14.93	878.	470.	890.	477.	959.	515.	982.	528.	1293.	701.
52	14.98	906.	486.	922.	494.	989.	532.	1013.	545.	1312.	711.
53	15.02	915.	491.	930.	499.	997.	536.	1021.	549.	1317.	714.
54	15.04	915.	491.	930.	499.	997.	536.	1021.	549.	1317.	714.
55	15.02	907.	486.	923.	495.	990.	532.	1014.	545.	1314.	712.
56	15.01	876.	469.	890.	477.	959.	515.	983.	528.	1296.	702.
57	14.86	871.	466.	875.	468.	943.	506.	967.	519.	1283.	695.
58	14.89	877.	469.	890.	476.	958.	514.	981.	527.	1292.	700.

Pin No. EBR-II	Peak kW/ft	Peak Temperatures									
		Coolant		Clad Outside		Clad Inside		Fuel Surface		Fuel Centerline	
		F	C	F	C	F	C	F	C	F	C
59	14.93	879.	470.	891.	477.	960.	515.	983.	528.	1294.	701.
60	14.93	877.	469.	890.	477.	958.	514.	982.	528.	1293.	701.
61	14.92	870.	466.	875.	468.	943.	506.	967.	520.	1285.	696.

Table B-15 Maximum Heat Rating and Temperatures, Mark-VA Fuel Pins, Position 3E2, Beginning-of-Life-Conditions

		Peak Temperatures											
		Coolant		Clad Outside		Clad Inside		Fuel Surface		Fuel Centerline	
Pin No. EBR-II	Peak kW/ft	F	C	F	C	F	C	F	C	F	C
1	15.02	887.	475.	895.	479.	963.	517.	987.	530.	1297.	703.
2	14.96	896.	480.	911.	488.	979.	526.	1002.	539.	1305.	707.
3	14.93	897.	480.	912.	489.	979.	526.	1003.	539.	1304.	707.
4	14.82	893.	479.	909.	487.	976.	524.	999.	537.	1300.	704.
5	14.71	883.	473.	891.	477.	958.	514.	981.	527.	1287.	697.
6	14.98	896.	480.	912.	489.	979.	526.	1003.	539.	1305.	707.
7	14.93	932.	500.	948.	509.	1013.	545.	1037.	558.	1325.	718.
8	14.89	941.	505.	956.	513.	1021.	549.	1044.	562.	1327.	719.
9	14.82	939.	504.	954.	512.	1019.	548.	1042.	561.	1324.	718.
10	14.71	928.	498.	944.	507.	1009.	543.	1032.	555.	1317.	714.
11	14.60	891.	477.	906.	486.	972.	522.	995.	535.	1292.	700.
12	14.93	898.	481.	913.	490.	980.	527.	1004.	540.	1304.	707.
13	14.89	941.	505.	956.	513.	1021.	549.	1044.	562.	1327.	719.
14	14.86	954.	512.	968.	520.	1033.	556.	1055.	569.	1332.	722.
15	14.80	955.	513.	969.	520.	1033.	556.	1055.	569.	1330.	721.
16	14.70	952.	511.	966.	519.	1029.	554.	1052.	567.	1326.	719.
17	14.60	936.	502.	951.	510.	1015.	546.	1038.	559.	1317.	714.
18	14.50	892.	478.	907.	486.	972.	522.	994.	535.	1289.	698.
19	14.83	896.	480.	911.	488.	977.	525.	1001.	538.	1300.	705.
20	14.83	940.	504.	955.	513.	1020.	549.	1043.	562.	1325.	718.
21	14.82	955.	513.	969.	520.	1033.	556.	1056.	569.	1331.	721.
22	14.77	957.	514.	970.	521.	1034.	557.	1056.	569.	1330.	721.
23	14.70	955.	513.	969.	520.	1032.	556.	1055.	568.	1327.	719.
24	14.60	951.	511.	965.	518.	1028.	553.	1050.	566.	1323.	717.
25	14.47	934.	501.	949.	509.	1012.	544.	1034.	557.	1312.	711.
26	14.32	889.	476.	903.	484.	967.	520.	990.	532.	1283.	695.
27	14.74	889.	476.	893.	479.	960.	516.	983.	529.	1288.	698.
28	14.73	929.	498.	945.	507.	1010.	543.	1033.	556.	1318.	714.

Pin No. EBR-II	Peak kW/ft	Peak Temperatures Coolant F C	Clad Outside F C	Clad Inside F C	Fuel Surface F C	Fuel Centerline F C
29	14.71	951. - 511.	965. - 518.	1029. - 554.	1052. - 566.	1327. - 719.
30	14.70	956. - 513.	969. - 520.	1032. - 556.	1055. - 568.	1327. - 719.
31	14.70	955. - 513.	968. - 520.	1032. - 555.	1054. - 568.	1327. - 719.
32	14.55	953. - 512.	966. - 519.	1029. - 554.	1051. - 566.	1322. - 716.
33	14.42	947. - 508.	961. - 516.	1023. - 551.	1045. - 563.	1316. - 713.
34	14.29	922. - 495.	937. - 503.	1000. - 538.	1023. - 550.	1302. - 706.
35	14.15	882. - 472.	885. - 474.	949. - 510.	972. - 522.	1268. - 687.
36	14.63	895. - 480.	909. - 487.	974. - 524.	997. - 536.	1294. - 701.
37	14.63	937. - 503.	952. - 511.	1016. - 546.	1038. - 559.	1318. - 714.
38	14.61	951. - 511.	965. - 518.	1028. - 554.	1051. - 566.	1323. - 717.
39	14.55	953. - 512.	966. - 519.	1029. - 554.	1051. - 566.	1322. - 717.
40	14.48	952. - 511.	965. - 518.	1028. - 553.	1050. - 565.	1319. - 715.
41	14.38	948. - 509.	961. - 516.	1023. - 551.	1045. - 563.	1315. - 713.
42	14.25	931. - 499.	945. - 507.	1008. - 542.	1030. - 554.	1304. - 707.
43	14.10	889. - 476.	901. - 483.	965. - 518.	987. - 530.	1275. - 691.
44	14.53	897. - 481.	909. - 487.	974. - 523.	997. - 536.	1291. - 699.
45	14.47	935. - 501.	949. - 510.	1012. - 545.	1035. - 557.	1312. - 711.
46	14.42	947. - 508.	961. - 516.	1023. - 551.	1045. - 563.	1316. - 713.
47	14.37	948. - 509.	961. - 516.	1023. - 551.	1045. - 563.	1314. - 712.
48	14.26	944. - 507.	958. - 514.	1020. - 549.	1042. - 561.	1310. - 710.
49	14.16	930. - 499.	944. - 507.	1006. - 541.	1028. - 553.	1301. - 705.
50	14.07	891. - 477.	902. - 483.	965. - 519.	987. - 531.	1275. - 690.
51	14.34	894. - 479.	905. - 485.	970. - 521.	992. - 533.	1284. - 695.
52	14.29	923. - 495.	938. - 503.	1001. - 538.	1023. - 551.	1302. - 706.
53	14.23	931. - 499.	945. - 507.	1008. - 542.	1030. - 554.	1304. - 706.
54	14.16	930. - 499.	944. - 507.	1006. - 541.	1028. - 553.	1301. - 705.
55	14.06	919. - 493.	934. - 501.	996. - 536.	1018. - 548.	1294. - 701.
56	13.96	889. - 476.	899. - 482.	962. - 517.	984. - 529.	1271. - 688.
57	14.15	887. - 475.	888. - 475.	952. - 511.	974. - 523.	1269. - 687.
58	14.10	892. - 478.	902. - 484.	966. - 519.	988. - 531.	1276. - 691.

Pin No. EBR-II	Peak kW/ft	Peak Temperatures									
		Coolant		Clad Outside		Clad Inside		Fuel Surface		Fuel Centerline	
		F	C	F	C	F	C	F	C	F	C
59	14.05	893.	479.	903.	484.	966.	519.	988.	531.	1274.	690.
60	13.94	890.	477.	900.	482.	963.	517.	985.	529.	1270.	688.
61	13.84	883.	473.	883.	473.	946.	508.	968.	520.	1258.	681.

Table B-16 Maximum Heat Rating and Temperatures, Mark-VA Fuel Pins, Position 4E2, Beginning-of-Life-Conditions

		Peak Temperatures				
		Coolant	Clad Outside	Clad Inside	Fuel Surface	Fuel Centerline
Pin No. EBR-II	Peak kW/ft	F C	F C	F C	F C	F C
1	13.79	916. - 491.	923. - 495.	984. - 529.	1005. - 541.	1277. - 692.
2	13.66	927. - 497.	941. - 505.	1001. - 539.	1022. - 550.	1285. - 696.
3	13.53	928. - 498.	942. - 505.	1001. - 538.	1022. - 550.	1282. - 694.
4	13.45	924. - 495.	937. - 503.	997. - 536.	1017. - 547.	1277. - 692.
5	13.36	911. - 488.	916. - 491.	975. - 524.	996. - 535.	1262. - 683.
6	13.73	929. - 498.	943. - 506.	1003. - 540.	1024. - 551.	1288. - 698.
7	13.60	969. - 521.	984. - 529.	1042. - 561.	1063. - 573.	1313. - 711.
8	13.45	978. - 526.	992. - 533.	1049. - 565.	1070. - 576.	1314. - 712.
9	13.35	976. - 524.	989. - 532.	1047. - 564.	1067. - 575.	1309. - 710.
10	13.27	963. - 517.	977. - 525.	1034. - 557.	1054. - 568.	1300. - 704.
11	13.18	920. - 493.	934. - 501.	992. - 533.	1012. - 544.	1268. - 686.
12	13.65	931. - 499.	945. - 507.	1004. - 540.	1025. - 552.	1286. - 697.
13	13.52	979. - 526.	993. - 534.	1051. - 566.	1071. - 577.	1316. - 713.
14	13.39	993. - 534.	1005. - 541.	1062. - 572.	1083. - 584.	1320. - 716.
15	13.26	993. - 534.	1005. - 540.	1061. - 572.	1081. - 583.	1316. - 713.
16	13.17	989. - 531.	1001. - 538.	1057. - 569.	1077. - 580.	1311. - 711.
17	13.09	971. - 522.	984. - 529.	1040. - 560.	1060. - 571.	1299. - 704.
18	13.00	920. - 493.	933. - 501.	990. - 532.	1010. - 543.	1262. - 683.
19	13.56	928. - 498.	941. - 505.	1001. - 538.	1022. - 550.	1282. - 694.
20	13.44	978. - 525.	991. - 533.	1049. - 565.	1069. - 576.	1313. - 712.
21	13.31	994. - 534.	1005. - 541.	1062. - 572.	1082. - 583.	1318. - 714.
22	13.18	994. - 534.	1005. - 541.	1061. - 572.	1081. - 583.	1314. - 712.
23	13.07	991. - 533.	1003. - 539.	1058. - 570.	1078. - 581.	1310. - 710.
24	12.98	987. - 530.	998. - 537.	1054. - 568.	1073. - 578.	1305. - 707.
25	12.92	968. - 520.	980. - 527.	1036. - 558.	1055. - 569.	1292. - 700.
26	12.87	916. - 491.	929. - 498.	985. - 530.	1005. - 541.	1256. - 680.
27	13.45	919. - 493.	921. - 494.	981. - 527.	1001. - 539.	1266. - 686.
28	13.34	966. - 519.	979. - 526.	1037. - 558.	1057. - 569.	1303. - 706.

Pin No. EBR-II	Peak kW/ft	Peak Temperatures									
		Coolant		Clad Outside		Clad Inside		Fuel Surface		Fuel Centerline	
		F	C	F	C	F	C	F	C	F	C
29	13.22	989.	532.	1001.	539.	1058.	570.	1078.	581.	1313.	712.
30	13.10	992.	533.	1003.	540.	1059.	571.	1079.	581.	1311.	711.
31	12.97	990.	532.	1001.	538.	1056.	569.	1076.	580.	1306.	708.
32	12.90	988.	531.	999.	537.	1054.	568.	1073.	579.	1303.	706.
33	12.85	982.	528.	993.	534.	1048.	565.	1068.	575.	1299.	704.
34	12.79	955.	513.	968.	520.	1023.	551.	1043.	561.	1281.	694.
35	12.72	909.	487.	909.	487.	965.	518.	984.	529.	1239.	671.
36	13.24	926.	497.	938.	503.	996.	536.	1016.	547.	1271.	689.
37	13.13	972.	522.	985.	530.	1042.	561.	1062.	572.	1301.	705.
38	13.00	988.	531.	999.	537.	1055.	568.	1074.	579.	1306.	708.
39	12.93	988.	531.	999.	537.	1055.	568.	1074.	579.	1304.	707.
40	12.87	987.	530.	998.	536.	1052.	567.	1072.	578.	1301.	705.
41	12.77	982.	528.	994.	534.	1048.	565.	1067.	575.	1296.	702.
42	12.72	964.	518.	976.	525.	1031.	555.	1050.	566.	1285.	696.
43	12.66	917.	492.	927.	497.	982.	528.	1002.	539.	1249.	676.
44	13.01	928.	498.	937.	503.	994.	535.	1014.	545.	1264.	685.
45	12.96	969.	521.	982.	528.	1038.	559.	1057.	570.	1294.	701.
46	12.89	983.	528.	994.	535.	1050.	565.	1069.	576.	1300.	705.
47	12.83	983.	528.	994.	535.	1049.	565.	1068.	576.	1298.	704.
48	12.73	979.	526.	991.	533.	1045.	563.	1065.	574.	1294.	701.
49	12.66	963.	517.	975.	524.	1030.	554.	1049.	565.	1282.	695.
50	12.58	919.	493.	928.	498.	983.	529.	1002.	539.	1247.	675.
51	12.92	925.	496.	933.	501.	990.	532.	1009.	543.	1259.	682.
52	12.85	957.	514.	970.	521.	1026.	552.	1045.	563.	1284.	696.
53	12.79	965.	518.	978.	526.	1033.	556.	1052.	567.	1287.	697.
54	12.72	964.	518.	976.	525.	1031.	555.	1050.	566.	1285.	696.
55	12.63	952.	511.	965.	518.	1020.	549.	1039.	559.	1275.	691.
56	12.55	917.	492.	926.	496.	981.	527.	1000.	538.	1245.	674.
57	12.81	917.	491.	917.	491.	970.	521.	989.	532.	1244.	673.
58	12.73	922.	494.	930.	499.	986.	530.	1005.	540.	1253.	678.

Pin No. EBR-II	Peak kW/ft	Peak Temperatures									
		Coolant		Clad Outside		Clad Inside		Fuel Surface		Fuel Centerline	
		F	C	F	C	F	C	F	C	F	C
59	12.68	923.	495.	930.	499.	986.	530.	1005.	541.	1251.	677.
60	12.59	920.	493.	927.	497.	982.	528.	1001.	539.	1247.	675.
61	12.51	911.	489.	911.	489.	963.	517.	982.	528.	1233.	667.

Table B-17 Maximum Heat Rating and Temperatures, Mark-VA Fuel Pins, Position 5E2, Beginning-of-Life-Conditions

		Peak Temperatures				
		Coolant	Clad Outside	Clad Inside	Fuel Surface	Fuel Centerline
Pin No. EBR-II	Peak kW/ft	F C	F C	F C	F C	F C
1	11.07	858. - 459.	867. - 464.	917. - 492.	934. - 501.	1172. - 633.
3	11.40	867. - 464.	880. - 471.	932. - 500.	949. - 509.	1189. - 643.
5	11.66	859. - 460.	872. - 467.	925. - 496.	943. - 506.	1193. - 645.
7	11.29	886. - 474.	900. - 482.	951. - 510.	968. - 520.	1199. - 649.
9	11.58	896. - 480.	910. - 488.	962. - 517.	980. - 526.	1213. - 656.
11	11.84	874. - 468.	889. - 476.	943. - 506.	961. - 516.	1209. - 654.
13	11.33	891. - 477.	905. - 485.	956. - 513.	973. - 523.	1203. - 651.
15	11.62	908. - 486.	921. - 494.	972. - 522.	990. - 532.	1220. - 660.
17	11.88	903. - 484.	917. - 492.	970. - 521.	988. - 531.	1226. - 663.
19	11.14	856. - 458.	856. - 458.	904. - 484.	921. - 494.	1166. - 630.
21	11.51	903. - 484.	916. - 491.	967. - 520.	985. - 529.	1214. - 656.
23	11.81	911. - 488.	924. - 496.	976. - 525.	994. - 534.	1226. - 663.
25	12.10	903. - 484.	918. - 492.	971. - 522.	990. - 532.	1232. - 667.
27	11.14	850. - 455.	852. - 456.	904. - 484.	921. - 494.	1169. - 632.
29	11.51	903. - 484.	917. - 492.	968. - 520.	986. - 530.	1215. - 657.
31	11.88	914. - 490.	927. - 497.	979. - 526.	997. - 536.	1230. - 665.
33	12.21	916. - 491.	930. - 499.	984. - 529.	1002. - 539.	1242. - 672.
35	12.54	861. - 461.	870. - 466.	928. - 498.	948. - 509.	1220. - 660.
37	11.51	893. - 478.	907. - 486.	959. - 515.	976. - 525.	1210. - 654.
39	11.88	913. - 489.	926. - 497.	979. - 526.	996. - 536.	1229. - 665.
41	12.32	917. - 492.	932. - 500.	986. - 530.	1005. - 540.	1245. - 674.
43	12.65	867. - 464.	871. - 466.	929. - 498.	949. - 509.	1220. - 660.
45	11.70	898. - 481.	913. - 489.	965. - 518.	983. - 528.	1218. - 659.
47	12.14	916. - 491.	930. - 499.	984. - 529.	1002. - 539.	1239. - 671.
49	12.54	910. - 488.	925. - 496.	981. - 527.	1000. - 538.	1249. - 676.
51	11.73	869. - 465.	884. - 473.	938. - 503.	956. - 513.	1205. - 651.
53	12.14	905. - 485.	920. - 493.	974. - 523.	992. - 533.	1234. - 668.
55	12.54	905. - 485.	921. - 494.	977. - 525.	996. - 536.	1247. - 675.

Pin No. EBR-II	Peak kW/ft	Peak Temperatures									
		Coolant		Clad Outside		Clad Inside		Fuel Surface		Fuel Centerline	
		F	C	F	C	F	C	F	C	F	C
57	11.95	854.	457.	870.	466.	925.	496.	944.	507.	1203.	650.
59	12.39	874.	468.	889.	476.	946.	508.	965.	518.	1223.	662.
61	12.80	868.	464.	884.	473.	943.	506.	963.	517.	1233.	667.

Table B-18 Maximum Heat Rating and Temperatures, Mark-VA Fuel Pins, Position 6E3, Beginning-of-Life-Conditions

		Peak Temperatures				
		Coolant	Clad Outside	Clad Inside	Fuel Surface	Fuel Centerline
Pin No. EBR-II	Peak kW/ft	F C	F C	F C	F C	F C
1	10.61	902. - 483.	907. - 486.	954. - 512.	969. - 521.	1180. - 638.
2	10.49	913. - 490.	924. - 496.	970. - 521.	985. - 530.	1190. - 643.
3	10.38	913. - 489.	923. - 495.	969. - 521.	984. - 529.	1186. - 641.
4	10.23	908. - 487.	918. - 492.	964. - 518.	978. - 526.	1179. - 637.
5	10.08	897. - 481.	898. - 481.	942. - 506.	957. - 514.	1159. - 626.
6	10.56	916. - 491.	926. - 497.	973. - 523.	988. - 531.	1193. - 645.
7	10.45	954. - 512.	965. - 518.	1010. - 543.	1025. - 552.	1220. - 660.
8	10.33	962. - 516.	972. - 522.	1016. - 547.	1031. - 555.	1221. - 661.
9	10.19	958. - 515.	968. - 520.	1012. - 544.	1027. - 553.	1215. - 657.
10	10.05	945. - 507.	955. - 513.	999. - 537.	1013. - 545.	1202. - 650.
11	9.90	905. - 485.	914. - 490.	958. - 514.	972. - 522.	1167. - 630.
12	10.51	918. - 492.	928. - 498.	974. - 523.	989. - 532.	1193. - 645.
13	10.39	963. - 517.	973. - 523.	1018. - 548.	1034. - 556.	1224. - 662.
14	10.27	976. - 524.	985. - 529.	1029. - 554.	1044. - 562.	1229. - 665.
15	10.17	975. - 524.	983. - 528.	1027. - 553.	1042. - 561.	1225. - 663.
16	10.01	969. - 521.	978. - 526.	1021. - 549.	1036. - 558.	1217. - 658.
17	9.87	951. - 511.	961. - 516.	1003. - 540.	1018. - 548.	1201. - 650.
18	9.71	906. - 486.	913. - 490.	956. - 513.	970. - 521.	1161. - 627.
19	10.42	915. - 490.	925. - 496.	971. - 521.	986. - 530.	1188. - 642.
20	10.32	962. - 517.	972. - 522.	1016. - 547.	1032. - 555.	1221. - 661.
21	10.23	977. - 525.	985. - 529.	1029. - 554.	1044. - 562.	1228. - 664.
22	10.11	976. - 525.	984. - 529.	1027. - 553.	1042. - 561.	1224. - 662.
23	9.98	973. - 523.	981. - 527.	1024. - 551.	1038. - 559.	1218. - 659.
24	9.83	967. - 520.	976. - 524.	1018. - 548.	1032. - 556.	1211. - 655.
25	9.75	949. - 509.	958. - 514.	1000. - 538.	1014. - 546.	1196. - 647.
26	9.67	903. - 484.	910. - 488.	953. - 512.	967. - 519.	1158. - 625.
27	10.32	906. - 485.	906. - 485.	952. - 511.	966. - 519.	1171. - 633.
28	10.23	950. - 510.	961. - 516.	1005. - 540.	1020. - 549.	1211. - 655.

Pin No. EBR-II	Peak kW/ft	Peak Temperatures Coolant F C	Clad Outside F C	Clad Inside F C	Fuel Surface F C	Fuel Centerline F C
29	10.13	972. - 522.	981. - 527.	1025. - 551.	1040. - 560.	1223. - 662.
30	10.04	975. - 524.	983. - 528.	1026. - 552.	1040. - 560.	1221. - 661.
31	9.94	973. - 523.	981. - 527.	1023. - 551.	1038. - 559.	1217. - 658.
32	9.86	970. - 521.	978. - 525.	1020. - 549.	1034. - 557.	1213. - 656.
33	9.79	963. - 517.	972. - 522.	1014. - 545.	1028. - 553.	1207. - 653.
34	9.70	937. - 503.	947. - 509.	989. - 532.	1004. - 540.	1187. - 642.
35	9.62	897. - 480.	897. - 480.	935. - 502.	949. - 510.	1143. - 617.
36	10.13	913. - 489.	921. - 494.	966. - 519.	981. - 527.	1178. - 637.
37	10.14	957. - 514.	966. - 519.	1010. - 543.	1025. - 552.	1212. - 656.
38	9.94	971. - 522.	979. - 526.	1022. - 550.	1036. - 558.	1216. - 658.
39	9.92	972. - 522.	979. - 526.	1022. - 550.	1037. - 558.	1215. - 657.
40	9.88	970. - 521.	978. - 525.	1020. - 549.	1035. - 557.	1213. - 656.
41	9.81	966. - 519.	974. - 523.	1016. - 546.	1030. - 555.	1209. - 654.
42	9.73	948. - 509.	957. - 514.	999. - 537.	1013. - 545.	1195. - 646.
43	9.65	904. - 485.	910. - 488.	953. - 512.	967. - 519.	1157. - 625.
44	9.95	915. - 490.	921. - 494.	964. - 518.	979. - 526.	1172. - 633.
45	9.92	954. - 512.	963. - 517.	1006. - 541.	1020. - 549.	1204. - 651.
46	9.90	967. - 519.	975. - 524.	1017. - 547.	1032. - 556.	1212. - 656.
47	9.88	967. - 520.	975. - 524.	1018. - 548.	1032. - 556.	1212. - 655.
48	9.81	964. - 518.	972. - 522.	1014. - 546.	1029. - 554.	1208. - 653.
49	9.75	948. - 509.	957. - 514.	1000. - 538.	1014. - 546.	1196. - 647.
50	9.69	907. - 486.	913. - 489.	955. - 513.	969. - 521.	1160. - 626.
51	9.90	911. - 489.	917. - 492.	960. - 516.	975. - 524.	1168. - 631.
52	9.88	942. - 506.	952. - 511.	995. - 535.	1009. - 543.	1195. - 646.
53	9.86	951. - 510.	960. - 516.	1003. - 539.	1017. - 547.	1201. - 649.
54	9.81	950. - 510.	959. - 515.	1001. - 539.	1016. - 547.	1199. - 648.
55	9.75	939. - 504.	949. - 509.	991. - 533.	1005. - 541.	1190. - 643.
56	9.69	905. - 485.	911. - 488.	954. - 512.	968. - 520.	1159. - 626.
57	9.86	904. - 484.	904. - 484.	942. - 506.	956. - 513.	1153. - 623.
58	9.84	909. - 487.	914. - 490.	958. - 514.	972. - 522.	1165. - 629.

Pin No. EBR-II	Peak kW/ft	Peak Temperatures									
		Coolant		Clad Outside		Clad Inside		Fuel Surface		Fuel Centerline	
		F	C	F	C	F	C	F	C	F	C
59	9.81	910.	488.	915.	491.	959.	515.	973.	523.	1165.	629.
60	9.75	907.	486.	912.	489.	956.	513.	970.	521.	1161.	627.
61	9.69	900.	482.	900.	482.	938.	503.	951.	511.	1146.	619.

Table B-19 Maximum Heat Rating and Temperatures, Mark-VA Fuel Pins, Position 6F1, Beginning-of-Life-Conditions

		Peak Temperatures									
		Coolant		Clad Outside		Clad Inside		Fuel Surface		Fuel Centerline	
Pin No. EBR-II	Peak kW/ft	F	C	F	C	F	C	F	C	F	C
1	9.33	905.	485.	905.	485.	946.	508.	960.	515.	1144.	618.
2	9.34	914.	490.	923.	495.	964.	518.	978.	526.	1158.	626.
3	9.36	916.	491.	925.	496.	966.	519.	980.	527.	1160.	627.
4	9.34	913.	490.	923.	495.	964.	518.	977.	525.	1158.	626.
5	9.32	903.	484.	903.	484.	944.	507.	958.	514.	1142.	617.
6	9.19	913.	489.	922.	494.	962.	517.	975.	524.	1153.	623.
7	9.18	951.	511.	960.	516.	1000.	538.	1014.	545.	1184.	640.
8	9.21	962.	516.	970.	521.	1010.	543.	1023.	551.	1192.	645.
9	9.21	962.	516.	970.	521.	1010.	543.	1023.	551.	1192.	645.
10	9.19	951.	510.	960.	516.	1000.	538.	1013.	545.	1184.	640.
11	9.19	911.	488.	920.	493.	960.	516.	974.	523.	1152.	622.
12	9.05	915.	491.	922.	494.	962.	516.	975.	524.	1149.	621.
13	9.06	959.	515.	967.	519.	1006.	541.	1019.	548.	1186.	641.
14	9.08	973.	523.	981.	527.	1019.	549.	1033.	556.	1196.	647.
15	9.08	975.	524.	983.	528.	1021.	550.	1035.	557.	1198.	648.
16	9.07	973.	523.	981.	527.	1019.	549.	1033.	556.	1196.	647.
17	9.06	958.	515.	967.	519.	1005.	541.	1019.	548.	1185.	641.
18	9.04	911.	489.	920.	493.	960.	515.	973.	523.	1148.	620.
19	9.03	913.	489.	919.	493.	958.	515.	972.	522.	1147.	619.
20	8.98	956.	514.	965.	518.	1003.	540.	1017.	547.	1182.	639.
21	8.93	972.	522.	979.	526.	1017.	547.	1031.	555.	1191.	644.
22	8.94	975.	524.	981.	527.	1019.	548.	1032.	556.	1193.	645.
23	8.94	975.	524.	981.	527.	1019.	548.	1032.	556.	1193.	645.
24	8.93	972.	522.	979.	526.	1017.	547.	1031.	555.	1191.	644.
25	8.98	956.	513.	964.	518.	1003.	539.	1016.	547.	1182.	639.
26	9.03	908.	487.	917.	492.	957.	514.	970.	521.	1146.	619.
27	9.01	905.	485.	905.	485.	940.	505.	953.	512.	1131.	611.
28	8.96	946.	508.	954.	512.	993.	534.	1006.	541.	1174.	634.

Pin No. EBR-II	Peak kW/ft	Peak Temperatures Coolant F C	Clad Outside F C	Clad Inside F C	Fuel Surface F C	Fuel Centerline F C
29	8.92	969. - 520.	976. - 524.	1014. - 546.	1027. - 553.	1189. - 643.
30	8.87	973. - 523.	979. - 526.	1017. - 547.	1030. - 554.	1189. - 643.
31	8.82	973. - 523.	979. - 526.	1016. - 547.	1030. - 554.	1188. - 642.
32	8.87	973. - 523.	979. - 526.	1017. - 547.	1030. - 554.	1189. - 643.
33	8.92	969. - 521.	976. - 525.	1014. - 546.	1027. - 553.	1189. - 643.
34	8.98	945. - 507.	954. - 512.	993. - 534.	1006. - 541.	1174. - 635.
35	9.03	900. - 482.	900. - 482.	938. - 504.	951. - 511.	1131. - 611.
36	8.94	911. - 488.	917. - 491.	956. - 513.	969. - 520.	1143. - 617.
37	8.90	954. - 512.	962. - 517.	1000. - 538.	1013. - 545.	1178. - 637.
38	8.84	969. - 521.	976. - 525.	1014. - 545.	1027. - 553.	1187. - 641.
39	8.83	971. - 522.	978. - 525.	1015. - 546.	1028. - 554.	1187. - 642.
40	8.83	971. - 522.	978. - 526.	1015. - 546.	1028. - 554.	1187. - 642.
41	8.86	969. - 521.	976. - 525.	1014. - 546.	1027. - 553.	1187. - 642.
42	8.83	954. - 512.	962. - 517.	1000. - 538.	1013. - 545.	1176. - 635.
43	8.97	908. - 487.	916. - 491.	955. - 513.	968. - 520.	1143. - 617.
44	8.87	913. - 489.	917. - 492.	956. - 514.	969. - 521.	1141. - 616.
45	8.86	953. - 512.	961. - 516.	999. - 537.	1012. - 545.	1176. - 636.
46	8.84	967. - 519.	974. - 523.	1012. - 544.	1025. - 552.	1185. - 641.
47	8.83	968. - 520.	975. - 524.	1013. - 545.	1026. - 552.	1185. - 641.
48	8.85	967. - 519.	974. - 523.	1012. - 544.	1025. - 552.	1186. - 641.
49	8.89	953. - 512.	961. - 516.	1000. - 538.	1013. - 545.	1177. - 636.
50	8.92	910. - 488.	917. - 492.	956. - 513.	969. - 520.	1142. - 617.
51	8.87	910. - 488.	915. - 490.	954. - 512.	967. - 519.	1139. - 615.
52	8.86	943. - 506.	951. - 511.	990. - 532.	1003. - 539.	1169. - 632.
53	8.84	952. - 511.	960. - 516.	998. - 537.	1011. - 544.	1175. - 635.
54	8.84	952. - 511.	960. - 516.	999. - 537.	1012. - 544.	1175. - 635.
55	8.88	943. - 506.	952. - 511.	990. - 532.	1003. - 540.	1170. - 632.
56	8.91	907. - 486.	914. - 490.	954. - 512.	967. - 519.	1140. - 616.
57	8.87	902. - 484.	902. - 484.	936. - 502.	949. - 509.	1125. - 607.
58	8.85	908. - 487.	914. - 490.	953. - 512.	966. - 519.	1138. - 615.

Pin No. EBR-II	Peak kW/ft	Peak Temperatures: Coolant F - C	Clad Outside F - C	Clad Inside F - C	Fuel Surface F - C	Fuel Centerline F - C
59	8.84	910. - 488.	916. - 491.	955. - 513.	967. - 520.	1139. - 615.
60	8.87	908. - 487.	914. - 490.	953. - 512.	966. - 519.	1139. - 615.
61	8.90	900. - 482.	900. - 482.	936. - 502.	949. - 509.	1126. - 608.

Appendix B References

B.1 D. C. Cutforth, et. al., "BURNOUT - Software to Calculate Fuel Pin Depletion in the EBR-II Core," Argonne National Laboratory, June 1991.

B.2 K. L. Basehore and N. E. Todreas, "SUPERENERGY-2: A Multiassembly, Steady-State Computer Code for LMFBR Core Thermal-Hydraulic Analysis," PNL-3379, COO-2245-57TR (August 1980).

B.3 S. K. Cheng and N. E. Todreas, "Hydrodynamics Models and Correlations for Bare and Wire Wrapped Hexagonal Rod Bundles - Bundle Friction Factors, Subchannel Friction Factors, and Mixing Parameters," Nuclear Engineering and Design (1986) 227-251.

B.4 M. S. Kazimi and M. D. Carelli, "Heat Transfer Correlations for Analysis of CRBRP Assemblies," Westinghouse Electric Corporation, CRBRP-ARD-0034, November 1976.

C APPENDIX: POWER AND FLOW DATA FROM THE OFF-NORMAL TRANSIENT ANALYSES

As discussed in Section 9.6, the off-normal transient safety analysis of the Mark-V and Mark-VA fuels consists of evaluation of the transients listed in Section 7.5. All transient analyses were performed using the SASSYS code except the analysis of event AN-5, for which the LIFE-METAL code was used. This appendix provides power and, for loss-of-flow (LOF) events, flow and power/flow ratio results for the events evaluated by SASSYS.

The specifications for the event analyses include the following:

- Nominal power = 62.5 MWt
  - -- Initial power for loss-of-flow events is 105% nominal power (65.625 MWt).
  - -- Initial power for transient overpower events, other than startup events, is 40% nominal power (25 MWt).
  - -- Initial power for startup events is 10^{-6} nominal power (62.5 Wt).
- Nominal flow = 9000 gpm @ 800°F (0.57 m^3/s @ 427°C, or 482 kg/s)
- Limiting Safety System Settings (Section 9.2):
  - -- Reactor outlet flow = 88% nominal
  - -- Reactor power = 115% nominal
  - -- Subassembly outlet temperature = T_{inlet} + 115% of the ΔT at nominal power
  - -- Period = 17 s
- Shutdown reactivity = -3.7$ in 0.45 s
- ANSI LWR decay power curve
- Zero auxiliary pump capacity
- Pump coastdown:
  - -- Clutch breaker trip: coastdown time of 23 s for pump 1, 25 s for pump 2
  - -- M-G output breaker trip: coastdown time of 32 s

- -- M-G input breaker trip: coastdown time of 80 s for pump 1, 88 s for pump 2
- Secondary pump tripped 6 s after scram, unless the initiator is a loss of normal power
- Reactivity insertion: 1¢/s for a single control rod runout
- Peaking factor = 1.26
- Uncertainty factors (Section 4.5):
  - -- Steady-state:
    - Cladding hot channel factor = 1.134
    - Fuel hot channel factor = 1.21
  - -- Transient:
    - Power = 1.07
    - Flow = 1.06
    - Fuel conductivity = 1.21
    - Cladding conductivity = 1.05
    - Film heat transfer coefficient = 1.13
- Mark-V: U-20Pu-10Zr fuel with 18-mil (0.46 mm) thickness of HT9 cladding and fuel slug diameter of 0.168 in. (4.27 mm)
- Mark-VA: U-20Pu-10Zr fuel with 15-mil (0.38 mm) thickness of 316SS cladding and fuel slug diameter of 0.173 in. (4.4 mm)
- Pin Geometry
  - -- Pin outside diameter = 0.23 in. (5.84 mm)
  - -- Wire wrap diameter = 0.042 in. (1.07 mm)
  - -- Wire wrap pitch = 6 in. (0.15 m)

The remainder of this appendix presents tables of normalized power (normalized to nominal power) for all transients analyzed with the SASSYS code. For loss-of-flow events, tables of normalized flow (normalized to nominal flow) and power-to-flow ratio are also given. Plots of the data in all tables are also included. The data shown are from the Mark-V fuel runs; the data for the Mark-VA cases are virtually identical and are not listed separately.

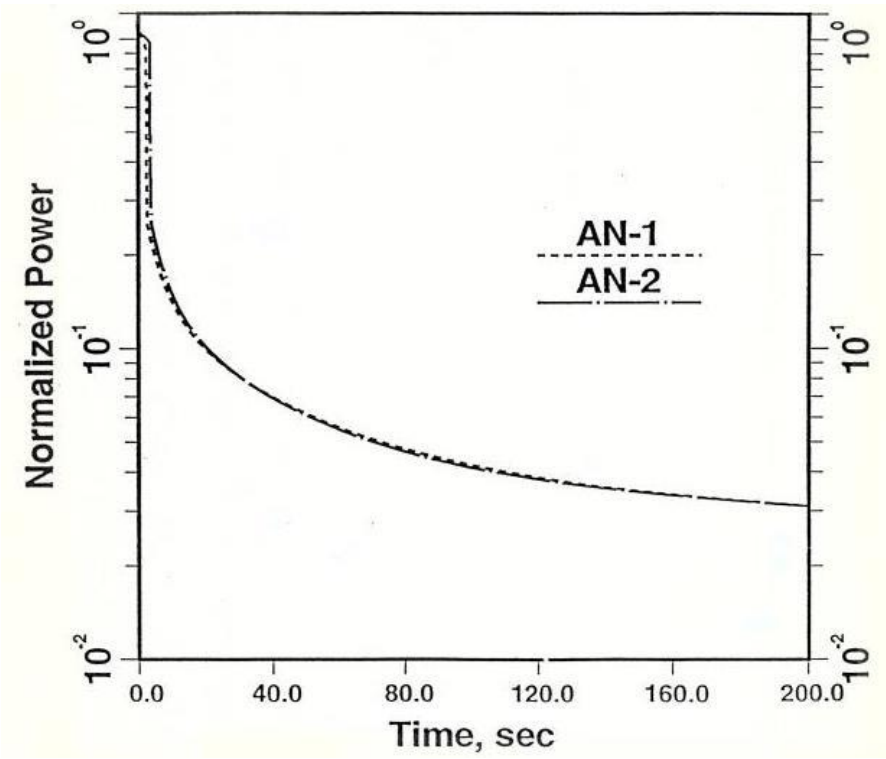

Figure C-1 Power Histories for Anticipated LOF Events in the 6-Row Core

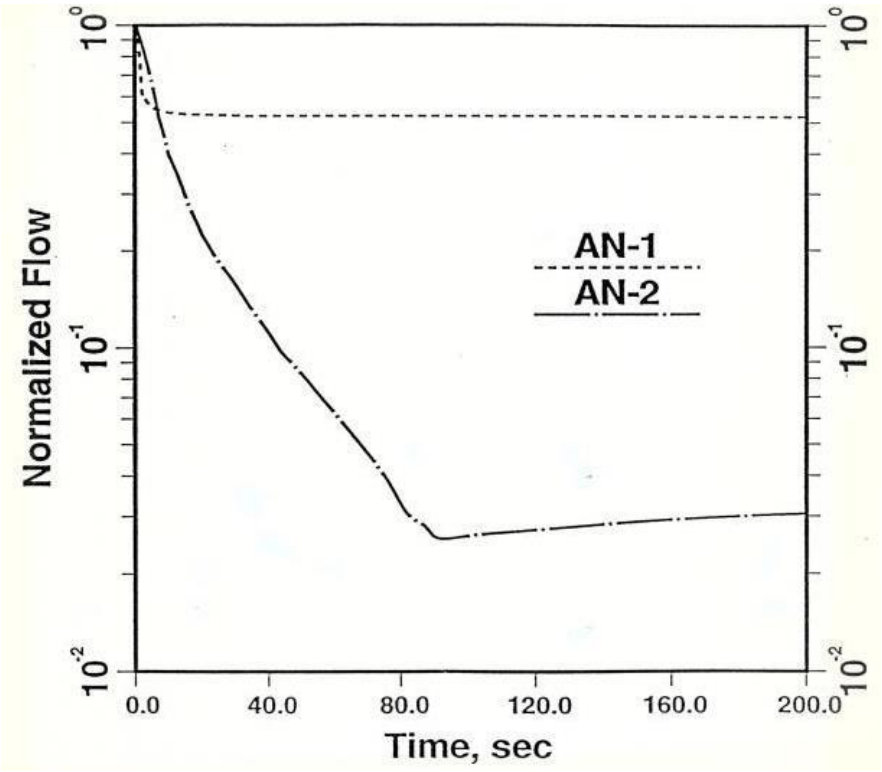

Figure C-2 Flow Histories for Anticipated LOF Events in the 6-Row Core

Table C-1 Power, Flow, and Power/Flow Ratio Histories for the AN-1 Transient

Time (s)	Normalized Power	Normalized Flow	Power/Flow Ratio
0.000	1.0500	1.0000	1.0500
1.000	1.0299	0.9227	1.1162
1.500	1.0105	0.8536	1.1838
2.000	0.9784	0.7590	1.2891
2.400	0.9533	0.6463	1.4750
2.500	0.4528	0.6368	0.7111
2.558	0.3964	0.6356	0.6236
2.645	0.3186	0.6368	0.5002
2.759	0.2648	0.6418	0.4127
3.084	0.2422	0.6487	0.3733
3.584	0.2283	0.6247	0.3654
4.084	0.2164	0.6163	0.3512
5.084	0.1963	0.5996	0.3275
6.084	0.1804	0.5931	0.3041
8.084	0.1565	0.5851	0.2675
10.084	0.1395	0.5786	0.2411
15.084	0.1132	0.5727	0.1977
20.084	0.0977	0.5696	0.1716
25.084	0.0871	0.5677	0.1535
30.084	0.0792	0.5664	0.1399
40.084	0.0680	0.5648	0.1205
50.084	0.0604	0.5649	0.1068
60.084	0.0547	0.5649	0.0968
80.084	0.0468	0.5650	0.0829
100.084	0.0417	0.5649	0.0738
120.084	0.0382	0.5649	0.0676
140.084	0.0357	0.5649	0.0631
160.084	0.0338	0.5649	0.0597
180.084	0.0323	0.5649	0.0571
200.000	0.0311	0.5649	0.0550

Table C-2 Power, Flow, and Power/Flow Ratio Histories for the AN-2 Transient

Time (s)	Normalized Power	Normalized Flow	Power/Flow Ratio
0.000	1.0500	1.0000	1.0500
1.000	1.0409	0.9592	1.0851
2.000	1.0263	0.8942	1.1477
3.000	1.0084	0.8276	1.2185
3.400	0.9999	0.8011	1.2482
3.500	0.5546	0.7943	0.6983
3.532	0.5011	0.7930	0.6319
3.575	0.4431	0.7898	0.5611
3.615	0.4037	0.7871	0.5129
3.661	0.3620	0.7844	0.4615
3.699	0.3266	0.7821	0.4176
3.728	0.3193	0.7802	0.4092
3.823	0.2690	0.7739	0.3476
4.013	0.2490	0.7602	0.3275
4.513	0.2334	0.7228	0.3230
5.013	0.2203	0.6926	0.3181
5.513	0.2089	0.6590	0.3170
6.013	0.1989	0.6259	0.3177
6.513	0.1900	0.5931	0.3204
7.013	0.1822	0.5602	0.3252
8.013	0.1686	0.5096	0.3309
9.013	0.1574	0.4680	0.3364
10.013	0.1480	0.4271	0.3465
12.013	0.1331	0.3763	0.3536
14.013	0.1219	0.3360	0.3626
16.013	0.1130	0.2958	0.3821
18.013	0.1058	0.2652	0.3992
20.013	0.0998	0.2388	0.4181

Time (s)	Normalized Power	Normalized Flow	Power/Flow Ratio
25.013	0.0882	0.1936	0.4559
30.013	0.0798	0.1649	0.4840
35.013	0.0733	0.1376	0.5326
40.013	0.0680	0.1158	0.5877
50.013	0.0601	0.0847	0.7093
60.013	0.0543	0.0632	0.8584
70.013	0.0498	0.0454	1.0960
80.013	0.0463	0.0289	1.6011
100.013	0.0412	0.0101	4.0679
120.013	0.0379	0.0106	3.5823
140.013	0.0355	0.0153	2.3139
160.013	0.0336	0.0198	1.7020
180.013	0.0322	0.0231	1.3937
200.000	0.0310	0.0253	1.2241

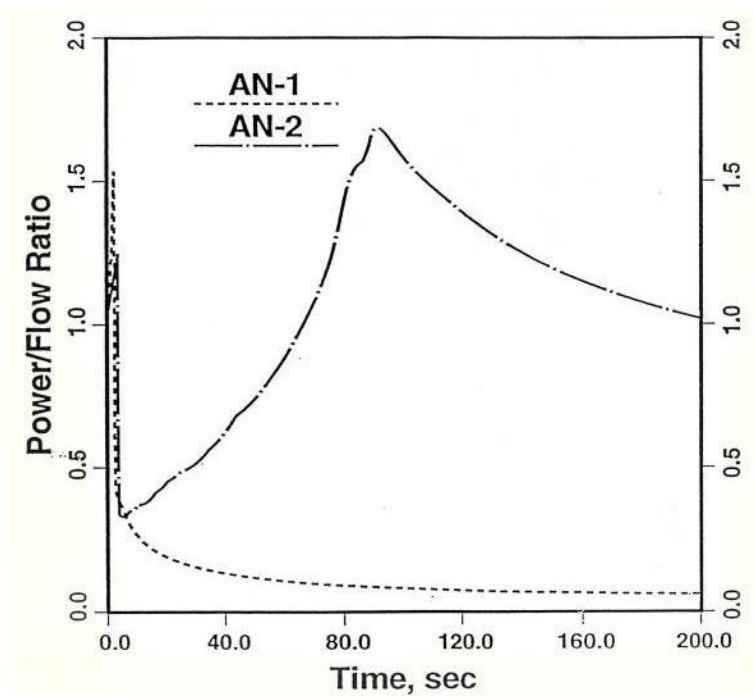

Figure C-3 Power/Flow Ratio Histories for Anticipated LOF Events in the 6-Row Core

Table C-3 Power History for the AN-3 Transient

Time (s)	Normalized Power	Time (s)	Normalized Power
0.00	0.4000	40.00	0.5269
1.00	0.4042	40.03	0.4872
2.00	0.4092	40.08	0.3947
3.00	0.4148	40.11	0.3605
4.00	0.4211	40.16	0.3234
5.00	0.4281	40.20	0.2860
6.00	0.4357	40.24	0.2747
7.00	0.4439	40.32	0.2223
8.00	0.4528	40.54	0.2078
9.00	0.4623	41.04	0.1905
10.00	0.4725	41.54	0.1761
12.00	0.4947	42.04	0.1640
14.00	0.5197	43.04	0.1449
16.00	0.5475	44.04	0.1304
18.00	0.5782	46.04	0.1090
20.00	0.6119	48.04	0.0942
23.00	0.6683	50.04	0.0833
25.00	0.7100	55.04	0.0660
28.00	0.7783	60.04	0.0556
30.00	0.8277	65.04	0.0485
33.00	0.8981	70.00	0.0434
35.00	0.9596		
38.00	1.0674		
39.00	1.1105		
39.40	1.1276		
39.90	1.1495		

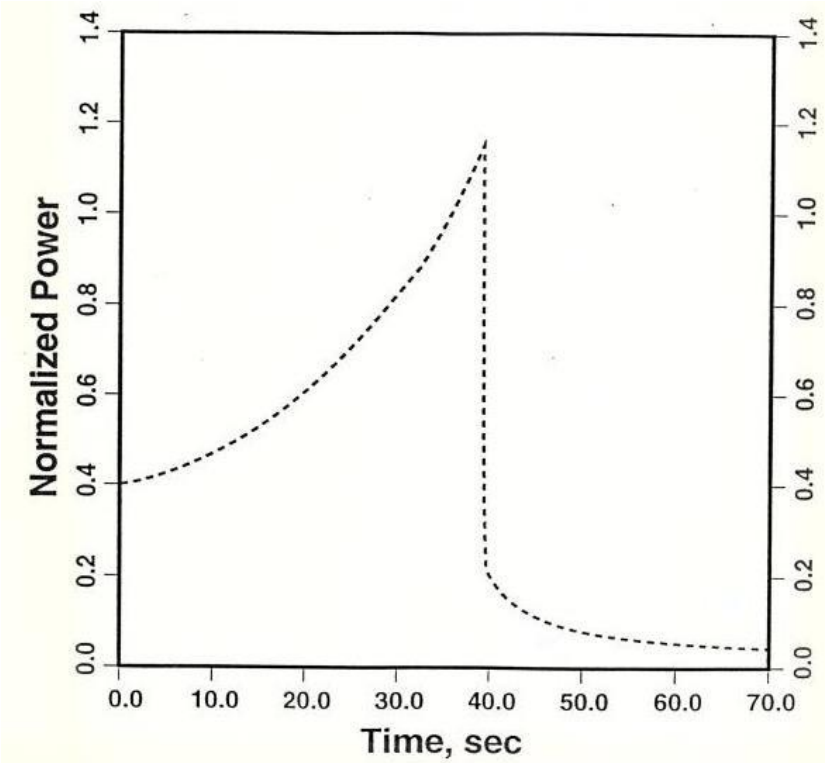

Figure C-4 Power History for Anticipated TOP Event AN-3 in the 6-Row Core

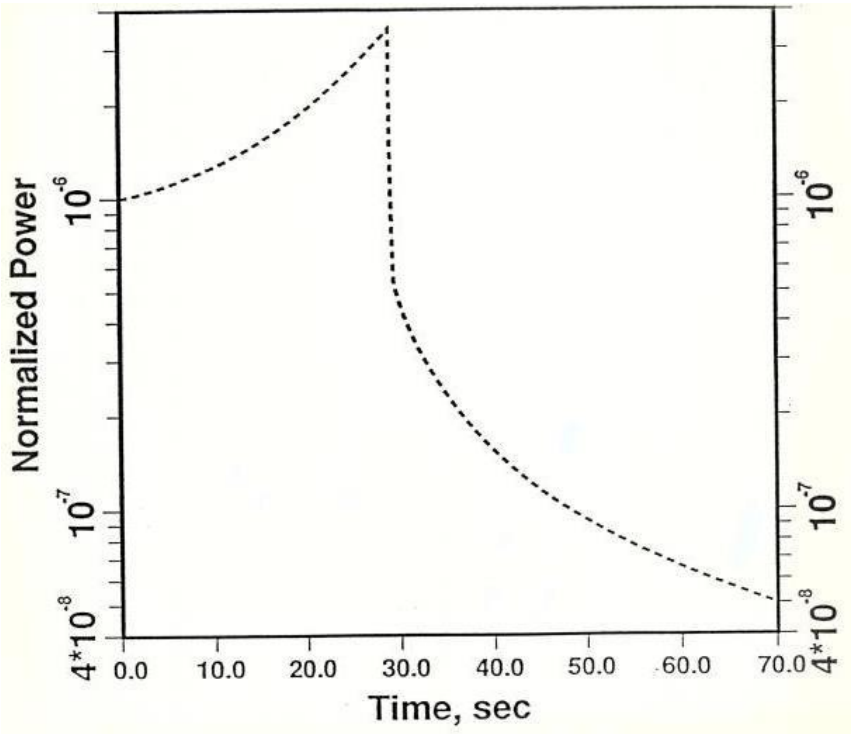

Figure C-5 Power History for Anticipated TOP Event AN-4 in the 6-Row Core

Table C-4 Power History for the AN-4 Transient

Time (s)	Normalized Power	Time (s)	Normalized Power	Time (s)	Normalized Power
0.00	1.0000E-06	19.00	1.8277E-06	30.02	4.5432E-07
0.20	1.0026E-06	20.00	1.9260E-06	30.52	4.1230E-07
0.40	1.0053E-06	21.00	2.0347E-06	31.02	3.7901E-07
0.60	1.0082E-06	22.00	2.1551E-06	32.02	3.2756E-07
0.80	1.0111E-06	23.00	2.2890E-06	33.02	2.8836E-07
1.00	1.0142E-06	24.00	2.4382E-06	35.02	2.3160E-07
1.20	1.0175E-06	25.00	2.6048E-06	40.02	1.5403E-07
1.50	1.0225E-06	26.00	2.7915E-06	45.02	1.1559E-07
2.00	1.0313E-06	27.00	3.0014E-06	50.02	9.2478E-08
3.00	1.0508E-06	28.00	3.2380E-06	60.02	6.5472E-08
4.00	1.0727E-06	28.50	3.3677E-06	69.91	5.0068E-08
5.00	1.0971E-06	28.90	3.4774E-06		
6.00	1.1240E-06	29.00	1.4002E-06		
7.00	1.1536E-06	29.02	1.2862E-06		
8.00	1.1861E-06	29.06	1.0967E-06		
9.00	1.2217E-06	29.10	9.7342E-07		
10.00	1.2606E-06	29.15	8.4685E-07		
11.00	1.3032E-06	29.18	7.4340E-07		
12.00	1.3498E-06	29.21	7.2307E-07		
13.00	1.4007E-06	29.28	6.1575E-07		
14.00	1.4564E-06	29.32	5.7173E-07		
15.00	1.5175E-06	29.42	5.2690E-07		
16.00	1.5844E-06	29.52	5.1211E-07		
17.00	1.6579E-06	29.62	4.9865E-07		
18.00	1.7387E-06	29.82	4.7488E-07		

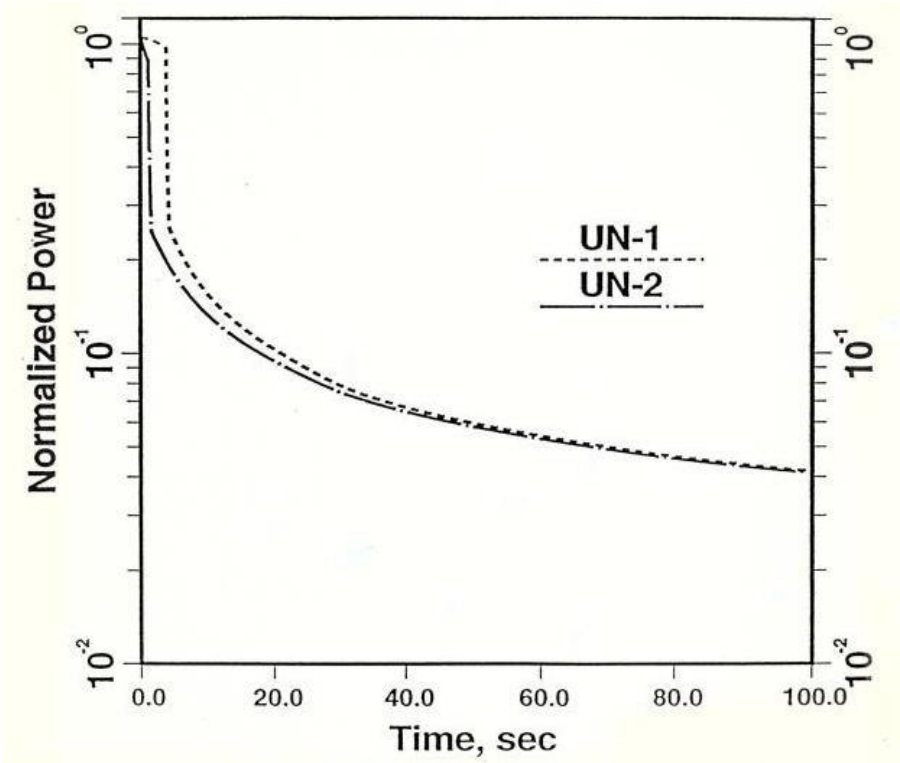

Figure C-6 Power Histories for Unlikely LOF Events in the 6-Row Core

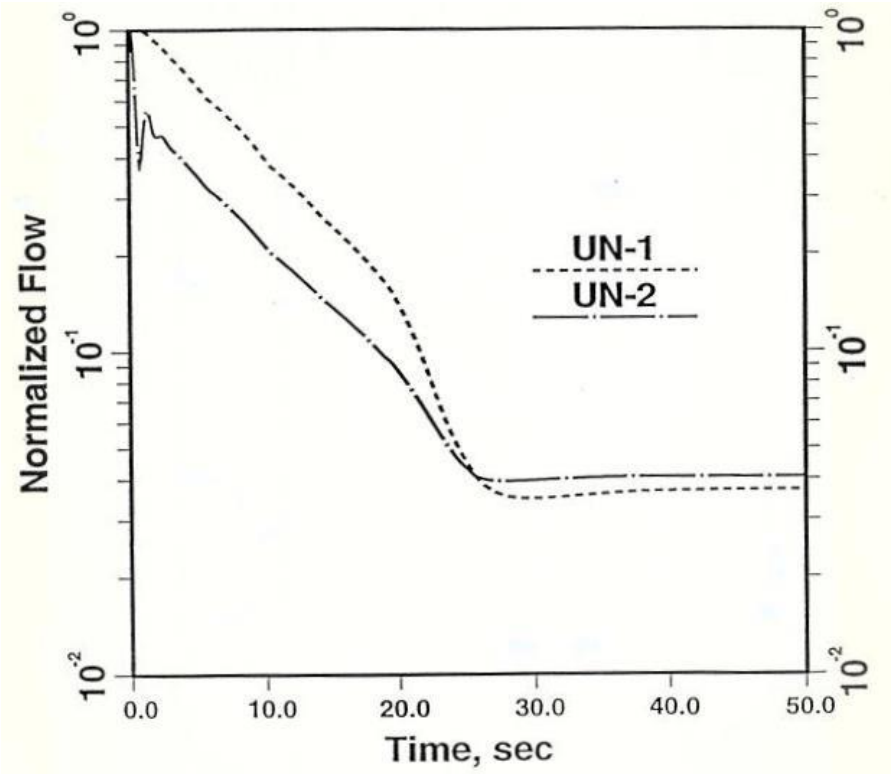

Figure C-7 Flow Histories for Unlikely LOF Events in the 6-Row Core

Table C-5 Power, Flow, and Power/Flow Ratio Histories for the UN 1 Transient

Time (s)	Normalized Power	Normalized Flow	Power/Flow Ratio
0.000	1.0500	1.0000	1.0500
1.000	1.0477	0.9899	1.0583
1.500	1.0434	0.9825	1.0620
2.000	1.0364	0.9411	1.1013
2.500	1.0277	0.9067	1.1334
3.000	1.0181	0.8619	1.1812
3.500	1.0064	0.8168	1.2321
3.900	0.9959	0.7860	1.2670
4.000	0.5534	0.7780	0.7113
4.032	0.5003	0.7765	0.6443
4.075	0.4423	0.7726	0.5725
4.115	0.4028	0.7693	0.5236
4.161	0.3613	0.7660	0.4717
4.198	0.3262	0.7632	0.4274
4.227	0.3191	0.7609	0.4194
4.322	0.2690	0.7533	0.3571
4.357	0.2585	0.7507	0.3443
4.512	0.2487	0.7367	0.3376
4.812	0.2390	0.7074	0.3378
5.012	0.2332	0.6920	0.3370
5.512	0.2202	0.6550	0.3361
6.012	0.2088	0.6148	0.3396
6.512	0.1988	0.5927	0.3354
7.012	0.1900	0.5659	0.3357
7.512	0.1821	0.5401	0.3372
8.012	0.1750	0.5146	0.3402
9.012	0.1628	0.4635	0.3512
10.012	0.1525	0.4127	0.3694
12.012	0.1363	0.3433	0.3971
14.012	0.1242	0.2844	0.4367
16.012	0.1147	0.2378	0.4824
18.012	0.1070	0.1960	0.5461

Time (s)	Normalized Power	Normalized Flow	Power/Flow Ratio
20.012	0.1006	0.1536	0.6553
22.012	0.0950	0.1057	0.8993
24.012	0.0900	0.0698	1.2901
26.012	0.0856	0.0491	1.7437
28.012	0.0817	0.0382	2.1377
30.012	0.0783	0.0321	2.4408
32.012	0.0753	0.0283	2.6638
34.012	0.0727	0.0258	2.8206
36.012	0.0704	0.0241	2.9246
38.012	0.0683	0.0229	2.9824
40.012	0.0664	0.0222	2.9979
42.012	0.0647	0.0218	2.9738
44.012	0.0632	0.0217	2.9167
46.012	0.0617	0.0218	2.8363
48.012	0.0604	0.0220	2.7438
50.012	0.0591	0.0223	2.6466
55.012	0.0563	0.0233	2.4153
60.012	0.0538	0.0243	2.2152
70.012	0.0496	0.0262	1.8957
80.012	0.0463	0.0279	1.6582
90.012	0.0437	0.0295	1.4809
100.012	0.0415	0.0307	1.3490
120.012	0.0381	0.0323	1.1764
140.012	0.0356	0.0331	1.0741
160.012	0.0337	0.0335	1.0072
180.012	0.0322	0.0336	0.9596
200.000	0.0310	0.0336	0.9230

Table C-6 Power, Flow, and Power/Flow Ratio Histories for the UN 2 Transient

Time (s)	Normalized Power	Normalized Flow	Power/Flow Ratio
0.000	1.0500	1.0000	1.0500
0.500	0.9835	0.8446	1.1644
0.800	0.9512	0.3747	2.5383
1.000	0.9296	0.4250	2.1875
1.200	0.9094	0.5466	1.6638
1.400	0.7728	0.6154	1.2558
1.500	0.3825	0.6210	0.6160
1.519	0.3777	0.6194	0.6097
1.585	0.3254	0.6098	0.5335
1.650	0.2927	0.5976	0.4898
1.783	0.2473	0.5631	0.4393
1.883	0.2436	0.5390	0.4520
2.083	0.2372	0.5088	0.4662
2.583	0.2242	0.5057	0.4433
3.083	0.2131	0.4842	0.4401
3.583	0.2032	0.4556	0.4459
4.083	0.1941	0.4369	0.4442
5.083	0.1785	0.3920	0.4553
6.083	0.1657	0.3506	0.4725
7.083	0.1550	0.3224	0.4807
8.083	0.1460	0.2945	0.4956
9.083	0.1382	0.2667	0.5181
10.083	0.1315	0.2391	0.5499
12.083	0.1204	0.2000	0.6018
14.083	0.1116	0.1674	0.6669
16.083	0.1044	0.1415	0.7382
18.083	0.0984	0.1181	0.8332
20.083	0.0932	0.0978	0.9530
22.083	0.0886	0.0756	1.1727
24.083	0.0845	0.0567	1.4903

Time (s)	Normalized Power	Normalized Flow	Power/Flow Ratio
26.083	0.0809	0.0444	1.8214
28.083	0.0777	0.0378	2.0560
30.083	0.0749	0.0345	2.1681
32.083	0.0724	0.0327	2.2135
33.083	0.0712	0.0321	2.2207
34.083	0.0701	0.0316	2.2215
36.083	0.0681	0.0309	2.2027
38.083	0.0663	0.0306	2.1665
40.083	0.0647	0.0305	2.1183
45.083	0.0610	0.0308	1.9771
50.083	0.0579	0.0314	1.8436
60.083	0.0528	0.0325	1.6266
70.083	0.0488	0.0335	1.4590
80.083	0.0457	0.0343	1.3300
100.083	0.0410	0.0355	1.1551
120.083	0.0377	0.0359	1.0500
140.083	0.0353	0.0359	0.9827
160.083	0.0335	0.0358	0.9366
180.083	0.0321	0.0355	0.9029

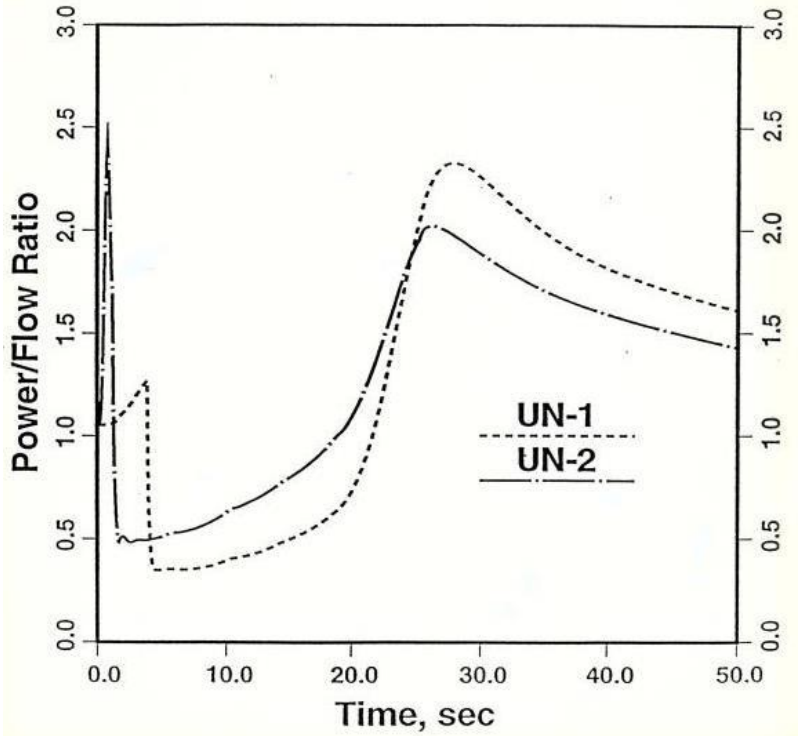

Figure C-8 Power/Flow Ratio Histories for Unlikely LOF Events in the 6-Row Core

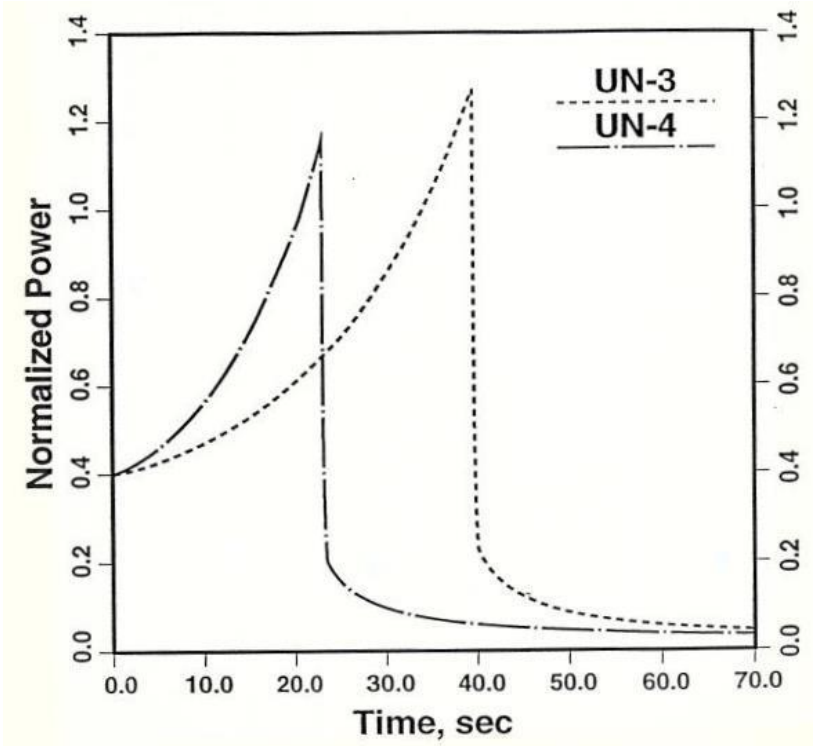

Figure C-9 Power Histories for Unlikely TOP Events UN-3 and UN-4 in the 6-Row Core (T_{inlet} = 690°F for UN-3)

Table C-7 Power History for the UN-3 Transient (T_{inlet} = 690°F)

Time (s)	Normalized Power	Time (s)	Normalized Power
0.000	0.4000	43.424	0.1752
1.000	0.4042	44.424	0.1540
2.000	0.4092	45.424	0.1382
3.000	0.4148	46.424	0.1255
4.000	0.4211	49.024	0.1018
5.000	0.4281	50.024	0.0951
6.000	0.4357	55.024	0.0730
7.000	0.4439	60.024	0.0604
8.000	0.4528	65.024	0.0521
9.000	0.4623	70.000	0.0462
10.000	0.4725		
15.000	0.5333		
20.000	0.6119		
25.000	0.7100		
30.000	0.8277		
35.000	0.9596		
40.000	1.1538		
41.000	1.1990		
41.400	1.2183		
41.500	0.5814		
41.560	0.4503		
41.666	0.3285		
41.779	0.2620		
41.879	0.2259		
42.424	0.2044		

Table C-8 Power History for the UN-4 Transient

Time (s)	Normalized Power	Time (s)	Normalized Power
0.000	0.4000	24.090	0.1892
1.000	0.4085	24.590	0.1736
2.000	0.4187	25.090	0.1607
3.000	0.4306	26.090	0.1411
4.000	0.4442	27.090	0.1263
5.000	0.4596	28.090	0.1146
6.000	0.4768	29.090	0.1050
7.000	0.4959	30.090	0.0971
8.000	0.5170	32.090	0.0848
9.000	0.5402	34.090	0.0758
10.000	0.5655	36.090	0.0690
12.000	0.6234	38.090	0.0636
14.000	0.6916	40.090	0.0593
16.000	0.7708	45.090	0.0513
18.000	0.8608	50.090	0.0458
20.000	0.9510	55.090	0.0417
22.000	1.0589	60.090	0.0386
23.000	1.1300	65.090	0.0361
23.200	1.1438	69.990	0.0340
23.300	1.1519		
23.400	0.5065		
23.424	0.4674		
23.474	0.3785		
23.557	0.3101		
23.710	0.2199		

Table C-9 Power History for the UN-5 Transient

Time (s)	Normalized Power	Time (s)	Normalized Power
0.000	1.0000E-06	74.000	5.3792E-01
1.000	1.0142E-06	76.000	8.1690E-01
2.000	1.0313E-06	78.060	1.0630E+00
4.000	1.0727E-06	78.260	1.0852E+00
6.000	1.1240E-06	78.460	1.1083E+00
8.000	1.1861E-06	78.560	1.1180E+00
10.000	1.2606E-06	78.660	1.1264E+00
15.000	1.5175E-06	78.760	1.1382E+00
20.000	1.9260E-06	78.860	1.1527E+00
25.000	2.6048E-06	78.960	4.0366E-01
30.000	3.8098E-06	78.979	3.6779E-01
35.000	6.1476E-06	79.061	2.5472E-01
40.000	1.1239E-05	79.190	1.7830E-01
45.000	2.4122E-05	79.343	1.3352E-01
50.000	6.3740E-05	80.034	1.1036E-01
52.000	1.0103E-04	81.034	8.8705E-02
54.000	1.6807E-04	83.034	6.2941E-02
56.000	2.9516E-04	86.034	4.1763E-02
58.000	5.5082E-04	90.034	2.7466E-02
60.000	1.1005E-03	95.034	1.8694E-02
62.000	2.3731E-03	100.034	1.3952E-02
64.000	5.5691E-03	105.034	1.1009E-02
66.000	1.4294E-02	110.034	9.0203E-03
68.000	3.9735E-02	115.034	7.5969E-03
70.000	1.1281E-01	120.000	6.5378E-03
72.000	2.8148E-01		

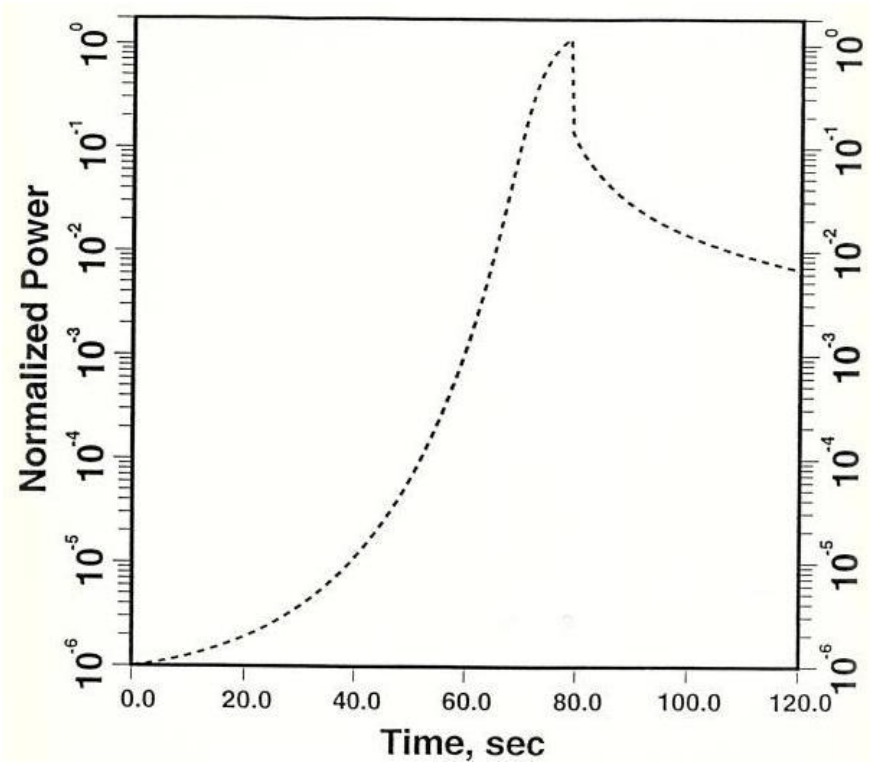

Figure C-10 Power History for Unlikely TOP Event UN-5 in the 6-Row Core

Nuclear Engineering Division
Argonne National Laboratory
9700 South Cass Avenue, Bldg. 208
Argonne, IL 60439-4842 www.anl.gov

Argonne National Laboratory is a U.S. Department of Energy laboratory
managed by UChicago Argonne, LLC